

Energy Systems in Electrical Engineering

Sri Niwas Singh  
Prabhakar Tiwari  
Sumit Tiwari *Editors*

# Fundamentals and Innovations in Solar Energy



Springer

# **Energy Systems in Electrical Engineering**

**Series Editor**

Muhammad H. Rashid, Florida Polytechnic University, Lakeland, USA

More information about this series at <http://www.springer.com/series/13509>

Sri Niwas Singh · Prabhakar Tiwari · Sumit Tiwari  
Editors

# Fundamentals and Innovations in Solar Energy

 Springer



*Editors*

Sri Niwas Singh  
Department of Electrical Engineering  
Indian Institute of Technology Kanpur  
Kanpur, Uttar Pradesh, India

Prabhakar Tiwari  
Department of Electrical Engineering  
Madan Mohan Malaviya University  
of Technology  
Gorakhpur, Uttar Pradesh, India

Sumit Tiwari  
Department of Mechanical Engineering  
Shiv Nadar University  
Dadri, Uttar Pradesh, India

ISSN 2199-8582

ISSN 2199-8590 (electronic)

Energy Systems in Electrical Engineering

ISBN 978-981-33-6455-4

ISBN 978-981-33-6456-1 (eBook)

<https://doi.org/10.1007/978-981-33-6456-1>

© The Editor(s) (if applicable) and The Author(s), under exclusive license to Springer Nature Singapore Pte Ltd. 2021

This work is subject to copyright. All rights are solely and exclusively licensed by the Publisher, whether the whole or part of the material is concerned, specifically the rights of translation, reprinting, reuse of illustrations, recitation, broadcasting, reproduction on microfilms or in any other physical way, and transmission or information storage and retrieval, electronic adaptation, computer software, or by similar or dissimilar methodology now known or hereafter developed.

The use of general descriptive names, registered names, trademarks, service marks, etc. in this publication does not imply, even in the absence of a specific statement, that such names are exempt from the relevant protective laws and regulations and therefore free for general use.

The publisher, the authors and the editors are safe to assume that the advice and information in this book are believed to be true and accurate at the date of publication. Neither the publisher nor the authors or the editors give a warranty, expressed or implied, with respect to the material contained herein or for any errors or omissions that may have been made. The publisher remains neutral with regard to jurisdictional claims in published maps and institutional affiliations.

This Springer imprint is published by the registered company Springer Nature Singapore Pte Ltd. The registered company address is: 152 Beach Road, #21-01/04 Gateway East, Singapore 189721, Singapore

# Contents

<b>1</b>	<b>Introduction to Solar Energy</b> .....	<b>1</b>
	S. N. Singh, Prabhakar Tiwari, and Sumit Tiwari	
<b>2</b>	<b>Solar Photovoltaic (PV) Generation</b> .....	<b>11</b>
	Umesh Agarwal, Naveen Jain, S. N. Singh, and Manoj Kumawat	
<b>3</b>	<b>Solar Thermal Power Generation</b> .....	<b>35</b>
	Rajeev Awasthi, Shubham Jain, Ram Kumar Pal, and K. Ravi Kumar	
<b>4</b>	<b>Innovative Applications of Solar Energy</b> .....	<b>79</b>
	Amandeep Singh and Janakarajan Ramkumar	
<b>5</b>	<b>Smart Energy System</b> .....	<b>93</b>
	Sachin K. Jain and S. N. Singh	
<b>6</b>	<b>A Holistic Review of Smart Grid Contribution Toward Energy Sustainability</b> .....	<b>117</b>
	Saad Umer Khan and Akhtar Kalam	
<b>7</b>	<b>Short-Term Solar PV Generation Forecast Using Neural Networks and Deep Learning Models</b> .....	<b>127</b>
	Shivashankar Sukumar, Naran M. Pindoriya, and Sri Niwas Singh	
<b>8</b>	<b>Off-Grid Solar Lighting Testing and Reliability</b> .....	<b>141</b>
	Supriya Rai, Birinchi Bora, Chandan Banerjee, and Arun Kumar Tripathi	
<b>9</b>	<b>Thermal Energy Storage for Solar Energy</b> .....	<b>167</b>
	Shubham Jain, Sumeet Kumar Dubey, K. Ravi Kumar, and Dibakar Rakshit	
<b>10</b>	<b>Solar Energy Pricing</b> .....	<b>217</b>
	Vivek Soni and Nitin Singh	
<b>11</b>	<b>Advances in Hybrid Solar System</b> .....	<b>231</b>
	P. Vipin Das, Navneet K. Singh, Rakesh Maurya, Asheesh K. Singh, and Sri Niwas Singh	

<b>12</b>	<b>Maximum Power Point Tracking of Photovoltaic Renewable Energy System Using a New Method Based on Turbulent Flow of Water-Based Optimization (TFWO) Under Partial Shading Conditions</b> .....	<b>285</b>
	Shohreh Nasri, Saber Arabi Nowdeh, Iraj Faraji Davoudkhani, Mohammad Jafar Hadidian Moghaddam, Akhtar Kalam, Saman Shahrokhi, and Mohammad Zand	
<b>13</b>	<b>Phase Change Materials and Its Applications</b> .....	<b>311</b>
	Anirudh Kulkarni, Rajat Saxena, and Sumit Tiwari	
<b>14</b>	<b>Sensitivity Analysis in Solar Systems</b> .....	<b>341</b>
	Desh Bandhu Singh, Sumit Tiwari, and Sanjay Kumar	
<b>15</b>	<b>Environmental Feasibility of Solar Hybrid Systems</b> .....	<b>367</b>
	Sumit Tiwari, Prabhakar Tiwari, V. K. Dwivedi, and G. N. Tiwari	
<b>17</b>	<b>Impact of the Photovoltaic Integration on the Hydrothermal Dispatch on Power Systems</b> .....	<b>397</b>
	Walter A. Carranza, Wilfredo C. Flores, Harold R. Chamorro, Margarita M. Diaz-Casas, Roozbeh Torkzadeh, Francisco Gonzalez-Longatt, Wilfredo Sifuentes, Vijay K. Sood, and Wilmar Martinez	
<b>18</b>	<b>Potential and Financial Analysis of the Floating PV in Hydropower Dams of Thailand</b> .....	<b>435</b>
	Wanwisa Peanpitak and Jai Govind Singh	
<b>19</b>	<b>Voltage Fault Ride-Through Operation of Solar PV Generation</b> ...	<b>467</b>
	Bonu Ramesh Naidu and Prabodh Bajpai	

# About the Editors

**Prof. Sri Niwas Singh** obtained his MTech and PhD in Electrical Engineering from Indian Institute of Technology Kanpur (IITK), India, in 1989 and 1995. Presently, he is Vice-Chancellor, Madan Mohan Malviya University of Technology Gorakhpur, and on leave from Professor (HAG), Department of Electrical Engineering, IITK. Before joining IIT Kanpur as Associate Professor, Dr. Singh worked with UP State Electricity Board as Assistant Engineer from 1988 to 1996, with Roorkee University (now IIT Roorkee) as Assistant Professor from 1996 to 2000 and with Asian Institute of Technology, Bangkok, Thailand, as Assistant Professor from 2001 to 2002. Dr. Singh received several awards including Young Engineer Award 2000 of Indian National Academy of Engineering (INAE), Khosla Research Award of IIT Roorkee, and Young Engineer Award of CBIP New Delhi (India), 1996. Prof. Singh is the recipient of Humboldt Fellowship of Germany (2005, 2007) and Otto-Monsted Fellowship of Denmark (2009–2010). Prof. Singh became the first Asian to receive 2013 IEEE Educational Activity Board Meritorious Achievement Award in Continuing Education. He is also the recipient of INAE Outstanding Teacher Award 2016 and IEEE R10 region (Asia-Pacific) Outstanding Volunteer Award 2016. Prof. Singh is IEEE (USA) Distinguished Lecturer of Industrial Application Society and Power & Energy Society. He is the recipient of Life-Time Achievement for Significant contribution to Energy Field 2018 and Prof. GK Dubey IEEE UP Section Life-time achievement Award 2018. His research interests include power system restructuring, FACTS, power system optimization & control, security analysis, wind power, etc. Prof. Singh has published more than 450 papers in international/national journals/conferences. He has supervised 43 Ph.D.s (30 completed & 13 under progress). He has also written 2 books, 11 book chapters and 4 monograms. He has completed three dozen of projects in India and abroad. Prof. Singh has been the editor of Springer book Lecture Notes on Electrical Engineering 509 and 609 of proceedings of ICAEDC 2017 & GUCON 2019, respectively. He has also been the editor isof Proceedings of ICRRM 2019 Published recently by Springer Nature Singapore in 2020. Dr. Singh was Chairman, IEEE UP Section for 2013–2014; IEEE Region 10 (Asia-Pacific) Conference and Technical Seminar Coordinator 2015–2018. Prof. Singh is currently IEEE R10 Vice-Chair Technical Activities 2019–2020 & IEEE India Council Chair 2019–2020.

**Dr. Prabhakar Tiwari** was born on April 20, 1975, in Ambedkar Nagar district of Uttar Pradesh, India. He got B.E. degree in Electrical Engineering from MMMEC, Gorakhpur; M.Tech. in Power Systems Engineering from IIT Delhi; and Ph.D. from JMI Central University. He has been involved in teaching various subjects of Electrical Engineering since the last 20 years. Dr. Tiwari has written 2 books and more than 70 papers in the different national & international journals and conferences. He has delivered more than 25 expert lectures on power systems, technical education and IEEE Awareness in different institutions of national & international repute. He has organized more than 20 conferences/STC/FDP/workshops/seminars. He was also awarded outstanding section Volunteer Award of IEEE UP Section for the year 2015. He had been Professor and Head, EEE & EE Department for 5 years. He was Organizing Chair & Convener of the 1st UPCON 2014, which is the one and only conference initiated and sponsored technically & financially by IEEE UP Section. Dr. Tiwari has supervised 6 Ph.D.s (1 completed and 5 under progress).

Currently, he is Associate Professor, EE Department, Madan Mohan Malaviya University of Technology, Gorakhpur, Uttar Pradesh. His major field of interest includes renewable energy, restructuring, deregulation, power system pricing, power system stability, smart grid and quality in technical education. He is Senior Member of IEEE and PES (Power and Energy Society), SGS (Smart Grid Society) and Education Society, Life Member of ISTE, Life Member of IE (India) and Joint Secretary of IEEE UP Section (for the year 2018 & 2019) and currently, Secretary, IEEE UP Section for the year 2020.

**Dr. Sumit Tiwari** is working with Shiv Nadar University, Dadri, Uttar Pradesh. He received the B.Tech. degree in Mechanical Engineering from the Uttar Pradesh Technical University, Lucknow (now AKTU). Further, he got M.Tech. and Ph.D. degree from the Indian Institute of Technology (IIT) Delhi. He got assistantship for his Ph.D. from “Ministry of New and Renewable Energy (MNRE)” assistantship. He worked with Professor Patrick Phelan’s Group, USA, as a research intern for 06 months under the fellowship named “Building Energy Efficiency Higher & Advanced Network (BHAVAN) Fellowship Program” which is a program executed by Indo-U.S. Science and Technology Forum (IUSSTF) and Department of Science and Technology (DST). He got Shrimati Vijay-Usha Sodha Research Award for the session 2018–2019 given by Center for Energy Studies, IIT Delhi. He also got second prize under “Best thesis award” in Ph.D. symposium organized by “Madan Mohan Malaviya University of Technology, Gorakhpur (U.P) INDIA & University of the Ryukyus, Okinawa, Japan”. He is working on various solar thermal technologies, namely, photovoltaic thermal (PVT) greenhouse drying system, PVT greenhouse heating system, PVT greenhouse biogas heating system, solar still, PVT air collector, PVT air collector integrated drying system, passive cooling of building, and solar adsorption cooling system, etc. He has published several SCI journal papers with high impact factor and international conference papers in his field. He has more than 12 years’ experience in teaching and research. He has also got several recognitions during his study as well as in teaching. He is working as a reviewer in more than 17 international SCI journals.

# Chapter 1

## Introduction to Solar Energy



S. N. Singh, Prabhakar Tiwari, and Sumit Tiwari

### 1.1 General

The sun is an ultimate source of energy, and all available forms of energies on earth, directly or indirectly, depend on it. It is a sphere of very hot gaseous substance having diameter of  $1.39 \times 10^9$  m with an average distance of  $1.5 \times 10^{11}$  m from the earth. The sun has temperature ( $T_s$ ) of 5777 K, and this temperature is maintained due to uninterrupted fusion reaction. Several fusion reactions have been proposed for production of the energy emitted by the sun; the most important being the one in which four photons of hydrogen unite to make helium (i.e., helium nucleus). The helium nucleus has less mass compared to four protons, which is converted to energy [1, 2].

In the history, the sun was the utmost cherished one among all Gods for the Egyptians, the Indians, Greeks, American Continent (indigenous inhabitants), and countless peoples from different religions [3]. In India, it was Surya, the god of the sun, the center of the world, and the source of heat, light, and life [4]. In the early script of “Bṛhad-Devata,” it is cited [5].

Archimedes, the philosopher, and mathematician (287–212 BC) used the flat reflecting surfaces to focus solar rays onto the wooden-made Roman ships. In AD 514, Proclus (Bishop) also repeated this feature to burn the fleet of enemies. During AD 1100–1180, a Byzantine writer, Ioannis Tzetsis, describes in his book Chiliades,

---

S. N. Singh  
Indian Institute of Technology, Kanpur, India

P. Tiwari (✉)  
Madan Mohan Malaviya University of Technology, Gorakhpur, India  
e-mail: [ptee@mmmut.ac.in](mailto:ptee@mmmut.ac.in)

S. Tiwari  
Shiv Nadar University, NH-91, Tehsil Dadri, Gautam Buddha Nagar, Uttar Pradesh, India

Vol. 3, the burning of the Roman ships by Archimedes [6, 7]. Vitellion, a mathematician, explained Archimedes' experiment in his book Optics [7]. Kemper [8] highlighted that an Egyptian Ibn Al-Haitan (about AD 1000) explored the burning of different materials using mirrors focusing on their surface by the sun's rays.

In Germany (Heidelberg), during 1615, Salomon de Caux (French scientist) revealed the first solar pump [9]. In 1774, Lavoisier (1743–94), the famous chemist, uses lenses to get solar concentration. It was also discovered that lenses can produce high temperatures (1780 °C) and were utilized for melting and exploring pure platinum properties [10]. John Ericsson (1803–89), based on Stirling cycle, built a steam engine operated by solar energy with an efficiency of 72.5% [11]. In 1890, V. A. Tsesarskii achieved a temperature of 3500 °C by focused radiation for melting metals and other materials [12]. Solar ponds were utilized to operate the engine for pumping water [13, 14]. Prof. Altenkirch (1936) firstly suggested the application of solar energy for air-conditioning [15, 16]. In Germany, the first heliostat was presented in 1912 [17]. Further, the tower system was examined based on central receiver installation by Prof. Francia [18].

The photovoltaic (PV) technology is the fastest rising industries globally. Continuous research is going on new PV materials and efficiency increment [19–21]. In 1839, the photovoltaic effect in which solar radiation can be directly converted into electricity was observed, the first time, by Becquerel [20, 21]. Due to sunlight, a part of energy is given to the farthest electron to move it from the valence band to the conduction band in the material, thus producing current. For silicon, 1.12 eV (electron volts) are needed for the electrons to jump from valence band to conduction band [22]. Further, it was found that the material, which absorbs large part of the solar spectrum, performs better [23].

According to [24–26], photovoltaic (PV) cell technologies are available based on various materials, having large market throughout the world. PV cell technologies can be divided into three generations, subjected to available natural resource and commercial viability. Different PV generations are:

- The first-generation PV systems that use the technology of crystalline silicon (c-Si) as well as multicrystalline (mc-Si) having efficiency closed to 24% and 20%, respectively.
- The second-generation PV systems are covered thin-film PV technologies and include three main families:
  - (a) Microamorphous silicon (a-Si/ $\mu$ c-Si) and amorphous silicon (a-Si);
  - (b) Cadmium telluride (CdTe);
  - (c) Copper indium gallium diselenide (CIGS) and copper indium selenide (CIS).
- The third-generation PV systems (organic PV) are in developing stage.

## 1.2 Merits of Solar Energy

There are several advantages for solar energy. Some of them are as follows:

- 
- It is free from pollutions
  - It is renewable in nature
  - Solar energy can be used for different ways, namely direct electricity generation (photovoltaics) or heat (solar thermal)
  - It requires small maintenance
  - No need of huge water, especially in solar PV systems
  - Quick installation makes it so popular
  - Light in weight so easy to mount anywhere, especially rooftop
  - It creates a very easy possibility for every consumer to become an energy producer by mounting rooftop with solar panel
  - Plays a very vital role to make energy sufficient, i.e., green buildings
  - Generation size may be very small to large value
  - It is one of the biggest hopes for global DC grid dreams
  - Fuel cost is zero and abundant at most of the places on the earth
  - No residual waste production from the fuel after generation
  - No noise pollution like other conventional generation sources
  - The real losses from the point of generation to point of utilization on average are least as solar plants are normally situated nearest to the loads
  - Very much suitable for remote areas for electrification
- 

## 1.3 Demerits of Solar Energy

Apart from the advantages, there are few concerns and challenges in the solar energy which are stated below:

- 
- It requires high initial investment
  - Weather dependent and intermittent supply
  - If solar energy generated cannot be utilized same time, it can be stored in large batteries. Cost of battery is high as well as having problem of disposal
  - Solar PV panels need more space compared to other technologies
  - Due to daytime, only power is generated; so for uninterrupted supply, battery storage is necessarily needed
  - Normally generation size is limited to MWs only
  - Generated voltage is DC only, so inverter is always needed to connect it to grid
  - When connected to grid, power quality is always an issue to provide access to grid
- 

(continued)



(continued)

- Utilization time of the panel is very less limited to daytime with threshold radiation necessary for generation
- Power generation has huge impact on pollution, dust, and other weather and environmental conditions

Truly speaking, the merits of solar generation out weight all the demerits and challenges. It is one of the best renewable powers and has huge potential.

### 1.4 Growth of Solar Power

Still, in the present time, 80% of world energy generation promotes pollution and climate change [27, 28]. To overcome the above stated problem, the progress and use of renewable energy resources (RES) have become extremely urgent. Solar energy is the best source which can fulfill the requirement of the world, i.e., 23,000 TW of energy available each year [29, 30]. It is an unlimited and effective energy source to harness huge application potentials owing to the reasonable and sustainable feature. The long-term solar photovoltaic potential of world is shown in Fig. 1.1.

The solar energy is extracted using two approaches: solar PV and solar thermal. From various perspectives, the solar PV is more popular than solar thermal. The harnessing technology of both the types of radiations is also altogether different though the innovative application of the solar thermal is making it increasingly popular nowadays. The installed capacity and annual addition of solar power are shown in Fig. 1.2.

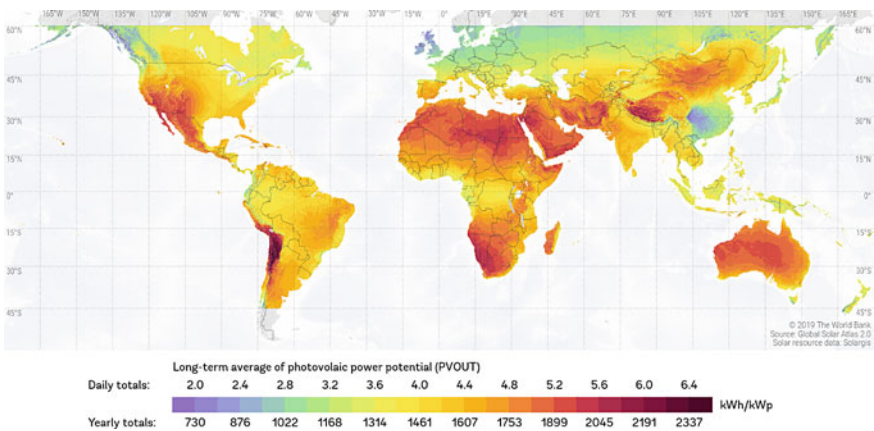
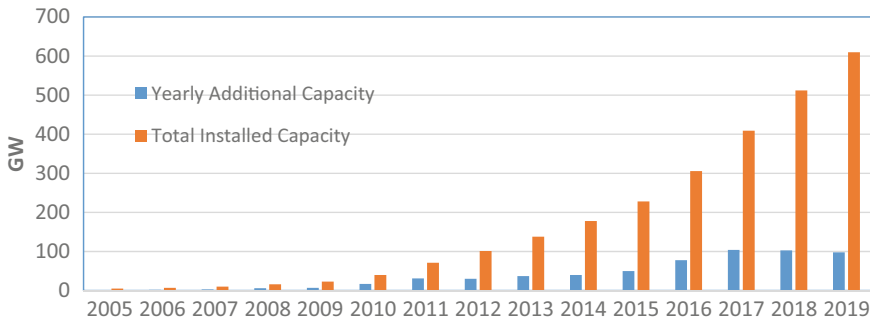


Fig. 1.1 Long-term average photovoltaic power potential ( Source <https://globalsolaratlas.info/global-pv-potential-study>)



**Fig. 1.2** Yearly solar power in world [31]

Ministry of New and Renewable Energy (MNRE), Government of India’s report [31] 2020–21 (Cumulative up to Aug 2020), is given in Fig. 1.2, which shows the seriousness of the Government of India toward solar technologies. The biogas plants in India till 31.08.2020 were 50.5 lakhs. The biogas target for FY 20–21 was 0.60 lakh plants but achieved only 0.09 lakhs (Table 1.1).

The cost of electrical power generated from solar PV keeps on decreasing, and it is now comparable to other renewable energy sources such as wind power. The

**Table 1.1** MNRE report 2020–21 (cumulative as on 31.8.2020) [31]

Program/scheme-wise physical progress in FY 2020–21 and cumulative up to Aug 2020 31			
	Target	Achievements (April–August 2020)	Cumulative achievements (as on 31.8.2020)
<i>(A) Grid-interactive power (capacities in MWp)</i>			
Solar power—ground mounted	9000.00	538.10	32,650.59
Solar power—rooftop	2000.00	573.42	3088.72
Wind power	3000.00	255.80	37,999.55
Small hydropower	100.00	56.80	4739.97
Biomass (bagasse)/cogeneration	200.00	173.37	9373.87
Biomass (non-bagasse), cogeneration/captive power	50.00	97.24	772.05
Waste to power	30.00	21.00	168.64
<b>Total</b>	<b>14,380.00</b>	<b>1715.73</b>	<b>88,793.39</b>
<i>(B) Off-grid/captive power (capacities in MW<sub>eq</sub>)</i>			
Waste to energy	10.00	3.61	201.81
Solar PV systems	500.00	10.98	989.37
<b>Total</b>	<b>510.00</b>	<b>14.59</b>	<b>1191.18</b>

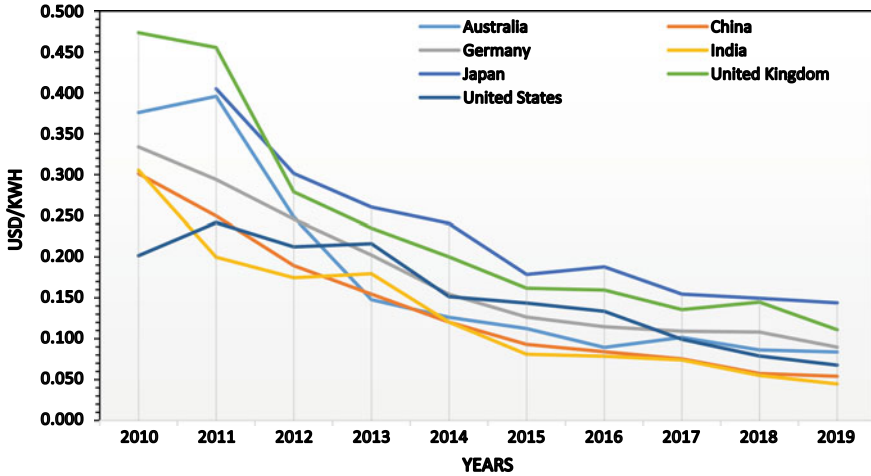


Fig. 1.3 Yearly cost solar power generation in different counties from 2010 to 2019 ( Source Author)

yearly cost solar power generation in different counties from 2010 to 2019 is given in Fig. 1.3. It can be seen from the figure that the cost of solar power generation in 2019 is the lowest in India due to various reasons.

## 1.5 Outline of the Book

This book is organized in 19 chapters including the introduction and is dedicated to most common and representative issues on solar energy. The first chapter discusses the history of solar power, its merits, and challenges. Chapter 2 highlights all aspects related to electricity generation from solar technology. A worldwide development of solar PV in terms of their perspective, existing strength, future scenario, drawbacks, and benefits is also discussed. Solar thermal power generation based on the line and point focusing solar concentrators is presented in Chap. 3 with detailed discussion on various components of the solar field, the recent developments, and environmental aspects of solar thermal power plants. Various challenges involved in hybrid solar power generation are also highlighted. Chapter 4 highlights the innovative applications of solar energy which are at the primitive stage of research and development but showing the promising results under specific conditions.

Chapter 5 introduces the concept of smart energy systems (SES) and presents the basic concept of Smart Grid, issues in integration of RESs, features of the smart energy systems from the recent literature, and challenges ahead in this domain. A holistic review of Smart Grid contribution toward energy sustainability is presented in Chap. 6. A smart grid system helps in achieving sustainable electrical energy initiatives by improving utilization of RES, optimal storage, increasing consumption

efficiency, and flexible T&D. Chapter 7 presents various neural network (NN) and deep learning (DL)-based approaches to forecast the solar PV generation, whereas Chapter 8 is dedicated to the off-grid solar lighting systems' testing and reliability analysis. Various charge controllers are discussed in this chapter.

Chapter 9 includes the technological development of latent, sensible, and thermochemical energy storage systems. Various thermal energy storage technologies with materials and their thermophysical properties used in diverse applications of solar energy have been outlined. Chapter 10 reviews the cost potential factors on solar energy pricing and a reflection on related factors. It also highlights and discusses the policy measures for accelerating future tariff reduction from solar energy. Various conventional and derived topologies of DC–DC/DC–AC converters for solar PV applications and the standards for solar PV integration are presented in Chap. 11. A cost optimization of solar PV HPS is investigated using Hybrid Optimization Model for Electric Renewables (HOMER) pro-software.

Maximum power point (MPP) tracking of photovoltaic renewable energy system using turbulent flow of water-based optimization (TFWO) under partial shading conditions has been investigated in Chap. 12. Results show that the TFWO has a better tracking capability with faster tracking speed and accuracy than particle swarm optimization (PSO) in obtaining the global MPP. Mathematical modeling and different computational approaches for studying phase change material (PCM)-based systems have been discussed in Chap. 13 for energy and building applications. This chapter provides a comprehensive review of PCMs, followed by a detailed description of various applications and research prospects. Chap. 14 deals with the application of sensitivity analysis of solar collectors and solar energy-based water purifier followed by the roadmap for the application of other solar systems which have the potential to mitigate some of the contemporary issues prevalent throughout the globe.

The environmental feasibility of solar hybrid systems having various solar PV cell technologies has been discussed in Chap. 15. Chapter 16 presents the issues and challenges in solar power interconnection in the exiting grid. The regulatory implications of solar energy integration with grid are also discussed in Chap. 16. Chapter 17 studies the effect on the operation of the Honduran power system with the incorporation of photovoltaic (PV) generation to compare the operation prior to the installation of such generation. The proposed optimal hydro-thermal dispatch of the system to reduce the marginal costs of operation in a medium-term study horizon is simulated using the Stochastic Dual Dynamic Programming (SDDP) software. In Chap. 18, the floating solar PV (FPV) systems in Thailand's hydropower dams are evaluated for their potential power production and economic benefits. Five cases of potential energy production were considered for financial analysis. In Chap. 19, a detailed methodology for retrofitting the existing PV units with crowbar circuit option or energy storage option is presented along with the design examples considering practical scenarios. A control strategy is presented in synchronous reference frame for facilitating the voltage fault ride-through operation of the SPV and the retrofitted SPV unit.

## References

1. Tiwari GN, Suneja S (1997) Solar thermal engineering systems. Narosa Publishing House, New Delhi
2. Tiwari GN, Goyal RK (1998) Greenhouse technology. Narosa publishing house, New Delhi, pp 252–311
3. Belessiotis VG, Papanicolaou E (2012) History of solar energy. *Ref. Module Earth Syst. Environ. Sci. Compr. Renew. Energy* 3:85–102
4. Anonymous (1981) Hemispherical bowl. *Sun World* 5(4):64
5. Delyannis A, Piperoglou E (1967–1972) Handbook of saline water conversion bibliography. Technical University of Athens, Athens, pp 2–9
6. Kapur J (1984) Surya, maker of the seasons, giver of life, lord of planets. *Sun World* 8(1):2–4
7. Aristotle (1952) *Meteorologica*. Harvard University Press, Cambridge, MA, p 480 (ISBN 9780674994362)
8. Telkes M (1943) Distilling water with solar energy. Report to Solar Energy Conversion Committee, MIT. [https://scholar.google.com/scholar\\_lookup?title=Distilling%20water%20with%20solar%20energy&author=M.%20Telkes&publication\\_year=1943](https://scholar.google.com/scholar_lookup?title=Distilling%20water%20with%20solar%20energy&author=M.%20Telkes&publication_year=1943)
9. Dickinson WC, Cheremisinoff PN (1980) Solar energy technology book, part A: engineering fundamentals. Marcel Dekker Inc., Butterworths, New York, p 912 (ISBN-13: 978-0824768720)
10. Delyannis E (2003) Historic background of desalination and renewable energy. *Sol Energy* 75:357–366
11. Jordan RC, Ibele WE (1956) Mechanical energy from solar energy. In: Proceedings of the world symposium on applied solar energy. Stanford Research Institute, Menlo Park, CA, USA, Phoenix, AZ, USA, pp 81–101, 1–5 November 1955
12. Böer KW (ed) (2005) The fifty years history of ISES and its national sections, vol 1. American Solar Energy Society Inc., Boulder, CO (Ch 17)
13. Mills DR (2001) Solar thermal electricity. In: Gordon J (ed) *Solar energy*. ISES, The State of the Art Chicago, IL p 724 (ISBN-10: 1902916239)
14. Robinson N (1956) Solar machines. In: Proceedings of the world symposium on applied solar energy. Stanford Research Institute, Phoenix, AZ, USA, Menlo Park, CA, pp 43–46, 1–5 Nov 1955
15. Adler S, Levite G, Tabor H (1964) The Altenkirch solar-cooled house. In: Proceedings of the UN conference on new sources of energy, vol 6. Rome, Italy, pp 60–65, 21–31 Aug 1961
16. Adler S, Levite G, Tabor H (1999) United nations/nations unies; Ibid, Selected reprints of papers by Tabor H (ed) *Solar energy pioneer*, vol 252. Balaban Publisher, ISES pp 75–88
17. Palz W (1978) Solar electricity: an economic approach to solar energy. UNESCO, Paris-Butterworths, London-Boston (ISBN-0408709103)
18. Francia G (1968) Pilot plants of solar steam generating stations. *Sol Energy* 12:51–59
19. Jäger-Waldau A (2006) European photovoltaics in worldwide comparison. *J Non-Cryst Solids* 352:1922–1927
20. Parida B, Iniyas S, Goic R (2011) A review of solar photovoltaic technologies. *Renew Sustain Energy Rev* 15:1625–1636
21. Razykov TM, Ferekides CS, Morel D, Stefanakos E, Ullal HS, Upadhyaya HM (2011) Solar photovoltaic electricity: current status and future prospects. *Sol Energy* 85:1580–1608
22. Kui-Qing P, Shuit-Tong L (2011) Silicon nanowires for photovoltaic solar energy conversion. *Adv Mater* 23:198–215
23. Goetzberger A, Hebling C, Schock HW (2003) Photovoltaic materials, history, status and outlook. *Mater Sci Eng: R: Rep* 40(1):1–46
24. Gangopadhyay U, Jana S, Das S (2013) State of art of solar photovoltaic technology. In: Proceedings of international conference on solar energy photovoltaics, vol 2013. (Article ID 764132, <https://doi.org/10.1155/2013/764132>)
25. Goetzberger A, Hebling C (2006) Photovoltaic materials, past, present, future. *Solar Energy Cells* 90:2170–2180

26. Sampaio PGV, González MOA (2017) Photovoltaic solar energy: conceptual framework. *Renew Sustain Energy Rev* 74:590–601
27. Schiermeier Q, Tollefson J, Scully T, Witze A, Morton O (2008) Energy alternatives: electricity without carbon. *Nature* 454:816–823. <https://doi.org/10.1038/454816a>
28. Lewis N (2007) Toward cost-effective solar energy use. *Science* 315(5813):798–801. <https://doi.org/10.1126/science.1137014>
29. Chu S, Majumdar A (2012) Opportunities and challenges for a sustainable energy future. *Nature* 488:294–303
30. Perez R, Zweibel K, Hoff T (2011) Solar power generation in the US: too expensive, or a bargain? *Energy Policy* 39:7290–7297. <https://doi.org/10.1016/j.enpol.2011.08.052>
31. MNRE report 2020–21 (Cumulative up to Aug 2020). <https://mnre.gov.in/the-ministry/physical-progress>

# Chapter 2

## Solar Photovoltaic (PV) Generation



Umesh Agarwal, Naveen Jain, S. N. Singh, and Manoj Kumawat

### 2.1 Introduction

The expansion in population and new living standards of human life are the main reasons for increased energy consumption. In the current situation, traditional energy sources are satisfying the energy demand by increasing the percentage of pollutants and greenhouse gases in the environment [52, 53]. Further, the conventional power plants have been originated to the serious disease as a variety of the respiratory system, effect on the sensory system, visibility related issues, deformation of the physical structure due to high contamination in the environment. The circumstances in most of the Asian countries are in a critical situation as China is facing about 17% of deaths annually due to air pollution [2]. Therefore, each country has targets to increase the percentage of contribution of the renewable energy resources that would be controlling the bulk amount of pollution contained in the environment. Solar photovoltaic (SPV) technology possesses good potential to meet global energy demand. In addition, this technology is more favorable due to worldwide availability, inexhaustible, wildlife safeguard energy resources among all available technologies.

In most underdeveloped countries, the SPV technology is a compact renewable source of electricity popularly used in rural areas. The SPV has supplied electricity for irrigation that is an essential application for rural areas. With the benefit of direct

---

U. Agarwal (✉) · N. Jain

Department of Electrical Engineering, College of Technology and Engineering, Udaipur,  
Rajasthan, India  
e-mail: [umeshbkb.agarwal@gmail.com](mailto:umeshbkb.agarwal@gmail.com)

S. N. Singh

Indian Institute of Technology Kanpur, Kanpur, Uttar Pradesh, India

M. Kumawat

Department of Electrical and Electronics Engineering, National Institute of Technology Delhi,  
New Delhi, India

conversion of sunlight into direct current (DC) electricity, the SPV systems possess other advantages also like the ease in operation and less manpower requirement as compared to other distributed energy resources. Absence of mechanically moving parts makes the operation quite silent and maintenance-free. Consequently, the SPV has established a low-cost approach relative to other green energy resources [52, 53]. Further, the SPV system has another advantage that it can be commissioned on top of roof and on the field without interfering to nearby lifestyles in rural as well as urban areas.

With the production of solar energy systems, which are expected to become more economical in the coming year, the per-watt expense of any solar energy systems has been diminishing over the last decade. Moreover, the government’s policies have motivated to increase the instated capacity of rooftop and solar water pump [41]. The demand of the world’s annual electricity has risen to 1000 GW and is projected to grow to 3000 GW by 2030. It is expected that about 1081 GW by the year 2030 will be supplied by the SPV systems [60].

The usage of green and clean solar energy has been pursued competitively in many nations, together with conventional fossil fuel-based power plants; thereby, it would render a noteworthy input to nationwide power production. In the European country, the SPV has approximate participation of 7.90% of the total demanding energy in Italy, 7.60% in Greece, and 7.00% in Germany. The solar photovoltaic power expanded at phenomenal levels, from capacity 3.7 GW in 2004 to 627 GW in 2019 as demonstrated in Fig. 2.1 [27].

In Fig. 2.2, China is at the top in this race of solarization with a capacity of nearly 205 GW till 2019, followed by European Union, USA, Japan, Germany, and India with a capacity of 131.7 GW, 75.9 GW, 63 GW, 49.2 GW, and 42.8 GW, respectively

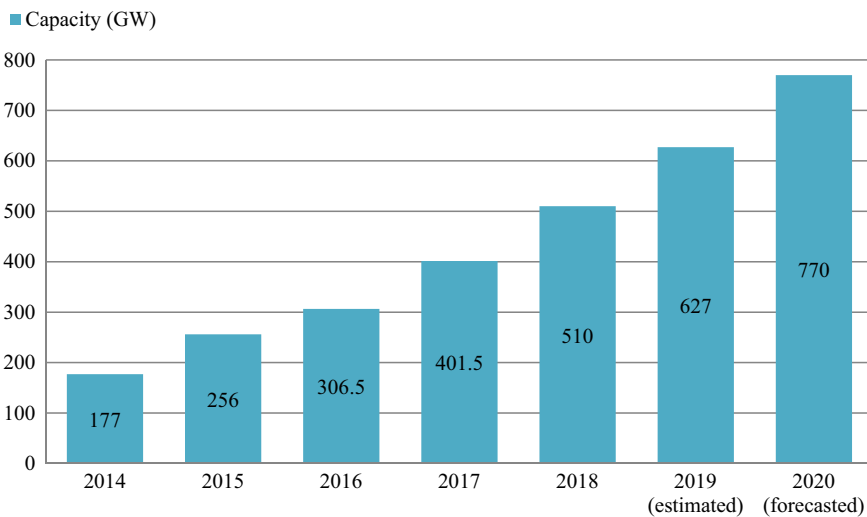


**Fig. 2.1** Global solar PV installed capacity (in GW) (source Author)



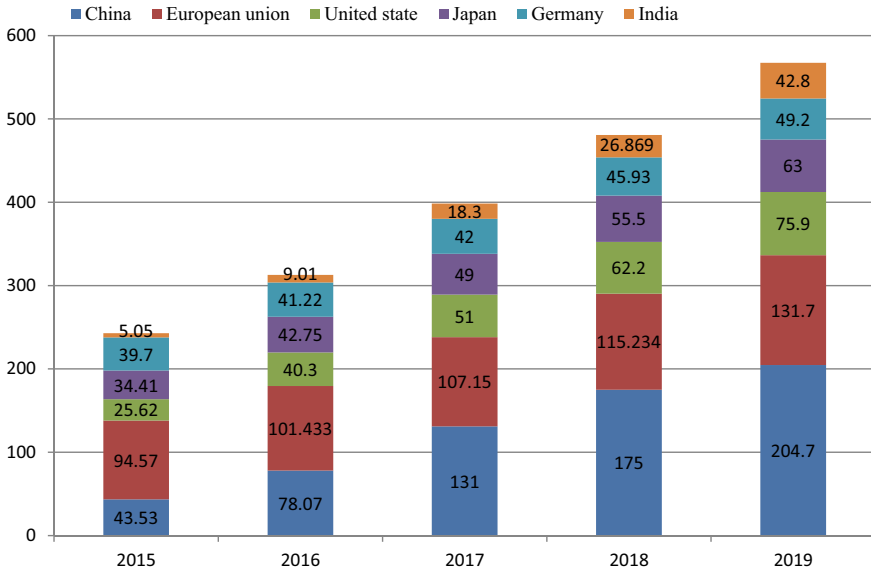


**Fig. 2.2** Country-wise solar PV installed capacity till 2019 (source Author). Note All capacities are in GW

[International Energy Agency (IEA)]. Australia is on the way to adopt a complete generation of electricity using renewable resources. In 2015, Australia dismantles its coal-fired plants of capacity 1300 MW as solar power dominates the energy market with production of 913 MW, more than produced by any other renewable energy resource [32].

India achieved the targets as 5.05 GW (2015), 9.01 GW (2016), 18.3 GW (2017), 42.8 GW (2019) using a grid-tied solar PV system. The Government of India aimed to attain 100 GW of power production using solar PV until 2022 under Jawaharlal Nehru National Solar Mission [Ministry of New and Renewable Energy (MNRE)]. France is also preparing to create a 1000-km solar road on the European border that would be capable of supplying ample electricity to power 5000 homes [38].

Overall, the SPV contribution amounts to nearly 3% of the world’s demand for electricity. The SPV’s contribution to de-carbonizing the energy mix is on the rise, and it saves up to 720 million tons of CO<sub>2</sub> equivalents by the end of 2019 based on the installed capacity. As a total,  $115 \times 10^6$  kW of SPV has been installed globally in 2019. The SPV has been contributed to reducing electricity generation concerned global CO<sub>2</sub> emission by 5.3% and energy-related emission by 2.2% [28].

## 2.2 Historic Development of Solar PV

The photovoltaic effect is not a new concept. Becquerel became first citizen in 1839, who observed the light to electricity production experimentally. In 1956, Daryl, Calvin and Gerald at “Bell Lab” in the USA coined the first viable Si cell having 4% output. Later on, the efficiency increased to 11% [52, 53]. In 1958, solar PV was first used in spacecraft to power the onboard devices. In 1964, the very first Nimbus spaceship was deployed by NASA, operated with the SPV array of 470 watts [44]. “The Institute of Energy Conversion” for research on thin-wafer SPV and solar thermal systems was established in 1972 by Delaware University. It was the first institute in this area. The building-integrated photovoltaic (BIPV) panels were first introduced at “4-Times Square Building.” The journey of solar PV is long; however, a brief development path for solar PV is given in Table 2.1 [61].

## 2.3 Fundamentals of PV system and Their Components

Solar PV system is the fundamental technique for directly transforming radiation energy to usable electrical power. It consists of power conversion devices, batteries to store electrical energy and most important photovoltaic modules. This section describes in detail about working, operating characteristics and parameters and apparatus of a PV scheme.

### 2.3.1 Solar Cell

Solar cell is a kind of transducer that directly transforming radiation energy to usable electrical power. It is generally made of Si and other semiconducting materials like GaAs, GaInAs, selenium, cadmium, etc. These cells are configured to make modules and array to obtain required voltage and current output.

### 2.3.2 Operating Principle

The fundamental building block of a SPV scheme is a solar cell. A lot of different materials are available and used for the construction of solar cells. However, silicon is still at the top position among them. It was observed in some of the semiconductors that they extract the electrical power from electromagnetic energy, and the solar cell operates on this effect only [1]. With a suitable structural design, these generated charged particles are separated to create an electric field that constitutes an electric current as shown in Fig. 2.3.

**Table 2.1** History of solar PV [25, 61]

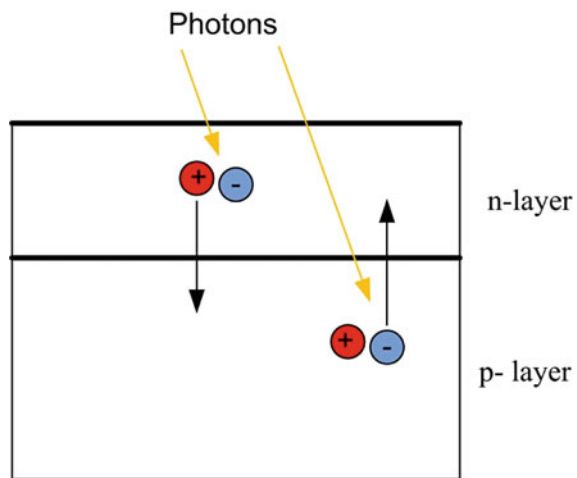
Year	Developments
1839	Physicist Edmond Becquerel investigated the light to electricity production effect while working with an electrolyte cell. He found that electricity production rises with light exposure [10, 22]
1860	The idea of a solar-powered steam engine was coined by French mathematician August Mouchet. In 1865, design of the solar-powered steam engine was developed [42]
1873	The photoconductive property of selenium was discovered by Smith [57]
1880	Samuel P. Langley developed the first instrument that can measure the solar irradiance. It was named ' <b>Bolometer</b> ' [36]
1883	Charles Fritts developed the first solar cell with 'selenium wafers'
1904	The photosensitive nature of copper and cuprous oxide mixture was invented by Wilhelm Hallwachs
1905	This year the article on the photoelectric effect of Albert Einstein was in print [20]
1908	Solar water heater using copper coils was developed by Bailey of the Carnegie Steel Company [12]
1918	Scientist Jan Czochralski introduced the process to develop single crystal silicon [18]
1932	The photovoltaic properties of Cadmium Sulfide (CdS) were revealed by Audobert and Stora
1954	The first commercial solar cell using silicon with 4% efficiency was fabricated by Chapin, Fuller and Pearson at Bell Lab in the USA. Later, efficiency of 11% was achieved [49, 50]
1957	Hoffman Electronics has created a 8% effective solar cell [6]
1958	Hoffman Electronics has created a 9% effective solar cell [6]
1958	Radios of Vanguard-I spaceship were powered by a small PV array first time. Afterwards, Explorer-3, Vanguard-2, and Sputnik-3 were launched with solar driven equipments on-board [19, 56]
1959	Hoffman Electronics developed a solar cell with 11% efficiency [6]
1959	The Explorer-6 spaceship was deployed with a PV array having 9600 cells [43]
1963	A commercial silicon-based photovoltaic module was invented by Sharp Corporation. The first lighthouse with 242 watts of SPV was installed by Japan
1964	The very first Nimbus spaceship was deployed by NASA, operated with the SPV array of 470 W [44]
1966	The first orbiting astronomical observatory with 1 kW of Solar PV system was launched by NASA
1970	Credit to develop a lower-cost solar cell goes to Elliot Berman, who brings the price down from \$100 per watt to \$20 per watt with the help of Exxon Corporation [3, 16, 31]
1972	Delaware University started 'The Institute of Energy Conversion' that support research in thin-wafer SPV and solar thermal systems
1973	World's first 'Solar One' solar-powered house was designed by Delaware University, USA
1976	The first amorphous silicon photovoltaic cell was developed by David and Christopher at RCA Laboratories [14]
1980	The thin-film solar cell composed using CuS/CdS exceeded 10% efficiency

(continued)

**Table 2.1** (continued)

Year	Developments
1981	Paul Mac Cready was the person who constructs the very first SPV energised plane with 16 thousand solar cells mounted on its wings, providing 3000 W of electrical energy
1982	The first 1000 kW solar PV plant was operated in Hisperia, California
1986	ARCO Solar has launched the first public domain thin-wafer SPV module in the world (G 4000)
1992	Cadmium telluride made solar cell with 15.9% efficiency was prepared by the South Florida University, which omits the restriction of 15% efficiency in thin-film cells
1994	The solar cell made using GaInP and GaAs crosses the efficiency of 30% was developed by The NREL
1999	In this year, building-integrated photovoltaic (BIPV) panels, a more energy-efficient building technique, were used in '4-Times Square' skyscraper in New York City
2000	BP Solarex had built two new Solar PV modules with thin-film with higher efficiencies in less area than break all the records in thin-film technology around the globe
2000	World's biggest solar cell production plant was started in Perrysburg, Ohio with a yearly solar module manufacturing capacity of 100 MW
2001	Santa Rita Jail installed a roof-mounted solar PV system of 1180 kW capacity installed by Power light Corporation in Dublin, California

**Fig. 2.3** Generation of mobile charge carriers due to photon energy in Solar PV  
(source Author)



A solar cell in essence is a  $p-n$  junction composed of two separate wafers of Si processed with a limited amount of trivalent or pentavalent atoms. For the formation of  $n$ -side, pentavalent impurities are added and for the  $p$ -layer, trivalent impurities are added having one vacant place to consume one electron. Once the two layers are combined together, the flow of  $e$  and holes started due to the concentration gradient. Electrons pass through  $n$  to  $p$  side and holes through  $p$  to  $n$  side. A field is developed

between the two layers, which restrict the further flow of charge carriers. This state is called equilibrium. This generated field attracts the e-from the *n* layer and holes from the *p* layer [1]. A *p-n* junction diagram presenting the influence of the aforementioned field is exhibited in Fig. 2.3. On both ends, metal connections are inserted to capture the charge carriers; thereby, current flows. The fingers like structure made by metallic strips to pass the light photons to the solar cells are engraved on sun-facing n-side [39].

Further, when the solar radiation strikes on the cell, three possibilities are there to happen: (i) Some photons may get reflected from the cell’s top surface, (ii) some may penetrate in the substrate, while (iii) some may pass without any significant effect due to less energy. The pairs of electron-hole are created owing to the breakdown of the band between silicon atoms. These pairs are generated on either side of the barrier. Due to the barrier potential, the minority charges are attracted toward the junction and drawn out in the reverse direction. In the *p*-side, minority charge carriers are electrons and in *n*-side, holes behave as a minority. This flow of minority charge carriers constitutes a small current in the solar cell. This current is basically irradiation dependent so-termed as “light-produced current.” This depends on the quality of solar cell current, since a higher value of light-originated current would produce more charge carriers, and thus more current will be flow in the system [39].

### 2.3.3 Analogous Electrical Network of a SPV

The electrical circuit drawn in Fig. 2.4 is analogous to the one-diode model of the solar cells. The following equations describe the behavior of its voltage with current [15].

$$I = I_L - I_D - I_{SH} \tag{2.1}$$

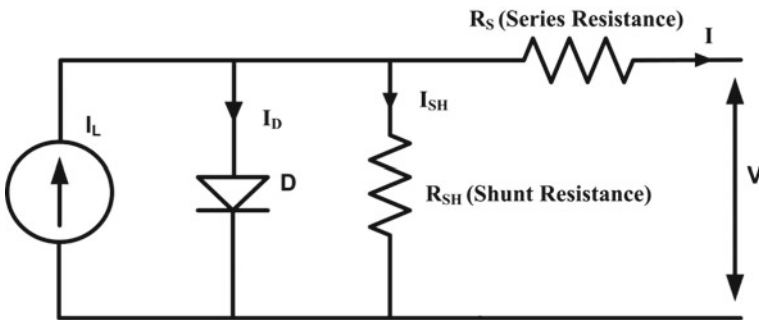


Fig. 2.4 One-diode representation of SPV (source Author)

where,

$$I_D = I_0 \left\{ \left( e^{\frac{q(V+IR_S)}{AKT}} \right) - 1 \right\} \quad (2.2)$$

$$I_{SH} = \frac{V + IR_S}{R_{SH}} \quad (2.3)$$

Therefore,

$$I = I_L - I_0 \left\{ \left( e^{\frac{q(V+IR_S)}{AKT}} \right) - 1 \right\} - \frac{V + IR_S}{R_{SH}} \quad (2.4)$$

where,  $I$ ,  $V$ ,  $I_0$  and  $q$  are the output current, the output voltage, the saturation current and charge on an electron, respectively. The quality of diode is identified by a factor termed as  $A$ , Boltzmann constant is given by  $k$ , and  $T$  represents the absolute temperature. It is bit difficult to explain the reason of existence of shunt resistance  $R_{SH}$ . The contacts and semiconductor material also offer some resistance, and it is represented by series-connected resistance  $R_S$ . Still, it is considered as the resistance offered by practical p-n junction and impurities cause a short-circuited path near the intersection. The  $R_S$  will preferably be zero and  $R_{SH} = \infty$ . This ideal situation, though, is not feasible although industrialists are seeking to mitigate the impact of both resistors to boost the outcomes.

The double-diode model incorporates the recombination phenomena and provides improved precision for the  $I$ - $V$  curve. The complexity of this model is more with respect to the one-diode configuration but at the same time, it is more accurate. This gives more scientifically reliable meaning to the internal parameters that may connect processes that exist within the solar wafer.

The electrical analogous circuit of the double-diode configuration having a current source connected in parallel with two diodes and two resistances  $R_S$  and  $R_{SH}$ . Figure 2.5 shows the double-diode model of the SPV [15].

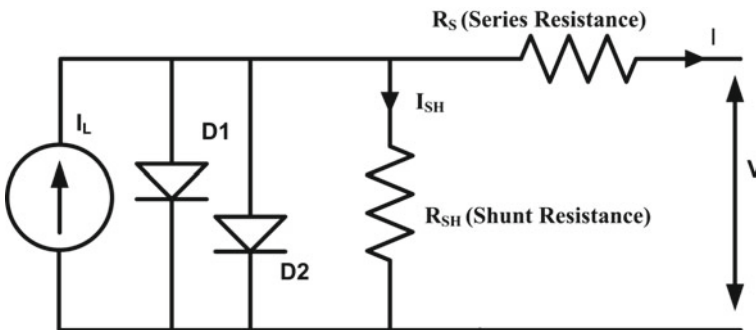


Fig. 2.5 Two-diode representation of SPV (source Author)

$$I = I_L - I_{D1} - I_{D2} - I_{SH} \quad (2.5)$$

where,

$$I_{D1} = I_{O1} \left\{ \left( e^{\frac{q(V+IR_S)}{A_1KT}} \right) - 1 \right\} \quad (2.6)$$

$$I_{D2} = I_{O2} \left\{ \left( e^{\frac{q(V+IR_S)}{A_2KT}} \right) - 1 \right\} \quad (2.7)$$

$$I_{SH} = \frac{V + IR_S}{R_{SH}} \quad (2.8)$$

Therefore,

$$I = I_L - I_{O1} \left\{ \left( e^{\frac{q(V+IR_S)}{A_1KT}} \right) - 1 \right\} - I_{O2} \left\{ \left( e^{\frac{q(V+IR_S)}{A_2KT}} \right) - 1 \right\} - \frac{V + IR_S}{R_{SH}} \quad (2.9)$$

### 2.3.4 Operating Parameters of Solar PV Cell ( $V_{OC}$ , $I_{SC}$ , $MPP$ )

The current–voltage characteristic reveals the two prime aspects of solar cells, which are the current  $I_{SC}$ , and voltage  $V_{OC}$  at shorted terminal and open terminal. The solar cell will generate zero power at both points. The opened terminal voltage  $V_{OC}$  can be obtained when current from the solar cell is nil and shunt resistance is ignored [29, 39]. Equation (2.10) shows the value of  $V_{OC}$ . Now, when the voltage becomes zero, the short-circuit current  $I_{SC}$  is obtained and remains more or less similar to the current  $I_L$  originates due to light as shown by Eq. (2.11)

$$V_{OC} = \frac{AKT}{q} \ln \left( \frac{I_L}{I_O} + 1 \right) \quad (2.10)$$

$$I_{SC} = I_L \quad (2.11)$$

The maximum power is produced by solar cells, when the multiplication of voltage and current is optimum, obtained by  $I$ - $V$  curve of solar PV.

### 2.3.5 Fill Factor ( $FF$ )

The fill factor ( $FF$ ) can be evaluated using the current at MPP ( $I_{MPP}$ ), the voltage at MPP ( $V_{MPP}$ ), voltage at open terminal ( $V_{OC}$ ) and the current at short circuit ( $I_{SC}$ ):

$$FF = \frac{V_{MPP} \times I_{MPP}}{V_{OC} \times I_{SC}} \tag{2.12}$$

In particular, the superiority of the cell is identified by fill factor. It is the true potential power ratio ( $I_{MPP}V_{MPP}$ ) to statistical one ( $I_{SC}V_{OC}$ ), in fact, that cannot be obtained. Due to the series resistance and shunt resistance of the diode, the voltage ( $V_{MPP}$ ) and current ( $I_{MPP}$ ) at MPP are still below the  $V_{OC}$  and the  $I_{SC}$ , respectively. The average FF is normally more than 0.70 [1, 39].

## 2.4 PV Systems

The characteristic curve of solar PV as revealed in Fig. 2.6, it tends to be seen that there is just one pinnacle working point named MPP. The most efficient PV management strategies are required to achieve optimal outputs from the solar PV spectrum, owing to the high capital expense of the solar PV array. In this regard, a DC-DC converter is placed in between the solar PV panel and load or storage device. By applying pulse width modulation (PWM) technique, the MPPT algorithm regulates the on-off sequence of DC-DC converter [39]. Figure 2.7 represents the basic building structure of solar PV.

The solar PV system has the following basic components.

### 2.4.1 PV Module

Many numbers of solar PV cells are combined to create a solar PV module. These PV cells have been connected in series to generate more voltage, and in parallel to generate more current. The whole structure is enclosed with tempered glass on

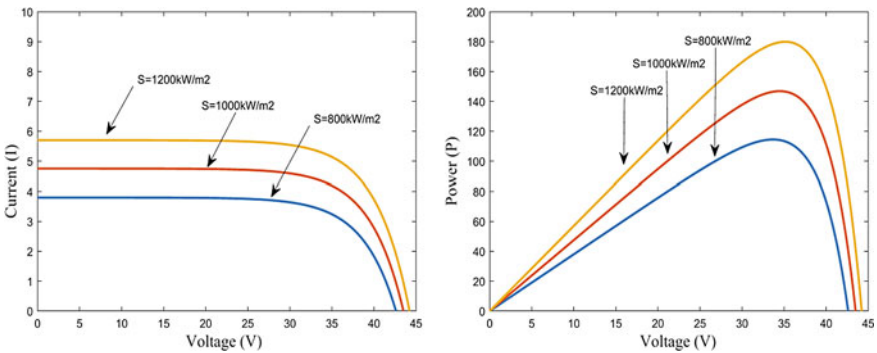
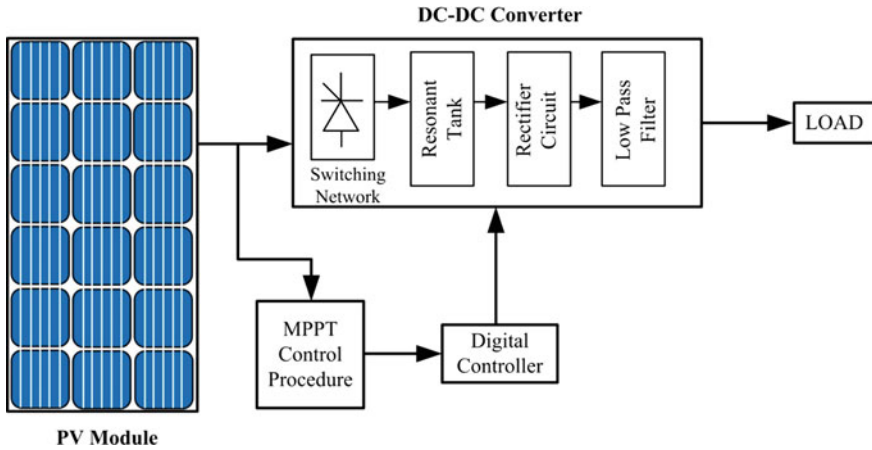


Fig. 2.6 Characteristic curves of solar cell (source Author)





**Fig. 2.7** Basic building structure of solar PV (*source* Author)

top, and the back has been covered with water-resistant laminated cover. For waterproofing, the sides are coated and an aluminum frame is used to keep all them as single mountable units. The electrical connections are provided in a connector box at panel back.

### 2.4.2 DC-DC Converter

The DC-DC converter has been utilized to acquire the maximum energy from the solar PV system. This converter individually regulates the performance of the panel through MPPT. DC converters and the microinverters both are analogous for the solar PV system, as both isolate the individual panels to maintain the required performance of the system.

### 2.4.3 Digital Controller

The digital charge manager is the backbone of the SPV system. The MPP can be tracked by it, and this energy is transferred to various types of batteries or load. The solar PV module delivers maximum power at some particular voltage, and this voltage is termed as maximum power voltage. This point of voltage is watched by the digital controller continuously with varying environmental as well as operational conditions.

### **2.4.4 MPPT Control Technique**

Maximum power point tracking, also known as MPPT, is a system that continuously adjusts the electrical parameters of the PV module to generate all the power they can generate. MPPT is a technique rather than a mechanical device that moves the solar panels in a sun-facing position all time. MPPT is a complete electronic device that alters the point of operation of the module to make sure that the utmost existing power is received. Further, the PV module draws out the maximum power using MPPT.

## **2.5 Types of Solar Cell**

The innovations in the sector of SPV are oriented toward achieving the goal of durable, highly efficient, and low-cost cells. Various versions of solar cells are available in the public domain, out of which 90% are wafer pattern silicon cells with a thickness of 180–200  $\mu\text{m}$  approximately. Single crystalline, multi-crystalline, amorphous silicon, cadmium telluride (CdTe), copper-indium-gallium-selenide (CIGS) and copper-indium-gallium-sulfide (CIGS<sub>2</sub>) are major types of silicon materials, which are needed for the more exploitation of the solar cell. Solar cells are split down into four groups depending on invention in manufacturing techniques, termed as era as per their popularity in the market. A comparative study of all four generations is given in Table 2.2 [7, 13, 32, 45, 52, 53].

### **2.5.1 The First Generation**

The crystalline silicon is used in the first age group of solar cells. This generation has been mostly used to construct the cells due to the easy fabrication. They are somewhat costly whenever required to make silicon wafer in pure form for solar PV. Due to the high power conversion efficiency, Si-based cells join a significant part of manufacturing of every type of solar cell. These cells are able to capture photons in the visible and outside the visible spectrum of light that is having an indirect band gap of 1.12 eV. Si makes solar cells manufacturing expensive because of the extremely advanced processing techniques and the expense of high-grade thin silicon layer. Moreover, it is less flexible and also bulky due to silicon. Further, the structure becomes costly due to heavy mechanical support [45].

**Table 2.2** Generations of solar PV [45]

Generation	Technology	Merits	Demerits
I-generation	Crystalline silicon wafer Monocrystalline (17–18%) Polycrystalline (12–14%)	<ul style="list-style-type: none"> <li>• High photo conversion efficiency</li> <li>• Well-established technology</li> <li>• Abundance of availability</li> </ul>	<ul style="list-style-type: none"> <li>• Costly</li> <li>• Required heavy mechanical structure for support</li> <li>• Less optical absorption</li> </ul>
II-generation	Thin-film (4–8%) CIGS (10–15%) CdTe (9–11%)	<ul style="list-style-type: none"> <li>• Relatively cheap</li> <li>• Can be made in a much thinner form</li> <li>• High optical absorption</li> </ul>	<ul style="list-style-type: none"> <li>• Less efficient</li> <li>• Less available material</li> <li>• Toxic (cadmium)</li> <li>• Less economic</li> </ul>
III-generation	Organic material Dye synthesized (9–10%) or Semiconductor-synthesized solar cell (39–40%)	<ul style="list-style-type: none"> <li>• High optical absorption</li> <li>• Cheaper</li> </ul>	<ul style="list-style-type: none"> <li>• Efficiency can be improved</li> <li>• Life is short which can also be improvised</li> </ul>
IV-generation	Perovskite PV and Hybrid (15–31%) Nano-crystal cell (7–8%)	<ul style="list-style-type: none"> <li>• High efficiency</li> <li>• More lifetime</li> <li>• Non-toxic</li> <li>• Low cost</li> </ul>	<ul style="list-style-type: none"> <li>• Less stable when used in PV</li> <li>• Thermally stable</li> </ul>

### 2.5.2 The Second Generation

The second-generation solar cells are usually manufactured by vacuum processed or by the accumulation of some chemical vapor. As compared to other era technologies, the second generation has been applied the chalcopyrite compounds such as CdTe or CIGS, and amorphous silicon wafer for the production of the solar cell. Despite low efficiency, they are comparatively inexpensive. These can be produced in much smaller and lighter sizes relative to their Si counterparts. Therefore, these cells are also known as thin-film solar cells. In respect to solar cells of the first generation, these have a direct band gap instead of the indirect band gap as in crystalline Si. While these film solar cells have a benefit of lower prices as compared to the first age of solar cells and certain drawbacks. The overwhelming majority of constituent elements of these cells are either more reactive (indium) in excess or extremely toxic (cadmium). Further, new manufacturing techniques for mass production will increase the cost of cells considerably. Such drawbacks and scale of economies have paved the technique for an alternative solar cell generation [45].

### ***2.5.3 The Third Generation***

With the introduction of organic material demonstrating photovoltaic characteristics, their ability to absorb less expensively and highly optically put them as an invention of the third generation. Other than organic solar cells, the dye- or semiconductor-sensitized solar cells (DSSCs) are another competitor that created to impact on the age of PV generation. The journey to compete with previously developed solar PV technologies was too long. The third generation involves the processing of solar PV using new technologies such as DSSC, organic PV (OPV), photo electrochemical (PEC) panels, and reduced cost quantum dots (QD) PV and tandem cells [45].

### ***2.5.4 The Fourth Generation***

In their development, “inorganic-in-organics” technology is integrated into fourth generation of cells. In order to develop the optronic characteristics of less expensive thin-film PVs, it involves the lower-cost property of organic material along with the constancy of specific inorganic nanostructures. In this generation of solar cells, problems associated with previous generations like higher cost, restricted flexibility, the volatility and the less efficiency are resolved. The fourth age includes perovskite-based PV and hybrid nano-crystal cells that are heading toward the development for the second age commercialized as cadmium telluride and copper-indium-gallium-selenide. The growing PV technologies are far away to accomplish the efficiency of 15 percentages. However, this generation has been achieved the same efficiency in the realistic condition [8, 9, 37, 45, 46].

## **2.6 Pros and Cons**

Sun-obtained power is a pollution-free and everlasting downstream of energy. It could provide independence to the users. However, solar energy is being taken as a prime alternative of conventional sources of energy to fulfill the energy demand in all developed and developing nations. Still, there are several shortcomings with application area and grid integration.

### ***2.6.1 Drawbacks of Solar Photovoltaic***

The high expenditure on equipment is the main issue that hurdles to promote solar power. In India, the average cost of installation of 1 kW rooftop solar photovoltaic (PV) is approximately INR 70,000. However, some states have given the subsidy.

However, a large payback period and less efficiency make the PV system less attractive for society [48]. The efficiency of the domestic rooftop has been varied between ranges from 10 to 20%. The crystalline structured solar power plant of 1 MW capacity (about 18% efficiency) demands land area of about 4 acres, at the same time thin-film panels (12% efficiency) would require 6 acres [26]. The performance of solar PV also gets affected by components such as batteries, inverters. Therefore, solar PV performance might be improved by utilizing efficient battery technologies and inverter design. However, shorter battery life and secure dumping of used batteries are also an important concern in the solar energy system. Despite this, batteries are large in size and bulky, thereby large space is required for installation [51].

Additionally, the scarcity of recycling facilities of used panels is one aspect of less development. Some materials as silver, tellurium, or indium are used to make panels that are precious and less available. The other constraints are high maintenance, deficiency of expert workers to meet the necessity to mount, manage, restore, assess, and finalize the solar power system [21]. Besides, dust on solar panels, cracks in panels, irregular use, overcharging of batteries, bypassing the charge controller are also some undeniable shortcomings that can lead to system damage. Furthermore, when there is no battery support, solar energy can only be harnessed for the period of daylight hours. Therefore, solar power is a less reliable source. Moreover, the large land requirement is also an important concern for the solar energy system. The location of land and pollution level in that area also affects the output of solar PV [34].

Another obvious shortcoming is voltage fluctuation due to the intermittent behavior of the sun and sudden change in weather conditions. It can interrupt the systems connected to PV. Also, there is a possibility of injection of DC in the grid which will lead to the failure of the distribution transformer [33]. These are some limitations of the solar energy system. Despite these, solar energy has lots of benefits that are making it, universally acceptable.

### ***2.6.2 Advantages of Solar Photovoltaic Generation***

It is a universally accepted fact that no energy source can beat the abundance of solar energy. Even, it can fulfill the world's electricity demand. The coal-fired plant emits approximately 0.63–1.64 kg of CO<sub>2</sub> while natural gas plant emits 0.27–0.91 kg per unit generation of electricity. The solar plant emits only 0.03–0.09 kg and the emission ratio of these three plants is 18:9.5:1. This comparison reveals the superiority of solar power in environmental friendliness than any other source. Approximately 25% of all GHG emission is due to the power plants (especially coal-fired). Therefore, solar power is the most feasible solution to mitigate the problem of global warming. Further, the use of solar power at the place of coal and gas power plant will be ecologically, financially, and publicly advantageous [32]. Furthermore, traditional coal and gas-fired power plant requires a large space and a large amount of water for their operation. On the other hand, solar power plant does not require any water

supply for their operation. Also, by-products of fossil fuel power plants (as in nuclear power plants) require great care and precaution. Presently, solar panels having more than 18% efficiency are also available at less cost [40, 55, 58].

Despite all the above benefits, solar power plant does not have a moving part so operation is noise-free and durable. Moreover, the maintenance cost is low. Also, solar plants are less prone to complete failure of a plant because either a cell or a panel only needs to be changed in failure.

## 2.7 Future of Solar PV Generation

Solar energy is probably the most ideal alternative to fulfill the hunger of energy in the near future as it is unrivaled as far as accessibility, cost adequacy, cleanliness, and output productivity contrasted with other sustainable sources of energy [26, 33]. Most of the research has been carried out to measure the solar energy flow between various components of photosynthetic substances [47]. The outcome of this research, efficiently contribute to the modernization of technologies to get far better results than what is as of now. It is found by scientists of the graphene group that the life span of perovskite cells can altogether be enhanced with introduction of a few layers of MoS<sub>2</sub> fragment as an active buffer boundary layer [4, 5, 11, 17, 23, 24, 30, 35, 54, 59]. Further, it was reported by the researchers' group in Hong Kong that perovskite-tandem solar cells with maximum light to electricity transfer efficiency, around the globe, of 25.5% have successfully been developed by them. At the time of the initial launch in 2009, the perovskite cell was having an efficiency of only 3.8% and now it is having 25.5%, which is a significant achievement [33]. Therefore, half-transparent perovskite cells have been developed to use in solar windows due to the ability of high power conversion and also blocking of infrared light while transmitting visible light [35]. It was shown that polymer poly (3,4-ethylene dioxathiophene) ought to have incredible potential for practical and most efficient perovskite cells as a hole delivering substance. A new research has been done by the team of MIT, USA. They developed a novel PV cell by combining two dissimilar sheets of solar photons absorbing materials to store up a larger spectrum of sunlight. Researchers have found that the device employed with a heat-resistant device, made up of tungsten and alumina layers can absorb the wider spectrum of sunlight and can deliver more electrical output.

The dye-sensitized solar cells were incorporated with the green polymer extracted from biodegradable waste and also experimented with the updated chitosan and crustacean's chitin to make the phthaloylchitosan, which increases the efficiency of the dye-sensitized cell more than 7%. The more efficient thin-wafer cells were developed using CdTe and Cu (In, Ga) Se<sub>2</sub> with an efficiency of around 16.5% and 20%, respectively. The light to electricity conversion efficiency of 14.1% was found in perovskite solar cells made by CH<sub>3</sub>NH<sub>3</sub>Pb<sub>0.75</sub>Sn<sub>0.25</sub>I<sub>3</sub> inverted structure [40]. In [23], the experiment of Freitag et al. represents that dye-sensitized solar cell has high efficiency under completely enclosed light condition. They obtained an open

terminal voltage of 1.1 V by the combination of two carefully fabricated sensitizers D35 and XY1, with the copper complex Cu (II/I) (tmby) as an oxido reduction agent (tmby, 4,4',6,6'-tetramethyl-2,2'-bipyridine).

## 2.8 Supportive Tools for Designing and Analysis of Solar PV

Before the execution of any solar power plant, it is required to study some aspects as a survey of the land, surrounding atmosphere, construction of structures, capacity consideration, and the requirement of equipment. With the help of software, manual work reduces to some extent. Therefore, details of some useful software for analysis and designing purpose of solar PV have been presented in Table 2.3.

## 2.9 Conclusions

Solar PV generation technologies have become well-organized and recognized around the world. Currently, many innovative mega-scale solar power projects are being placed or are still under production in both modernized and under-developed countries. The solar PV generation will remain the main source for the production of energy among all solar energy schemes. However, the prospective sector for standalone solar PV systems is required to be more innovated and promoted by the supportive policies. The cost of the solar PV generation system is reduced at remarkable prices in recent years. Still, the overall cost is high for the domestic utilities. Toward the overall development of the solar energy sector, some new strategies with subsidies are required. In near future, more efficient, reliable, and stable solar PV technologies will be available with the reduced cost of balance-of-system and overall PV system modules.

Throughout this segment, the global advancement of the solar photovoltaic system has been discussed including transformation of the solar PV technology starting from initial phase of the photovoltaic. Further, comparison and classification of generations of solar PV have been elaborated with the discussion of the fundamentals of the PV systems with their components, shortcomings, benefits, and possible prospects for the future. Therefore, regardless of a few downsides, solar PV technology is the greenest and the cleanest to satisfy the future energy demand of the world.

**Table 2.3** Brief of important software tools

S. No.	Software	Description
1	HOMER PRO Developed by NREL (National Renewable Energy Laboratory), USA	<ul style="list-style-type: none"> <li>• Various renewable and non-renewable sources of energy can be evaluated</li> <li>• More number of loads can be simulated</li> <li>• Performance parameters like fill factor, <math>V_{oc}</math>, <math>I_{sc}</math>, PF penalty can be incorporated for more precise calculation</li> </ul> <p>The detail is available at <a href="https://www.homerenergy.com/products/pro/pricing/index.html">https://www.homerenergy.com/products/pro/pricing/index.html</a></p>
2	PV F-Chart	<ul style="list-style-type: none"> <li>• Programming tool that calculates the photovoltaic system output including inverter and system model</li> <li>• It may be less suitable for calculation of PV power in real-world conditions</li> <li>• Results can be obtained in graphical form as well as in tabular form</li> </ul> <p>The demonstration is available at <a href="https://www.fchart.com/pvfchart/demo.php">https://www.fchart.com/pvfchart/demo.php</a></p>
3	PV Planner	<ul style="list-style-type: none"> <li>• Precise solar plant locator (iMap technology)</li> <li>• The interface is efficient and perceptible</li> </ul> <p>The detail is available at <a href="https://solargis.info/pvplanner/#tl=Google:hybrid&amp;bn=satellite">https://solargis.info/pvplanner/#tl=Google:hybrid&amp;bn=satellite</a></p>
4	PVSYST	<ul style="list-style-type: none"> <li>• User-friendly environment for architects, engineers, researchers and students</li> <li>• Simulates all the parameters of a practical PV system and generates a collective report</li> <li>• Permits the control over various designing factors</li> <li>• Bundled database from Photon publication that lists thousands of modules and inverter models</li> </ul> <p>The detail is available at <a href="https://www.pvsyst.com/en/software/download">https://www.pvsyst.com/en/software/download</a></p>

(continued)



Table 2.3 (continued)

S. No.	Software	Description
5	RETSCREEN	<ul style="list-style-type: none"> <li>• Inbuilt global weather data linked database of NASA Available for download from Canada National Resources at <a href="https://www.nrcan.gc.ca/energy/software-tools/7465">https://www.nrcan.gc.ca/energy/software-tools/7465</a></li> </ul>
6	System advisor model (SAM)	<ul style="list-style-type: none"> <li>• Availability of solar radiation data around the globe</li> <li>• Allows importing of TMY2, TMY3 and EPW data</li> <li>• In case grid-tied PV system, cost of energy can be estimated</li> <li>• Equipment and running cost of large power plants including system design and performance parameters</li> </ul> Available at <a href="https://sam.nrel.gov/download">https://sam.nrel.gov/download</a>
7	Solar PRO	<ul style="list-style-type: none"> <li>• Real-time analysis is the prominent feature</li> <li>• 3D visualization of overall system is possible</li> <li>• Inbuilt global weather data</li> <li>• Inbuilt facility to find the area of site and capacity of installation</li> </ul> The detail is available at <a href="https://www.lapsys.co.jp/english/products/where_to_buy/index.html">https://www.lapsys.co.jp/english/products/where_to_buy/index.html</a>
8	SUNDAT	<ul style="list-style-type: none"> <li>• Includes simulation features like partial or full shadow, structure design, electrical, mechanical system modeling and location analysis</li> <li>• Energy modeling via NREL SAM</li> <li>• SUNDAT is optimized for large-scale commercial or utility PV design</li> </ul> The detail is available at <a href="https://sundat.ftcsolar.com/index.php/register/">https://sundat.ftcsolar.com/index.php/register/</a>

(continued)

Table 2.3 (continued)

S. No.	Software	Description
9	Helioscope	<ul style="list-style-type: none"> <li>• 3D design</li> <li>• Rapid proposals</li> <li>• Single-line diagrams can be exported to the computer-aided design software</li> <li>• Up to 5000 kW systems</li> <li>• Global weather coverage</li> <li>• Shade reports</li> </ul> <p>The detail is available at <a href="https://www.helioscope.com/signup">https://www.helioscope.com/signup</a></p>
10	Solarius PV	<ul style="list-style-type: none"> <li>• For detailed financial and technological feasibility studies, the full, robust and creative method for grid-connected photovoltaic device design is combined with a broad variety of energy storage systems</li> <li>• Automatic single-line wiring diagram of the PV system</li> <li>• Professional financial analysis (photovoltaic system business plan)</li> </ul> <p>The detail is available at <a href="https://www.accasoftware.com/en/trial/solarius-pv">https://www.accasoftware.com/en/trial/solarius-pv</a></p>

## References

1. Assis A, Mathew S (2015) Fundamentals and modelling of a solar PV system. *Int J Adv Res Electr Electron Instrument Eng* 4(6) (2015)
2. Aggarwal A et al (2018) Clean and green India: is solar energy the answer? *IEEE Potent* 37:40–46
3. Alferov et al (1971) Solar-energy converters based on pn Al<sub>x</sub>Ga<sub>1-x</sub>As-GaAs heterojunctions. *Sov Phys-Semicond (Engl Transl) (United States)* 4(12)
4. Amu TL (2014) Performance optimization of tin halide perovskite solar cells via numerical simulation (Doctoral dissertation)
5. Ansari et al (2018) Frontiers, opportunities, and challenges in perovskite solar cells: a critical review. *J Photoche Photobio C Photoche Rev* 35:1–24
6. Asimov I (1962) My Son, the Physicist. *Scientific American and Hoffman Electronics*
7. Bagher AM et al (2015) Types of solar cells and application. *Amer. J Opt Photo* 3(5):94–113
8. Balema V (2009) Alternative energy photovoltaics ionic liquids, and MOFs. *Mat Matt*
9. Barnett AM et al (2001) High current, thin silicon-on-ceramic solar cell. *Sol Energy Mat Sol Cel* 66:45–50
10. Becquerel AE (1839) Investigating the effects of chemical radiation of sunlight using electric currents. *CR Acad Sci* 9(145):1
11. Besarati SM et al (2013) The potential of harnessing solar radiation in Iran: generating solar maps and viability study of PV power plants. *Renew Energy* 53:193–199
12. Butti K, Perlin J (1980) Solar water heaters in California, 1891–1930. *Coevo Quar (United States)*
13. Robert C (2010) Solar panel processing. *Archives Contemporains Editions, Philadelphia, USA*
14. Carlson DE, Wronski CR (1976) Amorphous silicon solar cell. *App Phys Lett* 28(11):671–673
15. Chaieb H, Sakly A (2015) Comparison between P&O and PSO methods based MPPT algorithm for photovoltaic systems. In: 2015 16th international conference on science and techniques of automatic control and computer engineering (STA) (2015)
16. Chapin DM et al (1954) A new silicon p-n junction photocell for converting solar radiation into electrical power. *J App Phy* 25(5):676–677
17. Chirumamilla M et al (2016) Multilayer tungsten-alumina-based broadband light absorbers for high-temperature applications. *Opt Mat Exp* 6:2704–2714
18. Czochralski J (1918) A new method for the measurement of the crystallization rate of metals. *J Phys Chem* 92:219–221
19. Easton RL, Votaw MJ (1958) Vanguard I IGY satellite. *Rev Sci Inst* 30(2):70–75
20. Einstein (1906) On the theory of light production and light absorption”. *Amer. Jou. of Phy.*, 1906, 199–206.
21. Ellabban O et al (2014) Renewable energy resources: current status, future prospects and their enabling technology. *Renew Sustain Energy Rev* 39:748–764
22. Fatet J (2006) Recreating Edmond Becquerel’s electrochemical actinometer: what can historical experiments replication teach us? July 2006
23. Freitag et al A (2017) Dye-sensitized solar cells for efficient power generation under ambient lighting. *Nat Photo* 11(6):372–378
24. Fu R et al (2015) Economic measurements of polysilicon for the photovoltaic industry: market competition and manufacturing competitiveness. *IEEE J Photovol* 5(2):515–524
25. Gevorkian P (2010) Alternative energy systems in building design. McGraw-Hill
26. Green MA, Emery K, King DL, Hisikawa Y, Warta W (2006) Solar cell efficiency tables (version 27). *Progr Photoval Res Appl* 14(1):45–51
27. International Energy Agency (IEA). Available at <https://www.iea.org>
28. Jäger-Waldau A (2020) Snapshot of Photovoltaic’s. *Energies* 13(4):930
29. Jain HK (2015) Study and implementation of maximum power point tracking algorithm for photovoltaic application (Master’s Dissertation)
30. Jiang X et al (2017) High-performance regular perovskite solar cells employing low-cost poly (ethylenedioxythiophene) as a hole-transporting material. *Sci Rep* 7:42564

31. Jordan et al (2013) Nanotechnology patent literature review: graphitic carbon-based nanotechnology and energy applications are on the rise. *Nanotech L Bus* 11:111
32. Kabir E et al (2017) Solar energy: potential and future prospects. *Renew Sustain Energy Rev* 82:9
33. Kannan N, Vakeesan D (2016) Solar energy for future world: a review. *Renew Sustain Energy Rev* 62:1092–1105
34. Kharcha P, Hansen J (2013) Coal and gas are far more harmful than nuclear power. *Sci Briefs-Nat Aeronaut Space Administr (NASA)*
35. Kim H et al (2016) Empowering semi-transparent solar cells with thermal-mirror functionality. *Adv Energy Mat* 6:1502466
36. Langley SP (1880) The bolometer. *Proc Am Metro Soc* 2:184–190
37. Liu C et al (2016) Highly efficient perovskite solar cells with substantial reduction of lead content. *Sci Rep* 6(1):1–8
38. Macdonald F (2016) France will install 1000 km of solar-panelled roads in the next 5 years. In: *Sciencealert*, Jan 2016
39. Masmoudi F et al (2016) Single and double diode models for conventional mono-crystalline solar cell with extraction of internal parameters. In: *13th International Multi-Conference on System Signals and Devices (SSD)*. IEEE, pp 720–728
40. McEvoy A, Castañer L, Markvart T (eds) (2013) *Solar cells: material, manufacture and operation*, 2nd edn. Elsevier
41. Ministry of New and Renewable Energy. Available at <https://www.mnre.gov.in>
42. Mouchot AB, Mouchot A (1869) *Solar heat and its industrial applications*. Gauthier-Villars, p 260
43. National Aeronautics and Space Administration (NASA), Explorer Programme. Available at <https://nssdc.gsfc.nasa.gov/nmc/spacecraft/display.action?id=1958-005A>
44. National Aeronautics and Space Administration (NASA), NIMBUS Programme (1964). Available at <https://nssdc.gsfc.nasa.gov/earth/nimbus.html>
45. Olaleru SA et al (2020) Perovskite solar cells: the new epoch in photovoltaics. *Sol Energy* 196:295–309
46. Oliva and Barron (2014) Dielectric coated Si or Ge QDs for improvement of solar cells. In: *Abstracts of papers of the American Chemical Society*
47. Dostál J, Pšenčík J, Zigmantas D (2016) In situ mapping of the energy flow through the entire photosynthetic apparatus. *Nat Chem* 8:705–710
48. Parkinson G (2015) Why solar costs will fall another 40% in just two years. *RE New Econ* 20 (2015)
49. Pearson G, Chapin D, Fuller C (1954) Bell labs demonstrates the first practical silicon solar cell. *Am Phys Soc (APS News)* 18(4)
50. Perlin J (1999) From space to earth: the story of solar electricity. *Earthscan*
51. Radivojevic et al (2015) Influence of climate and air pollution on solar energy development in Serbia. *Ther Sci* 19:32–32
52. Rathore et al (2019a) A comprehensive review of different types of solar photovoltaic cells and their applications. *Int J Amb Energy*:1–18
53. Rathore et al (2019b) Solar map of India under clear sky conditions. *Int J Sustain Energy* 38:415–446
54. Razykov TM et al (2011) Solar photovoltaic electricity: current status and future prospects. *Sol Energy* 85:1580–1608
55. Resch et al (200) Potentials and prospects for renewable energies at global scale. *Energy Policy* 36:4048–4056
56. Siry JW (1958) The Vanguard IGY Earth satellite program. In: *Proceedings of the fifth generation Assembly of CSAGI*
57. Smith W (1992) Effect of light on selenium during the passage of an electric current. *SPIE MILESTONE Ser MS* 56:3–3
58. Solar Foundation (2017) *National Solar Jobs Census 2013*. The Solar Foundation

59. Thongpron J, Kirtikara K (2006) Effects of low radiation on the power quality of a distributed PV-grid connected system. *Sol Energy Mat Sol Cel* 90:2501–2508
60. Tyagi et al (2013) Progress in solar PV technology: research and achievement. *Renew Sustain Energy Rev* 20:443–461
61. U. S. energy efficiency and renewable energy

# Chapter 3

## Solar Thermal Power Generation



Rajeev Awasthi, Shubham Jain, Ram Kumar Pal, and K. Ravi Kumar

### 3.1 Introduction

Sun radiates an enormous amount of solar energy every day. The source of energy in the sun is the nuclear fusion of two hydrogen nuclei into one helium nucleus at high pressure and temperature within the sun's core. The solar energy can be harnessed by its conversion into heat and electricity. Solar energy can be converted into electricity in two ways: solar photovoltaics and solar thermal technologies. Solar photovoltaics (PVs) convert solar radiation directly into electricity by utilizing the selective wavelength of solar radiation. This selective range of wavelength depends on the materials of the solar cells. However, solar thermal technologies utilize the entire solar spectrum available on the collector surface for thermal conversion irrespective of its wavelength. The collected thermal energy is converted into electricity by using a heat engine (e.g., steam and gas turbine, Stirling engine, etc.) or other thermoelectric generators. All these technologies for thermoelectric conversion must obey the second law of thermodynamics. According to this law, the efficiency of the process increases with the temperature of the process. Based on the operating temperatures, different working fluids came into the concept, e.g., organic fluids are used for power generation from the heat at low temperature, and the cycle is named as organic Rankine cycle (ORC). For higher cycle efficiency, water and synthetic oils are used as working fluids which operate at higher temperatures. This high temperature is achieved by concentrating solar radiation on the receiver, and these technologies are known as concentrating solar power (CSP) technologies. Hence, the electricity generation by solar thermal technologies involves the collection and concentration of solar radiation in the form of heat and its conversion into electricity. The limitation

---

R. Awasthi · S. Jain · R. K. Pal · K. Ravi Kumar (✉)  
Centre for Energy Studies, Indian Institute of Technology Delhi, New Delhi 110016, India  
e-mail: [krk@ces.iitd.ac.in](mailto:krk@ces.iitd.ac.in)

© The Author(s), under exclusive license to Springer Nature Singapore Pte Ltd. 2021  
S. N. Singh et al. (eds.), *Fundamentals and Innovations in Solar Energy*,  
Energy Systems in Electrical Engineering,  
[https://doi.org/10.1007/978-981-33-6456-1\\_3](https://doi.org/10.1007/978-981-33-6456-1_3)

of solar power generation technologies is the diurnal (day and night) and intermittent (hourly, daily, and seasonal) nature of solar radiation. Hence, dispatchability of the solar power generation is poor. Here, dispatchability is the ability of a power generating system to provide the required amount of power on demand regardless of the time and weather conditions. Therefore, it is necessary to employ either thermal energy storage (TES), auxiliary backup, or hybridize the solar power generation system with other fuel-based supplementary heating systems, which can improve the dispatchability of the solar power generation system.

### 3.2 The Layout of a Solar Thermal Power Plant

Solar thermal power plants are composed of three processes: collection and conversion of solar radiation into heat, conversion of heat to electricity, and thermal energy storage to mitigate the transient effects of solar radiation on the performance of the system. There are three blocks in a solar thermal power plant, as shown in Fig. 3.1 to achieve the above-mentioned processes such as

- (i) Solar field
- (ii) Thermal energy storage
- (iii) Power block.

The solar field has three basic components: concentrators, receiver, and tracking system. Concentrators reflect the solar radiation on the receiver, which is placed at the focal plane. The concentrated solar radiation is absorbed by the receiver and then converted into thermal energy by raising the temperature of a working fluid. The tracking mechanism is required to track the apparent motion of the sun. The apparent motion of the sun relative to the earth varies due to: (i) earth's rotation on its own

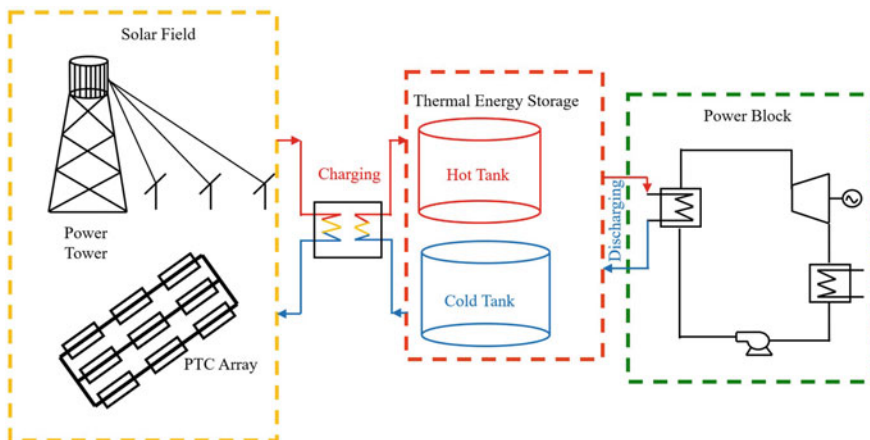


**Fig. 3.1** Layout of a solar thermal power plant. *Source* Author

axis and (ii) earth's revolution around the sun in an elliptical orbit. Both of these motions are mutually independent; hence, a two-axis tracking system is required to track the exact position of the sun in the sky.

The thermal energy storage is employed to reduce the effect of diurnal and seasonal variations in solar radiation on the performance of the solar thermal plant. Additionally, thermal energy storage increases the dispatchability of a solar thermal power generation system. Thermal energy storage technologies can be classified into three types: sensible heat storage, latent heat storage, and thermochemical energy storage. A sensible heat storage system stores the heat by raising the temperature of a storage media. The sensible heat storage material must have high specific heat to have high storage density. Latent heat storage system stores the heat by changing the phase of material either solid to solid/solid to liquid/liquid to gas/solid to gas. The material used for latent heat storage must have high latent heat. Thermochemical energy storage stores the heat due to enthalpy of reaction. The reactants are made to react by undergoing an endothermic reaction by absorbing the available heat. The stored energy can be retrieved by carrying out the reverse reaction.

The power block consists of heat exchangers, turbine, condenser, cooling tower, and alternator. The heated fluid from the solar field is used to drive the turbine, and the turbine shaft is coupled to the alternator, which generates electricity. The heat available at the turbine exit is rejected in the condenser and then to the ambient with the help of a cooling tower. The cooled fluid is again circulated to the solar field to collect the heat.

### 3.3 Classification of Solar Thermal Energy Technologies

The fundamental difference between solar thermal technologies is the difference in concentrator and receiver designs along with its tracking requirements. For achieving high fluid temperature, solar radiation needs to be concentrated. Hence, solar thermal collectors can be classified into the following categories (Fig. 3.2).

#### 3.3.1 *Non-Concentrating Collectors*

Non-concentrating collectors have the aperture area approximately equal to the absorber area. Hence, the concentration ratio for these types of collectors is unity. Flat plate collectors and evacuated tube collectors are examples of non-concentrating collectors. These collectors generate low temperature heat that can be used for domestic as well as process heating applications.

Flat plate collectors (FPCs) generally have a blackened absorbing surface to absorb the solar radiation, and the absorbed energy is transferred to the working fluid flowing inside the absorber tube/channel. The constructional details of the flat plate collector can be understood from Fig. 3.3a, b, respectively. The absorber plate is usually



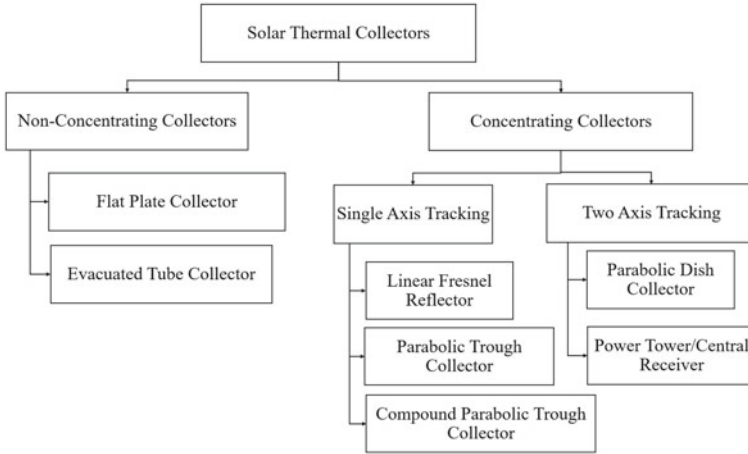


Fig. 3.2 Classification of solar thermal energy technologies. Source Author

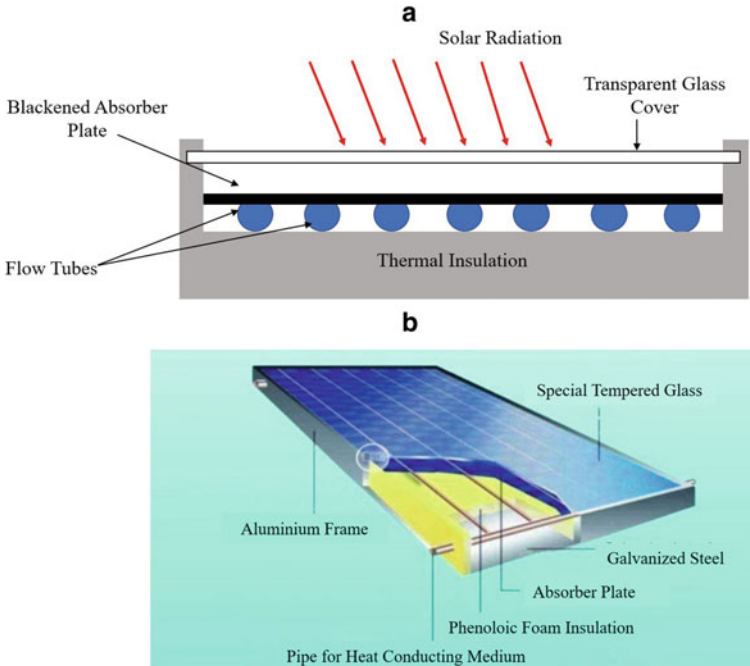
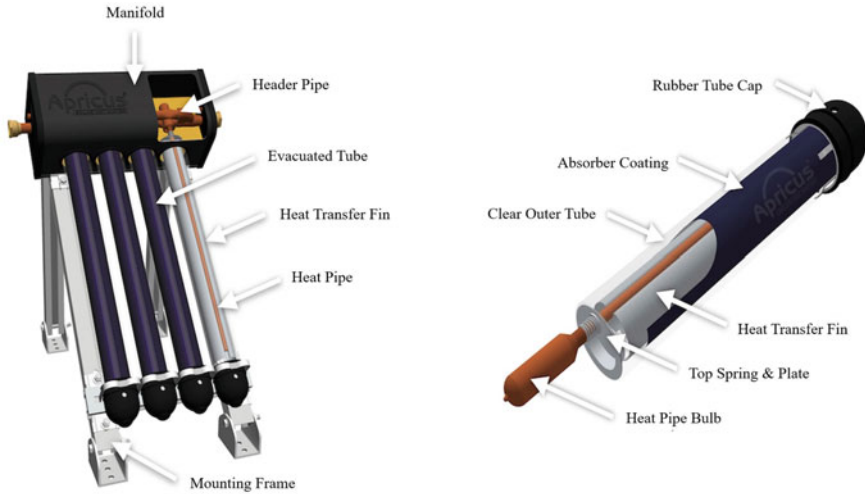


Fig. 3.3 (a) Schematic diagram of flat plate collector, (b) structure of flat plate collector [1]



**Fig. 3.4** Cut section view of evacuated tube collector [3]

covered by a transparent envelope to reduce the convective and radiative heat losses. The insulation is provided on the bottom and sides of the collector to reduce the conduction losses. Flat plate collectors are placed typically facing toward the south (in the northern hemisphere) and inclined at an angle equivalent to the latitude of the location. The configuration of these collectors is simple, and less maintenance is required. However, the obtainable temperature in FPCs is in the range of 80–100 °C. Hence, it is generally used for process heating applications, but in some cases, it is also used for power generation by using an organic Rankine cycle (ORC).

Evacuated tube collectors (ETCs) are similar to flat plate collectors, as shown in Fig. 3.4. In flat plate collectors, the losses from the absorber are still significant even after using the glass covers and insulation. In order to reduce the heat losses further, the absorber tube is placed in the sealed evacuated tubes. The evacuated glass tubes minimize the heat losses from the absorber. Hence, the operating temperature of ETCs is in the range of 100–120 °C [2]. Similar to the FPCs, the ETCs are also used for the process heating applications such as water and space heating and air dryers. ETCs are also used for power generation by using the organic Rankine cycle (ORC). Unlike the concentrating collectors, ETCs are placed in a stationary position at a particular orientation without a tracking system.

### 3.3.2 Concentrating Collectors

Concentrating collectors are also called concentrating solar power (CSP) technologies. A concentrating solar collector consists of a concentrator and a receiver. The concentrator is an optical system which concentrates the beam radiation on the

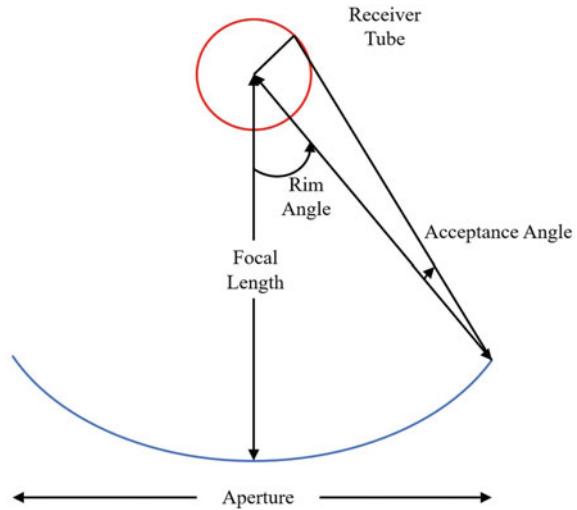
receiver. The receiver absorbs the concentrated solar radiation and converts it into the thermal energy by raising the temperature of the heat transfer fluid. Concentrating collectors provide energy at higher temperatures and require a tracking mechanism to track the apparent motion of the sun. The concentrating collectors are generally used for medium (150–300 °C) and high (>300 °C) temperature applications such as process heating and power generation. Linear Fresnel reflector, parabolic trough collector, compound parabolic collector, parabolic dish collector, and power tower are the different CSP technologies that can be used for power generation. These technologies will be discussed in detail in the upcoming sections of this chapter. Prior to the detailed discussion on the different CSP technologies, it is necessary to discuss the terminology used in the concentrating solar collectors.

### 3.4 Terminology Used in Solar Thermal Collectors

Solar thermal power generation requires high temperature, which needs the concentration of solar radiation. To compare the different solar thermal power generation systems, some key characteristics/parameters are important to analyze the performance of the power generation system. Some of those parameters are discussed as follows:

- **Aperture** is the plane of entrance for the solar radiation incident on the concentrator. It may also be defined as the plane joining the two extremes of the concentrator.
- **Concentration Ratio**
  - *Geometrical Concentration Ratio (GCR)* is the ratio of the area of the aperture to the area of the absorber.
  - *Optical Concentration Ratio (OCR)* is the ratio average energy flux integrated over the absorber surface to the flux available on the aperture.
  - *Local Flux Concentration Ratio (LCR)* is the ratio of the flux at any point on the receiver to the flux available on the aperture. LCR varies from point to point on the absorber.
- **Acceptance Angle** is the maximum angle by which the incident ray path may deviate from the normal to the aperture plane but still reaches the absorber surface (Fig. 3.5). The concentrators with a large acceptance angle do not require stringent tracking. However, smaller acceptance angles require frequent tracking to track the apparent motion of the sun.
- **Intercept Factor** is the fraction of the concentrated solar radiation intercepted by the absorber of a given size.
- **Rim Angle** is the angle between the centerline and the physical extremities of the mirror, which also depicts the relation between the focus to aperture ratio in parabolic trough concentrators (Fig. 3.5).

**Fig. 3.5** Terminologies in parabolic trough collector (PTC). *Source* Author



- **Optical Efficiency** of a solar collector may be defined as the ratio of the solar energy absorbed by the absorber to the solar radiation incident on the aperture. The following parameters that affect the optical efficiency of the solar concentrator are as follows:
  - Angle of incidence
  - Reflector shape
  - Refractive index
  - Accuracy of tracking
  - Extinction coefficient
  - Transmission losses
  - Absorptance of surface coating
  - Shading by the receiver
  - Thickness of the glazing
  - Dust on the glass surface
  - Cover transmission absorptance of the absorber

### 3.5 Concentrating Solar Thermal Technologies

Concentrating solar collectors are used to achieve high temperatures by concentrating direct beam radiation available over a large surface (concentrator/reflecting mirrors) onto a smaller area (receiver). The commercially available CSP technologies are namely linear Fresnel reflector, parabolic trough collector, parabolic dish collector, and power tower.

### 3.5.1 Linear Fresnel Reflector (LFR)

In linear Fresnel reflector (LFR), the incident direct solar radiation is concentrated by a series of linear Fresnel mirrors onto a downward facing receiver placed over the collectors, as shown in Fig. 3.6. The primary Fresnel reflector field is made of flat or curved parallel mirror stripes. The receiver in LFR consists of an absorber tube and a glass cover. The working fluid circulating inside the absorber tube gains enthalpy and is used for power generation. Concentration ratio in the range of 10–40 and temperature up to 500 °C can be achieved using the linear Fresnel reflectors [4, 5]. The benefits of LFR are the highest land-use factor and comparatively lower capital investment cost because of its constructive simplicity. It makes the LFR a potential and commercially adaptable CSP technology for power generation. A LFR system consists of (a) primary reflectors, (b) receiver consisting of absorber tube and glass cover, (c) tracking mechanism, and (d) control units.

#### 3.5.1.1 LFR Field

The primary reflectors in LFR are made of generally flat or curved glass reflectors or silver-coated glass, i.e., the reflecting surface is made of silver covered by glass covers to prevent the oxidation of the metallic reflectors. The primary reflectors can be continuous or the combination of multiple reflectors. The rows of primary reflectors are placed close to the ground on a strong mechanical structure. The placement close to the ground maximizes the structural stability against the wind load and also reduces the cost associated with the structural requirements. The LFR mirrors are generally

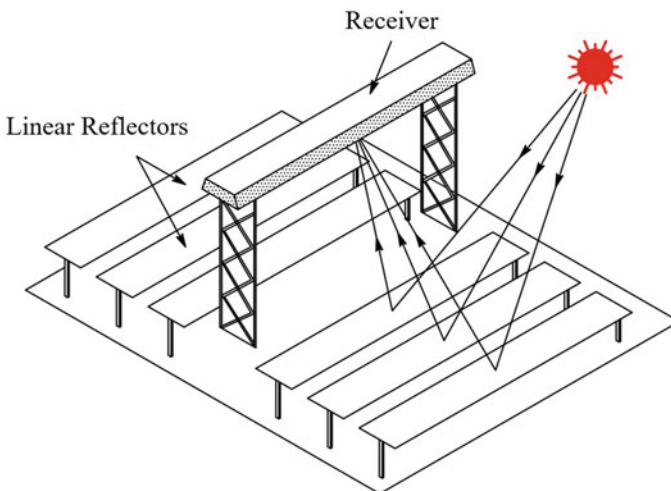


Fig. 3.6 Schematic of linear Fresnel reflector [6]

installed in the north–south direction and tracked with a single axis in an east–west direction to reflect the sun’s beam radiation on to a fixed linear receiver suspended over the rows of reflectors. The rows of reflectors are placed with a distance between the two consecutive rows to prevent the shading and blocking losses. These reflector rows are inclined at different angles depending upon the distance from the receiver and the incident solar radiation, but they track the apparent motion of the sun by the same angular velocity. Each module of primary reflectors is typically 12 meters long and 0.5–2 m wide. The modules are joined together to get the reflectors of the desired length. The concentrated solar radiation can be used for heating of water using a multitube cavity receiver or direct steam generation (DSG) using a single-tube receiver with a secondary reflector. The LFR with DSG technology is primarily used for power generating systems using the Rankine cycle (Sect. 3.6.1).

The area of the LFR field is decided based on the average direct normal irradiance (DNI) for the particular location, collection efficiency, and conversion efficiency. LFR systems traditionally use direct steam generation (DSG) technology, which eliminates the requirement of heat exchangers and heat transfer fluid. There are few LFR power plants with DSG, such as Novatec Solar PE-2 with 30 MW, Liddell steam augmentation system with 9.3 MWh<sub>th</sub>, Dhursar plant with 125 MW in Jaisalmer, Rajasthan [7–9]. These plants operate with saturated steam at about 55 bar. The modern LFR collectors can obtain a temperature up to 500 °C with molten salt as a working fluid and concentration ratio up to 50 [5, 10, 11].

The reflectors in LFR are made of the solar-grade mirror with low iron content because the iron content in the glass increases the absorption of solar radiation and reduces its reflectivity. The glass is coated with a silver layer with protective paint for the protection of reflective coating. The aluminum layer on a substrate is coated with SiO<sub>2</sub> for the prevention of abrasion and corrosion. The only limitation with aluminum-based reflector is the aluminum substrate may require pre-treatment to increase the adherence of the coating, which may change the absorptivity and other optical properties of the reflector [12, 13].

### 3.5.1.2 Receiver of LFR

In general, there are two types of receiver configurations being used with the LFR systems: an inverted trapezoidal cavity type with multiple tubes or a single tube type with a secondary reflector.

Trapezoidal cavity receiver with multiple tubes is most common with the LFR system, where the trapezoidal cavity is perfectly insulated from three sides (Fig. 3.7). On the aperture of the receiver, glass cover is used to reduce the convective and radiative heat losses and the oxidation of the surface coating of the absorber tubes [14]. This configuration is typically used for producing the steam up to saturated temperature conditions. The selective coating is used on the absorber tubes to increase its absorptivity and reduce emissivity. An increase in operating temperature increases heat losses from the receiver, and evacuating such a large cavity is very difficult.

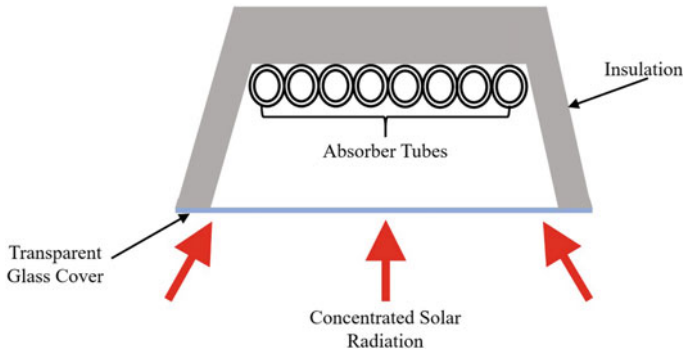


**Fig. 3.7** Trapezoidal cavity receiver with multiple tubes [16]

This is the major limitation of the trapezoidal cavity receiver, which results in higher convective losses from the absorber to the glass cover.

In a single-tube receiver, the tube is enclosed in an evacuated glass enclosure to reduce the convective heat loss. This type of receiver is typically equipped with a secondary concentrator, which is placed above the absorber tube to improve the intercept factor [15]. The external surface of the secondary reflector is insulated, and also, the outer surface of the absorber tube is coated with the selective coating to improve absorptivity and reduce emissivity.

The heat absorbed in the receiver by the HTF can be used for the power generation using the Rankine cycle. A typical solar thermal power generation system using the Rankine cycle is shown in Fig. 3.11. The only difference will be the replacement of parabolic trough collector (PTC) by the LFR in the solar field.

### 3.5.2 Parabolic Trough Collector (PTC)

In parabolic trough collector (PTC), a parabolic shaped concentrator is installed on a strong metallic structure that concentrates the sun's rays on the receiver placed on the focal axis of the parabola. The receiver converts the concentrated solar radiation into heat, and it can be collected by circulating the heat transfer fluid (HTF) flows through it. This HTF can be water, thermal oil, molten salt, or gas depending upon the operating temperature and applications. Concentration ratio up to 100 and temperature up to 500 °C can be achieved in parabolic trough collectors [17]. PTCs require single-axis tracking to track the diurnal motion of the sun. The high solar-to-thermal conversion efficiency, high flux density, versatility, modularity with the low investment cost make PTC as most popular CSP technology for power generation [18]. A parabolic trough collector consists of (a) parabolic concentrators, (b) receiver, (c) tracking mechanism, (d) support structure, and (e) control units (Fig. 3.8).

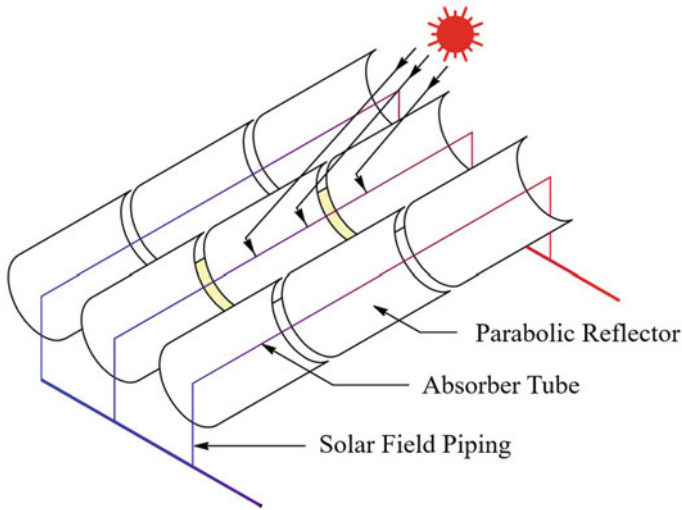


**Fig. 3.8** Schematic of parabolic trough collector [6]

In parabolic concentrators, the reflectors are generally made of either mirrors or aluminum sheets supported and mounted on a structure made up of mild steel or aluminum [19]. A hydraulic or mechanical tracking mechanism with sensors is employed to track the apparent motion of the sun continuously to minimize the cosine losses. The collector is typically placed by aligning the north–south axis and tracked continuously in the east–west direction to minimize the angle of incidence [20]. A single PTC module is designed based on the aperture area and the mirror length. These modules are installed in series to form a large collector that concentrates the solar radiation on the absorber. The absorber tube is encapsulated in an evacuated glass envelope to minimize the convective and radiative heat losses. Non-reflective coatings are used on the glass envelopes to minimize the reflective losses and achieve transmissivity more than 97% [21]. The heated fluid from the receiver can be used for power generation or process heating applications. PTC adopts both indirect steam generation and direct steam generation (DSG) configurations depending upon the applications. However, both of these configurations use the Rankine cycle for power generation.

In an indirect steam generation, the thermal oil is circulated inside the receiver that collects heat, and the heat is transferred to the water in a heat exchanger to generate the steam. The use of thermal oil in the PTC enables heat collection at higher temperatures based on the thermal properties of thermal oil and the design of PTC.

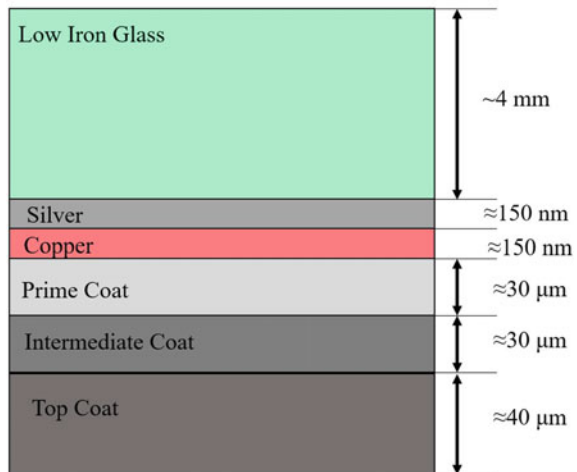


### 3.5.2.1 Concentrator of PTC

The concentrator in PTC is of parabolic shape, which concentrates the solar beam radiation incident perpendicular to the aperture plane on to the focal line. The parabolic concentrators are available in various aperture sizes. Most of the commercially available PTC solar power plants use parabolic concentrators of the aperture with 5.77 m (Eurotrough). However, recently large aperture PTC such as SkyFuel trough of 6 m and Ultimatetrough 7.5 m is under development for reducing the cost of the solar field. The length of PTC is decided by the stiffness of the reflector material since the longer modules reduce the number of pylons and the tracking units, which reduces the cost, e.g., one module of Heliotrough is 19 m long, and the assembly of modules controlled by one drive unit is 191 m long [22]. The rim angle for the commercially available Eurotrough solar collector is  $80^\circ$ . If the rim angle increases beyond the optimal value, the size of the absorber increases.

The typical structure of the silver-coated glass reflector is shown in Fig. 3.9. The silver-coated multilayered low iron content glass reflectors are generally used in commercial in PTC. The first layer below the glass is of reflective silver coating, and low iron content allows more transmission of the solar spectrum through the glass. More than 95% reflectivity can be obtained in the silver-coated mirrors [23]. Polished aluminum surfaces can also be used as a reflector in PTC. However, the reflectivity of the polished aluminum surface is 88.5%, which is less than that of silver-coated mirrors [24].

**Fig. 3.9** Typical structure of silver-coated glass mirror [25]



### 3.5.2.2 Receiver of PTC

The receiver consists of a metallic absorber tube, which is encapsulated in glass cover (Fig. 3.10). The metallic absorber tube and the glass cover are connected by metallic bellows, which compensates the effect of different expansion coefficients of the absorber and the glass cover. The receiver surface is typically coated with a selective coating to enhance its absorptivity and simultaneously reduce the emissivity. Black chrome or cermet is generally used as the selective coating due to ease in manufacturing and better economics [26, 27]. However, the use of glass cover reduces the transmittance due to an increase in reflective losses. To reduce these losses, an anti-reflective coating is provided on the glass cover surface. Additionally, the glass cover material should have low iron content in order to have low absorptance. For low-temperature ( $<300\text{ }^{\circ}\text{C}$ ) industrial applications, the annular space between the tubes is not evacuated. However, for the high-temperature requirements (above  $300\text{ }^{\circ}\text{C}$ ), the annulus between the absorber and glass cover is evacuated ( $5\text{--}10\text{ mbar}$ ) to reduce the convective heat losses. Furthermore, the metal-glass seal provides a tight annular gap between these tubes to maintain the vacuum for a longer duration. The getters (made of metallic compounds) are installed in the vacuum space to absorb the gas molecules that permeate into the vacuum annulus over time. The high cost and technical complexities associated with the evacuated receivers make them suitable for high-efficiency requirements where the poor economics is compensated with better thermal performance.

Generally, a stainless steel tube is used as an absorber placed at the focal line of the parabolic concentrator to form the external surface receiver. The diameter of the absorber usually varies from 25 to 150 mm depending on the size of the aperture of the collector.

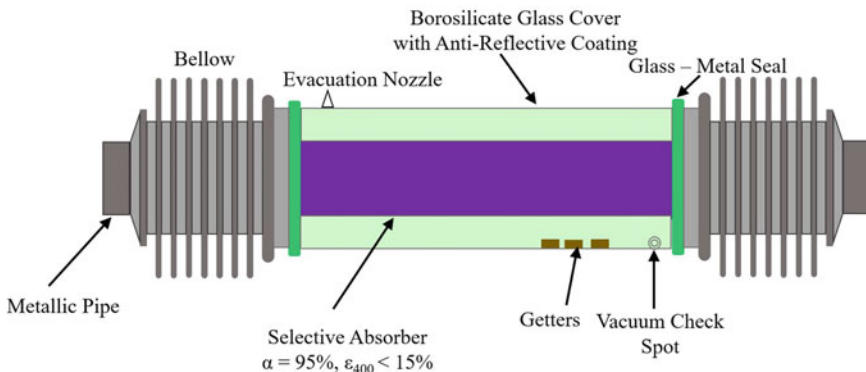


Fig. 3.10 Components of the receiver of PTC [28]

### 3.5.2.3 Power Conversion System

The energy absorbed by the working fluid (HTF) in the receiver can be utilized for powering the power block in the stand-alone power plant or to support the heat addition process in solar aided power plants. The commercial viability and technological maturity of parabolic trough technology make it suitable for both stand-alone power generation and hybridization with the conventional power plants. Based on the operating temperatures of the solar field and type of conventional power plant (for hybridization), the power conversion system may be considered based on the Rankine, Brayton, and combined cycle. The schematic diagram of a typical Rankine cycle-based solar thermal power plant with PTCs is depicted in Fig. 3.11. The overall performance of the power plants depends on its components such as turbine, heat exchangers, and condensers.

### 3.5.3 Central Receiver (CR)

In central receiver systems and also called as power tower systems, an array of dual-axis tracking-based reflectors (heliostats) placed on the ground focus sun rays at the receiver mounted on the centrally located tower (shown in Fig. 3.12). The high concentration ratio (more than 1000) and temperature (up to 1000 °C) can be achieved in the central receiver systems. These systems can be easily integrated with other power generation systems such as coal-fired thermal power plants, biomass-based thermal power plants, natural gas-based thermal power plants to form hybrid plants.

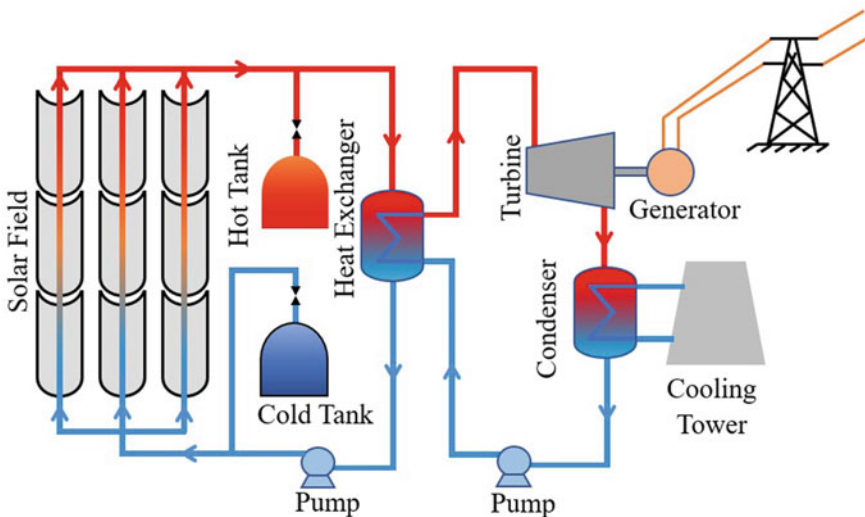
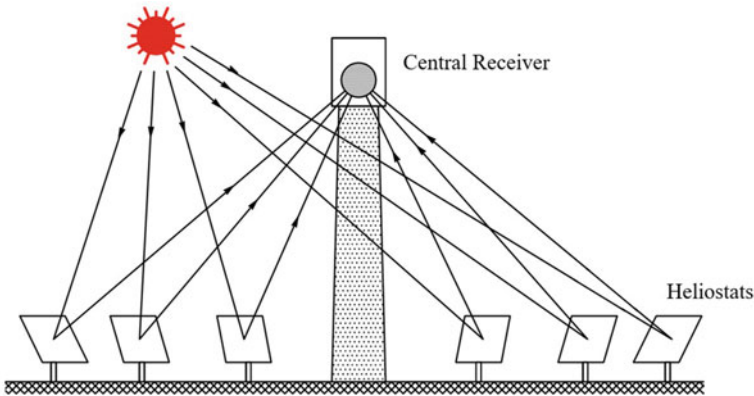


Fig. 3.11 Schematic of typical solar thermal power plant with PTC [29]



**Fig. 3.12** Subsystems of central receiver plant [6]

The annual capacity utilization of 0.4–0.8 can be achieved in such kind of hybrid systems [30, 31].

The central receiver technology is one of the most growing solar power generation technologies due to its superior performance as compared to other available technologies. The entire central receiver system can be classified into three subsystems, such as the heliostat field, receiver/tower system, and power conversion system (Fig. 3.12). The heliostat field consists of multiple reflectors that concentrate incident solar radiation on the receiver mounted on the central tower, where HTF passing through the receiver collects the concentrated thermal energy. The heated HTF is transferred to the power conversion system, where this energy is utilized to generate the electricity.

### 3.5.3.1 Heliostat Field

Heliostats are one of the major components of central receiver systems. Their cost accounts for 50% of the total cost of the plant [32]. The annual energy loss associated with the heliostat field is 47% of the overall annual energy loss from the plant [33]. The heliostat can be developed either by joining multiple low iron glass reflecting mirrors on a single frame or by stretching two membranes on the metallic ring support. The former design of heliostat requires a heavy foundation and has a high cost, while the later design is lightweight and has a low cost. The stretched membrane design is not used widely due to its less durability. Each heliostat is mounted on the metallic support structure, which can track the apparent motion of the sun in the azimuth and elevation axis. The motion to the support is provided with the help of a motor/gearbox system. Figure 3.13 shows the multimirror design of the heliostat. For obtaining a concave surface, multiple reflecting mirrors are mounted on a support structure. The focal length of the heliostat is kept equal to its distance from the receiver.

The design of the stretched membrane heliostat is shown in Fig. 3.14. Two different polymer membranes are stretched on the metallic ring structure to form a stretch

**Fig. 3.13** Multimirror design of heliostat [34]

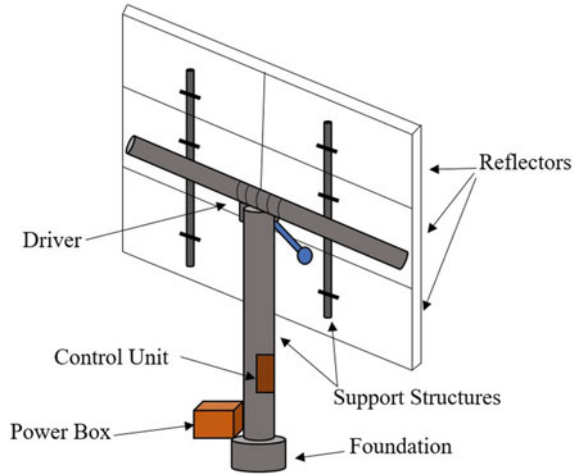
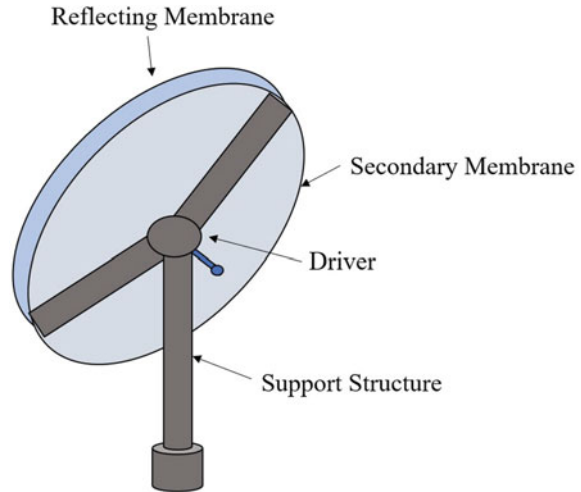


**Fig. 3.14** Stretched membrane design of heliostat [36]



membrane heliostat in which the polymer at the front was laminated by using the silver reflector. The vacuum created in the space between the two membranes of the heliostat can be adjusted to maintain a required focal length. The performance of the heliostat largely depends upon the reflectivity of the mirror, shading and blocking losses, and alignment or canting of each mirror facet mounted on the heliostat, which directly affects the overall performance of the plant. Various canting methods have been suggested in the literature to achieve better performance in power tower plants [35]. The wind load consideration is also necessary due to the large size of the mirrors.

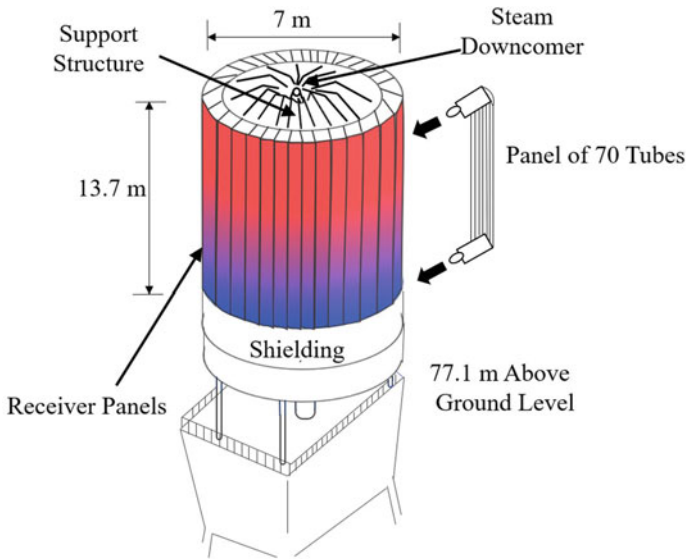


**Fig. 3.15** External receiver of Solar One power plant [33]

### 3.5.3.2 CR Receiver

The objective of the receiver is to absorb the concentrated solar radiation reflected from the heliostats and transmit it to the working fluid passing through it. Receivers are mounted on the top of the centrally located tower. Basically, receivers of the power tower are of two types: External receiver and cavity receiver.

#### External Receiver

In the external receiver, multiple small diameter (20–56 mm), boiler grade tubes are joined together to form a cylinder. The top and bottom of the tubes are connected with the header passage. The inlet and outlet of the tubes are at the bottom and the top, respectively. The external receiver of the Solar One power plant is shown in Fig. 3.15. The receiver is mounted on the tower of 77.1 m height. The 24 panels (bundle of tubes) have tubes of diameter 20–56 mm and length of 13.7 m. The material of fabrication and coating used is Incoloy 800 and pyromark, respectively [33]. The collection performance of the external receiver depends upon the size of the tubes and receiver. The heat losses associated with external receivers are high due to the large exposed area to the atmosphere.

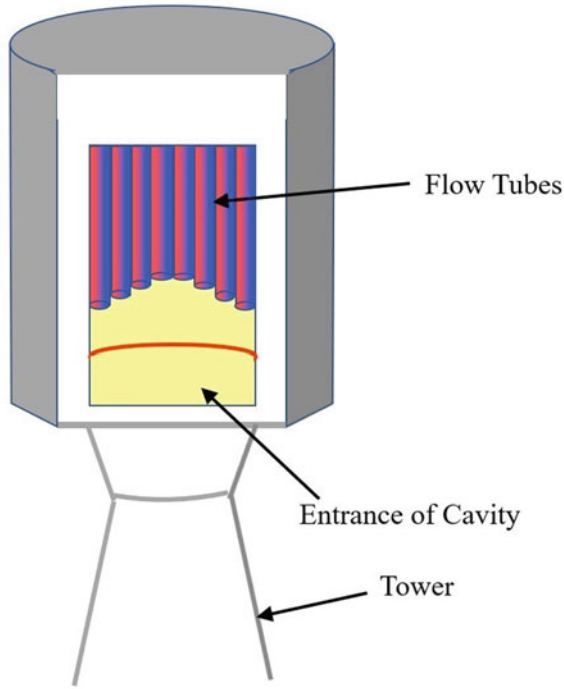


**Fig. 3.16** Schematic of cavity receiver of the solar tower [37]

### Cavity Receiver

Cavity receivers have been explored to minimize the convective heat loss from the large exposed surface of the external receiver, where the absorbing surface of the receiver is placed in the insulated cavity (Fig. 3.16). The size of the aperture area opening of the cavity is generally kept equal to one third or one half of the area of the heat-absorbing surface. Multiple cavities can be used in all four directions of the receiver to collect energy from the particular sector of the heliostats.

The receiver designs discussed so far are generally known as surface receivers or indirectly irradiated receivers because the HTF receives energy indirectly through an irradiated surface of the tube. The directly irradiated receivers are called as the volumetric receiver. In volumetric receivers, the porous substrate absorbs the concentrated solar radiation from the solar field inside the whole volume rather than on the surface. The HTF (usually gas) receives energy from the porous matrix by forced convection (Fig. 3.17).

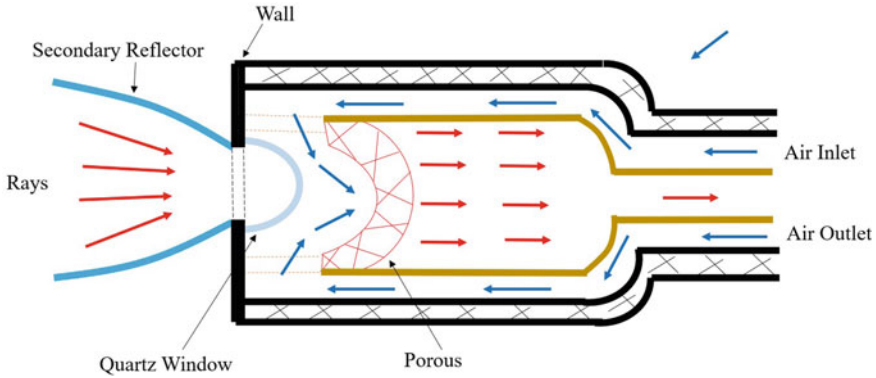


Fig. 3.17 Schematic of the volumetric receiver [34]

### 3.5.3.3 Power Conversion System

The energy collected by the working fluid (HTF) in the receiver can be utilized to operate the power block in the stand-alone power plant and to assist the heat addition process of the power cycle in solar aided power plants. The technical maturity of the central receiver system makes it an excellent technology for the hybridization with conventional power plants. The overall performance of the power conversion system depends upon the performance of its subsystems, such as the turbine, condenser and heat exchangers. Based on the operating temperature in the solar field, the power conversion system may be Rankine/Brayton/combined cycle. A typical Brayton cycle-based solar thermal power generation plant using CR is portrayed in Fig. 3.18. The optimization of the performance parameters in hybrid plants can lead to a better overall conversion efficiency of the plant.

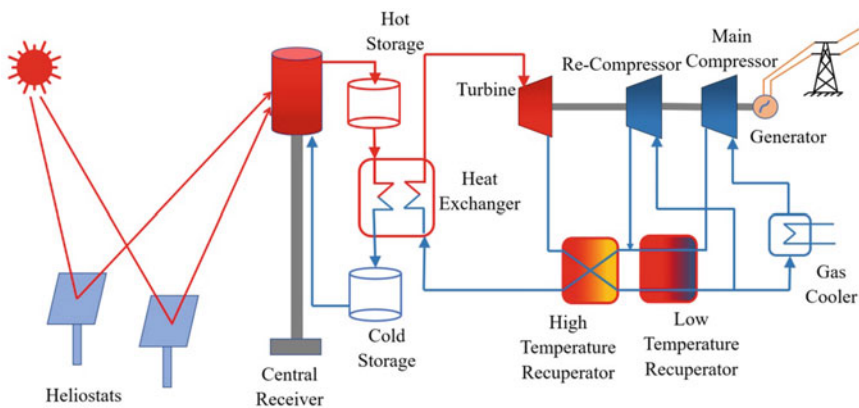


Fig. 3.18 Schematic of a typical solar thermal power plant with CR [38]



### 3.5.4 Parabolic Dish Collector

In parabolic dish collector (PDC), a paraboloid shaped reflector is used to focus the incident radiation on to the receiver placed at the focal point of the paraboloid dish. The absorbed concentrated radiation by the receiver can be utilized either for operating the Stirling engine or to heat the working fluid passing through the receiver. The energy collected using heat transfer fluid can be used to run the power cycle such as Rankine and Brayton cycle. The PDC offers a high concentration ratio, high optical, and conversion efficiency, which make them one of the most performing solar concentrators among other solar concentrating technologies. A solar dish concentrator consists of (a) paraboloid concentrator, (b) receiver having heat exchanger or Stirling engine system, (c) tracking system, and (d) other system control units (Fig. 3.19).

The paraboloid concentrator is made of metalized glass or plastic reflecting surface either as a continuous surface or as a combination of multiple reflectors, and it focuses incident radiation on the receiver mounted on the focal point of the dish. The concentrator is mounted on a strong metallic structure to sustain the wind load. Generally, the tracking system of the solar dish rotates the dish in a plane parallel to the horizontal earth surface (azimuth) as well as around the axis normal to it (elevation), so that the beam radiation incidents always normal to the aperture. The size of the focus depends upon the size of the parabola, focal distance, errors associated with the dish collector. Generally, in dish Stirling systems, the diameter of the dish ranges from 3 to 15 m [39]. The Stirling engine uses the energy of the heated fluid to move the piston and produce the mechanical work (rotation of the engine crankshaft). The rotation of the engine crankshaft can be transmitted to the generator to produce electricity.

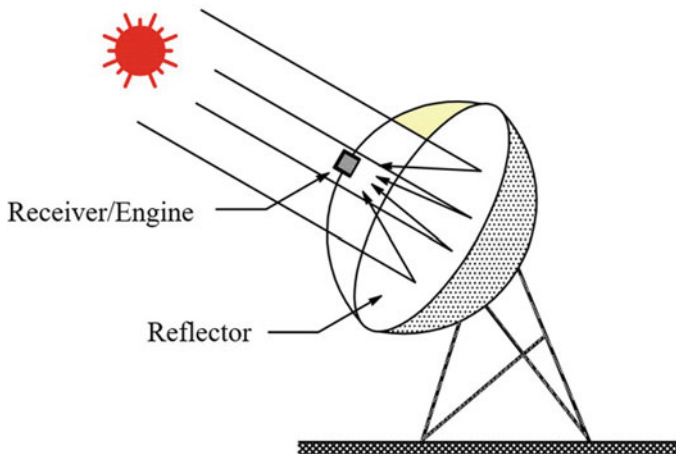


Fig. 3.19 Paraboloid dish collector [6]

**Table 3.1** Various technologies to develop parabolic dish concentrator [42]

S. No.	Concentrators	Description of the technology
1.	Glass faceted concentrator	Individual spherically curved glass reflector facets are mounted on a parabolic metal structure. These concentrators can achieve a high concentration ratio, but these structures are very heavy and require high investment
2.	Full surface parabolic concentrator	These are single surface approximate parabolic concentrators. It is generally available in a limited size
3.	Stretched membrane concentrator	A metallic or plastic sheet having a reflective coating can be stretched on the metallic ring to develop these concentrators. These are suitable for low size dishes only

### 3.5.4.1 Dish/Stirling Power Generation Technology

The thermal energy provided by the dish concentrator can be utilized to operate a Stirling engine, which works on a closed thermodynamic regenerative cycle with gaseous working fluid. Air, hydrogen, or helium is used as the working fluid in the Stirling engine. The work produced by the Stirling engine can be used to operate the generator coupled to it. In the Otto and Diesel cycle, the heat is generated internally into the engine cylinder due to the combustion of the fuel. In contrast, the Stirling engine can receive heat from the external source. The major components of the dish Stirling systems are as follows:

#### Dish Concentrator

The size of the dish concentrator is decided based on the requirement of the heat for the given applications. The modern solar dishes can achieve a temperature of up to 1500 °C and a concentration ratio up to 2000 [40, 41]. There are various technologies available by which the parabolic shape of the dish concentrators can be achieved (Table 3.1).

Typically, glass-based, polished aluminum or acrylic reflectors are used in most of the modern concentrators such as Eurodish, Suncatcher, and Big dish. It can achieve a reflectance of up to 95%. The low-cost reflected polymer films can also be used, but its reflectivity gets deteriorated over a period of time.

#### Receiver of PDC

Generally, cavity receivers are used in PDC, which have a small area of opening (aperture) to receive focused radiation. According to the method of heat transfer, receivers can be categorized into two categories: (a) direct illumination receiver

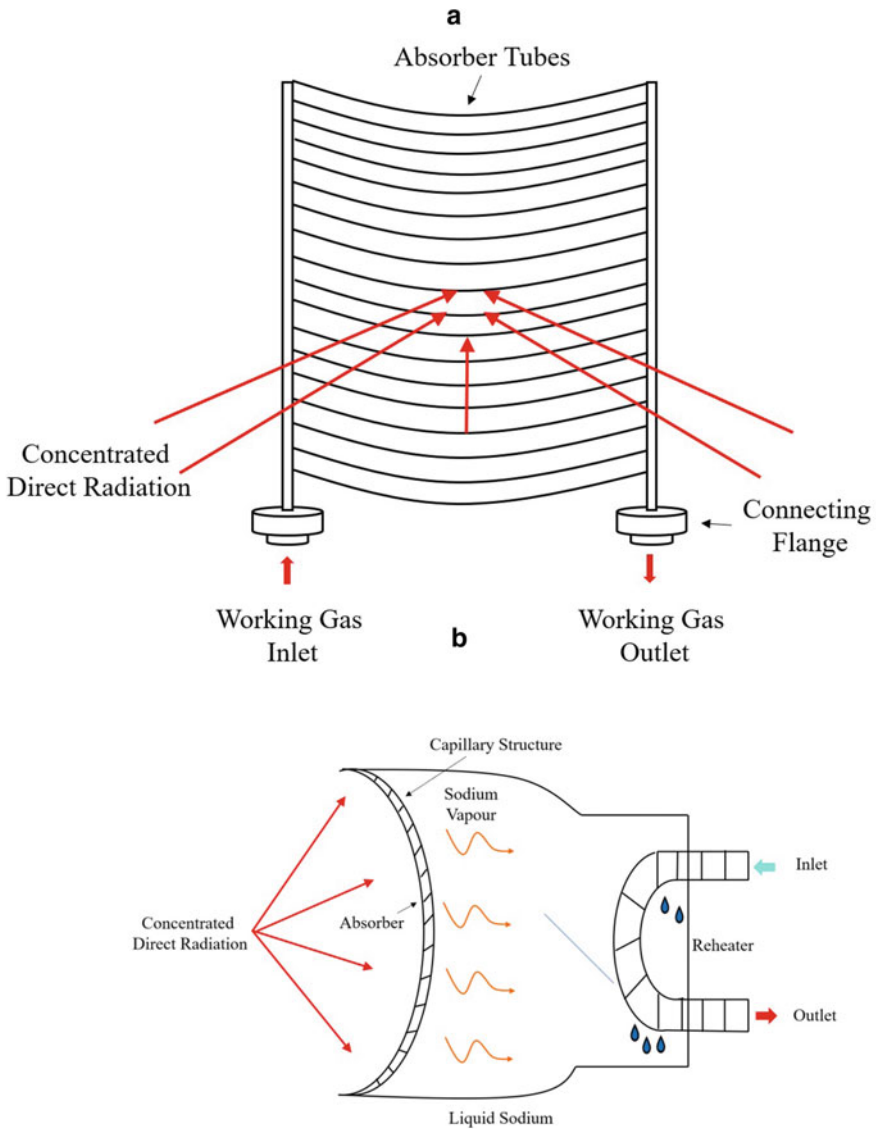


**Fig. 3.20** Receiver design principle, (a) Direct illumination receiver (DIR), (b) heat pipe receiver [40]

(DIR) and (b) heat pipe receiver. In DIR, the receiver collects the heat by absorbing concentrated solar radiation using heat transfer fluid in the form of liquid or gas when it passes through the small tubes in the receiver, and the received thermal energy can be utilized in the power cycle (Fig. 3.20a). In the heat pipe receiver, liquid metal (an intermediate fluid) absorbs the heat at the absorber surface of the receiver by

undergoing vaporization and transfers this heat to the working fluid of the power generation cycle by undergoing condensation on the tube in which the working fluid passes (Fig. 3.20b).

Solar dishes can also be used to produce steam, as in the case of PTC, central receiver, and LFR-based plants. The steam can be used to operate the steam turbine. The thermal energy collected in the dish system can also be utilized for operating the Brayton power cycle. The Stirling engine systems are the most preferred systems as compared to the other power generating systems due to its better conversion efficiency (40%), long cycle life, and low maintenance [39, 41]. The dish/Stirling systems have been tested mostly for decentralized power generation. Their performance evaluation for large-scale power plants is needed for the full-scale commercialization of this technology.

### Stirling Engines

Stirling engine has been designed by Scottish Presbyterian minister, Robert Stirling in 1816. Nowadays, there are various configurations of Stirling engines available such as Kinematic Engines (Alpha, Beta, and Gamma Stirling engines) and free-piston engines. Both the configurations of the Stirling engine have two different pistons sealed in closed volume. The piston in the kinematic engines is connected to a crankshaft to transmit the work to the generator, while the motion of the piston is not constrained by the crankshaft in the free-piston engines. Although the free-piston designs have low frictional losses, the extraction of energy is difficult in these designs. Many designs of free-piston Stirling engines integrated with the bounce chamber have been tested. Stirling engine works based on the Stirling cycle. The discussion on the Stirling cycle can be found in the Sect. 3.6.3.

The working of an Alpha-kinematic Stirling engine with a regenerator can be understood from Fig. 3.21. Due to the motion of piston in compression cylinder, the working gas is transferred to the warm space through the regenerator, where it gets heated due to the previously absorbed thermal energy and reaches the warm space. The temperature of the regenerator section decreases up to the temperature of the cold space; (Fig. 3.21a). The further heating of the gas is done in the warm space, which expands it isothermally and produces mechanical work; (Fig. 3.21b). After this stage, the piston in the working cylinder begins to close and forces the hot gas toward the cold space through the regenerator, where it transfers heat to the regenerator by undergoing isochoric operation; (Fig. 3.21c). The working gas achieves the temperature equal to the cold space, while the regenerator achieves the temperature equal to that in the hot space. Finally, the working gas is compressed isothermally, and the exhaust gas is transferred to the cold space (Fig. 3.21d). Figure 3.22 represents the power generation process of the dish/Stirling systems.

Every CSP technology has its own advantages and limitations, which are related to its design and operating parameters. Concentrating solar power generation systems based on PTC and CR are the more mature technologies as compared to the others. Table 3.2 represents the comparison of various available CSP technologies.

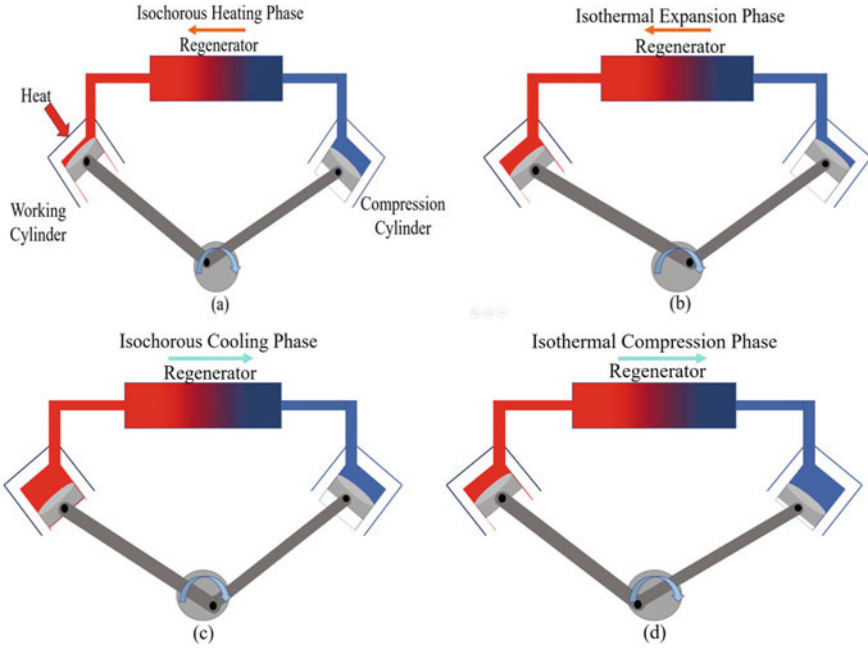


Fig. 3.21 Working of the Stirling engine [40]

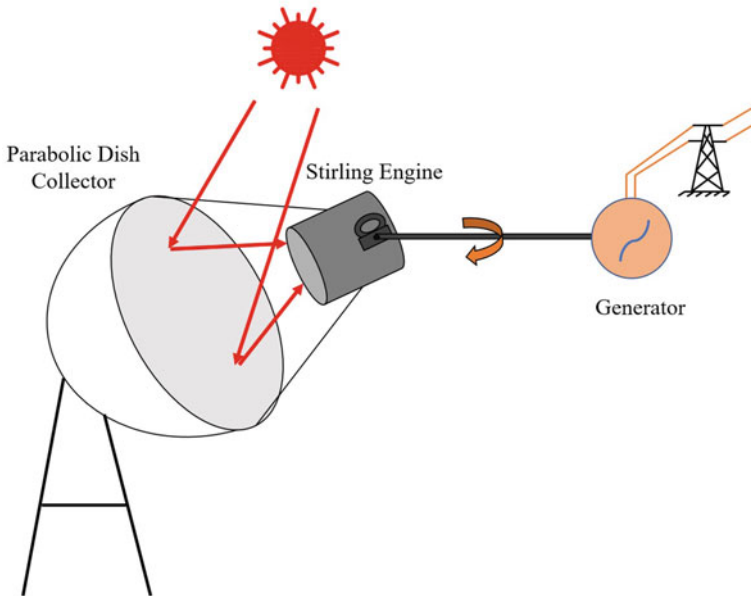


Fig. 3.22 Power generation using the dish Stirling system. Source Author

**Table 3.2** Comparison between CSP technologies [31, 43]

Characteristic parameters	LFR	PTC	CR	PDC
Collector optics	Line focus	Line focus	Point focus	Point focus
Receiver	Fixed	Mobile	Fixed	Mobile
Concentration ratio	$\geq 60$	70–80	$\geq 1000$	$\geq 1300$
Solar-to-electric conversion efficiency (%)	10–13	11–16	7–20	12–25
Technology development risk	Medium	Low	Medium	Medium
Typical capacity (MW)	10–200	10–300	10–400	0.01–0.025
Maturity of technology	Pilot project	Commercially proven	Commercially proven	Demonstration projects
Operating conditions (°C/bar)	260/50	380–540/100	540/100–160	555–750/NA

### 3.6 Power Generation Cycles

#### 3.6.1 Rankine Cycle

Rankine cycle was designed by William John Macquorn Rankine, who was a Scottish polymath and Professor at Glasgow University. Rankine cycle is a closed power cycle where the liquid working fluid is pumped to high pressure, and then, it is heated at constant pressure to convert it into vapor. This high-temperature and high-pressure vapor is then passed through the turbines to produce mechanical work. Afterward, the low-pressure vapor at the turbine outlet is condensed using condenser and cooling towers, and then, it is recirculated to the cycle again. The mechanical work obtained at the turbine shaft is used to run the alternator to generate electricity. The different modifications have been performed, such as reheating between the turbine stages and similarly, intercooling between the pumps in the Rankine cycle to increase its efficiency. Furthermore, regeneration in the Rankine cycle increases the mean temperature of heat addition by reducing the low-temperature heating of the feed stream in the boiler and replacing this by mixing of feed stream with a bled stream from the turbine stages.

Steam-based Rankine cycle is generally used for electricity generation in thermal power plants; either it is powered by fossil fuels such as coal, diesel or solar energy or nuclear power. The steam-based Rankine cycle ideally comprises four different processes, namely isentropic compression, isobaric heat addition, isentropic expansion, and isobaric heat rejection. These processes are depicted on the pressure–volume, temperature–entropy, and enthalpy–entropy diagrams, as shown in Fig. 3.23.

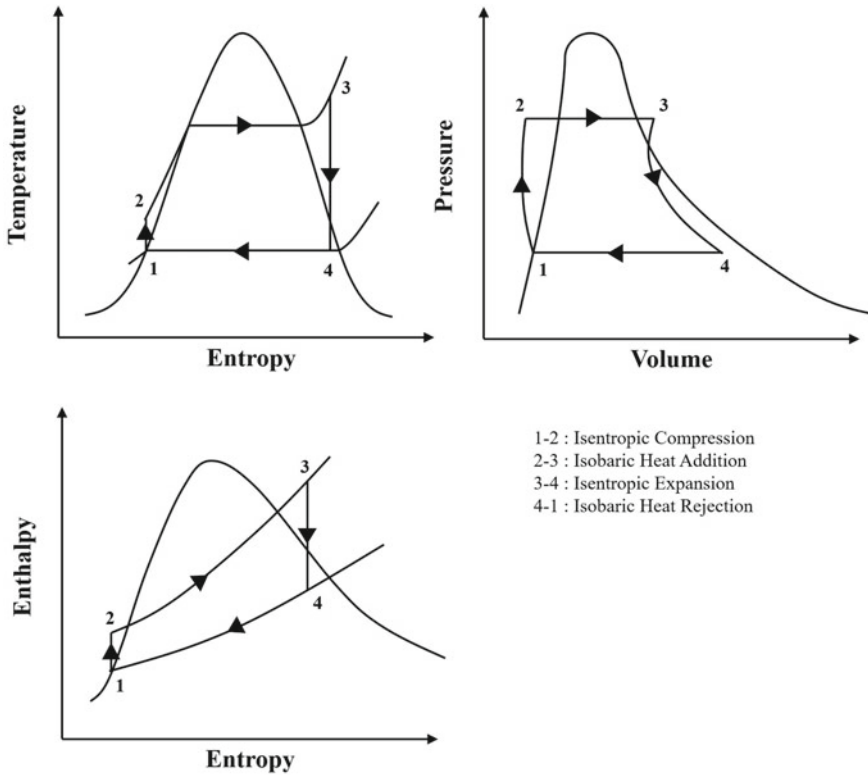


Fig. 3.23 Ideal Rankine cycle. Source Author

### 3.6.2 Brayton Cycle

In 1870, George Brayton proposed a cycle for reciprocating oil engine. Nowadays, it is being utilized for gas turbine power plants where compression and expansion of the working gas are done in separate rotating machinery. The ideal Brayton cycle comprises two reversible adiabatic (isentropic) processes and two isobaric (constant pressure) processes. Figure 3.24 represents the ideal Brayton cycle on pressure–volume and temperature–entropy coordinates. The working gas (air) is compressed isentropically from state 1 to 2 in a compressor. Heat addition to the high-pressure air coming from the compressor is done in a heat exchanger during isobaric process 2 to 3. The isentropic expansion of high-temperature and high-pressure air is done in a turbine during process 3 to 4. During this process, the power is generated, which can be further utilized to operate the generator for producing electricity. The air at state 4 is cooled down to state 1 at constant pressure in another heat exchanger and passes to the compressor again to repeat the cycle.

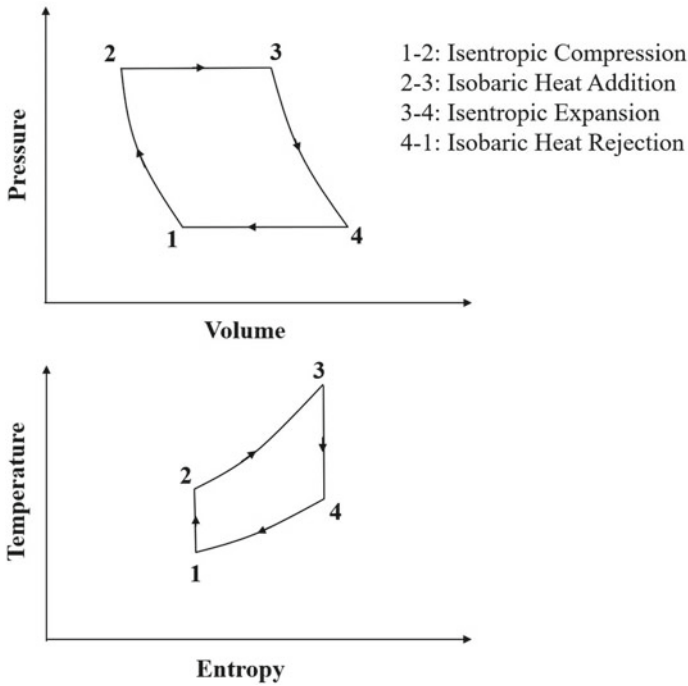


Fig. 3.24 Ideal Brayton cycle. *Source* Author

### 3.6.3 Stirling Cycle

The Stirling cycle is gaining the interest of the researchers from the last few years due to its high efficiency. Theoretically, it can achieve an efficiency equal to the Carnot efficiency. The engines based on the Stirling cycle are called external combustion engines because it can receive heat from the outside of the engine by burning any fuel or by concentrated solar radiation. The Stirling cycle is a closed thermodynamic cycle which ideally comprises four different processes, such as isothermal compression and isothermal expansion, isochoric heat addition, and isochoric heat rejection. These processes are represented on the pressure–volume and temperature–entropy coordinates in Fig. 3.25.

During the process 1–2, the working gas is compressed by utilizing the previously stored energy from the engine’s flywheel. The temperature at state 1 and 2 remains the same. The pressurized working gas at state 2, having minimum volume and minimum temperature, is heated from state 2 to state 3 by keeping the volume of the system constant. At state 3, the highest temperature and pressure are achieved in the system. During processes 3–4, the gas is allowed to expand and produce useful mechanical work, which is more as compared to the work utilized during the compression cycle. The net work produced can be utilized for generating electricity. Now, the engine



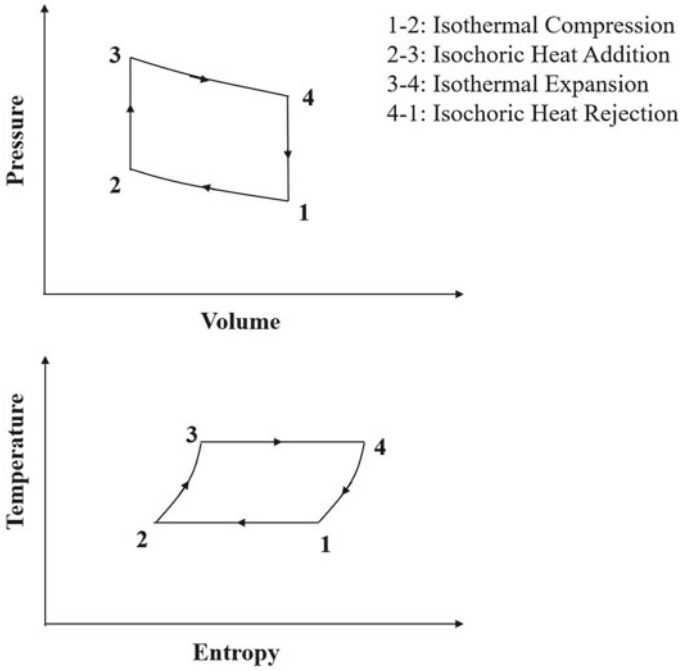


Fig. 3.25 Ideal Stirling cycle. Source Author

attains the state 1 again by rejecting heat during a constant volume process (from state 4 to 1).

### 3.7 Hybridization of CSP Systems

The CSP systems are economically suitable for electricity generation for locations having DNI greater than 2000 kWh/m<sup>2</sup>/year. The investment cost of the stand-alone CSP power plant is also very high. The transient nature of solar radiation and the unavailability of solar radiation during the night limit the dispatchability and reliability of the solar thermal systems for electricity generation. On the other hand, the conventional power plants face problems of environmental pollution, running out of fossil fuels, and hike in the price of fossil fuels. To overcome these problems, hybrid power generation systems can be developed where energy from solar and fossil fuel sources is used to generate electricity. Solar thermal power plants have enormous potential to be integrated with the existing conventional power plants. The integration of CSP systems with conventional power plants increases the efficiency, reduces the overall cost, and increases the dispatchability and reliability of the solar

power generation system. The CSP systems can be hybridized with coal, natural gas, biofuels, and geothermal energy.

The working fluid in the CSP system is heated by the concentrated solar radiation. The heated fluid can be used in the conventional power plant to produce electricity. The extent of the share of solar heat in the hybrid power generation system depends on technical feasibility. The share of solar heat in hybrid systems may be light, medium, and high. In light and medium hybrid systems, a small fraction of total energy is supplied by solar heat, and the role of CSP is less. The CSP system cannot generate electricity without the hybrid components of conventional systems. In the hybrid system with high solar share, the CSP share is more critical for power generation and can generate power without the fossil backup. The hybridization of CSP with conventional power plants includes hybridization with coal, hybridization with natural gas, hybridization with biofuels, and hybrid solar-CC (combined cycle) power plants.

### 3.7.1 Hybridization with Coal

The hybridization of CSP systems with the existing conventional coal power plant is one of the promising options to extract solar heat to augment with the coal power plants. The solar heat can be supplied either directly to the boiler for superheating or to preheat the boiler feedwater and air. Figure 3.26 shows the hybridized CSP plant where high-pressure steam is generated in the solar field and further added to the coal-fired boiler for superheating. The steam can be generated in the solar field by using PTC, LFR, or CR solar thermal systems. Here, the presence of two-phase flow at high pressure and temperature may induce thermal instability in the solar collectors.

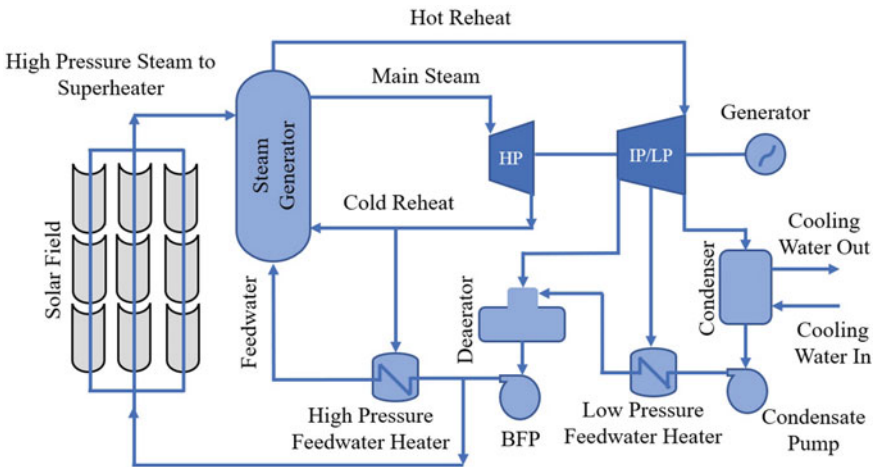


Fig. 3.26 Solar heat augmentation to the boiler for superheating [44]

The solar heat can be added to the coal power plant to preheat the boiler feedwater by the CSP system. This method is simpler as it eliminates the two-phase flow in the solar collectors as in the case of direct steam generation, and there is no requirement of the HTF-water heat exchanger as in the case of indirect steam generation. The coal-fired boiler is used to generate superheated steam to ensure a stable and efficient steam cycle. The heat losses from the solar field are also reduced because of lower operating temperatures (generally near or below 300 °C). The output of the plant increases as there is no extraction of bleed steam from the turbine for feedwater heating. Similarly, the preheating of air to the boiler by using the CSP system is another way of boiler preheating by using solar heat. The hybrid CSP with coal may generate 25% more electricity and has only 72% of the total investment cost as compared to stand-alone CSP plant [45]. The solar-to-electric conversion efficiency also increases as compared to the stand-alone solar thermal power plants.

### 3.7.2 Hybridization with Natural Gas

The gas turbine power generation system works on the Brayton cycle and typically operates as an open system. In a hybrid CSP-gas turbine power plant, the solar receiver is used to heat the pressurized air before the combustion. Figure 3.27 shows the process flow diagram of a hybrid CSP-gas turbine power plant. The solar heat added to the cycle at the stage of post-compression and pre-combustion. After this, adequate operating temperature is achieved by the combustion of fuels in the

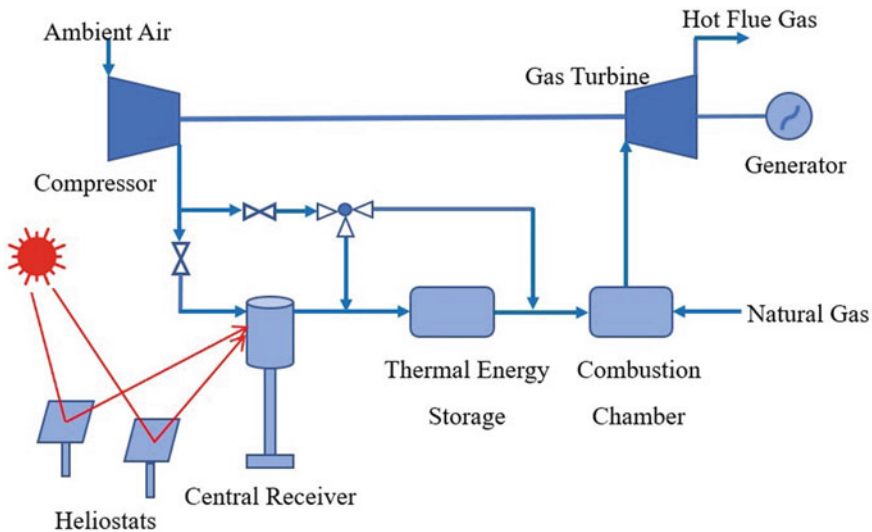


Fig. 3.27 Integration of solar heat with the gas turbine power plant [44]

combustion chamber. The variation in solar heat is compensated by controlling the fuel combustion. In a case study of the design of 30 MW hybrid CSP-gas turbine power plant, the annual overall efficiency increases from 15.9 (stand-alone solar thermal) to 19.0 (for hybrid) and capacity factor from 29.2 to 43.5% [46].

There is another way of hybridization of CSP and gas turbine working on a closed cycle. In this system, the pressurized air is heated by the solar receiver and then passes through the combustion chamber where the fuel is fired separately from the air stream. This hybridization concept is ideal for supercritical CO<sub>2</sub> because of the higher gas–volume ratio as compared to the air, which reduces the power consumed by the compressor. The hybridization of CSP with the gas turbine is more suitable as compared to coal power plants because of the potential to achieve higher solar fraction.

### 3.7.3 Hybridization with Biofuels

Hybridization of CSP systems with biofuels exhibits similar benefits as with conventional fossil fuel plants. The CSP systems can be integrated with various biomass sources such as stubble, forestry residues, wood waste, bagasse, and refuse-derived fuels. In hybrid CSP-biomass systems, the steam can be generated by biomass boiler in parallel with solar field steam generation systems. The biomass can also be applied to superheat the steam generated from the solar field to increase the power block efficiency. Another way of hybridization of the CSP system with biofuels is shown in Fig. 3.28. The heat transfer fluid from the solar field passed through the duct burner to further heat it at an adequate temperature level by combustion of biogas/syngas.

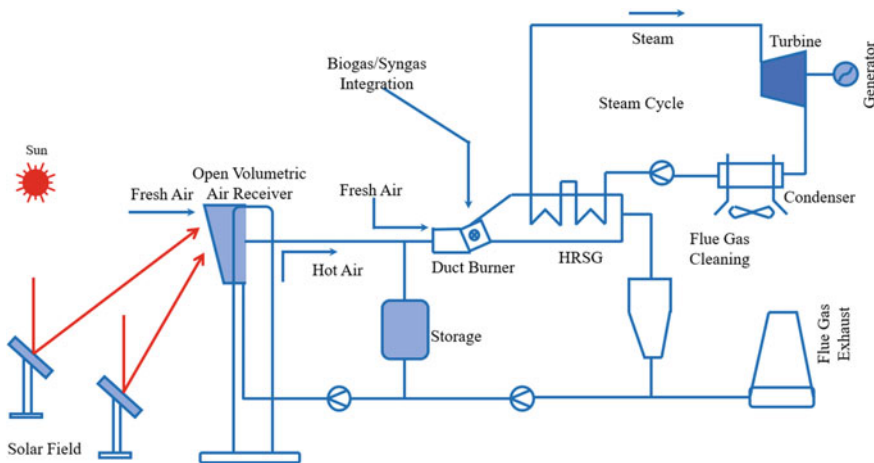


Fig. 3.28 Hybrid solar-biogas/syngas power plant [47]

The HTF further passes through the heat exchanger to generate steam to run the steam turbine.

### 3.7.4 Hybrid Solar-Combined Cycle Power Plants

The hybrid solar-natural gas combined cycle (CC) power plant is another way of hybridization of CSP systems. In a hybrid solar-CC power plant, the CSP system working on the Rankine cycle is integrated with the gas turbine power plant working on the Brayton cycle (Fig. 3.29). The hot gas that comes out from the gas turbine is used to generate steam in augmentation with the solar heat. The study has shown that the solar-CC power plant reduces the cost of solar electricity generation by 35–40% as compared to the stand-alone CSP system and improves the dispatchability of the CSP system [48].

## 3.8 Advancements in CSP

The electricity generation from CSP is getting more attention from the last four decades because of the large scope to reduce levelized cost of electricity (LCoE) by

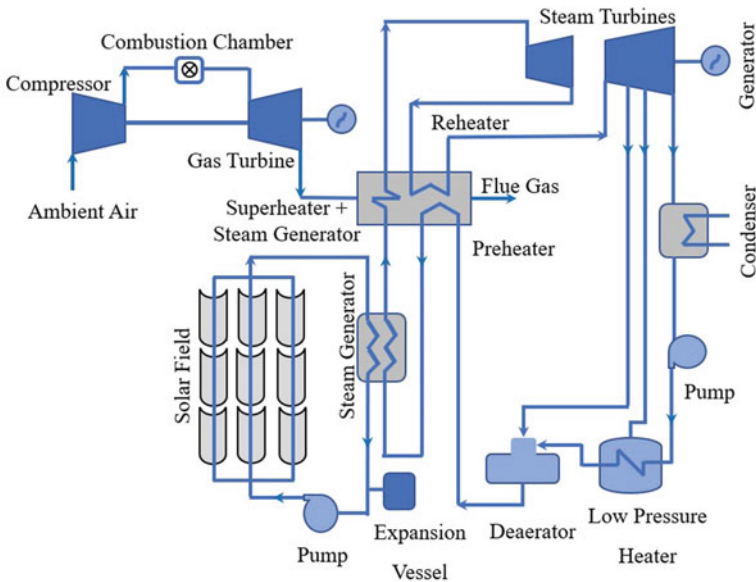


Fig. 3.29 Combined cycle power plant with solar heat augmentation [49]

advancements in the design of CSP components. The advancements in CSP components improve the thermal performance and reduce the overall cost of the plant. This is to make it economical and cost-competitive as compared to the other electricity generation systems. To overcome this challenge, many improvements have been continuously adopted in the solar reflector, receiver design, heat transfer fluid (HTF), heat absorption and transmission systems, power production systems, and thermal energy storage (TES) systems.

Solar reflectors (mirror/concentrator) are one of the important components of the solar collector which receives solar radiation. The characteristics of an efficient solar reflector are shown in Fig. 3.30. The small improvement in surface reflectance has a high impact on the annual performance of the solar field. Currently, the trends are going toward the development of thin silvered-glass reflectors because of high specularly and durability as compared to silvered-polymer mirrors. High reflectance can be achieved by a reduction in thickness of the transparent material (glass/polymer). The prototype mirrors have been developed, having reflectance more than 97%. Anti-soil coating on the mirror surface also improves the optical performance and life of the reflector.

Most of the existing CSP plants use oil and molten salt as HTF. Several alternative HTF/working fluids such as water/steam, molten salts, liquid metals, compressed gases (air, CO<sub>2</sub>, N<sub>2</sub> and He), and nano-fluids have been investigated for performance improvements in CSP. The HTFs should have good thermal and chemical stability, low vapor pressure, long life and should be available at affordable prices.

The integration of thermal energy storage (TES) with CSP enables the plants to operate as per the demand. TES also helps to reduce/eliminate the effect of clouds on the power plant operation and enables it to run during the nighttime when the solar radiation is not available. This reduces the LCoE and increases the dispatchability of the solar thermal power plant.

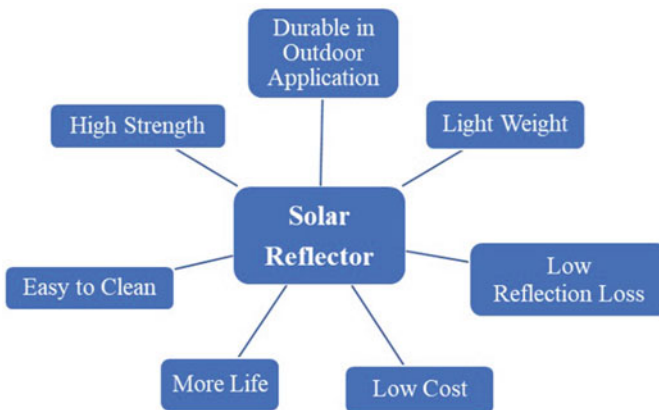


**Fig. 3.30** Characteristics of a solar reflector for better performance. *Source* Author

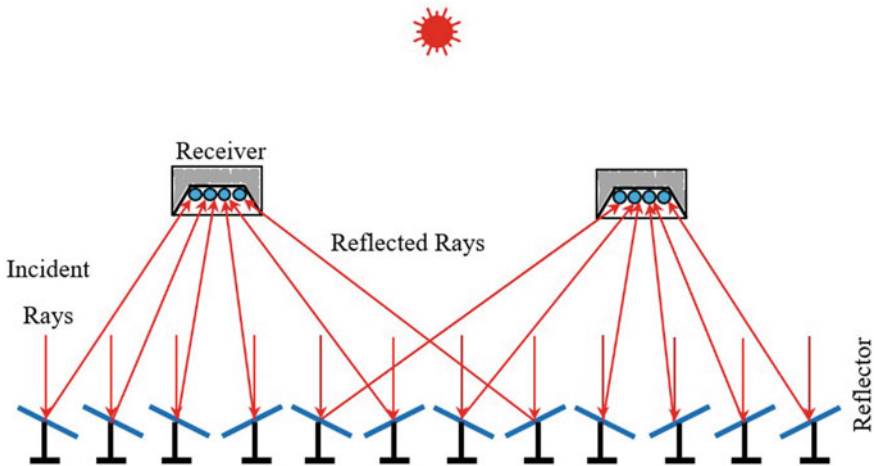


Fig. 3.31 Schematic of compact linear Fresnel reflector (CLFR) system [50]

### 3.8.1 Advancements in LFR

The conventional LFR system uses an inverted trapezoidal cavity receiver. The optical losses in the solar field and heat losses from the receiver are more in the conventional LFR power plants. The efficient utilization of ground and optical loss due to shading and blocking can be minimized by using the compact linear Fresnel reflector (CLFR) system (Fig. 3.31). In CLFR, two parallel receivers are used for each row of reflectors, and the mirrors are arranged in such a way that consecutive mirrors focus the incident solar radiation at the receiver on both sides.

The heat losses from the receiver can be minimized by using a secondary reflector (Fig. 3.32). The secondary reflector focuses all the reflected solar radiation to reach the receiver surface. This configuration enables a greater number of reflectors in the collector module, minimizes the convective heat loss, more homogeneous heating of the absorber tube, and could achieve high operating temperature (up to 500 °C).

### 3.8.2 Advancements in PTC

The conventional PTC power plants are based on indirect steam generation (ISG), where synthetic oils are used as heat transfer fluid (HTF). The oils have poor heat transfer characteristics, relatively high cost, and degradation in the properties due to continuous heating and cooling. The limitation of maximum operating temperature (~390 °C) reduces the thermal performance of the system. To overcome these problems, water/steam can be used as HTF/working fluid, and the steam can be generated in the solar collectors. In this case, there is no requirement of an oil–water heat

**Fig. 3.32** Schematic of the receiver with secondary reflector for LFR system [50]

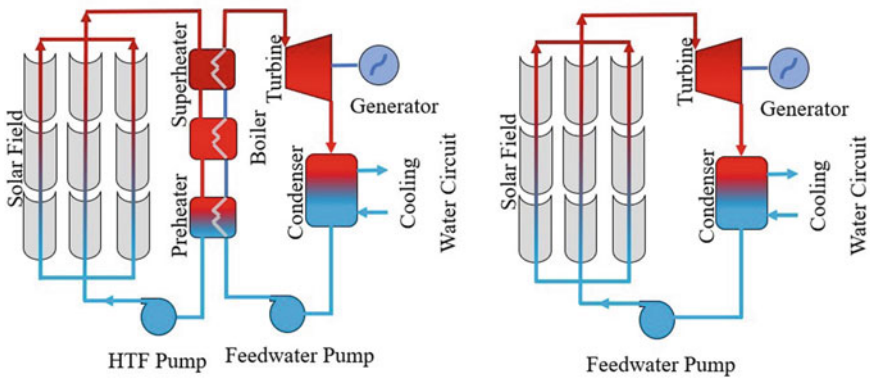
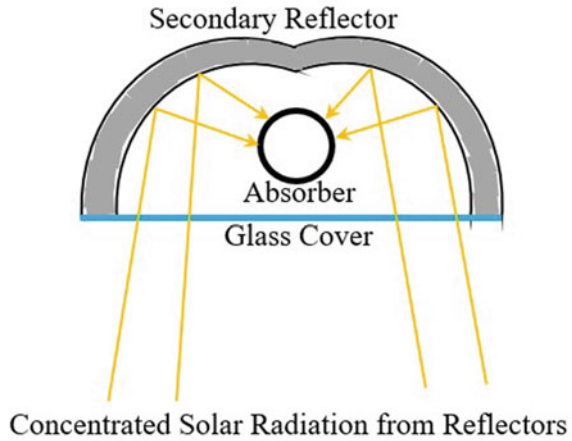


**Fig. 3.33** Schematic of (a) indirect steam generation PTC system and (b) direct steam generation PTC system [51]

exchanger and expensive HTF, which reduces the capital cost of the plant (Fig. 3.33). This is also called as direct steam generation (DSG). DSG in the solar field enables to generate steam at high temperature (up to 550 °C). There is a scope of cost reduction in the PTC solar power plant by employing a large aperture area solar collector. Research is under progress for the development of large aperture PTC.

### 3.8.3 Advancements in Central Receiver (CR) System

The current CR power plants use water/steam or molten salts as HTF/working fluid and operate on a Rankine cycle with a turbine inlet temperature <600 °C. The CR is



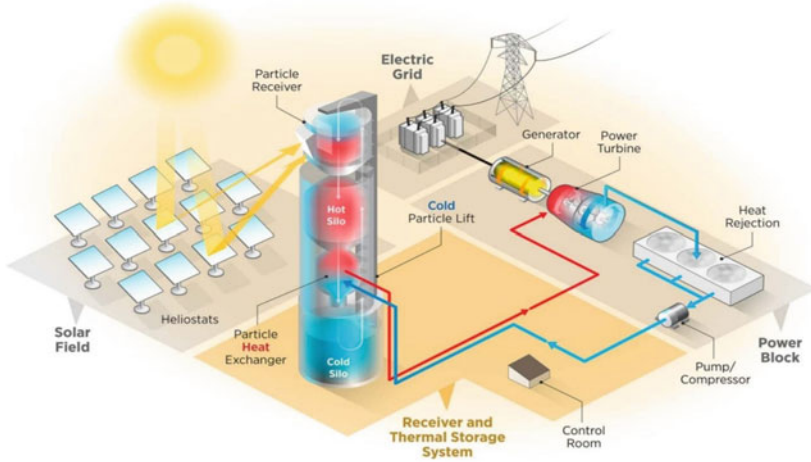


**Fig. 3.34** Falling particle receiver for the central receiver system [52]

a point focusing solar thermal technology having high concentration ratio and high temperature ( $>600\text{ }^{\circ}\text{C}$ ). Various receiver designs such as volumetric air receiver, falling particle receiver, and liquid metal receiver have been tested to achieve high temperature ( $>1000\text{ }^{\circ}\text{C}$ ) for power tower applications.

The falling particle receivers conceptualized by Sandia National Laboratories is a highly efficient receiver is designed with less cost for central receiver solar thermal technology to achieve high operating temperature ( $>1000\text{ }^{\circ}\text{C}$ ). The falling solid particles are heated by concentrated solar radiation and stored at high temperatures that can be used to heat the working fluid (Fig. 3.34). The cost of thermal energy storage is reduced significantly by directly storing the solid heated particles.

In the beam down concentrator concept of the power tower, the secondary reflector is used at the top of the tower to redirect the concentrated solar radiation to the receiver placed at the ground (Fig. 3.35). In this concept, all major equipment are placed at the ground. The easy installation, operation, and maintenance reduce the overall cost of a solar thermal power plant. Masdar Institute Solar Platform (MISP) developed a 100 kW solar beam down concentrator facility (Fig. 3.35) for research purposes [53]. The array of 45 mirrors are placed at the top of the tower (height 20 m) to redirect the solar radiation at the receiver which is placed at the ground.

The higher efficiency power cycles like an air-Brayton cycle, supercritical- $\text{CO}_2$  Brayton cycle, and ultra-supercritical steam cycle have been investigated for central receiver CSP systems. The performance of various power cycles with turbine inlet temperature is shown in Fig. 3.36. These advanced power cycles have the potential to make the future CSPs cost-competitive as compared to the other electricity generation systems.

$\text{CO}_2$  has been employed as HTF/working fluid in the Brayton cycle for power tower (Fig. 3.37).  $\text{CO}_2$  is non-toxic, low corrosive, non-flammable, and low-cost fluid



Fig. 3.35 Solar beam down concentrator facility at Masdar Institute Solar Platform (MISP) [53]

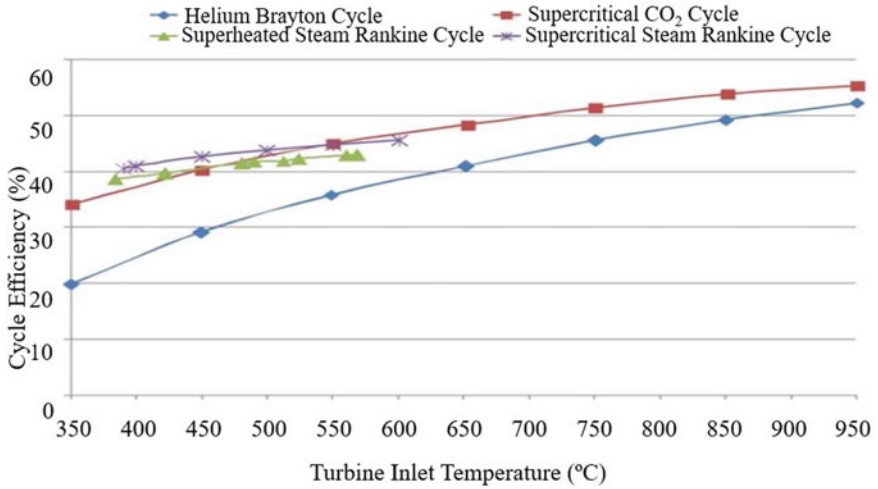


Fig. 3.36 Thermal performance of various power cycles with turbine inlet temperature [54]

having high density near the critical point. The compressor work is reduced in the supercritical-CO<sub>2</sub> Brayton cycle when CO<sub>2</sub> enters the compressor near the critical point. The single-phase reduces the operational complexity and can be integrated easily with sensible heat TES systems.

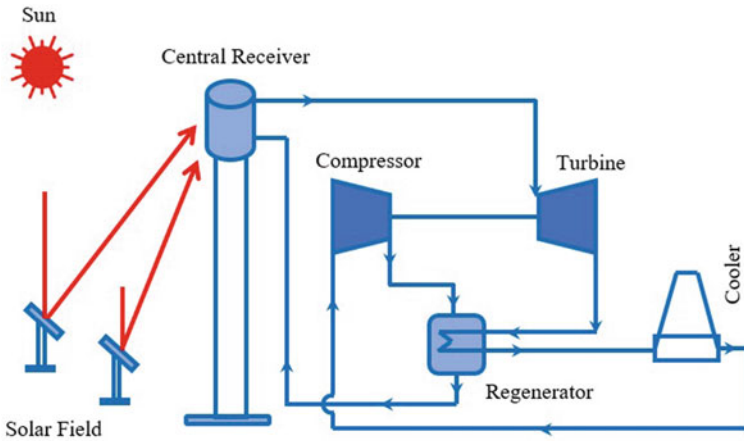


Fig. 3.37 Supercritical-CO<sub>2</sub>-based Brayton cycle for power tower [55]

### 3.9 Current Status of CSP Technology

The power generation for commercial applications using solar thermal technologies was started in 1985. In the present scenario, solar thermal technologies are getting more attention among other renewable energy technologies as it has high reliability and dispatchability because of its low-cost storage capability. The current status (until June 2020) of worldwide concentrated solar power projects is shown in Figs. 3.38, 3.39 and 3.40. The total capacity of concentrated solar power projects around the world is 8353 MW, among which 66% are operational, 17% are under

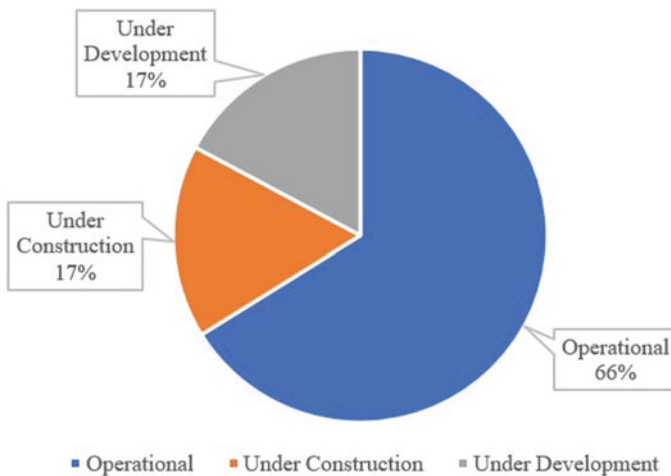


Fig. 3.38 Worldwide total plant capacity of CSP [56]

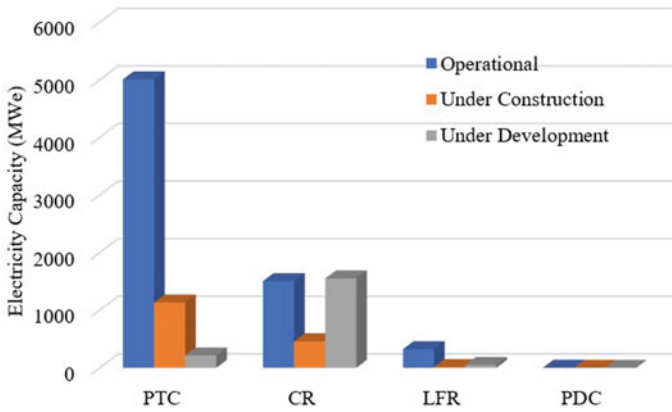


Fig. 3.39 CSP projects categorized by technology [56]

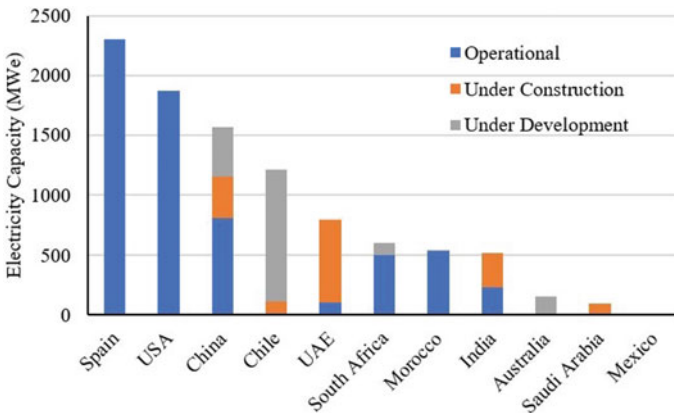


Fig. 3.40 Status of CSP projects in various countries by May 2020 [56]

construction, and 17% are under development [56]. PTC has the maximum installed capacity among all other solar thermal technologies followed by CR and LFR, as shown in Fig. 3.39. Presently, no power plant is operational using PDC solar thermal technology. Spain is the leading country in concentrated solar power generation, followed by the USA, China, Chile, and the UAE.

### 3.10 Summary

Solar energy is the most promising renewable source as it has the potential to fulfill the gap between energy demand and supply without any adverse impact on the environment. In a solar thermal energy system, solar collectors are used to convert solar radiation into heat. The non-concentrated solar thermal energy systems are used for low-temperature applications such as household heating applications and industrial process heating, whereas the concentrated solar thermal energy systems are used for high-temperature applications such as power generation and industrial process heating applications. In solar thermal power generation, solar collectors are used to collect the heat from the incident solar radiation. The heat extracted from the solar collectors is employed in the thermodynamic cycle to generate electricity. Linear Fresnel reflector (LFR), parabolic trough collector (PTC), central receiver (CR), and parabolic dish collector (PDC) are commercially available solar thermal technologies. The solar collector constitutes a concentrator (reflector) and receiver. Tracking systems are used to track the apparent motion of the sun so that the solar beam radiation incident on the aperture can be concentrated on the receiver. Rankine, Brayton, and Stirling cycle are commonly used thermodynamic cycles for solar thermal power generation. The integration of thermal energy storage and hybridization of solar thermal energy systems with conventional power generation systems improves the performance and dispatchability of the solar thermal systems. Advancements in the design of the solar thermal components improve the performance and consequently reduce the cost of electricity generation. This chapter discusses all the available CSP technologies and highlights the various design and operational parameters on which the overall efficiency of the solar power plants depends. The recent advancements in this field and various solar hybrid power generation technologies are also discussed. Harnessing solar energy for power generation is one of the most popular technologies in the field of power generation; therefore, efforts are being made to unlock its full potential.

### References

1. Flat Plate Solar Collector | Hi-MIN. <http://himinsun.com/4-7-flat-plate-solar-collector.html>. Accessed 21 Sept 2020
2. Abdalla FK, Paul W (2002) Optimum operating temperature for evacuated tube solar collectors. In: 40th Annual conference of the Australian and New Zealand solar energy society (ANZSES), pp 3–8
3. Solar Water Heaters, Hot Water Systems | Apricus Eco-Energy. <https://www.apricus.com/>. Accessed 21 Sept 2020
4. Calise F, D'Accadia MD, Santarelli M, Lanzini A, Ferrero D (2019) Solar hydrogen production: processes, systems and technologies. Academic Press
5. El Gharbi N, Derbal H, Bouaichaoui S, Said N (2011) A comparative study between parabolic trough collector and linear Fresnel reflector technologies. *Energy Procedia* 6:565–572. <https://doi.org/10.1016/j.egypro.2011.05.065>

6. Sharma C, Sharma AK, Aseri TK, Mullick SC, Kandpal TC (2015) Solar thermal power generation. In: Saxena P, Garg HP, Sastry OS, Singh SK (eds) *Advances in solar energy science & engineering*, vol 1. Today & Tomorrow's Printers and Publishers, pp 89–153
7. Haegel NM, Atwater H, Barnes T et al (2019) Terawatt-scale photovoltaics: transform global energy. *Science* 364(6443):836–838. <https://doi.org/10.1126/science.aaw1845>
8. Bogdanov D, Farfan J, Sadovskaia K, Aghahosseini A, Child M, Gulagi A, Oyewo AS, De Souza L, Simas N, Breyer C (2019) Sustainable electricity via evolutionary steps. *Nature Commun*, pp 1–16. <https://doi.org/10.1038/s41467-019-08855-1>
9. Kumar A (2017) A review on progress of concentrated solar power in India. *Renew Sustain Energy Rev* 79:304–307. <https://doi.org/10.1016/j.rser.2017.05.086>
10. Bellos E, Tzivanidis C, Papadopoulos A (2018) Optical and thermal analysis of a linear Fresnel reflector operating with thermal oil, molten salt and liquid sodium. *Appl Therm Eng* 133:70–80. <https://doi.org/10.1016/j.applthermaleng.2018.01.038>
11. Bellos E (2019) Progress in the design and the applications of linear Fresnel reflectors—a critical review. *Therm Sci Eng Progr* 10:112–137. <https://doi.org/10.1016/j.tsep.2019.01.014>
12. Almanza R, Hernández P, Martínez I, Mazari M (2009) Development and mean life of aluminum first-surface mirrors for solar energy applications. *Sol Energy Mater Sol Cells* 93(9):1647–1651. <https://doi.org/10.1016/j.solmat.2009.05.004>
13. Nostell P, Roos A, Karlsson B (1998) Ageing of solar booster reflector materials. *Sol Energy Mater Sol Cells* 54(1–4):235–246. [https://doi.org/10.1016/S0927-0248\(98\)00075-0](https://doi.org/10.1016/S0927-0248(98)00075-0)
14. Ahmed MH, Amin AMA (2015) Thermal analysis of the performance of linear fresnel solar concentrator. *J Clean Energy Technol* 4(5):316–320. <https://doi.org/10.18178/jocet.2016.4.5.304>
15. Heimsath A, Cuevas F, Hofer A, Nitz P, Platzer WJ (2014) Linear fresnel collector receiver: heat loss and temperatures. *Energy Procedia* 49:386–397. <https://doi.org/10.1016/j.egypro.2014.03.042>
16. Roostae A, Ameri M (2019) Effect of Linear Fresnel concentrators field key parameters on reflectors configuration, Trapezoidal Cavity receiver dimension, and heat loss. *Renew Energy* 134:1447–1464. <https://doi.org/10.1016/j.renene.2018.09.053>
17. Kodama T (2003) High-temperature solar chemistry for converting solar heat to chemical fuels. *Progr Energy Combust Sci* 29(6):567–597. Pergamon. [https://doi.org/10.1016/s0360-1285\(03\)00059-5](https://doi.org/10.1016/s0360-1285(03)00059-5)
18. Manikandan GK, Iniyan S, Goic R (2019) Enhancing the optical and thermal efficiency of a parabolic trough collector—a review. *Appl Energy* 235:1524–1540. <https://doi.org/10.1016/j.apenergy.2018.11.048>
19. Murtuza SA, Byregowda HV, Imran M (2017) “Experimental and simulation studies of parabolic trough collector design for obtaining solar energy. *Resour. Efficient Technol* 3(4):414–421. <https://doi.org/10.1016/j.refit.2017.03.003>
20. Kongkaiatpaiboon V, Nanan K, Eiamsa-ard S (2010) Experimental investigation of heat transfer and turbulent flow friction in a tube fitted with perforated conical-rings. *Int Commun Heat Mass Transfer* 37(5):560–567. <https://doi.org/10.1016/j.icheatmasstransfer.2009.12.015>
21. Schott PTR 70 Receiver (1992) [Online]. Available: [https://www.schott.com/english/applications/energy\\_environment.html](https://www.schott.com/english/applications/energy_environment.html)
22. Gunther S, Goemann M, Csambor S (2020) Parabolic trough technology. <https://docplayer.net/32427036-Chapter-5-parabolic-trough-technology.html>. Accessed 20 Aug 2020
23. RIO Glass. <http://rioglass.com/technology>
24. Alucoil Grupo Aliberico. Aluminum mirror—technical-details-ALMIRR. [Online]. Available: [www.alucoil.com](http://www.alucoil.com)
25. Avenel C, Raccurt O, Gardette J-L, Therias S (2019) Accelerated aging test modeling applied to solar mirrors. *npj Materials Degradation* 3(1):1–14. <https://doi.org/10.1038/s41529-019-0089-y>
26. Moya EZ (2012) *Parabolic-trough concentrating solar power (CSP) systems*. Woodhead Publishing Limited

27. Barriga J, Ruiz-De-Gopegui U, Goikoetxea J, Coto B, Cachafeiro H (2014) Selective coatings for new concepts of parabolic trough collectors. *Energy Procedia* 49:30–39. <https://doi.org/10.1016/j.egypro.2014.03.004>
28. Morales A, San Vicente G (2017) A new generation of absorber tubes for concentrating solar thermal (CST) systems. In: *Advances in concentrating solar thermal research and technology*, pp 59–73. <https://doi.org/10.1016/b978-0-08-100516-3.00004-6>
29. Solar T, Plant P, Soomro MI, Mengal A, Shafiq QN, Aziz S, Rehman U (2019) Performance improvement and energy cost reduction under different scenarios for a parabolic. *Processes* 7:1–23
30. Romero M, González-Aguilar J (2014) Solar thermal CSP technology. *Wiley Interdisc Rev Energy Environ* 3(1):42–59. <https://doi.org/10.1002/wene.79>
31. Behar O, Khellaf A, Mohammedi K (2013) A review of studies on central receiver solar thermal power plants. *Renew Sustain Energy Rev* 23:12–39. <https://doi.org/10.1016/j.rser.2013.02.017>
32. Kolb GJ, Davenport R, Gorman D, Lumia R, Thomas R, Donnelly M (2007) Heliostat cost reduction. In: *Proceedings of the Energy Sustainability Conference 2007*, pp 1077–1084. doi:10.1115/ES2007-36217
33. William G, Micheal BS (2001) Power from Sun. <http://www.powerfromthesun.net/Book/chapter10/chapter10.html>
34. He YL, Qiu Y, Wang K, Yuan F, Wang WQ, Li MJ, Guo JQ (2020) Perspective of concentrating solar power. *Energy* 198:117373. <https://doi.org/10.1016/j.energy.2020.117373>
35. Buck R, Teufel E (2009) Comparison and optimization of heliostat canting methods. *J Solar Energy Eng Trans ASME* 131(1):0110011–0110018. <https://doi.org/10.1115/1.3027500>
36. Geyer C, Milow M, Richter B (2015) Plataforma Solar de Almería. [Online]. Available: <https://www.psa.es/webeng/areas/ussc/synpet.php>
37. Li X, Kong W, Wang Z, Chang C, Bai F (2010) Thermal model and thermodynamic performance of molten salt cavity receiver. *Renew Energy* 35(5):981–988. <https://doi.org/10.1016/j.renene.2009.11.017>
38. Silva-Pérez MA (2017) Solar power towers using supercritical CO<sub>2</sub> and supercritical steam cycles, and decoupled combined cycles. Elsevier Ltd
39. Hafez AZ, Soliman A, El-Metwally KA, Ismail IM (2016) Solar parabolic dish Stirling engine system design, simulation, and thermal analysis. *Energy Convers Manage* 126:60–75. <https://doi.org/10.1016/j.enconman.2016.07.067>
40. Schiel W, Keck T (2012) Parabolic dish concentrating solar power (CSP) systems. In: *Concentrating solar power technology*, pp 284–322. <https://doi.org/10.1533/9780857096173.2.284>
41. Tsooutsos T, Gekas V, Marketaki K (2003) Technical and economical evaluation of solar thermal power generation. *Renew Energy* 28(6):873–886. [https://doi.org/10.1016/S0960-1481\(02\)00152-0](https://doi.org/10.1016/S0960-1481(02)00152-0)
42. Abbas M, Boumeddane B, Said N, Chikouche A (2011) Dish stirling technology: A 100 MW solar power plant using hydrogen for Algeria. *Int J Hydrogen Energy* 36(7):4305–4314. <https://doi.org/10.1016/j.ijhydene.2010.12.114>
43. Santos JJCS, Palacio JCE, Reyes AMM, Carvalho M, Freire AJR, Barone MA (2018) Concentrating solar power. *Adv Renew Energies Power Technol* 1(2):373–402. <https://doi.org/10.1016/B978-0-12-812959-3.00012-5>
44. Mills S (2018) Combining solar power with coal-fired power plants, or cofiring natural gas. *IEA Clean Coal Centre* 2(1):1–9. <https://doi.org/10.1093/ce/zky004>
45. Pierce W, Gauché P, Von Backström T, Brent AC, Tadros A (2013) A comparison of solar aided power generation (SAPG) and stand-alone concentrating solar power (CSP): a South African case study. *Appl Therm Eng* 61(2):657–662. <https://doi.org/10.1016/j.applthermaleng.2013.08.014>
46. Semprini S, Sánchez D, De Pascale A (2016) Performance analysis of a micro gas turbine and solar dish integrated system under different solar-only and hybrid operating conditions. *Sol Energy* 132:279–293. <https://doi.org/10.1016/j.solener.2016.03.012>

47. Coelho B, Oliveira A, Schwarzbözl P, Mendes A (2015) Biomass and central receiver system (CRS) hybridization: Integration of syngas/biogas on the atmospheric air volumetric CRS heat recovery steam generator duct burner. *Renew Energy* 75:665–674. <https://doi.org/10.1016/j.renene.2014.10.054>
48. Alqahtani BJ, Patiño-Echeverri D (2016) Integrated Solar Combined Cycle Power Plants: Paving the way for thermal solar. *Appl Energy* 169:927–936. <https://doi.org/10.1016/j.apenergy.2016.02.083>
49. Dersch J, Geyer M, Herrmann U, Jones SA, Kelly B, Kistner R, Ortmanns W, Pitz-Paal R, Price H (2004) Trough integration into power plants—a study on the performance and economy of integrated solar combined cycle systems. *Energy* 29(5–6):947–959. [https://doi.org/10.1016/S0360-5442\(03\)00199-3](https://doi.org/10.1016/S0360-5442(03)00199-3)
50. He YL, Wang K, Qiu Y, Du BC, Liang Q, Du S (2019) Review of the solar flux distribution in concentrated solar power: Non-uniform features, challenges, and solutions. *Appl Therm Eng* 149:448–474. <https://doi.org/10.1016/j.applthermaleng.2018.12.006>
51. de Sá AB, Pigozzo Filho VC, Tadrist L, Passos JC (2018) Direct steam generation in linear solar concentration: Experimental and modeling investigation—a review. *Renew Sustain Energy Rev* 90:910–936. <https://doi.org/10.1016/j.rser.2018.03.075>
52. Ho C (2016) Technology pathway—particle receivers. [Online]. Available: <https://www.osti.gov/servlets/purl/1429483>
53. Masdar Institute Solar Platform—Khalifa University. <https://www.ku.ac.ae/r-d-facilities/masdar-institute-solar-platform>. Accessed 18 Sept 2020
54. Dostal V, Hejzlar P, Driscoll MJ (2006) The supercritical carbon dioxide power cycle: comparison to other advanced power cycles. *Nucl Technol* 154(3):283–301. <https://doi.org/10.13182/NT06-A3734>
55. Al-Sulaiman FA, Atif M (2015) Performance comparison of different supercritical carbon dioxide Brayton cycles integrated with a solar power tower. *Energy* 82:61–71. <https://doi.org/10.1016/j.energy.2014.12.070>
56. Concentrating Solar Power Projects—National Renewable Energy Laboratory. <https://solarpaces.nrel.gov/projects>. Accessed 18 Sept 2020



# Chapter 4

## Innovative Applications of Solar Energy



Amandeep Singh and Janakarajan Ramkumar

### 4.1 Introduction

Photovoltaic cells (PVs) have shown its potential to mitigate climate change as a low-carbon technology. Solar panels are much more advanced than they are generally thought of, just as the big rooftop patterns of panels. The innovations in solar energy have widely ranged from the giant electric power plants to small LED battery chargers.

One of the mentionable large-scale innovative applications is the giant plant designs in the Japanese energy mix after the Fukushima disaster. US National Renewable Energy Laboratory (NREL) is coming up with switchable solar see-through windows built using organic photovoltaic technology [1].

It cannot be ignored that there are many small but prospective inventions. A miniaturized on-the-go solar panel with generator producing enough to recharge laptops and mobiles, solar-powered bike locks that provides keyless entry while connecting to the rider's mobile phone and can also detect theft, desalination units using high output solar spot light to extract salt and minerals from saline water, solar powered backpacks, solar fabrics, are a few mentions. This chapter sheds a light on a few novel inventions reported till date and the current and future applications of the technology. The readers are expected to be familiar with the recent advancements in solar technology and get motivated to contribute in making the earth greener.

The innovative applications in this chapter have been categorized as following.

- **Novel Concepts:** Ambitious and out-of-the box ideas have been discussed to intrigue the reader.
- **Improvements in PV cells:** Photovoltaic cell designs are being continuously improved to increase efficiency and reduce costs.

---

A. Singh · J. Ramkumar (✉)  
Indian Institute of Technology Kanpur, Kanpur, India  
e-mail: [jrkumar@iitk.ac.in](mailto:jrkumar@iitk.ac.in)

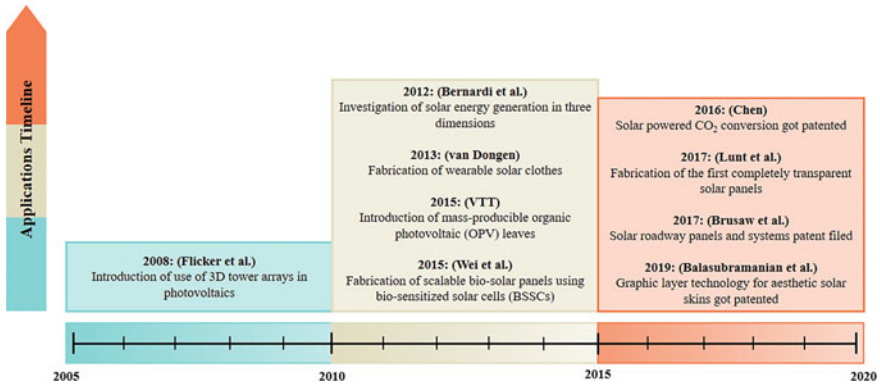


**Fig. 4.1** Timeline of different applications. *Source* Author

- **Biomimetics:** Imitating how nature captures and utilizes solar energy during photosynthesis.

The above categories will be discussed in detail in coming sections. Figure 4.1 shows a timeline of development of various solar applications being discussed in this chapter over the years along with their inventor/author(s).

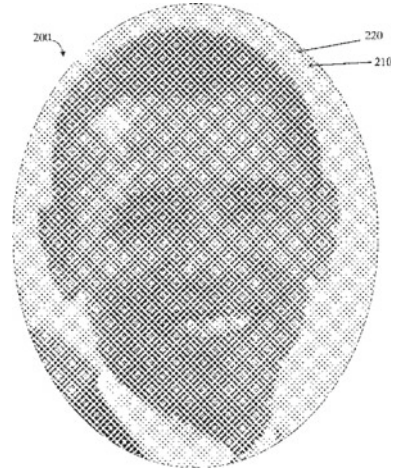
## 4.2 Novel Concepts

### 4.2.1 Aesthetic Solar Skins

SolarSkin is an aesthetic, screen protector like overlay that transforms the look of solar panels. This skin uses selective light filtration which transmits light to the panel while displaying a vibrant image of the skin. This technology finds its use in various applications like business branding, advertising, art, or general beautification. It also protects the modules against chemical and UV degradation. Different graphic layers are embodied on the solar modules in order to incorporate images/patterns. These graphic layers comprise of two types of layers: opaque-isolated regions and transparent continuous regions [2]. Many layers of isolated regions combine to form a recognizable image (Fig. 4.2).

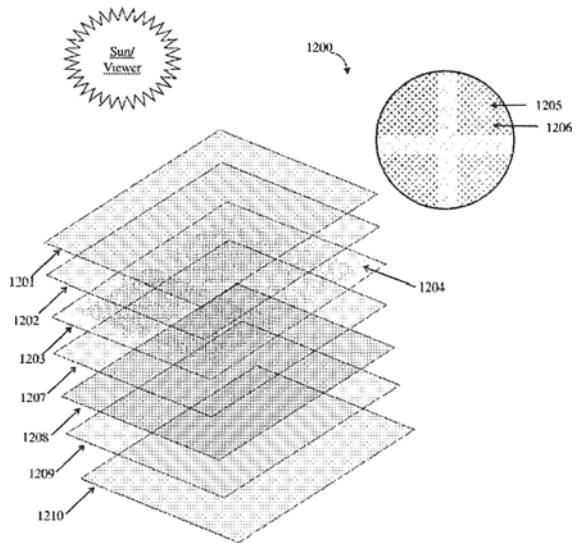
The isolated regions absorb certain wavelengths of radiation while reflect back certain other ranges to the eyes of the viewer. Graphic layers can be printed on isolated regions using various techniques like flatbed printing, inkjet printing, digital printing, laser printing, screen printing, etching, etc. Examples of transparent materials that can be used are glass, transparent plasticizers, polycarbonates clear coats, fluoropolymers, and polyesters. These materials can act as a protective layer that can

**Fig. 4.2** Opaque regions forming an image. *Source* [2]



increase the life of the module by protecting it from weather damage. Common adhesives used are polyvinyl butyl, silicone, ionomer, ethylene vinyl acetate, polyolefin (Fig. 4.3).

**Fig. 4.3** Opaque and transparent layers of SolarSkin. *Source* [2]



### 4.2.2 Solar Roadways

Solar roadways is an intelligent roadway system that converts solar energy into electricity using solar roadway panels. This application aims to increase the reach of solar panels by making them tough and weather resistant so that their use is not restricted by geographical location [3]. The invention aims to generate round-the-clock electricity using solar energy. Each solar tile comprises of three layers, namely: road surface layer, electronics layer, backplane [4].

The road surface layer is a glass panel that would bear the traffic and pedestrian loads. This layer is water-proof and transparent so that light can pass through to the panels underneath. The embodiment could be made from low iron float glass, engineered polymer interlayers, or rolled soda lime glass. The layer protects photovoltaic cells from microscopic impact stresses from traffic and Hertzian contact stresses by sharp objects. Strengthened glass may be textured to enhance traction capabilities [3].

The electronics layer consists of the monocrystalline photovoltaic cells having an efficiency of 14.47%. These solar cells are soldered or electrically attached in a spaced array. The DC electricity generated by the panel power the LEDs, heating element, sensor, and other components within the panels. Electromagnetic, piezoelectric, temperature, pressure and optical sensors could be used.

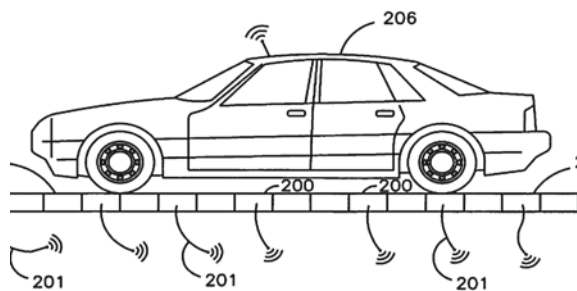
The backplane is the supportive surface below the roadway panels that carry grid connections. This layer is configured with conduits to house the power cables to and from the panels.

This invention comes with numerous advantages other than clean electricity generation. The LEDs embedded in the panels can illuminate the road at night. The heating element can melt winter snow on the road. Radio frequency signals may be used to track vehicles and provide precise GPS location. Safety signals like “stop” and “slow down” could be displayed to traffic (Fig. 4.4).

Exposure to severe environmental conditions like lightning strikes and electronic rust may damage the solar panels. Protective circuits made of metal oxide varasitors, gas tubes, and silicone avalanche diodes can divert excess electric current.

In spite of these advantages, solar roadways have a few major challenges that need to be addressed and can be taken as opportunity for the researchers which.

**Fig. 4.4** Embedded RF transceivers to track vehicles. *Source* [3]



Cost of building solar roadways and parking lots is extremely high. Technological advances in photovoltaics may bring this price down and offer improved efficiency in the future. Salt and rubber from tyres start to accumulate on the road which can be difficult to wash off. Solar roadways require high initial investments, but they generate revenue over time [4].

### 4.2.3 Wearable Solar Clothes

This research aims at bringing fashion designing and wearable technology together. Photovoltaic devices have excellent mechanical robustness and high conversion efficiency making them suitable portable electricity sources [5]. But due to their brittle nature, the use of solar cells has been limited [6]. Recent improvements in their elastic properties has made it practical to wear them.

Flexible solar cells can be divided into five different groups: perovskite solar cells (PSC), dye-sensitized, organic, and fiber shaped [5]. PSCs are ideal candidates for wearable devices because of their ability to form a thin electron absorption layer and superior efficiency of perovskite compared to other mechanisms. The photoactive perovskite layer in PSCs is embedded between two charge transport layers (Fig. 4.5).

Dye-sensitized solar cells (DSSCs) are the most economic photovoltaic devices because of low cost raw materials and the simple production processes. The principle behind their working is the generation of electron–hole pairs. It consists of three main parts, namely cathode, electrolyte, and highly sensitized photoelectrode (Fig. 4.6).

Flexible organic solar cells (OSCs) use carbon-based organic polymers instead of using hard, inorganic materials like silicon. Researchers built highly efficient OSCs by mixing sulfur-based thiol-ene reagents with semiconducting polymers [9]. The molecules blend and crosslink with the polymers to provide flexibility. The level of flexibility depends on the amount of thiol-ene. High amounts of thiol-ene can affect

**Fig. 4.5** Perovskite solar cells. *Source* [7]

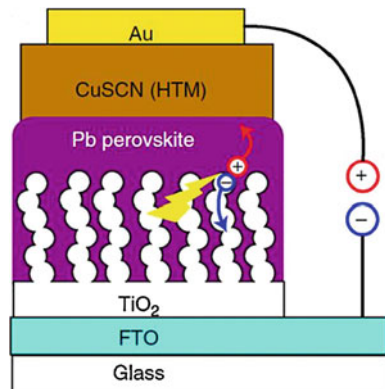
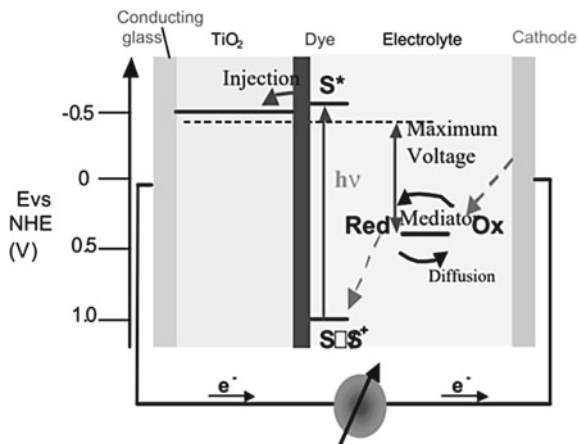


**Fig. 4.6** Dye-sensitized solar cells. *Source* [8]



efficiency, and in contrast, too less thiol-ene can cause it to crack easily. The sweet spot is achieved at an ideal amount of 20% thiol-ene.

Wire-shaped solar cells are low-dimensional solar cells having 3D light harvesting capability, excellent bending, superior stability (over ambient conditions), and exceptional flexibility [10]. Dye-sensitized, organic, and perovskite power mechanisms can be used to develop a wire-shaped solid-state solar cell. A solar cell in wire form was developed using Mn wires at low temperature via wet processing. Efficiency of these solar cells can be improved by coupling with Fe and Ti. These wire-shaped solar cells can be modified into fabrics and in turn woven into energy-producing garments [11]. These flexible materials, due to their flexibility and adaptability can be embedded into bags, clothes, aircrafts, cars, etc.

## 4.3 Improvements in PV Cells

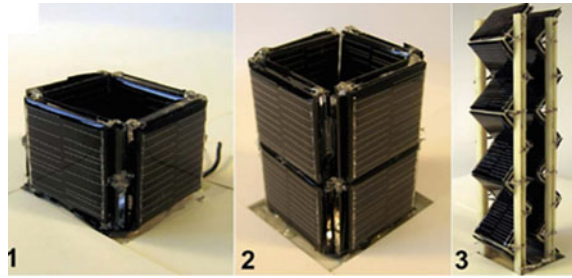
### 4.3.1 3D Photovoltaic Cells

Flat solar panel design is the most commonly used orientation for solar plants. Bulky and expensive solar trackers are used to optimize sunlight collection [12]. 3D PV cells can utilize the three dimensionality of sunlight. Two main advantages of 3D PV are re-absorption of reflected energy within the cells and effective collection of sunlight. Three dimensionality of light can be utilized in two ways: creating a 3D structure of conventional solar cells or using multiple beam epitaxy to grow a solar cell layer by layer [13].

A 3D tower assembly of solar cells would reduce the base area required. The daily energy generation for a simple open cube structure was measured to be 2.25 Wh [12]. This is a significant improvement compared to 1.22 Wh for a same area panel with a

**Fig. 4.7** 3DPV structures.

Source [12]



flat plate configuration. Computer simulations were run to find the optimal shapes that would increase the energy density generated. Generated energy was expressed as a function of coordinates of the cell and was maximized by optimizing the re-absorbed light and avoiding shading by neighboring cells (Fig. 4.7).

Three-dimensional solar cells were developed by depositing thin films of cadmium telluride over carbon nanotubes (CNT) towers. Photons rebound between these CNT towers and get multiple chances of absorption, thus increasing absorption efficiency. Theoretical models and computer simulations were used to modify geometrical characteristics (aspect ratio, perimeter, tower configuration, etc.) in order to maximize photon absorption. 3D cells generate 250–300% more power than that of a planar cell [13]. Power generation increased as the tower perimeter per unit area increased.

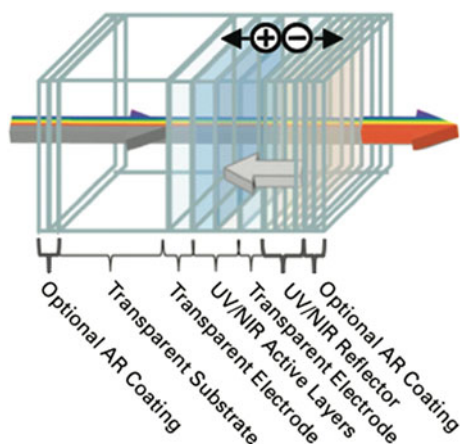
### 4.3.2 Transparent Solar Cells

The small energy density of photovoltaics necessitates large area deployment in order to meet high energy demands [14]. Low-cost, transparent, photovoltaic cells could overcome this obstacle as they could be integrated into window panes of buildings, air planes, boats, trains, etc. [15]. The non-transmitted light (around 20–30% in vehicles and 10–45% in buildings) from these windows could be used for power generation. Using inorganic, silicon-based solar cells are infeasible because of their limited flexibility, high costs, and band-like absorption spectrum limits [14].

Organic PV cells with chloroaluminium phthalocyanine (ClAlPc) and molecular acceptor as  $C_{60}$  that absorb ultraviolet light can be used. Broad-band antireflection (BBAR) coatings were deposited on their own quartz substrate and used as PV coatings. Indium tin oxide (ITO) cathodes and anodes were used, and their thickness was optimized to achieve maximum photocurrent (Fig. 4.8).

Thin-film photovoltaics (TPVs) is one of the most effective transparent solar cell technologies. They are either made by fabricating new materials and pastes to achieve transparency or by depositing pastes on fluorine-doped tin oxide (FTO) glass. Thickness of TPV cells is typically between nanometers to micrometers [16]. There are various ways of depositing a thin film on a substrate like physical vapor deposition (PVD), screen printing, electron deposition, chemical bath deposition

**Fig. 4.8** Transparent OPV cells. *Source* [15]



(CBD) technique, and pulsed layer deposition. Transparency of TPV cells can be increased by reducing the thickness of films in some materials like titanium oxide (Fig. 4.9).

Transparent photovoltaics are difficult to fabricate because the principles of photonic absorption essentially disagree with transparency [17]. Photons need to be absorbed by photovoltaics in order to generate electricity, whereas transparency means letting photons through. Highest transparency to efficiency ratio of 70%:8.2% was achieved using  $\text{TiO}_2$  nanotube film and transparent DSSC. Soon every window pane and electronic screen around us will be capable of generating electricity due to this promising technology.

**Fig. 4.9** Transparent TPV cells. *Source* [17]

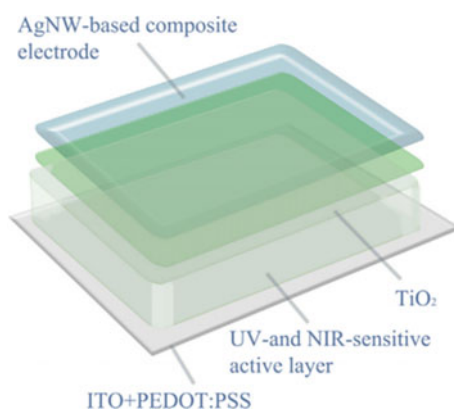
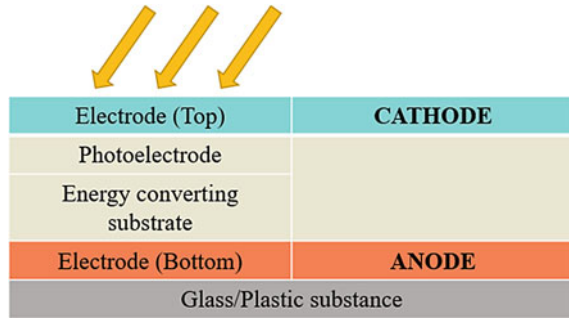




**Fig. 4.10** Schematic of PV paint. *Source* Author



### 4.3.3 Solar Paint

Installing solar panels is an expensive, labor intensive, and space-occupying process that makes the switch even more difficult [18]. Photovoltaic paint or solar paint is like normal paint but with billions of light-sensitive particles or quantum dots in the mix. Mostly, second- and third-generation PV materials based on hybrids, organic, and inorganic semiconductors are used for making solar paint [19]. The construction of PV paint is demonstrated in Fig. 4.10.

Solar paint solution can be processed in a number of ways, namely spin coating, doctor blading, printing (screen and printing), slot die coating, and successive ionic layer deposition. The most efficient solar paint ever is nano-ink  $Cu_2ZnSnS_4Se_{4(1-x)}$  developed using spin coating method and has an efficiency of 7.68% [20]. Centrifugal acceleration is used to spread the solution on a high spinning substrate in spin coating method. This results in a homogeneous film with low-defect density [21].

The efficiency of solar paint mostly depends on material selection, substrate, and deposition technique. Further research on thin-film photovoltaic paint can improve efficiency and make them effective for large-scale commercial applications.

## 4.4 Biomimetics

### 4.4.1 Solar Botanic Trees

Solar PV modules are mounted at a fixed angle and may not be the best at utilizing solar radiation due to fluctuating the angle of incidence. Moreover, the base area required for mounting these arrays is large and impractical for urban cities. A solar tree is a viable alternative because it can convert heat, light, and wind into clean energy using nano-thermoelectric, nano-photovoltaic, and nano-piezoelectric cells, respectively [22]. Very thin nano-thermoelectric cells convert heat from the sun into electricity using a semiconducting material like BiSbTe.

A thin photovoltaic cell with quantum dots would be used in order to confine electrons long enough till their energy can be extracted by thermoelectric transducers [23].

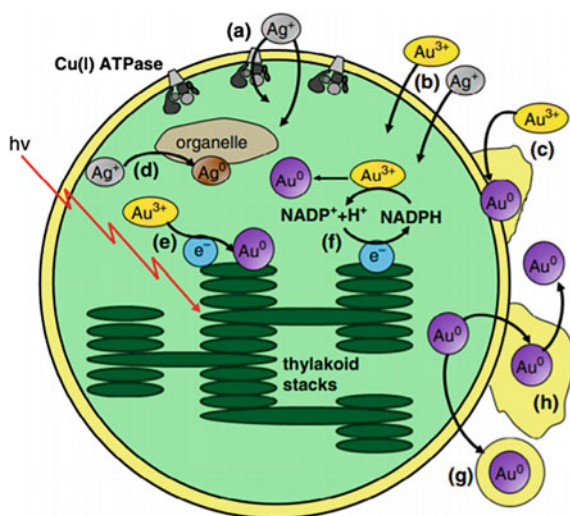
#### 4.4.2 Biosolar Cells

Biosensitized solar cells (BSSCs) are inspired by the phenomenon of electron ejection, triggered by photons, in light-activated proteins [24]. During photosynthesis, solar energy is captured to convert  $\text{CO}_2$  and  $\text{H}_2\text{O}$  into  $\text{O}_2$  and carbohydrates by microorganisms such as cyanobacteria or microalgae. Electrons flow to the cathode through extracellular transfer pathways during these reactions. Photons diffuse to the cathode from the anodic chamber and re-combine with oxygen and electrons to form  $\text{H}_2\text{O}$  [25].

Scalable biosolar panels were fabricated by assembling smaller individual BSSCs in a common microfluid channel [25]. Nine small biosolar cells connected in series produced a maximum power of  $5.59 \mu\text{W}$  at a voltage of 1.28 V. A proton exchanging membrane (PEM) was embedded between air-cathode and anode to reduce travel distance of protons thus reducing internal resistance (Fig. 4.11).

The biosolar cell device consists of four different layers each having different functionalities; (i) a transparent top layer of poly(methyl methacrylate) (PMMA) for capturing solar energy, (ii) a PMMA chamber anodic layer, (iii) PEM (Nafion 117) between the air-cathode and carbon cloth anode, and (iv) a bottom PMMA layer to expose available oxygen to the cathode (Fig. 4.12).

**Fig. 4.11** Photosynthesis of cyanobacteria cells. Source [26]



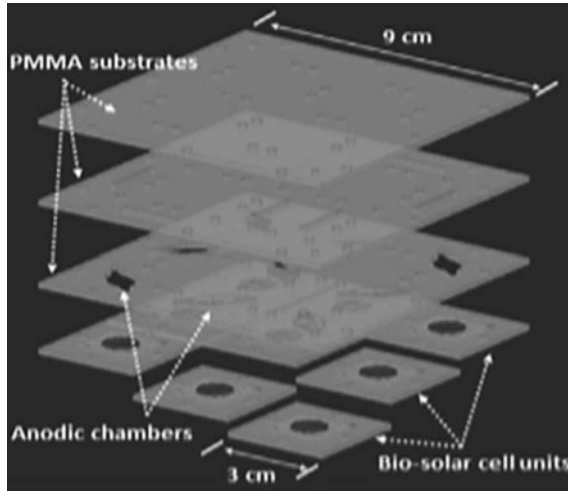


Fig. 4.12 Layers of a biosolar cell. Source [25]

Synechocystis cultures (PCC 6803) were grown at 30 °C in BG-11 medium containing 40 mg of  $K_2HPO_4$ , 1.5 g of  $NaNO_3$ , 36 mg of  $CaCl_2$ , 75 mg of  $MgSO_4$ , 1 mg EDTA, and 6 mg citric acid per one liter of distilled water. Constant illumination and aeration were supplied for 10 days using fluorescent lamps (Fig. 4.13).

Metabolic engineering and biology tools can be utilized to regulate gene expression of cyanobacteria to improve efficiency of biosolar cells [28]. Photosynthetic machineries like biochromophores, photosystems I and II, bacteriorhodopsin, and antenna proteins, that effectively capture the solar energy available and make use of it efficiently owing to the high light-to-electron conversion ratio, can be used in the future [28].

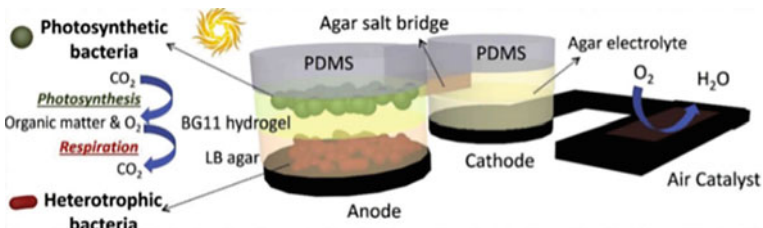


Fig. 4.13 Biosolar power system. Source [27]

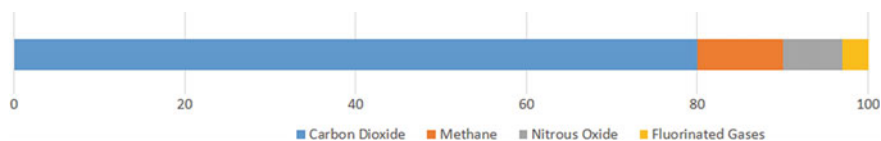


Fig. 4.14 Overview of GHGs in 2018. Source Author

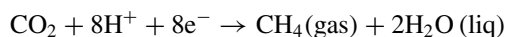
### 4.4.3 Solar-Powered CO<sub>2</sub> Conversion

It is known that the primary cause of global warming is greenhouse gases (GHGs) emissions such as CO<sub>2</sub>, CH<sub>4</sub>, N<sub>2</sub>O, HFCs, PFCs, and SF<sub>6</sub>. Emission of carbon dioxide (CO<sub>2</sub>) from fuel combustion accounts for the largest contribution of human activities in global GHG emissions. The global concentration of CO<sub>2</sub> in the atmosphere is ever increasing as shown in Fig. 4.14. Three approaches can be utilized to achieve a reduction in CO<sub>2</sub> emissions: (i) use of alternative energy source that are carbon-free, (ii) use of carbon-based energy sources efficiently, and (iii) use of carbon capture methods, storage of the captured CO<sub>2</sub>, and its use [29].

Three processes can be used for CO<sub>2</sub> conversion, namely photocatalysis, electrochemistry, and photo electrochemistry. Using electricity generated by solar energy to power a photoelectrochemical cell (PEC) is more efficient than conventional photocatalysis due to effective charge carrier separation [30].

Photoanode-driven PEC approach is a two-step process that resembles artificial photosynthesis: (i) photoanodic light-dependent reaction involving the photogenerated minority carriers by means of water oxidation (ii) cathodic reduction of CO<sub>2</sub> into hydrocarbon via a catalyst using the majority carriers generated by photons at the anode (Fig. 4.15).

The cathodic reaction is:



Reaction at the TiO<sub>2</sub> photoanode is:

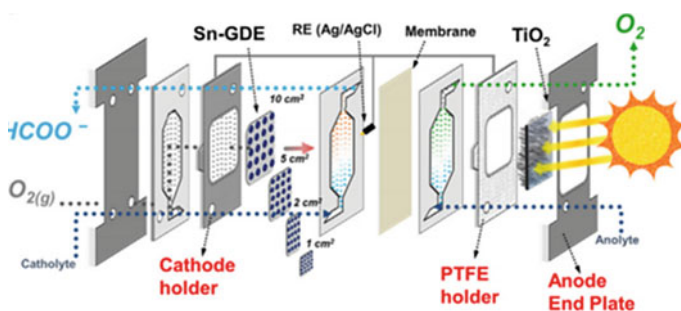
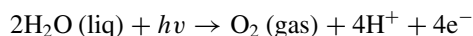


Fig. 4.15 PEC using TiO<sub>2</sub> photoanode. Source [30]



The photoanode comprises of  $\text{TiO}_2$  or  $\text{WO}$  nanotubes or nanowires,  $\text{PbS}$  or  $\text{CdS}$  quantum dots, and nano-structures of  $\text{Ag}$  or  $\text{Au}$ . The cathode is made from a diffusion layer containing a conductive gas with nano-structure electro-catalyst of  $\text{Cu}$  or  $\text{Co}$  [31].

## 4.5 Summary

Rising awareness about the negative impacts of conventional fuels on the environment leads to an increase in the demand for renewable and sustainable energy. Although a major share of the world's total energy is still derived from fossil fuels, demand for solar energy is rapidly increasing due to its abundance, low operating and maintenance costs, and negligible emissions. Almost all the world's solar energy is produced using photovoltaics at huge solar plants in remote locations which seems irrelevant to the masses.

The technologies discussed in this chapter illustrated the potential and wide applications of PV technology. From transparent solar windows and wearable solar clothes to solar roadways, one might see photovoltaics all around in the future; however, this cannot be called as the state of art review of the solar applications. Further, more work has to be done on these technologies before they are commercially viable and are available to the masses, in order to aim for the environmentally friendly manufacturing and society.

## References

1. Barlev D, Vidu R, Stroeve P (2011) Innovation in concentrated solar power. *Sol Energy Mater Sol Cells* 95(10):2703–2725
2. Balasubramanian S, Jody F (2019) Graphic layers and related methods for incorporation of graphic layers into solar modules. U.S. Patent US10256360B2
3. Brusaw D, Brusaw J (2017) Intelligent solar roadway system and solar roadway panels. U.S. Patent US20180102730A1
4. Kulkarni AA (2013) “Solar Roadways”—rebuilding our infrastructure and economy. *Int J Eng Res Appl (IJERA)* 1429–1436
5. Hashemi SA, Ramakrishna S, Aberle A (2020) Recent progress in flexible-wearable solar cells for self-powered electronic devices: energy & environmental science
6. Cross DT Sustainability times, wearable solar power is now another step closer to reality. <https://www.sustainability-times.com/low-carbon-energy/wearable-solar-power-is-now-another-step-closer-to-reality/>
7. Park N-G (2015) Perovskite solar cells: an emerging photovoltaic technology. *Mater Today* 18(2):65–72
8. Grätzel M (2003) Dye-sensitized solar cells. *J Photochem Photobiol C Photochem Rev* 4(2):145–153

9. Williams M Rice University News and Media Relations. Stretchy solar cells a step closer. <https://news.rice.edu/2018/11/07/stretchy-solar-cells-a-step-closer-2/>
10. Song W, Wang H, Liu G, Peng M, Zou D (2016) Nano Energy 19:1–7
11. Fan X, Zhang X, Zhang N, Cheng L, Du J, Tao C (2015) Wet-process fabrication of low-cost all-solid wire-shaped solar cells on manganese-plated electrodes. *Electrochim Acta* 161:358–363
12. Bernardi M, Ferralis N, Wan JH, Villalon R, Grossman JC (2012) Solar energy generation in three dimensions. *Energy Environ Sci* 5(5):6880
13. Flicker J, Ready J (2008) Simulations of absorbance efficiency and power production of three dimensional tower arrays for use in photovoltaics. *J Appl Phys* 103(11):113110
14. Lunt RR (2011) Bulovic V (2011) Transparent, near-infrared organic photovoltaic solar cells for window and energy-scavenging applications. *Appl Phys Lett* 98(11):113305
15. Stauffer NW MIT Energy Initiative, Transparent solar cells: <https://energy.mit.edu/news/transparent-solar-cells/#:~:text=Overview,they look or function today.&text=Their new@@@ solar cells absorb only infrared and ultraviolet light.>
16. Chopra KL, Paulson PD, Dutta V (2004) Thin-film solar cells: an overview. *Prog Photovolt Res Appl* 12:69–92
17. Husain AAF, Hasan WZW, Shafie S, Hamidon MN, Pandey SS (2018) A review of transparent solar photovoltaic technologies. *Renew Sustain Energy Rev* 94:779–791
18. Solar action alliance, solar paint-the paint of the future? <https://solaractionalliance.org/solar-paint/>
19. Khan SA, Rahman A (2019) Efficiency of thin film photovoltaic paint: A brief review. *7(6S):2277–3878*
20. Seo H, Son MK, Kim HJ, Wang Y, Uchida G, Kamataki K, Shiratani M (2013) Study on the fabrication of paint-type Si quantum dot-sensitized solar cells. *Jpn J Appl Phys* 52(10S):10MB07
21. Schilinsky P, Waldauf C, Brabec CJ (2006) Performance analysis of printed bulk heterojunction solar cells. *Adv Funct Mater* 16(13):1669–1672
22. Meghana KM, Sharavathi DJ, Kushma M, Manjula G (2016) Inspecting the results of renewable energy source of solar botanic trees using nano piezo electric elements. *Bonfring Int J Softw Eng Soft Comput* 6
23. Johnson A (2015) Solar botanic trees using nanoleaves: a energy harvesting production. *Int J Res Appl Sci Eng Technol (IJRASET)*. ISSN: 2321–9653
24. Somasundaran P, Chin M, Latosiewicz U, Tuller H, Barbiellini B, Renugopalakrishnan V (2011) Nanoscience and engineering for robust biosolar cells. *Bionanotechnology II*:427–454
25. Wei X, Lee H, Choi S (2016) Biopower generation in a microfluidic bio-solar panel. *Sens Actuators B Chem* 228:151–155
26. Jeffryes C, Agathos SN, Rorrer G (2015) Biogenic nanomaterials from photosynthetic microorganisms. *Curr Opin Biotechnol* 33:23–31
27. Mohammadifar M, Tahermia M, Choi S (2020) A miniaturized, self-sustaining, and integrable bio-solar power system. *Nano Energy* 104668
28. Ko SC, Lee HJ, Choi SY, Choi J, Woo HM (2018) Bio-solar cell factories for photosynthetic isoprenoids production. *Planta*
29. Kočí K, Obalová L, Laciný Z (2008) Photocatalytic reduction of CO<sub>2</sub> over TiO<sub>2</sub> based catalysts. *Chem Pap* 62(1):1–9
30. Irtem E, Hernández-Alonso MD, Parra A, Fàbrega C, Penelas-Pérez G, Morante JR, Andreu T (2017) A photoelectrochemical flow cell design for the efficient CO<sub>2</sub> conversion to fuels. *Electrochim Acta* 240:225–230
31. Chen B (2016) Solar powered CO<sub>2</sub> conversion: U.S. Patent: US 9,528,192 B1

# Chapter 5

## Smart Energy System



Sachin K. Jain and S. N. Singh

### 5.1 Introduction

The climate changes are now perceptible, and none other than our society is responsible for it. International professional community has acknowledged the concern about climate changes, and it is responding to this issue sincerely. New avenues are under exploration for environment-friendly future. Energy is one of the most crucial sectors that directly and significantly relates to the environment. A paradigm shift is required to manage energy resources efficiently in an environment-friendly manner. To meet out the total energy demand across the globe, the electricity has emerged as the most convenient and easy means due to many factors, such as easy transmission and simple control. On the other hand, the deteriorated environmental conditions have compelled us to look for alternatives of fossil fuels, especially coal and oil, and reduce dependency on them. The ambition of clean and sustainable energy supply relies on efficient and effective use of renewable energy sources (RES).

The intermittent nature of the RES requires special coordination and operational practices to exploit them to maximum possible extent. Smart energy system (SES) is one of the many directions explored by the researchers to achieve sustainable energy systems. Smart energy systems take an integrated holistic focus on the inclusion of more sectors (electricity, heating/cooling, transportation, industry, buildings, etc.) and allows for the identification of more achievable and affordable solutions to the

---

S. K. Jain (✉)  
IIITDM Jabalpur, Jabalpur, India  
e-mail: [skjain@ieee.org](mailto:skjain@ieee.org)

S. N. Singh  
IIT Kanpur, Kanpur, India  
e-mail: [snsingh@iitk.ac.in](mailto:snsingh@iitk.ac.in)

transformation into future renewable and sustainable energy solutions [1]. Among RES, solar energy is an important source of energy, which is provided by the sun in enormous amount in the form of heat and light. Variety of technologies are available to convert it into usable form, which can be broadly classified as: photovoltaics (PV) and solar-thermal.

Better utilization of solar energy using PV requires smart grid and microgrid, as these facilitates easy integration of PV systems. However, a significant portion of the total energy consumption is in the form of thermal, for cooling and heating applications. Also, energy conversion from one form to another involves significant losses, hence, it is always preferred to avoid energy conversion, if possible. Energy storage is one of the most researched areas in the past couple of decades, which will play crucial role in future sustainable energy solutions. Accordingly, a coherent system is required that will integrate multiple energy sectors with feasible strategies for economic, coordinated and optimal contribution of each sector for meeting out the rising energy demand of the globe. Such integrated systems have to be smart enough with pervasive computing, flexibility and ability to dynamically mitigate energy consumption through analysis of human behavior and environmental inferences. These systems can be termed as smart energy systems, which have the potential to meet out the growing energy demand with improved energy efficiency and utilization of clean and sustainable energy resources without any dependence on fossil fuels. Figure 5.1 shows a representative view of a smart energy system.

Last decade has seen significant interest and research contribution for the development of different aspects of smart energy systems, worldwide [2–5]. The different focus areas may be broadly classified as: necessity and viability of smart energy systems [6], grid integration of renewable energy sources [2, 7], energy storage [8–10], conceptual models of energy system [11–14], cyber-physical security [15], and many more. A brief review of the literature is presented here to get an overview of the smart energy systems.

The roots of the smart energy system can be traced in the challenges faced by the energy industry in the integration of renewable energy sources. The early articles [2, 7] that use the term smart energy system focused primarily on renewable energy integration to the smart grid for providing flexible electrical energy. The importance of energy storage was recognized at the similar time due to intermittent nature of the renewable energy sources [8, 9]. In 2012, Lund et al. [3] emphasized that exploration of renewable energy resources should not be looked upon as an isolated issue of electricity grid, but challenges of sustainable energy systems can be approached with all possible means of energy together. The paper presented the case of Skagen combined heat power (CHP) plant as a design case study of flexible energy systems. It is shown that smart energy systems may balance production and demand and may fulfil voltage and frequency stability requirements of the grid. Variety of energy resources as an integrated energy system requires smart energy meters that can monitor maximum possible utility services with communication facility. These will enable efficient management of energy resources with energy conservation.

Until initial few years of this decade, smart grid and smart energy system terms were considered synonymous, however, later the differences between the two



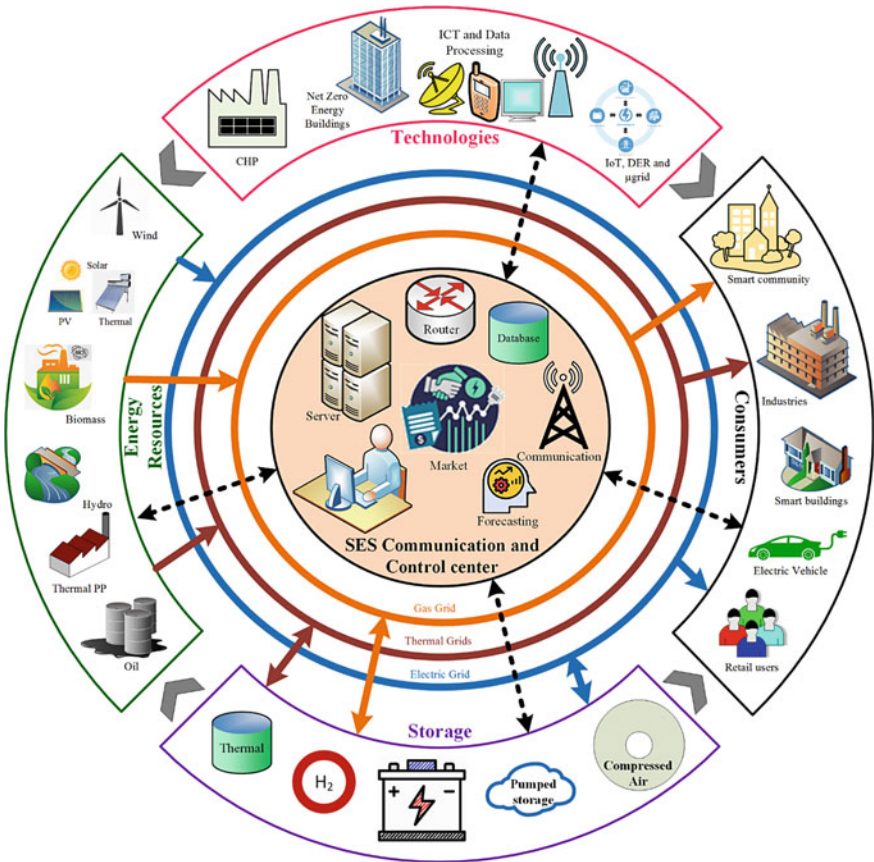


**Fig. 5.1** Smart energy system architecture. *Source* Author

emerged gradually. Smart grid research traditionally focuses on information and communication technology, smart energy meters, storage technologies, and local electric grids. Whereas, the smart energy system focuses on merging the electricity, thermal and transportation sectors, along with different energy storage techniques, which will enable integration of fluctuating renewable energy sources through the inherent flexibility feature in it [16]. Accordingly, SES should consider modelling of the future sustainable energy systems with the integration of different energy frameworks and interaction of key energy carriers, where production, conversion, storage, and consumption of different energy sources are analyzed within an intelligent framework. There have been case studies reported in the literature, which have confirmed the usefulness of smart energy systems [6]. Apart from the flexibility, the smart energy systems have the potential to promote the renewable energy sources by improving the economy and feasibility. Frede et al. [17] suggested that by integrating

the heat and power markets, the value of wind power can be ensured to be competitive and viable for sustainable wind power as compared to the most expensive heat alternative.

This chapter aims to introduce the concept of smart energy systems (SES). Accordingly, it presents the basic concept of smart grid, issues in integration of renewable energy sources, features of the smart energy systems from the recent literature and challenges ahead in this domain. Finally, it also discusses some models of SES and their relative comparison.

## **5.2 Components of SES**

Many definitions of the term smart energy system have been reported in the literature, which can be summarized as: Smart energy system is the well-coordinated integration of the smart electric grid, thermal energy system, smart gas network and transportation sector to attain the goal of clean energy in sustainable, efficient, economical and optimal manner such that renewable energy sources can be utilized to maximum possible extent. Accordingly, the components of smart energy system may be defined as:

### ***5.2.1 Energy Resource as Input to the System***

All kind of energy sources that supply energy to the consumers through the energy grid comes under this category. Although smart energy focuses on 100% renewable energy source-based energy supply network, the traditional energy sources cannot be excluded from it. The important aspect in energy resources, as a part of smart energy system, is proper coordination and optimal control of these resources to improve the energy efficiency and utilization factors of renewables. Some of the key energy resources are briefly explained in this section.

#### **5.2.1.1 Solar Energy**

Solar energy, provided by the sun in the form of solar radiation and light, is the supreme source of energy that is responsible for all our eco-system on Earth. For sustainable clean energy systems, solar energy is the most appropriate option. Many technologies have been developed and are under development for harnessing this abundant energy source for useful applications, such as, electricity, light, heat, etc. Among key technologies to harness the solar energy, photovoltaics and solar-thermal are widely used. Photovoltaic technology works on photovoltaic effect and directly converts solar energy contained in the photons into electricity using semiconductor material. In case of solar-thermal, the heat energy of the sunlight is used for space

or water heating. Solar-thermal technique is also used for electricity production using concentrating solar power plant, where the sun's energy is concentrated to boil water, which then drives the steam turbine-generator set. As such there is no drawback or adverse environmental effect of solar energy, its availability only during daytime makes it challenging as cost-effective, sustainable energy resource. Clouds significantly affect the solar output, which in turn affects the stable and smooth operation of solar energy system. Other shortcomings of solar energy system over other energy sources are requirement of vast land area and expensive technology.

### 5.2.1.2 Wind Energy

Wind energy is the ancient source of energy explored for water pumping, transportation, grain's grinding, etc. Today, it is one of the fastest-growing energy technologies, which has 623 GW of installed capacity by 2019 [18]. The reasons for this include, clean and sustainable energy source, reducing costs, improved technology for grid interconnection and handling intermittent nature, etc. Modern wind energy system uses wind turbines to capture kinetic energy from the wind to generate electricity. These can range from few kilowatt (kW) to megawatt (MW) ratings. Small size wind energy systems are used as distributed energy sources close to the consumer centers, while, large size plants are utility-scale plants that may be onshore or offshore. The pitfalls of wind energy include sound pollution, bird mortality, and large size of blades that makes its transportation and installation challenging.

### 5.2.1.3 Biomass Energy

Biomass is organic matter from natural means, such as plants and animals, which is used to produce usable energy through biomass technologies. Although it produces carbon dioxide during the processing or burning, it is considered renewable and sustainable source of energy because the produced carbon dioxide is almost balanced by the carbon dioxide captured in its own growth through the process of photosynthesis. Unlike the fossil fuels, which has carbon cycle of millions of years, biomass has carbon cycle of few months. The advantage of biomass energy is that its implementation is easy, fast and economic because it uses the same energy infrastructure as the fossil fuels. Biomass energy can use different organic materials, which can provide energy in different forms, as depicted in Table 5.1. Various technologies/processes are used for harnessing the biomass energy from organic matters, such as burning, fermenting, pyrolysis, gasification, anaerobic digestion, etc. Added benefits of biomass are that apart from energy, it can be used to produce some of the products that are otherwise derived from petroleum, such as, plastics.

**Table 5.1** Biomass energy materials and processes

Biomass item	Process	Remarks
Wood and its wastes	Burned to produce heat	Energy contents: 15 MJ/kg (Dried: 18 MJ/kg)
Crops and agricultural waste	Burned to produce heat or converted to liquid biofuels (e.g., bioethanol)	Energy contents: 4 MJ/kg (cut gross)
Food, waste, and garbage	Burned to produce heat or converted to biogas in landfills	It helps in garbage management
Animal dung and human sewage	Converted to biogas, which can be burned as a fuel	Always available at almost free cost
Vegetable oil and animal fat	Converted to liquid biofuels (e.g., biodiesel)	Can be used in diesel engines and as heating oil

Source Author

#### 5.2.1.4 Petroleum Oil

Petroleum oil, a complex mixture of hydrocarbons, is a fossil fuel that is used as energy source for traditional vehicles, electricity generation and industrial applications. Although electricity production from petroleum oil has reduced significantly in the last four decades from 23 to 3% in 2018, it still remains the dominant primary energy fuel with 32% of total energy share as per international energy agency IEA [19]. The fossil fuels are responsible for greenhouse gas emission, and hence pollutes the environment significantly. Being a non-renewable energy source, it is not possible to replace the extracted quantity in meaningful time, as it takes millions of years to form fossil fuels. The current focus of energy industry/experts is to find alternatives of these fossil fuels and to find out the ways for optimizing the use of these energy resources.

#### 5.2.1.5 Other Fossil Fuels

Coal and natural gas are other fossil fuels, which also contributes as primary energy source for electricity production, industrial applications and transportation purposes. These also emit toxic gases and are considered responsible for global warming. Apart from being culprit of polluting the environment, the depleting levels of fossils fuels are also a great concern for sustainable future energy systems. The research in this field is also aiming to develop the processes for minimizing its detrimental effects on the climate.

### **5.2.1.6 Other Energy Sources**

Hydel, nuclear, tidal, geothermal, etc. are other energy sources, which also participate in meeting out the total energy demand of the world. The energy from these sources is converted into electrical energy for real-world applications. In the last two decades, the share of nuclear energy has declined consistently, mainly because of two reasons: the risk of radiation hazard from nuclear plants and significant technological growth in renewable energy sectors, especially, wind and photovoltaic. The share of hydro energy is about 2.5% of total energy, whereas it is less than 1% for other renewable energy sources [19].

## **5.2.2 Energy Consumption**

The end-users of energy play crucial role in energy ecosystem. Energy consumers can be divided into the following broad sectors: transportation, industry, residential, agricultural, and commercial. The transport sector is the largest consumer with approximately one-third share in total energy consumption [19]. At present, majority of this energy demand is fulfilled by petroleum oil; therefore, this sector has attracted prime focus of the researchers for future sustainable energy system. Industrial consumption, which includes facilities and equipment used for manufacturing, mining, and construction is another sector followed by consumption in residential buildings and apartments. In residential buildings, lighting, home appliances, and heating/cooling system are main load points. Among these, heating/cooling system requires significant power and needs special attention in smart energy system. Commercial and agricultural sectors together contribute about 15–18% of total energy consumption on an average, worldwide. In the recent years, the share of natural gas has increased marginally in residential and commercial sectors that has reduced the oil consumption accordingly. According to IEA, the share of electricity has been almost same on a year-on-year basis, which suggests possible scope for the development of clean energy system with increased renewable energy resources participation in total energy consumption.

## **5.2.3 Communication and Control System**

The energy loads are supplied from different energy sources via energy transfer network systems. Depending on the form of energy source, these can be termed as smart electric grid, smart thermal grid, and smart gas grid. In smart energy systems, these different energy networks operate in an integrated manner, and hence, needs to have proper communication and control for better coordination among them. Smart energy system targets for improved energy efficiency, reduced emissions, cost-effective reliable supply of energy, and robust system after integration

of intermittent and uncertain renewable energy sources to the grid. Accordingly, data handling, computational resources, artificial intelligence, machine learning and advanced control techniques becomes important. Communication technology is the most basic requirement in any smart system with two-way exchange of information. Usman et al. [20] have discussed the key communication technologies for smart grid, which are equally applicable for smart energy system. At present, there is no single technology that can fulfill the expectations of smart energy system; however, a suitable combination of available options for different segments can serve the purpose. Among different technologies, power line communications (PLC), RF mesh, GSM, ZigBee, WiMAX, Wi-Fi, and dedicated fiber along high-voltage lines, etc. are frontrunners for research and deployment in smart energy system. A position paper of the Emerging Technical Committee Smart Grid Communications [21] mentions that future 5G networks promise to provide the quality of service of dedicated networks through a multi-purpose infrastructure and shall support high scalability for massively distributed smart grid deployments.

### **5.3 Enablers for Smart Energy System**

Driven by the global concerns about greenhouse gas emission, the innovative concept of smart energy system is shaping up to create an efficient and robust ecosystem for sustainable future energy system. Technological advancement has made it possible to realize the concept of smart energy system, and many recent and emerging technologies are contributing as enablers for a sustainable smart energy system. Figure 5.2 provides pictorial representation of key technology enablers for smart energy system. This section discusses some of these technologies and innovative concepts.

#### **5.3.1 *Information Communication Technology (ICT)***

The core idea of smart grid concept was to have two-way communication of the information between utility and consumers to improve the quality of power supply, customer satisfaction, and optimal utilization of the resources. In smart energy systems, the information and communication technology acts as nervous system, which provides energy management, coordination and scheduling of different resources, grid stability and control, demand management, automatic metering and billing, customer services, and other critical functions. ICT consists of data processing, computing, operations, information exchange and business service-related applications that ensure energy efficiency, reliability, productivity, and customer satisfaction. It not only facilitates seamless integration of renewables to the smart energy system, but also helps in managing the huge number of small and large size energy sources and associated subsystems.

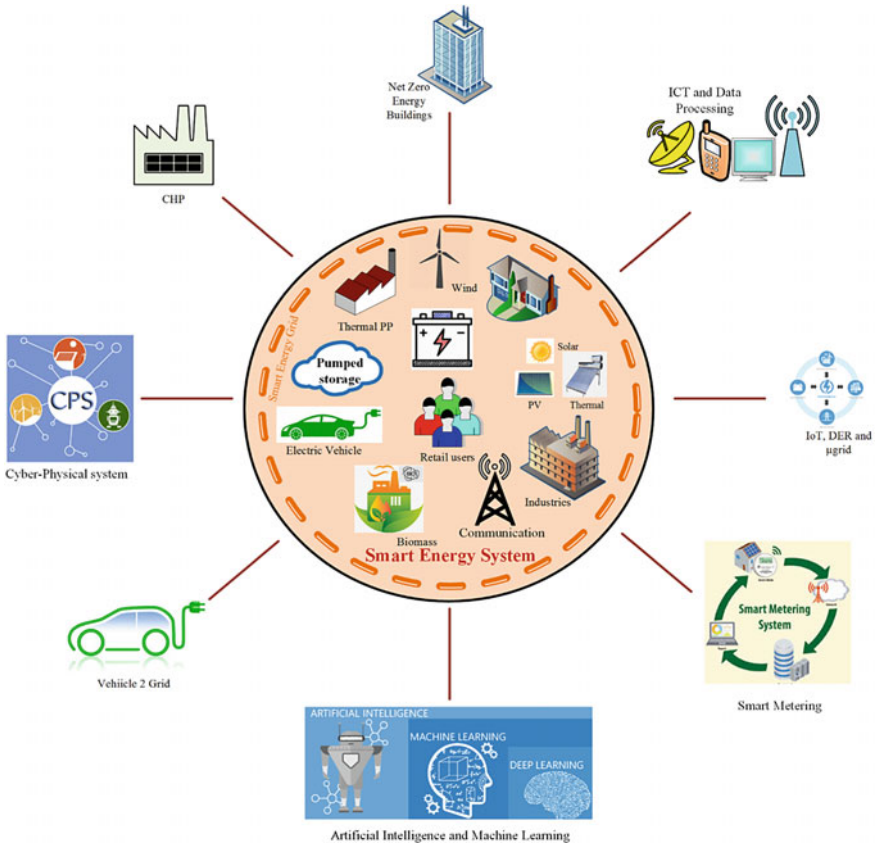


Fig. 5.2 Key enablers for smart energy system. Source Author

### 5.3.2 Combined Heat and Power (CHP) Plant

Combined heat and power (CHP) concept exploits the facts that residential buildings, industries, district heating/cooling systems consume considerable thermal energy and the traditional electricity generation involves wastage of sizable heat energy. In CHP, electricity and heat energy are generated simultaneously using a single fuel/source of energy; hence, it is referred to as cogeneration. This technology is a type of distributed energy generation, which may be typically located at individual buildings, district heating/cooling system or utility, where both electricity and thermal energy consumption occurs. The key features of CHP include significant improvement in energy efficiency, reduced greenhouse gas emission, reduced losses in distribution system, quick deployment, etc. Different CHP system configurations are reported in the literature, which might work with any of the available renewable or fossil fuels, e.g., biomass, gas, solar, diesel, etc.

### 5.3.3 *Internet of Things (IoT) and Cyber-Physical Systems*

The Internet of Things (IoT) is a technological innovation that interconnects computing systems, objects, machines, apparatus in an environment where the real and digital worlds meet to communicate with each other to enable compelling new business/technical models that support an increasingly complex system. The interconnection of the devices and apparatus follows a standard protocol, and every device/object is assigned a unique identification to allow the interconnection between the devices/objects without any human/computer intervention. This intelligent and pervasive environment forms the basis of the interconnected energy resources and other essential components of smart energy system. In an integrated and decentral-ized smart energy system, this technology offers rapid computations and optimum decision-making through real-time data sensing and transmission.

A cyber-physical system (CPS) is an interdisciplinary approach comprising of computing, digital and analog components, physical systems, which are controlled in integrated manner by computer-based algorithms. In cyber-physical systems, cyber capabilities are embedded in every physical component, and these physical and software components are deeply intertwined and interact with each other in ways that change with context. These exhibit multiple and distinct behavioral modalities and are able to operate on different spatial and temporal scales. Smart energy system needs synergizing various energy sources and loads from different domain, and cyber-physical system makes it possible through the orchestration of modern technologies. Smart energy systems involve remote access, monitoring and control of its elements, sensors and computing units in it are programmable. All these increase the vulnerability of these systems to cyber-attacks. The concept of cyber-physical security can be directly applicable to the smart energy system from protection of such security threats. Smart buildings can be developed as cyber-physical systems to implement smart energy systems at the local levels, thus avoiding distribution losses.

### 5.3.4 *Zero Energy Buildings*

The concept of a zero-energy building greatly supports smart energy system with considerable amount of renewables generation within the building, which is almost equal to the total energy consumption of the building, thereby resulting into zero consumption from the grid over a longer period of time. Zero energy building is expected to have low energy consumption as compared to traditional buildings and zero greenhouse gas emissions over a particular period of time. Net zero energy has been defined in the following four ways by National Renewable Energy Laboratory [22]: Net zero site energy, net zero source energy, net zero energy costs, net zero energy emissions. *Site energy* refers to the energy consumed and generated at a site, whereas *Source energy* refers to primary energy needed to extract and deliver energy to a site, including the energy that may be lost or wasted in the process of generation,



transmission and distribution. *Net zero energy cost* means that the building has zero energy utility bill over a definite period. A *net zero energy emission* building either uses no energy which results in emissions or offsets the emissions by exporting emissions-free energy.

In smart energy systems, the concept of net zero energy building can be used for all kind of energy requirements of the building and may be integrated with smart gas grid, smart thermal grid and smart electricity grid to get supplies from the utilities when building's own energy generation less than its total demand and to export the surplus energy to the grid, when on-site generation is more than consumption.

### ***5.3.5 Electric Vehicles and Vehicle to Grid***

Electric vehicle is very crucial element in smart energy system because it affects smart energy system in many ways. First, it is a special type of consumer that may use either electricity or other renewable energy sources as fuel, e.g., fuel cells. Second, it has energy storage capability that may significantly affect the operation and control of smart energy system. Third, it not only replaces the fossil fuel consumption by renewable sources, but also improves energy efficiency using regenerative braking and efficient drive system.

Promoting renewable energy sources and their integration to the grid is one of the prime motives of smart energy systems. Key renewable energy sources compulsorily require energy storage facility due to their intermittent nature and uncertainty, and energy storage is a costly affair as of now. The electrical vehicles along with the vehicle-to-grid (V2G) and grid-to-vehicle (G2V) technologies provide a ray of hope, where the battery storage of a group electric vehicles, which are parked most of the time, can be utilized in the management of renewable energy system and demand-supply unbalance. Although it is not as straightforward as it appears, new technological innovations are making it possible. Battery state of charge (SoC) and state of health (SoH) estimation are couple of such innovations, which might be very useful in fostering V2G and G2V technologies. Apart from renewable's integration, electric vehicles and associated V2G technology could be useful in peak curtailment and valley filling in demand curve, thereby enhancing the utilization of the resources.

### ***5.3.6 Smart Metering***

Smart meter is an interface between the consumer and utility that not only records the energy consumption details and related information but may also communicate between utility and consumer using a wireless communication network. Smart meters provide facility of integrated metering of thermal, electricity and gas, and are capable of monitoring and controlling the energy supply and associated parameters intelligently. These features are very supportive in both centralized and decentralized

energy management by the consumer or by the utility from remote. Such remote and decentralized energy management can be helpful in demand-response management, energy conservation, automatic billing, customer services, etc.

### ***5.3.7 Artificial Intelligence and Machine Learning***

The transformation of energy system to smart energy system requires intelligence embodied in it. Accordingly, artificial intelligence and machine learning become an important part of smart energy system, which provides necessary tools and means to handle challenges of integrating variety of energy sources and transportation sector in a smart energy system. The artificial intelligence is the ability of the system to learn from the environment and experience. In smart energy system, smart meters, sensors, and phasor measurement units provide a lot of data that carries information about the environment, and the historical data provides experience about the system events, operations, and responses to disturbances. Machine learning, through data analytics and deep learning provides understanding of the information and data gathered from different measuring devices for its proper application.

The applications of artificial intelligence and machine learning in smart energy system span variety of domains. One of the most important of these is forecasting. For efficient, effective, and optimal operation of smart energy systems, forecasting of weather information, consumption of different energy types at different times, wind and solar generation and energy price are crucial. Artificial intelligence can also provide energy usage and electricity trading patterns, which might be very useful in decision making. Virtual power plant and synthetic inertia are other domains, which not only ensures desired contribution of these in the system but also coordinates of various participants. Artificial intelligence can also be useful in demand-supply management through smart homes, which respond to the system by adjusting its consumption based on price or other parameters, e.g., supply frequency, time of use, etc.

Modeling of energy production at different time scales and condition monitoring of various component of the system has always been important for reliable and secure operation of the system. Artificial intelligence and machine learning can be very useful in these. A lot of research has been focused on artificial intelligence-based condition monitoring of the assets and modelling of different systems. These could be valuable in sensing irregularities in generation, transmission, distribution, or consumption in almost real time, and accordingly taking appropriate decisions/actions in autonomous mode. It can be helpful in maintenance planning and breakdown reduction. Another critical application of artificial intelligence and machine learning is in the management of electric vehicle's charging and discharging based on the battery storage status (SoC), usage pattern, price, and grid condition.

Artificial intelligence can help in reducing energy waste, energy costs, and enable maximum utilization of renewable energy sources. However, the challenges in this domain include unavailability of sufficient data for training and vulnerability of

such system to cyberattacks, as these are exposed to the world through network interconnection. This powerful tool, although, has shown its ability to handle such cyberattacks by learning itself from the past experiences and future intelligent predictions.

## 5.4 Energy System Analysis Models

Modeling and simulation are essential aspect for design, analysis, and planning of any system. Numerous models and software simulation tools are already available for various elements of energy system; however, analysis and design of integrated energy system requires comprehensive modelling and simulation package. The basic reason for this is that the models are application specific and it is not possible to include entire characteristics of the original physical system into a single model. It is well known that an approximate model is often more useful than an exact model because it is simple to work with and allows understating the original system in a better way. The energy system models can be at different scales, in terms of size or time horizon. A model may focus on any particular technology or specific location, or it may consider multiple energy sources, or variety of consumers, or broad view of regional or national level, it may be intended for planning, or prediction, or design, or analysis.

There are many agencies, such as international atomic energy agency (IAEA) [23], international renewable energy agency (IRENA) [24], national renewable energy laboratory (NREL) [25], Fraunhofer Institute for Solar Energy Systems [26], etc. who are actively engaged in modeling of energy systems. Some of these models/simulation tools are introduced here in brief. These models/simulation tools can be applied directly or can be incorporated with enhancement for smart energy system applications.

### 5.4.1 RETscreen

RETScreen [27] is a simulation software tool for management of clean energy systems, energy efficiency, renewable energy, and cogeneration project feasibility analysis as well as energy performance analysis. It helps in assessing and optimizing the technical and financial viability of potential clean energy projects and allows professionals to easily monitor and verify the actual performance of their installations. It is also capable of identifying additional energy savings/production opportunities. The software is available without any charge from [27] and can be used in any part of the world for analysis and performance evaluation of various types of renewable-energy and energy-efficient technologies. The software (available in multiple languages) also includes product, project, hydrology and climate databases, and a case study-based college/university-level training course.

RETScreen functioning is based on comparison between a base-case and a proposed-case. The base-case may be a conventional technology, and a proposed-case may be a clean energy technology. Accordingly, it is concerned relative cost of the energy from the proposed clean energy system as compared to the base-case for the same energy output. It considers initial cost, operational cost, greenhouse gas emission, etc. in making the decision. RETScreen can analyze up to a 50-year time horizon in monthly or yearly time steps. The advantage of this software tool in smart energy system analysis is that it can be applied to any energy system, however, the shortcoming is that although it can model all energy sectors, it cannot model transport sector.

#### ***5.4.2 Model for Analysis of Energy Demand (MAED)***

This model [28] evaluates future energy demands based on socioeconomic, technological and demographic development in medium- to long-term. Energy demand is disaggregated into a large number of end-use categories corresponding to different goods and services in each of the six economic sectors. The model relates systematically the specific energy demand for producing various goods and services identified in the model, to the corresponding social, economic and technological factors that affect this demand. Energy demand is disaggregated into a large number of end-use categories; each one corresponding to a given service or to the production of a certain good.

This model also allows the user to expand the pre-defined energy demand structure according to the needs and/or data availability. The key features of this model are: sector-wise disaggregated energy demand for six major economic sectors, Agriculture, Construction, Mining, Manufacturing, Service, and Energy; possibility of subdivisions of these sectors into sub-sectors, e.g. the energy demand in the Households sector can be disaggregated into rural and urban groups; transport sector includes various modes and fuels; computation of energy demand at the sub-sector and activity level; a systematic accounting framework for evaluating the effect on energy demand of a change in economics or in the standard of living of the population.

#### ***5.4.3 Wien Automatic System Planning (WASP)***

Wien automatic system planning [23] is a popular model for power system planning. User may define the constraints such as fuel availability, emission norms, etc. and the model determines the optimal long-term expansion plan, which is defined in terms of total discounted costs for a power-generating system. The cost function includes expenditures on account of capital investment, fuel, operation and maintenance, inventory, salvage, and unserved energy demand. The simulation is carried out using 12 load duration curves to represent each year, for up to a maximum duration of

30 years. The existing system information is needed as initial input, which can be represented in terms of technical, economic and environmental characteristics of existing power plants, which includes their capacity, operating levels, heat rates, outage rates, fuel and other operational costs, emission levels, etc. The key feature of this model is that it can simulate all kind of power plants, such as, fossil-fuel, nuclear, biomass, wind, tidal and hydro, however, in smart energy system analysis, the drawback of this model is that it can consider only electric energy sector.

#### ***5.4.4 System Planning Test (SPLAT) Model***

The System Planning Test (SPLAT) model [24] is based on renewable energy database, which consists of comprehensive and latest data on technology cost, performance and resource potentials. These customizable SPLAT models with provision of national and regional analyses and their respective input data allow policymakers and professional to evaluate investment options considering specific policy objectives. The SPLAT model can analyze future system prospects through a least-cost optimization framework for energy supply. This model uses projected power demand, demand profiles, fuel cost, capacity factor and plant availability factors as inputs and provides least-cost generation mix for the region. This model features comparison of simulation results with regional master plans.

#### ***5.4.5 IRENA FlexTool***

In the era, where world is rapidly adopting variable renewable energy sources, flexibility assessment of power grid becomes essential. Based on national capacity investment plans and forecasts, the IRENA FlexTool [24] makes power system flexibility assessments, which reflect full power system dispatch and offer a detailed view of flexible generation options, demand flexibility and energy storage, along with and sector-coupling technologies like power-to-heat, electric vehicles and hydrogen production through electrolysis. It provides an assessment of potential flexibility gaps and suggests a cost-effective mix of solutions to overcome the flexibility gaps. This data-driven model is significantly affected by the initial data. The key inputs for this tool are demand, the generation mix, fuel cost, variable renewable energy time series, etc. This model is available free of cost and has the ability to analyze system operations with a resolution of an hour or less, which is aligned with real-world system challenges.

### ***5.4.6 Integrated Energy System Model (IESM)***

The Integrated Energy System Model (IESM) [29] is developed by National Renewable Energy Lab. (NREL), which combines a power flow simulator, a home energy management systems, a market layer, and hardware-in-the-loop simulation. The IESM is developed as a system-of-systems (SoS) simulator wherein the above simulation models/systems are integrated in a virtual testbed. In smart energy system, this integrated model can be used to simulate and analyze the new market structures and emerging technologies, such as distributed energy resources, demand-response management, and energy storage so as to understand and test their impact on the system's ability to provide reliable electricity to all customers.

## **5.5 Role of Storage**

The smart energy system features integration of renewable energy sources, which are intermittent and uncertain; hence, the system will need enhanced flexibility. To balance energy supply and demand over time, it is necessary to store the energy over days, weeks, or months. Energy storage provides flexible means to balance the energy supply by storing surplus energy at some point of time and using it at the time of need. This will not only improve the energy efficiency significantly, but also allows better utilization of uncertain renewable energy sources. Hence, more renewables can be integrated to the grid without compromising the robustness and stability of the grid. In the emerging smart energy system, distributed renewable electricity generation is rising and consumers are expected to participate in the energy markets as “prosumers” and “prosumagers”. Energy storage can curtail the peaks in energy demand profile and will provide flexible solutions to market participants. Other benefits of energy storage might be reduction in emission levels by facilitating a more efficient use of the existing assets and by reducing the carbon content of the fuels. This section briefly discusses the key storage technologies that might be useful in smart energy system.

### ***5.5.1 Types of Energy Storage***

Although electrical energy storage has been a crucial challenge to the power community, significant development has been witnessed in the last few decades. In the smart energy systems, there are options of long-term and large capacity energy storage in the format other than electricity. The present energy storage technologies can be classified in short-term and long-term based on their storage capacity and storage time. Figure 5.3 presents classification of energy storage technologies.

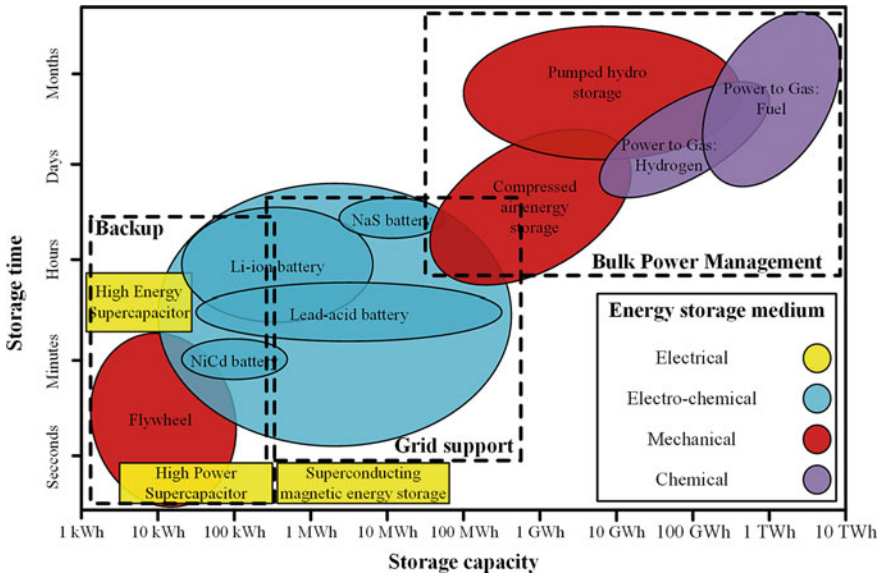


Fig. 5.3 An overview of energy storage technologies. Source Author

### 5.5.1.1 Pumped Hydro Storage

For bulk storage of electricity, pumped hydro storage is a popular technique. In this technique, water is pumped to a high-altitude reservoir during off-peak hours to store the energy in the form of potential energy. During peak demand, the water stored in the reservoir is used to generate electricity through hydro generator, and the released water is collected in lower reservoir. This storage technology is used for long-term storage of bulk energy. Use of pumped hydro storage is mainly determined by geographical and geological characteristics. In the European Union, pumped hydro storage accounted for 97% of electricity storage capacities in 2017. Pumped hydro storage is relatively cheaper for bulk energy storage capacity, however, long-term investment is required for this technology. Pumped hydro storage also provides ancillary services such as: frequency and voltage control to the power grid. The advantages of this storage technology are low self-discharge, good efficiency and small response time. At present, there are about 170 GW of pumped storage capacity in operation across the globe.

### 5.5.1.2 Compressed Air Energy Storage

In compressed air energy storage technology, air is pumped into an underground hole when surplus electricity is available. At the time of need, the stored compressed air from the underground cave is released back and heated, usually through natural gas.

This results in expansion of the air, which is used to generate electricity. This type of storage is used for medium term storage, for arbitrage, reserve, and other ancillary services. As reported in [30], only two compressed air energy storage facilities are operational, out of which one plant is in the USA (110 MW) and another in Germany (320 MW). This technology also has negligible self-discharge and response time of few seconds to few minutes; however, the efficiency is lower than pumped storage.

### 5.5.1.3 Flywheel

A flywheel is a mechanical device, which can store kinetic energy when it spins at high speed. The stored energy in the flywheel corresponds to its speed and can be released by slowing down its spin. This storage technique is not good for long-term energy storage; however, it is very convenient for load-leveling and load-shifting applications. The benefits of flywheel storage include very low response time, high efficiency, long-life cycle, and small maintenance costs. The disadvantages of this technology are requirement of vacuum chamber, mechanical complexity, and significant self-discharge. Since the demonstration of first commercial use of this storage technology in 2011 for grid regulation, many flywheel energy storage facilities are operational [30].

### 5.5.1.4 Battery Storage

This storage technology is based on electrochemical processes, where charging and discharging reactions are used for energy storage and retrieval. Dozens of different batteries are possible based on the electrode type. Figure 5.4 presents popular batteries for energy storage in smart energy systems. Lead-acid batteries use reaction between lead and sulfuric acid to generate electrons to produce energy. These have low energy density and low cost. These batteries are more common in vehicles, hence, can be useful in vehicle-to-grid and grid-to-vehicle energy transfer in electric/hybrid electric vehicles. These are also used in residential uninterrupted power supply systems.

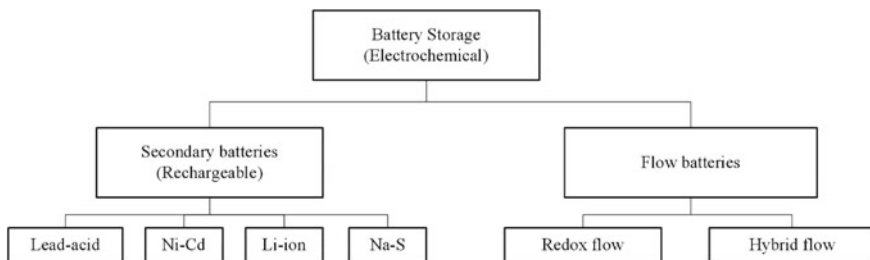


**Fig. 5.4** Battery storage technologies. *Source* Author



The nickel–cadmium (Ni–Cd) battery system uses nickel as positive electrode and cadmium as negative electrode. This battery was popular for portable devices like medical equipment and cameras, and these have been deployed in early age electric vehicles also up to the 1990s. However, the environmental concerns and toxicity resulted in limited applications of otherwise robust Ni–Cd batteries. These also have memory effect that causes a loss of capacity if a periodic full discharge cycle is not given.

A lithium-ion (Li-ion) battery is based on electrochemical charge/discharge reactions. It utilizes the flow of lithium ions from negative to positive electrode and release energy. These are very popular in the stationary field and worldwide more than 500 MW batteries are operating in grid-connected system. As reported in [30], Li-ion battery system with voltages up to 1 kV has been designed for grid support. Compared to other battery options, lithium-ion batteries have high energy density and are lightweight. The advantages of Li-ion batteries are their high energy and power density, high scalability, high efficiency and flexibility in power and energy. The applications of Li-ion batteries in power system include self-consumption of PV energy, contingency support of smart grids, ancillary services, frequency regulation, and support to better integration of large renewable plants into the electricity system.

Flow batteries, also known as redox (reduction–oxidation) batteries, operate in a similar way to fuel cells. It comprises two electrolytes, separated by ion or proton exchange membrane. Energy can be stored in the electrolytes by oxidizing one and reducing the other. This is achieved by increasing the potential difference between the two liquids. Similarly, electricity can be produced by reversing the process. Flow batteries are characterized by long life cycle and high energy efficiency, and hence these are found to suitable for the development of large-scale grid-connected energy storage system. However, the flow batteries are costly and suffer from the leakage problem of acidic fluids.

### 5.5.1.5 Power to Gas: Hydrogen Storage

Hydrogen energy storage is crucial in renewables integration and transition to smart energy system because it can provide long-term storage option in bulk amount. This belongs to the category of chemical energy storage, in which, the electricity is converted into hydrogen for storage purpose using electrolysis process that produce oxygen and hydrogen gases. The oxygen is simply released into the atmosphere, whereas hydrogen is compressed and stored for future need. Surplus electric energy from renewable or other sources may be used to produce and store hydrogen. At the time of need, the stored hydrogen can be re-electrified using fuel cells, which provides electricity output. It is also possible to generate electricity from hydrogen using gas turbines or engines. The characteristics of hydrogen energy storage systems are high volumetric energy density, low footprint in case of underground storage, and possibility of bulk energy storage. On the other side, low efficiency of the conversion chain, the high cost of electrolyzers and electricity are main drawbacks of this technique. Still, many power-to-gas projects are emerging across the globe, and some

of these envisage to use hydrogen in the transport sector. Like other bulk storage technologies, this is also useful in balancing seasonal and weekly fluctuations, and ancillary services.

#### **5.5.1.6 Power to Gas: Methane Storage**

Methane has emerged as an attractive alternative to the hydrogen for energy storage applications, as it can be easily produced by the process of methanation using hydrogen and carbon dioxide. The biggest motivation of using methane is its compatibility with the existing natural gas chain, and it can be injected into the natural gas grid without restriction for its use. Methane has better energy density than hydrogen and negligible self-discharge. Also, methanation provides the possibility to connect the electricity system with the market of other energy sources. The drawback of methane storage is its high cost and low efficiency.

#### **5.5.1.7 Supercapacitors**

The only technology to store electricity without any transformation is a capacitance; however, it's very low energy density, and hence, small storage capacity and short storage time used to be a big concern for any practical applications. A supercapacitor, also termed as electric double-layer capacitors (EDLCs), overcomes this challenge with very high capacitance values through its double-layer capacitance arrangement. Supercapacitors store electrical energy at an electrode–electrolyte interface. Supercapacitor is made of two metal plates with activated carbon coating, which results into bigger area for storing large amount of charge. These plates are immersed in an electrolyte, which is made of positive and negative ions dissolved in a solvent. Two charged layers separated by a small distance are produced on the surface with the application of voltage. Supercapacitors can be cycled millions of times without any significant change in its performance. It has low equivalent series resistance and provides high power density. Supercapacitors have the ability to perform at very low temperatures also, e.g.,  $-40\text{ }^{\circ}\text{C}$ . The shortcomings of supercapacitors include low energy density and low cell voltage. Supercapacitors find its applications in power management, frequency regulation and grid stability that may need fast charge/discharge cycles for short-term power requirements.

### ***5.5.2 Analysis on Energy Storage Technologies***

The key idea behind smart energy system is sustainable and energy efficient energy system, which relies on maximum utilization of renewable energy sources. Therefore, energy storage becomes crucial for smart energy system for balancing energy supply and demand. However, it is also a fact that energy storage options are very costly.

Usually, number of full-load hours is considered as a key parameter for determining the cost of any storage option. Battery storage is the costliest among different storage technologies. The average per unit cost of other storage technologies is comparable to each other, still, pumped hydro and compressed air storage are cheaper.

Being lowest in cost, pumped hydro storage has maximum shares of total storage capacity, while others except battery storage are gradually increasing with their maturity. Despite of the highest cost, battery storage is the second in the order, and are expected to play a crucial role in smart energy system. Therefore, largest growth across the world is witnessed in battery storage, and Li-ion batteries lead this growth with approximately 86% share in electricity storage using batteries. Also, there have been increasing interests in using the batteries of the electric vehicles for storage of electricity from the power grid and for the power grid at the time of dire need. For such systems, electric vehicles, power system and information technology integrated together bring up the concept of vehicle-to-grid (V2G), where electric vehicles act as a portable power plant providing electricity to the system as and when required.

## 5.6 Conclusion

Energy consumption of a country or an individual signifies its social, economic, and technological standing. However, its adverse effect on the climate persuades us to look for sustainable sources and systems for energy supply and consumption. Smart energy system is an integrated approach of multiple kind of energy sources, controlled and operated in an intelligent manner to reduce energy waste, facilitate easy grid integration of renewable sources, and optimal utilization of the resources. This requires amalgamation of many existing technologies and growth of several innovative technologies and methods.

This chapter discussed key components and important technology enablers of a smart energy system, which includes variety of energy sources that may be integrated to serve diverse energy consumers in an efficient way. Some of the existing, developing, and novel technologies are introduced, which are essential for achieving the objectives of smart energy system. Some of the useful software tools and models, which can be used to model a smart energy system for analysis and design, are presented with their key features and drawbacks. The importance of energy storage in realizing the smart energy system and various options of energy storage are also discussed in brief.

It can be summarized that smart energy system is one of the most important innovations in utilization of solar energy to maximum possible extent. A lot of social, technical and economic challenges need to be addressed in the coming days, some of them includes the design and management of a smart energy system, energy storage technology, energy market, etc.

## References

1. Lund H, Østergaard PA, Connolly D, Mathiesen BV (2017) Smart energy and smart energy systems. *Energy* 137:556–565. <https://doi.org/10.1016/j.energy.2017.05.123>
2. Guarnieri M, Liserre M, Sauter T, Hung JY (2010) Future energy systems: Integrating renewable energy sources into the smart power grid through industrial electronics. *IEEE Ind Electron Mag* 4(1):18–37. <https://doi.org/10.1109/MIE.2010.935861>
3. Lund H, Andersen AN, Østergaard PA, Mathiesen BV, Connolly D (2012) From electricity smart grids to smart energy systems—a market operation based approach and understanding. *Energy* 42(1):96–102. <https://doi.org/10.1016/j.energy.2012.04.003>
4. O'Dwyer E, Pan I, Acha S, Shah N (2019) Smart energy systems for sustainable smart cities: Current developments, trends and future directions. *Appl Energy* 237:581–597. <https://doi.org/10.1016/j.apenergy.2019.01.024>
5. Xu Y, Yan C, Liu H, Wang J, Yang Z, Jiang Y (2020) Smart energy systems: a critical review on design and operation optimization. *Sustain Cities Soc* 62:102369. <https://doi.org/10.1016/j.scs.2020.102369>
6. Bačeković I, Østergaard PA (2018) A smart energy system approach vs a non-integrated renewable energy system approach to designing a future energy system in Zagreb. *Energy* 155:824–837. <https://doi.org/10.1016/j.energy.2018.05.075>
7. Crossley P, Beviz A (2010) Smart energy systems: transitioning renewables onto the grid. *Renew Energy Focus* 11(5):54–56. [https://doi.org/10.1016/S1755-0084\(10\)70118-6](https://doi.org/10.1016/S1755-0084(10)70118-6)
8. Wade NS, Taylor PC, Lang PD, Jones PR (2010) Evaluating the benefits of an electrical energy storage system in a future smart grid. *Energy Policy* 38(11):7180–7188. <https://doi.org/10.1016/j.enpol.2010.07.045>
9. Krajačić G, Duić N, Zmijarević Z, Mathiesen BV, Vučinić AA, Da Graa Carvalho M (2011) Planning for a 100% independent energy system based on smart energy storage for integration of renewables and CO<sub>2</sub> emissions reduction. *Appl Therm Eng* 31(13):2073–2083. <https://doi.org/10.1016/j.applthermaleng.2011.03.014>
10. Lund H et al (2016) Energy storage and smart energy systems. *Int J Sustain Energy Plan Manage* 11:3–14. <https://doi.org/10.5278/ijsepm.2016.11.2>
11. Strasser T et al (2015) A review of architectures and concepts for intelligence in future electric energy systems. *IEEE Trans Indust Electron* 62(4):2424–2438. <https://doi.org/10.1109/TIE.2014.2361486>
12. Dominković DF, Dobravec V, Jiang Y, Nielsen PS, Krajačić G (2018) Modelling smart energy systems in tropical regions. *Energy* 155:592–609. <https://doi.org/10.1016/j.energy.2018.05.007>
13. Farmani F, Parvizimosaed M, Monsef H, Rahimi-Kian A (2018) A conceptual model of a smart energy management system for a residential building equipped with CCHP system. *Int J Electr Power Energy Syst* 95:523–536. <https://doi.org/10.1016/j.ijepes.2017.09.016>
14. Sorknæs P et al (2020) Smart energy markets—future electricity, gas and heating markets. *Renew Sustain Energy Rev* 119:109655. <https://doi.org/10.1016/j.rser.2019.109655>
15. Buza DI, Juhász F, Miru G, Fëlegyhàzi M, Holczer T (2014) CryPLH: protecting smart energy systems from targeted attacks with a PLC honeypot. In: *Lecture notes in computer science (including subseries lecture notes in artificial intelligence and lecture notes in bioinformatics)*, 2014, vol 8448, pp 181–192. [https://doi.org/10.1007/978-3-319-10329-7\\_12](https://doi.org/10.1007/978-3-319-10329-7_12)
16. Mathiesen BV et al (2015) Smart energy systems for coherent 100% renewable energy and transport solutions. *Appl Energy* 145:139–154. <https://doi.org/10.1016/j.apenergy.2015.01.075>
17. Hvelplund F, Möller B, Sperling K (2013) Local ownership, smart energy systems and better wind power economy. *Energy Strateg Rev* 1(3):164–170. <https://doi.org/10.1016/j.esr.2013.02.001>
18. Renewable energy statistics 2020 (2020)
19. World Energy Balances 2019—Analysis—IEA (2020) International energy agency, 2020 [Online]. Available <https://www.iea.org/reports/world-energy-balances-overview>. Accessed 01 Aug 2020

20. Usman A, Shami SH (2013) Evolution of communication technologies for smart grid applications. *Renew Sustain Energy Rev* 19:191–199. <https://doi.org/10.1016/j.rser.2012.11.002>
21. Schwefel H-P, Zhang Y-JA, Wietfeld C, Mohsenian-Rad H (2018) Emerging technologies initiative ‘smart grid communications’: information technology for smart utility grids
22. Torcellini P, Pless S, Deru M, Crawley D (2006) Zero energy buildings: a critical look at the definition; preprint
23. Energy Modelling ToolsIAEA [Online]. Available <https://www.iaea.org/topics/energy-planning/energy-modelling-tools>. Accessed 10 Aug 2020
24. Energy system models and data [Online]. Available <https://www.irena.org/energytransition/Energy-System-Models-and-Data>. Accessed 10 Aug 2020
25. van Beuzekom L (2015) Integrated energy system models (IESMs). National Renewable Energy Laboratory, 2015 [Online]. Available [https://nrel.github.io/iiESI.org/assets/pdfs/iiESI\\_102\\_omalley2.pdf](https://nrel.github.io/iiESI.org/assets/pdfs/iiESI_102_omalley2.pdf). Accessed 10 Aug 2020
26. Energy System Models at Fraunhofer ISE. Fraunhofer ISE, 2020 [Online]. Available <https://www.ise.fraunhofer.de/en/business-areas/power-electronics-grids-and-smart-systems/energy-system-analysis/energy-system-models-at-fraunhofer-ise.html>. Accessed 10 Aug 2020
27. RETScreen International. National Resources Canada, 2019 [Online]. Available <https://www.etscreen.net/>
28. User’s manual of model for analysis of energy demand. Vienna (2006)
29. Mittal S, Ruth M, Pratt A, Lunacek M, Krishnamurthy D, Jones W (2015) A system-of-systems approach for integrated energy systems modeling and simulation. In: Society for modeling and simulation international summer simulation multi-conference
30. Ajanovic A, Hiesl A, Haas R (2020) On the role of storage for electricity in smart energy systems. *Energy* 200:117473. <https://doi.org/10.1016/j.energy.2020.117473>

**Dr. S. K. Jain** received his M.Tech. in Electrical Engineering from Indian Institute of Technology Roorkee, in 2002 and Ph.D. in Power Systems from Electrical Engineering Department, Indian Institute of Technology Kanpur, in 2012. He worked as an Engineer (Projects) and Senior Engineer (Operations & Maintenance) with the largest power utility of India, viz. NTPC Ltd. from 2002 to 2007, where he was responsible for erection, testing, and commissioning of 400/132KV switchyard, variable frequency drive (VFD), generator protection and excitation system. After serving five years at NTPC limited, Dr. Jain joined Indian Institute of Information Technology, Design and Manufacturing Jabalpur as a Research Engineer, where he is an assistant professor at present.

He is a senior member of the largest professional body in engineering, IEEE (USA) and member of many prestigious technical societies like IE (India), IETE (India), and ISTE (India). He has undergone through many professional training programs at Bharat Heavy Electricals Limited (BHEL), Power Management Institute (PMI, NTPC), etc. He has been a recipient of General Manager Special Award at NTPC Rihand in 2005, POSOCO Power System Award (2013) and many best paper awards.

Dr. Jain has so far authored more than 40 research papers and has supervised 4 Phd students (2 ongoing), 21 Masters students (4 Ongoing). Dr. Jain has organized 5 conferences/workshops/QIP and serves as reviewer for more than 25 journals including IEEE Transactions on: Industrial Electronics, Power Delivery, Power System, Smart Grid, Education, Instrumentation and Measurement, etc.

**Prof S. N. Singh** obtained his M. Tech. and Ph.D. in Electrical Engineering from Indian Institute of Technology Kanpur, in 1989 and 1995. Presently, he is Vice-Chancellor, Madan Mohan Malviya University of Technology Gorakhpur and leave from Professor (HAG), Department of

Electrical Engineering, Indian Institute of Technology Kanpur, India. Before joining IIT Kanpur as Associate Professor, Dr Singh worked with UP State Electricity Board as Assistant Engineer from 1988 to 1996, with Roorkee University (now IIT Roorkee) as Assistant Professor from 1996 to 2000 and with Asian Institute of Technology, Bangkok, Thailand, as Assistant Professor from 2001 to 2002. Dr. Singh received several awards including Young Engineer Award 2000 of Indian National Academy of Engineering (INAE), Khosla Research Award of IIT Roorkee, and Young Engineer Award of CBIP New Delhi (India), 1996. Prof Singh is recipient of Humboldt Fellowship of Germany (2005, 2007) and Otto-monsted Fellowship of Denmark (2009–10). Prof Singh became the first Asian to receive 2013 IEEE Educational Activity Board Meritorious Achievement Award. He is also recipient of INAE Outstanding Teacher Award 2016 and IEEE R10 region (Asia-Pacific) Outstanding Volunteer Award 2016.

His research interests include power system restructuring, FACTS, power system optimization and control, security analysis, wind power, etc. Prof. Singh has published more than 440 papers in International/national journals/conferences and supervised 29 Ph.D. (11 Ph.D. under progress). He has also written two books—one on Electric Power Generation, Transmission and Distribution and second is Basic Electrical Engineering, published by PHI, India. Prof. Singh has completed three dozen of projects in India and abroad.

Prof. Singh was Chairman, IEEE UP Section for 2013 and 2014, and presently, he is IEEE Region 10 (Asia-Pacific) Conference and Technical Seminar Coordinator 2015–18. Prof Singh is also India Council Chairman-Elect 2017 of IEEE, the largest professional body in engineering.

# Chapter 6

## A Holistic Review of Smart Grid Contribution Toward Energy Sustainability



Saad Umer Khan and Akhtar Kalam

### 6.1 Introduction

The key contribution of the Smart Grid toward energy sustainability is from its information system. Data is central to decision making and the basis of accountability. There is a degree of resilience rooted in the Smart Grid system as it can quickly respond to disturbances of both information and physical systems [1]. The Smart Grid architecture supports interaction between physical and information systems with integrated processes for different applications [2]. The Smart Grid's information systems are reshaping governance by facilitating goal setting and policy formation. A holistic review is important when evaluating a broader goal such as sustainability, as sector-specific goals are usually in conflict and these interrelations are required to be studied before striving for meaningful goals rather than trendy social causes. Sustainability has come to focus because of the harmful implications of unsustainable practices of the industrial and information age driven by energy.

Current trends in smart cities are fueled by an increase in urbanization which in turn contributes to climate change. Electrification and decarbonization are at times opposing goals that can be balanced with new business models incorporating digitalization. Sustainability is a core objective of a smart city and is common to any definition produced by the participating members of the United Nations Economic Commission, but indicators or variables for individual communities may vary [3]. To integrate all the smart city services, a unified standard is required to connect all utilities and vendor components possibly under the umbrella of Smart Grid [4]. The following are some of the changes brought about by the Smart Grid revolution:

---

S. Umer Khan · A. Kalam (✉)  
College of Engineering and Science, Victoria University, Melbourne, Australia  
e-mail: [akhtar.kalam@vu.edu.au](mailto:akhtar.kalam@vu.edu.au)

S. Umer Khan  
e-mail: [saad.khan@live.vu.edu.au](mailto:saad.khan@live.vu.edu.au)

The electrical balance of plant (EBoP)	Increased share of renewable generation can affect grid stability and reliability because of its intermittent nature. Original Equipment Manufacturers (OEMs) are offering new solutions to address flexibility by including intelligent storage and infrastructure options
Energy Internet of Things or Internet of Energy (eIoT or IoE)	Energy efficiency can be improved by increasing the reliability of the grid. Predictive maintenance and process optimization can be achieved by data analytics
Transport and energy mobility	As the electric grid replaces the hydrocarbon-based fuel supply chain, charging infrastructure solutions are being developed to handle growing number of electrical vehicle

The majority of the world population is moving to urban centers and major cities, away from rural areas as the world population continues to increase which is forecasted to peak in the year 2100 at over 10 billion. The growth of cities in conjunction with an improvement in information and communication technologies (ICTs) is leading to large volumes of data also known as big data. This high-speed and high-volume data include resident's consumption data is making cities smarter and Smart Grid analytics is helping city planners to make key decisions related to policy, infrastructure, and operations leading to sustainable energy management.

For developed and developing countries not affected by major conflicts, the focus is toward upgrading and regeneration of infrastructure, instead of installing new greenfield sites. The Smart Grid is not meant to replace the existing electrical system which is not economically viable; instead, it offers new services and features on existing assets. It also provides solutions to integrate new systems with old without compromising on stability.

A Smart Grid facilitates energy sustainability by improving renewable energy utilization, improves renewable capacity, optimizes scheduling, and reduces line loss, behavior correction by demand response, and consumption efficiency [5].

The definition of a Smart Grid could vary from region to region, and the United State Department lays out the following functions for a Smart Grid system:

- Self-healing system in an event of power disturbance;
- Active participation of customers concerning demand response;
- Inbuilt resilience to physical and cyber-attacks;
- Ensure power quality suitable for modern usage;
- Provision for a variety of power storage and generation options;
- Compatibility for new products, services, and market structures; and
- Flexible operation of assets and increase asset performance.



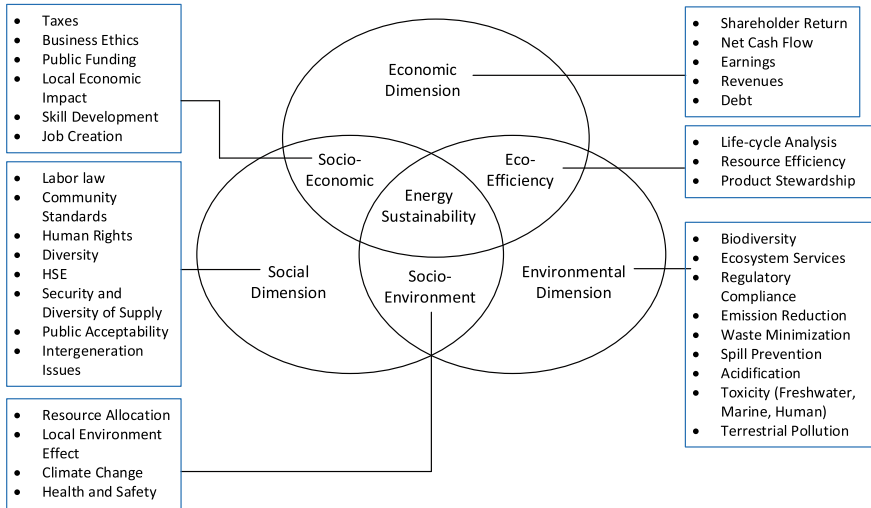


**Fig. 6.1** Sustainability as defined by key dimensions and their interactions. *Source* Author

### 6.1.1 Is Renewable Energy Sustainable?

Energy sources like wind, solar, hydro, and biomass are renewable by nature but not necessarily sustainable. Sustainability can be defined by three key dimensions and their interactions as illustrated in Fig. 6.1.

The environmental dimension of sustainability lists environmental indicators. One of the basic indicators is the net positive energy balance that is the renewable energy device should not cost more energy to produce for its intended operation life. Aside from the production side of assets, mining of non-renewable fuel and raw materials such as neodymium for wind turbines is equally bad for the environment. Similarly, hydropower dams can damage entire ecosystems and the disadvantages could spill into social dimensions causing conflict between or within nations.

Social dimensions contain the most complex indicators which can include demographics to the wage gap. Energy is the basic necessity of fulfilling needs on all levels of Maslow’s hierarchy of needs for a modern society. As the social dimension includes all stakeholders like customers, workers, investors, politicians, etc., this dimension and its interactions can be challenging to analyze. It is difficult to use a uniform template to analyze social aspects for each nation as each has its peculiar features. The world is more connected in the modern era, and international relations can at times weigh in heavier than other factors. What is sustainable for Germany may not be sustainable for North Korea?

The economic dimension contains simple but most influential indicators. Levelized cost, subsidies, economic activity, continuity of supply, financing options, and foreign exchange requirements can make an option sustainable or unsustainable.

Smart Grids can help create options suitable to address or mitigate the negative effects on all dimensions. Renewable energy sources when coupled with a Smart Grid including energy storage can provide sustainable energy solutions in competition to on-demand fossil energy sources.

There is no standardized methodology currently available to gauge the eco-efficiency of Smart Grid systems [6]. Sustainability in terms of processes needs to be evaluated as the conceptual systems are often overlooked during sustainability analysis [7]. A Smart Grid, when viewed in terms of future services, gives a higher sustainability score as the nature of the services can be multidisciplinary and across industries [8].

## 6.2 California's Renewable Energy Puzzle

In mid-August 2020, California faced rolling blackouts and public opinion blamed renewables for these events. The main season load for Californians is air conditioning, and 2020 has been one of the warmest recordings and one of the highest global temperatures. Independent System Operator (ISO) has clarified that:

This is a resource issue, not a renewable issue.

Around 50% of California's energy mix currently comprises renewable sources including large-scale hydro (California currently does not classify hydro as renewable). The 20-year shift to renewables has not made timely investments in storage in proportion to renewable projects replacing thermal power plants. It seems that policymakers were keen to ride on public opinion to close the power plant's contribution to carbon emissions, but the plan did not include the green alternative for a conservative scenario.

One of the rapidly implementable solutions being pushed is a drive to increase rooftop solar panels, batteries, and demand response programs for energy conservation. The existing conventional demand response program has made a difference as people have responded to the state's message by turning offload.

## 6.3 Energy Storage Is a Key Equalizer

The era of the modern grid is marked by a move from a traditional system where electricity is generated at remote central locations and subsequently distributed to geographically separated consumer centers to distributed energy generation, distributed storage, and varying consumption roles. The main deficiency in a traditional grid is lack of flexibility and hence limited energy management capabilities.

A Smart Grid requires groundbreaking systems to forecast and manage grid demand economically. Numerous power networks already have a substantial number of smart meters producing large consumption data. This linear data can be analyzed

in terms of performance and correlated with other events like weather to provide more meaningful insights.

The move leading to a Smart Grid has been accelerated by governmental regulatory and policy push promoting reliable and sustainable energy, which is possible by a combination of Smart Grid, integrated renewable generation, energy storage, and demand response management.

An integrated energy storage system provides the following advantages while ensuring grid reliability by meeting requirements of resilience and stability:

- Effective management of peak power demand;
- Provisions for renewable source penetration; and
- Reduces the infrastructure requirements by the management of peak load.

Commonly used energy storage systems used are listed in Fig. 6.2 of which battery storage is the most common application. Cities have opted to use one or a combination of energy storage systems.

The Smart Grid enables reduced carbon emissions by aiding the penetration and optimal utilization of distributed renewable energy resources coupled with energy storage. More work needs to be done to understand the effects of large-scale energy storage on power quality and grid stability. Current research trends include the optimization of energy storage operations, and any such initiative can only be realized within the framework of a Smart Grid or equivalent initiative.

Energy and reserve costs are opposing goals for which an optimal cost point can be established which can be realized for each energy storage type managed by a Smart Grid framework creating sustainable results [9]. Community-scale battery storage options can be a practical option but need a change in the network tariff

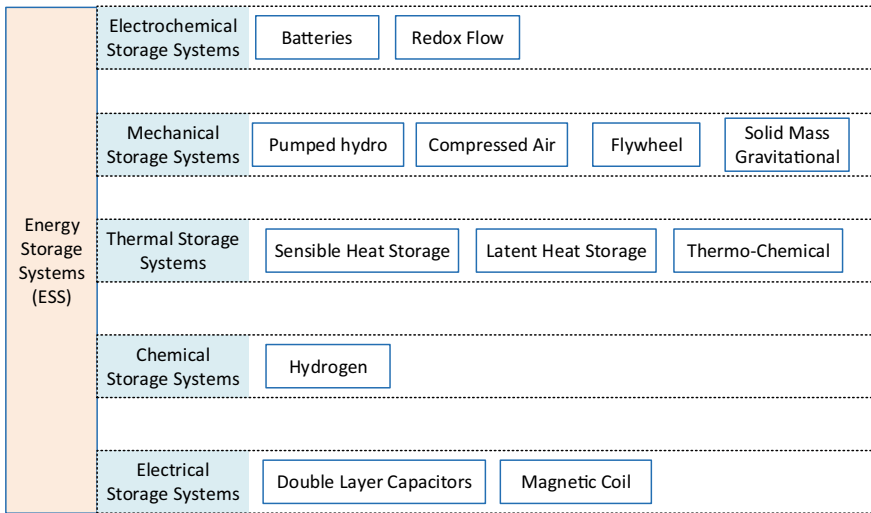


**Fig. 6.2** Commonly used energy storage systems. *Source* Author

structure. Residential-scale battery storage is already a viable option as the cost of battery systems has decreased over the years [10]. Future ICTs will enable the use of distributed battery storage and future tariff structure needs to accommodate these storage resources.

## **6.4 Information and Communication Technologies Realizing Sustainable Consumption**

ICTs are key to Smart Grid development in pursuit of goals such as sustainability via energy efficiency. The starting point in terms of the objective and constraints of ICT are as follows:

- Existing electrical system needs improvement to cut greenhouse emissions.
- Compromise between ICT-based energy consumption and energy saving by ICT-adopted Smart Grid.

Although the power systems need an ICT backbone to gather and analyze data generated from each system element, still the energy consumed by the ICT infrastructure should be kept in check. In addition, ICT system elements have a relatively short life cycle and obsolesce management, and legacy system integration can be an issue. As the energy footprint of ICT elements and devices continues to grow, the requirement for sensing, computing, and networking devices is going to increase the energy requirements. Collaboration with the telecom industry to provide auxiliary services to the Smart Grid will be fundamental to a cost-effective solution providing renewable resources management, load management, and existing grid functions.

Ongoing developments in energy networks are to adapt the present protection and control system toward a new communication framework suited for a Smart Grid's requirements. In the absence of a common reference architecture, artificial intelligence (AI) is playing an important role in integrating and optimizing energy consumption.

## **6.5 AI Role in the Integration of Renewable Energy and Optimization of Energy Consumption**

Renewable energy and specifically wind power have an unpredictability element which decides to store and transmit difficultly. The utility of a reliable power source is always more than an unpredictable energy source like the wind.

Google's London-based subsidiary DeepMind is developing solutions and employing machine learning to assist operators in quick, smart, and data-driven assessment of the utilization of their energy output. By the balancing of supply and demand, Google claims to improve the utilization by 20% above the baseline.

The system is striving to predict power output 24–36 h in advance of generation by a neural network trained on historic turbine output against weather forecasts. Google itself has reached its goal of 100% renewable sources.

This subsidiary is already using AI and the IoTs to decrease Google’s data center’s energy use by 30%. The system improves data center’s energy efficiency and reduces cooling load.

ICT will play a key role to influence consumption behavior, thereby increasing consumption efficiency and reducing wastage [11].

### 6.6 Renewable Energy Sources Integrated into the Power Grid with Smart Technologies

Renewable energy sources are diverse by nature and can vary in terms of scale, topology, and availability. Figure 6.3 shows the most popular and relatively clean renewable energy sources.

Renewable sources can support both islanded and grid-connected modes, but each source has different considerations in terms of grid connection. Renewable generation can solve today’s problems like sustainable energy, carbon emission targets, and energy security (both local availability and diversity). The main shortcoming of renewable sources is its variable nature but at the same time, reactive distributed generation in the context of the Smart Grid can reduce stress on the transmission system. Renewable energy sources can be characterized by the following:

- Scale or generation capacity;
- Location, which includes geographic location, installation form, and architecture; and
- Availability and variability that is instantaneous, daily, and seasonal variations.

In terms of size, a renewable energy source can be a residential installation or a utility-scale project whereas for hydro and wind various geographic constraints exist limiting options.

Whether the source is connected at the distribution or transmission level, a Smart Grid can manage a combination of distributed and central purchasing decisions. The intermittency evaluation of distributed solar can be far more complex than a central utility-scale solar installation.







Solar	Wind	Hydroelectric	Geothermal	Biomass	Tidal
					

Fig. 6.3 Popular and relatively clean renewable energy sources. Source Author

By treating renewable resources as smart assets for which the availability is variable but predictable, energy sustainability can be achieved. Only with basic decisions like sourcing, energy from a distance or near sources can reduce line losses, save energy, and extend asset life. In an event of a natural disaster like bushfires, earthquakes, and hurricanes when grid-connected resources are lost, distributed generation resources can form microgrids managed by smart services.

The futuristic principle needs to be employed while evaluating renewable energy sustainability that is sustainability for both the present and foreseeable future [12]. The same principle should be used when assessing the sustainability of the overall Smart Grid including generation.

## 6.7 New Developments in Flexible AC Transmission Systems (FACTS) Supporting Energy Sustainability

New technologies are available for single-phase modular static synchronous series compensator which injects a  $90^\circ$  of phase voltage to the line current, thereby manipulating the power flow on a line in real time. These technologies do not use transformers and use solid-state protection elements which reduce the installation time to a matter of weeks. These products give more options to system planners who can then use sustainable renewable resources and better manage transmission line capacities.

## 6.8 Conclusion

Individual systems and sub-systems for both renewable energy and Smart Grid may give varying sustainability impressions but a holistic approach considering the Smart Grid as the main system can give promising results. Future developments in energy storage, ICT, and automation will drive sustainable energy results.

## References

1. Chen S, Li K (2020) Distributed optimal control of transient stability for a power information physical system. 2020, 1393216
2. Cao JW, Wan Y-X, Tu G-Y, Zhang S-Q, Xia A-X, Liu X-F, Chen Z, Lu C (2014) Information system architecture for smart grids. *Chin. J. Comput.* **36**:143–167. 10.3724/SP.J.1016.2013.00143
3. Maria TA, Niamh M (2020) The concept of sustainability in smart city definitions, *Front Built Environ* 6(77)
4. Strielkowski W, Veinbender T, Tvaronavičienė M, Lace N (2020) Economic efficiency and energy security of smart cities. *Econ Res Ekonomska Istraživanja* 33(1):788–803
5. Hu Z, Li C, Cao Y, Fang B, He, L, Zhang M (2014) How smart grid contributes to energy sustainability. *Energy Procedia* 61:858–861

6. Moretti M, Djomo NS, Azadi H, May K, Vos K, Passel S, Witters N (2016) A systematic review of the environmental and economic impacts of Smart Grids. *Renew Sustain Energy Rev* 68:10.1016
7. Brown M, Zhou S (2012) Sustainable smart grids sustainability/sustainable smart grids, emergence of a policy framework. 10:1007
8. Nikolaidis P, Poullikkas A (2020) Sustainable services to enhance flexibility in the upcoming smart grids. In: Stagner J, Ting DK (eds) *Sustaining resources for tomorrow*. Green Energy and Technology, Springer, Cham
9. Mo JY, Jeon W (2017) How does energy storage increase the efficiency of an electricity market with integrated wind and solar power generation?—A case study of Korea. *Sustainability*, 9(10)
10. Dell RM, Rand David (2001) Energy storage—a key technology for global energy sustainability. *J Power Sources* 100:2–17
11. Bastida L, Cohen JJ, Kollmann A, Moya A, Reichl J (2018) Renewable and sustainable energy reviews. 103:455–462
12. Fuller RJ (2005) Renewable energy and sustainability—an evaluation. In: ANZSES Conference, Dunedin, (21)

# Chapter 7

## Short-Term Solar PV Generation Forecast Using Neural Networks and Deep Learning Models



Shivashankar Sukumar, Naran M. Pindoriya, and Sri Niwas Singh

### 7.1 Introduction

Renewable energy sources are the critical component of sustainable development as they reduce the dependency on fossil fuels for power generation, reduce greenhouse gas emission, and promote long-term energy security. Among the renewable energy sources, wind- and solar energy-based generations are in rapid growth. The installed capacity of grid-connected solar PV generation in India has increased to 36% of the overall grid-connected renewable power at the end of May 2019 [1]. While PV generation has a considerable potential to fulfill the growing electricity demand, the major challenge is its weather dependency, which leads to intermittency in its generation. The stochastic nature of PV generation can cause undesirable changes in the node voltages, voltage rise, and fluctuations in voltage and power in low-voltage distribution networks [2, 3]. This will result in an increase of the utility grid's overall operating cost [4, 5]. Moreover, the intermittency in solar PV generation of large utility scale plants will result in uncertainty during their participation in the local electricity markets. The uncertainty can be reduced by accurately forecasting solar PV generation. A reliable solar PV forecasting can provide vital information to utility scale PV operators for effective decision making. A day ahead forecast of solar PV generation for large utility scale plants with increased accuracy is crucial for utility scale solar PV plant's participation in the local electricity markets. The lack of accurate forecast will incur penalty and additional operating cost related to network balancing for the owners of utility scale solar PV plant [6]. For example,

---

S. Sukumar · N. M. Pindoriya (✉)

Department of Electrical Engineering, Indian Institute of Technology Gandhinagar, Gandhinagar, Gujarat, India

e-mail: [naran@iitgn.ac.in](mailto:naran@iitgn.ac.in)

S. N. Singh

Department of Electrical Engineering, Indian Institute of Technology Kanpur, Kanpur, UP, India

© The Author(s), under exclusive license to Springer Nature Singapore Pte Ltd. 2021

127

S. N. Singh et al. (eds.), *Fundamentals and Innovations in Solar Energy*,

Energy Systems in Electrical Engineering,

[https://doi.org/10.1007/978-981-33-6456-1\\_7](https://doi.org/10.1007/978-981-33-6456-1_7)



the central electricity regulatory commission (CERC) in India imposes penalty on operators or owners of utility scale renewable energy plant for deviating the error in forecast beyond 12% [7]. As a result, there is an interest in forecasting solar PV generation over different time horizons. Forecasting solar PV generation for very short term or short term is popular in the electricity market where the prediction time horizon ranges between seconds to 24 h.

The accuracy of solar PV generation forecasting depends on the type of models, historical data used, weather-dependant variables such as solar irradiance, air temperature, air pressure. However, in general view point, the forecasting techniques can be broadly classified as (i) persistence forecast, (ii) physical model, (iii) statistical techniques, and (iv) machine learning (ML) techniques. Persistence model is classic approach and adopts the concepts of today equal tomorrow. It has less computational cost and low time delay with reasonable accuracy. This model is generally used for short-term forecasting. Physical model involves forecasting generation based on meteorological information and surrounding atmosphere as inputs. This technique produce inaccurate predictions where there are changes in meteorological variables. However this technique produces high accuracy for long-term forecasting.

Statistical and ML models use historical solar PV and real-time generated data to forecast generation. Statistical models use mathematical equations to extract the pattern and carry out the processes of curve fitting. ML models relies on the ability of artificial intelligence to learn from experience in historical data and fine-tune its predictive ability using training runs. In ML techniques, powerful computers run numerous iterations to make final prediction. ML-based models have the ability to learn impossible nonlinear patterns without any formulations or equations. ML-based forecasting techniques are usually more accurate when compared to other forecasting techniques.

Artificial neural network (ANN) and deep learning (DL)-based models such as, multilayer perceptron neural network (MLPNN), recurrent neural network (RNN), convolution neural network (CNN), long short-term memory (LSTM), feed forward neural network, and feedback neural network (FBNN) are some main techniques of ML models used for application of solar PV forecast. In addition to forecasting solar PV generation, these methods are also used for solving complex problems in the field of pattern recognition, language processing, data mining, classification and filtering.

In this chapter, the authors attempts to solve the problem of short-term solar PV generation forecast on application of random vector functional link (RVFL) neural network and DL-based LSTM model. The solar PV power generation data obtained from rooftop solar PV plants installed at IIT Gandhinagar is used to develop and validate the forecast models.

## 7.2 Literature Review

In this section, variants of ANN and DL models are reviewed. Both DL and ANN have the ability to approximate nonlinear functions with high accuracy.

### 7.2.1 Artificial Neural Network (ANN)

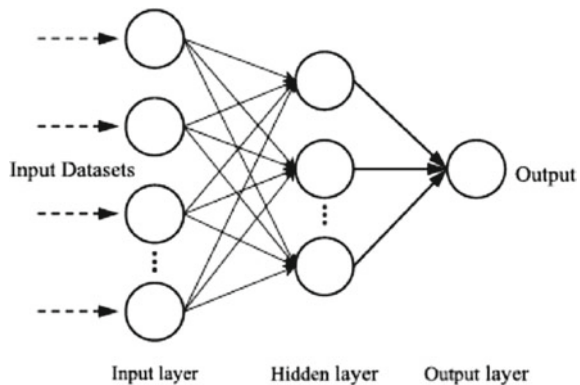
ANN is a nonlinear mapping between input and output and can recognize patterns from complex nonlinear data. The accuracy of ANN model and its variants relies on its input parameters, training algorithm, and structure configuration [8]. The basic neural network (NN) has three layers, namely input layers, hidden layers, and output layers, and is shown in Fig. 7.1 [9].

There are three stages for modeling any NN models, namely (i) design stage, (ii) training phase, and (iii) validation phase. In the design phase, the choice of features as input and output, architecture of ANN mode, number of layers, number of neurons in each layer, and selection of dataset for training and testing is made. Input feature data is given as input to ANN model as for training, and the weights of neurons in each layer is modified based on predetermined conditions. The trained model is tested against unseen data during the validation phase, and upon successful validation, the trained model is ready to make predictions.

The MLPNN structure is largely used in the literature to solve the problem of solar PV forecasting with increased accuracy when compared to other variants of ANN. MLPNN consists of an input and output layer and one or more hidden layers in its architecture. The hidden layers are characterized by the number of neurons. Generally, MLPNN is a composite of three or more layers of incoherently activating nodes. These nodes between different layers are connected together with certain amounts of weights, and it should be noticed that correlation between the number of nodes and the hidden layer is essential.

A Levenberg–Marquardt backpropagation (LM-BP) algorithm-based MLPNN was developed by authors of [10] to predict solar PV generation 24 h ahead for a solar plant in Italy. The simulation results demonstrated that the correlation between the forecasted and actual recorded values are 98% and 94% for sunny and cloudy days, respectively, and temperature, daily solar irradiance, and day of the month are used as input features to build the model.

**Fig. 7.1** Basic architecture of NN. *Source* Sobri et al. [3]



Similarly in [11], an MLPNN-based short-term and medium-term forecast of solar PV generation was developed. Correlation coefficient and root mean square error (RMSE) were used as performance metrics to compare actual value with the forecasted output. Application of implementing MLPNN and its variants for predicting solar PV generation can be found in [8, 9, 12–15]. Variation, improved and hybridization versions of NN's application in forecasting solar PV generation can be found in the literature. Improvising or hybridization is generally carried out to increase the accuracy. Application of meta-heuristic optimization techniques like particle swarm optimization (PSO), genetic algorithm (GA) for hyperparameter tuning of NN in order to improve the accuracy is also well researched in the literature [16–21].

### 7.2.2 *Deep Learning (DL) Models*

The aforementioned ANN and its variants models generally adopt shallow models as their core learning principle. Shallow models are NN models with one to two hidden layers; however, training the shallow models requires prior knowledge about the data and problem domain and moreover have difficult to carry out theoretical analysis. Therefore, the feature selection process highly relies on personal experience. Shallow models have limited generalization capability meaning it cannot generalize large set renewable energy data which is usually non-smooth and has complex patterns including noisy signals and chaotic nature of the weather system. Shallow model works well when the training dataset is relatively small, on the other hand poorly performed on big data. Widespread deployment of meters and sensors at power system networks generates large data sets, and application of shallow models on these datasets will suffer network instability and non-convergence of parameters [22].

DL is a promising branch of ML where it has strong generalization capability and can handle training of big data effortlessly, compared with shallow models [23]. It is an alternative of shallow models and is widely implemented in pattern recognition, image processing, fault detection, classification, and forecasting tasks [24, 25]. For example, a day-ahead forecasting of PV generation, based on deep belief network and gray theory-based data pre-processor, is proposed in [26]. The forecasting accuracy of the proposed model is found to be superior when compared with autoregressive integrated moving average (ARIMA), back propagation NN, radial basis function NN (RBF-NN), and support vector regression (SVR) models. The authors of [27] developed a deep convolution neural networks (DCNN) model to forecast solar PV generation from PV plants. Similarly, application of DL models such as stacked autoencoder, gate recurrent unit (GRU), LSTM, DBN, DRNN can be found in the literature [28–30].

### 7.3 Short-Term Solar PV Forecast Using RVFL and LSTM Models

In this chapter, we intend to highlight the methodology of one forecasting technique each from NN and DL models. Therefore, hybrid versions of random vector functional link (RVFL) networks from NN and LSTM from DL models are chosen for analysis. These models will be used to forecast solar PV generation in the short-term time horizon. Below given is the methodology of forecasting techniques,

#### 7.3.1 SARIMA Random Vector Functional Link (RVFL) Neural Network

The SARIMA-RVFL-based hybrid forecast model is considered in [31]. The input to the forecasting is raw data and is pre-processed using wavelet decomposition (WD) method. Then the transformed data is given as input to SARIMA and RVFL NN models to forecast a day-ahead prediction. The original was solar PV data always exhibits a variety of irregularities, such as fluctuation and spike. The irregularities have nonlinearity and non-stationarity features which deteriorate the forecasting performance. Therefore, the raw solar PV data is pre-processed using WD method to decompose the original signal into one low-frequency component and several high-frequency components. Generally, WD techniques are helpful in improving forecast performance because the decomposed sub-signals always exhibit better outliers and lower uncertainties [32].

The hybrid models of a combination of seasonal autoregressive integrated moving average (SARIMA) and RVFL NN model and the forecasting architecture are shown in Fig. 7.2.

The SARIMA structure has seasonality, autoregression, integration, and moving average components. They have the ability to clip non-stationary values from the analysed data. Moreover, they can capture the seasonal variation in the time series. SARIMA models are classified as statistical models, and the general governing equation is given by,

$$\emptyset(L)(1 - L)^d \emptyset(L)(1 - L^s)^D y_t = c + \theta(L)\theta(L)e_t \quad (7.1)$$

Here,  $y_t$  is time series,  $e_t$  is white noise, and  $L$  is the lag operator, and  $D$  represents the seasonal differentiation order,  $d$  represents regular differentiation order,  $\theta(L)$  represents seasonal moving average polynomial, and  $\Phi(L)$  represents seasonal autoregressive component.

NN and its variants are generally trained using error backpropagation method where the update algorithm may get stuck in local minima and the final solution depends on the learning rate. RVFL-based NN models overcome these disadvantages [33]. Figure 7.3 shows the structure of RVFL-based NN which consists of input layer,

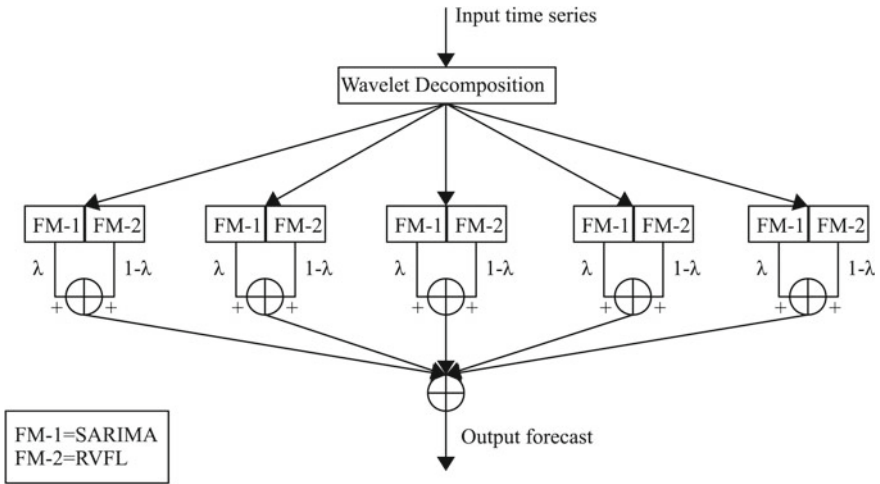


Fig. 7.2 Methodology of SARIMA-RVFL NN model. Source Kushwaha and Pindoriya [31]

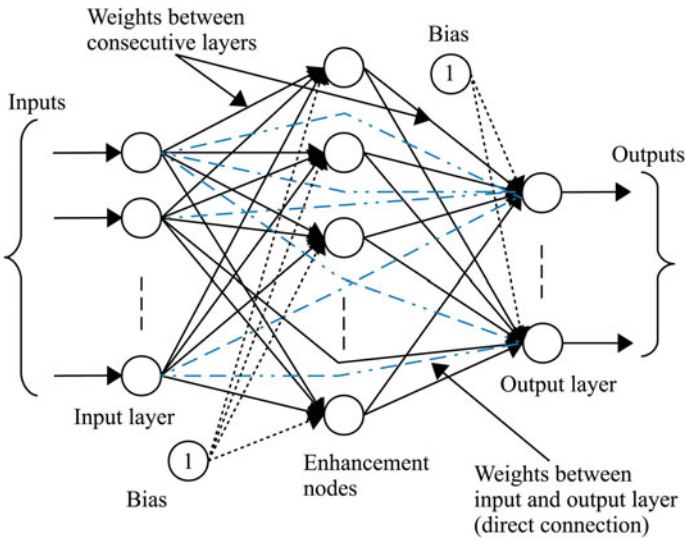


Fig. 7.3 Architecture of RVFL-NN. Source Kushwaha and Pindoriya [31]

enhancement nodes, and output layer. The weights between input and enhancement nodes are randomly chosen. Weights between the enhancement node and output layer can be obtained using ridge regression or Moore–Penrose pseudo-inverse methods. In addition to these linkages, there is a direct linkage between input and output layers.

### 7.3.2 Long Short-Term Memory (LSTM)

The LSTM are variants of recurrent neural networks (RNN). RNN has recurring connections between neurons which enables it to learn from current and previous information in order to find better solutions. When the RNN has more than two cells, it is difficult to obtain useful information due to the problem of vanishing gradients. In order to address the vanishing gradient problem, a special cell, namely “memory cell,” is built with additional neurons. Using the memory cell, LSTM is able to store useful information over an arbitrary period of time. In addition to it, LSTM has the ability to read, store, and erase necessary data from the memory. The architecture of the LSTM model is shown in Fig. 7.4.

## 7.4 Case Study at IIT Gandhinagar Campus

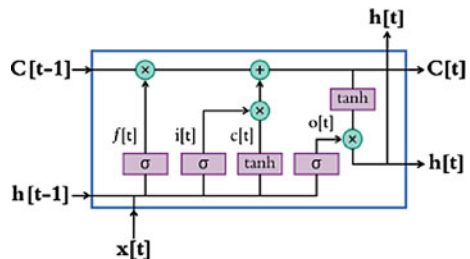
Solar PV system rated up to 500 kWp is installed at academic blocks, student’s hostel, and solar carport of IIT Gandhinagar campus. For this analysis, historical solar PV generation data obtained from 15 kWp solar panels installed at the rooftop of Beauki student’s hostel is used for the forecast model development purpose.

The performances of WD-RVFL, SARIMA-RVFL, and LSTM models are analyzed for solar PV generation data obtained during clear sky and cloudy/rainy weather conditions.

It should be noted by the readers, historical solar PV generation for clear sky and cloudy/rainy days from Beauki hostel collected between April 2017 and July 2017 was used for analysis on application of WD-RVFL and SARIMA-RVFL models. The data for the same can be taken from [31].

On the other hand, solar PV data for clear sky and cloudy/rainy days for Beauki hostel collected between April 2019 and July 2019 was used for analysis on application of LSTM-based DL model. Therefore, the data set considered for WD-RVFL, SARIMA-RVFL, and LSTM models is not the same.

Fig. 7.4 Architecture of LSTM. Source AlKandari et al. [28]



### 7.4.1 WD-RVFL Model to Forecast Clear Sky

The WD-RVFL model is used to forecast solar PV generation from rooftop PV at Beauki hostel. The raw solar PV data is given as the input to the WD model to generate low- and high-frequency components ( $A$ ,  $D1$ ,  $D2$ ,  $D3$ , and  $D4$ ). Figure 7.5 shows WD of solar PV power time series.

RVFL models for each of the frequency components are build to forecast the output. Each of the obtained forecast is summed up to obtain the actual forecast values. Here, radian basis activation function is used in the enhancement layer as its performance is better when compared to other activation function. The weights between the output and enhancement layer were done using pseudoinverse method. The solar PV generation forecast obtained for the clear sky data is shown in Fig. 7.6. The forecasted output from WD-RVFL is also compared with persistence, SARIMA, WD-SARIMA, and RVFL models, and it is found that WD-RVFL model performs better than other models. A comparison of performance metrics of solar forecasting using different techniques is shown in Table 7.1.

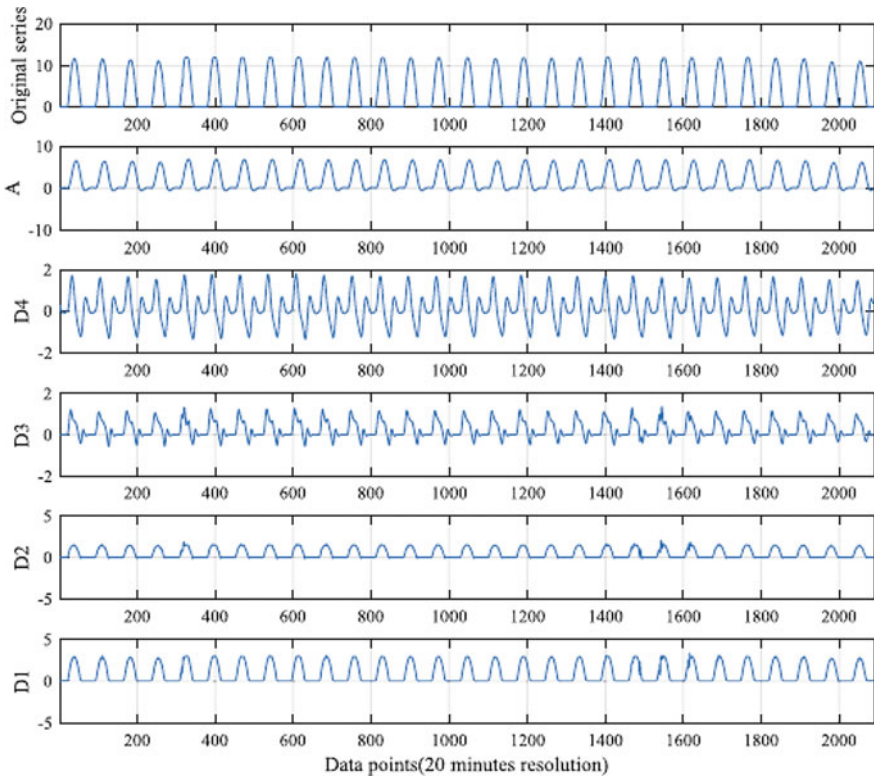
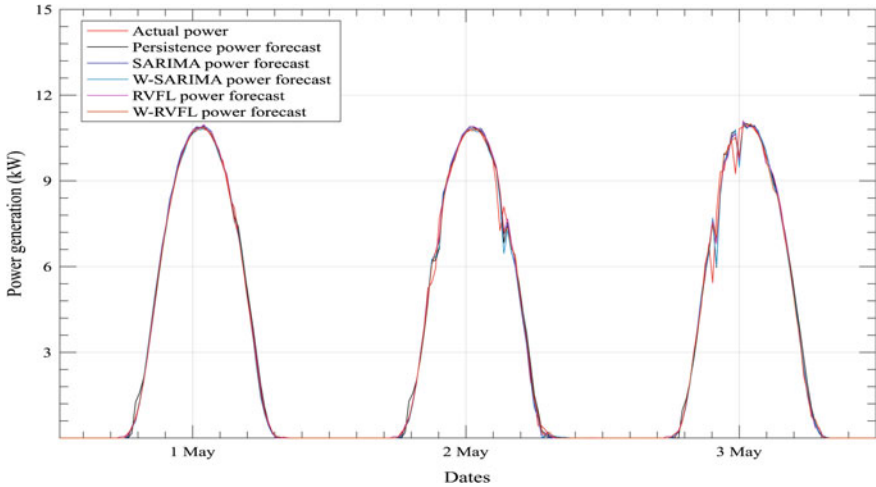


Fig. 7.5 WD of solar PV power time series. Source Kushwaha and Pindoriya [31]



**Fig. 7.6** Solar PV forecast obtained for clear sky days. *Source* Kushwaha and Pindoriya [31]

**Table 7.1** Performance comparison of forecast models

S. No.	Model	RMSE	R <sup>2</sup>	Error variance
1	Persistence	0.804	0.994	0.103
2	SARIMA	0.605	0.995	0.079
3	WD-SARIMA	0.763	0.992	0.125
4	RVFL	0.678	0.995	0.082
5	WD-RVFL	0.668	0.995	0.084

*Source* Kushwaha and Pindoriya [31]

### 7.4.2 SARIMA-RVFL to Forecast Rainy/Cloudy Day

SARIMA-RVFL model is used to forecast solar PV generation of rainy/cloudy days. On application of the different models, it is found that SARIMA-RVFL hybrid model performs better. The results of solar PV generation forecast and performance metrics are shown in Fig. 7.7 and Table 7.2, respectively.

### 7.4.3 LSTM to Forecast Clear Sky and Rainy/Cloudy Days

LSTM deep learning model is used to forecast the output power from solar PV plant. The forecasted output and performance metrics on application of LSTM-based DL model for forecasting solar PV generation is shown in Fig. 7.8 and Table 7.3, respectively. The results depicted below are for clear sky days,



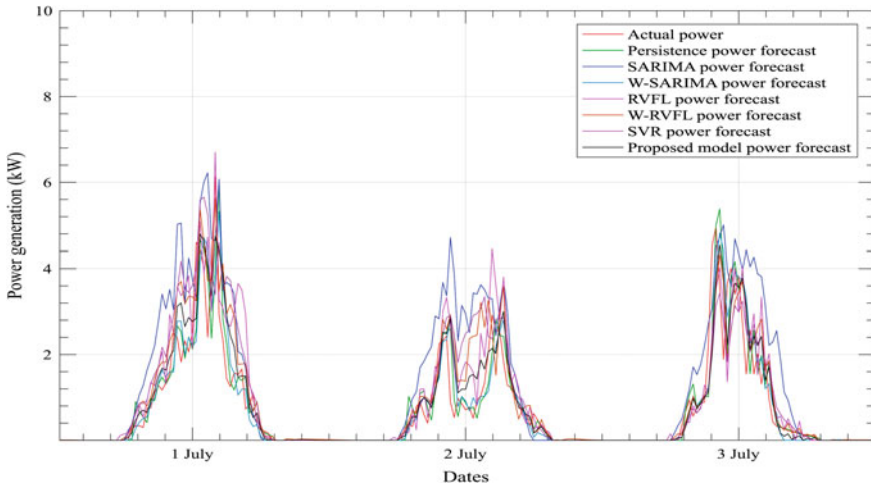


**Fig. 7.7** Solar PV forecast obtained for clear sky days. *Source* Kushwaha and Pindoriya [31]

**Table 7.2** Performance comparison of forecast models

S. No..	Model	RMSE	R <sup>2</sup>	Error variance
1	Persistence	1.021	0.906	1.043
2	SARIMA	1.091	0.892	1.191
3	WD-SARIMA	0.969	0.915	0.940
4	RVFL	1.006	0.908	1.005
5	WD-RVFL	0.952	0.918	0.906
6	SARIMA-RVFL	0.915	0.924	0.837

*Source* Kushwaha and Pindoriya [31]

**Fig. 7.8** Solar forecast for the day of clear sky. *Source* Authors

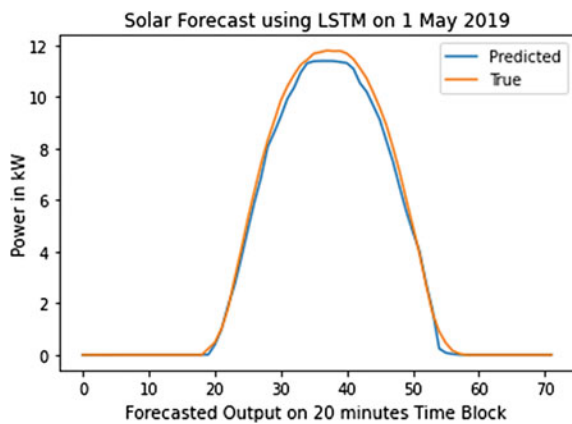


**Table 7.3** Performance comparison of forecast models for clear sky

Model	RMSE	R <sup>2</sup>	Error variance
LSTM	0.288	1.00	0.0532

Source Authors

The forecasted output and performance metrics for application of LSTM model for cloudy day is shown in Fig. 7.9 and Table 7.4, respectively.

Since the data considered for WD-RVFL, SARIMA-RVFL, and LSTM models is varying and it is needless to compare the performance of between the abovesaid forecasting models. However, forecasting the solar PV generation during clear sky is less challenging and straightforward. Even a reasonable model can predict the solar PV generation during clear sky from historical data. Therefore, based on the above statement, the authors would compare the performance metrics of solar PV generation for clear sky data for RVFL, WD-RVFL, and LSTM models. The tabular comparison is given below.

It can be noticed from Table 7.5, the LSTM model performs RVFL and WD-RVFL models while forecasting solar PV generation for clear sky. This may be because, (i) the LSTM model can consider large data points as input when compared to NN variants, and (ii) LSTM has a memory cell in its architecture which can learn from current and previous information in order to find a better solution. Moreover, the LSTM model used for this chapter work is a non-hyperparameter optimized model. Therefore, the efficiency of the LSTM model can be improved further by tuning the hyperparameter of the LSTM model.

**Fig. 7.9** Solar forecast for the day of cloudy day.  
Source Authors

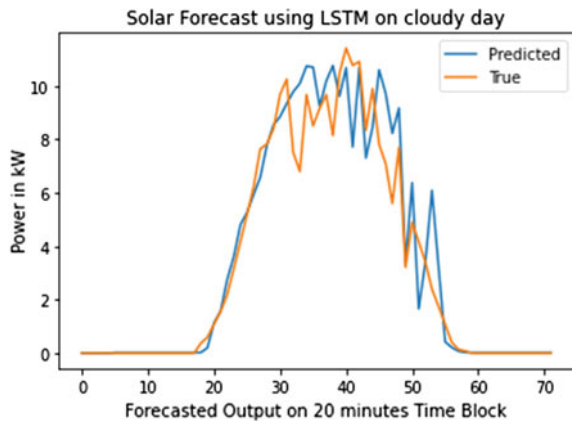


**Table 7.4** Performance comparison of forecast models for cloudy day

Model	RMSE	R <sup>2</sup>	Error variance
LSTM	0.907	0.93	0.914

Source Authors

**Table 7.5** Performance comparison of forecast models for clear sky day

Model	RMSE	R <sup>2</sup>	Error variance
RVFL	0.678	0.995	0.082
WD-RVFL	0.668	0.995	0.084
LSTM	0.288	1.00	0.0532

*Source* Authors

Accurate forecasting models to forecast generation from renewables are essential to take informed decisions. With the rapid development of information and communication technology (ICT) for large-scale control and monitoring of electrical systems, there has been an increase in installation of monitoring devices such as meter, sensors, ICT, and the Internet of Things (IoT)-based devices. These devices generate big data where DL-based hybrid models can handle big data to forecast the output power from renewable-based generation sources with high efficiency. This will assist the utility grid or utility scale PV plant owner to make informed decisions accurately resulting in reduction in cost of operation which will boost the revenue of owners of utility scale renewable plants.

## 7.5 Conclusion

In this chapter, the authors intend to solve the problem of short-term forecasting solar PV generation. Extensive literature on this problem is present; however, the authors focus on solving the solar PV generation forecasting problem using neural networks and deep learning models. Experiences from researchers show deep learning-based model's performances are superior to models based on neural networks. In this chapter, variants of NN model, namely RVFL- and DL-based LSTM models, are chosen and applied to solve the short-term solar PV forecasting problem on a realistic solar PV data set collected from IIT Gandhinagar solar network. Based on the result, the advantage of DL-based model over NN-based model is highlighted. This chapter is concluded by calling for more sophisticated and highly accurate forecasting models in view from renewable energy owner's perspective.

## References

1. The Ministry of New and Renewable Energy (MNRE). Government of India. <https://mnre.gov.in/>
2. Shivashankar S et al (2016) Mitigating methods of power fluctuation of photovoltaic (PV) sources—a review. *Renew Sustain Energy Rev* 59:1170–1184
3. Sobri S, Koohi-Kamali S, Rahim NA (2018) Solar photovoltaic generation forecasting methods: a review. *Energy Convers Manag* 156:459–497
4. Sukumar S et al (2018) Ramp-rate control approach based on dynamic smoothing parameter to mitigate solar PV output fluctuations. *Int J Electr Power Energy Syst* 96:296–305

5. Sukumar S et al (2018) Ramp-rate control smoothing methods to control output power fluctuations from solar photovoltaic (PV) sources—a review. *J Energy Storage* 20:218–229
6. Abhinav R, Pindoriya NM (2018) Opportunities and key challenges for wind energy trading with high penetration in Indian power market. *Energ Sustain Dev* 47:53–61
7. (2016) Framework on forecasting, scheduling and imbalance handling for variable renewable energy sources (Wind and Solar). Central Electricity Regulatory Commission (CERC)
8. Yadav AK, Chandel S (2014) Solar radiation prediction using artificial neural network techniques: a review. *Renew Sustain Energy Rev* 33:772–781
9. Zhu H, Li X, Sun Q, Nie L, Yao J, Zhao G (2015) A power prediction method for photovoltaic power plant based on wavelet decomposition and artificial neural networks. *Energies* 9:11
10. Mellit A, Pavan AM (2010) A 24 h forecast of solar irradiance using artificial neural network: application for performance prediction of a grid-connected PV plant at Trieste, Italy. *Sol Energy* 84:807–821
11. Izgi E, Öztopal A, Yerli B, Kaymak MK, Şahin AD (2012) Short–mid-term solar power prediction by using artificial neural networks. *Sol Energy* 86:725–733
12. Pang Z, Niu F, O’Neill Z (2020) Solar radiation prediction using recurrent neural network and artificial neural network: a case study with comparisons. *Renew Energy*
13. Galván IM et al (2017) Multi-objective evolutionary optimization of prediction intervals for solar energy forecasting with neural networks. *Inform Sci* 418:363–382
14. Benali L et al (2019) Solar radiation forecasting using artificial neural network and random forest methods: application to normal beam, horizontal diffuse and global components. *Renew Energy* 132:871–884
15. Ogliairi E, Grimaccia F, Leva S, Mussetta M (2013) Hybrid predictive models for accurate forecasting in PV systems. *Energies* 6:1918–1929
16. Kardakos E, Alexiadis M, Vagropoulos S, Simoglou C, Biskas P, Bakirtzis A (2013) Application of time series and artificial neural network models in short-term forecasting of PV power generation. In: Power engineering conference (UPEC). In: 2013 48th international universities. IEEE, pp 1–6
17. Chen S, Gooi H, Wang M (2013) Solar radiation forecast based on fuzzy logic and neural networks. *Renew Energy* 60:195–201
18. Mellit A, Sağlam S, Kalogirou S (2013) Artificial neural network-based model for estimating the produced power of a photovoltaic module. *Renew Energy* 60:71–78
19. Notton G, Paoli C, Ivanova L, Vasileva S, Nivet ML (2013) Neural network approach to estimate 10 min solar global irradiation values on tilted planes. *Renew Energy* 50:576–584
20. Prado F, Minutolo MC, Kristjanpoller W (2020) Forecasting based on an ensemble autoregressive moving average-adaptive neuro-fuzzy inference system–neural network-genetic algorithm framework. *Energy* 197:117159
21. Yang Z et al (2020) A novel competitive swarm optimized RBF neural network model for short-term solar power generation forecasting. *Neurocomputing*
22. Wang HZ, Li GQ, Wang GB, Peng JC, Jiang H, Liu YT (2017) Deep learning based ensemble approach for probabilistic wind power forecasting. *Appl Energy* 188:56–70
23. Tanveer A, Huanxin Chen (2019) Deep learning for multi-scale smart energy forecasting. *Energy* 175:98–112
24. Georg H, Matthias R (2018) Deep learning for fault detection in wind turbines. *Renew Sustain Energy Rev* 98:189–198
25. Zhang C, Chen CLP, Gan M, Chen L (2015) Predictive deep Boltzmann machine for multiperiod wind speed forecasting. *IEEE Trans Sustain Energy* 6(4):1416–1425
26. Chang GW, Lu HJ (2019) Integrating grey data preprocessor and deep belief network for day-ahead PV power output forecast. *IEEE Trans Sustain Energy* 99(1):1
27. Huaizhi W, Haiyan Y, Jianchun P, Guibin W, Yitao L, Hui J et al (2017) Deterministic and probabilistic forecasting of photovoltaic power based on deep convolutional neural network. *Energy Convers Manag* 153:409–422
28. AlKandari M, Ahmad I (2019) Solar power generation forecasting using ensemble approach based on deep learning and statistical methods. *Appl Comput Inform*

29. Li P et al (2020) A hybrid deep learning model for short-term PV power forecasting. *Appl Energ* 259:114216
30. Wang H et al (2019) A review of deep learning for renewable energy forecasting. *Energy Convers Manag* 198:11799
31. Kushwaha V, Pindoriya NM (2019) A SARIMA-RVFL hybrid model assisted by wavelet decomposition for very short-term solar PV power generation forecast. *Renew Energ* 140:124–139
32. Florian Z, Rick S (2018) Probabilistic mid and long-term electricity price forecasting. *Renew Sustain Energ Rev* 94:251–266
33. Zhang L, Suganthan P (2016) A comprehensive evaluation of random vector functional link networks. *Inf Sci* 367e368-1094e1105. <https://doi.org/10.1016/j.ins.2015.09.025>

# Chapter 8

## Off-Grid Solar Lighting Testing and Reliability



Supriya Rai, Birinchi Bora, Chandan Banerjee, and Arun Kumar Tripathi

### 8.1 Introduction

The electricity generation from renewable is a prominent center of attention for power generation in the current and forthcoming generation. The community of energy demand can be met by installing the SPV power plant. The power can also feed to the grid for revenue generation and as well as self-consumption. In general, SPV power plants are classified concerning operating loads integration with a grid for generation or self-consumption. The power electronics-based inverter is used for transforming the fickle direct current (DC) output into alternating current (AC) in constant frequency. It can be fed into a saleable electrical grid for local, off-grid, and electrical grid networks. The Ministry of New and Renewable Energy, Government of India, takes over research and development responsibility, international cooperation, and coordination promotion in India's renewable energy. Solar energy generation is receiving importance as it is a clean power and India has set a target of 175 GW by 2022, where the off-grid system gets main attraction due to uncertainty in availability of electricity in rural areas. Off-grid is a significant achievement in the families for striding and electrification [1] (Fig. 8.1).

On-grid power plants comprise SPV module, inverter, and the electricity grid. It is directly connected to the grid system without any autonomy storage and a backup

---

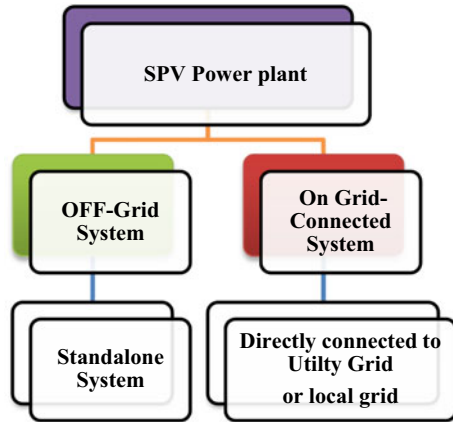
S. Rai (✉) · B. Bora · C. Banerjee · A. K. Tripathi  
National Institute of Solar Energy, Bandhwari, India  
e-mail: [supriya.ece.imps@gmail.com](mailto:supriya.ece.imps@gmail.com)

B. Bora  
e-mail: [birinchibora09@gmail.com](mailto:birinchibora09@gmail.com)

C. Banerjee  
e-mail: [chandanbanerjee74@gmail.com](mailto:chandanbanerjee74@gmail.com)

A. K. Tripathi  
e-mail: [aktripathi@nic.in](mailto:aktripathi@nic.in)

**Fig. 8.1** Types of SPV power plant. *Source* Author



plan. The consumers are allowed to use energy according to requirement own generated electricity requirement and suitability when the grid is available. They can feed the power to the grid and get tariffs against it. Off-grid systems are connected with battery and used for the stand-alone purpose. In the case of off-grid systems, solar power is used directly by the load during the sunshine period, and during the non-sunshine period, the load is fed through a battery, which is charged by the excess power produced during the sunshine period. The charge controller controls the charging or discharging process of the batteries. The hybrid system’s main components are the power conditioning unit (which houses inverter, charge controller, and data logger, etc.), storage battery, PV module, energy meters, transformer, and electricity grid. A hybrid system can store energy for the use of consumers and export all or excess generated electricity (Fig. 8.2).

**Stand-alone (Off-grid):** In an off-grid system, the inverter drives energy from solar batteries powered by SPV power plant without direct interface with the grid, which can be used to draw its energy to the household appliances used as DC source

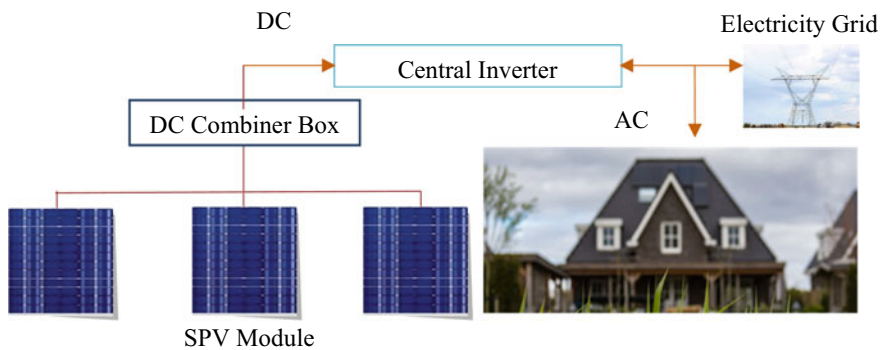


**Fig. 8.2** On-grid system designing. *Source* Author

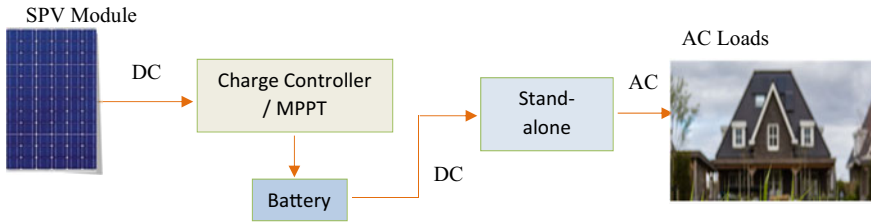


Fig. 8.3 Stand-alone system without grid interactive as alternative source. Source Author

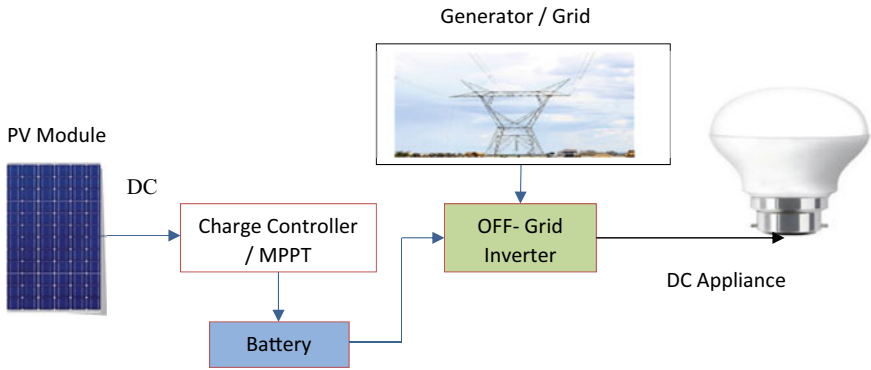


Fig. 8.4 OFF-grid inverter (without grid integration). Source Author

or convert into AC power. Various stand-alone inverters applications are also integrated as integral battery chargers to replenish the battery feeding to the source when available. Generally, interfacing with the utility grid does not require to have anti-islanding protection. Battery backup inverters are designed to pull energy from a battery, accomplish the battery charging through an onboard charger, and export excess energy to the utility grid (Figs. 8.3 and 8.4).

Solar photovoltaic (SPV) lighting system like portable solar lanterns, table lamp, task lights, torch, garden lights, road studs, fixed home lighting systems (HLS), and street lighting system (SLS) for rural, city, and highway roads are being used commonly. All these systems comprise the following components:

1. SPV module
2. Charge controller
3. Storage battery
4. Current driver or LED driver
5. Luminary-based house the LEDs.



## 8.2 SPV Module

There are different types of modules available in the market for use in off-grid applications: Monocrystalline silicon solar PV module, polycrystalline silicon solar PV module, and thin-film solar PV module. The commercial module with high reliability can perform without failure within a specified performance limit for a certain specified time. Some module design issues and fabrication issues bring the module's failure mechanism during long-term operation. The system can be broken into the sub-systems to estimate the reliability and analyze the data, establish the failure-time relationship, and study the mechanism and cause of failure. There are several ways to analyze the solar module defect to find the module's cause and failure. I-V curve analysis, IR imaging, electroluminescence, and diode test can be used to study these defects to analyze the defect. The failure modes can be identified by visual inspection or using laboratory tools. Instantaneous performance measurement data of the PV module in the outdoor condition is used to give a rating and estimate the degradation rate after a long term of exposure in the field. The list of equipment required to test the instantaneous SPV module performance in real-time measurement condition is given below.

- (a) *I-V* tracer
- (b) Angle of incidence measurement setup
- (c) Mesh with different transmissivity
- (d) Arrangement for cooling or heating the PV module
- (e) Spectroradiometer

Spectroradiometer is used to measure the spectrum of light used to estimate the mismatch factor and calculate the effective irradiance for the module technology tested. The spectroradiometer should be capable of measuring the spectrum of incident light in the wavelength range 280–1700 nm (Fig. 8.5).

Procedure for instant performance measurement of PV module under outdoor conditions [2–4]:

1. The irradiance should be more than 800 W/m<sup>2</sup>, and there should not be any rapid cloud movement. The better time to do the measurement is 11:00 AM to 2:00 PM.
2. Clean the module and connect the *I-V* tracer. Put the irradiance sensor on the same plane of the module.
3. AOI correction: Estimating the angle of incidence, and the real-time measured data is used. The incidence angle can be calculated in the plane of module applying formulae.

$$\theta = \cos^{-1}[\text{Sin}\delta\text{Sin}(\varphi - \beta) + \text{Cos}\delta\text{Cos}(\omega)\text{Cos}(\varphi - \beta)] \quad (8.1)$$

where  $\theta$  is the incidence angle,  $\varphi$  is the latitude,  $\beta$  is the tilt angle of the module,  $\delta$  is the declination, and  $\omega$  is the hour angle. The effect of AOI on the performance of

**Fig. 8.5** Spectroradiometers installed at a fixed tilt equal to latitude. *Source* Author



the PV module needs to be estimated for the distribution of AOI for the whole year.  $I_{scr}$  is the PV module short-circuit current at STC can be estimated as

$$I_{scr} = (I_{sc} * E_o) / [E_{poa} * (1 + \alpha_{Isc}(T_c - 25))] \tag{8.2}$$

The relative optical response is given as

$$f_2(AOI) = \frac{\left[ E_o \left( \frac{I_{sc}}{(1 + \alpha_{Isc}(T_c - 25)) * I_{scr}} \right) - ((E_{poa} - E_{dni} * \cos(AOI))) \right]}{[E_{dni} * \cos(AOI)]} \tag{8.3}$$

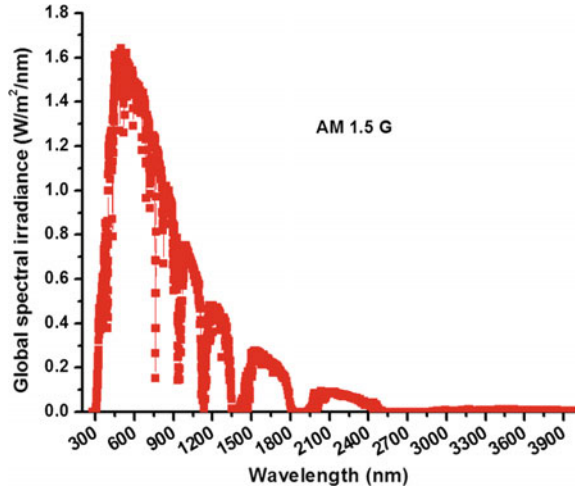
where

- $E_{dni}$  Normal direct solar irradiance ( $W/m^2$ ).
- $E_{poa}$  Global solar irradiance on the plane of array module ( $W/m^2$ ).
- $E_o$  Global solar irradiance at STC  $1000 W/m^2$ .
- AOI Angle between solar beam and module normal vector (degrees).
- $T_c$  Measured module temperature ( $^{\circ}C$ ).
- $\alpha_{Isc}$  Short-circuit current measurement temperature coefficient ( $1/^{\circ}C$ ).
- $I_{sc}$  Measured short-circuit current (A).

Solar irradiance falling on the SPV module is known as the effective irradiance. The effective irradiance with AOI effect on the PV module can be designed using

$$E_e = [E_{dni} * \cos(AOI) * f_2(AOI) + f_d * (E_{poa} - E_{dni} * \cos(AOI))] / E_o \tag{8.4}$$

**Fig. 8.6** AM 1.5 global spectrum as per IEC 60,904–3. *Source* Author



where  $f_d$  = fraction of diffuse irradiance used by the module, typically assumed = 1.

4. Spectral correction: If the radiation measuring device requires spectral correction, we need to measure the light’s incident spectrum. We need to estimate the effective irradiance in terms of light’s technology-specific spectral content by calculating the spectral mismatch factor. The MMF can be calculated by using the formula.

$$MMF = \frac{\int SR(\lambda)E_{AM1.5G}(\lambda)d\lambda}{\int E_{AM1.5G}(\lambda)d\lambda} \frac{\int E(\lambda)d\lambda}{\int SR(\lambda)E(\lambda)d\lambda} \tag{8.5}$$

where  $SR(\lambda)$  is the relative spectral response of the SPV module and  $E_{AM1.5G}$  defined as AM1.5G spectrum with effective solar irradiance ( $G_{eff}$ ) corrected by solar spectrum can be calculated by using the formula

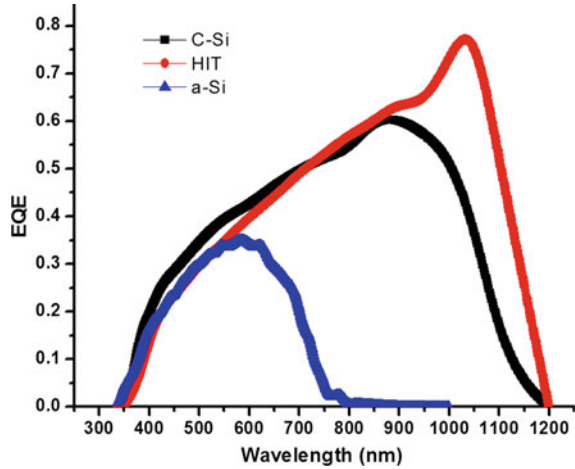
$$G_2 = \frac{G}{MMF} \tag{8.6}$$

5. Translation of performance measured data to STC by using the procedure as per IEC 60,891 (Fig. 8.6 and 8.7).

### 8.3 Charge Controller

The charge controller work on controlling electricity generation by a solar module acts as a voltage regulator. It protects the battery from overcharging and discharging rate. It provides optimal energy flow management within the system and regulates the

**Fig. 8.7** Spectral responses of PV modules. *Source* Author



voltage and current from the battery side to prevent the battery from overcharging and discharging and preventing reverse drainage from the batteries. It ensures deep cycle batteries that should not be overcharged during the day and do not supply backward power to the solar panels overnight when draining the batteries and maintaining a discharged cycle. Commercial solar charge controllers are three types:

1. Shunt-series charge controller
2. PWM charge controller
3. MPPT controller

The controller controlled set at four different set point for sensing the battery voltage.

- **Setting point regulation (VR):** The set point permitting the maximum voltage control flow in the battery reaches its voltage range. It sets a discontinuous battery charging to begin into regulated current delivery toward the battery. The set point is responsible for battery temperature operation on the specific battery longevity.
- **Low-voltages disconnect (LVD):** The low-voltage disconnect set point voltage where the load is disconnected from the battery preventing overdischarging. The allowable maximum depth of discharge and available capacity of the battery are estimated by system design and sizing process.
- **Low-voltage disconnect hysteresis (LVDH):** It shows the difference in the set point between the LVD set point and the battery’s reconnecting voltage. As the LVDH rapidly low down, it brings rapid on and off at a lower battery charging state by damaging the load and controller. In LVDH, the load remains off with extended periods until the array fully recharges the battery.
- **Shunt-Series Charge Controller:** This is battery charging technique with continuous trickle charger charging of the battery with its self-discharging rate using applied constant voltage and current. A trickle charging with automatic turned off operation where float charger is another simple forms trickle charger with an

automatic on/off switch. This charger senses when the battery voltage reaches a preset reference level, which corresponds to full charge or float charge and shuts off the current to the battery. When the battery discharges down to the second preset level, it turns the current back to the battery. This type of controller is also called a shunt–series-type charge controller.

It charges batteries in three stages—bulk stage, absorption stage, and float stage. Bulk stage charge batteries at current continually at 25% Ah rating are delivered.

**Absorption Stage** Absorption stage sets the platform at 20% of the charging of the battery. It feeds at a constant current similar to the absorption voltage, which depends on charging options, and current consumption decreases until the battery is completely charged. However, the current does not drop as per expectation. In this case, the battery might have permanent sulfation, which occurs when a battery is set at a low state of charge for weeks. The float voltage mode monitors the constant current mode technique where the battery voltage is maintained at an approximate volt of 2.25 V per cell, or 13.5 V for a 12 V designed battery. This charger maintains the performance lacked out from overcharging or below the electrolyte’s boiling, which decreases its performance. Here, voltage is reduced, and a current of less than 1% of the battery’s capacity is applied. It can lead the charging state without harming battery performance.

**The pulse width modulation (PWM) charge controller** plays a crucial role in the battery bank, allowing target voltage between the solar array and battery bank. This can work as switching on/off at a variable frequency with a variable duty cycle to maintain the battery very close to the voltage regulation set point and decrease its power applied to the battery gradually when it has fully charged. PWM is a process in which a signal is converted to pulses with widths that vary proportionally to the signal amplitude. PWM results in less stress on the batteries and extends battery life. PWM charge controller is generally more efficient than the on–off charge controller, and also it operates with three stages of battery charging—bulk, absorption, and float stage. Some PWM charge controller has another charging stage—“equalization stage” varies with four-stage chargers. The equalization stage is a charging process where the battery is overcharged, but some cells may have charge lower than others, so equalization brings them to full charge. PWM design allows the charge controller battery approach to make it full charge with generating less heat. Moreover, it charges efficiently without damaging the battery voltage (Fig. 8.8).

**MPPT Charge Controller:** The solar energy system is irradiation and temperature, which varies with time interval throughout the day according to seasonal and weather conditions. MPPT controllers set as an adaptive algorithm that tracks the maximum power point of the PV array and adjusts the incoming voltage maintaining the most efficient amount of power utilized by the system. With the maximum power point tracking controller, we can improve the PV system’s efficiency with the best algorithms to achieve the solar module’s peak power.

There are many types of algorithms used in the MPPT charge controller to improve solar energy efficiency, such as

- Incremental conductance (INC)

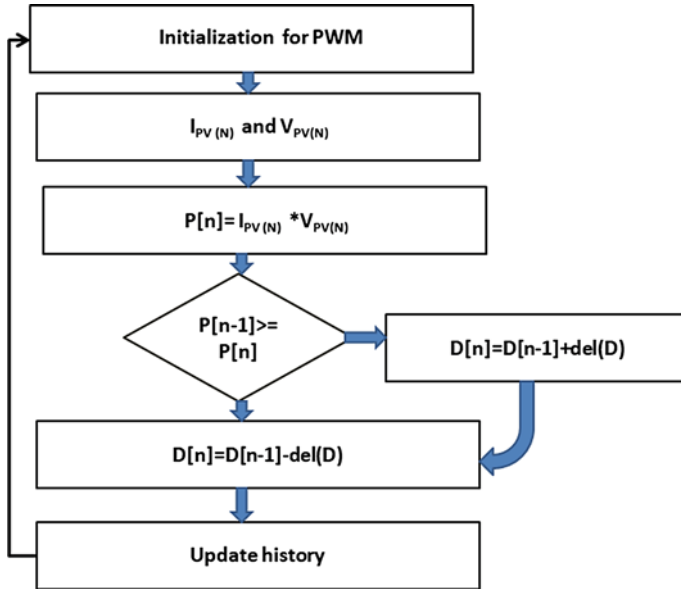


Fig. 8.8 PWM algorithm for battery charging and controller operation. Source Author

- Hill climbing or perturbation and observation (P&O)
- Artificial neural network (ANN)
- Fuzzy logic controller
- Particle swarm optimization

Other than these algorithms, it includes the open-circuit voltage control (OCVC), short-circuit current control (SCCC), feedback of power variation with voltage technique, feedback of power variation with current technique, single-input fuzzy controller for tracking MPP, ant colony optimization (ACO), and genetic algorithm (GA) methods. MPPT test procedure follows the EN50530 standard, which is European Standard and provides a procedure to measure the maximum power point tracking efficiently (MPPT) by inverter and charge controller, which are used in grid-connected and stand-alone photovoltaic systems. Based on static MPPT efficiency performance and conversion efficiency, the overall inverter efficiency is calculated. The dynamic MPPT efficiency is tested using maximum power tracking in real-time environmental conditions inside the laboratory using a charge controller or inverter. The different MPPT algorithm differentiates by the algorithm pattern followed by sensing voltage current, power, and slope. The incremental conductance brings to control the change of load and monitors  $Slope = \frac{\Delta I}{\Delta V}$ 's slope, while the perturb and observe manipulate load and monitor change in power  $Slope = \frac{\Delta P}{\Delta V}$ , continuously. The widely MPPT techniques applied in SPV applications are used in the different applications as off-grid system as LED street lighting, home appliances, solar vehicles, solar water pumping, etc., with control strategies method of direct,

indirect, or probabilistic technique. In direct control, the proficiency of PV generation data is not required. The PV panel operating point variations lead directly to the maximum PowerPoint. The techniques differentiated as perturb and observe, incremental conductance, fuzzy logic, feedback voltage, feedback current, and neural network were examined as direct methods. The indirect methods are utilized as P–V curves data for PV systems for different temperatures and intensity as a function obtained as empirical data. These indirect data extraction methods include the lookup table method, open-circuit, short-circuit sensing methods, curve fitting, etc. The fractional open-circuit voltage and current technique cannot be pursued for extracting the maximum power tracking accurately under varying environmental conditions, not considered for the effect of weather fluctuations of climatic conditions.

### **Perturb and Observe Condition**

Perturb and observe algorithm is the most commonly applied practicing the technique for tracking the maximum power point. This algorithm is easily implemented in the control parameter algorithm in array voltage, array current, and duty ratio of the power converter. This algorithm is made by incremental change in the array voltage if the power increases with the next perturbation.

The determination of duty cycle plays a crucial role in designing the MPPT controller to track maximum power point tracking algorithms with the step size ( $\Delta D$ ) is fixed general or varies by  $\Delta D$  affecting the MPPT overall efficiency cooperation with time response MPPT ripple. A MPPT system varies with step size can be able to distinguish steady-state and dynamic conditions.

The duty cycle is divided into four different cases.

Case 1: Delta  $P > 0$  power increases, delta  $V < 0$  voltage decreases, and  $\Delta D$  is subtracted.

Case 2: Delta  $P > 0$  power increases, delta  $V > 0$  voltage increases, and  $\Delta D$  is added.

Case 3: Delta  $P < 0$  power decreases, delta  $V < 0$  voltage decreases, and  $\Delta D$  is added.

Case 4: Delta  $P < 0$  power decreases delta  $V > 0$  voltage increases, and  $\Delta D$  is subtracted.

The  $\Delta D$  size affects the overall system efficiency is necessary for the selection of this parameter. Faster response in MPPT with  $\Delta D$  selection with larger variation is important for dynamic weather and cloudy condition. Steady-state weather conditions with  $\Delta D$  produce lower efficiency, increasing the size of ripples around maximum MPPT tracking.  $\Delta D$  is relatively small, and when the weather condition is in steady state, the MPPT system's efficiency is at its peak. That is, the operation point is as close as possible to the MPPT. HC method is based on the relationship between the PV array power and the switched mode DC–DC converter's switching duty cycle. The local maximum power point is achieved when the MPPT controller forces  $\Delta P/\Delta D$  to zero. By changing the ratio of the maximum output power can be obtained by using the derivative of PV output power with respect to voltage and equating this to zero

$$\frac{dP}{dV} = I + v \left( \frac{dI}{d(V)} \right) = 0 \text{ and condition brings}$$

$$\frac{dI}{dV} = \left( -\frac{I_{MMP}}{V_{MPP}} \right) \text{ at MPPT condition: } \frac{dP}{dV} = 0$$

While  $\frac{dP}{dV} > 0$  left move toward MPPT condition and  $\frac{dP}{dV} < 0$  move right of MPPT condition. The commercial controller designed for the off-grid system as pulse width modulation and maximum power point tracker (MPPT) is necessary as solar-controlled power systems for control flow of power from the solar module into batteries and monitoring the battery voltage. If the battery charge solar controller functions to monitor the battery voltage, it opens the charging circuit model if the voltage reaches its cutoff voltage level, working as a mechanical relay circuit and starting charging as it reaches its set point to succeed maximum capacity. PWM process states that the battery fully charges by decreasing the amount of power process as the battery is at fully charge state to extend the battery life and stress to the battery life floating point while MPPT turns the electronic tracking system continuously by comparing the battery charge level with solar output panel adjusting the voltage and current to the applied battery and conserving the power to track efficiently (Fig. 8.9).

The complexity of the different charge controllers is described in Table 8.1. This helps the researcher to sort out the complexity of designing for high efficient controller reliable in real-time condition battery management and tracking power efficiently (Fig. 8.10).

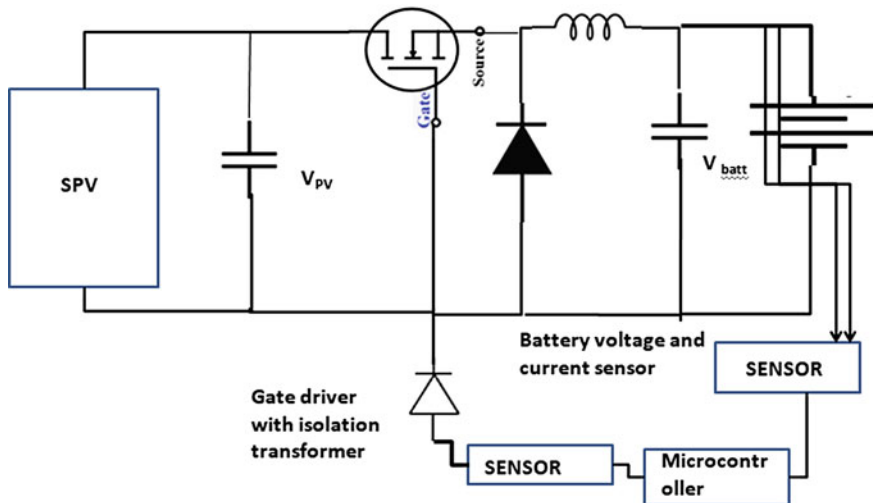
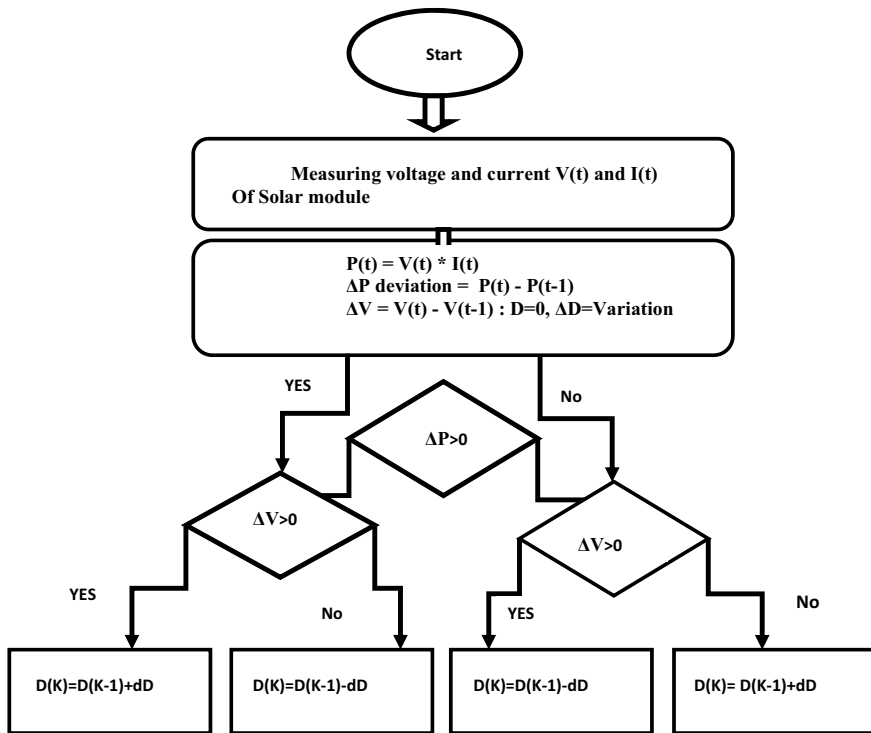


Fig. 8.9 Charge controller for MPPT tracking. Source Author



**Table 8.1** MPPT charge controller complexity in algorithm comparison (source Author)

MPPT technique	Software complexity	Hardware complexity	Tracking ability
P&O	Calculation of power and restoring of previous data	V(I) and I(V)sensor with memory state machine storing	Tracking power with suffering oscillation of incremental power
Incremental conductance (IC)	Calculating I, V, slope, power and restoring previous data	V(I) and I(V)sensor with memory multiplier	Determination of step size and tracking time
Open-circuit voltage control (OCVC) and short-circuit current control (SCCC)	Calculating $k * V_{oc}$ Or $k * I_{sc}$	Resistor divider	Radio metrically following open-circuit voltage It is directly influencing to estimate partial shading



**Fig. 8.10** Charge controller for P&O algorithm flowchart. Source Author

## 8.4 Battery Technology

**The battery** is the most commercial energy storage device in the SPV system stores the electrical energy as the usage of chemical form of energy generated by the SPV module during the sunshine condition and delivering during the night or non-sunshine hours. The electricity generated from the solar cell is DC, and as the battery also needs DC for charging, the battery power may be discharged during the hour of need. **Lead–acid batteries** most commercial used solar photovoltaic system, and in some cases **nickel–cadmium** battery has acceptable performance characteristics and life cycle cost for solar PV system applications. Batteries placed in solar lamps are made of use gel electrolyte technology with high deep discharging performance to operate in extreme ranges of .

Some technical parameters are used in the battery.

**Battery capacity (Ah)**—The ampere-hour capacity is expressed as current drawn from a battery that can provide over a specified period of time, for example, 120Ah battery C10 rate to end of discharge (EOD) of 1.75 V/cell. This means the battery can provide 12 amp utilized for 10 h to an end of discharge per cell.

**State of charge**—It expresses the present battery capacity working as a percentage form of maximum capacity. SOC is normally calculated using current integration to determine the change in battery capacity over time.

**EOD**—End of discharge level describes the battery string or cell voltage allowable to drop before affecting the load as 1.75 V or 21 V on a nominal 24 V system.

**Depth of discharge** is expressed as a percentage of maximum capacity discharge rate acceptable at least 70% DOD referring to deep discharge.

The two-step method charging method is the most efficient and commonly used method by charging the solar system battery. In the first step, a constant current is applied to charge 70% of the battery, and then a constant voltage is applied to maintain the battery to be fully charged. Also, it is not suitable for rapid charging technology. **Pulse charging method**—this method is used in the PWM charge controller. Simultaneously, the negative pulse charging method is used to eliminate polarization, so the temperature of the battery is low (approximately 4 °C), so the longevity of the battery life is increased. The C rating describes the rate of battery charging and discharging relatively to the maximum capacity. For example, we describe the discharge current discharge entire battery in 1 h for 1C rating battery while for example 20C with 2000 mAh total current is  $2 \text{ A} * 20 \text{ C} = 40 \text{ A}$  shows 40 A can be discharged for an hour without any severe precaution and safety. The second foremost credentials performance metric of the battery life cycle refers to the discharge current of energy in the battery life cycle with the discharge rate taken for reference. High capacity with larger operating temperature also affects the battery life cycle as it reduces the battery cycle, so it is essential for the industrial and commercial place to store the battery operating temperature at 10–30 °C. The Battery Test and Characterization Laboratory is recognized by the Bureau of Indian Standards (BIS), for IS 16270:2014 (Fig. 8.11, 8.12, 8.13 and 8.14).



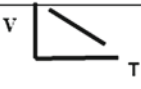
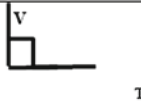
Charging type	Type of charging graph	Remarks
Constant Current		• It bring slow charging which is not good for parallel and series batteries.
CC-CC		• Faster charging but not good for Parallel /Series Batteries
Constant power		• Power limited by gassing voltage and current with slow charging.
CC-CV		• Applied for parallel battery charging with good charging rate

Fig. 8.11 Charging technique applied in vented lead–acid batteries. *Source* Author

The significant difference between the commercial batteries is differentiated discussed in Table 8.2.

### 8.5 System Designing in an Off-Grid System

Site potential for any location for monthly irradiance and peak sunshine hours necessary for designing the system provided location and site information for the predictive model. Daily irradiance is defined by monthly irradiance by the total number of days. For example, if the monthly irradiance is 104 kWh/m<sup>2</sup> and the number of days is 30 for June, the daily irradiance is 3.5 kWh/m<sup>2</sup>. The overall system performance plays a vital role in design and prediction of performance ratio calculation. The whole system losses include the whole system losses in the descriptive chart. Steps involved for SPV system sizing are described in the chart below, where energy consumption is defined by

$$\text{Energy (Wh)} = \text{Power (W)} * \text{Time (t)}$$

DC and AC losses accounted for separately as AC losses accounted for inverter losses while the DC system accounted for cabling losses (Fig. 8.15).

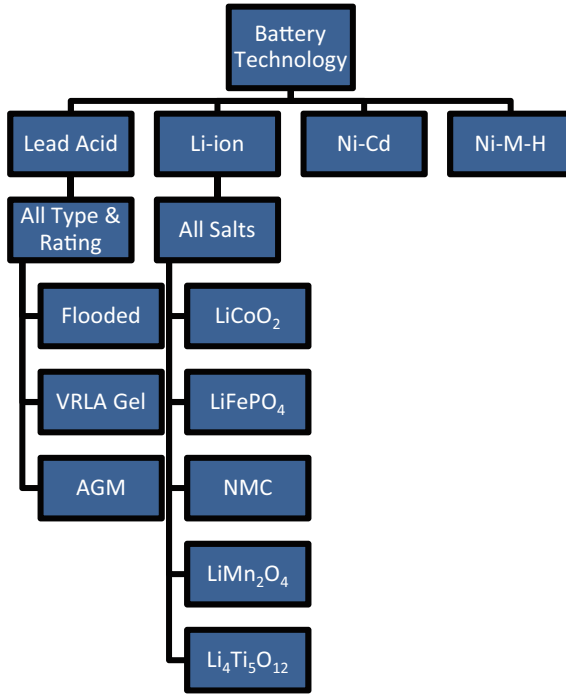


Fig. 8.12 Different types of commercial secondary batteries testing. Source Author

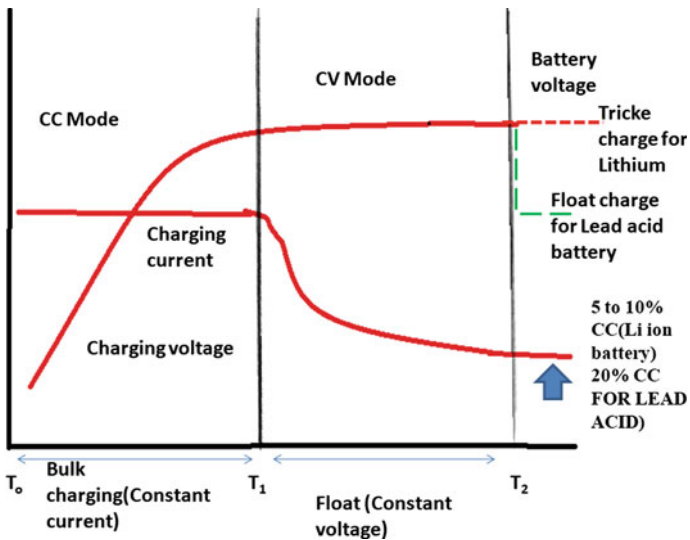
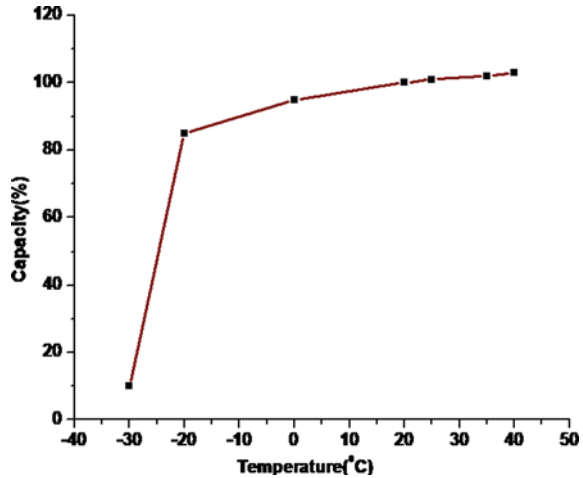


Fig. 8.13 Battery charging technique for solar batteries as CC–CV mode. Source Author

**Fig. 8.14** Capacity of battery behavior with temperature variation.  
Source Author



**Table 8.2** The significant difference between the commercial batteries is differentiated discussed

Parameters	Flooded lead–acid batteries	Lithium-ion batteries	Redox flow batteries
Lifetime span	Depending on the life cycle, it lasts up to 15 years or more; still proper maintenance is needed	High-quality batteries lasted for ten years	Longer life 25 years especially for vanadium With no cycle repetition
Charging technique	It takes several hours for charging 100%	It varies subsequently depending on the several factor ambient condition as it heated up at higher temperature expect three or longer hours charges	Recharged with replacing with electrolyte similar with auto gas tank
Cycling	200–300 discharged and charged state	5000–7000 cycle for possible for quality battery	No cycle limitation
Safety and maintenance	Regular maintenance, including adding water cleaning terminal and venting. It contains lead and sulfuric acid, which is corrosive. Gaseous hydrogen exploration brings gaseous hydrogen	Maintenance-free solid electrolyte with no water filling and refilling	Inherently safe as the electrolyte is not explored and catch fire
Cost	Cheapest applicable for SPV renewable energy Source	Expensive compared with lead–acid	Expensive due to advance organic technology, research leading to bring forward at lower cost effective

Source Author

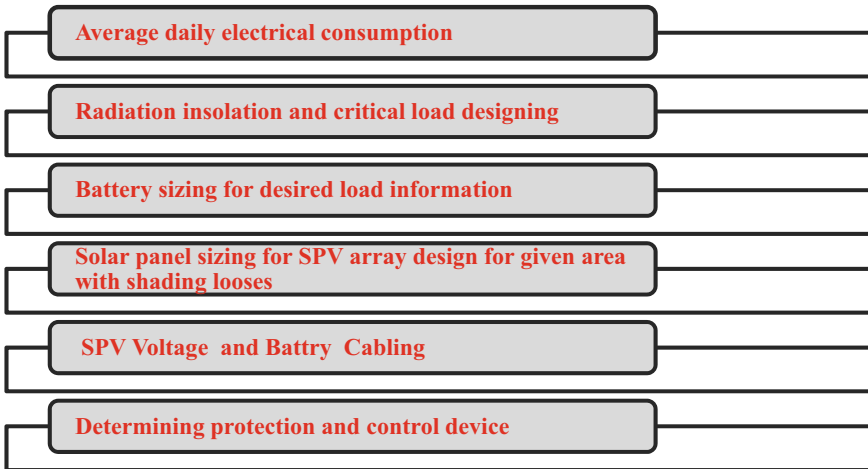


Fig. 8.15 Flow diagram for off-grid system designing. Source Author

Step 1: SPV peak power estimation design where energy when total peak generation is greater than consumption

$$E_{pv} = \text{Peak Power} * \text{Peak Sunshine Hour} * \text{PR}$$

where PR is performance ratio calculated by.

Performance ratio (PR): The performance ratio PR is expressed as the final SPV system yield,  $Y_f$ , divided by the reference yield,  $Y_r$  [1].

$$\text{PR} = \frac{Y_f}{Y_r} \tag{8.7}$$

The PV system yield,  $Y_f$ , is net energy output E divided by the nameplate value of DC power  $P_0$  installed PV array.

$$Y_f = \frac{E}{P_0} \text{ (kWh/kW) or (h)} \tag{8.8}$$

The reference yield,  $Y_r$ , is the total in-plane solar isolation  $Ht$  (kWh) divided by the PV's reference (STC) irradiation (kW). It represents an equivalent number of hours at the reference irradiance. It is a function of the location, orientation, and tilt angle of the PV array and varies day-to-day, month-to-month, and year-to-year as weather variability and seasonally change

$$Y_r = \frac{H}{G_0} \tag{8.9}$$

PR mainly depends on the module temperature. For reducing the seasonal effect and temperature effect, PR should be temperature normalized. This can be estimated by normalizing the instant output to 25 °C from the measured module temperature using the power temperature coefficient. While designing the charge controller system, voltage selection and design are done efficiently according to the system sizing.

The thumb rule selection is based on selecting 12 V system for less than 2 kW designed off-grid home appliances, while for 2–3 kW as 24 V system voltage. 3 – 5 kW system lies between 48 V, while 5–10 kW system has 96 voltage obeying the power law as  $V * I$  law where high voltage keeps DC current smaller applicable (Fig. 8.16).

The next designing step for system battery voltage depending on the cable losses and cable length. Battery voltage depending on battery cable losses is denoted as  $\epsilon$  as cable losses, section, and cable length denoted as  $S$  and  $L$ , peak array P

$$U_{BATT}^2 = \frac{(\rho * 2 * L * P)}{\epsilon * S} \tag{8.10}$$

As thumb rule installer prefers peak power less than 500 W 12 V<sub>dc</sub>, for peak power between 500 and 2000 W battery system voltage is 24 V, and more significant than 2000 W is 48 V. Likewise, DC cable sizing properties deal with double insulation cross-linked polyethylene compound with fire-resistant operating temperature. Battery capacity sizing design is defined by

$$\text{Battery capacity} = \left( \frac{E_{LOAD} * N_{day}}{V_{batt} * DOD * K_T} \right) \tag{8.11}$$

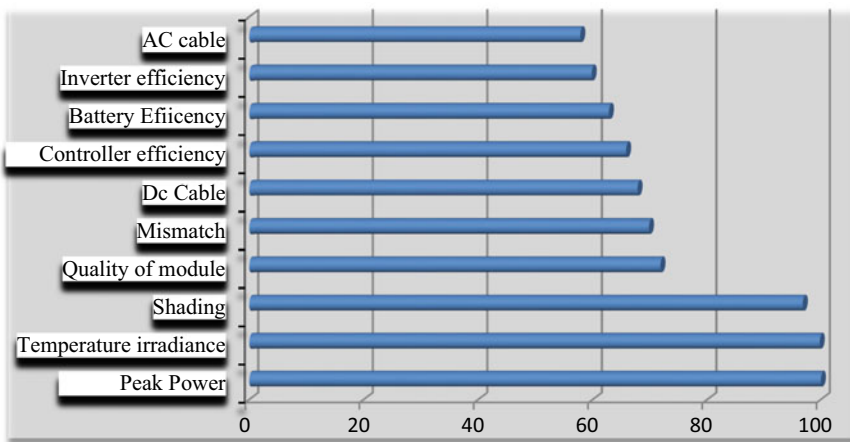


Fig. 8.16 Different type of system losses on the generation side. Source Author

$K_T$  is the minimum temperature condition.

$V_{Batt}$  = System voltage.

$E_{LOAD}$  = Daily electrical load.

DOD = Depth of discharge.

$N_{day}$  = Autonomy energy storage.

The selection of battery capacity is always more than energy consumption; adding the number of autonomy and the number of battery capacity provides enough energy to the electrical load when no energy is present. Battery bank introduces longevity of battery with a maximum depth of discharge. The capacity coefficient is introduced in battery temperature as a coefficient changing with temperature (Tables 8.3 and 8.4).

Inverter selection is based on the DC and AC side conversion based on the battery system voltage for AC side and electronic load in terms of frequency inverter power =  $1.25 * \text{Max } P_{AC}$  where sizing of charge controller is verified by the controller compatibility of PV array and battery voltage with the condition selectivity with the condition.

Cabling size also plays a prominent role in the system losses with the section of operating condition between SPV array controller batteries and inverter where SPV array is brought in the losses in DC controller cabling, DC combiner size maximum allowable losses maximized by 1% with allowable current losses up to 1% voltage drop of DC side is calculated by

$$\epsilon = \frac{\rho * 2 * L * I_{MPP}}{U_{MPP} * S_{selected}} \tag{8.12}$$

where  $S$  is the cross-sectional area, where voltage drop  $\epsilon$  is accepted less than 1%

**Table 8.3** Using  $k$  coefficient for the different temperature of batteries (source Author)

Operation battery coefficient	- 20 °C	- 10 °C	0 °C	10 °C	20 °C	30 °C	40 °C
Battery capacity coefficient $K_T$	0.8	0.85	0.90	0.95	1	1.04	1.10

**Table 8.4** Risk criteria for MPPT algorithms designing (source Author)

Serial No.	Sizing criteria	Risk in case of non-compliance criteria
1.	Maximum SPV array lower than nominal controller power	Controller failure defined as MPPT is not working stage
2.	Maximum open-circuit SPV must be lower than maximum controller voltage	It indicates controller failure damaging
3.	Maximum short-circuit SPV array sizing must be lower than maximum controller voltage	Controller failure mode as MPPT will not be in the working stage
4.	The controller in the suitable battery voltage	Failure in controlling an operation mode



**Example** If 7.2 W VDC LED lamp having 4 unit used for 5 h per day, 2 unit of 12 Vdc 6 W fan for 10 h per day and DC appliance working at 10 W for 2 h per day how to design a solar off-grid system?

Step 1: First step for designing the system design is to calculate the total appliances used for whole day

$$= (7.2 \times 5) + (6 \times 10) + (10 \times 2) \text{ W h/day} = 116 \text{ Wh/day.}$$

$$\text{SPV panels required energy} = 116 \text{ W h/day} \times 1.3 \text{ as lost energy as energy system.} \\ = 150 \text{ W h/day.}$$

Step 2: Size of SPV panel defined by available sunshine energy per day 4 h /day

$$\text{Total wattage of SPV panel} = 150/4 = 37.5 \text{ Wp.}$$

Step 3: Defining a battery sizing

$$\text{Batteries needed(Ah)} = (C_o(\text{Daily consumption (Ah)}) \times \text{Atonomy}) / \text{DOD} \quad (8.13)$$

$$\text{SOC} = \left(1 - \frac{\text{DOD}}{100}\right) \times 100 \quad (8.14)$$

SOC = State of charge.

DOD = Depth of discharge

The performance is analyzed by utilizing the energy to the load without charging and checking the number of hours the sample can burn when the battery is fully charged, dividing total watt-hours per day consumption by 0.85 for battery loss =  $116/0.85 = 136.47 \text{ W hr}$ .

The net energy is divided by 0.5 for the depth of discharge =  $136.47/0.5 = 272.94 \text{ W h}$ .

Battery voltage = 12 V.

Days of autonomy = 2 days.

Battery capacity =  $(272.94 \text{ W h}/12 \text{ V}) \times 2 = 45.49 \text{ A}$ .

Commercial battery is selected as 12 V 50 A for 2 day autonomy.

#### **Step 4: Charge controller selection.**

Standard sizing of solar charge controller practices for taking a short-circuit current ( $I_{SC}$ ) of the PV array and multiply it with 1.3 SPV module.

$P_m = 37.5 \text{ Wp}$ .

Panel voltage = 12 V.

Solar charge controller rating =  $37.5/12 = 3.125 \text{ A}$ .

The commercial solar charge controller should be rated 5 A 12 V or greater.

## 8.6 LED Lighting of Off-Grid System Appliances

The light-emitting diode (LED) is solid-state lighting comprised of n- and p-type layers where direct current is applied to the N side due to applied electrical pressure forces electrons jump across to the juncture to the P side crossed to fill holes on the other side to emit the energy. With the proper P and N materials, the energy is emitted as visible light, infrared, and ultraviolet LEDs for blue range. The basic terminology for defining the light is described below.

### Luminous flux

It is a fundamental technique of measuring electromagnetic radiation emitted by a given light source radiant flux. Luminous flux is the multiplication of radiant flux respective of wavelength, by the relative spectral sensitivity human sensitive visual system, associated wavelength range 380 nm to 780 nm.

$$\varphi = K_m \sum \psi_\lambda V_\lambda \lambda \tag{8.15}$$

$F$  Luminous flux (lumens).

$\sum \psi_\lambda$  Radiant flux in a small wavelength interval  $D\lambda$  (watts).

$V_\lambda$  The relative luminous efficiency function for the conditions.

$K_m$  Constant expressed as lumens/watt.

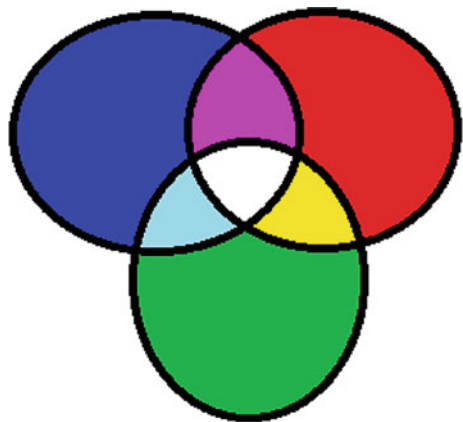
$\lambda$  = wavelength interval. For example if the green light radiates power in watt at 555 nm  $K_m$  1, red = 670 nm  $K_m$  0.1) and the radiating power in lm with 1 W LED radiate power is defined as lm:

Red light LED at 670 nm =  $683(\text{lm/W}) \times 0.1 (K_m) \times 1 (W) = 68.3 \text{ lm}$ .

Green light LED at 555 nm =  $683 (\text{lm/W}) \times 1 (K_m) \times 1 (W) = 683 \text{ lm}$  (Fig. 8.17).

Primary color brings as base colors used to generate other secondary colors through the mixing of color lights by adjusting red, green, blue (RGB). A secondary

**Fig. 8.17** Primary color design formation of a secondary color. *Source* Author



color is an intermediate form of colors by mixing equal quantities of two primary colors as are amber, cyan, and magenta.

Hue is the perception of a color for red, green, blue, etc., with saturation; high chroma is defined as it equals with high saturation. Low chroma defines low saturation broad spectrum for relative lightness or darkness of a color and is equivalent to one of the series of grays between white and black. For visibility of color temperatures from less than 2500 K to over 6000 K, it is defined as “white light,” producing specific color temperatures of white light, through color temperatures and availability varies by lamp type, wattage, and manufacturer design [5].

The light output (total luminous flux or lumen output) and other light output parameters (i.e., CCT, CRI, etc.) are measured by using an integrating sphere. Integrating sphere with a temperature-controlled system is designed to test photometric and colorimetric performance with dynamic temperature range as per IES LM-82 and LM-79 standard testing procedures [6]. The solid-state light engine is applied in a luminaries or fixture, and the thermal environment near the LEDs is altered by both the design and the application environment. By measuring a luminaire or fixture’s performance characteristics at various temperatures, one can model the expected light output by measuring the operating temperature. The most commonly used model is x CIE color space, a methodology for mapping perceived color onto the unit plane of an x, y, and z graph. This graph of x, y, and z chromaticity value defines the mapping of perceived color as a ratio of red, green, and blue color saturation. These three colors values are corresponding band-pass filtered with chromaticity mapping of any perceived hue or color as a simple locus on a unit plane. The light distribution varies from one type of system to others (i.e., unidirectional or omnidirectional light). The light distribution test is measured using the LUX meter or light meter after installing the system as specified by the user/ manufacturer or claimed by the user or standard testing procedure.

$$X = \int_{\lambda_1}^{\lambda_2} x(\lambda) * P(\lambda) d\lambda \quad (8.16)$$

$$Y = \int_{\lambda_1}^{\lambda_2} y(\lambda) * P(\lambda) d\lambda \quad (8.17)$$

$$Z = \int_{\lambda_1}^{\lambda_2} z(\lambda) * P(\lambda) d\lambda \quad (8.18)$$

X, Y, and Z are the trichromatic responses of the cones to a specified illumination signal.

$$x = \frac{X}{X + Y + Z}; y = \frac{Y}{X + Y + Z} \quad (8.19)$$

This intuitive sample provide the chromacity value of glow color red, then yellow, then white as they heated and lifetime brightness of an LED. The black body line or Planck, an locus, gives a single metric to characterize an illumination source, the CCT, expressed as Kelvin (K). CCTs as an example showing 2700–3000 K which are described as warm white, occupying a region with a yellower hue of white. CCTs of 3500–4000 K are described as neutral white, and CCTs of 4500–5500 K are described as cool white, for their bluish hue measured by  $x$  and  $y$  chromaticity coordinate.

### **Illuminance**

Illuminance is defined as luminous flux falling on the unit surface area. The unit of measurement of illuminance is defined as lumen/m<sup>2</sup> or lux. The illuminance incident on a surface is the most widely used electric lighting design criterion.

### **Luminance**

The luminance is calculated for the surface by luminous intensity emitting per unit on the projected surface area at a given direction. The unit of luminance is expressed in the candela/m<sup>2</sup>.

### **Candela (cd)**

Is defined as the intensity of a light source in one trending direction. This value represents the light output of directional lamps and luminaries supplied by the lamp manufacture and luminaries manufacturer.

### **Color Rendering Index (CRI)**

The color rendering index (CRI) is defined as the colors' reliability and appearance as the light source allowing the human eyes to recognize. A higher rendering index value is enviable for a light source as much as its efficiency on an excellent acceptance rated on a 100 scale. The driver circuit's efficiency is measured by measuring the input power from the battery, and the output of the driver fed to the LEDs. The driver circuit's output is measured as a function of the battery operating voltage, and the requirement to make sure the constant light output is that the driver output should not change more than  $\pm 3\%$  with the varying battery operating voltage. The charge controller's charging behavior is studied to know the type of the charge controller, whether it is MPPT/PWM/series regulated/ shunt regulated or any other type of the charge controller. Also, the compatibility of the charge controller with the battery and the module is checked. The MPPT-based charge controller is preferred. Charge controller efficiency needs to be more than 90%. To make the system thoroughly abuse-free, the system is tested for battery deep discharge protection, overcharge protection, reverse polarity protection, load short-circuit and open-circuit protection, and reverse current flow protection measure the effectiveness of a device converts electric current into useful output power (Fig. 8.18; Table 8.5).

$$\text{Driver efficiency is calculated by power factor} = \frac{\text{LED Real power output}}{\text{Apparent power of LED}} \quad (8.20)$$

**Fig. 8.18** Lux and CIE measurement instrument for LED application. *Source* Author

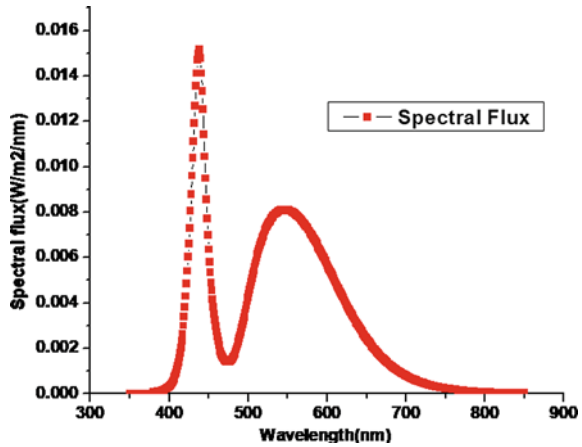


**Table 8.5** Efficacy and lifetime for commercial light application (*source* Author)

Lamp technology efficacy average life	Lamp technology efficacy average life	Lamp average lifetime efficacy
Candle light	0.2–0.3 lm/W	–
Incandescent lamp	8–15 lm/W	750–1500 h
Halogen lamp	10–35 lm/W	3000–5000 h
Pin-based CFL slight	50–85 lm/W	10,000–20,000 h
Linear fluorescent lamp	70–100 lm/W	15,000–45,000 h
Ceramic metal halide lamp	80–125 lm/W	10,000–32,000 h
LED lights	80 to 100 lm/W	Greater than 10,000 h

The efficacy of solar LED depends on the off state consumption of power di-arrangement of the thermal management system, power factor losses driving, and controlling operating voltage. The thermal management of LED defines the light beam from an LED, maintaining the cool perfectly efficient. A proper design heat sink and other thermal management features are crucial for improving operation, maximizing lifetime, and light output. As the junction temperature increases, the carrier lifetime time decreases. The driven factor brings the change in drive current, thermal pathway, and ambient temperature (Fig. 8.19).



**Fig. 8.19** Integrating sphere with temperature-controlled system. *Source* Author

An illustration showing 18 W LED rating draws 10 V-A. The driver's power factor performance is calculated by  $= 18 \text{ W}/21 \text{ VA}$ , which is 0.85 considered a higher power factor, while a CFL lamp rated with the same wattage draws 30 V-A with PF is 0.6 considered lower.

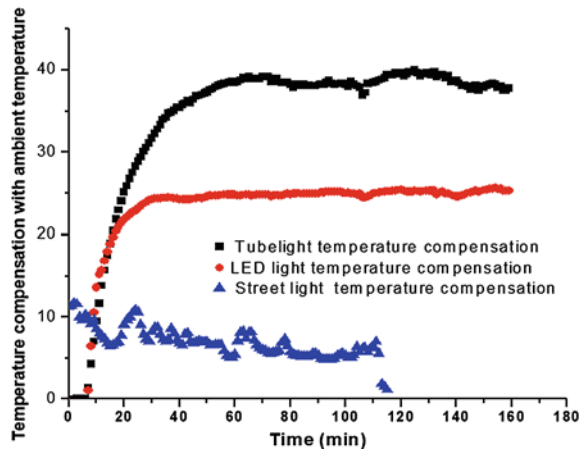
### Temperature Compensation

This test is conducted that the battery set points, i.e., battery charge regulation (BVR), low-voltage disconnect (LVD), and automatic load reconnect (LVR), are having the temperature compensation for proper charging of the battery irrespective of the operating temperature. For this test, the charge controller is kept inside a chamber, and these battery set points are measured in a temperature ranges from 0 to 50 °C and measuring the operating temperature cutoff. The LED body heat sink's housing is also monitored with the change with ambient temperature described below. If it gets heated up, it shows less isolation with the driver circuit and harms the other semiconductor components in the circuit and decays its running hour time [6] (Fig. 8.20).

## 8.7 Conclusion

The off-grid application of LED lighting system is explained in this chapter. The overall performance off-grid design considers higher reliability, system performance's longevity with higher durability, proper installation maintenance, and safety measures should be followed in project execution. The accelerated testing of the product in the test laboratory or in the field can increase the reliability in the field conditions.

**Fig. 8.20** Temperature compensation of LED and street light. *Source* Author



## References

1. <https://mnre.gov.in/solar/standard-specs-cost>
2. Bora B, Sastry OS, Kumar A, Renu, Bangar M, Prasad B (2016) Estimation of most frequent conditions and performance evaluation of three photovoltaic technology modules. *ASME J Sol Energy Eng* 138(5):054504–054504–6. <https://doi.org/10.1115/1.4034202> (2016)
3. Series resistance measurement of solar PV modules using mesh in real outdoor condition. In: 5th International conference on advances in energy research, ICAER 2015, 15–17 December 2015, Mumbai, India, *Energy Procedia* 90:503–508 (2016)
4. IEC 60891:2009 Photovoltaic devices—procedures for temperature and irradiance corrections to measured I–V characteristics
5. IES LM-79–08: Method of electrical and photometric measurements of solid state lighting (LED) products
6. IESNA LM-82–12 (The approved method for determining photometric properties as a function of temperature for LED light engines and integral lamps)

# Chapter 9

## Thermal Energy Storage for Solar Energy



Shubham Jain, Sumeet Kumar Dubey, K. Ravi Kumar, and Dibakar Rakshit

### 9.1 Introduction

The increase in global energy consumption and the depletion of conventional energy resources have triggered efforts to explore sustainable renewable energy resources. The adverse effect of conventional fuel-based energy systems on the environment, such as pollution and CO<sub>2</sub> emission, can be mitigated by integrating them with suitable renewable energy resources along with energy storage. Solar energy technology has risen as the prominent renewable energy resource for various energy applications due to its abundant availability. The intermittent nature of solar energy is one of the major challenges in the utilization of this form of energy in various applications. The integration of appropriate storage technology can overcome this challenge. One of the potential energy storage technologies to store energy from solar energy is thermal energy storage (TES). The thermal energy storage is one of the critical parts of any solar energy system. Energy is stored in the form of heat/cold in the working medium of thermal energy storage, which can further be utilized for various applications. The entire working cycle of the TES comprises three different processes, such as the charging, heat retaining, and discharging process. The energy collected from the solar collectors is supplied to the storage medium in the charging process. In contrast, the stored heat has been retrieved from the storage medium during the discharging process (Fig. 9.1). In the heat retaining process, the stored energy is retained in the medium for a specific period. The energy stored in TES solely depends on the inherent characteristics of the storage medium and the temperature difference between the source of energy and the storage medium.

The varying demand for energy requires proper energy redistribution between source and end user. Solar energy system integrated with TES can fulfill the peak

---

S. Jain · S. K. Dubey · K. R. Kumar (✉) · D. Rakshit  
Centre for Energy Studies, Indian Institute of Technology, Delhi, India  
e-mail: [krk@ces.iitd.ac.in](mailto:krk@ces.iitd.ac.in)



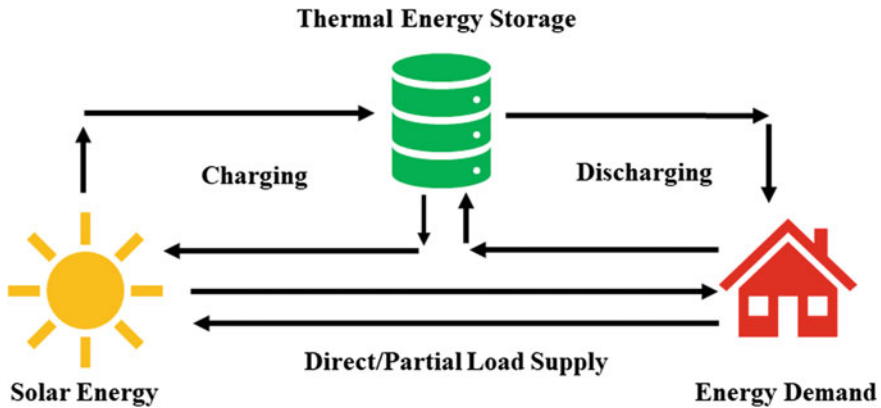
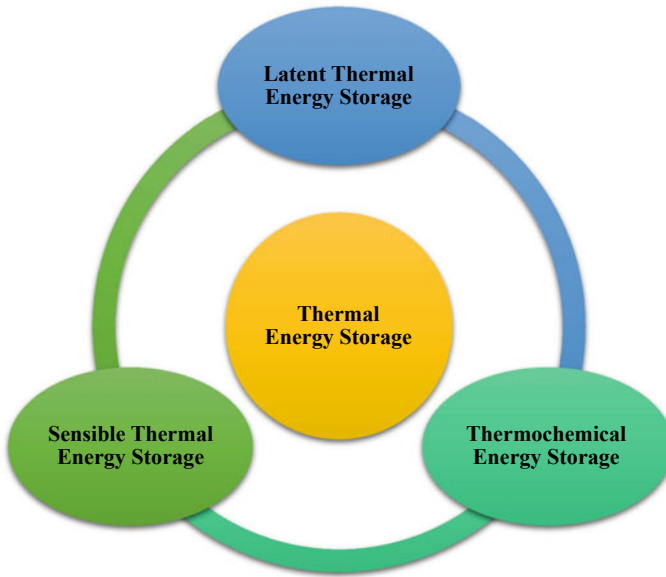


Fig. 9.1 Operation of thermal energy storage. *Source* Author

and fluctuating energy demands and provides high energy security. TES provides operational flexibility and better capacity utilization (extent up to which system uses its overall rated capacity) in the system. The improved performance of solar energy systems incorporated with TES results in economical operation as compared to the solar energy systems without TES. The overall efficiency of the energy systems is interrelated with energy conservation. Hence, any improvement in the energy conservation approach in the system can lead to increased efficiency. The TES can be characterized based on the following performance parameters:

- **Power Density:** It is the energy transfer rate per unit mass or volume of the storage medium.
- **Energy Density:** It is the amount of energy accumulated in a given mass or volume of the storage medium.
- **Storage Period:** It defines the duration of energy storage. It can vary from hours to months.
- **Response Time:** It is the rate of storing/releasing energy in/from the storage to balance the load demand. It can vary from seconds to minutes.
- **Charging/Discharging Time:** It is the time required to charge/discharge the storage system.
- **Discharge Rate:** It is the measure of the rate at which accumulated energy in the storage is discharged.
- **Self-Discharge:** It is the energy dissipation during idle time.
- **Cycle Life:** It represents the maximum number of charging/discharging cycles that can be operated into the entire life span of the storage.
- **Round-Trip Efficiency:** It is the ratio of the energy retrieved to the energy stored in the storage.
- **Cost:** It comprises capital as well as the operational cost of the energy storage.

The aforementioned performance parameters play an important role in the selection of appropriate storage technology for specific energy applications. The high



**Fig. 9.2** Classification of TES. *Source* Author

energy and power density directly represent the storage capability of the TES. The round-trip efficiency indicates how efficiently the storage technology can be utilized by minimizing energy losses. Efforts are being made by the researchers to develop cost-effective TES technology having a better cycle life. Based on the process of storing energy, thermal energy storage technologies may be classified into three categories, such as sensible thermal energy storage (STES), latent thermal energy storage (LTES), and thermochemical energy storage (TCES) (Fig. 9.2). In a sensible thermal energy storage system, the heat is stored/released by increasing/decreasing the temperature of the storage medium, while LTES stores/releases energy by undergoing the phase change process. The TCES stores/releases energy in the form of the enthalpy of the corresponding chemical reaction. Every type of TES has its own merits and demerits, which should be considered during the selection of the appropriate storage technology according to the specific application (Table 9.1). The detailed description of these technologies is provided in the subsequent sections.

## 9.2 Sensible Thermal Energy Storage

The roots of the STES technology can be found in our old historical building structures where rocks and stone are used to keep the inner space cool during summer

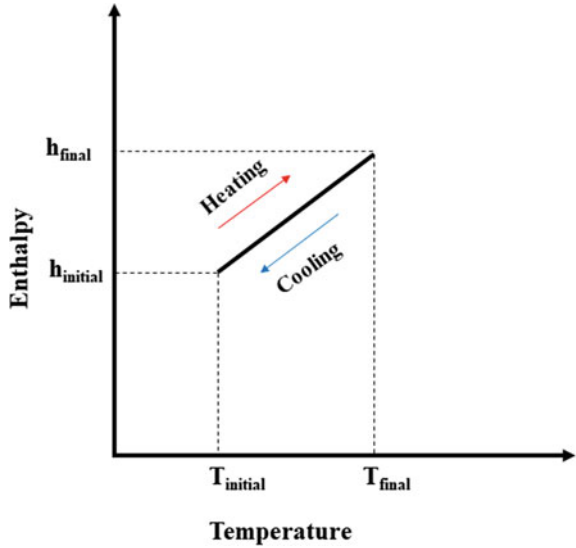
**Table 9.1** Comparison between STES, LTES, and TCES [1]

	STES	LTES	TCES
Capacity (kWh/t)	10–50	50–150	120–250
Power (MW)	0.001–10.0	0.001–1.0	0.01–1.0
Efficiency (%)	50–90	75–90	75–100
Storage period	Days/seasonal	Hours/seasonal	Hours/days
Advantages	<ul style="list-style-type: none"> <li>• Reliable and inexpensive</li> <li>• Simple system and easy operation</li> <li>• Low cost and eco-friendly</li> <li>• High thermal conductivity</li> </ul>	<ul style="list-style-type: none"> <li>• Moderate energy density (better than STES)</li> <li>• Isothermal operation</li> <li>• Available in wide range of melting temperatures</li> </ul>	<ul style="list-style-type: none"> <li>• Highest energy density</li> <li>• Compact system</li> <li>• Operates at atmospheric temperature</li> <li>• Negligible heat losses</li> </ul>
Disadvantages	<ul style="list-style-type: none"> <li>• Low energy density</li> <li>• Huge volume required for storage</li> <li>• High heat losses and self-discharge</li> <li>• High construction cost and geological constraints</li> </ul>	<ul style="list-style-type: none"> <li>• Low thermal stability</li> <li>• Corrosion</li> <li>• Low thermal conductivity</li> <li>• High cost</li> <li>• Supercooling</li> </ul>	<ul style="list-style-type: none"> <li>• Expensive</li> <li>• Design and operational complexities</li> </ul>
Present status	<ul style="list-style-type: none"> <li>• Matured technology and large-scale deployment have been done</li> </ul>	<ul style="list-style-type: none"> <li>• Technology is in pilot-scale testing phase, and several laboratory-scale prototypes have been developed</li> </ul>	<ul style="list-style-type: none"> <li>• Unmatured technology and laboratory-scale testing have been done</li> </ul>

and hot during winter. Nowadays, this technology has emerged as a promising technology for diverse energy applications due to the development of advanced materials. The STES stores energy by altering the temperature of the working medium without undergoing any phase change process (Fig. 9.3). The working cycle of STES comprises two processes, such as sensible heating (charging process) and sensible cooling (discharging process). The energy stored per unit mass in STES is directly proportional to the specific heat and the difference between the initial and final temperatures of the storage media. The materials having high specific heats and high operating temperatures are preferred in STES because they can store more thermal energy. However, the higher temperature of the storage medium leads to higher heat losses to the surrounding. So, insulation plays an essential role in STES. The sensible heat stored in kJ ( $Q$ ) during charging of STES can be expressed in terms of specific heat in kJ/kg K ( $c_p$ ), mass in kg ( $m$ ), and temperature difference in °C ( $\Delta T$ ) as follows:

$$Q = mc_p \Delta T = mc_p (T_{\text{final}} - T_{\text{initial}}) \quad (9.1)$$

**Fig. 9.3** Sensible heating/cooling. *Source* Author

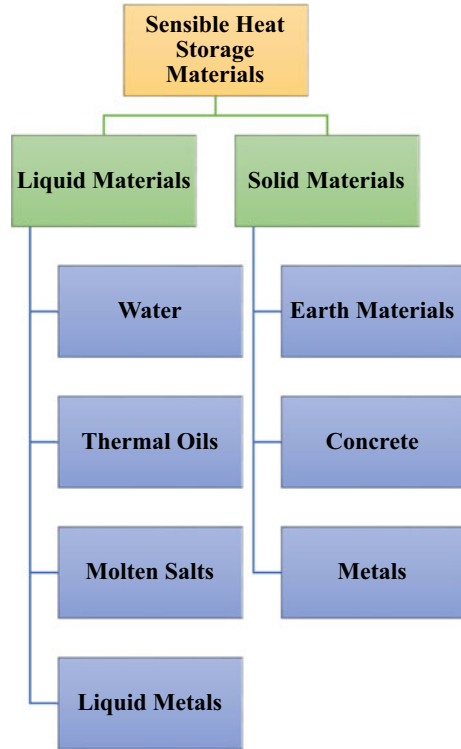


$$\Rightarrow Q = V \cdot (\rho \cdot c_p) \cdot (T_{\text{final}} - T_{\text{initial}}) \tag{9.2}$$

Here,  $\rho \cdot c_p$  is the volumetric heat capacity of the STES (in  $\text{kJ/m}^3 \text{K}$ ).

The energy stored during charging can be retrieved during the discharging process. The efficiency of STES depends on the inherent characteristics of the medium of storage. The materials having high energy density and thermal conductivity are preferred for storing high energy in a compact space. The thermal and chemical stability of the material and non-reactivity with the container material is necessary for developing STES, having a long cycle life. The structural stability of the storage is judged based on the compressive strength and fracture toughness of the material. The use of non-toxic and non-explosive materials is necessary to develop eco-friendly STES technologies. Generally, sensible storage mediums provide a low-cost storage option for many energy applications, which makes it widely adopted thermal storage technology. The sensible thermal storage materials can be classified into two distinct categories, such as solid and liquid sensible heat storage materials (Fig. 9.4). Gaseous materials are usually not preferred as a sensible heat storage media due to their high specific volume. Rocks, pebbles, refractory bricks, and metals such as steel and cast iron are used as the solid sensible heat storage media, and oil, water, inorganic salts, etc., are used as the liquid sensible heat storage media in STES (Table 9.2). The flowability of liquid sensible materials provides some operational flexibility to the storage. The low-cost storage can be made by using solid materials.

**Fig. 9.4** Classification of sensible heat storage materials. *Source* Author



### 9.2.1 Solid Sensible Heat Storage Materials

Solid sensible heat storage materials are one of the economical media to store thermal energy. These materials have been used in various solar energy applications for the past many years. The solid materials used in sensible thermal energy storage are as follows.

#### 9.2.1.1 Earth Materials

The commonly used earth materials are gravels, sand, and rocks. The better thermal conductivity, significant storage capacity, nonflammability, non-toxicity, and the lowest cost make these materials suitable for storing thermal energy in diverse solar applications such as solar power generation, solar cooking, desalination, and solar drying. The packed bed configuration of storage is the most suited configuration for storing thermal energy in earth materials in a large quantity [8]. In space heating applications, earth materials have been utilized in the packed bed storage as the filler materials and air have been utilized as the heat transfer fluid (HTF). The heat

**Table 9.2** Sensible heat storage materials [2–7]

Materials	Density (kg/m <sup>3</sup> )	Specific heat at 20 °C (kJ/kg K)	Thermal conductivity at 20 °C (W/m K)	Thermal capacity (MJ/m <sup>3</sup> K)
Concrete	2200–2700	0.75–1.13	0.9–2.0	1.68–3.0
High alumina concrete	2400	0.98	0.2	2.35
Reinforced concrete	2200	0.85	1.5	1.87
Cement mortar	1900–2000	0.64	0.6–0.7	1.19–1.30
Castable ceramic	3500	0.86	1.4	3.03
Alumina ceramic	3800–4000	0.75–0.88	18.0–33.0	2.83–3.48
Silicon carbide ceramic	3200	0.75	120	2.40
Brick	1700–1800	0.84	0.5–0.7	1.419–1.51
Brick magnesia	3000	1.13–1.15	5.0–5.1	3.39–3.45
Silica fire brick	1800	1.00	1.5	1.82
Soil (clay)	1500	0.88	1.3	1.27
Soil with gravel	2000	1.84	0.5	3.68
Silica-based refractory	2300	0.86	1.8	2.01
Copper	8300–9000	0.38–0.41	372.0–385.0	3.17–3.72
Iron–cast iron	7200–7900	0.46–0.83	29.3–73.0	3.34–6.61
Aluminum	2700	0.89–0.94	204.0–238.4	2.41–2.55
Lead	11300	0.13	35.3	1.48
Steel–cast steel	7800	0.57–0.60	40.0–50.0	4.45–4.68
Steel slag	3000	0.99	2.0–3.5	2.96
Cofalit	3100	0.80–1.03	1.4–2.7	2.49–3.22
Graphite	2200–2300	0.40–0.61	122.0–155.0	0.88–1.37
Sodium chloride	2200	0.85–0.86	6.5–7.0	1.83–1.86
Molten salts	500–2600	1.50	0.2–2.0	1.35–3.90
Mineral oil	800	2.6	0.1	2.0
Synthetic oil	900	2.10–2.30	0.1	1.89–2.07
Liquid sodium	900	1.30	71	1.10
Water	1000	4.18	0.6	4.17

capacity, thermal conductivity, density, porosity, cost, and availability are the parameters that need to be considered for selecting appropriate earth material for the given applications.

### **9.2.1.2 Concrete Block**

Concretes are a mixture of gravel, sand, and cement, where cement acts as a binder. Concrete blocks are the low-cost and eco-friendly sensible heat storage materials having significant thermophysical properties. Due to the excellent mechanical properties, concrete does not require any storage container, which reduces the cost of the storage. When concrete-based sensible heat storages are operated for many high-temperature thermal cycles, then it can lead to the swelling of the concrete structure, which further can generate the cracks in the structure.

### **9.2.1.3 Metals**

Metals are also used as sensible heat storage in many applications. Metals can store/release heat at a faster rate as compared to the other storage materials due to their high thermal conductivity and diffusivity. Therefore, the heat transfer area required for the metallic storage medium is less than the other mediums. Aluminum, steel, cast iron, zinc, and copper are some of the preferred metals which are used in STES. The solid industrial waste such as metal slag and metal chips can also be used as the storage medium. Metals are preferred for high-temperature (200–700 °C) storage applications [4]. It is to be noted that the cost of the metal-based STES is much higher as compared to other STES materials.

## ***9.2.2 Liquid Sensible Heat Storage Materials***

Storing thermal energy in the liquid sensible heat storage medium is a widely adopted storage technology in solar energy applications. The liquid materials used in sensible thermal energy storage are as follows.

### **9.2.2.1 Water**

It is one of the widely used sensible heat storage materials due to its easy availability, low cost, significant specific heat, nonflammable and non-toxic nature. It is also used as the heat transfer fluid in various applications. It is used in the form of ice, water, and steam in cold storage, medium temperature storage (below 100 °C), and steam accumulator, respectively. The high vapor pressure of water increases the material cost of the container.

**Table 9.3** Thermophysical properties of thermal oils used in concentrating solar power plants [9]

Properties	Therminol VP-1	Xceltherm 600	Syltherm XLT	Dowtherm A
Composition	Diphenyl oxide/biphenyl	Paraffinic mineral oil	Dimethyl polysiloxane	Diphenyl oxide/biphenyl
Max bulk temperature (°C)	400	316	260	400
Melting point (°C)	12	—	−111	12
Atmospheric boiling point (°C)	257	301	200	257
Kinematic viscosity (mm <sup>2</sup> /s)	2.48	15.5	1.1	2.56
Density (kg/m <sup>3</sup> )	904	736	660	897
Thermal conductivity (W/m K)	0.11	0.12	0.06	0.1083
Specific heat capacity (kJ/kg °C)	2.075	2.643	2.171	1.63
Thermal storage capacity (MJ/m <sup>3</sup> °C)	1.876	1.945	1.433	1.462

**9.2.2.2 Thermal Oils**

The organic fluids having excellent heat transfer characteristics are used as the HTF as well as the storage fluid in various solar energy applications. Table 9.3 shows various thermal oils used in solar power plants. These oils remain in the liquid phase at the higher temperature (up to 250 °C at atmospheric pressure) as compared to water, so it can be used for high-temperature heat transfer as well as heat storage applications. Owing to low vapor pressure than water, thermal oils require a low thickness of material for containers and pipes. Thermal oils do not freeze in pipes as molten salts during direct storage, where they have used as the HTF as well as the storage fluid because thermal oils have a low melting point ( $\leq 12$  °C). The specific heats of thermal oils ( $\sim 2$  kJ/kg K) are lower than water, and their cost is also high; nevertheless, they are one of the reliable materials for energy storage in various applications.

**9.2.2.3 Molten Salts**

The stability issues of thermal oils at high temperature ( $\geq 400$  °C) limit its applications in many energy systems. In those systems, molten salts are preferred for heat transfer fluid as well as storage media. Table 9.4 shows the thermophysical properties of various molten salts used in solar energy applications. The high volumetric storage



**Table 9.4** Thermophysical properties of molten salts used in the solar energy applications [10–13]

Properties	Solar salt	Hitec	Hitec XL	Na-K-Li nitrates
Composition	NaNO <sub>3</sub> (60%)-KNO <sub>3</sub> (40%)	NaNO <sub>3</sub> (7%)-KNO <sub>3</sub> (53%)-NaNO <sub>2</sub> (40%)	NaNO <sub>3</sub> (7%)-KNO <sub>3</sub> (45%)-Ca(NO <sub>3</sub> ) <sub>2</sub> (48%)	NaNO <sub>3</sub> (28%)-KNO <sub>3</sub> (52%)-LiNO <sub>3</sub> (20%)
Melting point (°C)	220	142	120	130
Stability limit (°C)	600	535	500	600
Viscosity (Pa s)	0.00326	0.00316	0.00637	0.03
Density (kg/m <sup>3</sup> )	1899	1860	1992	–
Thermal conductivity (W/m K)	0.55	0.2	0.52	–
Heat capacity (kJ/kg K)	1.1	1.56	1.45	1.091

capacity, stability at the high temperature, high boiling point, and low vapor pressure make the molten salts one of the preferred materials in concentrating solar power plants. The major drawback of molten salts is its very high melting point due to which it solidifies in the pipes when there is no heat source (during off-sunshine hours). Although the melting point of the pure salts can be reduced by making a eutectic mixture of two or more salts, they still have a high melting point. The high viscosity of molten salts increases the pumping power requirements of the storage systems, such as direct two-tank sensible storage of solar power plants. The selection of container material requires special attention because molten salts are corrosive in nature.

### 9.2.2.4 Liquid Metals

Liquid metals possess excellent heat transfer characteristics. Generally, the liquid metals having a low melting point are preferred in this category to store thermal energy (Table 9.5). The high thermal conductivity, negligible vapor pressure, and significant heat capacity make them a potential candidate as HTF and heat storage media. The large difference between the melting and boiling points of liquid metals provides them a wide operational temperature range as compared to the other materials. The very high cost and susceptibility to corrosion are the major obstacles in the wide utilization of liquid metals in various energy-related applications.

**Table 9.5** Thermophysical properties of liquid metals used in concentrating solar applications [11]

Properties	Na	Na (22.2%)-K (77.8%)	Pb (44.5%)-Bi (55.5%)
Melting point (°C)	98	-12	125
Stability limit (°C)	883	785	1533
Viscosity (Pa s)	0.00021 (at 600 °C)	0.00018 (at 600 °C)	0.00108 (at 600 °C)
Density (kg/m <sup>3</sup> )	1042	780	10300
Thermal conductivity (W/m K)	46.0 46 (at 600 °C)	26.2 (at 600 °C)	12.8 (at 600 °C)
Heat capacity (kJ/kg K)	1.25 (at 600 °C)	0.87 (at 600 °C)	0.15 (at 600 °C)

### **9.2.3 Sensible Thermal Energy Storage Systems**

There are various TES systems in which sensible heat storage materials are used to store thermal energy collected from solar collectors. One such popular sensible thermal energy storage system is water heat storage. Solar water heating storage system stores thermal energy collected by either flat plate solar collector or evacuated tube solar collector in the form of the enhanced sensible heat of the water. The efficient utilization of sensible heat storage materials in diverse solar energy applications depends upon the proper design of the TES. The operating parameters also play a critical role in the designing of the storage system. The sensible storage materials can directly be used in the solar energy systems itself, or a separate storage system can be integrated with the solar energy system. A separate storage system can be operated in either a direct or indirect mode of operation. In the direct mode of operation, the fluid which receives energy from the source and the fluid which is utilized as the medium of storage will be the same. In contrast, both the fluids will be different in the case of an indirect mode of operation. The existing STES technologies which have been utilized in various solar energy applications for the past many years are discussed in the following sections.

#### **9.2.3.1 Single-Tank Thermocline Storage**

Single-tank sensible heat storage filled with liquid HTF provides an economical option to store thermal energy. In CSP plants, the single-tank thermocline storage is being used from the past many years. The same HTF, which collects energy from the solar field, also acts as the storage medium in the insulated single-tank thermocline storage. The hot HTF stored in the tank can be utilized in the power cycle at the time of need. During charging, the hot fluid was fed at the top, and cold fluid is drawn from the bottom. The flow is reversed during the discharging operation (Fig. 9.5). The hot fluid (at the top half of the tank) remains separated from the cold fluid (at the bottom half of the tank) due to the thermal stratification (buoyancy difference).

In another configuration, the low-cost filler material can be used as the primary storage medium in the tank, and liquid HTF is used as the secondary medium of storage as well as to maintain the thermocline. It decreases the overall cost of the system by reducing the required quantity of costly liquid HTF [14, 15].

#### **9.2.3.2 Two-Tank Storage**

Two-tank sensible heat storage is one of the most widely used thermal energy storages in concentrating solar plants. Two-tank thermal storage can be classified into direct and indirect two-tank thermal storage. In the direct two-tank TES (Fig. 9.6), the same fluid is used as the HTF in the solar field as well as the storage media in the storage tanks.

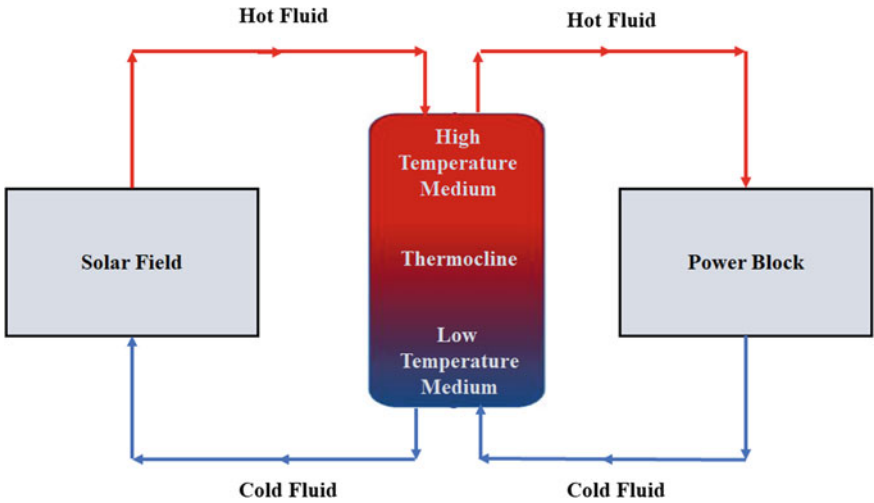


Fig. 9.5 Single-tank thermocline storage for concentrated solar thermal power plant. Source Author

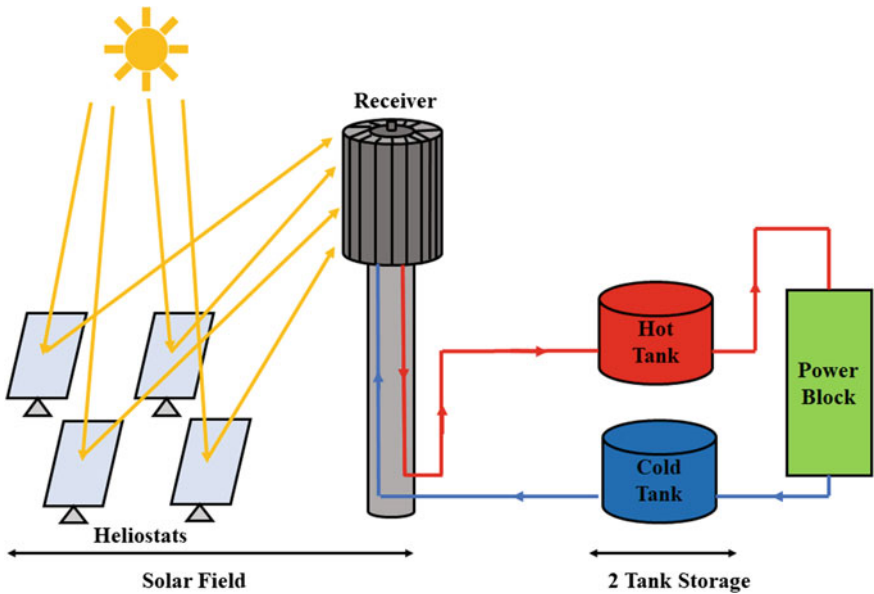
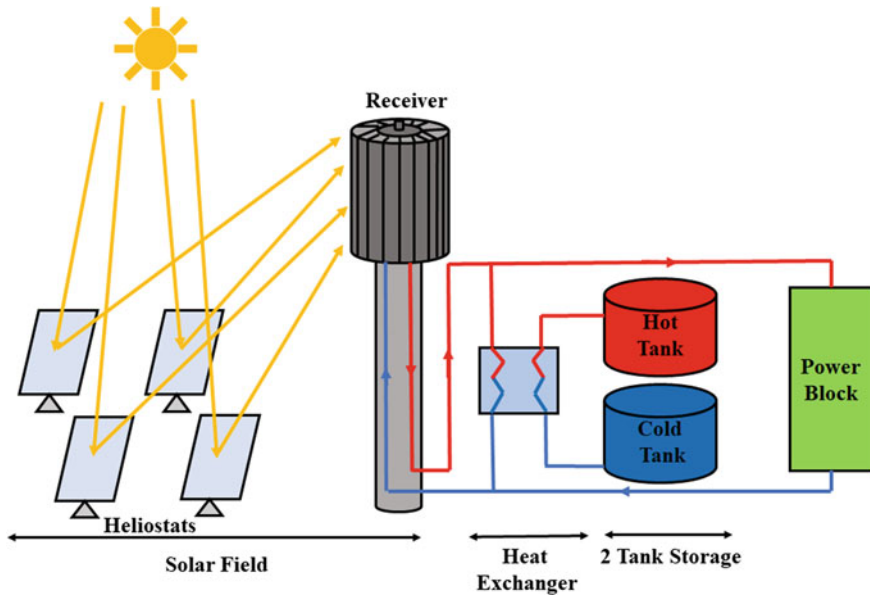


Fig. 9.6 Direct two-tank sensible heat storage in central receiver-based concentrating solar thermal power plant. Source Author



**Fig. 9.7** Indirect two-tank sensible heat storage in central receiver-based concentrating solar thermal power plant. *Source* Author

During the charging cycle, the HTF is pumped from the cold tank and collects energy from the solar field, and it is stored in the hot tank. During the discharging cycle, the stored energy in the hot tank can be utilized for generating steam in the power cycle. In contrast, in the indirect configuration of two-tank storage (Fig. 9.7), separate fluids are used in the solar field and storage tanks. A heat exchanger is provided to facilitate the heat transfer between the HTF of the solar field and storage fluid. During sunshine hours, the energy collected by the HTF which is passing through the solar collectors can be fed directly to the power block to generate electricity. The excess energy can be supplied to the storage medium with the help of an intermediate heat exchanger. The storage fluid can store the thermal energy in the hot tank, which can further be utilized for generating the steam during off-sunshine hours and cloudy weather conditions. Both the modes of operations have its own advantages and disadvantages, which need to be considered during the selection of the appropriate two-tank storage. Generally, thermal oils are used as the HTF in the parabolic trough solar collector field, and salts are used as the storage fluid in indirect two-tank storage. Due to the low operating temperature range of thermal oils and low boiling points ( $\leq 400$  °C), the vapor pressure rises quickly at the temperature higher than the boiling point of the respective oil. It can lead to the leakage of costly thermal oils. In that case, low-cost salts can be used as the HTF in the solar field as well as the storage fluid (direct two-tank storage). It will eliminate the need for a costly heat exchanger between the solar field and two-tank storage. On the other hand, the high melting point of molten salts can lead to the freezing of HTF in the



**Fig. 9.8** Two-tank molten salt storage of Andasol solar power station located in Spain [16]

solar field during the unavailability of the heat source. The requirement of trace heating/auxiliary heaters, anti-freezing, and the draining mechanism will add the extra cost to the system. In early concentrating solar plants, direct two-tank storages were used, but nowadays, indirect two-tank storages are being preferred. Figure 9.8 shows the two-tank molten salt storage of the Andasol solar power station located in Spain.

### 9.2.3.3 Steam Accumulator

The low volumetric energy density restricts the direct use of saturated as well as superheated steam in the storage. Instead, pressurized water having a high temperature can be used for storing thermal energy in steam accumulators. It is a promising technology which has been widely utilized in CSP plants as well as conventional power plants as a buffer storage system. In the direct steam generation (DSG)-based solar thermal plants, the steam can directly be stored as the high-temperature pressurized water in the steam accumulators. This eliminates the need for auxiliary components such as heat exchanger and additional pumps, which are being utilized in molten salt-based storages. The steam accumulators also eliminate the limitation of the maximum allowable temperature of common oil-based storages and eliminate the cost of intermediate heat exchangers. Water has significant heat capacity and can be used for high-temperature heat transfer as well as storage fluid. The high-temperature steam from the solar field can be fed into the steam accumulator based on the Ruth accumulator system (Fig. 9.9), where it starts condensing in the water, which is already

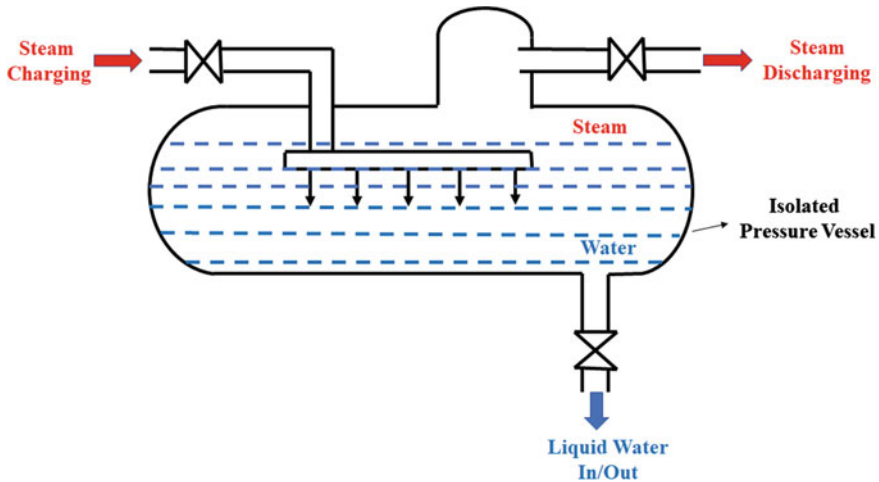


**Fig. 9.9** Schematic of a steam accumulator [17]

filled in the accumulator (covering 50–90% of the total volume of the accumulator). Due to the condensation of the high-temperature pressurized steam, the temperature and pressure of the filled water increase. However, most of the energy received from steam is stored in the form of the sensible heat of the water, but some part is also stored directly as the steam over the water. The water at high temperature and highly pressurized state can be converted into saturated steam by flash evaporation, while it is exposed to the low-pressure atmosphere. Generally, steam accumulators are manufactured in cylindrical shapes, and carbon steel is used as the material of fabrication, which can withstand high temperature and pressure.

For the appropriate designing of the steam accumulators, it is necessary to focus on the thermomechanical stability of the system for multiple charging/discharging cycles. It directly affects the life span of the storage. Steam accumulators can be vertical and horizontal in orientation, but horizontal steam accumulators are preferred because it provides a large surface area of water to condense the steam. The size of the accumulator depends on the required storage capacity. Generally, multiple units are preferred for storing a large amount of energy due to its easy transportation and maintenance. The major drawback of steam accumulators is its short storage period. Steam accumulators are used to overcome the effect of inappropriate weather conditions on the operation of the CSP plants for a short period of time. It cannot be utilized for extending the operation of the plant after sunset and during the long duration of cloudy conditions. The steam accumulator-based storage system having a storage capacity of 20,000 kWh, which is utilized in commercial power tower plant PS10 located in Spain (Fig. 9.10), can provide 50 min of operational capacity at 50% turbine load [18].



Fig. 9.10 Steam accumulators of PS10 power tower plant, Spain [16]

#### 9.2.3.4 Underground Thermal Energy Storage

The ground (clay, rock, soil, sand) can be a potential storage medium for storing thermal energy at low temperatures ( $\leq 80^\circ\text{C}$ ). Due to the low operating temperature, underground thermal storages are more suited to the water and space heating/cooling applications at the domestic and district level [19]. The thermal energy collected from the solar collectors can be stored in the underground storage during the charging process, and later it can be retrieved from the storage. Underground spaces can also be used for storing cold fluid. Generally, underground storages are referred as seasonal storage, i.e., in cold areas, they store excess thermal energy in summer and utilize that energy in winter. There are different configurations available in which underground space can be utilized for storing thermal energy, which are aquifer storage, borehole storage, pit storage. Aquifer storage stores energy in the natural underground water reservoir and its surrounding porous matrix.

There are two different underground wells of warm and cold water that are used to store energy. The water from the cold well can be passed through the solar collectors to gain thermal energy, and then it can be stored in the warm well. Later this warm water can be utilized for the space heating and water heating applications (Fig. 9.11). Aquifers are location specific and depend upon the geological and hydrogeological conditions of the site. Borehole storage is the closed-loop underground thermal energy storage where a vertical heat exchanger surrounded by the grouting materials such as Portland cement, silica sand, and bentonite is inserted into the drilled boreholes to transfer the thermal energy to the underground rocks. After receiving the energy from the source, the heat transfer fluid can transfer that energy to the



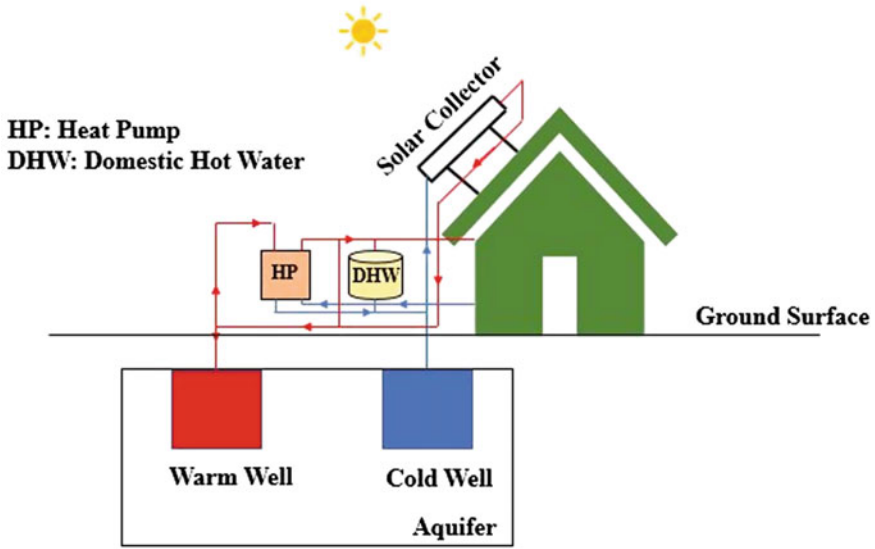


Fig. 9.11 Aquifer storage [20]

underground rocks (Fig. 9.12). However, the presence of a heat exchanger in the borehole provides flexibility to use any HTF as per the operating temperature of the respective applications; it also increases the overall cost of the system. Underground oil wells and mining sites can be used as the pit thermal energy storage where the

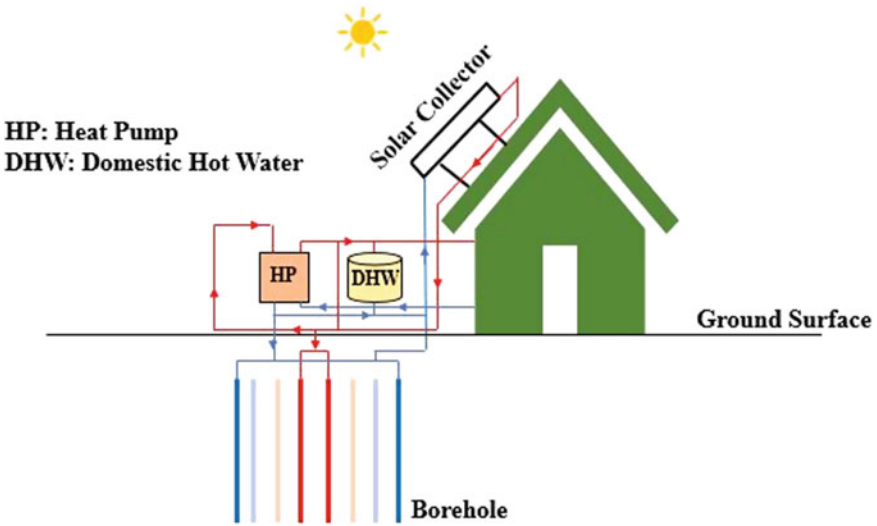


Fig. 9.12 Schematic of borehole storage [20]

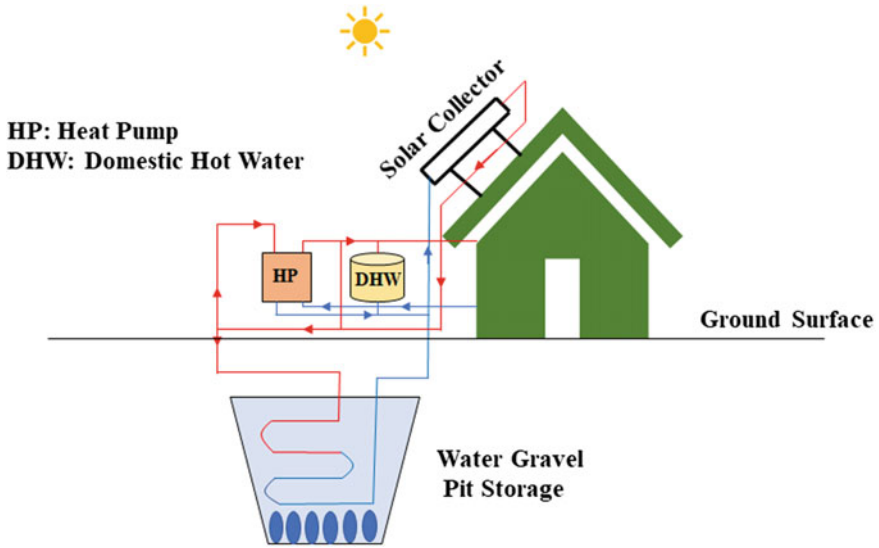
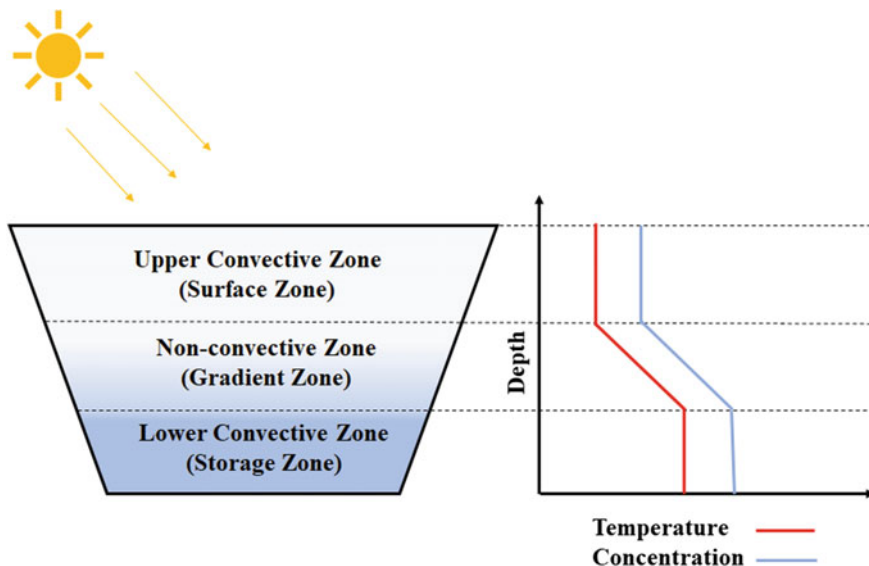


Fig. 9.13 Pit storage [20]

thermal energy of the warm/cold water can be stored. These underground storages are lined with plastic (HDPE) and filled with water or gravel. Top of the pit storage is insulated to reduce thermal losses. The thermal energy of the warm water can be transmitted to the different layers of the pit storage either by direct contact or through the heat exchanger tubes installed at different layers (Fig. 9.13). From an economic perspective, aquifer and pit storages are the favorable storage technologies due to their low cost.

### 9.2.3.5 Solar Pond

In lakes and ponds, the sun rays heat the water, which decreases the density of the water. The less-dense water moves to the surface and loses its energy to the atmosphere. The repetition of this process keeps the temperature of the lake and ponds nearly equal to the atmospheric temperature. In the solar pond, the natural convection of the heated water is restricted by creating the salt gradient. The bottom region of the solar pond is made densest by dissolving salt in it. Due to the high density of the bottom region, the water cannot lift to the upper region even after it gets heated. According to the presence of salt, the solar pond can be divided into three different zones, such as upper convective zone (surface zone), intermediate non-convective zone (gradient zone), and lower convective zone (storage zone) (Fig. 9.14). The highly dense lower convective zone (LCZ) stores energy, while the intermediate non-convective zone (NCZ) insulates it due to the salt gradient developed in it.



**Fig. 9.14** Various zones of the salt gradient in the solar pond [21]

The upper convective zone (UCZ) has low salinity water or freshwater generally at atmospheric temperature.

The sun rays reach the black painted absorber surface at the bottom and sides of the pond due to the significant transparency of water to the visible radiation and heat the absorber surface. Further, the heat is transferred to the salty water in the storage zone. The gradient zone traps this energy in the storage zone itself. The stored thermal energy can be utilized for many low-temperature applications. The conduction losses from the storage zone can be minimized by using proper insulation on the bottom and side surfaces of the pond. Owing to the substantially low thermal conductivity of water, if the appropriate thickness of the intermediate non-convective zone is maintained then the heat losses from the top region, i.e., UCZ, can be reduced. In this way, the solar pond acts as the solar collector as well as a sensible thermal storage system. At the location where large land area, significant solar radiation, and water are available, this technology can be utilized to store solar thermal energy. In Bhuj (India), a 6000 m<sup>2</sup> solar pond supplies energy to the dairy industry [22].

Owing to the low cost, the solar pond has been utilized for many solar energy applications for the past many years, such as solar desalination [23] and electricity generation using thermal energy generator [24]. Researchers have fabricated the mini solar pond having a salt gradient in it and a shallow solar pond without having a salt gradient inside it for small size storage applications. Initially, the energy is absorbed either by the black painted inner surface of the pond or by a black rubber kept at the bottom of the pond. To retain the thermal energy in the system for a longer duration, two glass covers were used. These solar ponds were utilized in integration with solar

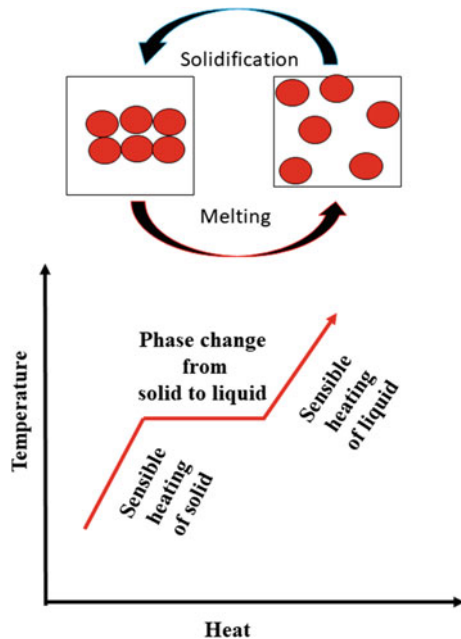
stills, and it was found that these storage systems are capable of improving the daily performance of the solar stills [25, 26].

### 9.3 Latent Thermal Energy Storage

The latent heat storage materials store energy in the form of phase transition enthalpy by undergoing a phase change process at nearly a constant temperature. These materials are commonly known as phase change materials (PCMs). Although the solid–liquid, liquid–gas, solid–gas, and solid–solid phase transformations can store energy, owing to a better enthalpy of phase transition and acceptable volume change, solid–liquid phase transitions are preferred for storing energy in LTES. During the melting cycle (charging cycle) of PCM, it absorbs heat, which increases the vibrational energy of its atoms or molecules. The atomic bonds loosen due to the absorbed energy, and material changes its phase from solid to liquid (Fig. 9.15).

A reverse process occurs during the solidification cycle (discharging cycle) of the PCM, and it releases the stored energy. The heat absorbed/released during the charging/discharging cycle is termed as latent heat. It is important to note here that the latent heat represents the energy of phase transition only. It does not contain the heat stored/released during the process in which the temperature of medium changes significantly, which is often termed as sensible heat. It can be understood from the example of the melting of ice. If heat is supplied to the ice, it absorbs heat at a

**Fig. 9.15**  
Melting/solidification  
process and melting curve  
[27]



nearly constant temperature in the form of latent heat until it completely melts. If further heat is supplied to the liquid water, then it starts absorbing heat in the form of sensible energy, and its temperature starts rising. However, the LTES stores energy in the form of sensible and latent heat both, but the energy stored during phase change remains much higher than its counterpart. The latent heat stored during solid–liquid and liquid–gas transformation is known as latent heat of fusion and latent heat of vaporization, respectively. The heat stored/released during the solid–liquid phase transition of the PCMs can be expressed as:

$$Q = \int_{T_i}^{T_m} mc_{ps}dT + m\beta L + \int_{T_m}^{T_f} mc_{pl}dT \quad (9.3)$$

$$\Rightarrow Q = m[c_{ps}(T_m - T_i) + \beta L + c_{pl}(T_f - T_m)] \quad (9.4)$$

where  $c_{ps}$ ,  $c_{pl}$  are the specific heats of PCM in the solid state and liquid state, respectively.  $\beta$  and  $L$  are the fraction of PCM melted and latent heat of fusion, respectively.  $T_i$ ,  $T_m$ , and  $T_f$  represent the initial temperature, melting temperature, and final temperature of the PCM, respectively. The efficient design and development of the PCM-based storage depend on the appropriate selection of the PCM. The desirable properties of the PCMs are as follows:

- **Thermophysical Properties:** The selection of the melting point of the PCM should be made according to the applications. The PCM should be capable of storing large energy per unit volume; i.e., it should have high latent heat. The high specific heat of the PCM permits additional heat storage as its sensible energy. The heat transfer rate in LTES depends on the thermal conductivity of the PCM; higher the thermal conductivity, better will be the heat transfer rate. For the structural point of view, the volume changes of PCM during phase transition and the vapor pressure should be low.
- **Chemical Properties:** The better chemical and thermal stability of the PCM makes the LTES durable for the multiple operational cycles. The PCM should be non-toxic, nonflammable, and eco-friendly.
- **Kinetic Properties:** The PCMs having a good nucleation rate are preferred in LTES. The congruent melting of PCM improves the performance of the storage. The solidification/melting cycles of the PCM should be reversible, and there should be no or less supercooling.
- **Economic Properties:** For the development of economically viable LTES, the cost of the PCM should be low, and it should be readily available. The recyclable PCMs are preferred over non-recyclable PCMs.

PCMs can be categorized broadly in three distinct categories, such as inorganic PCMs, organic PCMs, and eutectic PCMs (Fig. 9.16). Every type of PCMs has certain advantages and disadvantages associated with them. The selection of the appropriate PCM based on requirements of the particular application is necessary for the fruitful utilization of these materials in storage technology. PCMs are available in a diverse

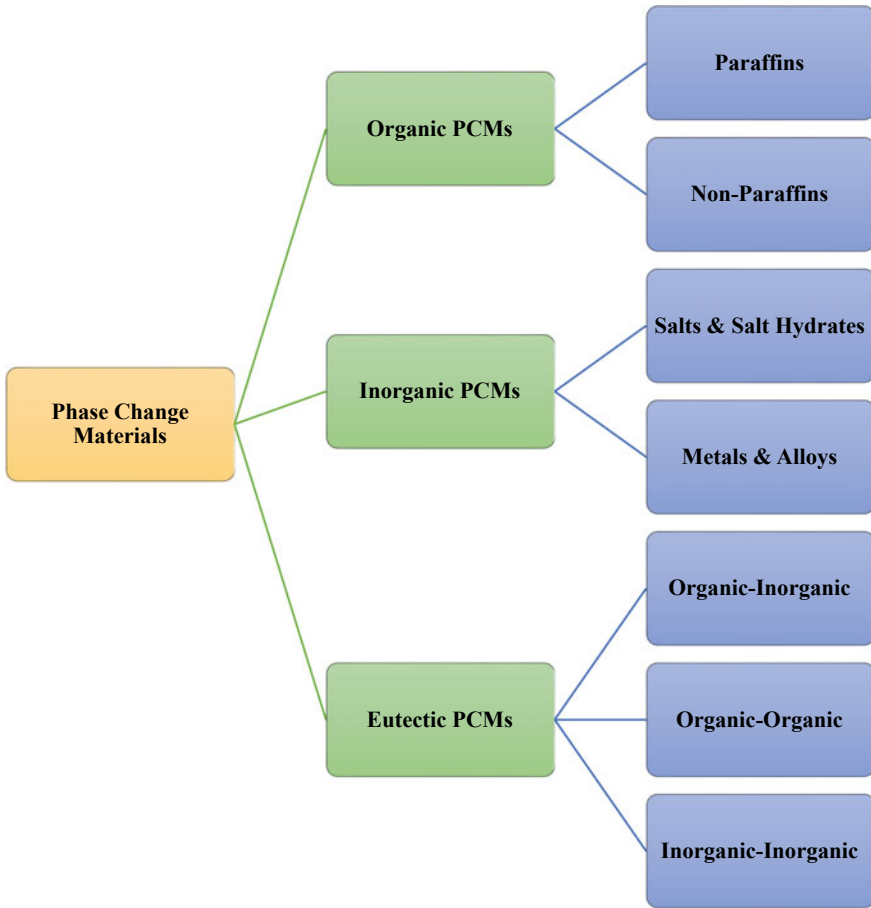


**Fig. 9.16** Classification of phase change materials. *Source* Author

range of thermal properties, which can be efficiently utilized for storage applications in various solar energy systems.

### 9.3.1 Organic PCMs

Organic PCMs are readily available in a wide range of temperatures. The melting without phase segregation and low or no supercooling makes them a prominent material for storing latent energy. Organic PCMs are usually non-corrosive due to which it is compatible with many container materials. These PCMs can further be classified into the groups of paraffins and non-paraffins.

### 9.3.1.1 Paraffins

The paraffin having straight-chain alkanes is used as the latent heat storage materials where the length of the chain directly indicates the melting temperature of the paraffins (Table 9.6). Longer the chain, higher will be the melting point. Their chemical formula is  $\text{CH}_3-(\text{CH}_2)_{(n-2)}-\text{CH}_3$ ; here, “n” represents the no. of “C” atoms.

**Table 9.6** Thermophysical properties of paraffins used in the LTES and their properties [28–31]

Materials	Melting temperature (°C)	Latent heat (kJ/kg)	Density (kg/m <sup>3</sup> )	Thermal conductivity (W/m K)	Storage capacity (MJ/m <sup>3</sup> )
Decane (carbon atoms-10)	−29.65	202	726 (liquid)	–	147
Pentadecane (carbon atoms-15)	10	205–210	765–768 (liquid)	–	157–161
Eicosane (carbon atoms-20)	36.7	247	785 (solid), 778 (liquid)	0.15	192
Triacontane (carbon atoms-30)	65.4	252	806	–	203
Tetracontane (carbon atoms-40)	81.5	272	817	–	222
Pentacontane (carbon atoms-50)	92	276	825	–	228
Hexacontane (carbon atoms-60)	99	279	831	–	232
Heptacontane (carbon atoms-70)	105.5	281	836	–	235
Hectane (carbon atoms-100)	115.25	285	846	–	241
Rubitherm RT-5	5	180	880 (solid), 770 (liquid)	–	158.4
Paraffin wax	32–32.1	251	830	0.514 (solid), 0.224 (liquid)	208
Medicinal paraffin	40–44	146	830	0.5 (solid)	121
Commercial paraffin wax	52.1	243.5	809.5 (solid), 771 (liquid)	0.15 (solid)	197.1
Bees wax	61.8	177	950	–	168

Pure paraffins are costly because it requires high refinement. So, the low-cost technical grade paraffins are preferred for LTES, which are actually the by-product of oil refining. Generally, paraffins are incompatible with the plastic containers and can be stored in metal-based containers. The sufficient availability of paraffins for a wide range of melting temperatures, moderate latent heat, congruent melting, low cost, low vapor pressure, low volume change, and negligible supercooling increases its adaptability in various energy applications. The thermal conductivity of paraffins is low, and they are moderately flammable. These drawbacks can be overcome by proper designing of the storage systems.

### 9.3.1.2 Non-paraffins

Esters, fatty acids, alcohols, and glycols come under this category, which have good heat storage capability in terms of significant latent heat. Fatty acids ( $R-COOH$ ) obtained from natural oils can be an appropriate substitute material for pure paraffins. The fatty acids have low thermal conductivity, and their high-volume change during phase transition and instability at the high temperature, which limits its applications. Fatty acid esters having chemical formula  $R-COO-R'$ , where  $R$  and  $R'$  are alkyl groups, can also be utilized as the PCMs. Esters have low supercooling and are chemically stable, but these PCMs also have the drawbacks of low thermal conductivity and unpleasant odor like fatty acids. For medium temperature storage applications such as waste heat recovery and solar heating, alcohols are preferred. They possess the highest melting temperature and latent energy of fusion among other non-paraffin PCMs. Polyethylene glycols (PEGs) are one of the most used glycols in LTES. PEGs have the highest supercooling among all other paraffin and non-paraffin PCMs. The non-paraffins have diverse properties where every type of material possesses unique advantages and disadvantages. The low thermal conductivity, instability at high temperatures, is the major shortcoming of non-paraffins. Table 9.7 shows various non-paraffin PCMs used in solar energy applications.

### 9.3.2 Inorganic PCMs

The inorganic PCMs have high energy densities and high melting temperatures as compared to most of the organic PCMs. In high-temperature solar applications, inorganic PCMs are preferred over organic PCMs because their enthalpies do not degrade with the operating cycles. These materials can be classified in the salts, salt hydrates, and metallic.



**Table 9.7** Thermophysical properties of non-paraffins used in LTES [28–31]

Materials	Formula	Melting temperature (°C)	Latent heat (kJ/kg)	Density (kg/m <sup>3</sup> )	Thermal conductivity (W/m K)	Storage capacity (MJ/m <sup>3</sup> )
<i>Fatty acids</i>						
Caprylic acid	CH <sub>3</sub> (CH <sub>2</sub> ) <sub>6</sub> .COOH	16	148.6	981 (solid), 901 (liquid)	0.149 (liquid)	145.8
Lauric acid	CH <sub>3</sub> (CH <sub>2</sub> ) <sub>10</sub> .COOH	42	171	870 (liquid)	0.149	148.8
Myristic acid	CH <sub>3</sub> (CH <sub>2</sub> ) <sub>12</sub> .COOH	54	190	860 (liquid)	–	163.4
Palmitic acid	CH <sub>3</sub> (CH <sub>2</sub> ) <sub>14</sub> .COOH	64	185.4	989 (solid), 850 (liquid)	0.162 (liquid)	183.4
Stearic acid	CH <sub>3</sub> (CH <sub>2</sub> ) <sub>16</sub> .COOH	69	209	940 (liquid)	0.097	196.5
<i>Esters</i>						
Isopropyl palmitate	C <sub>19</sub> H <sub>38</sub> O <sub>2</sub>	11	100	–	–	–
Butyl stearate	C <sub>22</sub> H <sub>44</sub> O <sub>2</sub>	18	123	–	0.21 (solid)	–
Methyl palmitate	C <sub>17</sub> H <sub>34</sub> O <sub>2</sub>	27	163.2	–	–	–
Vinyl stearate	C <sub>20</sub> H <sub>38</sub> O <sub>2</sub>	27	122	–	–	–
<i>Alcohols</i>						
Xylitol	C <sub>5</sub> H <sub>12</sub> O <sub>5</sub>	92.7–94.5	232–263.3	1520	–	353–400
D-sorbitol	C <sub>6</sub> H <sub>14</sub> O <sub>6</sub>	97	110	1490	–	163.9
Erythritol	C <sub>4</sub> H <sub>10</sub> O <sub>4</sub>	117–118	315–344	1480 (solid), 1300 (liquid)	0.733 (solid), 0.326 (liquid)	466–509
D-mannitol	C <sub>6</sub> H <sub>14</sub> O <sub>6</sub>	165–168	294–341	1489–1520	0.19 (solid), 0.11 (liquid)	438–518

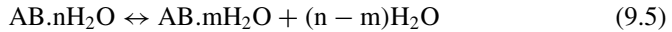
(continued)

**Table 9.7** (continued)

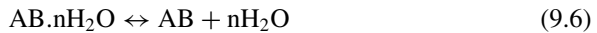
Materials	Formula	Melting temperature (°C)	Latent heat (kJ/kg)	Density (kg/m <sup>3</sup> )	Thermal conductivity (W/m K)	Storage capacity (MJ/m <sup>3</sup> )
<i>Glycols</i>						
Diethylene glycol	(HOCH <sub>2</sub> CH <sub>2</sub> ) <sub>2</sub> O	-10	247	1200 (liquid)	-	296
Triethylene glycol	C <sub>6</sub> H <sub>14</sub> O <sub>4</sub>	-7	247	1200 (liquid)	-	296

### 9.3.2.1 Salts and Salt Hydrates

Salts are utilized for high-temperature storage applications. They have high energy density but low thermal conductivity. Salts can be utilized in LTES, either in pure form or in the form of hydrates (Table 9.8). Salt eutectic mixtures are also used in many storage systems. The alloys of inorganic salts and water having chemical formula  $AB \cdot nH_2O$  are referred to as the salt hydrates. The dehydration of salt hydrates results either in its anhydrous form or in the dehydration of salts in the form having fewer moles of  $H_2O$ .



or



When salt hydrate melts, the solid crystal releases the water. The anhydrous salts cannot be dissolved in the stoichiometric volume of water present in the hydrated salt. The less hydrated salt settles down in the storage and creates phase segregation. This irreversible melting of the salt hydrates is called the incongruent melting. The poor nucleation properties and its consequence due to the incongruent melting are the major shortcomings of salt hydrates. Although the salt hydrates have some other demerits, such as significant supercooling and irreversible phase transition, its high storage capacity and thermal conductivity make it one of the feasible choices for latent heat storage applications.

### 9.3.2.2 Metals and Alloys

Metallic PCMs offer excellent thermal conductivities and volumetric energy density (Table 9.9). However, the cost of these PCMs remains high as compared to the other, but for low volume storages, these PCMs are the most preferred PCMs. These PCMs have not been considered as the general-purpose LTES mediums due to its low latent heat per unit weight, which creates the problem of excess weight. These PCMs can be stored in metal and ceramic containers. During multiple thermal cycles, their microstructures can be changed due to segregation, oxidation, and precipitation. To avoid this, inert gas atmosphere is needed, which further can lead to the absorption of inert gas in the metal during phase transition cycles. It can change the thermophysical properties of the metal. The operational complexities have reduced its adaptability in energy storage applications.

**Table 9.8** Thermophysical properties of PCMs based on salt and salt hydrate [28, 29, 31]

Materials	Formula	Melting temperature (°C)	Latent heat (kJ/kg)	Density (kg/m <sup>3</sup> )	Thermal conductivity (W/m K)	Storage capacity (MJ/m <sup>3</sup> )
<i>Salt hydrates</i>						
Calcium chloride hexahydrate	CaCl <sub>2</sub> .6H <sub>2</sub> O	29	190.8	1802 (solid), 1562 (liquid)	1.088 (solid), 0.540 (liquid)	343.8
Sodium phosphate dibasic dodecahydrate	Na <sub>2</sub> HPO <sub>4</sub> .12H <sub>2</sub> O	36	280	1520 (solid)	0.514 (solid), 0.476 (liquid)	425.6
Barium hydroxide octahydrate	Ba(OH) <sub>2</sub> .8H <sub>2</sub> O	78	265.7	2070 (solid), 1937 (liquid)	1.225 (solid), 0.653 (liquid)	550
Magnesium chloride hexahydrate	MgCl <sub>2</sub> .6H <sub>2</sub> O	117	168.6	1569 (solid), 1440 (liquid)	0.694 (solid), 0.570 (liquid)	264.5
<i>Nitrate salts</i>						
Sodium nitrate	NaNO <sub>3</sub>	306	172	2261 (solid)	0.5	388.9
Potassium nitrate	KNO <sub>3</sub>	335	266	2109 (solid)	0.5	561
<i>Carbonate salts</i>						
Sodium carbonate	Na <sub>2</sub> CO <sub>3</sub>	854	276	2533 (solid), 1972 (liquid)	–	699.1
Potassium carbonate	K <sub>2</sub> CO <sub>3</sub>	897	236	2290 (solid)	–	540.4
<i>Chloride salts</i>						
Zinc chloride	ZnCl <sub>2</sub>	280	75	2907 (solid)	0.5	218
Sodium chloride	NaCl	802	420	2160 (solid)	–	907.2
<i>Sulfate salts</i>						
Sodium sulfate	Na <sub>2</sub> SO <sub>4</sub>	884	165	2680 (solid)	–	442.2
Lithium sulfate	LiSO <sub>4</sub>	858	84	2220 (solid), 2003 (liquid)	–	186.5

(continued)

**Table 9.8** (continued)

Materials	Formula	Melting temperature (°C)	Latent heat (kJ/kg)	Density (kg/m <sup>3</sup> )	Thermal conductivity (W/m K)	Storage capacity (MJ/m <sup>3</sup> )
<i>Fluoride salts</i>						
Lithium fluoride	LiF	850	1044	2640 (solid). 1810 (liquid)	–	2756.2
Sodium fluoride	NaF	996	794	2558 (solid). 1948 (liquid)	–	2031.1
<i>Hydroxide salts</i>						
Sodium hydroxide	NaOH	318	165	2100 (solid)	–	346.5
Potassium hydroxide	KOH	380	150	2040 (solid)	–	306

**Table 9.9** Thermophysical properties of metals and their alloys used as the PCMs [28, 29]

Materials	Melting temperature (°C)	Latent heat (kJ/kg)	Density (kg/m <sup>3</sup> )	Thermal conductivity (W/m K)	Storage capacity (MJ/m <sup>3</sup> )
<i>Metals</i>					
Zinc (Zn)	419	113	7140 (solid)	116	806.8
Aluminum (Al)	660	397	2707 (solid), 2375 (liquid)	204	1074.7
Copper (Cu)	1084	208	8960 (solid), 8020 (liquid)	401	1863.7
<i>Alloys</i>					
Zn/Mg (53.7%/46.3%)	340	185	4600 (solid)	–	851
Al/Mg/Zn (59%/33%/6%)	443	310	2380 (solid)	–	737.8
Si/Al (86%/12%)	576	560	2700 (solid)	–	1512
Zn/Cu/Mg (49%/45%/6%)	703	176	8670 (solid)	–	1525.9

**Table 9.10** Thermophysical properties of eutectic PCMs [5, 29, 32, 33]

Materials	Melting temperature (°C)	Latent heat (kJ/kg)	Density (kg/m <sup>3</sup> )	Thermal conductivity (W/m K)	Storage capacity (MJ/m <sup>3</sup> )
<i>Organic–organic</i>					
Stearic acid–palmitic acid (36%/64%)	53	182	971	2.34 (solid)	165.6
Urea–acetamide (38/62)	53	224	1216	0.510 (solid)	262.8
<i>Inorganic–inorganic</i>					
KNO <sub>3</sub> -KOH (80/20)	214	83	1905	0.88 (solid)	154.8
NaNO <sub>2</sub> -NaNO <sub>3</sub> (55/45)	233	163	2210	0.64 (solid)	349.2
<i>Organic–inorganic</i>					
Urea-NaNO <sub>3</sub> (71-29)	83	187	1502	0.75 (solid)	273.6
Urea-KNO <sub>3</sub> (77/23)	109	195	1416	0.810 (solid)	266.4

### 9.3.3 Eutectics

Eutectics are the PCMs having two or more amalgamated materials having congruent melting points (Table 9.10). They melt and solidify irreversibly without phase segregation. Although they have low heat capacities and latent heat, the desirable properties of the eutectic PCMs can be obtained by varying the weight proportion of amalgamated materials in the mixtures. This quality makes them one of the prominent latent heat storage mediums for the future.

### 9.3.4 Latent Thermal Energy Storage Systems

The latent heat storage materials are utilized for a wide range of solar energy applications. These materials are utilized in the photovoltaic (PV) and photovoltaic/thermal (PV/T) systems to improve their performance by reducing the operating temperature [34, 35]. These materials have also been tested to improve the nocturnal performance of solar stills [36]. Apart from this, the use of the PCMs to store energy in solar cookers has been studied by various researchers [37]. Many other applications can also be found in the previous literature, such as in space heating and solar drying. LTES technology has a high potential of being utilized for diverse energy applications. Generally, for indirect use, latent heat storage systems are designed in either the shell and tube configuration or macro-encapsulated packed bed configuration. These configurations improve the heat transfer between the HTF and the PCM.

### 9.3.4.1 Macro-encapsulated Packed Bed Storage

Macro-encapsulated packed bed storage is the widely adopted LTES configuration, which not only improves the performance of the inbuilt PCM; it also maintains an efficient charging/discharging operation. In this configuration, a significant volume of the PCM is enclosed by a shell, and multiple discrete units of such type are put together into a storage tank (Fig. 9.17). The HTF can pass over these units through voids for exchanging heat during the charging/discharging cycles. One of the potential advantages of macro-encapsulation of the PCMs is it provides a self-sustaining structure to the PCM and eliminates the chance of reaction with its surrounding. It also improves the thermal conductivity of the PCM, which is one of the major limitations of most of the PCMs. For the durability of this system, the shell materials should have better thermal and chemical stability, and it should not be reactive to the encapsulated PCM. The typical containers which are used for the macro-encapsulation of PCMs are bottles made of polyethylene and polypropylene, mild steel cans and tin-plated metal cans, etc. The shape of macro-encapsulation can be sphere, rectangular, cylindrical, etc. The tank used in this application is similar to the tanks which are used in other storage systems. The flow passage of the HTF plays a vital role in the overall performance of the packed bed storage. It should be designed in such a way that HTF should maintain a large heat transfer area in contact with

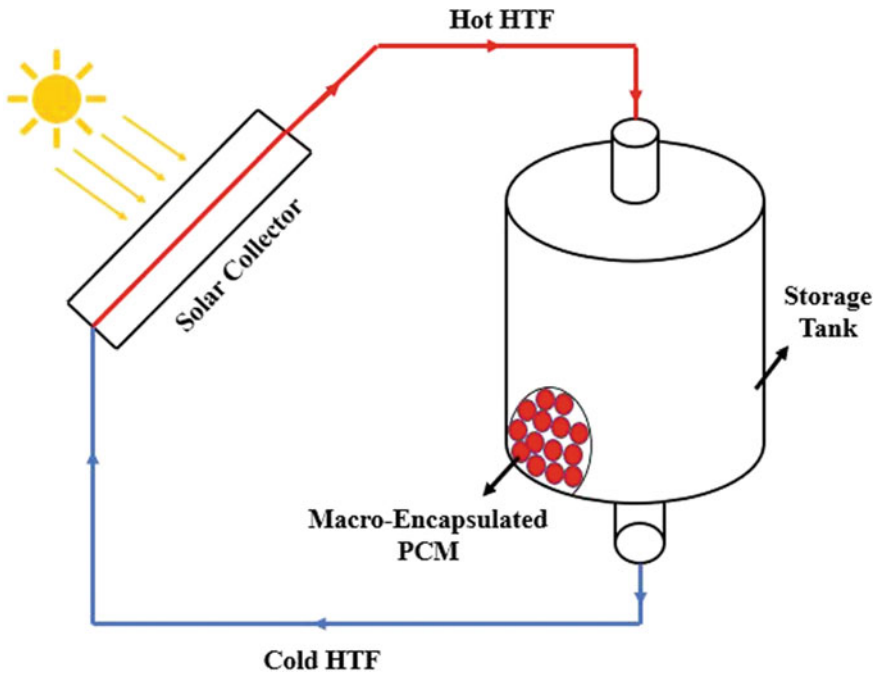


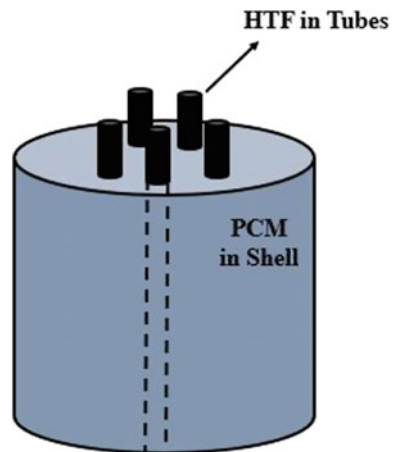
**Fig. 9.17** Charging of macro-encapsulated packed bed storage. *Source* Author

the capsules, and there should be less pressure drop in the flow passage. During the charging operation of the storage, the hot HTF from any energy source passes over the capsules, which transfer heat to the encapsulated PCM through the shell. The energy stored in the melted PCM can be retrieved by passing cold HTF over it during discharging operation. The major performance parameters of the packed bed storage are the void fraction, inlet temperature, flow velocity of the HTF, and overall bed size [38]. The high finite temperature difference between the HTF and PCM leads toward better heat transfer. Researchers have utilized this storage configuration for solar air heating purposes, where the air itself is used as the HTF [39]. This technology has been explored for solar cooking applications as well, where energy collected from the solar collectors has been transferred to the packed bed storage, and the stored energy further be utilized for cooking applications [40].

**9.3.4.2 Shell and Tube Latent Heat Storage**

Another potential configuration for LTES is shell and tube configuration. In this configuration, generally, the PCM is stored at the shell side, and HTF passes through the tube side (Fig. 9.18). There are various parameters such as the diameter and length of the shell as well as the tube, inlet mass/volume flow rate and temperature of the HTF, and the number of tubes, which influence the performance of the shell and tube-based TES. The temperature difference between the shell side PCM and tube side HTF is the major driving force for the melting/solidification process in the storage. Higher the inlet HTF temperature, better will be the heat transfer. The high mass flow rate of HTF can improve the performance of the storage. Hence, the optimization of the mass flow rate is necessary for the efficient operation of the storage. Researchers have tested shell and tube storage for CSP applications and highlight the role of various geometrical parameters [41]. The large length and the

**Fig. 9.18** Schematic of shell and tube-based LTES.  
 Source Author





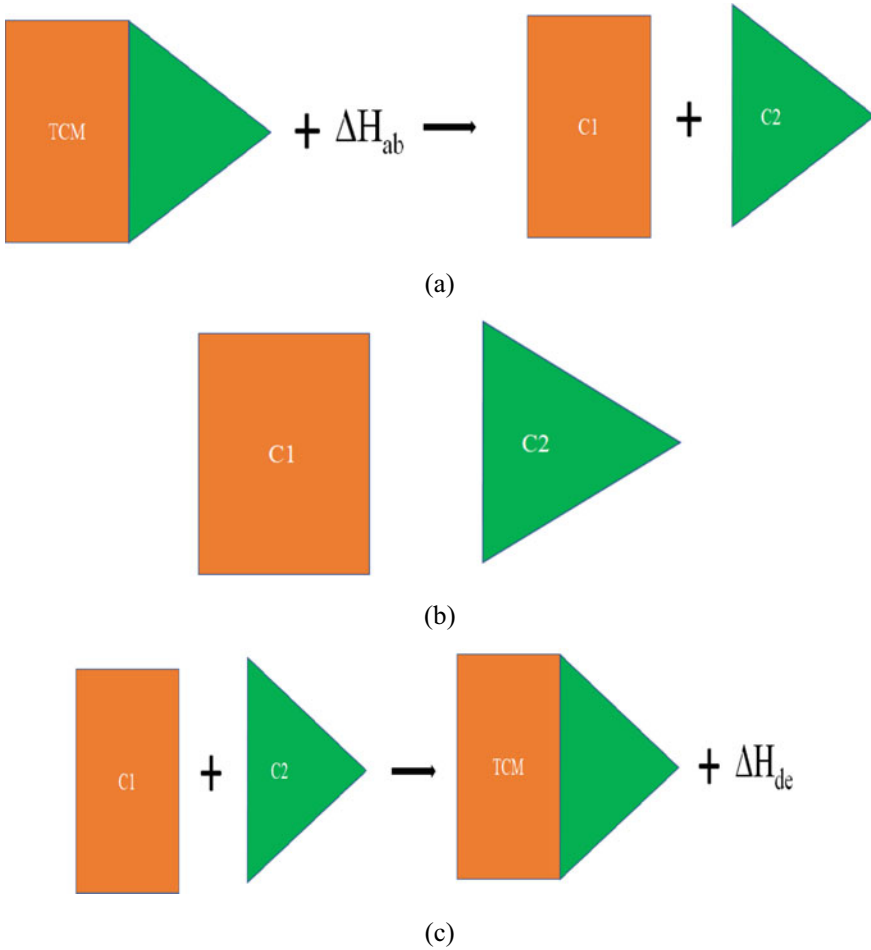
small diameter of the tubes can improve the effectiveness of the storage, but the small diameter can lead to a large pressure drop in the flow passage.

## 9.4 Thermochemical Energy Storage

In this technique, the thermal energy is stored in the form of a chemical reaction. A chemical reaction which is reversible in nature is preferred to store thermal energy. To understand the phenomenon, let us consider the example of a chemical reaction in analogy with phase change material.



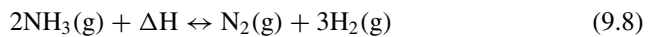
Here in the above reaction, TCM is thermochemical material similar to PCM in the latent heat storage technique. The thermal energy equivalent of enthalpy of absorption of the reaction is stored in the chemical reaction. This supplied energy to the TCM initiates dissociation reaction and dissociates the TCM into two or more compounds, i.e., compounds C1 and C2 in the reaction. When it is required to utilize the stored energy, the reaction is reversed, i.e., compounds C1 and C2 combine, and energy equivalent to the enthalpy of desorption of reaction is released during the reverse chemical reaction. From the above example, it can be clearly understood that the storage of energy is performed by an endothermic chemical reaction where heat equivalent to the enthalpy of absorption is stored, and the discharge of energy is performed by exothermic chemical reaction. The mechanism of thermochemical energy storage can be divided into three different steps, such as charging, storage, and discharging of energy. The charging of energy is an endothermic chemical reaction where the thermal energy from sources like solar collectors can be supplied to TCM. The TCM gets dissociated into two or more compounds like C1 and C2 in Fig. 9.19a. The dissociated compounds C1 can be ammoniate, hydroxide, carbonate, and hydrate, while C2 can be ammonia, water, carbon dioxide, and hydrogen. The storage of energy includes the storage of dissociated compounds separately, as shown in Fig. 9.19b. The dissociated compounds are stored at nearly ambient temperature due to which there is either no heat loss or very minimal heat loss as compared to other storage techniques. Discharging of energy is an exothermic chemical reaction where the thermal energy is supplied to the end-use applications when required. During the discharge, the dissociated compounds react together at definite temperature pressure conditions to release the heat, as shown in Fig. 9.19c. To discuss the thermochemical energy storage in detail, it is necessary to understand terminology turning temperature ( $T^*$ ). Turning temperature is the temperature at which reaction rate constant ( $k$ ) is unity. Turning temperature is calculated as the ratio of reaction enthalpy to reaction entropy ( $T^* = \Delta H/\Delta S$ ) [42]. It indicates the required temperature to carry an endothermic or exothermic reaction. The thermochemical energy storage can be classified either based on the physical state or based on the chemical composition of the reacting compounds in the chemical reaction (Fig. 9.20).



**Fig. 9.19** Principle of thermochemical energy storage (a) charging, (b) storage, and (c) discharging of heat. *Source* Author

### 9.4.1 Ammonia System

The TCM materials such as ammonia and ammonium bisulfate get dissociated when heat at high temperature is supplied to it. The feasibility of an ammonia-based thermal energy storage system was studied in 1995 [43]. The reaction of ammonia is an example of a gas–gas phase reaction, while the ammonia bisulfate reaction is an example of a liquid–gas reaction. The two reactions are mentioned and discussed below one by one.



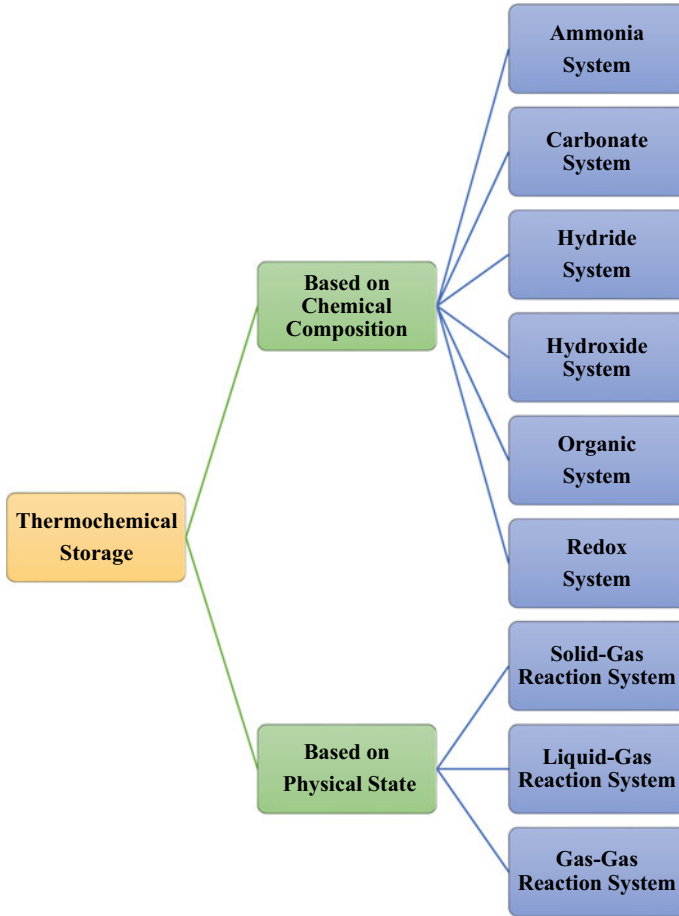
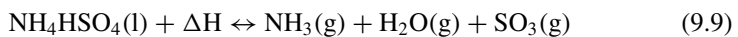


**Fig. 9.20** Classification of thermochemical energy storage. *Source* Author

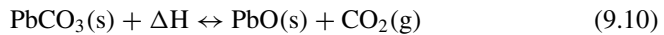
Ammonia has an enthalpy of absorption 66.9 kJ/mol and enthalpy of desorption 53 kJ/mol. Ammonia as gas is dissociated into nitrogen and hydrogen both as a gas; hence, it comes under the category of gas–gas reaction. The reaction takes place at temperature 996 °C at 10–300 bar pressure range with an energy density of 2682 MJ/m<sup>3</sup> [44, 45]. The TCM cost is low with simple reaction, high enthalpy of reaction, and high energy density. There are few disadvantages associated with ammonia, such as low reversibility, high operating pressure, the need for catalyst (Fe/Co), and hydrogen and nitrogen handling difficulty. Let us take another example of an ammonia system-based thermochemical energy storage



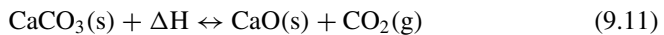
Liquid ammonium bisulfate absorbs high-temperature heat and dissociates into gaseous compounds, ammonia, sulfur trioxide, and water vapors. This is an example of a liquid–gas reaction. The absorption and desorption reaction temperatures are 1473 and 996 °C, respectively, at 1–2 bar operating pressure range. The reaction enthalpy of ammonium bisulfate is 336 kJ/mol, and the energy storage density is 3096 MJ/m<sup>3</sup> [44, 46]. Similar to the ammonia reaction, this system also has high energy storage density and high enthalpy of reaction. This reaction does not require any catalyst, but the product formed in the chemical reaction is corrosive and toxic in nature.

### 9.4.2 Carbonate System

The carbonates of metal, such as lead (Pb) and calcium (Ca), can store thermal energy at high temperatures. Metal carbonates are solid in nature and dissociate into oxides of metal, which is also solid, and carbon dioxide as a gas. This system comes under the category of solid–gas reaction. The two TCMs which come under the carbonate category are discussed below.



Lead carbonate has a relatively lesser reaction enthalpy 88 kJ/mol and energy storage density 1090.8 MJ/m<sup>3</sup> [47]. The absorption and desorption temperature of this reaction is 996 and 846 °C at pressure up to 10 bar. No catalyst is required for the reaction, and the by-product handling is relatively easier. The reversibility of the reaction and toxic nature of PbO are the challenges associated with lead carbonate. Another example of the carbonate system is calcium carbonate, which follows the reaction, as shown below.



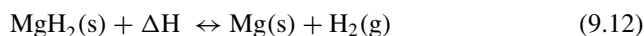
The dissociation of all the metal carbonates is similar and produces metal oxide and carbon dioxide. Calcium carbonate is also in the category of solid–gas reaction. The absorption and desorption temperature of this TCM is 1406 and 1429 °C. Calcium carbonate has a relatively better reaction enthalpy 178 kJ/mol and energy storage density 2491.2 MJ/m<sup>3</sup> [47, 48]. Calcium carbonate has a lesser cost and good availability, and no catalyst is required for the reaction. Few challenges associated with the calcium carbonate system are its irreversibility, agglomeration at the higher temperature, and volume change during the reaction. Major metal carbonate systems have issues of irreversibility due to which their application at a commercial scale is not possible. Some other metal carbonates are listed in Table 9.11 with their thermochemical properties.

**Table 9.11** Thermochemical properties of carbonate materials for thermochemical energy storage [49]

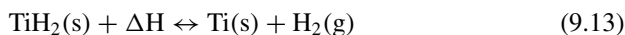
TCM	Turning temperature (°C)	Reaction enthalpy (kJ/mol)	Gravimetric energy storage density (kJ/kg)
ZnCO <sub>3</sub>	120	68.32	544.9
CdCO <sub>3</sub>	290	96.57	560.1
MgCO <sub>3</sub>	300	98.98	1174
SrCO <sub>3</sub>	1220	202.34	1370.65
BaCO <sub>3</sub>	1555	165.09	836.6

### 9.4.3 Hydride System

Several metals react with hydrogen to form metal hydrides and release thermal energy (exothermic reaction). Metal hydrides came in existence for hydrogen storage application initially, but later in the 1970s, the use of metal hydride for thermal energy storage was started. Very few materials were known at that time for the temperature application up to 200 °C. Later with development in research on ionic and complex metal hydrides, the energy storage was possible for temperature up to 1000 °C. Lithium (Li)-based metal hydride was the first metal hydride which was studied and found suitable for high-temperature applications [50]. The high cost of Li makes the thermal energy storage system expensive. Later, magnesium (Mg)-based hydrides attracted the researchers due to its low material cost. The most common metal hydride which can be used for thermal energy storage application is magnesium (Mg)-based metal hydride.



Magnesium-based metal hydride comes under the category of solid–gas reaction. Magnesium hydrides have a large range of operating temperatures and pressure from 750 to 1000 °C with a pressure up to 100 bar. The reaction enthalpy and energy storage density of magnesium metal hydride are 75 kJ/mol and 2088 MJ/m<sup>3</sup>, respectively [51]. Magnesium metal hydride has comparatively good reversibility with low cost and easily available materials. The disadvantages associated with magnesium hydride are slow reaction kinetic, high operating pressure, sintering, and need of a catalyst. Titanium, well known for anticorrosive property and high-temperature resistance, is also explored for thermal energy storage at high temperatures.

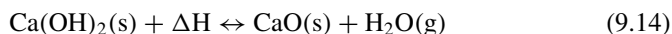


The operating temperature range of titanium hydride is 900–1000 °C, with a pressure range of 1–3 bar. The reaction enthalpy and experimental energy storage density of magnesium metal hydride are 150 kJ/mol and 2926.8 MJ/m<sup>3</sup>, respectively [52]. Titanium metal hydride reaction also comes in the category of solid–gas reaction

similar to magnesium hydride. Titanium metal hydride possesses good reversibility and high reaction enthalpy, and no need for a catalyst makes it a suitable candidate for thermal energy storage. However, the high specific weight of titanium reduces the gravimetric storage capacity significantly. Metal hydrides are in the advanced research phase for thermal energy storage applications. Several models and prototypes of metal hydride-based thermochemical energy storage have been developed with good storage capacity, good cyclic stability, and ease in operation.

#### 9.4.4 Hydroxide System

The dehydration of metal hydroxide requires energy, and this is used to store the thermal energy in hydroxide systems. The major metal hydroxides have relatively lower operating temperatures except for calcium and barium hydroxide. Magnesium hydroxide has the highest enthalpy of reaction, but calcium hydroxide ( $\text{Ca}(\text{OH})_2$ ), being reversible, easily available, and low-cost material, has been studied extensively for high-temperature thermal energy storage. The feasibility of  $\text{Mg}(\text{OH})_2$  was verified by studying its reaction kinetics for the application of a chemical heat pump [53]. The poor heat transfer performance, cyclic stability, and sintering of Mg particles restricted the use of  $\text{Mg}(\text{OH})_2$  for thermal energy storage applications.



The operating temperature range of calcium hydroxide is 950–1000 °C, with pressure up to 2 bar. The enthalpy of reaction and energy storage density for calcium hydroxide are 104 kJ/mol and 1573.2 MJ/m<sup>3</sup>, respectively.  $\text{Ca}(\text{OH})_2$  comes under the category of solid–gas reaction. Calcium hydroxide is a reversible, low-cost material and operates at low pressure. The major challenges with calcium hydroxide are agglomeration and sintering of its particles. Some of the famous metal hydroxides have been listed in Table 9.12 with their thermochemical properties.

#### 9.4.5 Organic System

Methane gas ( $\text{CH}_4$ ) is one of the most popular organic compounds and used for the production of synthesis gas ( $\text{CO} + \text{H}_2$ ), also popular as syngas. The two methods of syngas production are endothermic chemical reaction, and these methods are discussed here for the application of thermal energy storage.



The mentioned reaction is well known as methane steam reforming or steam reforming. The major application of this reaction is hydrogen production. As this is

**Table 9.12** Thermochemical properties of hydroxide materials for thermal energy storage [49]

TCM	Turning temperature (°C)	Reaction enthalpy (kJ/mol)	Gravimetric energy storage density (kJ/kg)
Zn(OH) <sub>2</sub>	55	49.60	498.96
Ni(OH) <sub>2</sub>	70	47.84	516
Be(OH) <sub>2</sub>	70	51.27	1191
Cd(OH) <sub>2</sub>	125	59.95	409.4
Mn(OH) <sub>2</sub>	190	67.07	754
Mg(OH) <sub>2</sub>	265	77.74	1333
Sr(OH) <sub>2</sub>	755	88.58	728.3
Ba(OH) <sub>2</sub>	1005	93.46	545.47

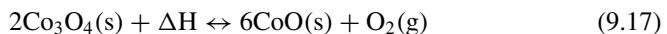
an endothermic reaction, hence it is also used to store thermal energy. The absorption and desorption temperature of this reaction is 1496 and 1076 °C at a wide pressure range from 20 to 150 bar. The reaction enthalpy and energy storage density of this thermochemical reaction are 250 kJ/mol and 28.08 MJ/m<sup>3</sup>, respectively [54]. Another reaction of methane with carbon dioxide, also known as dry reforming, is an endothermic reaction and can be used for thermal energy storage.



The absorption and desorption temperature of this reaction is the same as the reaction of methane with steam, but the operating pressure is comparatively lower at 3.5 bar. The reaction enthalpy and energy storage density of this thermochemical reaction are 247 kJ/mol and 27.72 MJ/m<sup>3</sup>, respectively [54]. Both these reactions come under gas–gas type reaction and have high reaction enthalpy. The challenges associated with these two thermochemical methods are low energy storage density, the need for a catalyst, low reversibility, and high cost of methane.

#### 9.4.6 Redox System

Oxides of metal undergo a reduction reaction, which is an endothermic reaction. Redox systems are also known as metal oxide systems. Oxides of cobalt (Co), barium (Ba), and manganese (Mn) are the most popular in this category. Let us discuss cobalt oxide with the reduction reaction, as mentioned below:

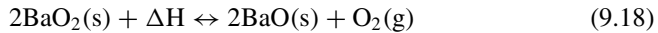


Oxide of cobalt has an operating temperature 1416–1446 °C in a pressure range from 0 to 1 bar. The reaction enthalpy and energy storage density of this thermochemical reaction are 205 kJ/mol and 1062 MJ/m<sup>3</sup>, respectively [55]. This reaction

**Table 9.13** Thermochemical properties of metal oxides for thermal energy storage [49]

TCM	Turning temperature (°C)	Reaction enthalpy (kJ/mol)	Gravimetric energy storage density (kJ/kg)
Cr <sub>5</sub> O <sub>12</sub>	105	126.17	279.1
Li <sub>2</sub> O <sub>2</sub>	145	34.22	745.9
MgO <sub>2</sub>	205	21.43	380.6
PbO <sub>2</sub>	295	55.23	230.9
Sr <sub>2</sub> O <sub>5</sub>	325	68.06	210.4
PtO <sub>2</sub>	420	62.8	276.5
Mn <sub>2</sub> O <sub>3</sub>	915	90.03	190.1
Fe <sub>2</sub> O <sub>3</sub>	1360	232.61	485.6
Mn <sub>3</sub> O <sub>4</sub>	1700	194.63	850.6
V <sub>2</sub> O <sub>5</sub>	1710	176.59	970.9

comes under the category of solid–gas type reaction. This reaction is reversible with high reaction enthalpy and does not require any catalyst. The toxic nature of CaO and oxygen handling difficulty are the disadvantages associated with this thermochemical reaction.



Barium peroxide has operating temperature 1236–1326 °C in a pressure range from 0 to 10 bar. The reaction enthalpy and energy storage density of this thermochemical reaction are 77 kJ/mol and 1180.8 MJ/m<sup>3</sup>, respectively [56, 57]. This reaction comes under the category of solid–gas type reaction. The reaction does not require any catalyst and has low operating pressure. The reversibility of the reaction, sintering, agglomeration, and oxygen handling difficulty are a few challenges associated with barium oxide. Several oxides were studied, and it was reported in the study that oxides of barium, cobalt, manganese, copper, and iron are suitable for high-temperature applications [58]. Cobalt oxide (Co<sub>3</sub>O<sub>4</sub>) has the best reversibility and energy storage density among the other oxides. Some popular metal oxides with their thermochemical properties have been listed in Table 9.13.

#### 9.4.7 Utilization of Thermochemical Energy Storage in Solar Thermal Applications

Thermal energy is required in various process industries for their operations, power generation, and space heating applications [52]. Thermochemical energy storage can be one of the best possible options for thermal energy storage in solar thermal power plants. Let us consider one such example of thermochemical energy storage using



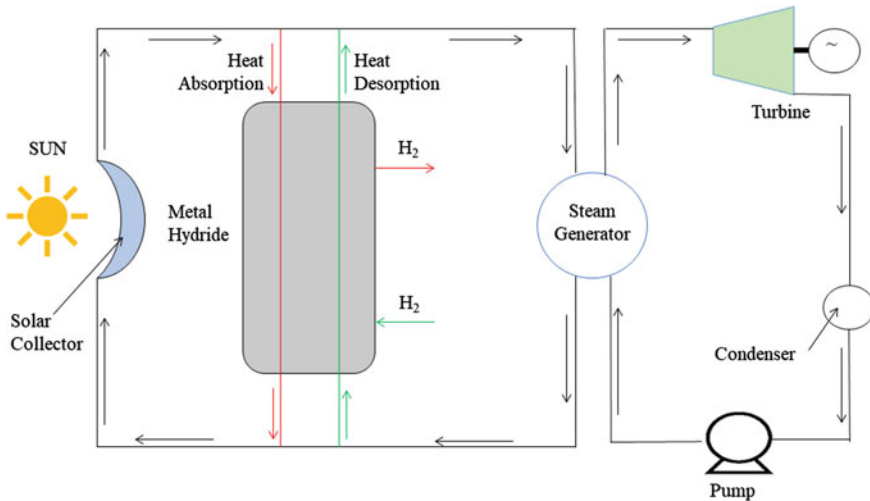


**Fig. 9.21** Schematic of solar thermal power plant with thermochemical energy storage system.  
*Source* Author

metal hydride discussed earlier. Consider a metal hydride-based thermochemical energy storage system integrated with a solar thermal power plant, as shown in Fig. 9.21. The schematic includes the solar field, energy storage, and power cycle. The hydride-based thermochemical energy storage unit consists of a metal hydride system to store thermal energy. Let us discuss the working of a metal hydride-based thermochemical energy storage system in detail. During the daytime, a part of the thermal energy collected in the solar field is supplied to the thermal energy storage unit. The red color line indicates the storage of thermal energy. During the endothermic reaction, metal hydride stores thermal energy equivalent to reaction enthalpy. This endothermic reaction leads to the dissociation of the metal hydride into metal and hydrogen, as shown in Fig. 9.21. The liberated hydrogen from metal hydride can be stored separately, which can further be utilized during the discharging cycle. In this way, the thermal energy supplied from the solar field to the storage system gets stored in the metal hydride. This stored energy, when required by the power plant during non-sunshine hours, can be released by supplying the hydrogen to metal. The green color line indicates the discharging process. The discharged thermal energy is supplied to the heat exchanger to produce superheated steam. Similarly, the stored energy can be used in various process applications in the industries. The selection of TCM is made based on the application parameter, where the heat is to be utilized.

## 9.5 Economic Aspects of TES

The successful deployment of any technology in various applications depends upon the cost involved in technology development. The cost involved in the TES technologies can be categorized as the capital cost and operational and maintenance costs. The capital cost includes cost related to the design and construction of the TES and cost involved in the development of various components such as instrumentations, pipes, fittings, and insulation. The cost involved in the parasitic load, such as pumping, trace heating, refilling, and other operational costs, is associated with the operational cost. System Advisor Model (SAM) developed by National Renewable Energy Laboratory can be utilized for the financial study of renewable energy projects [59]. There are many financial models that are given for commercial and residential renewable energy systems. SAM may provide the information related to the various costs involved in the renewable energy system integrated with TES based on the input parameters such as design parameters of solar collectors, storage, and operation strategy. To understand the cost matrix of the TES system, Nithyanandam and Pitchumani et al. [60] model can be referred. Based on this model, the cost of the entire TES system can be categorized into different sections, as follows [28]:

- **Container Cost:** The configurations such as packed bed and shell and tube have high cost as compared to the single tank and single concrete block. The preferred and cost-effective materials used for the fabrication of the storage container are mild steel and reinforced concrete. The most used insulation material is fiberglass. The cost matrix of the container is linked to the storage density. Lower the density, larger will be the size of the storage as well as higher the container cost.
- **Storage Material Cost:** Storage cost can be calculated by using cost per unit mass of the material. Water, sand, and gravels are cheap storage mediums, while organic PCM, thermochemical reactors, and thermal oils are costly mediums.
- **Overhead Cost:** It includes the miscellaneous cost such as pipes and fitting cost, and instrumentation cost.
- **Design-Specific Cost:** It includes the heat exchanger cost and cost associated with the implementation of various performance enhancement techniques. The cost associated with the implementation of various performance enhancement techniques should be justified by the superior performance of the TES. For the development of the TES, which can work efficiently at very high temperature, the cost of the used materials increases drastically. So, the selection of the material plays a vital role in the development process.

Most of the STES technologies are economical in terms of materials, design, and operation. Its cost varies from 0.11 to 11.12 \$/kWh [1]. The geometrical simplicity and easy availability make STES an economical technology. LTES and TCES are complicated and also relatively expensive. Although these technologies have a high energy density, the storage material and the system design make it expensive. Due to the low thermal conductivity of the PCMs, LTES requires better heat transfer arrangements, which increases its cost further. The complexities associated with the

reactor design, costly storage material, and heat transfer equipment are the major sources of the increased cost of the TCES. The cost of LTES and TCES can be found in the range of 11.12 to 55.6 \$/kWh and 9 to 111 \$/kWh, respectively [1].

## 9.6 Current and Future Outlook of TES Technologies

Nowadays, TES technology is being utilized in many energy-related applications [61–63], but there are few demerits of these technologies which restricts its utilization in diverse applications. The STES technology is a cost-effective technology, but its low energy density is one of the major obstacles in its utilization in a wide range of applications. Similarly, the low thermal conductivity is the major problem associated with PCMs, which needs to be overcome for its large-scale deployment because it hampers the heat transfer process in the LTES. The process complexities have to be minimized for utilizing TCES technology. Researchers are developing many new age TES technologies as well as improving the existing TES technologies to get full-scale benefits of these technologies. The hybrid sensible heat and latent heat storage system have been developed by the researchers, which can overcome the problem of the quick temperature drop of the STES during the discharging process, and it improves the energy density of sensible storage systems [64, 65]. There are various heat transfer intensification techniques that have been highlighted in the previous literature which can overcome the problem of the poor heat transfer associated with the PCMs. These techniques are: the use of the extended surfaces, the use of nanofluids, cascading of multiple PCMs in a single unit, in-building of low-density porous materials in the PCM, integration of heat pipes in the LTES, etc. [66–69]. The use of fins is one of the most preferred heat transfer enhancement techniques in PCM-based storage due to its low cost and easy fabrication. The use of cascade PCMs maintains uniformity in the heat transfer process during the melting/solidification of the PCMs. Heat pipes improve the available heat transfer area in the system, which enhances the thermal performance of the LTES. For improving the thermal conductivity of the PCMs, nano-sized metallic particles are being used, which reduces the response time of the system [70, 71]. The low-density metal foams and metal matrices are being used to intensify the thermal performance of the PCMs, which also reduces the response time of the LTES. Various innovative designs of the TES, such as shell and tube design, encapsulated packed bed design, and triplex tube design, have also been explored by researchers, which provides better heat transfer in the system. Thermochemical energy storages are currently under the research phase, and few laboratory-scale models have been developed, as discussed in the earlier sections. The major challenges associated with thermochemical energy storage systems are enhancement of thermal conductivity, cyclic stability, thermal stability, heat exchanger efficiency, energy storage density, and reversibility of thermochemical materials. These properties can be improved by changing the chemical composition, adopting more advanced manufacturing techniques, and improving the design of the thermochemical energy storage systems. There are various parameters that are involved in the design and

operation of the TES. To obtain the best thermal performance from the TES system, it is necessary to choose these parameters appropriately. The studies on the optimized design of TES and implementation of the various heat transfer enhancement techniques in the TES are one of the growing fields of research in this area.

## 9.7 Summary

Thermal energy storage is one of the essential parts of any energy system. It improves the overall efficiency of the system as well as it reduces the operating cost of the system. Apart from this, the integration of TES with the energy systems also reduces the CO<sub>2</sub> emission and manages the mismatch between demand and supply. In solar energy applications, it provides a sustainable solution to the problem of the intermittent nature of solar energy. The thermal energy can be stored in the form of sensible heat, enthalpy of phase transition, and enthalpy of the chemical reaction. The materials used in the diverse storage applications have been discussed in this chapter. The potential merits/demerits of the available thermal energy storage systems have been highlighted. There are certain requirements, which need to be fulfilled for the efficient designing of the TES. These requirements are high energy density and thermal conductivity of the storage medium, better thermal and chemical stability of the TES materials, compatibility of the storage media with the container material, better heat transfer between storage medium and HTF, low thermal losses to the environment, reversible charging/discharging, and better control on the operation. TES systems have been developed in various innovative designs, which improve the charging/discharging performance of the storage. The existing TES technologies and their operating strategies have been discussed. A discussion on the cost associated with the TES technologies has been highlighted here. Various ongoing researches in this area have been discussed. The correction in the mismatch between demand and supply of the energy systems by using TES can improve the dispatchability of the overall system. TES contributes to fulfilling the energy demand of the society in an efficient and eco-friendly manner. It decreases the dependency on conventional fuels, which degrade the atmosphere. Although TES technologies are one of the most sought technologies due to its extreme importance in various applications, there are many problems associated with it, which need to be overcome for its efficient utilization in diverse energy applications. A coordinated effort to develop high performance and cost-effective TES technologies can unlock the doors of the maximum benefits of the TES technologies for various applications.

## References

1. Sarbu I, Sebarchievici C (2018) A comprehensive review of thermal energy storage. Sustainability (Switzerland) 10(1). <https://doi.org/10.3390/su10010191>

2. Xu C, Li X, Wang Z, He Y, Bai F (2013) Effects of solid particle properties on the thermal performance of a packed-bed molten-salt thermochemical storage system. *Appl Therm Eng* 57(1–2):69–80. <https://doi.org/10.1016/j.applthermaleng.2013.03.052>
3. Khare S, Dell'Amico M, Knight C, McGarry S (2013) Selection of materials for high temperature sensible energy storage. *Sol Energy Mater Sol Cells* 115:114–122. <https://doi.org/10.1016/j.solmat.2013.03.009>
4. Hussain F, Rahman MZ, Nair A (2020) Chapter 6 Energy storage technologies. Elsevier Inc
5. Gil A, Medrano M, Martorell I, Lázaro A, Dolado P, Zalba B, Cabeza LF (2010) State of the art on high temperature thermal energy storage for power generation. Part 1-Concepts, materials and modellization. *Renew Sustain Energy Rev* 14(1):31–55. <https://doi.org/10.1016/j.rser.2009.07.035>
6. Tiskatine R, Oaddi R, Ait El Cadi R, Bazgaou A, Bouriden L, Aharoune A, Ihlal A (2017) Suitability and characteristics of rocks for sensible heat storage in CSP plants. *Solar Energy Mater Solar Cell* 169:245–257. <https://doi.org/10.1016/j.solmat.2017.05.033>
7. Suresh C, Saini RP (2020) Review on solar thermal energy storage technologies and their geometrical configurations. *Int J Energy Res* 44(6):4163–4195. <https://doi.org/10.1002/er.5143>
8. Calvet N, Gomez JC, Faik A, Roddatis VV, Meffre A, Glatzmaier GC, Doppiu S, Py X (2013) Compatibility of a post-industrial ceramic with nitrate molten salts for use as filler material in a thermochemical storage system. *Appl Energy* 109:387–393. <https://doi.org/10.1016/j.apenergy.2012.12.078>
9. Kenda ES, N'Tsoukpoe KE, Ouédraogo IWK, Coulibaly Y, Py X, Ouédraogo FMAW (2017) Jatropa curcas crude oil as heat transfer fluid or thermal energy storage material for concentrating solar power plants. *Energy Sustain Dev* 40:59–67. <https://doi.org/10.1016/j.esd.2017.07.003>
10. Goods SH, Bradshaw RW (2004) Corrosion of stainless steels and carbon steel by molten mixtures of commercial nitrate salts. *J Mater Eng Perform* 13(1):78–87. <https://doi.org/10.1361/10599490417542>
11. Fernández AG, Ushak S, Galleguillos H, Pérez FJ (2014) Development of new molten salts with  $\text{LiNO}_3$  and  $\text{Ca}(\text{NO}_3)_2$  for energy storage in CSP plants. *Appl Energy* 119(3):131–140. <https://doi.org/10.1016/j.apenergy.2013.12.061>
12. González-Roubaud E, Pérez-Osorio D, Prieto C (2017) Review of commercial thermal energy storage in concentrated solar power plants: Steam versus molten salts. *Renew and Sustain Energy Rev* 80:133–148. <https://doi.org/10.1016/j.rser.2017.05.084>
13. Baharoon DA, Rahman HA, Omar WZW, Fadhl SO (2015) Historical development of concentrating solar power technologies to generate clean electricity efficiently—a review. *Renew Sustain Energy Rev* 41:996–1027. <https://doi.org/10.1016/j.rser.2014.09.008>
14. Brosseau D, Kelton JW, Ray D, Edgar M, Chisman K, Emms B (2005) Testing of thermochemical filler materials and molten-salt heat transfer fluids for thermal energy storage systems in parabolic trough power plants. *J Solar Energy Eng Trans ASME* 127(1):109–116. <https://doi.org/10.1115/1.1824107>
15. Reddy KS, Jawahar V, Sivakumar S, Mallick TK (2017) Performance investigation of single-tank thermochemical storage systems for CSP plants. *Sol Energy* 144:740–749. <https://doi.org/10.1016/j.solener.2017.02.012>
16. Skumanich A (2020) CSP: Developments in heat transfer and storage materials—renewable energy focus. <http://www.renewableenergyfocus.com/view/17095/csp-developments-in-heat-transfer-and-storage-materials/>. Accessed 24 August 2020
17. Steinmann WD, Eck M (2006) Buffer storage for direct steam generation. *Sol Energy* 80(10):1277–1282. <https://doi.org/10.1016/j.solener.2005.05.013>
18. Solucar (2006) 10 MW solar thermal power plant for southern Spain. [Online]. Available [http://ec.europa.eu/energy/res/sectors/doc/csp/ps10\\_final\\_report.pdf](http://ec.europa.eu/energy/res/sectors/doc/csp/ps10_final_report.pdf)
19. Schmidt T, Mangold D, Müller-Steinhagen H (2004) Central solar heating plants with seasonal storage in Germany. *Sol Energy* 76(1–3):165–174. <https://doi.org/10.1016/j.solener.2003.07.025>

20. Hesarakı A, Holmberg S, Haghighat F (2015) Seasonal thermal energy storage with heat pumps and low temperatures in building projects—a comparative review. *Renew Sustain Energy Rev* 43:1199–1213. <https://doi.org/10.1016/j.rser.2014.12.002>
21. Kurt H, Halici F, Binark AK (2000) Solar pond conception—experimental and theoretical studies. *Energy Convers Manag* 41(9):939–951. [https://doi.org/10.1016/S0196-8904\(99\)00147-8](https://doi.org/10.1016/S0196-8904(99)00147-8)
22. Kumar A, Kishore VVN (1999) Construction and operational experience of a 6000 M2 solar pond at kutch, India. *Sol Energy* 65(4):237–249. [https://doi.org/10.1016/S0038-092X\(98\)00134-0](https://doi.org/10.1016/S0038-092X(98)00134-0)
23. Appadurai M, Velmurugan V (2015) Performance analysis of fin type solar still integrated with fin type mini solar pond. *Sustain Energy Technol Assess* 9:30–36. <https://doi.org/10.1016/j.seta.2014.11.001>
24. Singh B, Gomes J, Tan L, Date A, Akbarzadeh A (2012) Small scale power generation using low grade heat from solar pond. 49:50–56. <https://doi.org/10.1016/j.proeng.2012.10.111>
25. Ramadan MRI, Khallaf AM (2011) Thermal performance of an active single basin solar still (ASBS) coupled to shallow solar pond (SSP). *DES* 280(1–3):183–190. <https://doi.org/10.1016/j.desal.2011.07.004>
26. Ramadan MRI, Salem N (2008) Thermal performance of a single-basin solar still integrated with a shallow solar pond. 49:2839–2848. <https://doi.org/10.1016/j.enconman.2008.03.002>
27. Fleischer AS (2015) Thermal energy storage using phase change materials. 9783319209210
28. Alva G, Lin Y, Fang G (2018) An overview of thermal energy storage systems. *Energy* 144:341–378. <https://doi.org/10.1016/j.energy.2017.12.037>
29. Mehling LF, Cabeza H (2008) Heat and cold storage with PCM: an up to date introduction into basics and applications. Springer, Heidelberg, Berlin
30. Alva G, Liu L, Huang X, Fang G (2017) Thermal energy storage materials and systems for solar energy applications. *Renew Sustain Energy Rev* 68:693–706. <https://doi.org/10.1016/j.rser.2016.10.021>
31. Jankowski NR, McCluskey FP (2014) A review of phase change materials for vehicle component thermal buffering. *Appl Energy* 113:1525–1561. <https://doi.org/10.1016/j.apenergy.2013.08.026>
32. Pereira da Cunha J, Eames P (2016) Thermal energy storage for low and medium temperature applications using phase change materials—a review. *Appl Energy* 177:227–238. <https://doi.org/10.1016/j.apenergy.2016.05.097>
33. Cabeza LF, Castell A, Barreneche C, De Gracia A, Fernández AI (2011) Materials used as PCM in thermal energy storage in buildings: a review. *Renew Sustain Energy Rev* 15(3):1675–1695. <https://doi.org/10.1016/j.rser.2010.11.018>
34. Huang MJ, Eames PC, Norton B (2004) Thermal regulation of building-integrated photovoltaics using phase change materials. *Int J Heat Mass Transf* 47(12–13):2715–2733. <https://doi.org/10.1016/j.ijheatmasstransfer.2003.11.015>
35. Su D, Jia Y, Alva G, Liu L, Fang G (2017) Comparative analyses on dynamic performances of photovoltaic–thermal solar collectors integrated with phase change materials. *Energy Convers Manag* 131:79–89. <https://doi.org/10.1016/j.enconman.2016.11.002>
36. El-Sebaıı AA, Al-Ghamdi AA, Al-Hazmi FS, Faidah AS (2009) Thermal performance of a single basin solar still with PCM as a storage medium. *Appl Energy* 86(7–8):1187–1195. <https://doi.org/10.1016/j.apenergy.2008.10.014>
37. Sharma SD, Iwata T, Kitano H, Sagara K (2005) Thermal performance of a solar cooker based on an evacuated tube solar collector with a PCM storage unit. *Sol Energy* 78(3):416–426. <https://doi.org/10.1016/j.solener.2004.08.001>
38. Regin AF, Solanki SC, Saini JS (2008) Heat transfer characteristics of thermal energy storage system using PCM capsules: a review. *Renew Sustain Energy Rev* 12(9):2438–2458. <https://doi.org/10.1016/j.rser.2007.06.009>
39. Karthikeyan S, Ravikumar Solomon G, Kumaresan V, Velraj R (2014) Parametric studies on packed bed storage unit filled with PCM encapsulated spherical containers for low temperature solar air heating applications. *Energy Convers Manag* 78:74–80. <https://doi.org/10.1016/j.enconman.2013.10.042>

40. Kumaresan G, Vigneswaran VS, Esakkimuthu S, Velraj R (2016) Performance assessment of a solar domestic cooking unit integrated with thermal energy storage system. *J Energy Storage* 6:70–79. <https://doi.org/10.1016/j.est.2016.03.002>
41. Pirasaci T, Goswami DY (2016) Influence of design on performance of a latent heat storage system for a direct steam generation power plant. *Appl Energy* 162:644–652. <https://doi.org/10.1016/j.apenergy.2015.10.105>
42. Abedin AH (2011) A critical review of thermochemical energy storage systems. *Open Renew Energy J* 4(1):42–46. <https://doi.org/10.2174/1876387101004010042>
43. Anggraini AR, Oliver J (2019) 濟無No Title No Title. *J Chem Inf Model* 53(9):1689–1699. <https://doi.org/10.1017/CBO9781107415324.004>
44. Garg HP, Mullick SC, Bhargava AK (1985) Solar thermal energy storage. *Sol Therm Energy Storage*
45. Dunn R, Lovegrove K, Burgess G (2012) A review of ammonia-based thermochemical energy storage for concentrating solar power. *Proc IEEE* 100(2):391–400. <https://doi.org/10.1109/JPROC.2011.2166529>
46. Wentworth WE, Chen E (1976) Simple thermal decomposition reactions for storage of solar thermal energy. *Sol Energy* 18(3):205–214. [https://doi.org/10.1016/0038-092X\(76\)90019-0](https://doi.org/10.1016/0038-092X(76)90019-0)
47. Kato Y, Harada N, Yoshizawa Y (1999) Kinetic feasibility of a chemical heat pump for heat utilization of high-temperature processes. *Appl Therm Eng* 19(3):239–254. [https://doi.org/10.1016/s1359-4311\(98\)00049-0](https://doi.org/10.1016/s1359-4311(98)00049-0)
48. Kato Y, Yamada M, Kanie T, Yoshizawa Y (2001) Calcium oxide/carbon dioxide reactivity in a packed bed reactor of a chemical heat pump for high-temperature gas reactors. *Nucl Eng Des* 210(1–3):1–8. [https://doi.org/10.1016/S0029-5493\(01\)00421-6](https://doi.org/10.1016/S0029-5493(01)00421-6)
49. André L, Abanades S, Flamant G (2016) Screening of thermochemical systems based on solid-gas reversible reactions for high temperature solar thermal energy storage. *Renew Sustain Energy Rev* 64:703–715. <https://doi.org/10.1016/j.rser.2016.06.043>
50. Caldwell RT, McDonald JW, Pietsch A (1965) Solar-energy receiver with lithium-hydride heat storage. *Sol Energy* 9(1):48–60. [https://doi.org/10.1016/0038-092X\(65\)90161-1](https://doi.org/10.1016/0038-092X(65)90161-1)
51. Sheppard DA, Paskevicius M, Humphries TD, Felderhoff M, Capurso G, Bellosta von Colbe J, Dornheim M, Klassen T, Ward PA, Teprovich JA, Corngale C, Zidan R, Grant DM, Buckley CE (2016) Metal hydrides for concentrating solar thermal power energy storage. *Appl Phys A Mater Sci Process* 122. <https://doi.org/10.1007/s00339-016-9825-0>
52. Paskevicius M, Sheppard DA, Williamson K, Buckley CE (2015) Metal hydride thermal heat storage prototype for concentrating solar thermal power. *Energy* 88:469–477. <https://doi.org/10.1016/j.energy.2015.05.068>
53. Kato Y, Yamashita N, Kobayashi K, Yoshizawa Y (1996) Kinetic study of the hydration of magnesium oxide for a chemical heat pump. *Appl Therm Eng* 16(11):853–862. [https://doi.org/10.1016/1359-4311\(96\)00009-9](https://doi.org/10.1016/1359-4311(96)00009-9)
54. Fedders H, Harth R, Höhlein B (1975) Experiments for combining nuclear heat with the methane steam-reforming process. *Nucl Eng Des* 34(1):119–127. [https://doi.org/10.1016/0029-5493\(75\)90161-2](https://doi.org/10.1016/0029-5493(75)90161-2)
55. Pelay U, Luo L, Fan Y, Stitou D, Rood M (2017) Thermal energy storage systems for concentrated solar power plants. *Renew Sustain Energy Rev* 79(January):82–100. <https://doi.org/10.1016/j.rser.2017.03.139>
56. Fahim MA, Ford JD (1983) Energy storage using the BaO-BaO reaction cycle. *Chem Eng J* 27(1):21–28
57. Bowrey RG, Jutsen J (1978) Energy storage using the reversible oxidation of barium oxide. *Sol Energy* 21(6):523–525. [https://doi.org/10.1016/0038-092X\(78\)90078-6](https://doi.org/10.1016/0038-092X(78)90078-6)
58. André L, Abanades S, Cassayre L (2017) High-temperature thermochemical energy storage based on redox reactions using Co-Fe and Mn-Fe mixed metal oxides. *J Solid State Chem* 253(March):6–14. <https://doi.org/10.1016/j.jssc.2017.05.015>
59. Home—system advisor model (SAM). <https://sam.nrel.gov/>. Accessed 08 July 2020
60. Nithyanandam K, Pitchumani R (2014) Cost and performance analysis of concentrating solar power systems with integrated latent thermal energy storage. *Energy* 64:793–810. <https://doi.org/10.1016/j.energy.2013.10.095>



61. Crespo A, Barreneche C, Ibarra M, Platzer W (2018) Latent thermal energy storage for solar process heat applications at medium-high temperatures—a review. *Solar Energy* 192:3–34. <https://doi.org/10.1016/j.solener.2018.06.101>
62. Saxena R, Rakshit D, Kaushik SC (2019) Phase change material (PCM) incorporated bricks for energy conservation in composite climate: a sustainable building solution. *Sol Energy* 183:276–284. <https://doi.org/10.1016/j.solener.2019.03.035>
63. Saxena R, Rakshit D, Kaushik SC (2020) Experimental assessment of phase change material (PCM) embedded bricks for passive conditioning in buildings. *Renew Energy* 149:587–599. <https://doi.org/10.1016/j.renene.2019.12.081>
64. Zauner C, Hengstberger F, Mörzinger B, Hofmann R, Walter H (2017) Experimental characterization and simulation of a hybrid sensible-latent heat storage. *Appl Energy* 189:506–519. <https://doi.org/10.1016/j.apenergy.2016.12.079>
65. Okello D, Foong CW, Nydal OJ, Banda EJK (2014) An experimental investigation on the combined use of phase change material and rock particles for high temperature (~350 °C) heat storage. *Energy Convers Manag* 79:1–8. <https://doi.org/10.1016/j.enconman.2013.11.039>
66. Akhilesh R, Narasimhan A, Balaji C (2005) Method to improve geometry for heat transfer enhancement in PCM composite heat sinks. *Int J Heat Mass Transf* 48(13):2759–2770. <https://doi.org/10.1016/j.ijheatmasstransfer.2005.01.032>
67. Amin M, Putra N, Kosasih EA, Prawiro E, Luanto RA, Mahlia TMI (2017) Thermal properties of beeswax/graphene phase change material as energy storage for building applications. *Appl Therm Eng* 112:273–280. <https://doi.org/10.1016/j.applthermaleng.2016.10.085>
68. Cao Y, Faghri A (1991) Transient two-dimensional compressible analysis for high-temperature heat pipes with pulsed heat input. *Num Heat Transf Part A Appl* 18(4):483–502. <https://doi.org/10.1080/10407789008944804>
69. Fukai J, Kanou M, Kodama Y, Miyatake O (2000) Thermal conductivity enhancement of energy storage media using carbon fibers. *Energy Convers Manag* 41(14):1543–1556. [https://doi.org/10.1016/S0196-8904\(99\)00166-1](https://doi.org/10.1016/S0196-8904(99)00166-1)
70. Saxena R, Dwivedi C, Dutta V, Kaushik SC, Rakshit D (2020) Nano-enhanced PCMs for low-temperature thermal energy storage systems and passive conditioning applications. *Clean Technol Environ Pol.* 0123456789. <https://doi.org/10.1007/s10098-020-01854-7>
71. Singh RP, Kaushik SC, Rakshit D (2018) Solidification behavior of binary eutectic phase change material in a vertical finned thermal storage system dispersed with graphene nano-plates. *Energy Convers Manag* 171(April):825–838. <https://doi.org/10.1016/j.enconman.2018.06.037>



# Chapter 10

## Solar Energy Pricing



Vivek Soni and Nitin Singh

### Chapter Key highlights

- Solar energy pricing comprising of cost of its components, mainly of PV, installation, and handling cost.
- Solar PV module costs account for only around 20% of solar. Thus, financing costs account for the largest component—over 50% of solar energy tariffs.
- In recent years, the tariffs dropped to a record low of INR 2.44 per kWh for utility-scale solar-based energy generation.
- Historically, equipment-related factors have been the major drivers of tariff reduction, accounting for 73% of the solar tariff reduction in recent years.
- The decline in financing costs accounting for the remaining roughly 27% of the tariff decline.
- However, there could be a role reversal—changes in financing costs could drive future declines in solar tariffs.
- Improvements in the financing costs for solar energy projects can partly be explained by declining commercial bank benchmark lending rates, growing familiarity with solar technologies, favorable policy ecosystem resulting in lowered risk perceptions among debt financiers, and intense competition at auctions.
- The impact of equipment-related factors is likely to be less significant in solar tariff decline in the years ahead.

---

V. Soni (✉)

Bharatiya Vidya Bhavan's Usha and Lakshmi Mittal Institute of Management, New Delhi, India  
e-mail: [vivek.soni@alumni.iitd.ac.in](mailto:vivek.soni@alumni.iitd.ac.in)

N. Singh

Motilal Nehru National Institute of Technology, Allahabad, India

## 10.1 Introduction

Solar energy pricing is regarded as primary sign of growing economic activity. The price of round-the-clock solar energy had become comparable to the average price of electricity generated from thermal power. As a vital component of the solar system, cost of PV module found in many studies is one of the major costs contributing the solar energy pricing, and other factors included operations and maintenance cost and cost of other equipment like inverters and batteries used in the solar generation system. For instance, cost decreased in various components of large-scale solar due to factors such as increased demand, government subsidies, and increasing environmental concerns. In fact, in the recent time, some markets generate renewable energy more cheaply than fossil fuels.

Factors such as rapidly increasing integration of renewable energy (RE) in the grid, continuously falling solar panel prices and supportive policies framed by the government are steadily leading to the increase in renewable electricity market in India. In the field of solar electricity in particular, the annual solar PV electricity production increased from 4 TWh in 2005 to 247 TWh in 2015 [1]. Now, the Government of India intends to achieve 175,000 MW of renewable energy integration by 2022, out of which 100,000 MW will be from solar. The target of 100,000 MW solar project or plant will be achieved through the deployment of 40,000 MW of rooftop solar projects and 60,000 MW of large and medium-scale solar projects.

This large-scale integration of solar power to the grid creates new challenges and opportunities for the consumers, producers, and generators, because of the unique siting, operational, and ownership characteristics of solar power as compared to other conventional centralized resources. The main concerns about PV integration are the economic justification for solar power [2]. Soon after the announcement of the revised targets by the Government of India, the average solar electricity prices have declined, making the business for the renewable generation more robust and reliable. Record low winning tariffs of INR 2.44 per kWh for solar and INR 2.43 per kWh for wind energy generation in the past few years indicates government interests for optimized renewable energy prices to expand large consumer base (CERC Determination of levelised generic tariff for FY 2019–20; Press Information Bureau 2017, Government of India 2018 [3, 4]).

The solar energy price is also experienced by and vulnerable to many other factors related to social and environmental conditions [5]. They also introduce risks and inherent uncertainties in the energy sector. The risks associated in solar segment of energy sector depend on various cost components and size of projects.

The decline in solar tariffs of the renewable is mainly due to the influence of declining equipment costs and the competitive bidding post-electricity act 2003 ([6]; Crisil [7]; Shrimali et al. [8]). It is seen that PV module contributes significantly to the tariff and the other important factors such as financial costs, running cost (operating and maintenance cost), and most importantly the subsidies offered by the government influences the tariff/price of the solar energy.

Literature on solar energy pricing includes where the LCOE and internal rate of return (IRR) are calculated by using the Monte Carlo method (Geissmann et al. 2016) giving probabilistic ranges to all of the variables. This methodology allows us to obtain the probability of the possible scenarios. Other authors have used the Monte Carlo method to study a wide variety of realistic problems. The Monte Carlo method has been applied in several previous works in the field of renewable energy generation (Tomosk et al. 2017; Heck et al. 2016), where LCOE and IRR are used as common economic evaluation tools.

The solar pricing methodology approach proposed in this paper is acceptable because this is regularly used in previous work carried out, showing excellent performance. The approach for solar energy pricing shown in this chapter is innovative as it allows financing costs on PV grid parity from a realistically point of view for a wide area. The methodology used for solar energy pricing is easily applicable to other countries by adjusting the economic and energy parameters.

In the recent times of COVID-19 situation, the solar energy sector also faced delays in land acquisition and in setting up of power evacuation infrastructure as contributing factors to its projects not meeting deadlines. To achieve a reduction of the solar energy tariff in the future, the interpretation of key factors must be understood, so that the future policies for maximizing the profits of generation companies and reduction in tariff for consumers can be designed in the competitive markets. It was also a reality check that the project proponent was unable to fulfill its contractual obligations for these milestone capacity scaling projects and reduced the power at only Rs. 2.44/unit, India's lowest to date.

Few solar energy pricing issues include land acquisitions in solar-based power projects which could not be completed on time under a Central PSU auction. Additionally, there were bottlenecks due to inadequate transmission infrastructure. Moreover, the challenges are not enough; a couple of issues were found related to grid operations by Discoms that also add another dimension.

The focus of this chapter is to identify the major factors that affect the solar power pricing and to identify the drivers that will affect the future price. Further, the investigation of equipment and non-equipment-related factors on the decline in the renewable energy tariffs, specifically, the solar one, is also analyzed. Lastly, this chapter highlights areas that represent opportunities to increase the competitiveness of solar electricity tariffs in the years to come and discusses the policy measures that could accelerate future tariff reduction.

## 10.2 Methodology of Solar Energy Pricing

There are different components that decide total solar prices, such as photovoltaic installation costs, solar panels, mounting structure, inverters, and operating and maintenance costs along with some rescue value of the technology used. All of those are determinants of solar energy pricing. Many studies with different assumptions are

found related to determination of energy cost (levelised cost, i.e. LOCE). The deterministic calculation methodology allows us to reach several conclusions. In small installations, grid parity depends on the financial model and the cost of the installation. In middle-scale installations, grid parity is already achieved, except for some geographical cases with an annual yield of 1100 kWh/kWp. Large-scale installations can be connected without any tariff as the cost of energy is lower than the retail cost of energy at any case.

It is also important to note that the depreciation values of components are not considered except for solar modules[9]. The costs of all other components are fixed except for that of PV modules. Depending on the three sizes of installation considered, i.e., 500, 50 and 5 kW, cost of each component is considered except the cost of the PV panels. There could be multiple scenarios of cost determination. Let us examine the scenarios of solar pricing calculations in three different cases, i.e., 5, 50 and 500 kW. The aim of such kind of estimation of solar energy pricing, considering pessimistic values, is to set the minimum value for the LCOE.

Many studies have calculated the solar energy pricing using various approaches and methods. The Monte Carlo method has been evaluated precisely for all the variable inputs if grid parity is achieved. In this chapter, the representative cases, where the LCOE is lower than the retail cost of energy, have been presented.

First case of 5 kW (inverter power) is the worst case scenario where a 10 % rate of interest and 1100 kWh/kWp yield have been estimated manually.

Table 10.1 indicates PV module cost, system cost, LCOE, and internal rate of return.

The financial parameters, such the interest rate, loan duration and amount loaned, significantly affect the IRR. While determining solar energy price, it could be determined that the LCOE would reach the retail electricity cost at an interest rate of 4% for any module cost (Carlos et al. 2019).

The second case corresponds to a PV installation of 50 kW. This case is summarized in Table 10.2.

This is the case where deterministic calculation method is used which determines the LCOE that may reach to the retail energy cost at the interest rate of 6% for any module cost. The third case of a PV installation of 500 kW can be understood from Tables 10.3, 10.4 and 10.5.

**Table 10.1** Comparison of levelized cost of energy (LCOE) and internal rate of return (IRR) based on a recovery factor at 10% interest, for the 5 kW case

PV module cost (/Wp)	System cost (€)	LCOE (/kWh)	IRR (%)
1	15,464	0.2756	4.811
0.8	14,012	0.2514	3.83
0.6	12,560	0.2271	2.68
0.4	11,108	0.2029	1.31
0.2	9656	0.1787	0.4

Source Carlos et al. 2019: Remarks: Cost figures are in Euros and are indicative

**Table 10.2** Comparison of LCOE and IRR based on a recovery factor at 10% interest (50 kW) case

PV module cost (/Wp)	System cost (€)	LCOE (/kWh)	IRR (%)
1	118,580	0.2154	2.049
0.8	104,060	0.1911	0.53
0.6	89,540	0.1669	1.39
0.4	75,020	0.1427	3.97
0.2	60,500	0.11841	7.46

Source Carlos et al. 2019: Remarks: Cost figures are in Euros and are indicative

**Table 10.3** Comparison of LCOE and IRR based on a recovery factor at 10% interest 500 kW case

PV module cost (/Wp)	System cost (€)	LCOE (/kWh)	IRR (%)
1	1,022,45	0.1585	0.316
0.8	877,250	0.1385	1.67
0.6	732,050	0.1184	4.36
0.4	586,850	0.0984	8.02
0.2	441,650	0.07834	14.52

Source Carlos et al. 2019: Remarks: Cost figures are in Euros and are indicative

**Table 10.4** LCOE over a range of interest rates (50,000 W inverter, deterministic method)

PV module cost (/Wp)	System cost (€)	LCOE (/kWh)				
		Interest rate (%)				
		12	10	8	6	4
1	1,022,450	0.2149	0.1881	0.1625	0.1386	0.1166
0.8	877,250	0.1869	0.1638	0.1419	0.1214	0.1025
0.6	732,050	0.1588	0.1396	0.1213	0.1042	0.0884
0.4	586,850	0.1308	0.1154	0.1007	0.087	0.0743
0.2	441,650	0.1027	0.0911	0.0801	0.0697	0.0602

Source Carlos et al. 2019: Remarks: Cost figures are in Euros and are indicative

**Table 10.5** Comparison of the LCOE based on the different annual yields for 500 kW

PV module cost (/Wp)	System cost (€)	Annual yield (kWh/kWp)	Case 1	Case 2	Case 3	Case 4	Case 5
			1100	1200	1300	1400	1500
1	1,022,450	0.188	0.174	0.162	0.151	0.143	0.143
0.8	877,250	0.164	0.152	0.141	0.132	0.125	0.125
0.6	732,050	0.14	0.129	0.121	0.113	0.107	0.107
0.4	586,850	0.115	0.107	0.1	0.094	0.089	0.089
0.2	441,650	0.118	0.11	0.103	0.097	0.091	0.091

Source Carlos et al. 2019: Remarks: Cost figures are in Euros and are indicative

### 10.3 Solar Price Competition, Auctions and Reversal Changes

The cost of generating electricity from solar PV systems has fallen over time. A major factor behind this decline has been the continual decrease in the price of solar modules. The solar module is the principal component in PV systems. These declines have brought the price of solar generated electricity closer to the price of electricity generated from other energy resources, but a gap remains. Competition is an significant factor seen in the energy sector, where under imperfect competition, the impact on the price of cost changes will depend on how the energy market reacts to cost change.

Competitive procurement acts as price discovery for solar energy pricing. On examining the Indian market, it is evident that energy prices have been fallen faster than what government and regulators, and a few planners have captured in traditional renewable energy. The process of competitive procurement allows private sector actors to bid a plant price based on the actual costs of doing business. At international level, methodology for energy prices and manner of energy business is found slightly different across the countries like Brazil, South Africa including India. It is also evident that that in competitive auctions in such countries have led to immediate average price cut of 29–50%. However, approaches in developed countries are differed from the others, where government considers a few additional cost components such as investment against the environmental protection, energy efficiency improvement, operating and maintenance, compares solar cost with other energy options, and finally set energy prices is quite high. But auctions in their countries have led to a further decrease in the LCOE.

Competitive procurement for solar system is the method for purchasing a part of system through an open and competitive process where multiple bidders are engaged in the process. In fact, competitive framework is focal point to the development of a low-cost and high-renewable electricity sector because it provides a platform for tendering projects transparently. The process can also help to reduce harmful greenhouse gas emissions and bring cleaner sources of energy to the energy consumers. In this regard, reverse auctions have emerged as the latest examples of competitive procurement, resulting in considerably lower global prices than historical prices. Hence, cheaper solar energy prices also allow cash-impooverished utilities and ultimately the consumer to pay less for electricity supplied by solar system. This further affects public and utility desire to buy more solar energy.

In particular, the reverse auctions are type of competitive procurement in which the lowest price wins, as opposed to a silent auction where prices are bided up. Generally, the regulatory processes of pre-qualification before the auction to choose preferred bidders govern these auctions. Reverse auctions enable government agencies to dedicate resources to advance planning and consultation. The regulator sets a certain level of capacity and/or energy that is required at a certain price and fills the capacity until that level is met. Auctions are framed into multi-round programs, where each successive round establishes more confidence and pushes prices lower. Over the

time, the reverse auctions have resulted in low prices for solar energy projects in many countries including Mexico (2.69 cents/kWh), Chile (2.91 cents/kWh), Zambia (6.02 cents/kWh), and United Arab Emirates (2.99 cents/kWh) over the past six months, often at prices comparable to natural gas.

## 10.4 Impact of Changes in Module Costs and Financing Costs on the Future Trajectory of the LCOE

Financial costs have a significant influence on the LCOE calculation. With regard to financing the costs of PV plants, the levelized cost of energy (LCOE) can be used to calculate the required system and finance expenses necessary to achieve grid parity [10, 11]. To take into account the effect of financing costs, the risk of the investment would have to build into the interest rate. The LCOE is not the same as the electricity cost, but it is similar to the total price paid by consumers while considering as many realistic costs as possible. When assessing LCOE against grid parity, all system and project costs should be taken into account. These costs include PV modules, structures, inverters, cables, and installation.

Grid parity is a condition where power generation from renewable energy sources such as solar costs more or less the same as traditional sources. When grid parity is achieved for photovoltaic (PV) installations, all electrical energy produced can be sold at the same cost as it is purchased from the grid [12]. Several factors are to be into account, such as the possible subsidies or special economic regimes of the PV generators and the financing costs of this type of installation.

Feed-in tariffs (FITs) are fixed electricity rates charged to solar energy producers for each energy unit generated and inserted into the grid. The private players are investing just because of its lucrative and stable nature see a few of investment options. The pricing structure that the FIT offers is vital in determining the growth rate of the PV industry and the investments made by private investors and the government, and therein lies the future of the industry [13].

PV is one the most encouraged sources of energy generation (Badcock 2010), where profitability ratios, financial conditions, and the quantification of risks are all clearly known (Helms et al. [14]). In addition, the inclusion of batteries in solar pricing determination can improve the profitability of grid-connected PV installations if the tariff policy allows optimizing revenues by managing the charge and discharge of the batteries [15]. Recently, many countries in the world, including USA, have set new targets for the levelized cost of electricity(LCOE) from solar PV. Reducing further PV costs by a factor of two to three from the values of recent last few years—requires improvements in technology performance and reliability as well as reductions in hardware, operations and maintenance, and soft costs [16].

In addition, more cost reductions are carried out through lowering project capital cost. Project capital costs, or sometimes known as the financing costs, are the costs associated with raising funds to build and operate a project. They typically come

in two forms: the upfront costs associated with arranging funds (deal setup costs) and the costs required to pay back the sources of capital for providing project funds, plus profit. There are few factors which influence financing costs and include the amount of risk associated with achieving the investor's desired rate of return, the level of marketplace competition for available projects and sources of capital (i.e., the balance of supply and demand), and, to a lesser extent, the time and effort required to arrange a financial transaction.

Major research and development efforts related to lowering the solar price have been made. Although this has already reduced the cost of PV financing, further reducing the perceived risk of cash flows to PV investors may reduce the cost of capital and increase the amount of profit. This leverage expense is debt as a percentage of overall expenditure in photovoltaic projects. Few R&D areas could enable lower capital costs and increase advantage through lower perceived risks and increased competition. Improving performance, reliability, operations and maintenance, and testing of photovoltaic products are focused on reducing technology risk. There could be other multiple areas like reducing solar resource risk, reducing risk of declining PV, electricity value, and reducing electricity off-taker risk. In addition to above, public and private activities such as analysis, data aggregation, and industry working groups and collaboration which may involve some R&D activities as well would further reduce the cost of financing, often by enabling financing transactions to occur more quickly with less effort and reducing the upfront costs associated with arranging financing for PV projects.

## **10.5 Contours of SEP: Policy, Market, and Societal-Led Interventions**

By reducing some of the risks perceived by the private sector, leveraging financing and increasing capital flows for R&D, policy plays a central role in the deployment of renewable energy technologies. There are major obstacles in the industry over and above technical barriers. Renewable projects will require large investments in infrastructure, which the private sector might consider risky, unless they have sufficiently funded consistent incentives. In the form of incentives, policy can also sustain industry sales until manufacturers achieve cost reductions from learning opportunities and economies of scale. The USA and China have historically taken different approaches to policymaking in the energy sector, partly because they have different needs and priorities and partly because they have different systems of government. These factors can make it difficult to analyze policies, or to find common ground for cooperation on policy-related matters. In view of the important role that policy will continue to play in the efforts of both countries to increase the use of renewable energy, this chapter highlights the strategic approaches adopted by China and the USA and discusses some areas of common interest. It also outlines possible business limitations and addresses prospects for improving market infrastructure.



Renewable energy is going to be an important source for power generation in near future, because we can use these resources repeatedly to produce useful energy. Wind power generation is considered as having lowest water consumption, lowest relative greenhouse gas emission, and most favorable social impacts. It is considered as one of the most sustainable renewable energy sources, followed by hydropower, photovoltaic, and then geothermal. As these resources are considered as clean energy resources, they can be helpful for the mitigation of greenhouse effect and global warming effect. Local employment, better health, job opportunities, consumer choice, improvement of life standard, social bonds creation, income development, demographic impacts, social bonds creation, and community development are achieved by the proper usage of renewable energy system. Along with the outstanding advantages of these resources, some shortcomings also exist such as the variation of output due to seasonal change, which is the common thing for wind and hydroelectric power plant; hence, special design and consideration are required, which are fulfilled by the hardware and software due to the improvement in computer technology.

## 10.6 Conclusion

This chapter presented a picture of solar energy pricing, methodology, and its implications to India's solar system. Indian energy sector needs to accelerate its solar energy capacity addition in order to meet its renewable energy (RE) targets. Besides policy commitments, the cost competitiveness of solar tariffs facilitates the uptake of renewable power. This chapter focuses on the major determinants of solar tariffs, disaggregating the impact of equipment-related factors and financing costs (costs of debt and equity). This chapter finds that financing costs account for the largest component—over 50% of RE tariffs. Further, equipment-related factors have been the major drivers of tariff reduction historically, accounting for 73% of the solar tariff reduction. However, this chapter demonstrates that there could be a role reversal—changes in financing costs could drive future declines in both solar and wind tariffs. This necessitates the de-risking of these sectors through suitable policy-led and market-led interventions in order to lower financing costs [17].

Energy pricing-related computational and empirical capabilities are also enabling a new era of “systems by design” in energy sector. This includes scientific theory, modeling, simulation, high-performance computing, data management and analysis, algorithms, software, and high-throughput experimental techniques to enable the prediction, design, engineering, and experimental characterization of materials in PV and solar arrays manufacturing. These capabilities can offer so many optimal solutions and consumer's expectations in India's solar energy, basically to extract potential to develop new materials, technologies, and systems more rapidly and at lower cost than traditional approaches. Many R&D institutions have development

of such capabilities as its central focus [18]. In Indian context, many of state electricity commissions and regulators are using advanced scientific tools for energy cost calculations and make available to energy technology developers.

Auctions are also seen as one of the lucrative option in determining solar energy pricing, and at a high-level, they require that key stakeholders come together to institute the requisite technical, legal, and regulatory processes prior to auction rollout. It is very much important for efficient auctions, basically to ensure the component of supply is available for introducing new solar projects as well as the electrical grid is susceptible to incorporate them as variable energy sources. At a more granular level, solar energy stakeholders should develop a consensus around the goals they would like to achieve and how these goals will be reflected in auction design to support reducing the solar energy pricing further. Pre-auction planning including site selection, grid connection plans, environmental impact studies, resource studies, as well as standardized solar energy purchase and interconnection agreements, can all smooth the path forward. Solar energy stakeholders will need to focus on the level of competition and performance goals that are acceptable for the context of country. While mature markets should have price-determined auctions, emerging markets should also concentrate on establishing the supply chain, for example by realistic local content laws, evenly spaced timelines for auctioning to enable local business growth. In the cases of markets where there is not a prior track record of competition, this may mean starting small to boost competition before downward price pressure sets in. As transformation in the solar industry increases, capacity targets could simultaneously increase. While solar prices tend to be higher where utility creditworthiness is a significant challenge, tools exist to address market risk, such as guarantees and capital grants, to garner more competition. Solar energy pricing step can be taken to increase the probability of financial closure and project execution, such as project bond conditions to reduce the risk of non-completion and lowball bidding, the availability of concessional funding, site-specific resource measurements, guidelines on equipment, and capacity factor requirements.

## **10.7 Implication to India's Energy Renewable Energy Vision**

Solar energy pricing plays a central role in both the energy sector and the promotion of environmental sustainability, thereby promoting India's efforts to fulfil its RE vision. India's photovoltaic solar ambition is a little optimistic looking 20 GW target in 2022. The proposed mission anticipated and deemed somewhat unlikely given the upcoming changes in structure and economy.

Whatever the concerns about a mega solar project strategy's long-term feasibility, momentum in India's solar power market has also been toward a positive outlook for optimal energy mix. For example, a new deal between the US export and import bank and the Indian renewable agencies (like IREDA) has opened the doors on a potential

\$1 billion in finance to facilitate solar technology exports. Private capital is also apparently set to flood into India's solar sector. In addition, India's solar ambitions require investment. Inevitably, those seeking to penetrate Indian solar territory have plenty of investment goals. Efforts are also being made to address some of the main structural issues which posed barriers to inward investment. In addition to policy measures, better financial opportunities and increased expertise and awareness, there is also evidence of building up in the supply chain.

Solar energy pricing is also influenced by the system components requirements, their manufacture, fabrications, and import–export statistics. In this regard, Indian solar companies have seen to be highly dependent on China in terms of importing components. Modules account for nearly 60% of a solar power project's total cost. It is estimated that over 80% of solar cells and modules are imported from the different country because of its competitive pricing compared to domestic manufactures. Chinese companies due to their competitive pricing dominate the fast-growing domestic market for solar components. India imported solar photovoltaic (PV) cells, panels, and modules the recent past years.

As per different reports, Indian solar industry largely depends on China for procurement of raw material. The same is not the case for wind equipment, but for solar about 85% of cells and modules are still imported, mostly from other countries like China. China has been working vigorously to scale up not only the generation of renewable energy, but also production and manufacturing and is currently the world's largest exporter and installer of solar panels, wind turbines, batteries, and electric vehicles. Specific to solar China is fully integrated with polysilicon production, to wafers, cells, s and modules.

India has a domestic manufacturing capacity of only 11 GW for panels and 3 GW for solar cells, although some capacity remains unutilized due to price and quality concerns. With the world facing more frequent changes, Indian solar market is looking at rapid changes for diversification of trade markets, particularly making it more reliance energy sector. The opportunity will improve capabilities of Indian manufactures in domestic manufacturing of solar equipment.

Solar energy sector is also looking to play a larger role in global energy supply chains in the backdrop of the disruption caused by the pandemic. With the self-reliance program, India currently has considered in scaling up a domestic manufacturing capacity beyond 3 GW for solar cells and recently awarded a manufacturing-linked solar contract that will help in establishing additional solar cell and module manufacturing capacity. Here, clean energy projects now account for more than a fifth of India's installed power generation capacity, with the country becoming one of the top renewable energy producers globally with ambitious capacity expansion plans. In this context, China remains India's second largest trading partner after the USA. India's exports to China rose 3.8% to \$17.1 billion in 2019, while imports contracted 7.5% to \$68.3 billion during the same year.

However, one can keep in the mind that near-term development and execution of renewable Energy (RE) projects are not hampered with our plant set under self-reliance manufacturing. A dedicated strategy is need of the hour, and to scale up local manufacturing, Indian manufacturing industry look forward to putting in place

a long-term policy, coupled with infrastructure and the right incentives to support the same. Another essential investment consideration is in R&D, policymakers, and top experts, as they need to think about complete vertical integration if we are aiming to be a self-sufficient manufacturer of solar equipment. It is not enough to set up units to make cells, modules, or wafers. It should also need to gear up production of ancillaries including inverters, glass, back sheets, etc.

Besides boosting domestic manufacturing, our country should also need to take a forward-looking approach to the manufacturing of equipments for renewable. No doubt, battery technology is all set to be a game changer, as it addresses the intermittency of renewable and can transform electric mobility [19]. Many initiative of Energy Efficiency Services Limited (EESL) is appreciated. It is believed that this segment will become critical for the growth of RE in coming years. Unfortunately, China has taken an early lead in developing battery technology, but it is still at a nascent stage and India has a good chance at competing on this front [20]. Innovations are high in India as compared to China, and one should take note that India is not short on skill, expertise, land, or man-power—reducing our import dependency on solar equipment by ramping up domestic capabilities is not an easy task, but it can be achieved in the interests of “Make in India,” competitive pricing and also technological advancement.

In fact, a good dedicated energy sector-focused approach is the way that could be instead of restricting imports, perhaps incentivizes the local manufacturers and skiing peoples. The pro-active approach in turn realization of the dream will take a long-term view and stay committed to the notion of making India a manufacturing hub, irrespective of our international relations.

## 10.8 Key Recommendations

Based on the study on solar energy pricing presented in this chapter, the following critical recommendations are derived from the study.

- De-risk the RE sector through explicit subsidies or measures translating into lower return expectations for investors.
- Enforce contractual provisions to minimize instances of payment delays or power purchase agreement (PPA) renegotiation.
- Safeguard RE developers against long payment delays with payment security mechanisms.
- Facilitate timely land acquisition to streamline the process of solar park development.
- Ensure contractual provisions that safeguard against curtailment risk by guaranteeing a minimum level of off-take of RE generation.
- Design financial instruments, such as guarantees that mitigate curtailment risks for developers.

## References

1. International Energy Agency (2020) Energy policy review. India 2020, IEA Publications
2. Tervo E, Agbim K, Deangelis F, Kyung H (2018) An economic analysis of residential photovoltaic systems with lithium ion battery storage in the United States. *Renew Sustain Energ Rev* 94:1057–1066
3. Government of India (2017) CERC Determination of levelled generic tariff for FY 2019–20 under Regulation 8 of the Central Electricity Regulatory Commission (Terms and Conditions for Tariff determination from Renewable Energy Sources) regulations
4. Press Information Bureau (2018) Press release on year end review of Ministry of New and Renewable, Govt. of India
5. Chawla K, Aggarwal M, Dutt A (2020) Analyzing the falling solar and wind tariff. ADBI Working Paper Series. Feb 2020. ADBI Publications
6. IRENA (2019) Renewable power generation costs in 2018. International Renewable Energy Agency, Abu Dhabi IRENA
7. Crisil (2017) A sector report on solar energy. Credit rating information services of India limited, CRISIL Publications. New Delhi, India
8. Shrimali G, Trivedi S, Srinivasan S, Goel S, Nelson D (2016) Cost-effective policies for reaching India's 2022 renewable targets. *Renewable Energy* 93(2016):255–268
9. Rábago KR (2013) The value of solar tariff: net metering 2.0. 2013. Elisabeth Haub School of Law at Pace University
10. Branker K, Pathak MJM, Pearce JM (2011) A review of solar photovoltaic levelized cost of electricity. *Renew Sustain Energ Rev* 15:4470–4482
11. Szabó S, Jäger-Waldau A, Szabó L (2010) Risk adjusted financial costs of photovoltaics. *Energ Pol* 38:3807–3819
12. Dufo-López R, Bernal-Agustín JL (2013) Photovoltaic grid parity in Spain. In: *Lecture notes in electrical engineering*, vol 178. Springer: Berlin/Heidelberg, Germany. ISBN 9783642315275
13. Sarasa-Maestro CJ, Dufo-López R, Bernal-Agustín JL (2013) Photovoltaic remuneration policies in the European Union. *Energ Pol* 55:317–328
14. Helms T, Salm S, Wüstenhagen R (2015) Investor-specific cost of capital and renewable energy investment decisions. In: Donovan CW (ed) *Renewable Energy Finance*, Imperial College Press, London, pp 77–101
15. Pena-bello A, Burer M, Patel MK, Parra D (2017) Optimizing PV and grid charging in combined applications to improve the profitability of residential batteries. *J Energ Storage* 13:58–72
16. Jäger K, Isabella O, Smets AHM, van Swaaij RACMM, Zeman M (2014) Solar energy fundamentals, technology, and systems. Delft University of Technology
17. Chawla K, Aggarwal M (2012) Anatomy of solar tariff, council of energy, environment, and water. CEEW Policy Brief CEEW Publications, New Delhi, India
18. Gulaliyev MG, Mustafayev ER, Mehdiyeva GY (2020) Assessment of solar energy potential and its ecological-economic efficiency: Azerbaijan case. 12:1116
19. Li Y, Gao W, Ruan Y (2018) Performance investigation of grid-connected residential PV-battery system focusing on enhancing self-consumption and peak shaving in. *Renew Energ* 127:514–523
20. Nengroo SH, Kamran MA, Ali MU, Kim D, Kim M, Hussain A, Kim HJ (2018) Dual battery storage system: an optimized strategy for the utilization of renewable photovoltaic energy in the United Kingdom. *Electronics* 7:177

# Chapter 11

## Advances in Hybrid Solar System



**P. Vipin Das, Navneet K. Singh, Rakesh Maurya, Asheesh K. Singh,  
and Sri Niwas Singh**

### 11.1 Introduction

Today, the substantial growth of renewable energy source (RES) is increasingly prominent to cope with issues such as global energy security, environmental pollution issues, and achieving sustainable development. Wind generation, solar PV, bio-fuel, geothermal, and hydropower stations are the major contributors among the various RESs [1–3]. However, the meteorological conditions-dependent RES, e.g., solar PV and wind power, are characterized by strongly intermittent generation.

The capacity of various RESs is shown in Fig. 11.1 [4]. Among the various RESs, solar PV is selected as a candidate in this chapter, being the most accessible type of RES. Table 11.1 shares the advantages of using solar PV over other RESs. The recent development and increment in solar PV across the globe are given in [5]. The recent development in technology and solid-state electronics caused drastic development in the operation and control of solar PV system [6]. Material development also accelerates the development of solar PV. Many types of solar PV cells are available in the market today. Polycrystalline, mono-crystalline, amorphous silicon, cadmium telluride solar cell, and bio-hybrid solar cell are the major types of solar PV cells available in the market [7]. At present, the solar system is used in two applications based on the technology. The first one is solar thermal technology, using in the heating application, and the other one is solar PV uses in power generation applications. This chapter deals with solar PV systems and their applications in power systems [8].

---

P. Vipin Das (✉) · N. K. Singh · A. K. Singh  
Motilal Nehru National Institute of Technology Allahabad, Allahabad, India  
e-mail: [vipindas504@gmail.com](mailto:vipindas504@gmail.com)

R. Maurya  
Sardar Vallabhbhai National Institute of Technology Surat, Surat, India

S. N. Singh  
IIT Kanpur, Kanpur, India

**Fig. 11.1** Status of RESs around the globe. *Source* Author

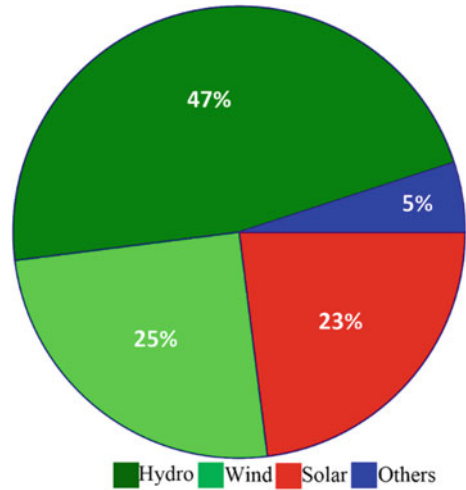


**Table 11.1** Shortcomings of other RESs over solar PV

Small hydro	Wind	Biomass
<ul style="list-style-type: none"> <li>• Large investments and tie required to develop the dams</li> <li>• Building the dam may affect the ecosystem</li> </ul>	<ul style="list-style-type: none"> <li>• The variation in wind pattern is varying significantly with respect to location</li> <li>• Specific location is required to install wind farm</li> <li>• The wind farm location can be far from the load centers</li> </ul>	<ul style="list-style-type: none"> <li>• The burning of biomass creates environmental pollution</li> </ul>

*Source* Author

In power system applications, the solar PV system is available in grid-connected and off-grid topologies [9]. In the grid-connected applications, the solar PV system is intended to provide power to the loads, but delivering the excess power to the utility, based on the agreement. In the off-grid (also known as a stand-alone system) application, the solar PV system will deliver the power to a particular load or a community load. However, the intermittent nature of power generation by the solar PV is the significant drawbacks of the system, which is being attempted to mitigate using the maximum power point tracking (MPPT) system [10].

There are several research works available on MPPT techniques and operation. Perturb and observe MPPT, incremental conductance MPPT, fractional open-circuit voltage MPPT, short circuit current MPPT, and some soft-computing-based MPPT are among the most common MPPT techniques available for solar PV system [11]. The power-electronic converters, such as DC-DC unidirectional converters, DC-DC bi-directional converters, and inverters, have become a vital part of the solar PV system. The efficiency of the power-electronic converters has a direct effect on the solar PV system performance. Also, many control strategies are developed to

improve the performance of power-electronic converters [12]. These controllers and converters jointly improve the solar PV system performance.

Various technical/material developments in energy storage systems (ESS) help to increase the deployment of solar PV in power system applications. Battery ESS and supercapacitors are the most commonly used ESS in solar PV applications. However, research papers are available based on other ESS, such as superconducting magnetic energy storage, pumped hydro, and flywheel energy storage [13]. The use of ESS helps to increase the self-consumption of solar PV generated power, thus, improve the overall system efficiency. The use of ESS imposes the application of an energy management system (EMS) in the solar PV system. The EMS is the control strategy for charging/discharging the battery efficiently, depending on the load demand and power available from solar PV [14].

For solar PV utilization, with its maximum benefits, there are several control algorithms developed by researchers [15]. The energy management system (EMS), maximum power point tracking (MPPT), and inverter control are the common controllers used in the solar PV system. In the following section, each control strategy is reviewed extensively.

Hybridization with other RESs is another solution to cope up with the intermittent nature of the solar PV system. There are several examples of hybridizing, the solar PV system with the wind turbine, fuel cell, small hydropower plant, and many other RESs, for performance improvement.

However, very efficient and intelligent control techniques are required in such a system to operate. The works available in the literature present many hybridized solar PV system. The hybrid solar PV system is mainly used in stand-alone solar PV generating stations. In grid-connected solar PV applications, there are several factors to handle [16]. The frequency and voltage violation at the point of common coupling are the significant issues faced during the interconnection of the solar PV with the grid. This variation may result in a grid collapse, which may lead to a blackout. These grid connection issues can be solved using proper grid synchronization techniques [17]. There are many phase-locked loop techniques available to synchronize the solar PV system with the grid—among which, some techniques are reviewed in this chapter. The power quality (PQ) issues, islanding, and standards related to grid-connected PV are discussed in detail. Here, various power-electronic converters and their control mechanisms are also reviewed. The Indian and international guidelines and standards for solar PV hybrid systems are explained to understand the global phenomenon of solarization. Finally, the simulation results are presented to provide better insight for readers regarding operation and control of the solar PV HPS.

## 11.2 Integration of Solar PV in Distributed Generation

There are two different architectures to integrate solar PV to the power system, namely stand-alone and grid-connected architecture. This section extensively reviews the various combinations of different RES and ESS with the solar PV.



### ***11.2.1 Grid-Connected Solar PV***

In a solar-grid structure, the solar PV is connected directly to the grid through power-electronic interfaces. This configuration is extensively reviewed in the literature and gained the attention of several researchers [18]. There are several standards available to integrate solar PV to the grid, defined by various national and international agencies [19]. Depending on the power range and power-electronic interface configuration, the four types of grid-connected configurations are shown in Table 11.2. These are available with/without an energy storage system (ESS) [20].

### ***11.2.2 Grid Synchronization***

There are several methods available to synchronize the solar PV system with the grid [21]. The main objective of synchronization is to match the frequency, magnitude, and phase angle of the solar PV inverter with the same parameters on the grid side. The various phase-locked loop (PLL) techniques are available in the literature to synchronize the solar PV with the utility grid [22].

### ***11.2.3 The Phase-Locked Loop (PLL)***

Phase-locked loops (PLL) are the most commonly used techniques for synchronizing incoming time-variable signals to the grid. The PLL consists of three basic blocks, such as phase detector, loop filter, and voltage-controlled oscillator, as shown in Fig. 11.6. The input voltage at the PCC is fed to the phase detector, to be compared with the voltage output of the voltage-controlled oscillator for producing the error signal. The loop filter filters this error signal. Among, several topologies available in the literature; some important PLLs are summarized in Table 11.3.

### ***11.2.4 Impact of Integrating Solar PV to the Grid***

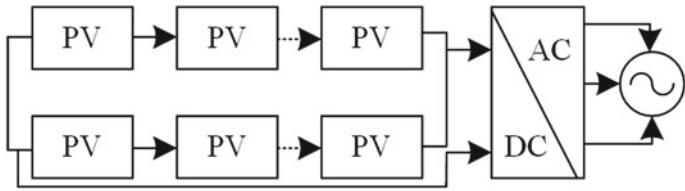
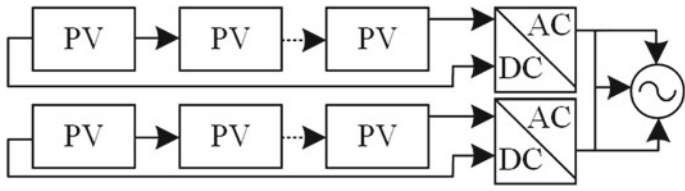
The high penetration of solar PV to the grid can create various negative impacts on the grid. The significant impacts of solar PV integration to the grids may result in (i) power quality (PQ) issues, (ii) increased reactive power requirement, and (iii) islanding.

#### **(a) Power quality issues**

Harmonics are the primary PQ issues caused due to integration of the solar PV system into the grid. The presence of inverter causes harmonics during the DC/AC conversion in system containing nonlinear loads. These harmonic currents introduce voltage drops in the system, further resulting in waveform distortion of the supply

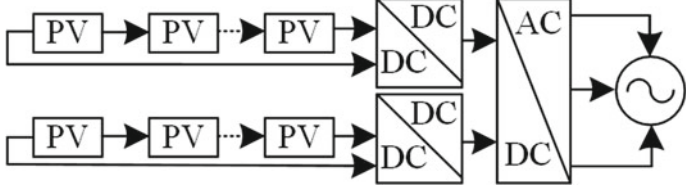
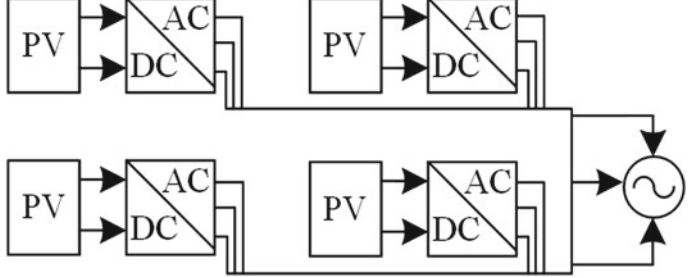
voltage. Also, the presence of harmonics in the system causes resonance in the power system, leading to malfunctioning and permanent failure of the equipment. Several controllers are available in the literature to mitigate harmonics caused by solar PV inverters [23]. The most common PQ issues of the Indian power system are addressed in [24].

**Table 11.2** Various topologies of the grid-connected solar PV system

<i>i. Central topology configuration</i>	
Configuration	 <p><b>Fig. 11.2</b> [19]</p>
Description	The series and parallel combinations of solar PV modules are connected to a central inverter. This topology is used in power ranges 100–1000 kW
Benefits	The centralized inverter is easy to control and employed for high-power applications
Drawbacks	Since it uses large DC cables, the cable losses are more, damage of single string can cause shut down of the power plant, high installation cost, MPPT become non-reliable due to different $V-I$ characteristic of various solar PV modules
<i>ii. String topology configuration</i>	
Configuration	 <p><b>Fig. 11.3</b> [19]</p>
Description	The solar PV modules are connected in series to form the string, and each string is connected to different inverters. This configuration is typically used for the power ranges 0.4–2.0 kW
Benefits	The MPPT is more reliable than the central configuration, system robustness increased
Drawbacks	Due to the presence of inverters, the system is bulky, high installation cost, and the cable losses are still high due to the presence of large DC cables
<i>iii. Multi-string topology configuration</i>	

(continued)

**Table 11.2** (continued)

<p>Configuration</p>	 <p><b>Fig. 11.4</b> [19]</p>
<p>Description</p>	<p>The solar PV modules are connected in series to form a string, and each string is connected to DC-DC converters. These DC-DC converters are connected in parallel, and this output is connected to a central inverter. This configuration is typically used in the power range of 1.5–6.0 kW</p>
<p>Benefits</p>	<p>The MPPT is more reliable than the central configuration; consequently, system robustness increased</p>
<p>Drawbacks</p>	<p>The bulky system, the presence of DC-DC converter increases system cost</p>
<p><i>iv. AC modules topology configuration</i></p>	
<p>Configuration</p>	 <p><b>Fig. 11.5</b> [19]</p>
<p>Description</p>	<p>Each solar PV modules are connected with separate inverters, and these inverters are connected and finally integrated with the grid</p>
<p>Benefits</p>	<p>Simple configuration, increased system reliability</p>
<p>Drawbacks</p>	<p>The bulky and costly system</p>

**(b) Increased reactive power requirement**

Usually, the solar PV inverters are operated at unity power factor, as, the small residential solar PV prosumers produce solar PV energy to gain more incentives based on their kWh yield, not on the kVAR yield. As a result, the reactive power requirements met by the solar PV system becomes minimal, which forces the grid

to supply more reactive power. It makes the distribution transformers to operate at low-power factor [25]. Several controllers are available in the literature to mitigate this drawback [26].

(c) **Islanding**

Islanding is the condition when the load is supplied by the solar PV system, in the absence of a grid. This is a dangerous situation, which is harmful for the personals during maintenance of the grid. To avoid such situations, the solar PV inverter shall be capable to detect the islanding, and disconnect the solar PV system during a grid downtime. This ability of solar PV inverter is known as anti-islanding. Several anti-islanding methods are available in the literature [27].

### 11.2.5 Standards for Grid-Connected Solar PV System

Various agencies/institutions provided specific standards and regulations for the grid-connected solar PV system. Some of the important standards are reviewed and tabulated in Table 11.4 [28].

### 11.2.6 PV-Based Stand-alone System

The stand-alone solar PV system is indented to supply loads in an isolated area, where the conventional grid is absent. There are several configurations of stand-alone solar PV systems available in the literature [29]. Some of the stand-alone configurations are reviewed here.

(a) **Solar-battery system**

A stand-alone solar PV–battery hybrid power system is shown in Fig. 11.12, where battery is used to mitigate the intermittency of the solar PV generation [30]. Generally,

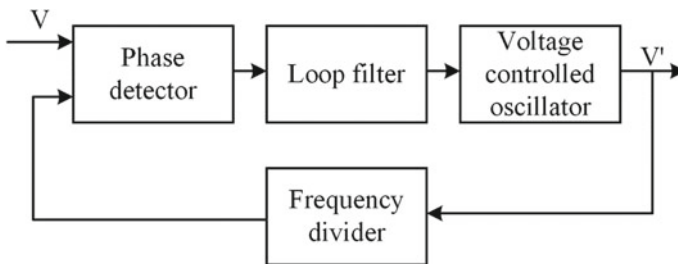


**Fig. 11.6** Generalized block diagram of PLL [19]

**Table 11.3** various PLL topologies

i. SRF PLL

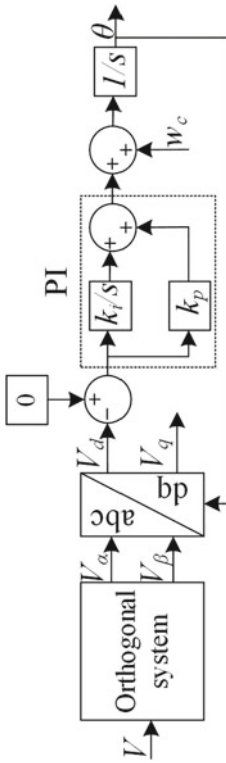


**Fig. 11.7** Synchronous reference frame (SRF) PLL [19]

Description

The working of the system is based on the SRF theory. The three-phase voltage signal is converted to the direct- and quadrature-axis components. The direct axis component is passed through the PI controller to generate the phase angle

(continued)

Table 11.3 (continued)

ii. ZCD PLL

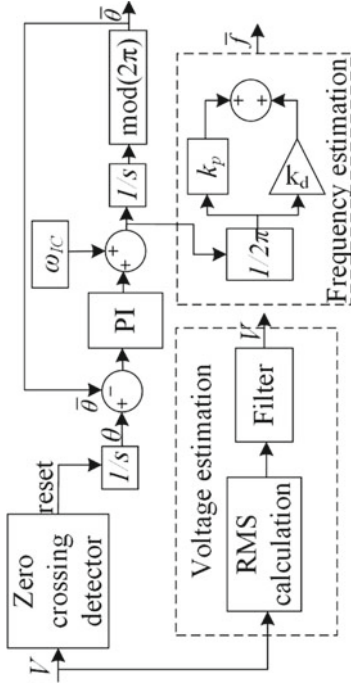


Fig. 11.8 Zero crossing detector (ZCD) PLL [19]

Description

The reference phase angle in this PLL is generated by the ZCD method. The reference phase angle is compared with the actual values; a zero error signal indicates the proper synchronization

(continued)

Table 11.3 (continued)

iii. HT PLL

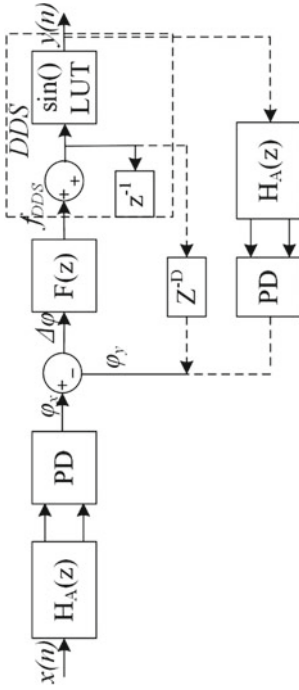


Fig. 11.9 Hilbert transform (HT)-based PLL [19]

Description

Here, the reference phase angle is generated by the Hilbert transform. The working principle is the same as that of other PLL types

(continued)

Table 11.3 (continued)

iv. PT PLL

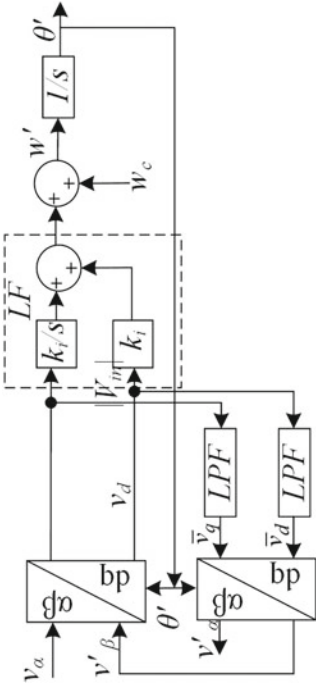


Fig. 11.10 Parks transformation (PT)-based PLL [19]

Description

The Parks transformation is used to convert the three-phase voltage to direct- and quadrature-axis components

(continued)



Table 11.3 (continued)

i. CT PLL

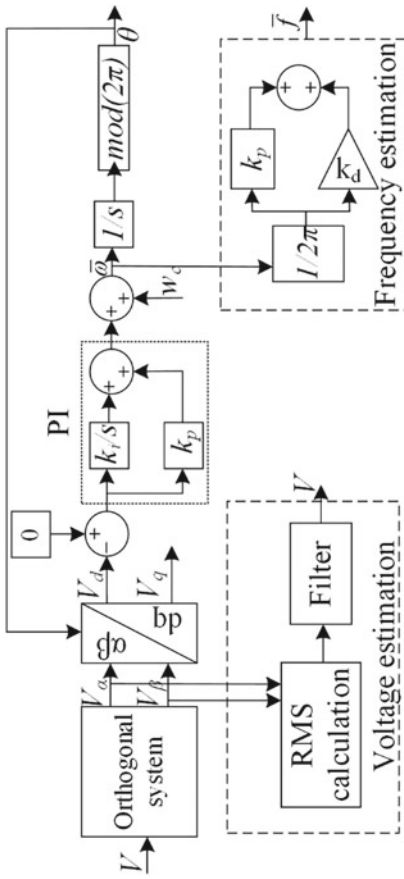


Fig. 11.11 Clark's transformation (CT)-based PLL [19]

Description

The Clarks transformation is used to convert the three-phase voltage to direct- and quadrature-axis components

**Table 11.4** Standards for integrating solar PV system with the grid

Standard	Title
<i>Grid integration</i>	
IEEE 1547-2003	“Standard for Interconnecting Distributed Resources with Electric Power Systems”
DIN EN 50530 2011	“Overall efficiency of grid-connected photovoltaic inverters”
IEEE, 2030, 2011	“Draft guide for smart grid interpretability of energy technology and information technology operation with the electric power system, and end-user applications and loads”
IEC 62446 2009	“Grid-connected photovoltaic systems—Minimum requirements for system documentation, commissioning tests, and inspection”
<i>Solar PV converters</i>	
IEC 61727 2002	“Photovoltaic (PV) systems Characteristics of the utility interface”
DIN EN 61683 2000-08	“Photovoltaic systems Power conditioners Procedure for measuring efficiency (IEC 61683:1999)”
IEEE 921, UL1741 2010	“Standards for inverters, converters, and controller for use in the independent power system”
<i>Testing and design</i>	
CEI 62124 2004	“Photovoltaic (PV) stand-alone systems—Design verification”
DIN EN 62108 (VDE 0126-33) 2008-07	“Concentrator photovoltaic (CPV) modules and assemblies Design qualification and type approval (IEC 62108:2007)”
IEEE 1547.1 2005	“Standard for conformance test procedures for equipment interconnecting distributed resources with the electric power system”
<i>Measurements</i>	
IEEE 929, 2000	“Recommended practice for utility interface of the photovoltaic system”
IEC 61000-4-15 2010	“Electromagnetic compatibility testing end measurement technique”
IEC 60904-8, 2014	“Photovoltaic devices—Part 8: Measurement of spectral responsivity of a photovoltaic (PV) device”
IEC 61829 2015	“Photovoltaic (PV) array On-site measurement of current-voltage characteristics”
IEC 61724 1998	“Photovoltaic system performance monitoring Guidelines for measurement, data exchange, and analysis”

(continued)

**Table 11.4** (continued)

Standard	Title
IEEE 512, 1999	“IEEE recommended practices and requirements for harmonic control in electrical power systems”
EN 50160, 1999	“Public distribution voltage quality”
<i>Islanding procedure</i>	
IEC 62116 2008	“Utility-interconnected photovoltaic inverters—Test procedure of islanding prevention measures”
DIN EN 62116 (VDE 0126-2): 2012	“Test procedure of islanding prevention measures for utility-interconnected photovoltaic inverters (IEC 62116:2008, modified)”
IEC 60364-7-712 2002	“Electrical installations of buildings—Part 7-712: Requirements for special installations or locations—Solar photovoltaic (PV) power supply systems”
<i>Safety precautions</i>	
VDE 0126-1-1 2006	“Automatic disconnection device between a generator and the public low-voltage grid”
IEC 60269-6, 2014	“Low-voltage fuses—Part 6: Supplementary requirements for fuse-links for the protection of solar photovoltaic energy systems”
IEC 62109-1, 2010	“Safety of power converters for use in photovoltaic power systems—Part 1: General requirements”
DIN EN 61730-2 2007–10	“Photovoltaic (PV) module safety qualification—Part 2: Requirements for testing (IEC 61730-2:2004, modified)”

Source Author

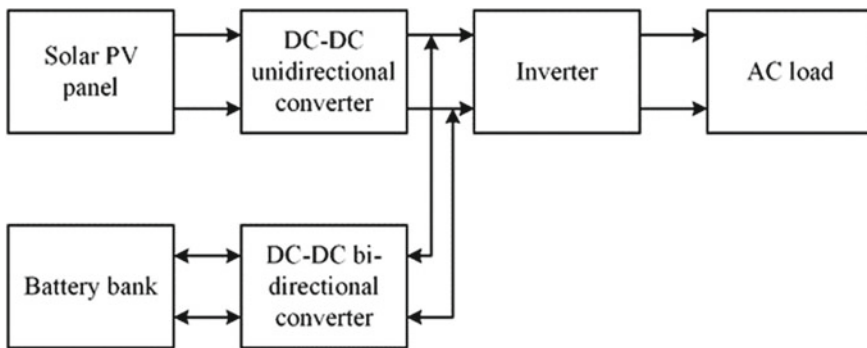


**Fig. 11.12** Stand-alone solar PV ESS HPS. Source Author

solar PV is supposed to meet the load demand. Still, in some of the cases, the power production from solar PV becomes lesser than the load demand depending on the solar irradiance. In such cases, the battery is responsible to provide power to the load. The working of this system is based on a power management system (PMS). The PMS continuously measures the load power and solar PV power. If the solar PV power is higher than the load power, the excess power is stored into the battery. However, if the solar PV power is lesser than the load power, the battery supplies the load demand. There are several control algorithms available in the literature to execute PMS in the solar PV-battery hybrid power system [31].

**(b) Solar-wind-energy storage system**

Solar-wind-energy storage system stand-alone HPS is widely exploited in literature [32]. Since the RES are stochastic due to climate dependency, an energy storage system (ESS) is necessary in this case. The typical configuration of such HPS is shown in Fig. 11.13. In this case, similar to the case of solar PV-battery power system, the priority will be given to solar PV and wind sources. In the absence of these RESs, the battery will support the load using a PMS [31]. In literature, various ESS such as supercapacitors, battery, and superconducting magnetic energy storage are used in this configuration [33].

**(c) Solar-diesel system**

Hybridization of solar PV with diesel generator is the most commonly available configuration among the various solar PV-based HPS. In this case, the priority for meeting the load will be given to solar PV due to its clean power production. In the

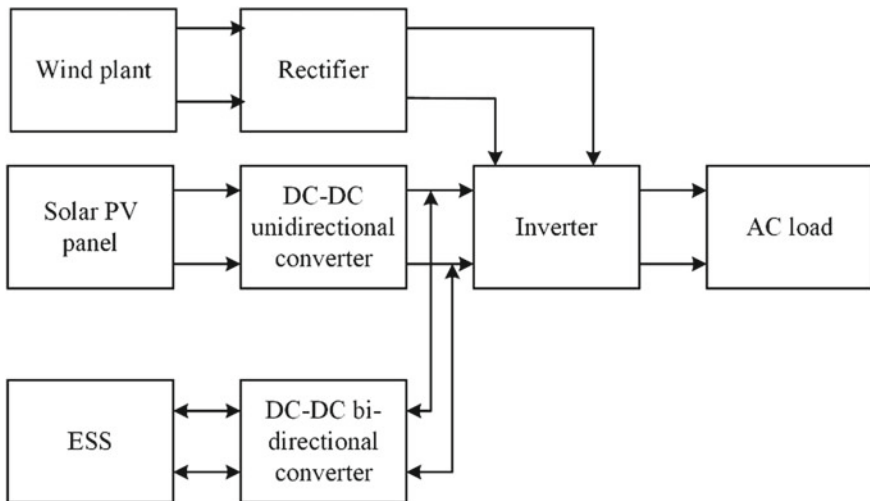


**Fig. 11.13** Stand-alone solar PV/wind/ESS HPS. *Source* Author

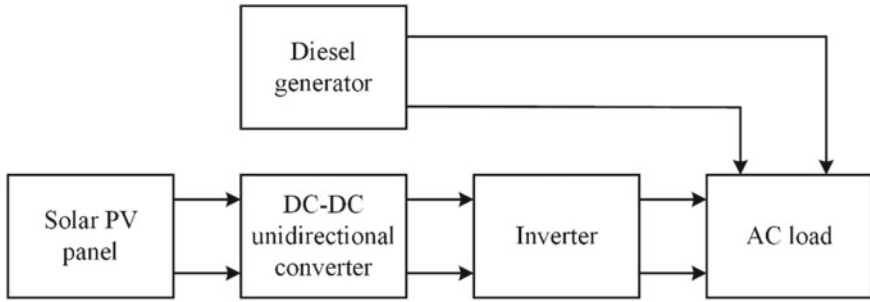


**Fig. 11.14** Stand-alone solar PV/diesel generator HPS. *Source* Author

absence of solar PV, the diesel generator will support the load. A configuration of this HPS is shown in Fig. 11.14 [34].

**(d) Solar-fuel cell system**

In recent years, the solar PV hybridization with a fuel cell (FC) has become very popular [35]. The development in the FC accelerates the use of this configuration. This configuration becomes most eco-friendly when the hydrogen fuel for the FC is generated using the solar PV. Similar to the case of solar PV-battery HPS. Here, the excess solar PV power generation is used to produce hydrogen, and the produced hydrogen is stored in the hydrogen tanks. This stored hydrogen can be used as fuel for the FC during off solar PV hours. Thus, the continuity in supply can be maintained. A configuration of this HPS is shown in Fig. 11.15.

Apart from these configurations, several other configurations of stand-alone solar PV HPS can be seen from various works of literature [36]. Table 11.5 presents a comparison of pros and cons of various available solar PV HPS.

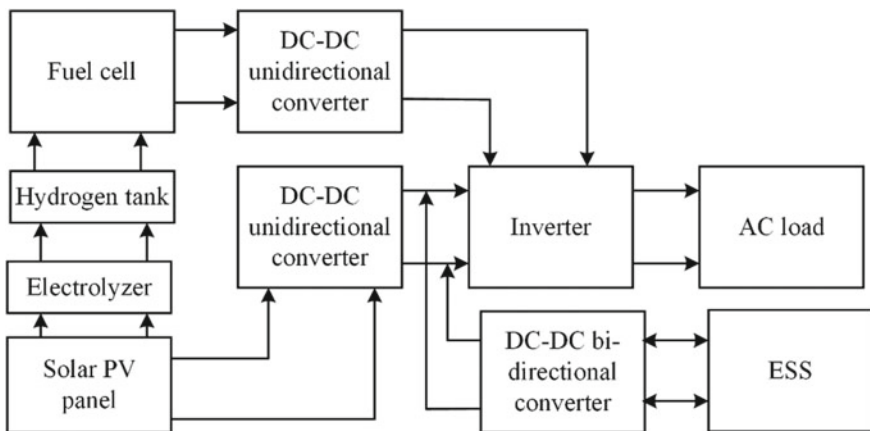


**Fig. 11.15** Stand-alone solar PV/fuel cell/ESS HPS. *Source* Author

**Table 11.5** Comparison of solar PV HPS topologies

Type	Topology	Pros	Cons
Grid-connected	Solar PV-wind [37]	<ul style="list-style-type: none"> <li>• Less expensive due to the absence of ESS</li> <li>• The net metering facility offsets the price for electricity used from the grid</li> <li>• Grid is a cost-effective system</li> <li>• The solar PV system proprietor can gain extra income by selling the power</li> </ul>	<ul style="list-style-type: none"> <li>• The system will become isolated in the absence of a grid</li> <li>• The reverse power flow from the solar PV system to the grid is dangerous during grid maintenance</li> </ul>
	Solar PV-wind-fuel cell [38]		
	Solar PV-wind-small hydro [39]		
	Solar PV-small hydro [40]		
Islanded system	Solar PV-wind-ESS [41]	<ul style="list-style-type: none"> <li>• A better solution to power areas, where the electricity network is not available</li> </ul>	<ul style="list-style-type: none"> <li>• The system is costly due to the presence of ESS</li> <li>• The intermittent nature of RESs make the system control strategy complex</li> <li>• The system highly depends on environment conditions</li> <li>• The surplus energy wastage can happen in case of low ESS capacity</li> </ul>
	Solar PV-diesel [42]		
	Solar PV-diesel-ESS [43]		
	Solar PV-wind-diesel [44]		
	Solar PV-wind-diesel-ESS [45]		
	Solar PV-fuel cell-ESS [46]		
	Solar PV-wind-fuel cell-ESS [47]		

Source Author

### 11.2.7 Policies of Indian Perspective

The development of RES in India begins with the establishment of the Commission of Alternate Sources of Energy (CASE) in 1981 by the department of science and technology (DST). Later, this commission changed to the department of new energy sources (DNES) in the year 1982 and became a full-fledged ministry in the year 1992. Now, the ministry of new and renewable energy sources (MNRE) is a responsible to develop policies and missions about RES under the government of India (GoI). The GoI has developed many missions to develop solar PV in the country; some of them are discussed briefly in [48]. Highlights of National Solar Mission in this concept are summarized below.

#### Jawaharlal Nehru National Solar Mission (JNNSM) 2010

The JNNSM, also known as the national solar mission, was developed as a plan of “National Action Plan on Climate Change (NAPCC).” This mission was planned to be accomplished in three phases. The phase-1 (2010–2012) planned to install

rooftop solar PV panels, and phase-2 (2013–2017) was the continuation of phase-1. By phase-3 (2017–2022), the GoI planned to achieve the installation of 100 GW solar PV. This JNNSM was revised in 2014 and to accomplish the target GoI planned many policies as below:

- Kisan Urja Suraksha evam Utthaan Mahabhiyan-planned for agriculture sector solarization.
- The MNRE issued guidelines for grouping solar PV inverters based on the Bureau of Indian Standards (BIS).
- The MNRE issued operational guidelines to implement phase-two of its grid-connected rooftop solar program, planning 22 GW of rooftop solar PV.
- The MNRE came out with new benchmark costs for off-grid SPV systems and solarization of grid-connected agricultural pumps for the year 2019–20.
- The MNRE issued new guidelines incorporating changes in the project timelines for the development of solar parks in the country.
- MNRE releases guidelines for installing an off-grid solar PV system in 2020.
- The guidelines for the integration of DER and grid connection are given in [49].

### **11.3 Advancements in Modeling and Applications of Hybrid Power Systems**

As discussed in Sect. 2, the integration of the solar PV system to the existing power system is accelerated by several policies and standards. The advancement in power-electronic and control technologies also helped to speed-up the solar PV deployment. In the following section, the various power-electronic converter topologies and control techniques developed for solar PV HPS are reviewed extensively.

#### ***11.3.1 Power Converters Topologies for the Solar PV HPS***

Power-electronic converters are the vital parts of a solar PV HPS, without which the integration of solar PV is impossible. Power-electronic converters for solar PV HPS can be broadly divided into three parts, viz., DC-DC unidirectional converter, DC-AC inverters, and DC-DC bi-directional converters. The various topologies of these converters are reviewed extensively in this section.

### 11.3.2 DC-DC Unidirectional Converter

The efficiency of power, which is delivered to the load/grid, is highly influenced by DC-DC unidirectional converter employed. The DC-DC unidirectional converters can be classified into two categories, non-isolated and isolated types.

#### (a) Non-isolated DC-DC unidirectional converters

The solar PV module voltage is generally very low and nonlinear in the range of 12–120 V. This low-voltage forces the application of DC-DC unidirectional converters. Among the DC-DC unidirectional converters, the boost type topologies are most widely used in solar PV applications due to their high gain. There are several boost type DC-DC unidirectional converter topologies that are available in the literature. Earlier, the conventional boost converters as shown in Fig. 11.16 were used in solar PV applications, but several topologies derived from these basic structures are available, also. Some of the derived boost converter topologies are reviewed in this section. The non-isolated DC-DC boost converters are again classified into three categories, based on the voltage gain and the power rating, as shown in the chart.

#### (b) Low gain low-power converters

This converter is used in low-power applications, where the less conversion ratio is required. The various topologies that lie under this category are explained in detail below.

##### 1. Conventional boost converter

The structure of a conventional boost converter is shown in Fig. 11.16. This converter consists of a diode, MOSFET as power-electronic switches and a capacitor, inductor as passive elements. The duty ratio of these converters is given in Eq. (11.1). To achieve high gain, this converter needs to be operated at an extreme duty ratio of

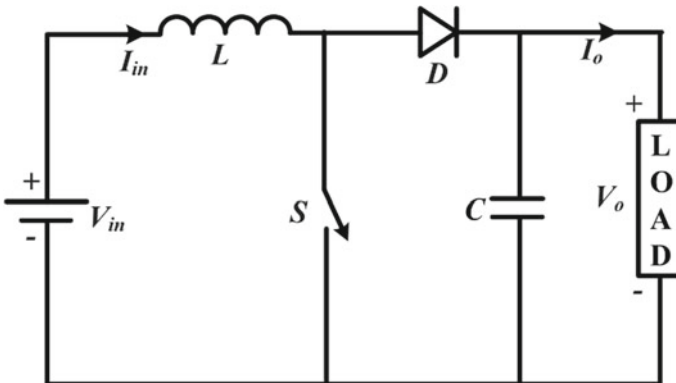
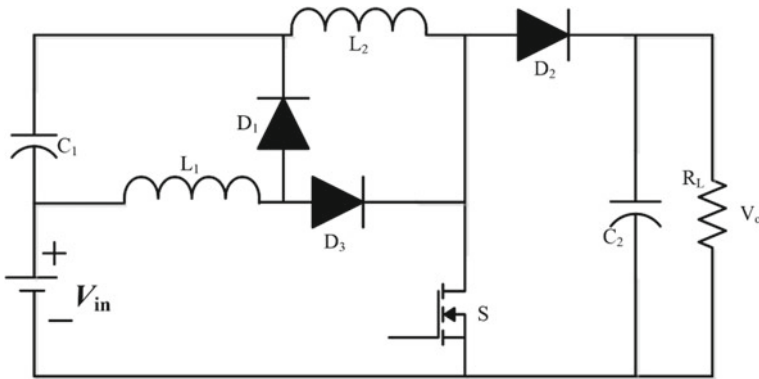


Fig. 11.16 Conventional boost converter [58]





**Fig. 11.17** Quadratic boost converter [58]

0.9, which is practically impossible due to the switching characteristics of diode and MOSFET switches. Thus, practically the duty ratio is limited in the range of 0.5–0.8 [50].

$$\frac{V_o}{V_{in}} = \frac{1}{1 - D} \quad (11.1)$$

## 2. Quadratic boost converters [51]

Figure 11.17 shows the structure of the quadratic type boost converter. The voltage gain of these converters is twice as that of conventional boost converters. So high voltage can be achieved with the same duty ratio. However, the maximum practical gain is limited to 10, beyond which the diode exhibits reverse recovery phenomenon.

## 3. Cascaded boost converter [52]

To achieve high gain, in some cases, the cascading of conventional boost converters are used. The primary issue related to this configuration is the low efficiency, due to the cascading. Their structure and operation are detailed in [52].

## 4. Integrated cascaded boost converter [53]

In this topology, the two switches are integrated to reduce the control complexity.

A comparison of low gain low-power type boost converters, based on the voltage gain and component count, is presented in Table 11.6.

### (i) Low gain high-power converter

These converters are used in applications, where high power and low voltage are required. The interleaved boost converter is the most popular type of low gain high-power converter. The interleaved boost converters are reviewed from many works

**Table 11.6** Comparison of low gain low-power DC-DC boost converter

Topology	Voltage gain	Component count
Conventional boost converter	Less than 5	4
Quadratic boost converter	4	8
Cascaded boost converter	5	8
Integrated cascaded boost converter	10	9

*Source* Author

available in the literature [54]. These converters are developed by interleaving of the switches and components in the conventional boost converter. The voltage gain of these converters is the same as that of the conventional boost converters, but the power rating increased due to the interleaving technology. The interleaving technology additionally helps to reduce the input and output current ripples [54]. Depending on the number of interleaved switches, the interleaved boost converters can be classified as two-phase, three-phase, and four-phase converters. The low gain of the order of 5 is the drawback of these converters.

## (ii) High gain low-power converters

There are several topologies of high gain low-power boost converters available in the literature. Some of the critical converters under this category are discussed here.

### 1. Three-level boost converters [55]

The three-level boost converter gain is twice as that of the conventional boost converter. The voltage stress experienced by the switches is half in comparison with the conventional boost converter. However, due to the high voltage gain, the reverse recovery problem in the diode is severe in this converter.

### 2. Voltage doubler [56]

The circuit diagram of the voltage doubler topology is shown in Fig. 11.18. The voltage output of these converters is double as that of the input voltage. This converter consists of a diode and a capacitor. The capacitor stores the energy and discharge to the output as twice the input voltage.

### 3. Coupled inductor-based boost converter [57]

In this boost type converter, a coupled inductor is used either at the output stage or at the input stage. High voltage gains can be achieved in these type of converters by adjusting the turn's ratio of the coupled inductor. Several research papers are available on the design and development of these converters. Figure 11.19 shows the circuit diagram of the coupled inductor-based boost converter.

The other converters in these categories are summarized in Table 11.7. Many other derived boost converter topologies can be found in literature [58].

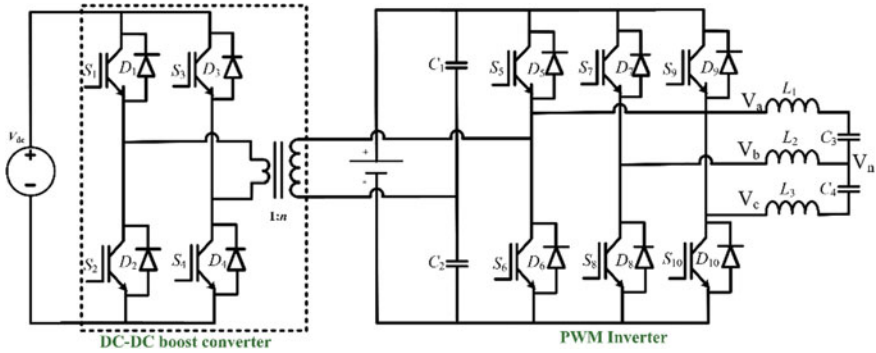


Fig. 11.18 Voltage doubler [58]

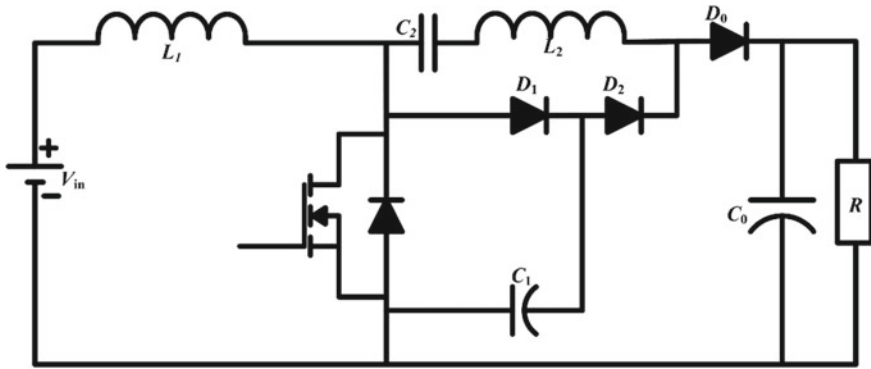


Fig. 11.19 Coupled inductor-based DC-DC boost converter [58]

(a) Isolated DC-DC boost converters

In this type of boost converters, the input stage is isolated from the output stage using high-frequency transformers or coupled inductors. Such isolation is necessary for grid-connected applications and the applications, where reliable power transfer with reduced electromagnetic interference is required [59]. With the help of transformers or coupled inductors, isolated converters with either a single-stage or two-stage can be developed [59]. Figure 11.20 shows the structure of a single-stage isolated DC-DC boost converter. Many topologies of isolated DC-DC boost converters with coupled inductors are reported in the literature [60]. In these type boost converters, the coupled inductor stores energy in one cycle and discharge in the next cycle [60]. A comparison chart of isolated and non-isolated type DC-DC boost converter is given in Table 11.8.

**Table 11.7** Summary of high gain low-power and high-power DC-DC boost converters

Topology	Voltage gain		Component count		Features
	Min.	Max.	Min.	Max.	
Voltage lift topology	9.5	15.3	12	15	<ul style="list-style-type: none"> <li>• Fewer voltage stresses</li> <li>• Reduced current ripple</li> <li>• Increased reliability with decreased component count</li> </ul>
Flying capacitor		5		7	<ul style="list-style-type: none"> <li>• Limited gain</li> <li>• High voltage stress</li> <li>• Simple structure</li> <li>• Not suitable for high current applications</li> </ul>
Multilevel switched capacitor (SC) technology	9	12	10	20	<ul style="list-style-type: none"> <li>• Modular structure</li> <li>• Fewer voltage stresses</li> <li>• Limited voltage gain</li> <li>• The higher number of components</li> </ul>
Voltage multiplier cell	9.5	15.8	10	22	<ul style="list-style-type: none"> <li>• High component count</li> <li>• Fewer voltage stresses</li> <li>• Limited gain</li> <li>• Poor voltage regulation</li> </ul>
Multiphase converters	5	9.5	9	26	<ul style="list-style-type: none"> <li>• Reduced device rating</li> <li>• More component counts</li> <li>• Less input current ripple</li> </ul>

Source Author

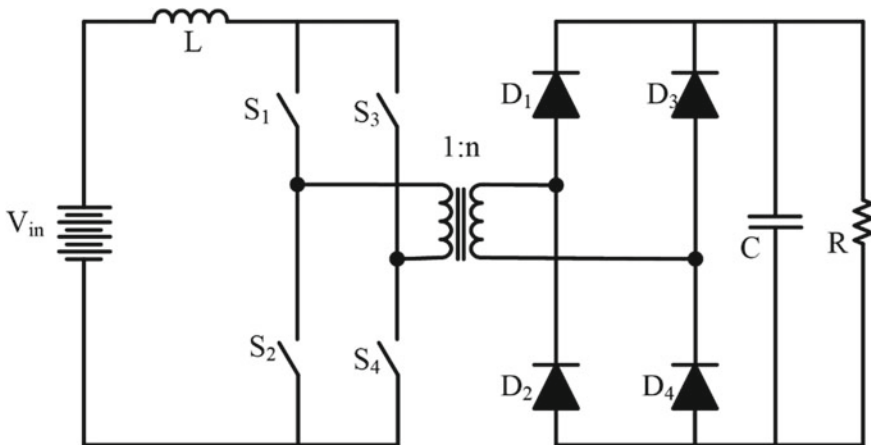


**Fig. 11.20** Isolated DC-DC boost converter [59]

**Table 11.8** Comparison between non-isolated and isolated boost converters

Non-isolated converter	Isolated converter
Simple structure • Less weight • Input and output stages are electrically connected • Suitable for low and medium power applications	High-power applications • Less electromagnetic interference • Input and output stages are electrically isolated • The coupled inductor needs to be designed carefully for high gain applications

Source Author

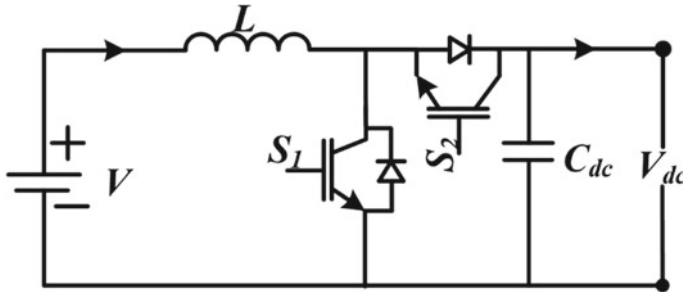


**Fig. 11.21** DC-DC buck-boost converter [59]

### 11.3.3 Bi-Directional DC-DC Converters

The increased use of ESS in HPS forces to use bi-directional type converters. The basic structure of the bi-directional converter is the buck-boost topology, as shown in Fig. 11.21. These converters work with the help of an EMS. If the solar PV power is greater than the load demand, then the buck mode of the buck-boost converter will be activated to store the excess energy to the ESS. During low solar PV generation time, the ESS discharges through the boost mode operation of the buck-boost converters. Dual active bridge (DAB) as shown in Fig. 11.22 is another useful and most popular bi-directional type converter used in solar PV applications. DAB converters are suitable for high-power applications [61]. The control strategy depends on the phase shift between the two AC voltage waveforms across the isolation transformer [62].

### 11.3.4 Inverters

Inverters in solar PV HPS is used for power conversion from DC to AC. The design of inverters needs extra care since it defines the quality of power injected into the grid. Three-phase and single-phase inverters are widely used in solar PV applications [63].

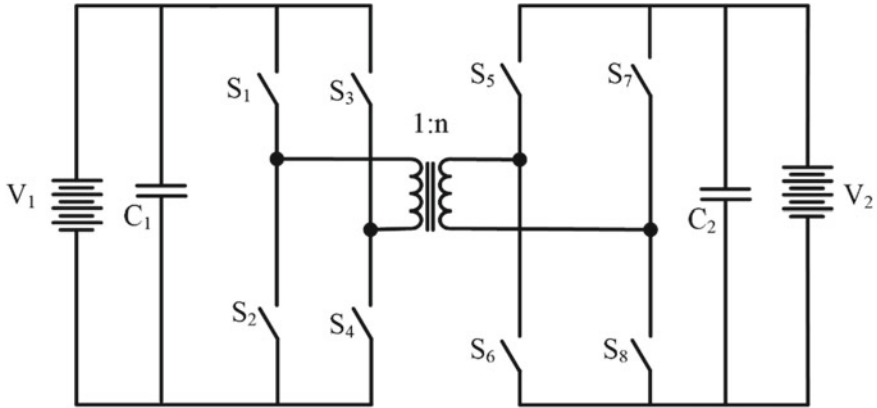


Fig. 11.22 DC-DC DAB converter [59]

(a) Full-bridge inverters

Full-bridge inverters are the most commonly used inverter for grid-connected solar PV applications. The basic structure of a full-bridge inverter is shown in Fig. 11.23. Unipolar, bipolar, and hybrid modulation strategies are applied in full-bridge inverters [64]. In some literature, the combination of unidirectional and bi-directional topologies is also used [65].

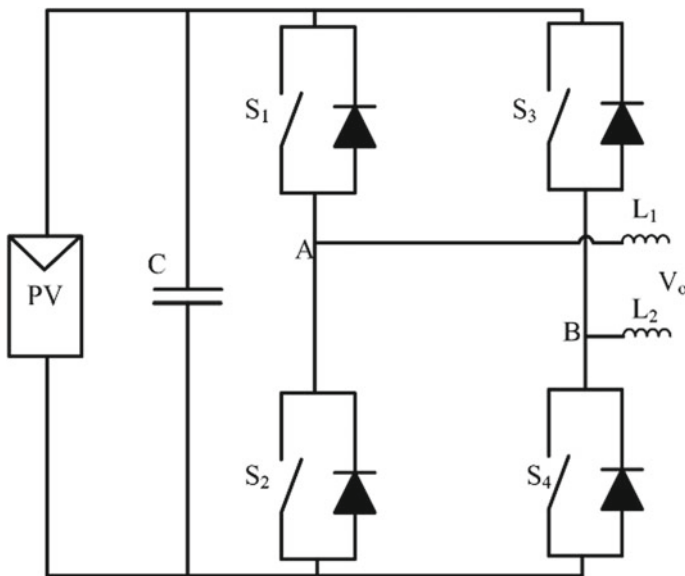


Fig. 11.23 Full-bridge inverter [19]

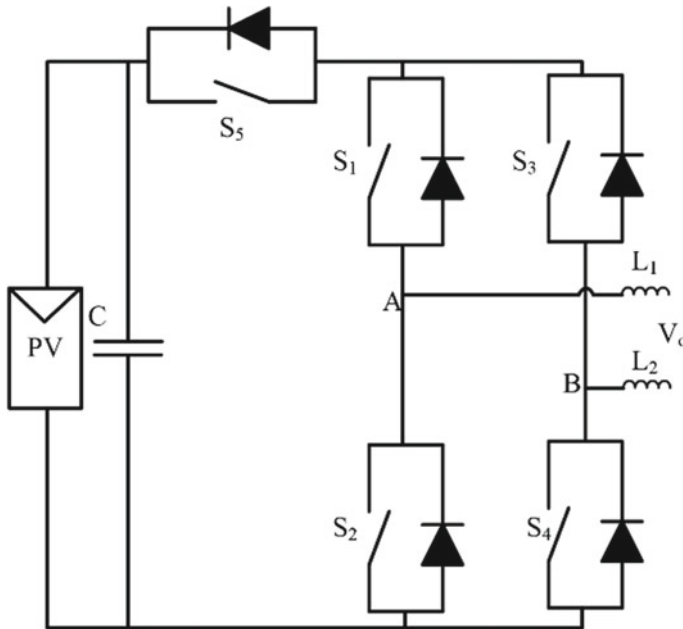


Fig. 11.24 H5 inverter [19]

(b) **H5 inverters**

H5 inverter topology is one of the most efficient inverter topologies applicable in solar PV HPS. It has another advantage of having common mode current. Figure 11.24 depicts the conventional H5 inverter topology. Many other derived H5 inverters topologies are also available in the literature [66].

(c) **HERIC inverters**

The HERIC stands for a *highly efficient and reliable inverter concept* [67]. The basic structure of the HERIC inverter is shown in Fig. 11.25. The HERIC structure is developed by inserting a bypass element at the AC side, as depicted in Fig. 11.25. This bypass element helps to control the reactive power exchange, thus, increases efficiency. The leakage current and electromagnetic interference in these inverters are shallow than other inverter topologies.

(d) **REFU inverter topology**

Figure 11.26 shows the circuit structure of a REFU inverter. This inverter is also developed by inserting a bypass element to generate zero voltage with the minimum loss [68]. This topology also featured with high efficiency and low leakage current as in the case of HERIC topology, as shown in Fig. 11.26.

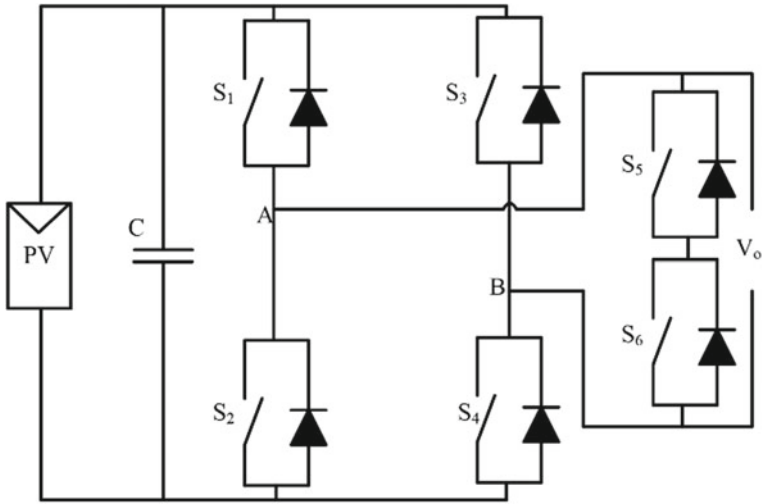


Fig. 11.25 HERIC inverter [19]

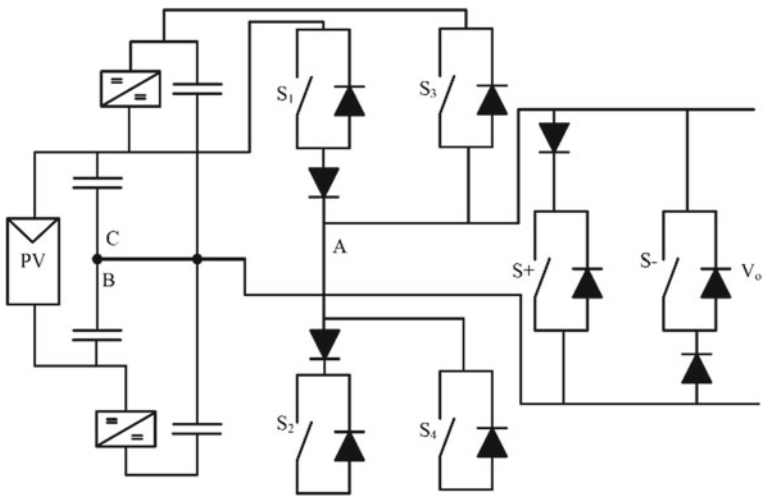


Fig. 11.26 REFU inverter [19]

(e) **Full-bridge zero voltage rectifier (FB-ZVR)**

The FB-ZVR is derived from the full-bridge topology. This converter is featured with high efficiency and zero voltage generation with minimal losses. The higher efficiency of 96% is achieved in this topology [69]. The primary circuit structure of this topology is shown in Fig. 11.27. This topology has advantages like low electromagnetic interference and leakage current.



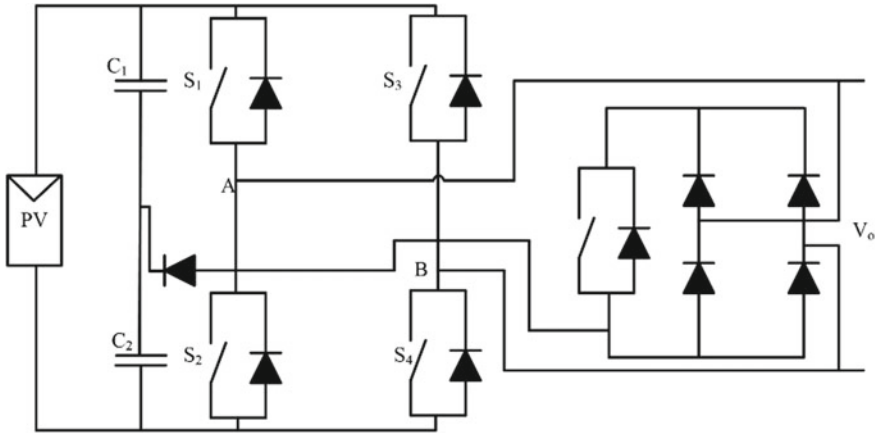


Fig. 11.27 Full-bridge zero voltage rectifier inverter [19]

(f) **Neutral point clamped (NPC) inverter**

This inverter topology is the typical type used in solar PV application due to its versatility and can be used as a three-phase and single-phase with different levels [70]. The structure of this topology is shown in Fig. 11.28. The NPC topology is featured with high efficiency, low leakage current, and almost zero EMI.

(g) **Flying capacitor inverter**

The structure of a flying capacitor inverter topology is presented in Fig. 11.29. The capacitor in this topology floats concerning the ground potential, which is the reason behind the name [71].

Other than the explained topologies, many derived inverter topologies such as cascaded bridge-type topologies, Z sourced inverter, and many other can be seen in the available literature [63].

## 11.4 Control Techniques

The development of new control techniques boosts the deployment of the solar PV system. This control system is the brain of the solar PV system based on which the entire system works. The control system in a solar PV can be classified into three major classifications, as explained in the following sub-sections.

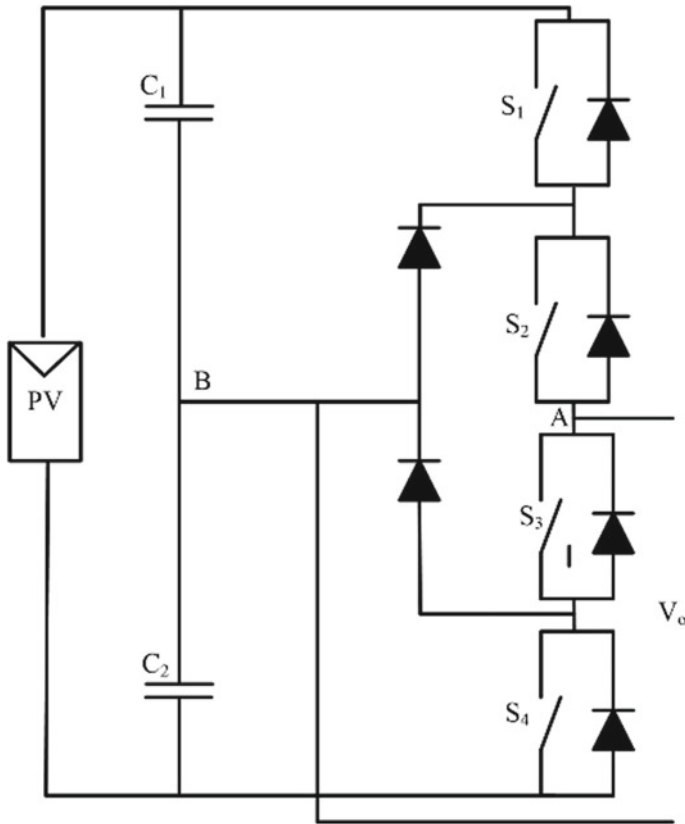


Fig. 11.28 Neutral point clamped (NPC) inverter [19]

### 11.4.1 Maximum Power Point Tracking Controllers

The MPPT controllers are an integral part of a solar PV system. The stochastic nature of solar PV power production forces the use of MPPT control to track the maximum power point concerning the irradiance variations [72]. The MPPT algorithm compares the generated PV voltage with the reference voltage corresponding to the maximum power to generate a switching signal for the DC-DC boost converter. There are several MPPT algorithms available in the literature; and most popular MPPT techniques are reviewed here, [73]. The MPPT techniques depend on three parameters, namely irradiance, temperature, and load. The  $I-V$ - and  $P-V$  characteristics of the solar PV system vary concerning irradiance and temperature, as demonstrated in Fig. 11.30. As discussed in the figure, the maximum power point will change concerning the irradiance and temperature level, and the MPPT controller tracks the maximum power during each irradiance and temperature levels.

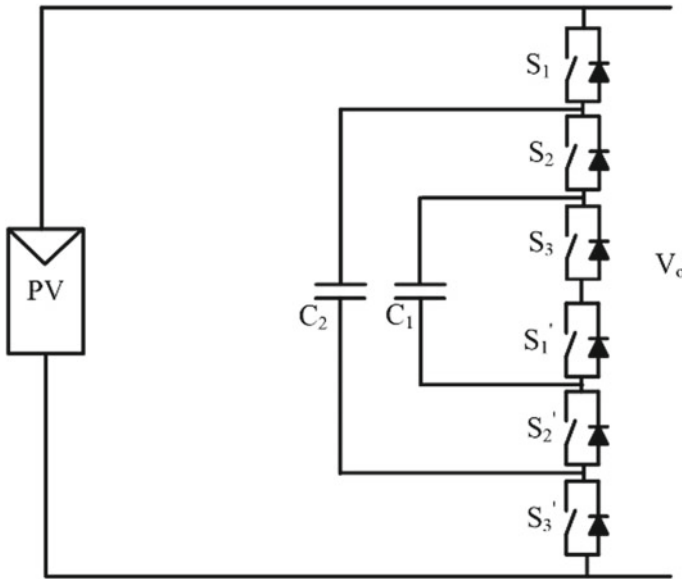


Fig. 11.29 Flying capacitor inverter [19]

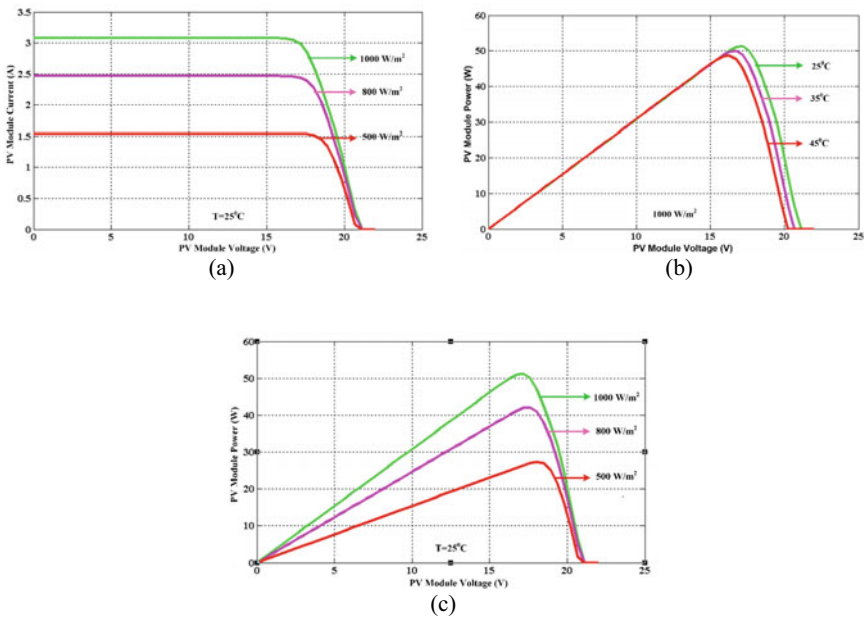


Fig. 11.30 Change in solar PV output **a**  $I$ - $V$  characteristics with change in irradiance, **b**  $P$ - $V$  characteristics with change in temperature, **c**  $P$ - $V$  characteristics with change in irradiance. *Source* Author

### (a) **Criteria for MPPT selection**

Since there are several methods to extract maximum power from the solar PV panel, the selection criteria of MPPT has become an important task. Some classifications, such as implementation, sensors, cost, and efficiency, are mentioned as some criteria for the selection of MPPT in literature [74]. Each criterion is explained briefly as follows;

- (i) **Implementation:** Implementation deals with the easiness of practical implementation of the MPPT in the solar PV system. Some MPPT methods are straightforward to implement, and some are very complicated in terms of controller complications. The researcher should know about the complexity of each MPPT before implementing it.
- (ii) **Sensors:** The number of sensors is another factor to be considered for precise tracking of the maximum power. The sensors are used to sense the temperature, irradiance, voltage, and current output from the solar PV panel, so a minimum of four sensors are required for accurate tracking. Some modified MPPT are available in the literature with a reduced number of sensors.
- (iii) **Cost:** Minimization of cost is the main aim of every researcher in the modern world. The cost of MPPT depends on the methodologies and the number of sensors required. To reduce the cost, one should use an MPPT technique having reduced number of sensors with reduced control complexity.
- (iv) **Efficiency:** Efficiency of the MPPT is defined as the ability to track maximum solar PV power accurately. Some MPPT techniques will oscillate at the maximum power point, which will reduce the overall efficiency of the entire solar PV system.

### (a) **Classification of MPPT**

The MPPT is classified according to the tracking strategy. The various MPPT available in the literature are tabulated in Table 11.9:

There are several other MPPT controllers are available in the literature [94]. The explanation for these techniques is omitted here, due to space constraints.

## ***11.4.2 Solar PV Inverter Control***

### (a) **Pulse width modulation techniques**

Pulse width modulation (PWM) is the standard technique used to generate switching pulses for inverters. PWM generates pulses with constant amplitude by modulating the carrier signal with the reference signal. Generally, square wave or sinusoidal waves are used as the reference signal, and sawtooth or triangular signals are used as carrier signals [95].

**Table 11.9** Various MPPT techniques practiced in solar PV system

Tracking techniques	Tracking methods	Description
Constant parameter tracking	Constant voltage method [75]	In this method, the voltage of the solar PV panel is regulated to the maximum point by comparing it with a fixed reference voltage. This is the simplest MPPT technique
	Open-circuit voltage [76]	This MPPT technique works on the relation; i.e., the open-circuit voltage of solar PV is directly proportional to the maximum power point voltage ( $V_{MPP}$ ). The MPPT system continuously measures the open-circuit voltage and update the $V_{MPP}$ accordingly
	Short circuit current [77]	Similar to the open-circuit voltage method, this MPPT technique is based on the linear relation between current at maximum power point ( $I_{MPP}$ ) and the short circuit current. The MPPT continuously monitors the short circuit current and update the $I_{MPP}$ accordingly
	Temperature gradient [78]	This MPPT technique is based on the relation between the open-circuit voltage and temperature gradient. The MPPT continuously monitors the temperature change and updates the MPP same in the case of the open-circuit voltage method
	Current/voltage feedback [79]	This method is similar to the constant voltage method. The MPPT technique is based on the comparison between actual solar PV current (voltage) and reference current (voltage)
Tracking based on measurements and comparison	Look-up table [80]	This tracking is based on the predefined temperature and irradiance values. The controller cross-checks the saved values and updates the MPP based on each climatic condition

(continued)

**Table 11.9** (continued)

Tracking techniques	Tracking methods	Description
	Load I/V maximization [81]	This is based on the optimization technique. Here, the controller tries to maximize the load voltage and current. Ultimately, this will result in maximizing the solar PV output
Trial and error tracking	Perturb and observe (P&O) [82]	This is the most commonly used MPPT technique. In this method, the control system will keep on searching the PV curve to obtain the MPP. There are several derived P&O MPPT techniques available in the literature
	Three-point weight comparison [83]	This is one of the improved versions of P&O MPPT technique. In this, the control algorithm will check only three points on the PV curve
	Online MPP search [84]	In this method, the control algorithm will compare the maximum reference power with the actual power and obtain the MPP when the difference between reference power and actual power becomes zero
	Droop control [85]	In this method, the control algorithm tries to maintain the dc-link voltage. This DC-link voltage regulation ultimately results in MMPT
Tracking based on mathematical calculation	Incremental conductance [86]	In this method, the conductance is calculated from the voltage and current. This calculated conductance is used to find the MPP
	Sliding mode controller [87]	The sliding mode controller is used to track the actual PV curve with the reference PV curve
	Differentiation method [88]	In the differentiation method, the solar PV curve is modeled as a differential equation, and MPP is obtained by solving the differential equation

(continued)

**Table 11.9** (continued)

Tracking techniques	Tracking methods	Description
	Curve fitting [89]	In this method, various data fitting-based numerical methods are experimented to track the actual PV curve with the reference PV curve.
	Ripple correlation control [90]	This method calculates the ripples produced, when the solar PV is connected to a power-electronic converter. Then, these calculated ripples are reduced to obtain the MPP
Soft-computing-based tracking	Fuzzy logic controller [91]	
	Neural network [92]	
	Swam controller and other natural-inspired techniques [93]	

Source Author

**(b) Single Pulse Width Modulation**

In this modulation technique, only one pulse will be generated in a one-half cycle. Rectangular signals are modulated with triangular signals, as shown in Fig. 11.31, to generate pulses [96].

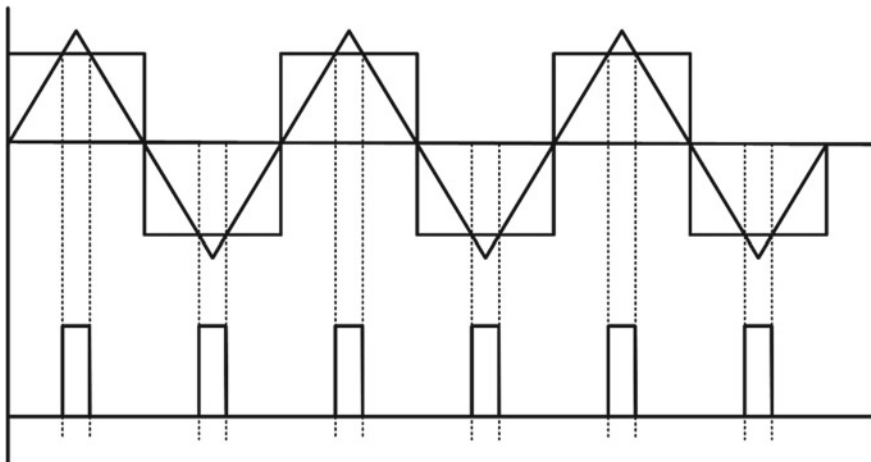


**Fig. 11.31** Single pulse width modulation. Source Author

(c) **Multiple Pulse Width Modulation**

Multiple pulses per phase can be generated using this modulation technique. The waveforms for generating multiple PWM are shown in Fig. 11.32. Here, the triangular signal with high frequency is modulated with the rectangular signal [97].

(d) **Sinusoidal Pulse Width Modulation**

In this modulation technique, the triangular carrier wave with high frequency is modulated with the sinusoidal waveform. The schematic waveforms for generating pulses using sinusoidal PWM are shown in Fig. 11.33.

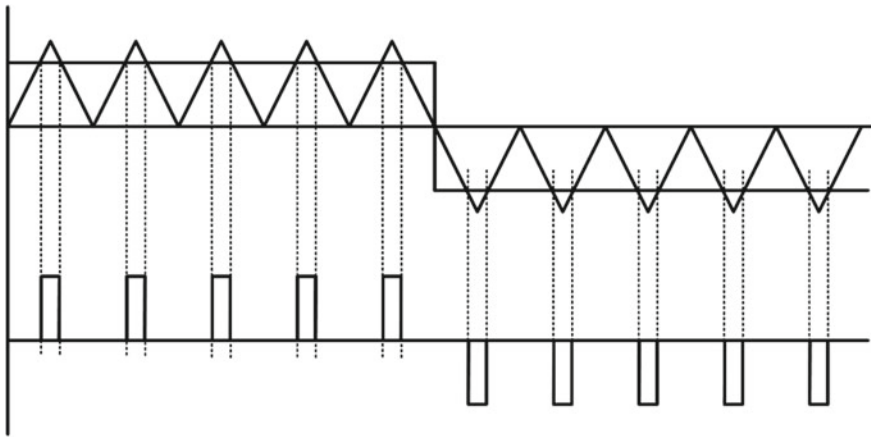


Fig. 11.32 Multiple pulse width modulation. *Source* Author

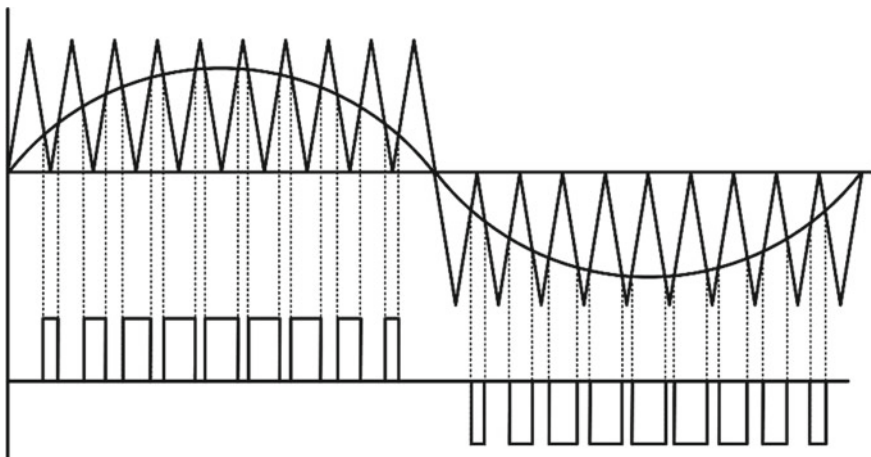


Fig. 11.33 Sinusoidal pulse width modulation. *Source* Author



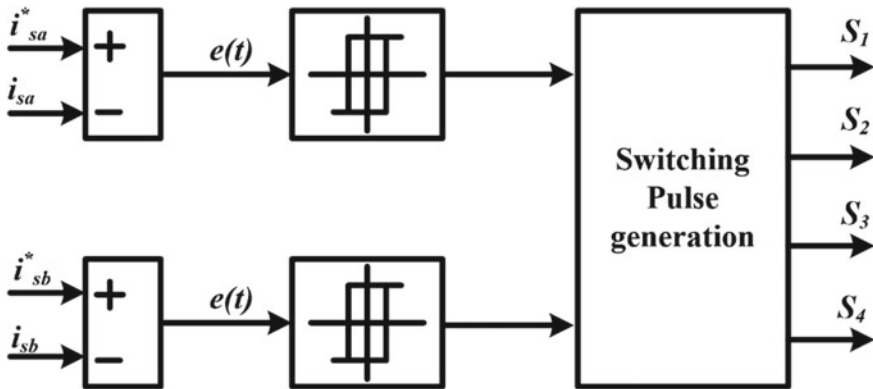


Fig. 11.34 Fixed-hysteresis current controller [98]

### (e) Fixed-Hysteresis Current Controller

Hysteresis current controller technique is the common pulse generation technique used in grid-connected inverters. In grid-connected inverters, the grid current becomes the control parameter, so the hysteresis current control technique is most suitable in such cases. The schematic diagram for generating pulses using a hysteresis current controller is shown in Fig. 11.34. Here, the actual current signals are compared with the reference signals, and the error signals are passed through the hysteresis band. The output from the hysteresis band is fed to the switching signal generation block [98].

Other than the standard techniques explained here, many more inverter techniques are available in the literature [99].

## 11.5 Applications for the Performance Enhancements

The performance of the solar PV system can be improved with the help of control strategies discussed in previous sections. Here, some applications are discussed to improve the performance of solar PV or to maximize solar PV utilization.

### 11.5.1 Energy Management for the Hybrid Power Systems

The energy management system (EMS) is a vital control part of the hybrid power system. The primary power flow in a solar PV system hybridized with a battery ESS is shown in Fig. 11.35. Generally, the EMS is based on the power available from solar PV and load power. The EMS in the given system can be divided into three

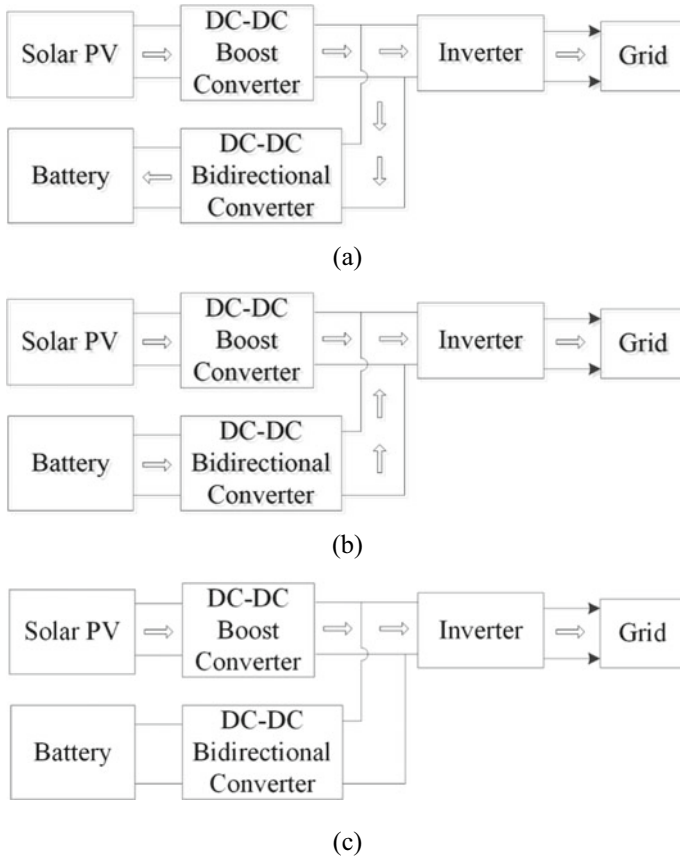


**Fig. 11.35** Power flow in a solar PV/ESS HPS during **a** surplus power condition, **b** deficient power condition, and **c** battery idle condition. *Source* Author

modes depending on the power available from solar PV. This can be explained as follows.

Mode 1: Solar PV power ( $P_{PV}$ )  $\geq$  Load power ( $P_{Load}$ )

In this mode, the solar PV power is sufficient to support the load, and the excess power is diverted to the battery.

Mode 2: Solar PV power ( $P_{PV}$ )  $\leq$  Load power ( $P_{Load}$ )

In this mode, the solar PV power is insufficient to feed the entire load; in such a situation, the excess power required by the load is provided from the battery.

Mode 3: Solar PV power ( $P_{PV}$ ) = Load power ( $P_{Load}$ )

This is the rare mode, where the solar PV power is sufficient to support the load, and the battery remains idle.

Other than the conventional EMS algorithms, many researchers are working on this topic, and several EMS can be seen in the literature [100]. The proper use of EMS can increase the self-consumption rate.

### 11.5.2 *Self-consumption Maximization*

The maximum economic and environmental benefits from a solar PV system can be extracted by maximizing the self-consumption. The term self-consumption can be defined as the maximum utilization of solar PV generated power without wasting it. The use of ESS in the system is one of the prominent techniques to increase solar PV self-consumption. Other than using ESS, electric vehicles can be used to increase self-consumption. The generated power from solar PV can be used to charge the EV batteries; thus, reducing the wastage of energy. The EV infrastructure in solar PV-based HPS can be used either centralized or distributed concept. The integration of EV to the solar PV HPS can be seen from the literature [101].

## 11.6 Economic Feasibility of Hybrid Solar Power Systems

The economic analysis of the solar PV HPS in this chapter is conducted using the HOMER Pro software. A HOMER Pro model of the solar PV hybridized with a diesel generator and the battery energy storage is developed. The actual values of the load and solar irradiance pattern available in the HOMER Pro server are used for analysis. The system is tested for both grid-connected and stand-alone modes.

### 11.6.1 *Economic Modeling of the System [102]*

The economic model in HOMER Pro is an optimized model to reduce the cost of power generation. The cost associated with the system can be divided into three categories:

Capital cost ( $C_C$ ): Cost required as capital expenditure to start the project.

Replacement cost ( $C_R$ ): Replacement cost includes replacing the faulted items and spare parts.

Operation cost ( $C_O$ ): The operation cost includes the cost associated with running the system.

The optimization problem can be defined as follows;

$$\text{Min } F = \sum C_C + C_R + C_O \quad (11.2)$$

The cost of energy (COE) and the net present cost (NPC) are used to analyze the economic feasibility of the system. COE is the 'average cost per kWh' of useful electricity produced by the system. The NPC is the present value of installation and operation costs of the system over its lifetime. It is calculated according to the total annualized cost (\$/year) and capital recovery factor.

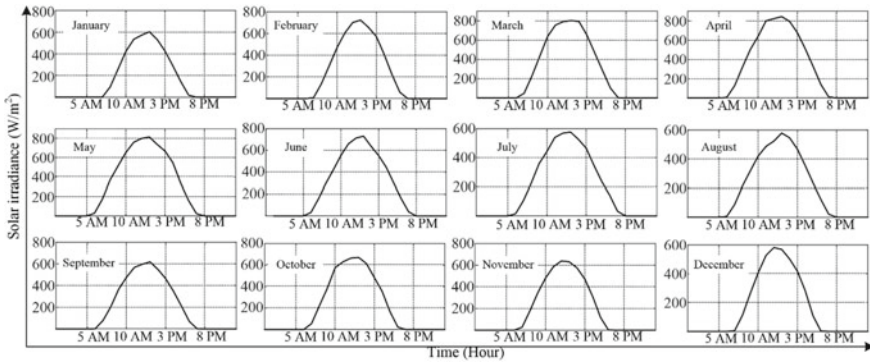


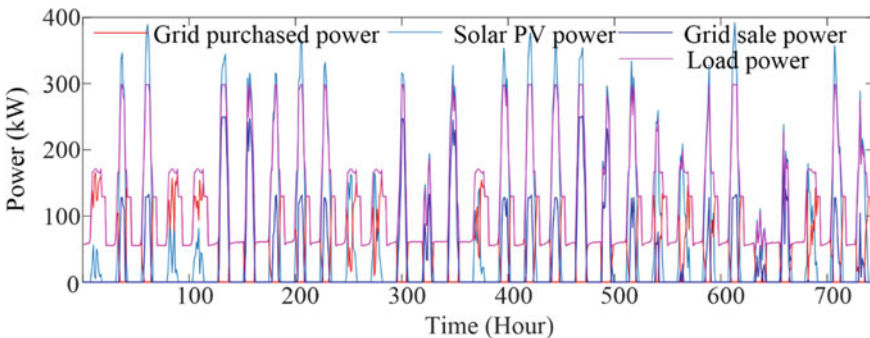
**Fig. 11.36** Monthly average solar PV irradiance. *Source* Author

The monthly average solar PV irradiance pattern used for the HOMER Pro analysis is shown in Fig. 11.36.

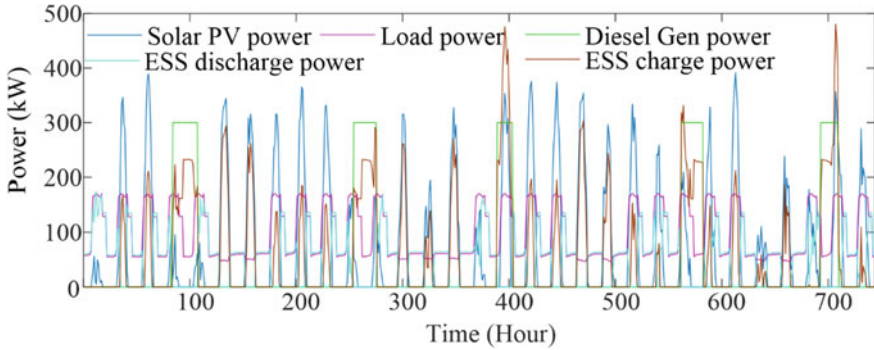
The total electrical load served by various components in the system, such as solar PV, diesel generator, and the grid for grid-connected operation, is shown in Fig. 11.37. The same figure is plotted for January for a better understanding of how each component is responded to maintain the load-generation balance.

Figure 11.38 shows the power generated by various sources in the case of a grid-connected solar PV hybrid system. The power purchased from the grid during deficiency in solar PV power generation and the power sold to the grid during the surplus power generation are also demonstrated in Fig. 11.38.

The comparison of COE and NPC for different combinations of hybrid systems is shown in Table 11.9. In the first system, the load is assumed to be served by the grid alone. In the second system, the load is served by a hybrid solar PV-grid-connected system. In the third system, the entire load is supported by the stand-alone solar PV



**Fig. 11.37** Power generation and consumption in grid-connected solar PV hybrid power system. *Source* Author



**Fig. 11.38** Power generation and consumption in stand-alone solar PV hybrid power system. *Source* Author

**Table 11.10** COE and NPC comparison of various topologies

System	COE (US \$ per kWh)	NPC (US \$)
Load served by grid only	0.1500	1,703,649
Off-grid solar PV-diesel-ESS	4.49	51,022,210
Grid-connected solar PV	0.0745	1,060,110

*Source* Author

system. From the comparison table, it can be seen that the COE is lesser if a grid-connected solar PV system supplies the load. The COE for the stand-alone system is higher in comparison with the remaining two systems. From Table 11.10, it can be concluded that the stand-alone system is advisable only if the grid connectivity is not available. This proof for the above-mentioned claim can be seen from the literature [103].

### 11.7 A Case Study on Hybrid Solar System in the DC Microgrid

Figure 11.39 shows the proposed circuit for the integration of three sources. As depicted in figure, the solar module is connected in the first leg of the converter to supply energy to load by the boost converter. It will supply energy using the MPPT method to load. The battery is connected by second leg of the converter, which is used as a bi-directional converter storing energy from sources and releasing it when no energies are available during charging. It will work as a buck converter mode while discharging it will work as a boost converter. The supply grid is connected to the third leg through a transformer from 230 V, 50 Hz supply. The transformer is

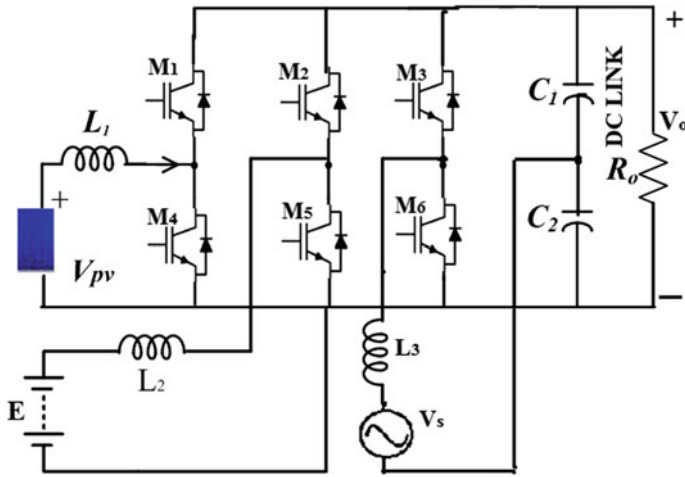


Fig. 11.39 Circuit diagram of the converter used in the system. Source Author

used to step down the voltage to 15 V AC supply for the converter. The converter works as a voltage doubler, rectifying the voltage to DC, giving it to loads. In this figure,  $L_1, L_2, L_3$  are inductors,  $C_1, C_2$  are output capacitors, and  $M_1, M_2, M_3, M_4$  are IGBTs of the converter.

### 11.7.1 Modes of Operations

In this study, energy management is performed to increase the independence of the hybrid system toward the utility grid. According to the requirement of loads, the input energy sources are given different priorities. The operating modes of the system can be described in the following sub-sections, and the flowchart is provided in Fig. 11.40.

*Mode 1:* If solar PV energy and grid supply are available and battery status is not full, then the solar PV module supplies power to load, as shown in Fig. 11.41a. The battery will charge from the solar PV module, and the grid supply remains off. When the solar PV panel is operating, then the battery is charging through a buck converter. Here, IGBT 4 is operated, thus, the inductor  $L_1$  is storing energy the output capacitor  $C_1, C_2$  is discharging through the load, and it acts as a source to the buck converter as IGBT2 is operated, and the input inductor of the battery is storing energy. IGBT 4 is turned off and the stored energy of the inductor  $L_1$  starts to discharge through diode of IGBT1 to the capacitor  $C_1, C_2$  as well as the load. The IGBT2 is turned off so the inductor  $L_2$  is discharging at the same time.

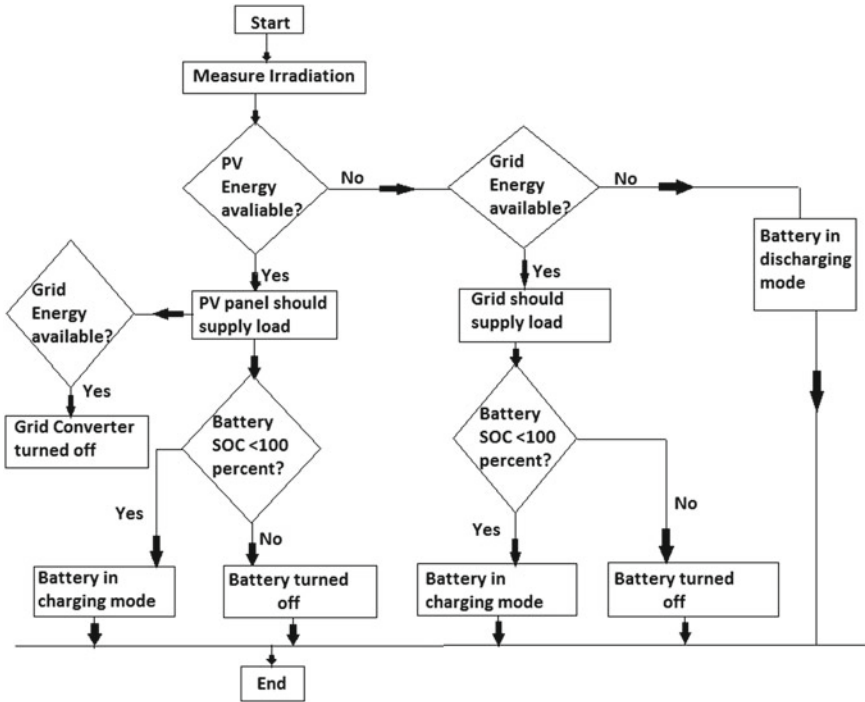


Fig. 11.40 Energy management algorithm. Source Author

*Mode 2:* If solar PV energy and grid supply are available and the status of the battery is full, then the PV module supplies power to load, and the battery will be in idle mode, i.e., no charging and discharging and grid remains off.

*Mode 3:* If solar PV energy is not available and grid supply is available, and battery status is also not full. Grid supplies power to load, and the battery will charge from grid supply, and solar PV remains off due to unavailability of sun energy. The grid supply is connected to the load. With the voltage doubler technique, the AC power is transferred to the DC-link, and the battery is charged at the same time. In that case, both converters will work independently.

*Mode 4:* If PV energy is not available and grid is available, and battery status is full, then battery will be turned off, and grid supplies power to load.

*Mode 5:* If solar PV energy is not available and grid is not available, and the battery status is full, then the solar PV module remains off, and the battery supplies power to load. The battery is connected to load as boost converter then IGBT 5 is operated then the inductor  $L_2$  charges and capacitors  $C_1, C_2$  starts to discharge through the load. Then, IGBT 5 is turned off, and anti-parallel diode of IGBT 2 is operated, then the inductor  $L_2$  discharges and the capacitor starts  $C_1, C_2$  to charge through the battery, and also energy is transferred to load.

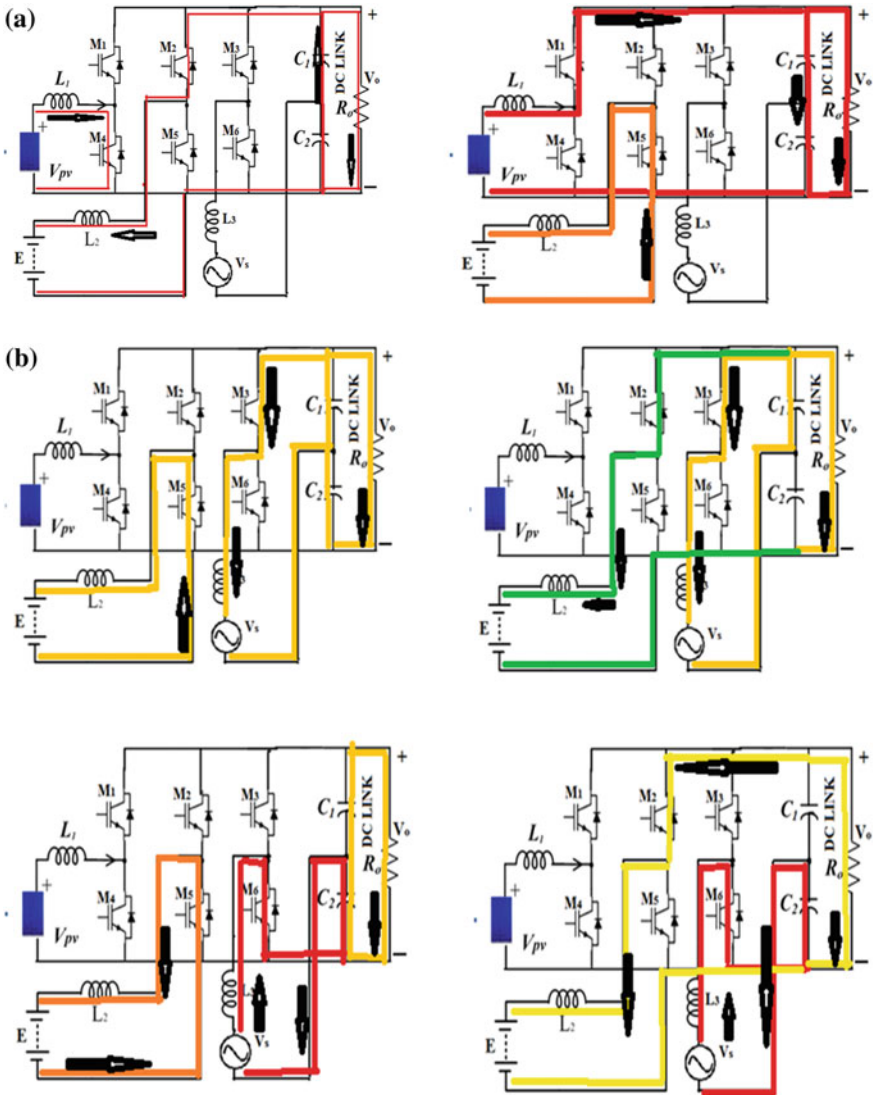


**Fig. 11.41** a PV panel supplying power to load and battery charging (source Author). b AC supply supplying power to load and battery charging at the same time (source Author). c Discharging of battery to supply power to load (source Author)



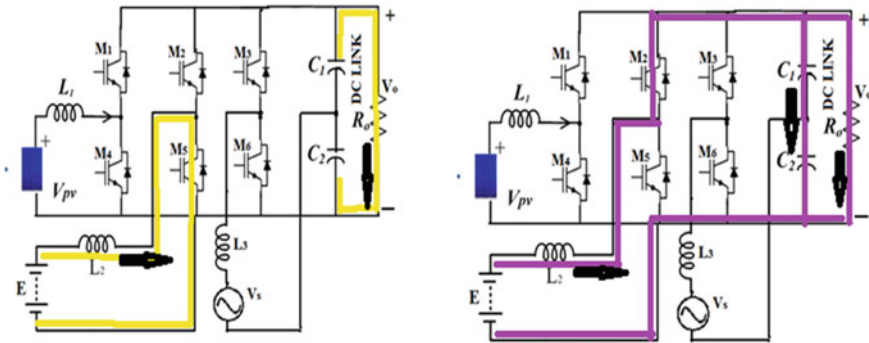


Fig. 11.41 (continued)

### 11.7.2 Closed-Loop Control Strategy of System

#### (a) The control technique for PV panel

To extract maximum power from the PV panel, the incremental conductance method is employed in the first leg of the voltage source converter, which acts as a boost converter. A boost converter provides constant DC-link output voltage with a small variation in output voltage. The PV cell voltage, current, and power are used as input to the controller to operate the DC-DC boost converter, which modifies the duty ratio of the boost converter to track MPP.

#### (b) Bi-directional control of battery management system

Simplified battery charging profile has four distinct operating modes: bulk, absorption, equalization, and maintenance. In the bulk mode, the charger limits the maximum charging current to a preset value ( $I_{MAX}$ ) while monitoring the battery voltage. In the absorption mode, the charger elevates the voltage to 70–90% while monitoring the current. When it has reached this point, the battery is between 70 and 90% state of charge (SOC). When the current decreases to a preset value, the charger enters the equalization mode, when it has reached this point, the battery is at 90% SOC. Equalizing is an overcharge performed on lead-acid batteries after they have been fully charged. This function equalizes the cell voltages in a battery module. When a PV source or grid is available, then the battery will be in constant current charging mode by buck converter overcharging is made by constant voltage charging. Still, when they are not available, then the battery will be in constant voltage discharging mode by the boost converter. In this case, the battery acts as a boost converter to supply power to load. Here, the output voltage is sensed and compared with a reference voltage and fed to the PI controller. The output of the PI controller is compared with the repeating sequence to get desirable gating pulses (Fig. 11.42).

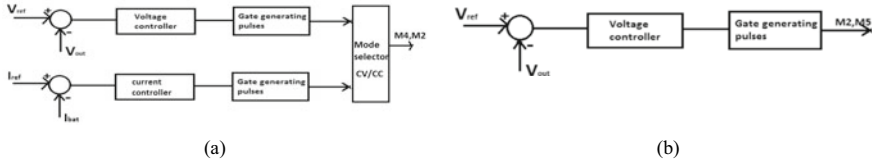


**Fig. 11.42** Closed-loop control for **a** battery charging; **b** battery discharging. *Source* Author

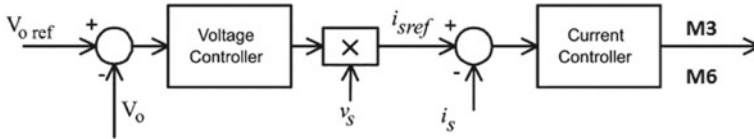


**Fig. 11.43** Closed-loop control scheme of voltage doubler. *Source* Author

**(c) The control technique for voltage doubler circuit**

The classical control scheme includes a voltage controller, typically a proportional-integrative (PI) controller, which controls the DC-link voltage constant. To ensure the improved PQ feature, the output of the PI controller is multiplied with unity sinusoidal input voltage to obtain the input current reference ( $i_{sref}$ ) and compared with input current  $i_f$  as depicted in Fig. 11.43. After that switching signals are obtained for  $M_6$  and  $M_3$ . The fast-current controller studied controls the input current, so the high input power factor is achieved. The objective of this control is used to maintain highly sinusoidal input current and keeps in phase with the voltage to make the input power factor closed to unity.

**(d) Simulation results**

A Simulink model of the proposed converter rated as per specification tabulated in Table 11.11 is developed to investigate the system performance. Initially, PV power generation is assumed to be greater than load demand and the SOC of battery is considered to be 50%. As PV panel with open-circuit voltage of 21 V is connected through first leg of VSC and battery of 12 V, 12 Ah is connected on second leg of VSC, and reduced AC supply main of 16 V, 50 Hz, is connected to third leg of VSC as shown in Fig. 11.39. The output voltage of 48 V, DC is achieved when PV panel received solar irradiation of 1000 W/m<sup>2</sup>. The simulation study is carried out for 1.5 s under steady-state conditions. During this time, PV panel supplies power to load of 30 Ω at 48 V, DC and simultaneously charges the battery for 1.5 s. At time instant 1.5 s, the solar irradiation falls below 500 W/m<sup>2</sup>, then the load and battery is feed by AC supply main due to unavailability of sufficient solar power. In other words, the AC supply grid supplies power to DC load and charge the battery at a constant current of 1.5 A. It is also observed that the output voltage is maintained constant voltage of 48 V during aforesaid operations. The waveforms of various parts are

**Table 11.11** Specification of the system under consideration

S. No.	Parameters	Specification
1	Inductance $L_1$	3 mH
2	Inductance $L_2$	1 mH
3	Capacitance $C_1, C_3$	10 mF
4	Inductance $L_3$	8 mH
5	Solar panel $V_{oc}, I_{sc}$	21 V, 4 A
6	Solar array	5 module in parallel
8	Switching frequency	5 kHz
9	Battery capacity	20 Ah
10	Battery full charged voltage	13 V
11	Battery nominal charged voltage	12 V
12	Solar panel $V_{mp}$	18 V
13	Solar panel current $I_{mp}$	3 A

shown in Fig. 11.44. It is observed in Fig. 11.44b that when power is fed by supply main, converter draws current from supply main at unity power factors.

In order to evaluate the system efficiency while solar PV charging the battery and feeding power to DC load, the power supplied to the load is to be estimated as follows:

Power supplied by solar panel = PV voltage \* input current of PV panel =  $22 * 4.5 = 99$  W.

The power delivered to DC load = output voltage \* load current =  $48 * 1.6 = 77$  W.

The power supplied to the battery while charging =  $12 * 1.5 = 18$  W. Thus, the total power supplied to DC load and battery =  $77 + 18 = 94.8$  W. Therefore, the efficiency of the system is evaluated as 95.5%. When supply main is providing power to load and charging battery after 1.5 s, the input power supplied by supply main is evaluated as  $15 * 6.4 = 95.45$  W. Thus, the system efficiency of 99.3% is achieved.

The similar analysis has been carried out under various operating conditions and analytical results are tabulated in Table 11.12. It is further verified by simulation results. Analysis shows that the efficiencies of the different systems are almost above 90%, indicating negligible losses in the system. If solar power is converted to AC, then the efficiencies will be lesser, hence, we use the DC grid for home appliances.

## 11.8 Summary

This chapter is intended to briefly explain the various solar PV HPS with the help of recent literature. The various system topologies of the solar PV HPS, such as

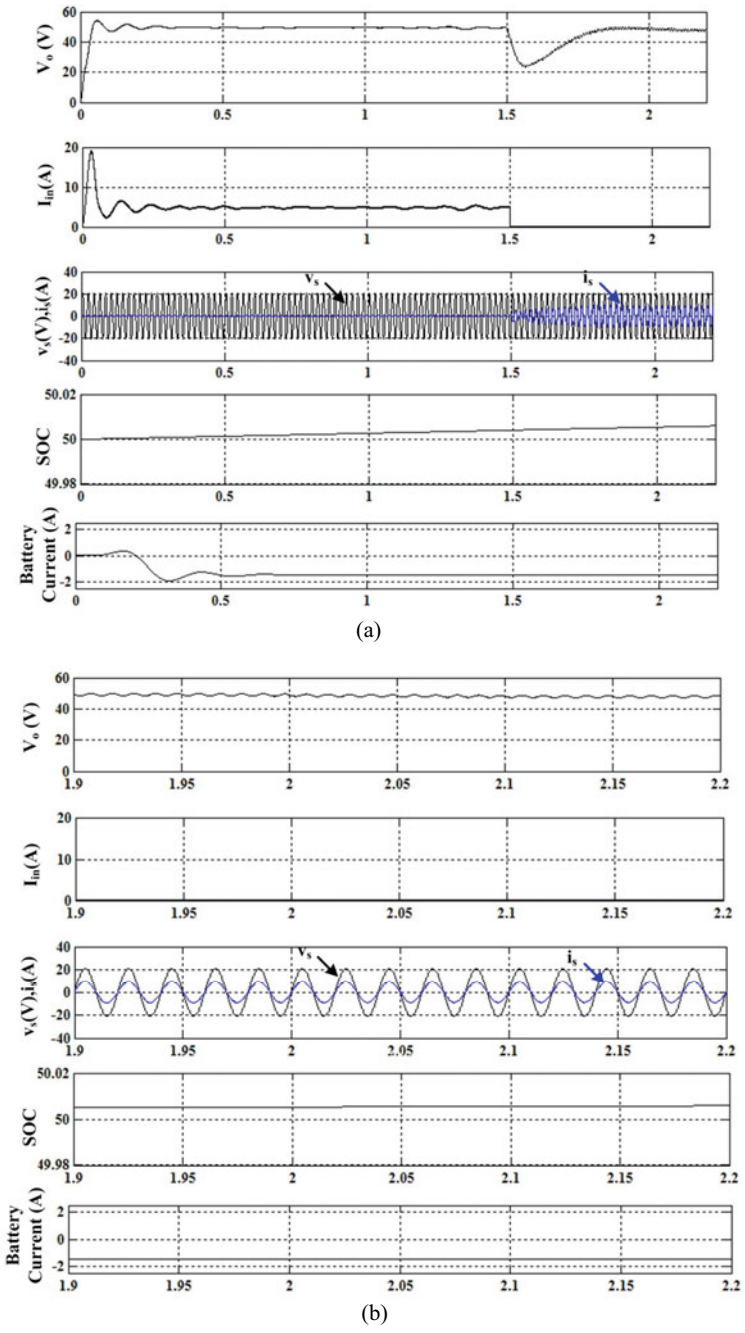


**Fig. 11.44** Results of proposed system when power is fed from **a** PV panel and **b** AC supply main.  
 Source Author

**Table 11.12** Results of different parameters of MATLAB simulation

Load ( $\Omega$ )	The input current of PV panel (A)	Battery charging current (A)	Input AC current (A)	Battery discharge current (A)
30	4.5	1.5	6.4	15
14	8.5	1.5	12.0	22
15	9.0	3.0	13.3	23
11	10.2	1.5	14.4	25

Source Author

grid-connected and stand-alone systems are explained with their pros and cons. The national and international standards for solar PV HPS installation and integration are also provided. The power-electronic converter topologies used in solar PV HPS are extensively reviewed. Various techniques for improving the self-consumption of the solar PV system are explained. The economic analysis of the solar PV system in grid-connected and stand-alone mode is analyzed with the help of HOMER Pro. The HOMER Pro simulation shows the grid-connected system is more economical than the off-grid system. Finally, a case study of a hybrid system is proposed and the simulation model is developed using the MATLAB<sup>®</sup>/Simulink platform. The results for the MATLAB<sup>®</sup>/Simulink simulation are presented and the results are discussed.

**Acknowledgements** The authors would like to acknowledge Mr. Vivek Pandey, from Power System Operation Corporation Limited, India for his valuable and constructive suggestions during the preparation of the chapter.

## Annexure 1

See Figs. 11.2, 11.3, 11.4, 11.5, 11.6, 11.7, 11.8, 11.9, 11.10, 11.11, 11.23, 11.24, 11.25, 11.26, 11.27, 11.28 and 11.29.

## Annexure 2

See Figs. 11.16, 11.17, 11.18 and 11.9.

## Annexure 3

See Figs. 11.20, 11.21 and 11.22.

## References

1. Mohtasham J (2015) Review article—Renewable energies. *Energy Procedia* 74:1289–1297
2. Ogbonnaya C, Abeykoon C, Damo UM, Turan A (2019) The current and emerging renewable energy technologies for power generation in Nigeria: a review. *Therm Sci Eng Prog* 13:100390
3. Lehtola T, Zahedi A (2019) Solar energy and wind power supply supported by storage technology: a review. *Sustain Energy Technol Asses* 35:25–31
4. International Renewable Energy Agency—IRENA (2019) Future of solar photovoltaic: deployment, investment, technology, grid integration and socio-economic aspects. IRENA
5. IRENA (2020) Renewable energy capacity highlights, 31 March 2020. Irena 1–3
6. Mehmood H, Tauqueer T, Hussain S (2018) Recent progress in silicon-based solid-state solar cells. *Int J Electron* 105:1568–1582
7. Gul M, Kotak Y, Muneer T (2016) Review on recent trend of solar photovoltaic technology. *Energy Explor Exploit* 34
8. Khan J, Arsalan MH (2016) Solar power technologies for sustainable electricity generation—a review. *Renew Sustain Energy Rev* 55:414–425
9. Karthikeyan V, Rajasekar S, Das V, Pitchaivijaya K, Singh A (2017) Smart energy grid design for island countries. *Green Energy Technol*. <https://doi.org/10.1007/978-3-319-50197-0>
10. Mao M et al (2020) Classification and summarization of solar photovoltaic MPPT techniques: a review based on traditional and intelligent control strategies. *Energy Rep* 6:1312–1327
11. Eltawil MA, Zhao Z (2013) MPPT techniques for photovoltaic applications. *Renew Sustain Energy Rev* 25:793–813
12. Hossain MZ, Rahim NA, Selvaraj J et al (2018) Recent progress and development on power DC-DC converter topology, control, design and applications: a review. *Renew Sustain Energy Rev* 81:205–230
13. Mostafa MH, Abdel Aleem SHE, Ali SG, Ali ZM, Abdelaziz AY (2020) Techno-economic assessment of energy storage systems using annualized life cycle cost of storage (LCCOS) and levelized cost of energy (LCOE) metrics. *J Energy Storage* 29
14. Azuatalam D et al (2019) Energy management of small-scale PV-battery systems: a systematic review considering practical implementation, computational requirements, quality of input data and battery degradation. *Renew Sustain Energy Rev* 112:555–570
15. Bakar AL, Tan CW (2019) A review on stand-alone photovoltaic-wind energy system with fuel cell: system optimization and energy management strategy. *J Clean Prod* 221:73–88
16. Brinkel NGB et al (2020) Impact of rapid PV fluctuations on power quality in the low-voltage grid and mitigation strategies using electric vehicles. *Int J Electr Power Energy Syst* 118:105741
17. Jaalam N, Rahim NA, Bakar AHA, Tan CK, Haidar AMA (2016) A comprehensive review of synchronization methods for grid-connected converters of renewable energy source. *Renew Sustain Energy Rev* 59:1471–1481
18. Eltawil MA, Zhao Z (2010) Grid-connected photovoltaic power systems: technical and potential problems—a review. *Renew Sustain Energy Rev* 14:112–129
19. Chatterjee S, Kumar P, Chatterjee S (2018) A techno-commercial review on grid connected photovoltaic system. *Renew Sustain Energy Rev* 81:2371–2397
20. Moon S, Yoon SG, Park JH (2015) A new low-cost centralized MPPT controller system for multiply distributed photovoltaic power conditioning modules. *IEEE Trans Smart Grid* 6:2649–2658
21. Panigrahi R, Mishra SK, Srivastava SC, Srivastava AK, Schulz NN (2020) Grid integration of small-scale photovoltaic systems in secondary distribution network—a review. *IEEE Trans Ind Appl* 56:3178–3195
22. Golestan S, Guerrero JM, Vasquez JC (2017) Single-phase PLLs: a review of recent advances. *IEEE Trans Power Electron* 32:9013–9030
23. Liang X, Andalib-Bin-Karim C (2018) Harmonics and mitigation techniques through advanced control in grid-connected renewable energy sources: a review. *IEEE Trans Ind Appl* 54:3100–3111

24. Quality P (2015) Swachh power
25. Gayatri MTL, Parimi AM, Pavan Kumar AV (2018) A review of reactive power compensation techniques in microgrids. *Renew Sustain Energy Rev* 81:1030–1036
26. Ellis A et al (2012) Review of existing reactive power requirements for variable generation. *IEEE Power Energy Soc Gen Meet* 1–7. <https://doi.org/10.1109/pesgm.2012.6345555>
27. Kunte RS, Gao W (2008) Comparison and review of islanding detection techniques for distributed energy resources. In: 2008 40th North American power symposium, NAPS2008, pp 1–8. <https://doi.org/10.1109/naps.2008.5307381>
28. Wu YK, Lin JH, Lin HJ (2017) Standards and guidelines for grid-connected photovoltaic generation systems: a review and comparison. *IEEE Trans Ind Appl* 53:3205–3216
29. Chauhan A, Saini RP (2014) A review on Integrated Renewable Energy System based power generation for stand-alone applications: configurations, storage options, sizing methodologies and control. *Renew Sustain Energy Rev* 38:99–120
30. Choi BY, Noh YS, Ji YH, Lee BK, Won CY (2012) Battery-integrated power optimizer for PV-battery hybrid power generation system. In: 2012 IEEE vehicle power and propulsion conference, VPPC 2012, pp 1343–1348. <https://doi.org/10.1109/vppc.2012.6422686>
31. Hong J, Yin J, Liu Y, Peng J, Jiang H (2019) Energy management and control strategy of photovoltaic/battery hybrid distributed power generation systems with an integrated three-port power converter. *IEEE Access* 7:82838–82847
32. Arabali A, Ghofrani M, Etezadi-Amoli M, Fadali MS (2014) Stochastic performance assessment and sizing for a hybrid power system of Solar/Wind/Energy Storage. *IEEE Trans Sustain Energy* 5:363–371
33. Nema P, Nema RK, Rangnekar S (2009) A current and future state of art development of hybrid energy system using wind and PV-solar: a review. *Renew Sustain Energy Rev* 13:2096–2103
34. Girma Z (2017) Techno-economic analysis of photovoltaic pumping system for rural water supply in Ethiopia. *Int J Sustain Energy* 36:277–295
35. Thounthong P et al (2011) Energy management of fuel cell/solar cell/supercapacitor hybrid power source. *J Power Sources* 196:313–324
36. Akikur RK, Saidur R, Ping HW, Ullah KR (2013) Comparative study of stand-alone and hybrid solar energy systems suitable for off-grid rural electrification: a review. *Renew Sustain Energy Rev* 27:738–752
37. Chen YM, Liu YC, Hung SC, Cheng CS (2007) Multi-input inverter for grid-connected hybrid PV/wind power system. *IEEE Trans Power Electron* 22:1070–1077
38. Coelho RF, Schimtz L, Martins DC (2011) Grid-connected PV-wind-fuel cell hybrid system to supply a critical DC load. In: 2011 IEEE 33rd international telecommunications energy conference (INTELEC), pp 1–9
39. Agarkar BD (2011) A review on hybrid solar/wind/ hydro power generation system. *Int J Curr Eng Technol*. <https://doi.org/10.14741/ijcet/22774106/spl.4.2016.38>
40. Olatunde O, Hassan MY, Abdullah MP, Rahman HA (2020) Hybrid photovoltaic/small-hydropower microgrid in smart distribution network with grid isolated electric vehicle charging system. *J Energy Storage* 31:101673
41. Datta U, Kalam A, Shi J (2018) Hybrid PV-wind renewable energy sources for micro-grid application: an overview. *Hybrid-renewable energy systems in microgrids: integration, developments and control*. Elsevier Ltd. <https://doi.org/10.1016/b978-0-08-102493-5.00001-7>
42. Ismail MS (2002) Design of a Pv/diesel stand alone hybrid system for a remote community in palestine. *Ieee* 2:599–606
43. Lan H, Wen S, Hong YY, Yu DC, Zhang L (2015) Optimal sizing of hybrid PV/diesel/battery in ship power system. *Appl Energy* 158:26–34
44. Ngan MS, Tan CW (2012) Assessment of economic viability for PV/wind/diesel hybrid energy system in southern Peninsular Malaysia. *Renew Sustain Energy Rev* 16:634–647
45. Dufo-López R et al (2011) Multi-objective optimization minimizing cost and life cycle emissions of stand-alone PV-wind-diesel systems with batteries storage. *Appl Energy* 88:4033–4041

46. Ghenai C, Salameh T, Merabet A (2020) Technico-economic analysis of off grid solar PV/fuel cell energy system for residential community in desert region. *Int J Hydrogen Energy* 45:11460–11470
47. Nelson DB, Nehrir MH, Wang C (2006) Unit sizing and cost analysis of stand-alone hybrid wind/PV/fuel cell power generation systems. *Renew Energy* 31:1641–1656
48. Harish SM, Raghavan SV (2011) Redesigning the national solar mission for rural India. *Econ Polit Wkly* 46:51–58
49. Mukhopadhyay S, Soonee SK, Joshi R, Rajput AK (2012) On the progress of renewable energy integration into smart grids in India. In: IEEE power and energy society general meeting. <https://doi.org/10.1109/PESGM.2012.6344933>
50. Wai RJ, Shin LZ (2011) Total sliding-mode voltage tracking control for DC-DC boost converter. In: Proceedings of the 2011 6th IEEE conference on industrial electronics and applications, ICIEA 2011, vol 58, pp 2676–2681
51. Leyva-Ramos J, Ortiz-Lopez MG, Diaz-Saldierna LH, Morales-Saldaña JA (2009) Switching regulator using a quadratic boost converter for wide DC conversion ratios. *IET Power Electron* 2:605–613
52. Walker GR, Sernia PC (2004) Cascaded DC-DC converter connection of photovoltaic modules. *IEEE Trans Power Electron* 19:1130–1139
53. Dreher JR et al (2012) High step-up voltage gain integrated DC/DC converters. In: 2012 3rd IEEE international symposium on power electronics for distributed generation systems (PEDG), pp 125–132. <https://doi.org/10.1109/pedg.2012.6253990>
54. Yao G, Chen A, He X (2007) Soft switching circuit for interleaved boost converters. *IEEE Trans Power Electron* 22:80–86
55. Rodrigues JP, Mussa SA, Barbi I, Perin AJ (2010) Three-level zero-voltage switching pulse-width modulation DC-DC boost converter with active clamping. *IET Power Electron* 3:345–354
56. Vasic M et al (2019) Ultraefficient voltage doubler based on a GaN resonant switched-capacitor converter. *IEEE J Emerg Sel Top Power Electron* 7:622–635
57. Azizkandi ME, Sedaghati F, Shayeghi H, Blaabjerg F (2020) Two- and three-winding coupled-inductor-based high step-up DC-DC converters for sustainable energy applications. *IET Power Electron* 13:144–156
58. Sri Revathi B, Prabhakar M (2016) Non isolated high gain DC-DC converter topologies for PV applications—a comprehensive review. *Renew Sustain Energy Rev* 66:920–933
59. Forouzes M, Siwakoti YP, et al (2017) Step-up DC-DC converters: a comprehensive review of voltage-boosting techniques, topologies, and applications. *IEEE Trans Power Electron* 32:9143–9178
60. Jeremy LJ, Ooi CA, Teh J (2020) Non-isolated conventional DC-DC converter comparison for a photovoltaic system: a review. *J Renew Sustain Energy* 12
61. Shao S, Chen H, Wu X, Zhang J, Sheng K (2019) Circulating current and ZVS-on of a dual active bridge DC-DC converter: a review. *IEEE Access* 7:50561–50572
62. Shao S et al (2019) optimal phase-shift control to minimize reactive power for a dual active bridge DC-DC converter. *IEEE Trans Power Electron* 34:10193–10205
63. Jana J, Saha H, Das Bhattacharya K (2017) A review of inverter topologies for single-phase grid-connected photovoltaic systems. *Renew Sustain Energy Rev* 72:1256–1270
64. Xiao HF, Lan K, Zhang L (2015) A quasi-unipolar SPWM full-bridge transformerless PV grid-connected inverter with constant common-mode voltage. *IEEE Trans Power Electron* 30:3122–3132
65. Zhang L, Sun K, Xing Y, Zhao J (2016) A family of five-level dual-buck full-bridge inverters for grid-tied applications. *IEEE Trans Power Electron* 31:7029–7042
66. Victor M, Greizer F, Kaufungen, Bremicker S, Alheim, Hibler U (2008) Method of converting a direct current voltage from a source of direct current voltage, more specifically from a photovoltaic source of direct current voltage, 2
67. Tang Z et al (2019) Hybrid UP-PWM scheme for HERIC inverter to improve power quality and efficiency. *IEEE Trans Power Electron* 34:4292–4303



68. González R, López J, Sanchis P, Marroyo L (2007) Transformerless inverter for single-phase photovoltaic systems. *IEEE Trans Power Electron* 22:693–697
69. Kerekes T, Teodorescu R, Rodríguez P, Vázquez G, Aldabas E (2011) A new high-efficiency single-phase transformerless PV inverter topology. *IEEE Trans Ind Electron* 58:184–191
70. Barghi Latran M, Teke A (2015) Investigation of multilevel multifunctional grid connected inverter topologies and control strategies used in photovoltaic systems. *Renew Sustain Energy Rev* 42:361–376
71. Buticchi G, Concari C, Franceschini G, Lorenzani E, Zanchetta P (2012) A nine-level grid-connected photovoltaic inverter based on cascaded full-bridge with flying capacitor. In: 2012 IEEE energy conversion congress and exposition (ECCE 2012), pp 1149–1156. <https://doi.org/10.1109/ecce.2012.6342688>
72. Verma D, Nema S, Shandilya AM, Dash SK (2016) Maximum power point tracking (MPPT) techniques: recapitulation in solar photovoltaic systems. *Renew Sustain Energy Rev* 54:1018–1034
73. Ram JP, Babu TS, Rajasekar N (2017) A comprehensive review on solar PV maximum power point tracking techniques. *Renew Sustain Energy Rev* 67:826–847
74. Karami N, Moubayed N, Outbib R (2017) General review and classification of different MPPT techniques. *Renew Sustain Energy Rev* 68:1–18
75. Yu GJ, Jung YS, Choi JY, Kim GS (2004) A novel two-mode MPPT control algorithm based on comparative study of existing algorithms. *Sol Energy* 76:455–463
76. Shimizu T, Hashimoto O, Kimura G (2003) A novel high-performance utility-interactive photovoltaic inverter system. *IEEE Trans Power Electron* 18:704–711
77. Kasa N, Iida T, Iwamoto H (2000) Maximum power point tracking with capacitor identifier for photovoltaic power system. *IEE Proc Electr Power Appl* 147:497–502
78. Park M, Yu IK (2004) A study on the optimal voltage for MPPT obtained by surface temperature of solar cell. *IECON Proc (Ind Electron Conf)* 3:2040–2045
79. Jain S, Agarwal V (2004) A new algorithm for rapid tracking of approximate maximum power point in photovoltaic systems. *IEEE Power Electron Lett* 2:16–19
80. Kim Y, Jo H, Kim D (1996) New peak power tracker for cost-effective photovoltaic power system. *Proc Intersoc Energy Convers Eng Conf* 3:1673–1678
81. Salas V, Olías E, Lázaro A, Barrado A (2005) New algorithm using only one variable measurement applied to a maximum power point tracker. *Sol Energy Mater Sol Cells* 87:675–684
82. Femia N, Petrone G, Spagnuolo G, Vitelli M (2005) Optimization of perturb and observe maximum power point tracking method. *IEEE Trans Power Electron* 20:963–973
83. Roy CP, Naick BK, Shankar G (2013) Modified three-point weight comparison method for adaptive MPPT of photovoltaic systems. In: IET conference 2013, pp 146–156
84. Sharaf AM (2007) A novel photovoltaic online search algorithm for maximum energy utilization, pp 192–197
85. Shadmand MB, Balog RS, Abu-Rub H (2014) Model predictive control of PV sources in a smart DC distribution system: maximum power point tracking and droop control. *IEEE Trans Energy Convers* 29:913–921
86. Safari A, Mekhilef S (2011) Simulation and hardware implementation of incremental conductance MPPT with direct control method using cuk converter. *IEEE Trans Ind Electron* 58:1154–1161
87. Yang B et al (2018) Perturbation observer based fractional-order sliding-mode controller for MPPT of grid-connected PV inverters: design and real-time implementation. *Control Eng Pract* 79:105–125
88. Xiao W, Dunford WG, Palmer PR, Capel A (2007) Application of centered differentiation and steepest descent to maximum power point tracking. *IEEE Trans Ind Electron* 54:2539–2549
89. Farayola AM, Hasan AN, Ali A (2017) Curve fitting polynomial technique compared to ANFIS technique for maximum power point tracking. In: 2017 8th international renewable energy congress (IREC). <https://doi.org/10.1109/irec.2017.7926047>

90. ESRAM T, Kimball JW, Krein PT, Chapman PL, Midya P (2006) Dynamic maximum power point tracking of photovoltaic arrays using ripple correlation control. *IEEE Trans Power Electron* 21:1282–1290
91. Algarín CR, Giraldo JT, Álvarez OR (2017) Fuzzy logic based MPPT controller for a PV system. *Energies* 10
92. Lin WM, Hong CM, Chen CH (2011) Neural-network-based MPPT control of a stand-alone hybrid power generation system. *IEEE Trans Power Electron* 26:3571–3581
93. Farajdadian S, Hosseini SMH (2019) Optimization of fuzzy-based MPPT controller via metaheuristic techniques for stand-alone PV systems. *Int J Hydrogen Energy* 44:25457–25472
94. Ahmad R, Murtaza AF, Sher HA (2019) Power tracking techniques for efficient operation of photovoltaic array in solar applications—a review. *Renew Sustain Energy Rev* 101:82–102
95. Urmila B, Subbarayudu D (2010) Multilevel inverters: a comparative study of pulse width modulation techniques. *Int J Sci Eng Res* 1:3–7
96. Kim S-H (2017) Pulse width modulation inverters. *Electr Motor Control*. <https://doi.org/10.1016/b978-0-12-812138-2.00007-6>
97. Grant DA, Jose S (2012) (12) United States Patent 2
98. Mohseni M, Islam SM (2010) A new vector-based hysteresis current control scheme for three-phase PWM voltage-source inverters. *IEEE Trans Power Electron* 25:2299–2309
99. Zeb K et al (2018) A comprehensive review on inverter topologies and control strategies for grid connected photovoltaic system. *Renew Sustain Energy Rev* 94:1120–1141
100. Zia MF, Elbouchikhi E, Benbouzid M (2018) Microgrids energy management systems: a critical review on methods, solutions, and prospects. *Appl Energy* 222:1033–1055
101. Denholm P, Kuss M, Margolis RM (2013) Co-benefits of large scale plug-in hybrid electric vehicle and solar PV deployment. *J Power Sources* 236:350–356
102. Ahmad J et al (2018) Techno economic analysis of a wind-photovoltaic-biomass hybrid renewable energy system for rural electrification: a case study of Kallar Kahar. *Energy* 148:208–234
103. Parida A, Chatterjee D (2017) Cost effective utility-solar photovoltaic based hybrid scheme for institutional buildings: a case study. *IET Gener Transm Distrib* 11:1102–1110

# Chapter 12

## Maximum Power Point Tracking of Photovoltaic Renewable Energy System Using a New Method Based on Turbulent Flow of Water-Based Optimization (TFWO) Under Partial Shading Conditions



**Shohreh Nasri, Saber Arabi Nowdeh, Iraj Faraji Davoudkhani, Mohammad Jafar Hadidian Moghaddam, Akhtar Kalam, Saman Shahrokhi, and Mohammad Zand**

---

S. Nasri

Department of Electrical Engineering, Najafabad Branch, Islamic Azad University, Najafabad Isfahan, Iran

e-mail: [shohrenasri@yahoo.com](mailto:shohrenasri@yahoo.com)

S. A. Nowdeh

Golestan Technical and Vocational Training Center, Gorgan, Iran

e-mail: [saber.arabi17@gmail.com](mailto:saber.arabi17@gmail.com)

I. F. Davoudkhani

Department of Electrical Engineering, Khalkhal Branch, Islamic Azad University, Khalkhal, Iran

e-mail: [faraji.iraj@gmail.com](mailto:faraji.iraj@gmail.com)

M. J. H. Moghaddam · A. Kalam (✉)

College of Engineering and Science, Victoria University, Melbourne, Australia

e-mail: [akhtar.kalam@vu.edu.au](mailto:akhtar.kalam@vu.edu.au)

M. J. H. Moghaddam

e-mail: [mohammad.hadidianmoghaddam@live.vu.edu.au](mailto:mohammad.hadidianmoghaddam@live.vu.edu.au)

S. Shahrokhi

Department of Electrical Engineering, Sanandaj Branch, Islamic Azad University, Sanandaj, Iran

e-mail: [shahrokhi.saman@yahoo.com](mailto:shahrokhi.saman@yahoo.com)

M. Zand

Young Researchers and Elite Club, Borujerd Branch, Islamic Azad University, Borujerd, Iran

e-mail: [dr.zand.mohammad@gmail.com](mailto:dr.zand.mohammad@gmail.com)

© The Author(s), under exclusive license to Springer Nature Singapore Pte Ltd. 2021

285

S. N. Singh et al. (eds.), *Fundamentals and Innovations in Solar Energy*,

Energy Systems in Electrical Engineering,

[https://doi.org/10.1007/978-981-33-6456-1\\_12](https://doi.org/10.1007/978-981-33-6456-1_12)

## 12.1 Introduction

Today, most of the renewable energy technologies are reliable and inexpensive in comparison with traditional fossil fuel power plant, including new photovoltaic (PV) energy [1, 2]. The demand for PV systems has expanded in reason of benefits as simple availability of radiation and eco-friendly aspect. So, maximum power point tracking (MPPT) of PV systems should be considered, especially in the conditions of climate change [3, 4]. The MPPT control is important to improve the efficiency of PV systems. On the other hand, PSC leads to multiple peaks in  $I$ - $V$  characteristics of the PV system. Therefore, it is necessary to study the achievement of the maximum power point in PSC and an algorithm should be used that guarantees the maximum power point in the conditions of changes in the working point. On the other hand, in recent years, different types of DC/DC converters have been used in the PV system. By optimally adjusting the converter duty cycle and controlling the converter switching, the maximum power of the PV system can be achieved. Therefore, the study of using different types of DC/DC converters in MPPT problem solving, especially in PSC, is very important [5, 6]. P&O and IC methods are two very suitable methods used to solve the MPPT under uniform irradiance conditions [7–9]. However, PV modules are exposed to PSC, which is a real problem and responsible for most of the power reductions and mismatches [10]. When the PV module operates under these conditions, the voltage power curves will have several local peak points [11, 12]. In order to address the effects of PSC on  $P$ - $V$  curves, conventional MPPT algorithms have undergone some modifications and improvements. Some of these are based on configuration and require additional power circuits to perform the maximum point power tracking operation [13]. Therefore, the overall efficiency will decrease. Some other methods are based on fuzzy controller to solve the MPPT [14], extreme sequence searcher control [15], and artificial neural networks (ANNs) [16]. ANNs are one of the methods applied to solve the MPPT. This method is commonly used to estimate MPP relative to stochastic weather conditions as well as to enhance turbulence algorithms and incremental observation and guidance [17]. Meta-heuristic algorithms like genetic algorithm (GA) [18] and differential evolution (DE) [19], have also been used to solve the MPPT problem. In [20], ant colony optimization is applied for MPPT solution. Although the application of this method has been demonstrated through simulation, it is difficult to implement and implement in a hardware database. In [21], fuzzy logic is used to adjust the parameters of PSO and ACO. In [22], artificial intelligence is used to track the MPP of the PV system as well as optimization algorithms such as GA and PSO have examined the performance of various methods. A method to improve the PV efficiency is proposed using a MPPT algorithm using the golden search optimization (GSO) algorithm [23]. The GSO search law causes it to converge and can handle rapid changes in atmospheric parameters, and it can also converge to the maximum point of global power under PSCs. In [24], a new algorithm is presented for MPPT in large PV systems under partial shadow conditions. In this study, the traditional disturbance and observation method (P&O) and PSO algorithm have been used to achieve this goal. In [25], the

colony bee algorithm (ABC) is used to track and improve the efficiency of MPPT in PV systems under PSC and the results are evaluated with the PSO. In [20], the MPPT method based on the ACO is presented which is implemented between the load and the PV system to extract the maximum power. In this study, the capability of the proposed method in PSC has been investigated. In [26], the grey wolf optimizer—crow search algorithm (GWOCSA) is used to solve the MPPT problem of the PV system in PSC. In [27], the sine–cosine algorithm (SCA) is proposed to achieve the maximum efficiency of the PV system by optimally adjusting the duty cycle of the DC/DC converter under conditions of radiation changes and PSC. In [28], the grasshopper optimization algorithm (GOA) is proposed to extract the PV maximum power in the conditions of radiation changes and PSC. In [29], the moth flame optimizer perturb and observe (MFO-P&O) method has been implemented to track the maximum power point of the PV system in conditions of rapid radiation changes as well as various PSC patterns.

In this chapter, a new method named turbulent flow of water-based optimization (TFWO) algorithm is proposed for MPPT solution of PV systems. The TFWO algorithm [30] is a convenient and simple method without control parameters and is independent from system initial conditions to achieve the global peak power of the PV system via direct control of the DC/DC buck–boost converter duty cycle in different atmospheric conditions. In this study, the duty cycle of DC/DC converter is considered as an optimization variable that the output power of the PV system is optimally determined by the TFWO method for the optimal duty cycle. That is, in the proposed method with the optimal duty cycle, the MPP of the PV system is extracted. The capability of the TFWO method in terms of different PSCs is evaluated. Also, the effect of using buck–boost converter compared to boost converter has been analyzed and compared. In this study, the output power of the PV system due to each of the PSC patterns has been evaluated. Also, to verify the TFWO, the results are compared and analyzed with the well-known PSO method. The tracking performance of the proposed method in achieving the global optimal point in PSC has been investigated, and also the results of the proposed methods have been evaluated.

## 12.2 PV Cell Modeling

The equivalent circuit of this PV cell model is shown in Fig. 12.1.

The  $I$ - $V$  characteristic equation of the PV module is achieved by [24].

$$I = N_p \left( I_{pv} - I_s \left( e^{\frac{q(V+IR_s)}{aN_sKT}} - 1 \right) \right) - \frac{V + IR_s}{R_{sh}} \quad (12.1)$$

where  $V_t$  is the thermal voltage of the PV cell is replaced by the thermal voltage of the module, i.e.,  $V_t = \left( \frac{N_sKT}{q} \right)$ .  $N_s$  and  $N_p$  are the PV cells number with series and parallel connection, respectively.  $a$  is a constant indicates the ideality of the diode.

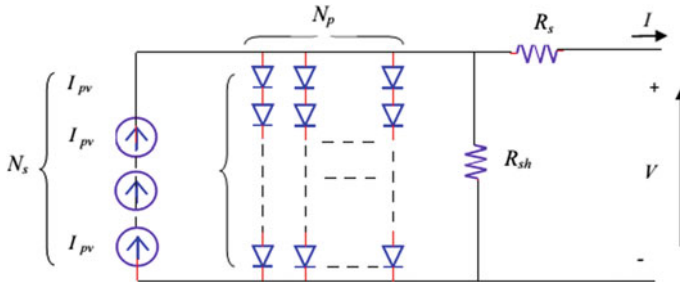


**Fig. 12.1** Single-diode model of PV cell [24]

The current of PV cells through light (radiation) is linearly related to the amount of radiation and is affected by temperature as follows [24]:

$$I_{pv} = \left( \frac{G}{G_{STC}} \right) (I_{pvn} + K_i (T - T_{STC})) \tag{12.2}$$

$I_{pvn}$  is nominal current generated by light generated under standard radiation conditions ( $G_{STC}$ ), and the standard temperature ( $T_{STC}$ ) is related to the standard test conditions (1000 W/m<sup>2</sup> and 25 °C). The nominal photocurrent is defined as follows [24]:

$$I_{pvn} = \left( \frac{R_s + R_{sh}}{R_s} \right) I_{scn} \tag{12.3}$$

$I_{scn}$  represents the nominal short-circuit current.

### 12.3 PV System Under PSC

Figure 12.2 and (a) shows a PV array with a series connection of two modules with a characteristic curve under standard radiation and PSC. When one of the modules is under PSC, instead of one peak, two peaks appear in the characteristic curve of  $V-I$  and  $P-V$ . In PSCs, the PV module is damaged due to the hot spot. Bypass diodes are used to prevent the modules from being damaged by heat. Therefore, to enhance the PV efficiency and prevent waste of PV energy, it is necessary to use the intelligent MPPT method.

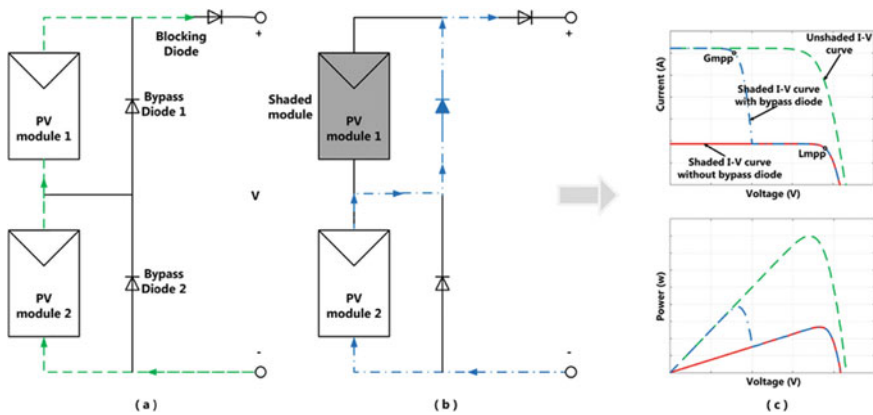


Fig. 12.2 PV array **a** in standard condition **b** in PSC **c** curves of  $I-V$  and  $P-V$  in standard and PSC [25]

## 12.4 Proposed MPPT Method and Implementation

### 12.4.1 Description of MPPT System

MPPT system is shown in Fig. 12.3. PV voltage and current are measured, and their product is calculated by a multiplier and applied to the MPPT method. A duty cycle named  $d$  is generated by the MPPT algorithm based on TFWO, and the converter is activated. The value of  $d$  is selected as the population member position in the TFWO method, and the corresponding output power is considered as fitness of the population member. Therefore, the TFWO algorithm identifies the optimal  $d$  for a typical operational point.

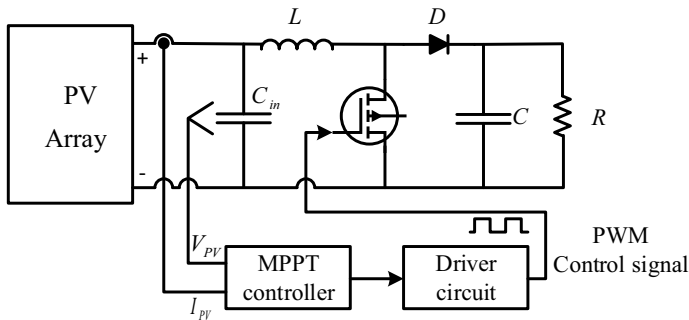


Fig. 12.3 Block diagram of TFWO-based MPPT. Source Author

## 12.4.2 Overview of TFWO

TFWO-based optimization is applied to achieve the MPPT algorithm for the PV system operating under direct PSC with direct control method. To achieve MPPT based on TFWO, each response of the algorithm population member is presented as duty cycle optimization variable. The TFWO algorithm is inspired by water whirlpool motion. The whirlpool is one of the random phenomena in nature. The center of the whirlpool is a pit with suction and draws everything in based on centrifugal force. Sometimes, there are several vortices next to each other, which in addition to breaking objects inside also affect each other. To formulate the TFWO algorithm, several whirlpools have been used in such a way that each of these whirlpools tries to pull objects into their center according to their distance from them. The population of the TFWO algorithm is divided into  $N_{Wh}$  whirlpools (groups). The best member of each group is the tensile strength of the whirlpool, which creates a hole and a tensile force in the center of the whirlpool [29].

The following are the steps for implementing the TFWO algorithm.

### 12.4.2.1 Vortex Formulation

In the first stage, the  $N_{Wh}$  members or vortex group are generated arising from the equal division of the primary population ( $X^0$ , including  $N_p$  members). The powerful member of any vortex set that has the best value of the objective function  $f$  is regarded as a vortex. Then, the selected vortex absorbs other objectives ( $X$ , contains  $N_p - N_{Wh}$  objectives).

### 12.4.2.2 he Effects of Vortex on Its Set and Other Vortexes

Each vortex ( $Wh$ ) is like a vacuum hole that exerts a centrifugal force on the position of its members ( $X$ ) and tries to pull them into itself. Since each  $j$ th vortex is denoted by position  $Wh_j$ , it tends to equate the position of member  $i$ th ( $X_i$ ) with its position as  $X_i = Wh_j$ . However, due to the distance between the vortices ( $Wh - Wh_j$ ) and the different values of the objective function ( $f$ ), some deviations ( $\Delta X_i$ ) are formed, in which case the new position  $i$ th is defined as  $X_i^{new} = Wh_j - \Delta X_i$ . Figure 12.4 shows the effect of vortices on their target members.

According to Fig. 12.4, the target members ( $X$ ) approach to the center of their vortex at a specific angle ( $\delta$ ) that is changing at any given moment (repetition in the algorithm). The value of new angle in situation  $i$  is obtained as follows [30]:

$$\delta_i^{new} = \delta_i + \text{rand}_1 * \text{rand}_2 * \pi \quad (12.4)$$

Equation (12.5) is used to obtain the vortices with the highest and lowest amount of weighed distance among all the targets. Then,  $\Delta X_i$  can be modeled and calculated



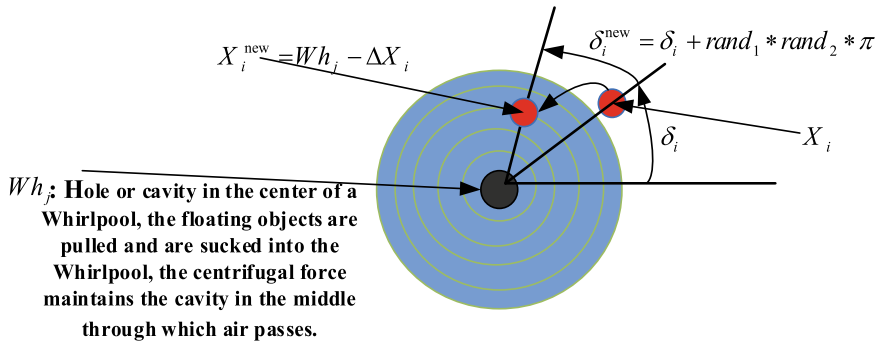


Fig. 12.4 Recommended model of vortex for optimization objectives [30]

by using Eq. (12.6). Equation (12.7) is used to update the position of members as follows [30]:

$$\Delta_t = f(Wh_t) * |Wh_t - \text{sum}(X_i)|^{0.5} \tag{12.5}$$

$$\Delta X_i = \cos(\delta_i^{\text{new}}) * (Wh_f - X_i) - \sin(\delta_i^{\text{new}}) * (Wh_w - X_i) \tag{12.6}$$

$$X_i^{\text{new}} = Wh_j - \Delta X_i \tag{12.7}$$

where  $Wh_f$  and  $Wh_w$  are the amount of vortices with highest and lowest values of  $\Delta_t$ , respectively; and  $\delta_i$  is the  $i$ th target angle.

The pseudo-codes 1 and 2 show the recommended model for updating target situation as follows [30]:

**Pseudo-code (1)**

```

for  $t = 1 : N_{Wh}$ 
 $\Delta_t = f(Wh_t) * |Wh_t - \text{sum}(X_i)|^{0.5}$ 
end
 $Wh_f = Wh_t$  with minimum value of  $\Delta_t$ 
 $Wh_w = Wh_t$  with maximum value of  $\Delta_t$ 
    
```

```

 $\delta_i^{\text{new}} = \delta_i + \text{rand}_1 * \text{rand}_2 * \pi$ 
 $\Delta X_i = \cos(\delta_i^{\text{new}}) * (Wh_f - X_i) - \sin(\delta_i^{\text{new}}) * (Wh_w - X_i);$ 
 $X_i^{\text{new}} = Wh_j - \Delta X_i;$ 
    
```

**Pseudo-code (2)**

```

 $X_i^{new} = \min(\max(X_i^{new}, X^{min}), X^{max});$ 
if  $f(X_i^{new}) \leq f(X_i)$ 
 $X_i = X_i^{new};$ 
 $f(X_i) = f(X_i^{new});$ 
end
    
```

**12.4.2.3 Centrifugal Force**

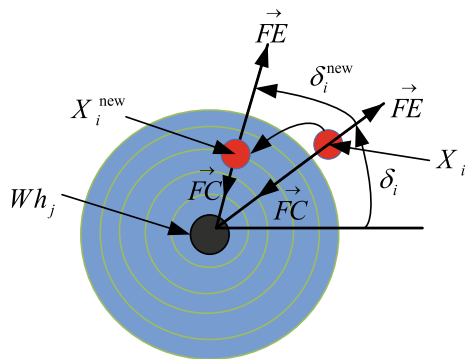
Although on the one hand the attraction force attracts the mobile objects, on the other hand they move away from the respective center by the centrifugal force. Newton’s law of motion states that a stationary object remains at rest and a mobile object moves at the same rapidity and direction unless an unbalanced force is applied to them. When the object moves to a new position, it can be said that the centrifugal force ( $FE_i$ ) overcomes the attraction force of the vortex. Equation (12.8) states that the centrifugal force acts on one dimension of the decision variables. For this purpose, the centrifugal force is obtained by considering the angle between the object and the vortex. Based on the uniform distribution in the range of zero and one, if the value of this force is more than a random value, then the centrifugal force for a selective and random direction is obtained from Eq. (12.9) as follows [30]:

$$FE_i = ((\cos(\delta_i^{new}))^2 * (\sin(\delta_i^{new}))^2)^2 \tag{12.8}$$

$$x_{i,p} = x_p^{min} + x_p^{max} - x_{i,p} \tag{12.9}$$

The pseudo-code 3 is presented in Fig. 12.5 [30]:

**Fig. 12.5** Various types of forces in a vortex [30]



**Pseudo-code (3)**

```

FEi = ((cos(δinew))2 * (sin(δinew))2)2.
if rand < FEi
  p = round(1 + rand * (D - 1));
  xi,p = xpmin + xpmax - xi,p;
  f(Xi) = f(Xinew);
end

```

**12.4.2.4 Interactions Between the Whirlpools**

As vortices pull their surrounded objects toward themselves, each vortex tends to plunge other vortex into its own hole. In order to model this effect, the nearest vortex is obtained based on its objective function and the lowest amount of Eq. (12.10). Then, Eqs. (12.11) and (12.12) are considering for updating the position of vortex as follows [30]:

$$\Delta_t = f(\text{Wh}_t) * |\text{Wh}_t - \text{sum}(\text{Wh}_j)| \quad (12.10)$$

$$\Delta \text{Wh}_j = \text{rand}(1, D) * |\cos(\delta_j^{\text{new}}) + \sin(\delta_j^{\text{new}})| * (\text{Wh}_f - \text{Wh}_j) \quad (12.11)$$

$$\text{Wh}_j^{\text{new}} = \text{Wh}_f - \Delta \text{Wh}_j \quad (12.12)$$

where  $\delta_j$  is the value of the  $j$ th angle of vortex hole.

The pseudo-codes 4 and 5 are presented follow [29]:

**Pseudo-code (4)**

```

for t = 1 : NWh - {j}
  Δt = f(Wht) * |Wht - sum(Whj)|
end
Whf = Wh with minimum value of Δt

```

$$\text{Wh}_j^{\text{new}} = \text{Wh}_f - \Delta \text{Wh}_j;$$

$$\Delta \text{Wh}_j = \text{rand}(1, D) * |\cos(\delta_j^{\text{new}}) + \sin(\delta_j^{\text{new}})| * (\text{Wh}_f - \text{Wh}_j);$$

$$\delta_j^{\text{new}} = \delta_j + \text{rand}_1 * \text{rand}_2 * \pi.$$

**Pseudo-code (5)**

```

Whjnew = min(max(Whjnew, Xmin), Xmax);
if f(Whjnew) <= f(Whj)
Whj = Whjnew;
f(Whj) = f(Whjnew);
end

```

To conclude, if the strongest vortex among the new members of the vortex set has more power, it will be considered as a new vortex in the next iteration. Pseudo-code 6 describes this phenomenon as follows [30]:

**Pseudo-code (6)**

```

if f(Xbest) ≤ f(Whj)
Whj ↔ Xbest
f(Whj) ↔ f(Xbest)
end

```

Flowchart of the MPPT based on TFWO method is shown in Fig. 12.6.

**12.4.2.5 Implementation of TFWO**

In this study, to solve MPPT problem based on TFWO algorithm, the objective function of the problem of maximizing the power of the PV system for the optimal duty cycle of the DC/DC converter is formulated as follows:

$$\text{Maximize } P_{PV}(d) \quad (12.13)$$

The optimization constraint related to the converter duty cycle is presented as follows:

$$d_{\min} < d < d_{\max} \quad (12.14)$$

where  $d_{\min}$  and  $d_{\max}$  are the min and max values of the duty cycle, respectively, which are considered between 0 and 1.

The population of the TFWO algorithm has been updated by

$$\Delta d_i = \cos(\delta_i^{\text{new}}) * (Wh_f - d_{i,\text{old}}) - \sin(\delta_i^{\text{new}}) * (Wh_w - d_{i,\text{old}}) \quad (12.15)$$

$$d_{i,\text{new}} = Wh_j - \Delta d_i \quad (12.16)$$

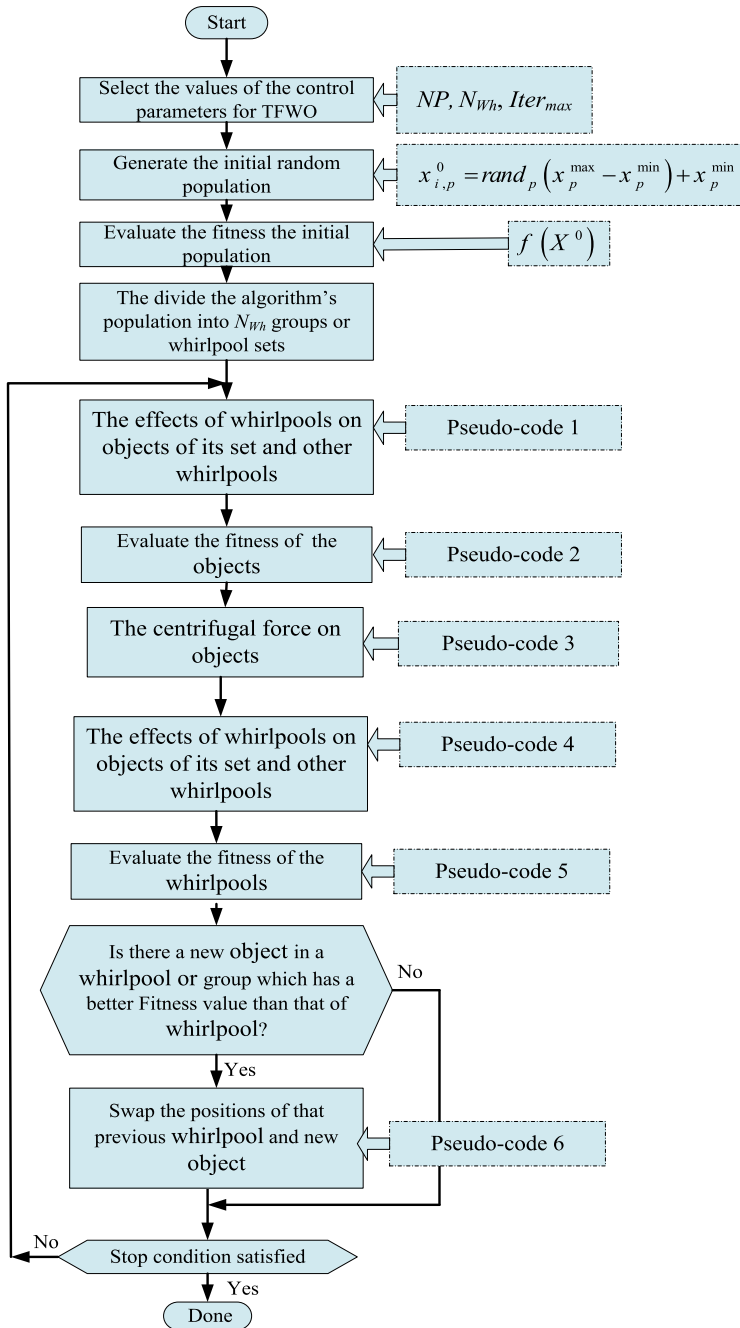


Fig. 12.6 Flowchart of the MPPT based on TFWO method [29]

To determine duty cycles, the controller sequentially generates the PWM signal based on  $d_i$ , then can measure the PV voltage ( $V_{PV_i}$ ) and the PV current ( $I_{PV_i}$ ) and calculate the power ( $P_{PV_i}$ ) of each  $d_i$  duty cycle. The objective function for each duty cycle is defined as [24]:

$$P(d_i^k) > P(d_i^{k-1}) \quad (12.17)$$

where  $i$  is the population number and  $k$  is the iteration number of the algorithm. Due to changes in weather conditions, the amount of power produced by the PV panel changes, the population of the algorithm must be re-quantified according to the following logic to achieve the global peak of PV power.

$$\frac{|P_{PV_{new}} - P_{PV_{old}}|}{P_{PV_{old}}} \geq \Delta P_{pv}(\%) \quad (12.18)$$

In case of inequality of the above equation, a new MPP search is performed. So, according to the TFWO method, the optimal duty cycle guarantees the maximum output power of the PV system.

## 12.5 Simulation Results

In this section, the simulation results of MPPT problem based on TFWO method in partial shadow conditions are presented. The PV system consists of two PV modules with series connection; a DC/DC converter is implemented under test conditions. In this research, two types of converters including boost and buck boost converters have been used to establish the voltage relationship between PV modules and load. One of the most important goals of this research is the comparative evaluation of each converter presented in MPPT problem. In other words, in the first step, the MPPT problem is solved by using the TFWO method based on the boost converter, and then, the buck boost converter is replaced instead of the boost converter and the results of the two converters are compared with each other. The parameters of the PV module and DC/DC converters are presented in Tables 12.1 and 12.2, respectively.

In this section, a simulation method including a Simulink and a single-diode model for a PV module is adopted to evaluate the feasibility and efficiency of the proposed MPPT algorithm.

Table 12.3 shows the parameters of the PV module for single-diode model. The various characteristics of  $V-I$  and  $P-V$  related to PV modules are shown in Fig. 12.7. Also, the Simulink block model of PV system with the PV controller is presented in Fig. 12.8. Numerical values of radiation related to different patterns including a standard pattern and 3 radiation patterns are also presented in Table 12.4.

**Table 12.1** Parameters of PV modules used in (BP SX 80) [25]

Parameter	Value
Maximum power generated	80 W
Open-circuit voltage	22.1 V
Maximum power voltage	17.6 V
Short-circuit current	4.8 A
Maximum power current	4.6 A
Temperature coefficient	-0.080 V/°C
Structure	2S1P

**Table 12.2** Parameters of inverter [25]

Parameter	Value
Switching frequency (fs)	50 kHz
Capacitor (C)	470 μF
Inductor (L)	1.82 MHz
Internal resistance of inductor	0.394 Ω

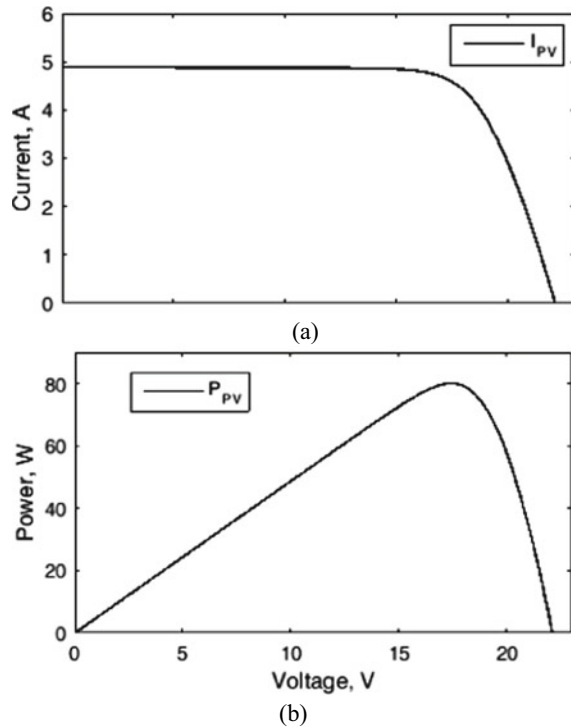
**Table 12.3** Parameters of the PV module for single-diode model [25]

Parameter	Value
$I_o$	4.8902
$I_s$ diode	1.5439
$n$	0.29653
$R_s$	0.22473
$R_{sh}$	466.7217

To evaluate the efficiency of the MPPT algorithm based on TFWO and also to investigate the effect of different converters on the maximum power point tracking, four scenarios are defined as follows:

- Scenario 1 Power pursuit of the PV system with different partial shadow patterns based on TFWO method;
- Scenario 2 Power pursuit of the photovoltaic system with changes in radiation and partial shadow pattern based on the TFWO method;
- Scenario 3 Comparison of the performance of TFWO method with PSO method in MPPT problem solution; and
- Scenario 4 Investigating the effect of different DC/DC converters on MPPT problem solving.
- Scenario 5 The parameter values of the TFWO and PSO algorithms are presented in Table 12.5.

**Fig. 12.7** characteristics of the **a**  $V-I$  and **b**  $P-V$  related to photovoltaic modules.  
 Source Author



### 12.5.1 Results of the First Scenario

The first scenario is to validate MPPT method based on the proposed TFWO to track the general MPP point under transient and permanent SPs. The power and current characteristics in terms of the voltage of the PV module for four SPs are presented in Fig. 12.9. For SP1, the radiation is uniform on all PV sub-modules.

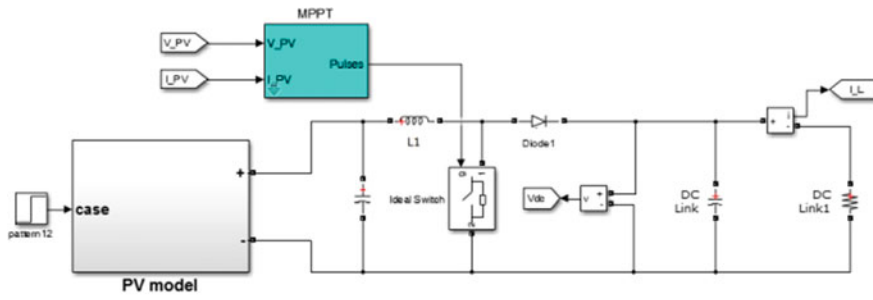
For each pattern of SP, the TFWO algorithm is implemented 100 times. Table 12.6 shows that MPPT based on proposed TFWO is able to successfully track public MPP. The power values of PV module in SP are shown in Fig. 12.10.

### 12.5.2 Results of the Second Scenario

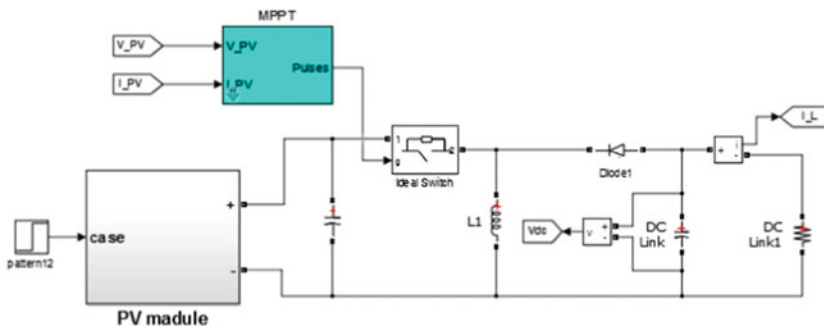
The ability to find general MPP is crucial for new weather conditions. In order to demonstrate the ability to track MPPT based on proposed TFWO under transient irradiation conditions, three stages are considered as follows:

- Stage 1 Changing SP1–SP2
- Stage 2 Changing SP1–SP3





(a)



(b)

**Fig. 12.8** Schematic of PV system **a** boost converter, **b** buck boost converter. *Source* Author

**Table 12.4** Numerical values of radiation [25]

Radiation pattern	Radiation value			
SP1	1000	1000	1000	1000
SP2	1000	500	1000	1000
SP3	1000	700	100	1000
SP4	1000	500	100	1000

### Stage 3 Changing SP1–SP4

Figures 12.11, 12.12, and 12.13 show the characteristics of power, voltage, current, and related cycle for stages 1, 2, and 3. The  $T_s$  MPPT sampling time is set to 0.06 s, and the value of  $\Delta P_{pv}$  (%) (amplitude of power fluctuations in steady state) is set to 2%. When the SP changes from a uniform condition to a relatively shady condition in tenths of a second, the proposed MPPT algorithm can find the general MPP for the new SP.

**Table 12.5** Parameter values of the TFWO and PSO algorithms

Parameter of PSO	Values	Parameter of TFWO	Values
Number of particles	10	Number of particles	10
Number of repetitions	200	Number of repetitions	200
Inertia coefficient	0.9 and 0.4	Number of vortices	10
Personal guidance coefficient	1.2	–	–
Social guidance coefficient	1.6	–	–

Source Author

### 12.5.3 Results of the Third Scenario

In this section, a comparative study of MPPT is performed based on the proposed and PSO methods. At the first step, a comparison is performed based on the presented indicators in Table 12.7. Both algorithms are implemented with ten repetitions for each SP presented in Table 12.4. It can be seen that when the photovoltaic array operates under shadow conditions, the MPPT algorithm based on TFWO has a superior in view of number of successful convergences. Also, in view of accuracy and average convergence value, the MPPT algorithm based on TFWO has a faster convergence rate toward maximum global power point (GMPP) in comparison with MPPT algorithm based on PSO. But, in SP4 shadow conditions, the convergence time of PSO is less than TFWO.

Figure 12.14 shows the generated power by TFWO and PSO algorithms, which can be compared with the criteria of maximum output power (Pmax) and sitting time. Table 12.8 shows the output power of each algorithm. For the first case, the TFWO algorithm has been able to track the MPP with very high accuracy and the amount of PSO algorithm is close to it. Also, for SP2 and SP3, both algorithms have reached to almost maximum power and have been able to reach GMPP. But for SP4, both algorithms have been far from the GMPP, and even after much searching and repetition of the algorithm (100 repetitions), they were not able to reach the GMPP. Therefore, this problem is investigated in the next section, because it seems that the GMPP has been out of reach for the boost converter that is not able to transfer maximum power.

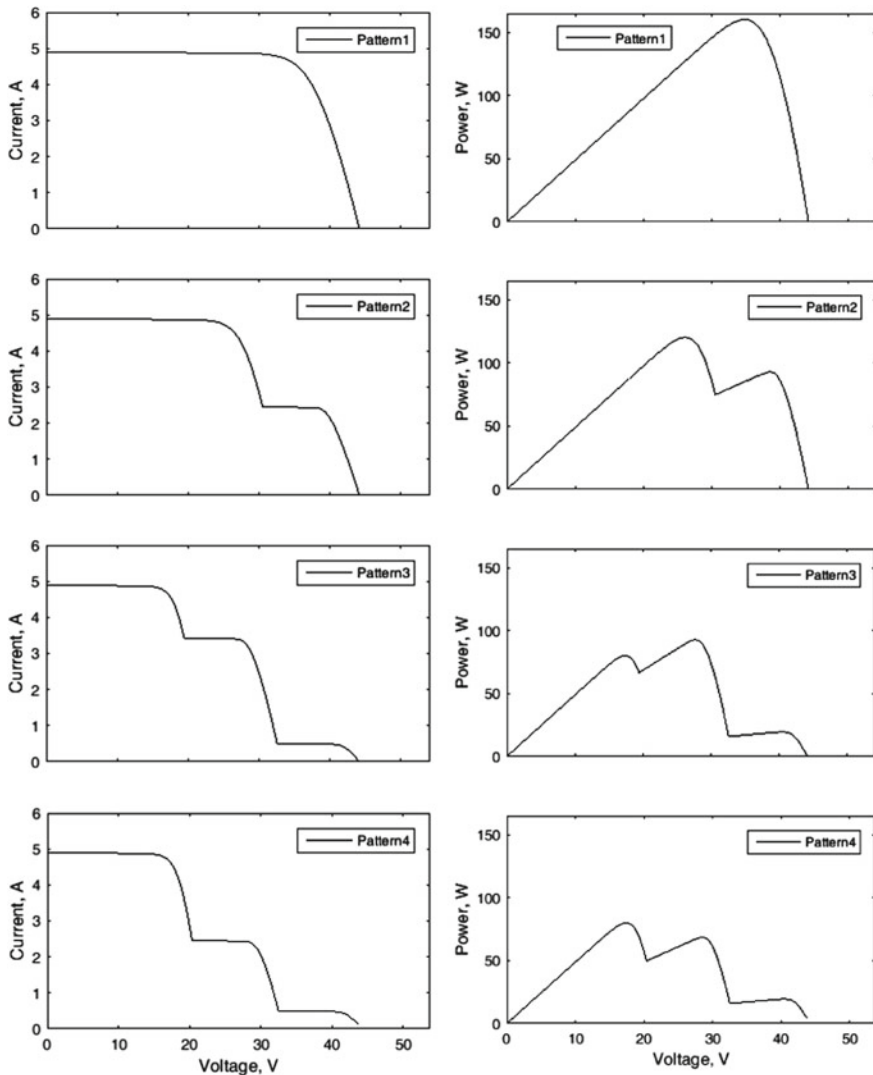


Fig. 12.9 Current and power characteristics of the module under different patterns of SPs. Source Author

### 12.5.4 Results of the Fourth Scenario

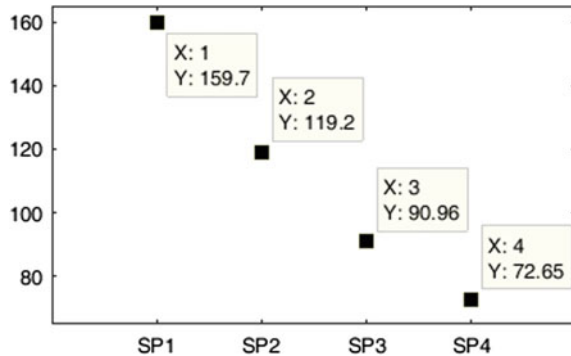
Due to the fact that each type of converter has a specific working area and a certain maximum transferable power, in SP4 mode, it was observed that PSO and TFWO algorithms were not able to reach GMPP, because the GMPP point is not in the working area of the boost converter and it is practically impossible to achieve this

**Table 12.6** MPPT performance based on TFWO presented under various SPs

Radiation pattern	Ideal output power (W)	Output power by TFWO with boost converter (W)	Output power by TFWO with buck–boost converter (W)
SP1	160	159.7	159.7
SP2	120.1	119.2	120
SP3	92.73	90.96	91.68
SP4	80.06	72.65	78.12

Source Author

**Fig. 12.10** Extracted power of MPPT based on proposed TFWO for various SPs.  
Source Author



with a boost converter. In other words, the boost converter is not able to transfer the maximum power and limit the efficiency of the MPPT algorithm, so it cannot follow GMPP. Therefore, in this section, the buck–boost converter is replaced instead of the boost converter and the simulation process is repeated. The results are presented in Table 12.9 and Fig. 12.15. A maximum power of 159.7 W is extracted by both converters when the PV module is not under a partial shadow, but the buck–boost converter converges 50.32% faster than the boost converter and achieves to GMPP. Also, in the case of partial shadow SP2 with equal convergence speed, the buck–boost converter transmits 120 W of power, but the boost converter transmits a maximum of 119.2 W of power. In addition, in SP3 conditions, the buck–boost is both faster and more accurate than the boost. In this case, the buck–boost transmits 91.68 W of power, but the boost transmits 90.96 W of power, and this power advantage is accompanied by 22% further speed of convergence. According to Table 12.9, in the case of SP4 radiation, the boost converter is not able to reach GMPP. Therefore, it has a maximum transmission capacity of 72.66 W with both TFWO and PSO algorithms, which is a long distance up to 80.06 W of maximum power. By replacing the buck–boost converter, maximum output power has been increased from 72.65 to 78.12 W due to its wider operation range.

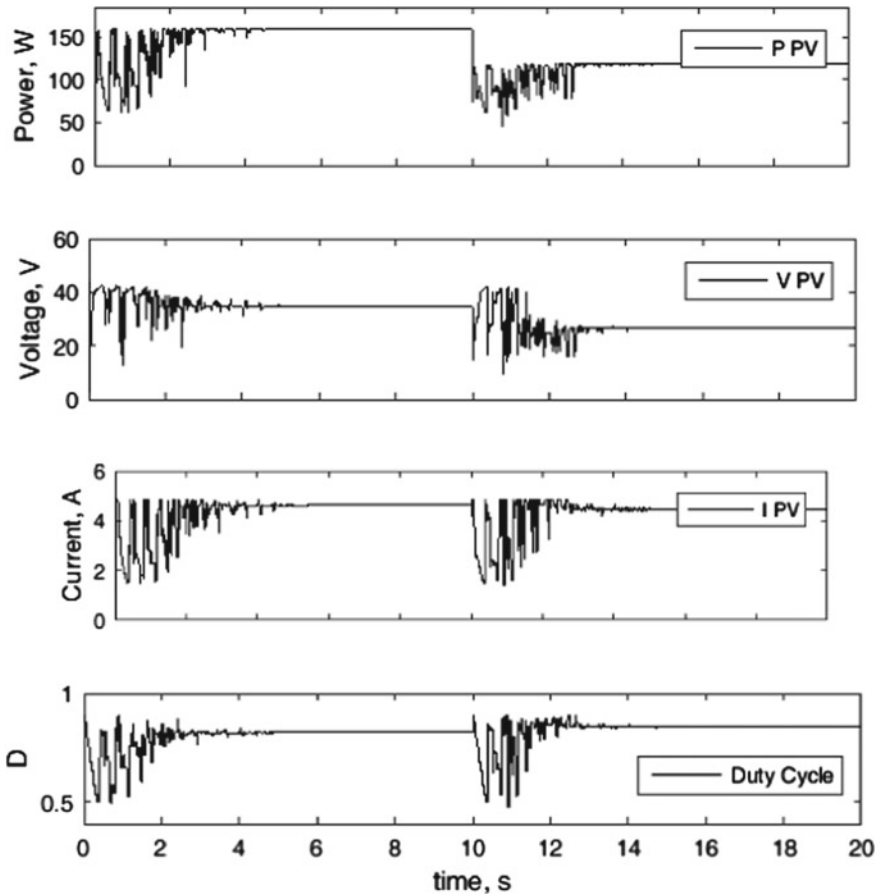


Fig. 12.11 SP changes from SP1 to SP2. Source Author

## 12.6 Conclusion

In this chapter, the TFWO algorithm, which is an intelligent method with easy implementation and without control parameters, is used to solve MPPT and achieve GMPP of PV system with direct control of operation cycle of DC/DC converter. In this study, the TFWO algorithm optimizes operating cycle of DC/DC converter according to maximizing the extracted PV power. The capability of the TFWO is evaluated in terms of different patterns of SPs and radiation changes. Also, to verify the proposed TFWO, the results are compared and analyzed with PSO method. In addition, the effect of using buck–boost converter in comparison with boost converter in terms of problem solution is evaluated with different PSC. The feasibility of the TFWO is confirmed by analyzing different SPs on a PV system. The simulation results showed that TFWO had a better tracking performance than PSO algorithm in finding

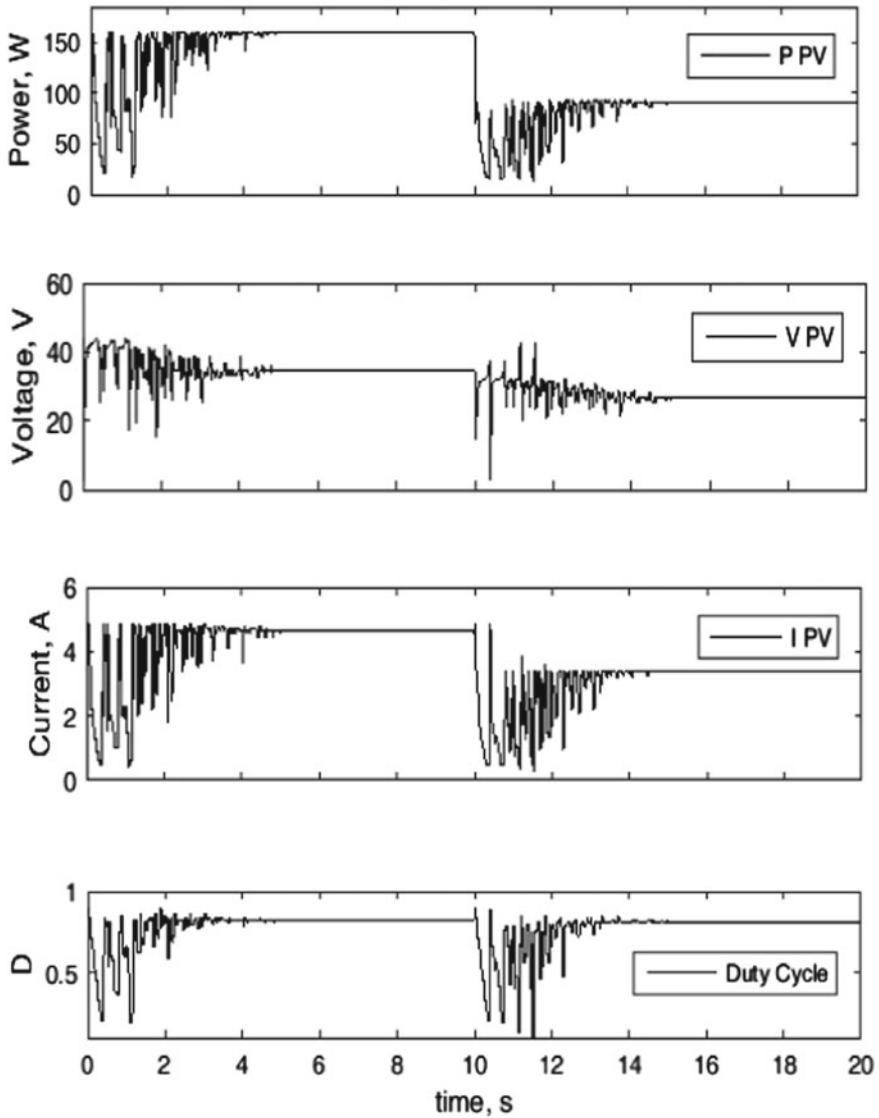
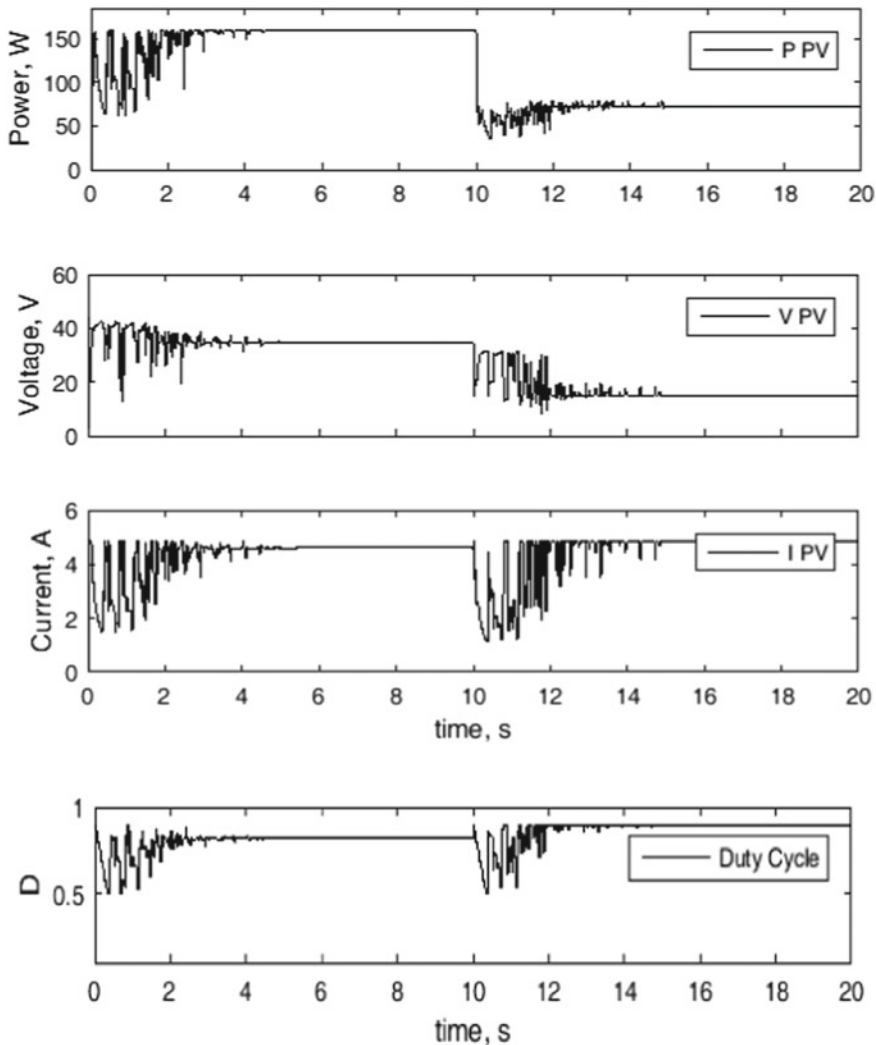


Fig. 12.12 SP changes from SP1 to SP3. Source Author

the maximum point of general power under shadow and variable weather conditions. Also, the results showed that the TFWO method requires quantitative control parameters and this method is independent of initial conditions. In this chapter, simulation process was implemented with four scenarios. In the first scenario, it was observed that the TFWO is able to successfully follow GMPP. In the second scenario, when the SP changed from a uniform condition to a relatively shady condition in tenths of



**Fig. 12.13** SP changes from SP1 to SP4. *Source* Author

a second, the TFWO is able to find the GMPP for the new SP. In the third scenario in comparison with the TFWO with the PSO method, the results showed that when the PV array works under shadow conditions, the TFWO performs better than PSO in terms of the number of successful convergences. Also, in terms of accuracy and average value of convergence, the TFWO has a higher speed of convergence toward GMPP in comparison with PSO. The results showed that the DC/DC converter, an interface between the PV module and the load, has a great impact on the convergence speed and accuracy of the maximum power point. DC/DC converter must be selected so that GMPP is within the operation range of the DC/DC converter so that

**Table 12.7** Comparison between MPTT algorithms based on TFWO and PSO under different SPs

Radiation pattern	Algorithm	Convergence rate to GMPP (%)	Accuracy (%)	Number of cycles
SP1	TFWO	99.68	99.86	8.44
	PSO	99.13	99.45	11.44
SP2	TFWO	98.56	99.78	7.64
	PSO	96.28	99.03	16.16
SP3	TFWO	97.48	99.76	10.66
	PSO	96.68	99.14	15.16
SP4	TFWO	96.33	99.56	9.38
	PSO	93.84	98.38	9.30

Source Author

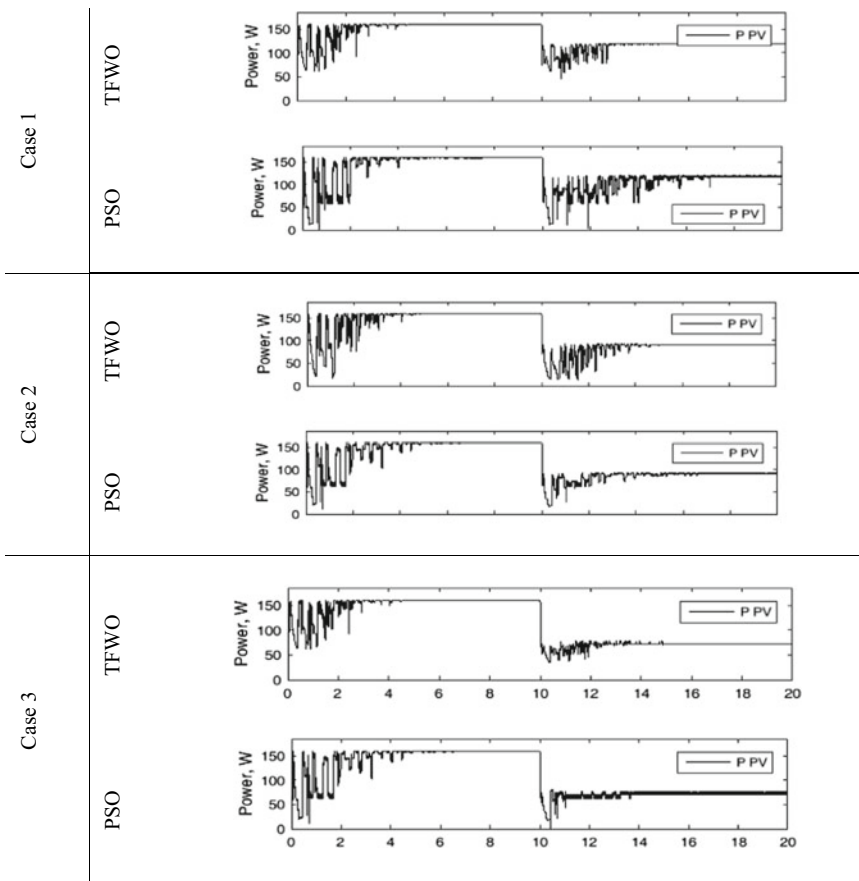


**Fig. 12.14** Comparison of generated power by TFWO and PSO. Source Author



**Table 12.8** Comparison of MPTT algorithms based on TFWO and PSO under different SPs

Radiation pattern	Algorithm	GMPP (W)	$P_{max}$ (W)	Accuracy (%)	Settling time (s)
SP1	TFWO	160	159.7	99.81	3.04
	PSO		159.3	99.56	4.12
SP2	TFWO	120.1	119.2	99.25	2.75
	PSO		118.55	98.71	5.82
SP3	TFWO	92.73	90.96	98.09	3.84
	PSO		90.72	97.83	5.46
SP4	TFWO	80.06*	<b>72.65</b>	<b>90.74</b>	2.45
	PSO		<b>72.59</b>	<b>90.67</b>	3.35

Source Author

\*Maximum power achievable by boost converter is 72.66 W

**Table 12.9** Comparison of boost and buck–boost converters performance with TFWO algorithm under different SPs

Radiation pattern	GMPP (W)	Converter type	$P_{max}$ (W)	Accuracy (%)	Settling time (s)
SP1	160	Boost	159.7	99.81	3.04
		Buck–boost	159.7	99.81	1.51
SP2	120.1	Boost	119.2	99.25	2.75
		Buck–boost	120	99.92	2.76
SP3	92.73	Boost	90.96	98.09	3.84
		Buck- boost	91.68	98.87	3.01
SP4	80.06*	Boost	72.65	90.74	2.45
		Buck–boost	<b>78.12</b>	<b>97.58</b>	3.34

Source Author

\*Maximum power achievable by boost converter is 72.66 W

the algorithm can follow the maximum power. The results cleared that in one of the simulated atmospheric conditions, the boost converter is not able to transfer the maximum generated power, and then, it limits the efficiency of the MPPT algorithm while, by using the buck–boost converter, due to having a wide operation range, it has the ability to follow the GMPP with fast and high accuracy in comparison with the system equipped by boost converter.

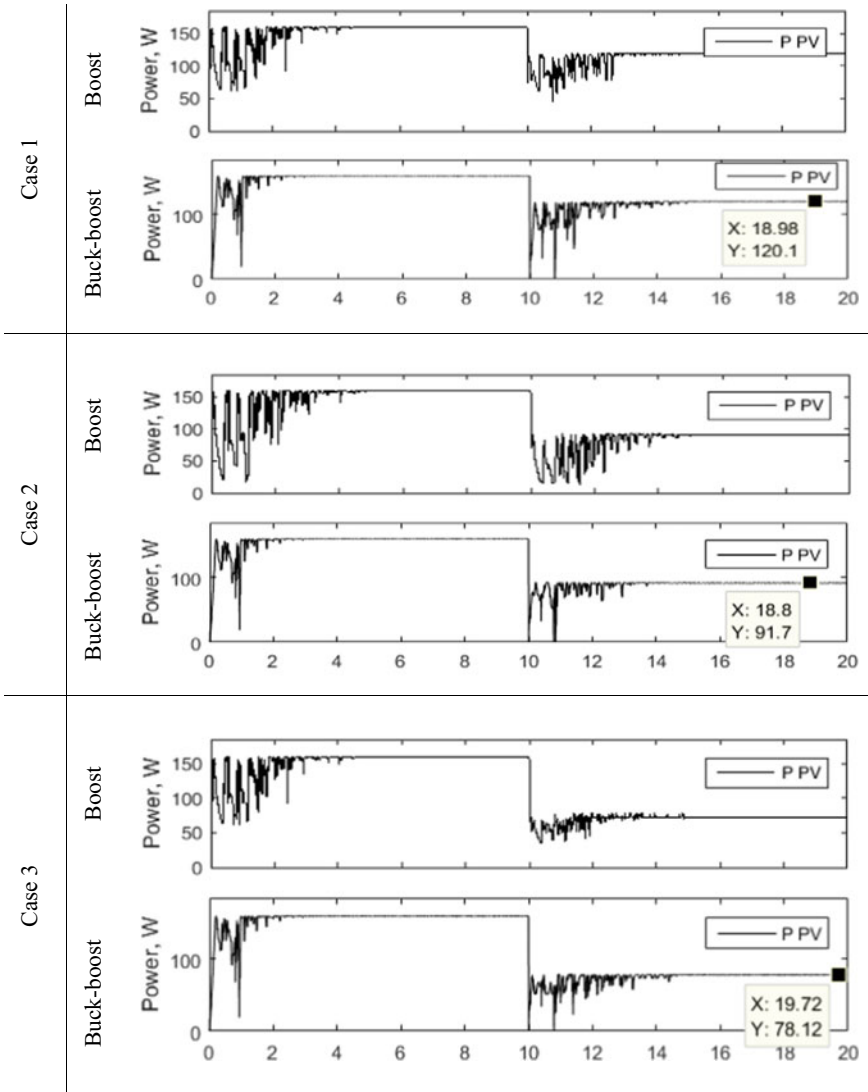


**Fig. 12.15** Comparison of transmitted power by boost and buck-boost converter by TFWO algorithm. *Source* Author

### References

1. Naderipour A, Abdul-Malek Z, Noorden ZA, Davoudkhani IF, Nowdeh SA, Kamyab H, Chelliapan S, Ghiasi SMS (2020) Carrier wave optimization for multi-level photovoltaic system to improvement of power quality in industrial environments based on Salp swarm algorithm. *Environ Technol Innov*:101197

2. Nowdeh SA, Davoudkhani IF, Moghaddam MH, Najmi ES, Abdelaziz AY, Ahmadi A, Razavi SE, Gandoman FH (2019) Fuzzy multi-objective placement of renewable energy sources in distribution system with objective of loss reduction and reliability improvement using a novel hybrid method. *Appl Soft Comput* 77:761–779
3. Mousazadeh H, Keyhani A, Javadi A, Mobli H, Abrinia K, Sharifi A (2009) A review of principle and sun-tracking methods for maximizing solar systems output. *Renew Sustain Energy Rev* 13(8):1800–1818
4. Kamarzaman NA, Tan CW (2014) A comprehensive review of maximum power point tracking algorithms for photovoltaic systems. *Renew Sustain Energy Rev* 37:585–598
5. Nowdeh SA, Moghaddam MJH, Babanezhad M, Davoodkhani IF, Kalam A, Ahmadi A, Abdelaziz AY (2019) A novel maximum power point tracking method for photovoltaic application using secant incremental gradient based on newton raphson. In: *Solar photovoltaic power plants*. Springer, Singapore, pp 71–96
6. Anzalchi A, Sarwat A (2015, Apr) Artificial neural network based duty cycle estimation for maximum power point tracking in photovoltaic systems. In: *SoutheastCon 2015*. IEEE, pp 1–5
7. Lin CH, Huang CH, Du YC, Chen JL (2011) Maximum photovoltaic power tracking for the PV array using the fractional-order incremental conductance method. *Appl Energy* 88(12):4840–4847
8. Esram T, Chapman PL (2007) Comparison of photovoltaic array maximum power point tracking techniques. *IEEE Trans Energy Convers* 22(2):439–449
9. Salas V, Olias E, Barrado A, Lazaro A (2006) Review of the maximum power point tracking algorithms for stand-alone photovoltaic systems. *Sol Energy Mater Sol Cells* 90(11):1555–1578
10. Woyte A, Nijs J, Belmans R (2003) Partial shadowing of photovoltaic arrays with different system configurations: literature review and field test results. *Sol Energy* 74(3):217–233
11. Patel H, Agarwal V (2008) MATLAB-based modeling to study the effects of partial shading on PV array characteristics. *IEEE Trans Energy Convers* 23(1):302–310
12. Velasco-Quesada G, Guinjoan-Gispert F, Piqué-López R, Román-Lumbreras M, Conesa-Roca A (2009) Electrical PV array reconfiguration strategy for energy extraction improvement in grid-connected PV systems. *IEEE Trans Industr Electron* 56(11):4319–4331
13. Kobayashi K, Takano I, Sawada Y (2006) A study of a two stage maximum power point tracking control of a photovoltaic system under partially shaded insolation conditions. *Sol Energy Mater Sol Cells* 90(18):2975–2988
14. Karatepe E, Hiyama T (2009) Artificial neural network-polar coordinated fuzzy controller based maximum power point tracking control under partially shaded conditions. *IET Renew Power Gener* 3(2):239–253
15. Lei P, Li Y, Seem JE (2011) Sequential ESC-based global MPPT control for photovoltaic array with variable shading. *IEEE Trans Sustain Energy* 2(3):348–358
16. Salam Z, Ahmed J, Merugu BS (2013) The application of soft computing methods for MPPT of PV system: a technological and status review. *Appl Energy* 107:135–148
17. Xu J, Shen A, Yang C, Rao W, Yang X (2011, Sept) ANN based on IncCond algorithm for MPP tracker. In: *2011 sixth international conference on bio-inspired computing: theories and applications (BIC-TA)*. IEEE, pp 129–134
18. Messai A, Mellit A, Guessoum A, Kalogirou SA (2011) Maximum power point tracking using a GA optimized fuzzy logic controller and its FPGA implementation. *Sol Energy* 85(2):265–277
19. Taheri H, Salam Z, Ishaque K (2010, Oct) A novel maximum power point tracking control of photovoltaic system under partial and rapidly fluctuating shadow conditions using differential evolution. In: *2010 IEEE symposium on industrial electronics and applications (ISIEA)*. IEEE, pp 82–87
20. Jiang LL, Maskell DL, Patra JC (2013) A novel ant colony optimization-based maximum power point tracking for photovoltaic systems under partially shaded conditions. *Energy Build* 58:227–236
21. Valdez F, Melin P, Castillo O (2014) A survey on nature-inspired optimization algorithms with fuzzy logic for dynamic parameter adaptation. *Expert Syst Appl* 41(14):6459–6466

22. Kermadi M, Berkouk EM (2017) Artificial intelligence-based maximum power point tracking controllers for photovoltaic systems: comparative study. *Renew Sustain Energy Rev* 69:369–386
23. Kheldoun A, Bradai R, Boukenoui R, Mellit A (2016) A new golden section method-based maximum power point tracking algorithm for photovoltaic systems. *Energy Convers Manage* 111:125–136
24. Sundareswaran K, Palani S (2015) Application of a combined particle swarm optimization and perturb and observe method for MPPT in PV systems under partial shading conditions. *Renew Energy* 75:308–317
25. Soufyane Benyoucef A, Chouder A, Kara K, Silvestre S (2015) Artificial bee colony based algorithm for maximum power point tracking (MPPT) for PV systems operating under partial shaded conditions. *Appl Soft Comput* 32:38–48
26. Davoodkhani F, Nowdeh SA, Abdelaziz AY, Mansoori S, Nasri S, Alijani M (2020) A new hybrid method based on gray wolf optimizer-crow search algorithm for maximum power point tracking of photovoltaic energy system. In: *Modern maximum power point tracking techniques for photovoltaic energy systems*. Springer, Cham, pp 421–438
27. Chandrasekaran K, Sankar S, Banumalar K (2020) Partial shading detection for PV arrays in a maximum power tracking system using the sine-cosine algorithm. *Energy Sustain Develop* 55:105–121
28. Ram BK, Chidambararaj N (2020) Grasshopper optimization algorithm utilized Xilinx controller for maximum power generation in photovoltaic system. *Evolving Syst*:1–14
29. Nowdeh SA, Moghaddam MJH, Nasri S, Abdelaziz AY, Ghanbari M, Faraji I (2020) A new hybrid moth flame optimizer-perturb and observe method for maximum power point tracking in photovoltaic energy system. In: *Modern maximum power point tracking techniques for photovoltaic energy systems*. Springer, Cham, pp 401–420
30. Ghasemi M, Davoudkhani IF, Akbari E, Rahimnejad A, Ghavidel S, Li L (2020) A novel and effective optimization algorithm for global optimization and its engineering applications: turbulent flow of water-based optimization (TFWO). *Eng Appl Artif Intell* 92:103666

# Chapter 13

## Phase Change Materials and Its Applications



Anirudh Kulkarni, Rajat Saxena, and Sumit Tiwari

### *Nomenclature*

$C$	Specific heat capacity, kJ/kg K
$\Phi$	Nano-fluid volume fraction
$D$	Equivalent diameter, m
Nu	Nusselt number
$F$	Packing factor
Re	Reynolds number
$W$	Width, m
Pe	Pecklet number
$h$	Convective heat transfer coefficient, W/m <sup>2</sup> K
Pr	Prandtl number
$H$	Sensible enthalpy, J
$k$	Thermal conductivity, W/m K
$I$	Solar radiation intensity, W/m <sup>2</sup>
$A$	Cross-sectional area
$L$	Length, m
$\delta$	Thickness of the material
$L_f$	Latent heat of fusion, J

---

A. Kulkarni · R. Saxena (✉)  
Department of Mechanical Engineering, School of Technology, Pandit Deendayal Energy  
University, Raisan, Gandhinagar, India  
e-mail: [rajat.saxena@sot.pdpu.ac.in](mailto:rajat.saxena@sot.pdpu.ac.in)

R. Saxena  
Department of Chemical Engineering, School of Technology, Pandit Deendayal Energy  
University, Raisan, Gandhinagar, India

S. Tiwari  
Department of Mechanical Engineering, Shiv Nadar University, Gautam Buddha Nagar, India

$\sigma$	Stefan–Boltzman constant, $W/(m^2K^4)$
$\dot{m}$	Mass flow rate, kg/s
$\varepsilon$	Emissivity of glass
$p$	Pressure, $N/m^2$
$t$	Time
$s$	Liquid fraction
$\mu$	Viscosity of fluid
$B$	Constant parameter
$\kappa$	Boltzman constant
$T$	Temperature, K
$U$	Overall heat transfer coefficient, $W/m^2 K$

### ***Subscripts***

$u$	Horizontal component of the velocity, m/s
$a$	Ambient
$v$	Vertical component of the velocity, m/s
$b$	Backplane
$x$	Distance in flowing direction, m
$c$	Solar cell
$y$	Distance in normal direction, m
$g$	Glass
$\alpha$	Absorption coefficient
$p$	PCM layer
$\alpha_t$	Thermal diffusivity, $m^2/s$
ref	Reference value at reference conditions
$\alpha_{mt}$	Indicator function to mark different fluids
$w$	Water
$\eta$	Photovoltaic efficiency
$f$	Fluid
$\beta$	Temperature coefficient of PCM
$c$	Coil tube through which fluid flows
$\beta_t$	Thermal expansion coefficient, $1/K$
np	Nano-particle
$\tau$	Transmission coefficient
bf	Base fluid
$\gamma(T)$	Melt function
nf	Nano-fluid
$F'$	Flat plate collector efficiency factor
$s$	Solid
$\rho$	Density
$l$	Liquid
$V$	Volume

ref Reference value

## 13.1 Introduction

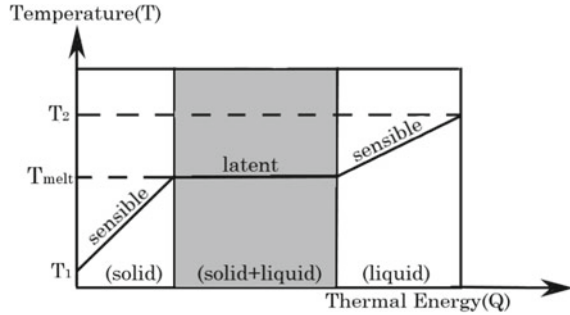
Energy consumption around the world is increasing, while the resources available for sustenance of life on earth are limited. For ensuring the supply of energy to our future generations, it is vital to realize the necessity of conserving energy and use it judiciously. The researchers are working on multiple solutions to this problem. One such solution can be using **Phase Change Materials (PCMs)**. When material transforms from one phase to another, it absorbs or releases energy which is called 'latent heat'. The temperature of phase change is such that it may be exploited for the application. Another significant advantage is a large amount of heat associated with the phase change, which makes the storage size compact, due to its high energy density. There are several applications that are being discussed here to compile the scattered information available in the literature. The general perception, as seen in most of the studies, is they target an application, thus, limiting the scope of the study. This chapter, however, discusses various applications of phase change materials starting from environmental management to human comfort solutions, some of which are still not discussed elsewhere. This study focuses on imparting knowledge on simulation studies, methods to simulate the phase change materials followed by the experimental studies being carried out for buildings energy conservation, and various storage systems for low, medium, and high-temperature applications. For understanding the process, it is first essential to understand the concept of phase change material and its working.

### 13.1.1 *PCM and Its Working*

Materials undergo phase transition when the heat is absorbed or released. This occurs mostly at a constant temperature, for pure substances, known as the melting or boiling point, depending it is a solid–liquid or liquid–gas phase transition. The process solid–liquid phase transition can be understood from Fig. 13.1.

In the solid phase, the material absorbs heat, and consequently, its temperature rises. This continues until melting temperature is reached. Further, the temperature stops rising, and the energy supplied is stored in the form of internal energy, which results in phase change or melting of the material. This heat, absorbed by the material to undergo a phase change, is referred to as latent heat of the material. The reason for researchers being interested in this latent heat is its magnitude which is much higher compared to the sensible heat. Another important aspect is that this energy

**Fig. 13.1** Temperature profile for solid–liquid phase transition for pure substances (Source Author)



is absorbed or released at constant or over a narrow range of temperature. This is useful for many applications which are discussed subsequently in this chapter. The following equations can represent the heat stored for sensible and latent heat storage:

$$Q_{\text{sensible}} = m \cdot C_p \cdot \Delta T \quad (13.1)$$

$$Q_{\text{latent}} = m \cdot L \quad (13.2)$$

where  $Q_{\text{sensible}}$  is the amount of heat stored by sensible heat storage materials with subsequent rise/fall in temperature, denoted by  $\Delta T$  as shown in Eq. 13.1. The heat stored in latent heat storage material,  $Q_{\text{latent}}$ , is given by the product of mass and latent heat capacity of the material at the phase change temperature (Eq. 13.2).

### 13.1.2 Advantages of Using a PCM

As discussed already, the advantage of using PCM is their large heat storage capacity and storing/retrieval of heat at an almost constant temperature known as the phase change temperature. Due to the enormous magnitude of this heat that can be stored, the volume of storage reduces substantially—thus saving on the mass of material required and space to store it. The constant temperature heat storage adds to the application part of PCMs, where the temperature is critical for the heat source. For example, in the case of the solar thermal power plant, the heat can be retrieved at a constant temperature from the storage, which can be transferred to the heat transfer fluid in the cycle.

Another advantage is explored in case of the building where a range of temperature variation is narrow, and these PCMs can be suitable for maintaining the comfort temperature and reduce the temperature fluctuations within the building thereby, resulting in energy savings. Similarly, advantages are observed in the case of PV panels, batteries, and electronic circuits where PCMs can be advantageous in controlling the temperature and avoiding overheating.



### 13.1.3 Scope of Present Study

The scope of this study is first to classify different thermal energy storage materials. Then comparing the suitability of their application, adjudge them based on their properties and highlight various research prospects that exist for PCMs to become a commercially viable solution soon. This study also highlights different approaches used to model PCMs followed by experimental analysis carried out by many researchers on various PCM applications. The potential of PCM application varies from environment conservation to various engineering solutions that may be usefully implemented in many industrial applications. This study would also discuss different commercial products available and that can be developed using PCMs.

## 13.2 PCM as Thermal Energy Storage Material

### 13.2.1 Classification

The energy storage materials can be classified, as shown in Fig. 13.2. This study, however, focuses on different phase change materials. The phase transition can be solid–liquid, solid–gas, liquid–gas, and solid–solid. It is observed that in all these cases, the energy associated with each can be tremendous. In the case of solid–gas and liquid–gas phase changes, the change in volume is quite high. Thus, solid–liquid phase transitions are of significant concern and studied worldwide. Solid–liquid PCMs are subdivided into two types organic and inorganic based on their chemical composition and chemistry. The thermal conductivity of these PCMs is observed to be low in general. Thus, researches are being carried out for PCM enhancement to

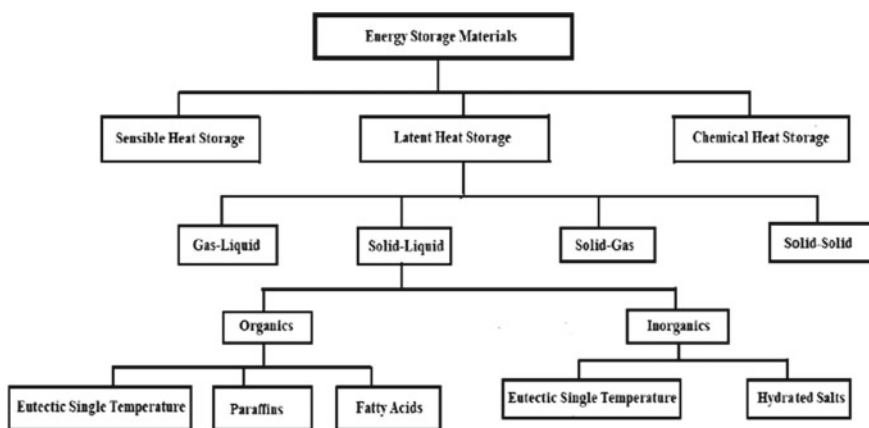


Fig. 13.2 Storage material classification [1]

increase their effective thermal conductivity. This is discussed in detail in Sect. 13.3 of this chapter. It is also observed that organic PCMs seem more promising due to their cyclic stability and non-corrosive nature compared to inorganic PCMs; however, their cost is also relatively higher. Inorganic PCMs, on the other hand, are cheap but they also have supercooling effect. It is defined as the change in melting and solidification temperature. It is observed that the material needs to be cooled below its freezing point to initiate the nucleation to take place, resulting in the starting of the solidification.

The research is being carried out to find suitable nucleating agents that may be added to avoid the supercooling to take place in case of inorganic PCMs. Another category of PCMs is eutectics which can be either organic or inorganic. It is the mixture of two or PCMs mixed such that they melt at ordinary melting temperature. These eutectics can be cheap and more stable. Thus, these materials are also researched for various applications.

### ***13.2.2 Parameters for PCM Selection***

Selection of PCM is of crucial importance and is dependent on the type of application for which it is to be applied. For example, PCMs with low thermal conductivity are suitable for cooling load reduction in hot climatic condition and should be used on the outer side exposed to the sun [2]. Whereas, for cold climatic conditions, higher thermal conductivities are desirable. With higher thermal conductivity, the charging rate of PCM during the day is faster, and it readily discharges during the night by releasing heat to the inside. Thus, the inside temperature can be maintained warmer for a longer duration during the off-sunshine hours, reducing the auxiliary heating load within the building [3]. Therefore, PCM properties are of prime importance. Another critical parameter for PCM is its phase change temperature and temperature of application. It is necessary to map the PCM based on the temperature of use as suitable PCM would result in better thermal characteristics [4]. Thus, mapping of the right PCM is mandatory for the desired output. Furthermore, in building perspective, if PCMs have a solidification temperature lower than the minimum temperature of the place solidification may not occur. Hence, the material would only behave as sensible heat storage on a subsequent day. Therefore, two significant parameters are the requisite properties of PCM, and the temperature of application based on which PCM should be carefully selected.

### ***13.2.3 Properties and Characterization***

PCM properties are of critical importance. The properties of PCM can fall in the following categories:

**Thermal Properties:** Phase change temperature/range, latent heat capacity, specific heat, thermal conductivity, volume change ratio (critical during phase change)

**Chemical Properties:** Cyclic stability, compatibility, corrosion characteristics, phase segregation (must not occur), sub-cooling/supercooling, flammability (should be non-inflammable), environment friendly, and non-polluting

**Economics:** Easily available, low cost, and should be recyclable.

For determining the PCM properties, it is necessary to characterize them. It plays a critical role in terms of PCM selection for design, modeling, and experimentation for various applications. The knowledge available in the literature is limited and also inaccurate in some cases [5]. Another important aspect is the procedure followed for carrying out the characterization. It is observed that the characterization must be carried out as per the application, or else the results may vary [6]. Inorganic PCMs show the tendency of sub-cooling, also referred to as supercooling, i.e., there is a difference in melting and solidification temperature. The latter is lower compared to the prior. This generally goes unreported as in many cases only melting, or solidification cycles are studied and illustrated. In contrast, in actual practice, both melting and solidification cycles must be studied simultaneously to avoid erroneous results in simulations, etc. This phenomenon must be accounted for in the modeling, which is generally neglected, and is of critical importance especially when temperature variation is small, as in the case of buildings, etc. Thus, accurate information on the thermophysical properties of PCMs is critically necessary. The latent heat, specific heat, melting and solidification temperature, and supercooling can be accurately determined by differential scanning calorimeter (DSC). For measuring the thermal conductivity, the thermal conductivity meter is used. The measurement is generally done by two methods, i.e., steady state and transient. The steady-state methods include guarded hot plate and heat flow meter techniques both based on Fourier's law. This, however, is suitable for only solid materials (PCM, however, exists in dual-phase solid-liquid during the operation) and requires long waiting time period to establish a stable temperature gradient within the specimen. However, with technological advancement, there are other methods also available of thermal conductivity measurement for both solid as well as liquid phases, using steady-state methods, in short duration of time. The transient method measures thermal conductivity within seconds. Thus, these methods are gaining popularity. Different transient techniques used are the transient plane source (TPS), transient hot wire (THW), and laser flash.

### ***13.2.4 PCM Enhancement***

PCM enhancement may be referred to as methods to improve the workability of PCMs. Mostly, all PCMs have an inherent problem of poor thermal conductivity. Thus, studies have been carried out for useful thermal conductivity improvement by increasing the surface area with the use of fins [7–9] or by addition of nanoparticles

[10], graphene, and carbon nanotubes [11], etc. It is necessary to identify the need for enhancement and application. For example, nano-enhanced PCMs may be a viable solution for buildings, but they may not be economically feasible. However, for cooling application in space or enhancement of dispatch, ability for storage application in spacecraft, automobiles, defense systems, water heating, etc., may be feasible as well as affordable.

Another critical aspect is inherent PCM issues such as sub-cooling, stability, their incorporation, etc. Each has a different solution to overcome these problems. For example, to avoid sub-cooling suitable additives known as surfactants can be mixed to PCMs. Similarly, for enhanced stability, stabilizing agents can be added. PCMs for incorporation are often encapsulated (micro and macro) depending on the application and cost constraints. There are several pieces of research on coating and encapsulations for PCMs [12–14] for various applications. Thus, it is needed to be understood that the PCM enhancement method must be selected based on the specific requirement of the application and of course the financial constraints.

## 13.3 Numerical Modeling of PCM

### 13.3.1 General Practice

Since the phase change materials (PCM) exhibit solidification and melting, which includes phase transitions, the heat conduction problem can be modeled as a Stefan problem. In such a problem, two different domains are assumed to exist, viz. solid and liquid. These phases are differentiated by a moving interface, a sharp surface front. Usually, this surface front is maintained at the specific melting temperature, a constant latent heat capacity, and has a zero thickness interface of the surface front [15, 16]. A phase change process of such a kind needs attention, and the calculations need to be performed throughout the domain. A single domain approach is very convenient in such numerical calculations since the same system of Navier–Stokes–Boussinesq equations is evaluated inside both liquid and solid phases. In the case of enthalpy porosity approach [17], an explicit treatment is not given to the melt interface, but an entity referred to as the liquid fraction is defined as the cell volume to be in liquid form. The liquid fraction is linked with each grid of the domain. It is evaluated at every iteration of the simulation by balancing enthalpy. Needless to mention that if a non-isothermal phase change is assumed (discussed in detail below), in the semisolid region, the liquid fraction values vary between 0 and 1. A more straightforward approach to handle this semisolid region is to model it as a porous region. In that case, the solid and liquid regions have porosity values of 0 and 1, respectively. It can be attained by explicitly setting the velocity to zero in finite volume methods or by applying penalty models in finite element methods based on viscosity or Carman–Kozeny relation. With these assumptions, the transport equations are given as [18].

Continuity equation:

$$\frac{\partial \rho}{\partial t} + \frac{\partial(\rho u)}{\partial x} + \frac{\partial(\rho v)}{\partial y} = 0 \quad (13.3)$$

X—momentum equation:

$$\begin{aligned} \frac{\partial(\rho u)}{\partial t} + \frac{\partial(\rho u u)}{\partial x} + \frac{\partial(\rho v u)}{\partial y} &= \frac{\partial}{\partial x} \left( \mu \frac{\partial u}{\partial x} \right) + \frac{\partial}{\partial y} \left( \mu \frac{\partial u}{\partial y} \right) \\ &\quad - \frac{\partial p}{\partial x} - \eta \frac{(1-s)^2}{s^3 + b} u \end{aligned} \quad (13.4)$$

Y—momentum equation:

$$\begin{aligned} \frac{\partial(\rho v)}{\partial t} + \frac{\partial(\rho u v)}{\partial x} + \frac{\partial(\rho v v)}{\partial y} &= \frac{\partial}{\partial x} \left( \mu \frac{\partial v}{\partial x} \right) + \frac{\partial}{\partial y} \left( \mu \frac{\partial v}{\partial y} \right) - \frac{\partial p}{\partial y} \\ &\quad - \eta \frac{(1-s)^2}{s^3 + b} v + \frac{\rho_{\text{ref}} g \beta (h - h_{\text{ref}})}{c_p} \end{aligned} \quad (13.5)$$

Energy equation:

$$\frac{\partial(\rho H)}{\partial t} + \frac{\partial(\rho u H)}{\partial x} + \frac{\partial(\rho v H)}{\partial y} = \frac{\partial}{\partial x} \left( \alpha_t \frac{\partial H}{\partial x} \right) + \frac{\partial}{\partial y} \left( \alpha_t \frac{\partial H}{\partial y} \right) + S_H \quad (13.6)$$

The energy equation consists of sensible enthalpy, which is derived from  $H = \int_{T_{\text{ref}}}^T c_p dT$  [19, 20]. The thermal diffusivity,  $\alpha_t = k / \rho C_p$  is multiplied with advection of enthalpy in the above equation. Also,  $u$ ,  $v$ ,  $x$ ,  $y$ ,  $p$ ,  $\mu$ , and  $\rho$  represent the horizontal component of velocity, the vertical component of velocity, horizontal direction, vertical direction, pressure, dynamic viscosity, and density, respectively. Moreover, the Boussinesq approximation holds and is introduced in the Y—momentum equation, wherein  $\beta_t$ ,  $\rho_{\text{ref}}$ , and  $h_{\text{ref}}$  represent coefficient of thermal expansion, and density and enthalpy (reference values), respectively.

### 13.3.2 Types of Grid Techniques Used to Model PCM

There are three approaches to solve the above Stefan problem, based on the choice of grid generation [21, 22],

- Fixed grid method: As the name suggests, the spatial nodes' grid that is utilized for discretizing the domain stays fixed while the simulations progress. The problem is evaluated using state functions and auxiliary constitutive formulations that assists the tracing of the phase change phenomenon because of solidification or

melting. The approach is most common among the studies based on the numerical technique which are available in abundance.

- Deformed grid method: The interfaces or sharp fronts during melting/solidification are traced by moving grid points instead of being fixed. The essence of the Stefan problem is captured through this approach by the deforming grid (Stefan condition) when the solution is calculated.
- Hybrid method: A combination of the above two methods can be applied by coupling the solutions of discretized PDEs solved using a pseudo-fixed grid, along with a local front tracking using the deformed grid method.

In this chapter, only the fixed grid method is discussed as it is most used. Further, this grid method is the simplest of the three to solve problems in the thermal engineering field with phase changes. There are primarily two types of phase changes involved: isothermal and non-isothermal. The equations above show the realistic non-isothermal process, wherein three phases exist. In the case of the isothermal process, however, only solid and fluid phases are considered.

### ***13.3.3 Handling the Energy Equation***

#### **13.3.3.1 Overview**

Based on handling of the energy equation, broadly three different methods are popular in the literature, viz. methods based on enthalpy discussed above, apparent calorific capacity method, and heat source method. In the enthalpy method, a dominant role is played by the enthalpy for distinguishing sensible and latent heat parts for both isothermal and non-isothermal phases changes. If a proper scheme is applied to handle the numerical calculations, it is faster than any other method for PCM modeling. In an apparent calorific capacity method, the sensible and latent heat energy parts are clubbed together for further simplicity. In the heat source method, the source term involves latent heat for obtaining differential equations based on temperature for a proper solution. Usually, in the cases of gradual phase changes, the apparent calorific method is chosen, while the other two methods are widely used when the phase change occurs in small temperature ranges. However, the calorific method is computationally inefficient with coarser grids and large time steps. For this method to be computationally accurate, the grids need to be closely spaced along with very small time step values. Moreover, the convergence is difficult to achieve as the latent heat may be underestimated in this method. If the phase changes occur at a fixed temperature, it is difficult to apply the calorific method. On the other hand, application of heat source method requires serious under relaxation, which calls for further investigation on finding the optimum under relaxation factor values. Further, round off errors exist in case if the melting occurs over a wide temperature range. Hence, one can see the wide applicability of the enthalpy–porosity technique and its popularity among the researchers.

In the above equations, following the heat source method, the source term involving latent heat is

$$S_H = \frac{\partial(\rho\Delta H)}{\partial t} + \frac{\partial(\rho\Delta H)}{\partial x} + \frac{\partial(\rho\Delta H)}{\partial y} \quad (13.7)$$

When the fixed grid technique is used for modeling the melting and solidification, the major difficulty lies in considering the mass and heat transfer conditions near the phase change. An appropriate volume source term should, therefore, be introduced. In the above equation,  $\Delta H$  represents latent heat content. It should be noted that this heat content is a function of temperature and can be written in terms of latent heat of the material as  $\Delta H = sL_f$ . The term “ $s$ ” is often referred to as the liquid fraction and is derived as a temperature gradient between the solidus and liquidus temperatures.

A parameter “ $A$ ” is defined in the momentum equations, which helps retaining velocity its respective value in the solid and fluid regions. As a method to do that, it is defined as [23]

$$B = -n \frac{(1-s)^2}{s^3 + b} \quad (13.8)$$

It should be noted that two constants  $n$  and  $b$  are introduced in the above equation. The purpose of these constant is to maintain the mathematical feasibility of this condition. The constant  $b$  is often retained to a lower value in the range of  $10^{-3}$ , while the constant  $n$  is kept at a sufficiently large value of  $10^9$  in order to avoid division by zero. The aim is to transit the velocity from solid to other phases smoothly to confirm smooth convergence.

### 13.3.3.2 Phase Field Method

It is well known that PCMs have lower thermal conductivity values that leads to a slower rate of charging and discharging. The overall heat transfer rate is affected and, in turn, reduces efficiency. Among the different techniques to overcome this problem, a convenient method is to embed PCMs in porous metal foams with high thermal conductivity. Usually, a representative elementary volume is considered in the case of porous media modeling, wherein the fluid-saturated porous solid aggregates are held to be distributed appropriately. Further, homogenization is applied to achieve a continuum model (volume-averaged). The phase field method (PFM) contains a squishy zone, like the above case, and excludes interfacial energy balance. A free energy density function is key motivation in the case of PFM. This force is liable for the progress of the phase switch zone. Also, PFM utilizes a phase field variable that depends on position and time to ascertain whether the phase is solid or fluid. The resultant method is applicable in capturing dendritic evolution (non-equilibrium) during the supercooled melt solidification [24].

### 13.3.3.3 Volume of Fluid Method

Another approach to model the multiphysical phenomena is coupling volume of fluid (VoF) method with a solid–liquid phase change in the Eulerian frame. Since the introduction of the enthalpy method by Voller and Prakash [25], there have been immense efforts in handling the phase change. The VoF approach was proposed by Hirt and Nichols [26] and has been an excellent technique to capture the interface with the help of an indicator function to mark different fluids. In this approach, the PCM and gas phase are assumed to be two-phase immiscible incompressible fluid along with a fixed grid method.

Equations (13.1)–(13.4) would remain the same in this approach due to the presence of the enthalpy method. However, the VoF method includes an indicator function  $\alpha_{mt}$  to mark different fluids:

$$\alpha_{mt} = \begin{cases} 1 & \text{cell contains first fluid} \\ 0 < \alpha_{mt} < 1 & \text{cell contains the interface} \\ 0 & \text{cell contains second fluid} \end{cases}$$

The first fluid is PCM, while the second fluid is the gas to be modeled. The volume fraction equation can be written as

$$\frac{\partial \alpha_{mt}}{\partial t} + \nabla \cdot (\alpha_{mt} \mathbf{u}) + \nabla \cdot (\mathbf{u}_r \alpha_{mt} (1 - \alpha_{mt})) = 0 \quad (13.9)$$

In the above equation,  $\mathbf{u}_r = \mathbf{u}_1 - \mathbf{u}_2$ , is the relative velocity between the PCM and the gas phase. Moreover, another source term has to be included in momentum equations related to the surface tension force ( $\sigma_s$ ), given by,

$$S_\sigma = \sigma_s \nabla \cdot \left( \frac{\nabla \alpha_{mt}}{|\nabla \alpha_{mt}|} \right) \nabla \alpha_{mt} \quad (13.10)$$

The specific enthalpy can also be considered as the sum of sensible and latent heat values, to give,

$$H = \int_{T_{ref}}^T c_p dT + \alpha_{mt} \gamma(T) L_f = c_p (T - T_{ref}) + \alpha_{mt} \gamma(T) L_f \quad (13.11)$$

Unlike the previous case,  $\gamma(T)$  is introduced here as the melt fraction, and it depends on temperature and the latent heat of fusion ( $L_f$ ). It attains zero value in the solid zone, and 1 in the liquid zone, while it ranges between 0 and 1 in the mushy zone. The parameter A or Darcy-type source term is introduced in this method like the earlier approach.

If Eq. 13.12 and the energy equation, Eq. 13.6, are combined and written in a concise form, the following equation is obtained



$$\frac{\partial(\rho c_p T)}{\partial t} + \nabla \cdot (\rho u c_p T) = \nabla \cdot (\kappa \nabla T) - \alpha_{\text{mt}} L_f \left[ \frac{\partial \rho \gamma}{\partial t} + \nabla \cdot (\rho u \gamma) \right] + T_{\text{ref}} \left[ \frac{\partial(\rho c_p)}{\partial t} + \nabla \cdot (\rho u c_p) \right] \quad (13.12)$$

### 13.3.4 *Sophisticated Tools Available*

The above methods discussed have a wide range of applicability. However, there are sophisticated tools available which implement these models for specific applications. The commercial packages COMSOL, FLUENT, and HEATING do provide the option to model PCMs out of the box with some level of customization to implement new models. Mostly, they implement heat source (or heat capacity) method and can be used to simulate different applications based on the finite element, finite volume, and finite difference method, respectively [27].

An abundance of pre-packaged applications is focused on the thermal management through the usage of PCM in the whole building design. Such applications help designers and manufacturing companies to focus more on inventive ideas to develop the energy and thermal performance of buildings. Aspects such as dynamic involvement among all thermal-based elements linked with ease and comfort and energy consumption are accounted that includes building envelope, air conditioning, lighting, and control devices. There are many articles about listing tools capable of handling the dynamic behaviors of a building and its systems [28].

#### 13.3.4.1 **EnergyPlus**

EnergyPlus [27] is one among many of such tools. It uses the conduction transfer functions (CTFs) to approximate heat transfer in building envelope. Moreover, it has a conduction finite difference (CondFD) solution algorithm, which uses a semi-implicit finite difference scheme. The scheme is based on heat capacity method, and the latent heat evolution is considered using an auxiliary enthalpy–temperature data set. In the latest versions of the software, a fully implicit scheme can be found, providing numerical flexibility. Some limitations of this software include the compulsion to use a lower time step size, using 1/3rd of the default node space, and PCM hysteresis is left unaccounted, which may cause a discrepancy in the results.

#### 13.3.4.2 **TRNSYS**

TRNSYS consists of several “TYPES” modules are linked together, making it a modular program. In such a program, the output of one model is linked with the

input of another model [29]. Such a program can be useful in modeling complex building systems, wherein existing TYPES can be used, or new modules can be created, and it can be easily integrated into the TRNSYS package. Furthermore, external applications can also be linked into TRNSYS. The program has by default several models for phase change heat transfer. However, most of the times propriety research modules opt like TYPE36, TYPE58, TYPE204, TYPE1270, and so on.

#### **13.3.4.3 ESP-r**

ESP-r is a UK-based simulation tool that is of dynamic energy type [30]. It is used for modeling the thermal, visual, and acoustic performance of buildings. The effective heat capacity and additional heat source methods are used by default in ESP-r. Again, fine time steps are necessary to obtain sufficiently accurate results in this tool.

#### **13.3.4.4 BSim**

BSim is another dynamic simulation-oriented program, and it is based in Denmark. It has an attractive graphical user interface which helps the users to get oriented easily. It is based on heat capacity method using the quasi-steady state in building modeling. Overall, it gives accurate behavior of PCM but with a fine value of time step and can be used for continuous heating and cooling and heating with low initial temperature (below the melting point of PCM).

#### **13.3.4.5 Others**

There are other research-based tools as well like PCMExpress, RADCOOL, and CoDyBa. PCMExpress is a German-based planning and simulation program mainly used for thermal management of buildings. The tool assumes a building that floats freely, and one can simulate various types of building materials and weather conditions. Such a simulation helps the decision-making process during the early design stage. RADCOOL has been designed for cooling and heating system based in the USA [28].

### **13.4 PCM Applications**

PCM application can be broadly classified based on the temperature of application. The first is for low or medium temperature applications that refer to temperature range up to 150 °C and second for high-temperature application where the temperature is above 150 °C. The application domain for both these temperature domains has been enlisted and discussed below.

### 13.4.1 PCM Application for Low and Medium Temperature Range

#### 13.4.1.1 PCM Application as an Environment Management Solution

With global warming becoming a threat, people living in hilly areas are facing problems of melting glaciers and water shortage, leading to population migration. A researcher and engineer (Sonam Wangchuk) in Ladakh found a unique solution by using water in the form of ice as storage. The phase change concept was used to store the runaway water during winters in the form of huge stupas saving around 200 million liters of water in each stupa. The downstream water is made to pass through pipes, and flow is controlled using the valves. During the night at sub-zero temperature, the water is sprinkled which solidifies immediately and settles forming a stupa. The structure is grown big enough such that it could sustain and hold. This unique structure is called as the “Ice Stupa” and is shown in Fig. 13.3.

The Ice Stupa holds the Guinness Book of the world record of the most massive human-made ice structure, which is a simple application of water as phase change



**Fig. 13.3** Ice Stupa by Sonam Wangchuk (*Credit* Rolex awards; <https://www.rolex.org/rolex-awards/environment/sonam-wangchuk>)

material. These structures melt during April and provide water to the locals for irrigation, etc., when it is most required. This unique concept has helped to replenish the melting glaciers and helped the locals to sustain life in Ladakh, Himalayas, in India.

### 13.4.1.2 PCM Application in Buildings

PCM application in buildings is of interest for researchers across the globe. For maintaining a lower inside temperature, the building in olden days was built with thick walls that are they aimed at increasing the thermal mass of the buildings. To mimic that, PCM integration can be a viable solution. Due to the high storage capacity of PCMs, the thinner walls, integrated with PCM, can provide similar thermal shielding effect.

Figure 13.4 shows a schematic diagram of the working of a PCM, within a building envelope. The figure shows four different scenarios of a typical summer day (hot climatic condition), i.e., morning 8 am, evening 4 pm, night 8 pm, and early morning 4 am over a 24-hour cycle to understand the concept behind the incorporation of PCMs within a building. At 8 am, the sun is up, and solar radiation starts falling on the exterior walls/surfaces. The temperature starts rising. As the day progresses, the surface temperature tends to increase further. The surface temperature

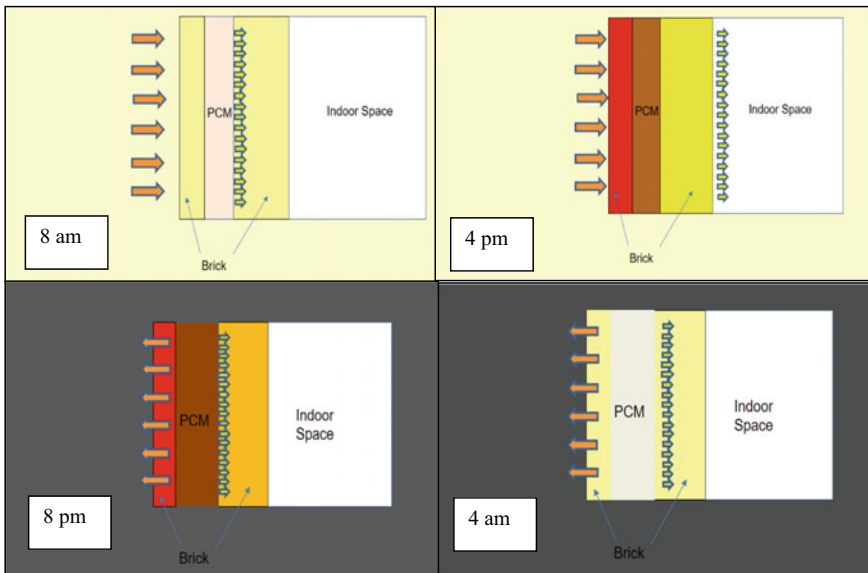


Fig. 13.4 Schematic to depict the working of a PCM within a building ( Source Author)

rises above the ambient temperature due to solar air effect [4]. The inside temperature is comparatively cooler. Thus, heat transfer starts taking place from outside to the inside.

As the temperature on the outer surface rises, the heat flow to the inside also increases. The temperature rises until the PCM melting temperature is reached. Now with the addition of heat, the PCM starts melting, and the temperature of the PCM layer is stagnant at its melting temperature. Now two heat flows occur one due to the temperature difference between outside layer and PCM, and other between PCM temperature and temperature on of the inside layer. The difference between the two is stored within the PCM and is utilized as phase change latent heat. This continues until complete melting of the PCM takes place. As depicted at 4 pm, the PCM is completely melted, and the temperature on the inside starts rising. However, at sunsets, the temperature on the outside goes down, as shown at 8 pm. The temperature of PCM is higher than both the ambient temperature and the inside surface temperature. Two heat flows circuits are formed, one from PCM to the inside and other from PCM to the outside. Now, since resistance is less due to lower wall thickness on the outer side, and there is a higher temperature difference, more heat is discharged outside. Only a small amount flows to the inside; thus, PCM gets discharged (releases heat) and solidifies, as shown at 4 am, in the diagram. The overall heat flowing to the inside over a 24-hour cycle can be reduced by 12–15% [31]. It is necessary to get discharged at night to be available to absorb heat the next day. This can be ensured by careful selection and benchmarking of PCMs [32]. PCMs need to be mapped to a particular climatic condition based on the melting temperature of the PCM and the climatic conditions of the location to ensure daily charging and discharging of the PCM and effective utilization.

Kaushik et al. [33] modeled PCM incorporated building in 1981. There were a series of studies that followed [34–38]. These studies were carried out for cold climatic conditions. In Indian perspective, studies were initially carried out by Pasupathy et al. [39] and Kant et al. [40] followed by experimental studies carried out for New Delhi by Saxena et al. [14]. These studies showed a temperature reduction up to 6 °C with PCM incorporated brick compared to the conventional ones. It is first necessary to understand the amount of solar radiation falling on to the surface. The solar radiation falling on a surface data is available for different places. However, the radiation falling on various wall surfaces is to be calculated. Typical values for the solar radiation falling on different surfaces are calculated based on the radiation data available for May first week as shown in Fig. 13.5.

The temperature of the surface exposed to sunlight is higher than the ambient temperature. As discussed, this is due to the solar air effect [43]. This temperature generated at the surface is responsible for heat transfer to take place. The difference in this surface temperature and the inside temperature acts as the driving potential for heat transfer to take place. This has been modeled by several researchers [44–48] and heat flow to the inside for different scenarios, climatic conditions and wall parameters have been discussed. Further, experimental studies have been carried out for PCM incorporated bricks [41, 49–51] showing energy savings up to 15% over 24 h cycle and peak heat transfer reduction up to 50% during the day for both hot

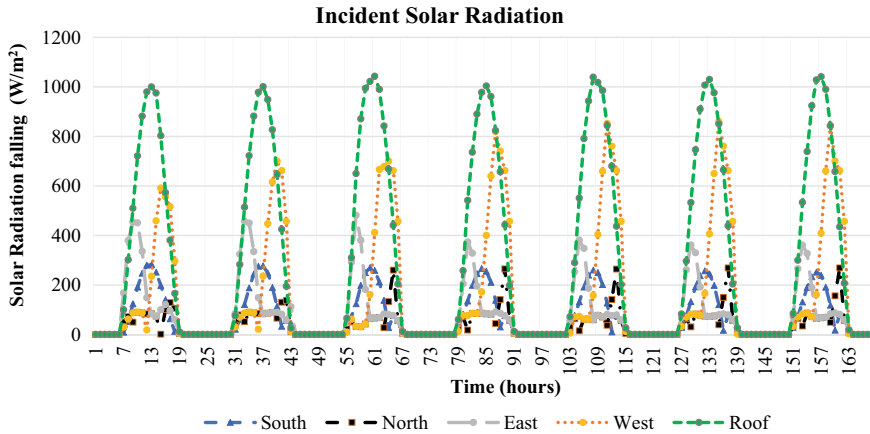


Fig. 13.5 Calculated values of incident solar radiation falling over different surfaces [42]

as well cold climatic conditions. There have been studies on PCM incorporated wall boards [52, 53]. However, leakage issues need to be addressed before the actual implementation of these PCM boards as a retrofit solution. The studies on actual PCM incorporated rooms have also been carried out by a few researchers for cold climatic conditions [54–58]. The results show a significant lowering of heat transfer. Still, detailed economic analysis and feasibility study need to be carried out followed by the investigation of cheaper PCM alternatives, thus, making PCM buildings as a solution for future energy-efficient buildings.

### 13.4.1.3 Constant Temperature Solar Drying and Space Heating Application

India is the second-largest producer of the fruits and vegetables in the world with a production of 259 million MT with wastage of nearly 4.6–15.9% in fruits and vegetables annually. As per latest estimates by the Associated Chambers of Commerce of India, our country loses approximately INR 926 B (US\$ 14.33 B) after harvest every year, due to rejection at the farm gate, lack of proper storage facilities, and delays in the distribution process. Thus, food preservation can be critical for agricultural countries like India. The general meaning of food preservation is to extend their shelf life by preservatives that retard their rate of spoilage. These can be achieved by various techniques like drying, cooling, storing at a constant temperature, etc. Drying is an efficient way easy to handle and enhances crop life in such a way that its nutritional value can be retained. In the drying process of certain food products, the temperature is the crucial parameter. In the current situation, farmers are accustomed to use open-air sun drying process for drying and preserving their agricultural products. This causes browning of products, resulting in deterioration of food quality. If we use solar dryer integrated with phase change material (PCM), providing constant



**Fig. 13.6** Solar drying setup with PCM storage at Pandit Deendayal Petroleum University ( *Source Author* )

temperature heating of food products and simultaneously storing the excess solar energy into the form of latent heat during the day which can provide warmth during night hours as well. Thereby quality of the crop can be restored as well as browning phenomena can be avoided. The PCM incorporated solar dryer setup is shown in Fig. 13.6.

The target is a sustainable technology for the preservation of several items like vegetables, medicinal plants, fruits, etc., using constant temperature-controlled drying. Another initiative by the National Institute of Solar Research (Government of India) has developed solar dryer cum space heating system based on evacuated tube collectors and used PCMs for temperature-controlled drying and heating. These systems have been installed in Ladakh, are under testing phase, and have shown excellent results in terms of space heating as well as fruit drying.

#### **13.4.1.4 Thermal Management of Photovoltaic (PV) Modules and Electric Circuits**

There has been a significant increase in the use of PV for power generation over the past decade to harness renewable energy from solar. There have been researches carried out that shows that temperature control of the module increases their efficiency. Brano et al. [59] developed the thermal model analysis of the crystalline PV-PCM system using the finite difference method. It was found that the discharging of PV panels is essential for efficient working of the system, and there needs to be good thermal contact between PV and PCM.

Indartono et al. [60] used petroleum jelly as PCM on the backside of 10-watt-peak monocrystalline solar panel in Indonesia outdoor conditions and found that the average power and efficiency increased by 7.3 W and 6%. Abdelrazik et al. [61] did an experimental validation for a PVT/PCM system. The setup was the same old setup as everyone with PCM at the back and cooling fluid in between the PCM. The PCM used here was paraffin wax mixed with different concentrations of graphene

nano-platelets along with pure water as cooling fluid. The experiment was conducted in two different conditions: one in winter and other in summer. The PVT/PCM was highly efficient in summer with an electrical efficiency enhancement of 22% versus 6.9% in the winter when compared to stand-alone PV.

Fayaz et al. [62] explored a novel design of a thermal collector made up of aluminum. The experiment was conducted for PV, PVT, and PVT-PCM systems to observe, evaluate, and analyze efficiency under different operating conditions. The experiment consisting of the PVT-PCM system was conducted using paraffin wax (commercial code name A44-PCM). For the PV-thermal hybrid systems, water flows through the serpentine thermal collector, which is passively driven by the overhead water tank. It was observed that there was a reduction in the temperature of PV cell by 8.3 and 8.1 °C in case of PVT, and 12.8 and 12 °C in the case of the PVT-PCM system from the PV module, experimentally and numerically, respectively. Similarly, the electrical efficiency obtained for the PVT-PCM, PVT, and PV systems numerically is 14, 13.85, and 13.72% when compared to experimental values of 13.87, 13.74, and 13.56%.

Waeli et al. [63] used time-varying equations to get results that are more accurate by cooling PV module with both PCM and nano-fluid.

Drawing of a mathematical model in the context of the proposed collector: (a) equivalent thermal circuit of PVT, (b)–(e) glass, PV, wax layer, and tube coil, respectively.

For glass

$$(\rho CV)_g \frac{dT_g}{dt} = \alpha_g I(t) - \left[ U_{ga}(T_g - T_a) + \frac{k_g A_g (T_g - T_c)}{\delta_g} + \sigma \epsilon_g A_g (T_g^4 - 9.3 \times 10^{-6} T_a^6) \right] \quad (13.13)$$

For cell

$$(\rho CV)_c \frac{dT_c}{dt} = (1 - \alpha_g) I(t) - \frac{k_g A_g}{\delta_g} T_g + \left( \frac{k_g A_g}{\delta_g} - \frac{k_c A_c}{\delta_c} \right) T_c + \frac{k_c A_c}{\delta_c} T_p \quad (13.14)$$

For PCM

$$(\rho CV)_p \frac{dT_p}{dt} = \frac{k_c A_c}{\delta_c} T_c - \left( \frac{k_c A_c}{\delta_c} + h A_c \right) T_p + h A_c T_a - \dot{m} C_f T_f + \dot{m} C_f T_{fin} \quad (13.15)$$



### 13.4.1.5 Heating and Cooling Applications

Heating required for cold places is often quite large, for example, in the UK alone the heating power needed comprises one-fifth of the total power consumption. Further, hot water is required for household requirement, in hospitals, and restaurants for cleaning and sanitization purposes. One way is to use electrical power to generate heat, and another option is to use solar heat energy, store it, and use as and when required. Thus, the energy loss due to conversion can be avoided, and more of renewable power can be used. Similarly, the exhaust heat available at the end of the power cycle can be used for space heating applications. This has been implemented in some places as a pilot project in some of the cold countries. Use of PCMs as storage in these systems can enhance the heat storage capacity as latent heat storage can be 50 times more than the sensible heat storage [64]. Another important aspect is using solar energy for heating. The solar radiation is available during the day. However, the requirement of hot water/heat is more during late evening or early morning hours when the sun is not available. To bridge this gap between demand and solar availability, PCM can play a significant role in terms of storing the heat during the sunshine hours and providing it during the off-sunshine hours. Studies show that temperature stability and hold is more for PCM solar heating system compared to any sensible heating system. The PCM utilization for heating applications has been researched where waste heat from various systems and sub-systems can be stored and used for allied applications and result in a substantial amount of energy savings. A numerical study carried out for the UK suggested that PCM water heating application can result in the lowering of CO<sub>2</sub> emissions by 11% [65]. Another study is on nano-enhanced PCM for solar water heating application [66]. Thus, PCM application for heating application has enormous potential.

PCM can also be applied for industrial heating applications where constant controlled heat is required, for example, in the sugar industry for drying the moisture to obtain sucrose. Similarly, it can be applied in the dairy industry to produce different milk products like butter, ghee, condensed milk or khoa, etc.

Besides heating, PCMs can be used as a cooling option. One such application used since decades is desert coolers. In desert coolers, the water evaporates cooling the incoming air which is forced out after cooling through the fan. Another example is earthen pots used since ages in India, where water changes its phase from liquid to gas cooling the water inside the pots. These are used in households in India during the summer season. Further, researches are being carried out using the solid–liquid phase transition for solar-assisted cooling application in case of adsorption cooling to overcome the problem of intermittent solar radiation as a heat source during off-sunshine hours. These applications are still under research stage, and systems are being developed and tested for different ambient temperature scenarios.

### 13.4.1.6 Battery Thermal Management for Electric Vehicles

With the advent of electric vehicles, there have been significant researches concentrated on battery life and efficiency. Currently, lithium-ion (Li-ion) batteries are considered as the most promising technology for the storage of electrical energy, and one of the critical parameters is its working temperature range. Acceptable temperature range of EVs is between  $-20$  and  $60$  °C, while the optimum temperature range is  $15$ – $35$  °C. The temperatures above  $60$  °C possess a severe threat of causing thermal runaway in Li-ion batteries [67]. Cooling systems are therefore needed to be designed which should be lightweight and compact and should not act as a parasite on battery pack as most active cooling systems, thereby decreasing overall EV efficiency. The system should be able to perform well in adverse climatic condition and should be cost-effective and environment-friendly. For cold countries, air cooling is a viable option. However, for countries like India, the temperature of ambient air is not sufficient to cool the batteries sufficiently. Thus, there is a need for incorporating an additional cooling system. Using PCM can be a feasible solution as a passive cooling alternative used in combination with an active cooling system. Rangappa et al. [68] have reported a hybrid cooling system that uses outcomes of the computational fluid dynamics simulations. This system maintains the temperature within  $313$  K ( $40$  °C) for the battery using a  $9$ -mm-thick pure phase change material (PCM) under heat generation rate of  $30,046$  W/m<sup>3</sup>. The coolant flow rate can be increased beyond  $2$  L/min to achieve better performance of the system. Verma et al. [67] have studied prismatic and cylindrical lithium-ion batteries based on their performance in a high ambient. PCM utilization for battery thermal management is still at the research stage, and experimental setup for testing the battery characteristics is being carried out.

### 13.4.1.7 Wearable PCM Devices

PCM application for buildings and battery temperature control has already been discussed, and it is seen that PCM can be suitable to application for given temperature range. Similarly, in PCM incorporated fabric design solutions can be used for maintaining the comfort temperature. For instance, consider two cases of firefighter and an army officer in combat stationed in posts in extreme climate, both are exposed to extremes of temperature. Firefighters or an army officer posted in hot climatic condition of say a desert location has very few options to maintain a cold temperature. PCM fabric-based uniforms can be used for such situations as they could store extreme heat and maintain cooler/tolerable temperature for more duration. In the case of firefighters, even a few more extra minutes can be lifesaving. PCMs with enhanced storage capacity can help in sustaining the harsh environment for a longer duration. These jackets can be charged in base camps or during the night when the temperature is relatively lower. There are some products already available in the market used to relieve sprained muscle, etc., using ice packs, etc. There can be many other potential applications for these PCM fabrics which are under investigation.

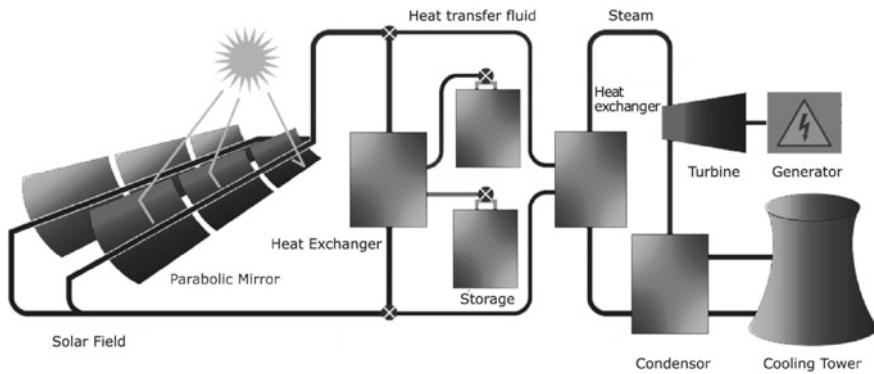


**Fig. 13.7** Layout of parabolic trough based solar thermal power plant [70]

### 13.4.2 PCM High-Temperature Applications

PCM high-temperature application has been used for ages. However, their use in the form of heat storage is a concept which was introduced later, i.e., in the last fifty years or so. Melting of substances and minerals is carried out at higher temperatures, and their solidification time defines their crystal lattice structure based on which solid–solid phase distinction occurred. Many other factors such as the inclusion of foreign particles also affected the properties such as strength. However, with precise knowledge of the amount of heat stored and its impact on the rearrangement of atoms at lattice structure level, the use of these materials for various heat storage applications and as heat transfer fluid has been studied. These materials are suitable for solar thermal power generation as they can serve as storage materials as well as heat transfer fluid at high temperature. Vignarooban et al. [69] studied various materials and compared different materials and their suitability in the application for solar thermal power generation. A typical layout of a solar thermal power plant is shown in Fig. 13.7.

Figure 13.7 shows the use of storage system to absorb the excess heat during the day, which can be utilized during the off-sunshine hours. The storage materials can also act as heat transfer fluids. The typical values of heat transfer coefficient, melting temperature, and working range are shown in Table 13.1. The use of PCMs in solar thermal power has been implemented only a few plants. The major limiting factor is their cost and due to lower cost of power through solar PV. Thus, a lot of research is required for finding suitable cheaper alternatives such that power generation through solar thermal also becomes cost-effective and implementable solution rather than just a feasible solution.

**Table 13.1** Comparison of different materials employed for solar thermal power plants [69]

Materials	Value of heat transfer coefficient 'h'	Advantages	Limitation
<b>Thermal oil</b>			
Biphenyl/diphenyl oxide (Therminol VP-1) (12–393 °C)	It ranges between 1000 and 3500 $Wm^{-2} K^{-1}$ . It increases with temperature and is maximum at around 580 °C	<ul style="list-style-type: none"> <li>• It is non-corrosive, and studies are being carried out to increase the heat capacity by adding <math>SiO_2</math> nanoparticles</li> <li>• Operating pressures are not very high</li> </ul>	<ul style="list-style-type: none"> <li>• Low operating temperature range hence often not used for high-temperature power plants</li> <li>• Owing to the low specific heat and high cost, it cannot be used as storage material and neither as power cycle working fluid</li> <li>• Relatively costly</li> </ul>
<b>Molten Salts</b>			
Solar salt (220–600 °C)	It ranges between 3600 and 6700 $Wm^{-2} K^{-1}$ . It increases with temperature High density, specific heat capacity, thermal stability, and lower vapor pressure values at high-temperature values	<ul style="list-style-type: none"> <li>• It has high “h” and relatively cheaper compared to the thermal oils and molten metals</li> <li>• Can be used as HTF as well as for storage due to reasonably good specific heat and relatively higher density</li> <li>• Non-polluting, non-flammable, more abundant thus relatively cheaper to thermal oils and molten metals</li> </ul>	<ul style="list-style-type: none"> <li>• It has a high melting point of 220 °C, thereby increasing the need and cost of heat tracing</li> <li>• Upper range temperature is 600 °C thus power cycle efficiency is restricted</li> <li>• Corrosion problem in pipes</li> </ul>
Hitec (142–535 °C)	It ranges between 1500 and 4000 $Wm^{-2} K^{-1}$ . It increases with temperature	<ul style="list-style-type: none"> <li>• Hitec has a the melting point of 142 °C which is much lower than that of the solar salt</li> <li>• It is cheaper than the solar salt</li> </ul>	<ul style="list-style-type: none"> <li>• The higher operating temperature is restricted to 500 °C which can be enhanced to 535 °C with the use of few additives</li> <li>• Need of heat tracing still quiet high</li> <li>• They pose corrosion problems with cast iron which can be greatly reduced with the use of stainless steel pipes and nickle-based alloy pipes</li> </ul>

(continued)

**Table 13.1** (continued)

Materials	Value of heat transfer coefficient 'h'	Advantages	Limitation
Hitec XL (120–500 °C)	It ranges between 400 and 6800 Wm <sup>-2</sup> K <sup>-1</sup> . Value is low at lower temperatures due to high viscosity thereby smaller values of Reynolds number	<ul style="list-style-type: none"> <li>• Its melting point temperature is 120 °C which is relatively lower than Hitec and solar salt</li> <li>• Higher specific heat than the solar salts thus a better material for storage</li> </ul>	<ul style="list-style-type: none"> <li>• Higher operating temperature is only 500 °C</li> <li>• Heat tracing is required</li> <li>• To avoid corrosion, stainless steel pipes are to be used</li> <li>• More viscous than the other two salts</li> </ul>
<b>Liquid Metals</b>			
Na (98–883 °C)	It ranges between 28,000 and 18,000 Wm <sup>-2</sup> K <sup>-1</sup> . The value of heat transfer coefficient decreases due decrease in thermal conductivity with the increase in temperature	<ul style="list-style-type: none"> <li>• Higher values of heat transfer coefficients hence higher rate of heat transfer</li> <li>• High range of working temperatures (98–883 °C)</li> </ul>	<ul style="list-style-type: none"> <li>• Specific heat capacity values are lower. Hence, liquid metals cannot be economically feasible for storing owing to higher unit cost as the storage density is lower</li> <li>• Contact with hydrogen and water possibly results in combustion</li> <li>• Stainless steel or ceramic (SiC) pipes are to be used to minimize corrosion</li> <li>• Heat tracing required</li> <li>• Four times more costlier than solar salt</li> </ul>
Lead bismuth eutectic (LBE) (125–1670 °C)	It ranges between 10,600 and 11,900 Wm <sup>-2</sup> K <sup>-1</sup> . Thermal conductivity increases with temperature, hence "h" also increases	<ul style="list-style-type: none"> <li>• Higher values of heat transfer coefficients, hence higher rate of heat transfer</li> <li>• It melts at around 125 °C, and boiling point is around 1500 °C; therefore, a wide range of operating temperatures</li> </ul>	<ul style="list-style-type: none"> <li>• Cost of LBE is 26 times that of the solar salt</li> <li>• Heat tracing required</li> <li>• Ceramic pipes to be used to minimize corrosion, which are relatively costlier</li> </ul>

### 13.5 Limitations and Future Recommendations

In the case of PCMs, the major challenge is the availability and choice of correct PCMs as per the desired application. Another critical parameter is currently the cost of PCMs available and researched, which is quite high. Thus, the payback period for PCM incorporated systems is very high. In modeling perspective, it must be commented that simulation of PCMs is tricky and involves many assumptions and approximations. The in-house codes developed by various research groups to

model PCM for different applications have not been included for the sake of brevity. However, such an exhaustive list of codes and their merits and demerits shall benefit both novice and experts alike.

The silver lining in PCM research is that with time as the research is being carried out, the cheaper alternatives are being found, for example, PCM bricks prepared and showcased by Saxena et al. [71] the cost of brick came down from INR 2600 to just INR 90. Thus, with material research and using cheaper alternatives, followed by addressing their stability and other issues, the PCMs application can have a bright future for many applications as discussed. Concisely, the research prospects in case of PCMs are enormous but require a lot of efforts for turning it from a feasible solution to an optimal one.

## 13.6 Conclusions

This chapter provides a comprehensive review of PCM and its application. It includes data  $n$  different PCMs and their modeling. Numerical modeling of PCMs has several uses, especially related to the building energy optimization, which are discussed. Most popular techniques and methods, along with their merits and demerits, have been illustrated. Furthermore, details on the governing equations and the importance of various source terms variables have been discerned. It is observed that most numerical studies prefer enthalpy-based methods due to their simplicity and ease of modeling. Moreover, the models that incorporate heat capacity or source methods require a short time step value to attain the desired accuracy and, hence, results in a significant slowdown. Further, most sophisticated tools for PCM modeling related to the entire building are based on heat capacity methods. It should be noted that still a lot of work is required in this field, as most of the programs available are still computationally expensive and need substantial time step values.

About the experimental application of PCMs, it essential to state that still a lot of research is required to find suitable PCMs in affordable costs. The experiments show that the use of PCM is a feasible solution. However, due to the cost implications, the use of PCMs is still limited and restricted. PCM application in buildings, solar drying, and heating applications can be cost-effective with proper design implementation and shorter payback period. Whereas for storage applications for high temperature, it is still economically not a viable solution. The focus is also on the thermal enhancement of PCMs as per thermal conductivity and stability in case of inorganic PCMs and eutectics.

## References

1. Zalba B, Marín JM, Cabeza LF, Mehling H (2003) Review on thermal energy storage with phase change: materials, heat transfer analysis and applications. *Appl Therm Eng* 23:251–283. [https://doi.org/10.1016/S1359-4311\(02\)00192-8](https://doi.org/10.1016/S1359-4311(02)00192-8)
2. Saxena R, Agarwal N, Rakshit D, Kaushik SC (2020) Suitability assessment and experimental characterization of phase change materials for energy conservation in Indian buildings. *J Sol Energy Eng* 142. <https://doi.org/10.1115/1.4044568>
3. Mi X, Liu R, Cui H, Memon SA, Xing F, Lo Y (2016) Energy and economic analysis of building integrated with PCM in different cities of China. *Appl Energy* 175:324–336. <https://doi.org/10.1016/J.APENERGY.2016.05.032>
4. Saxena R, Rakshit D, Kaushik SC (2020) Review on PCM application for cooling load reduction in Indian buildings. In: *Solar energy-system, challenges and opportunities*. pp 247–275
5. Singh RP, Xu H, Kaushik SC, Rakshit D, Romagnoli A (2019) Charging performance evaluation of finned conical thermal storage system encapsulated with nano-enhanced phase change material. *Appl Therm Eng* 151:176–190. <https://doi.org/10.1016/J.APPLTHERMALENG.2019.01.072>
6. Khan A, Saikia P, Saxena R, Rakshit D, Saha S (2019) Microencapsulation of phase change material in water dispersible polymeric particles for thermoregulating rubber composites—a holistic approach. *Int J Energy Res* 49:4925. <https://doi.org/10.1002/er.4925>
7. Hoogendoorn CJ, Bart GCJ (1992) Performance and modelling of latent heat stores. *Sol Energy* 48:53–58. [https://doi.org/10.1016/0038-092X\(92\)90176-B](https://doi.org/10.1016/0038-092X(92)90176-B)
8. Singh RP, Xu H, Kaushik SC, Rakshit D, Romagnoli A (2019) Effective utilization of natural convection via novel fin design and influence of enhanced viscosity due to carbon nano-particles in a solar cooling thermal storage system. *Sol Energy* 183:105–119. <https://doi.org/10.1016/j.solener.2019.03.005>
9. Singh RP, Kaushik SC, Rakshit D (2018) Solidification behavior of binary eutectic phase change material in a vertical finned thermal storage system dispersed with graphene nanoplates. *Energy Convers Manag* 171:825–838. <https://doi.org/10.1016/J.ENCONMAN.2018.06.037>
10. Pise AT, Waghmare AV, Talandage VG (2013) Heat transfer enhancement by using nanomaterial in phase change material for latent heat thermal energy. 2:360–366
11. Teng TP, Cheng CM, Cheng CP (2013) Performance assessment of heat storage by phase change materials containing MWCNTs and graphite. *Appl Therm Eng* 50:637–644. <https://doi.org/10.1016/j.applthermaleng.2012.07.002>
12. Saxena R, Dwivedi C, Dutta V, Kaushik SC, Rakshit D (2020) Nano-enhanced PCMs for low-temperature thermal energy storage systems and passive conditioning applications. *Clean Technol Environ Policy* 1–8. <https://doi.org/10.1007/s10098-020-01854-7>
13. Aguayo M, Das S, Maroli A, Kabay N, Mertens JCE, Rajan SD, Sant G, Chawla N, Neithalath N (2016) The influence of microencapsulated phase change material (PCM) characteristics on the microstructure and strength of cementitious composites: experiments and finite element simulations. *Cem Concr Compos* 73:29–41. <https://doi.org/10.1016/j.cemconcomp.2016.06.018>
14. Chang TC, Lee S, Fuh YK, Peng YC, Lin ZY (2017) PCM based heat sinks of paraffin/nanoplatelet graphite composite for thermal management of IGBT. *Appl Therm Eng* 112:1129–1136. <https://doi.org/10.1016/j.applthermaleng.2016.11.010>
15. Lamé G, Clapeyron BP (1831) Mémoire sur la solidification par refroidissement d'un globe liquide. *Ann. Chim. Phys.* 47:1831
16. Stefan J (1889) Über einige probleme der theorie der wärmeleitung. *Sitzer. Wien. Akad. Math. Naturw.* 98:473–484
17. Hunter LW, Kuttler JR (1989) The enthalpy method for heat conduction problems with moving boundaries. *J Heat Transf* 111:239–242. <https://doi.org/10.1115/1.3250668>

18. Goyal P, Dutta A, Verma V, Thangamani I, Singh RK (2013) Enthalpy porosity method for CFD simulation of natural convection phenomenon for phase change problems in the molten pool and its importance during melting of solids. In: COMSOL conference, p 10
19. Voller VR (1990) Numerical heat transfer, part B: fundamentals: an international journal of computation and methodology fast implicit finite-difference method for the analysis of phase change problems. *Numer Heat Transf* 17:155–169. <https://doi.org/10.1080/10407799508928838>
20. Brent AD, Voller VR, Reid KJ (1988) Enthalpy-porosity technique for modeling convection-diffusion phase change: application to the melting of a pure metal. *Numer Heat Transf* 13:297–318. <https://doi.org/10.1080/10407788808913615>
21. Augspurger M, Udaykumar HS (2016) A Cartesian grid solver for simulation of a phase-change material (PCM) solar thermal storage device. *Numer Heat Transf Part B Fundam* 69:179–196. <https://doi.org/10.1080/10407790.2015.1097106>
22. Sheikholeslami M (2018) Numerical modeling of nano enhanced PCM solidification in an enclosure with metallic fin. *J Mol Liq* 259:424–438. <https://doi.org/10.1016/j.molliq.2018.03.006>
23. Chakraborty PR (2017) Enthalpy porosity model for melting and solidification of pure-substances with large difference in phase specific heats. *Int Commun Heat Mass Transf* 81:183–189. <https://doi.org/10.1016/j.icheatmasstransfer.2016.12.023>
24. Sweidan AH, Heider Y, Markert B (2020) Modeling of PCM-based enhanced latent heat storage systems using a phase-field-porous media approach. *Contin Mech Thermodyn* 32:861–882. <https://doi.org/10.1007/s00161-019-00764-4>
25. Voller VR, Prakash C (1978) A fixed grid numerical modelling methodology for convection diffusion mushy region phase change problems. *Int J Heat Mass Transf* 30:1709–1719
26. Hirt CW, Nichols BD (1981) Volume of fluid (VOF) method for the dynamics of free boundaries. *J Comput Phys* 39:201–225. [https://doi.org/10.1016/0021-9991\(81\)90145-5](https://doi.org/10.1016/0021-9991(81)90145-5)
27. Al-Saadi SN, Zhai Z (2013) Modeling phase change materials embedded in building enclosure: a review. *Renew Sustain Energy Rev* 21:659–673. <https://doi.org/10.1016/j.rser.2013.01.024>
28. Tabares-Velasco PC, Christensen C, Bianchi M (2012) Verification and validation of EnergyPlus phase change material model for opaque wall assemblies. *Build Environ* 54:186–196. <https://doi.org/10.1016/j.buildenv.2012.02.019>
29. Kuznik F, Virgone J, Johannes K (2010) Development and validation of a new TRNSYS type for the simulation of external building walls containing PCM
30. Heim D, Clarke JA (2004) Numerical modelling and thermal simulation of PCM-gypsum composites with ESP-r. *Energy Build* 36:795–805. <https://doi.org/10.1016/j.enbuild.2004.01.004>
31. Saxena R, Rakshit D, Kaushik SC (2018) Experimental assessment of characterised PCMs for thermal management of buildings in tropical composite climate. In: 4th world congress on mechanical, chemical, and material engineering (MCM'18)
32. Navaro L, Solé A, Martín M, Barreneche C, Olivieri L, Tenorio JA, Cabeza LF (2019) Benchmarking of useful phase change materials for a building application. *Energy Build* 182:45–50. <https://doi.org/10.1016/j.enbuild.2018.10.005>
33. Kaushik SC, Sodha MS, Bhardwaj SC, Kaushik ND (1981) Periodic heat transfer and load levelling of heat flux through a PCCM thermal storage wall/roof in an air-conditioned building. *Build Environ* 16:99–107. [https://doi.org/10.1016/0360-1323\(81\)90026-3](https://doi.org/10.1016/0360-1323(81)90026-3)
34. Hadjieva M, Stoykov R, Filipova T (2000) Composite salt-hydrate concrete system for building energy storage. *Renew Energy* 19:111–115. [https://doi.org/10.1016/S0960-1481\(99\)00024-5](https://doi.org/10.1016/S0960-1481(99)00024-5)
35. Ismail KAR, Castro JNC (1997) PCM thermal insulation in buildings. *Int J Energy Res* 21:1281–1296. [https://doi.org/10.1002/\(SICI\)1099-114X\(199711\)21:14%3c1281:AID-ER322%3e3.0.CO;2-P](https://doi.org/10.1002/(SICI)1099-114X(199711)21:14%3c1281:AID-ER322%3e3.0.CO;2-P)
36. Stritih U (2003) Heat transfer enhancement in latent heat thermal storage system for buildings. *Energy Build* 35:1097–1104. <https://doi.org/10.1016/j.enbuild.2003.07.001>
37. Mehling H, Cabeza LF (2008) Applications for heating and cooling in buildings. Heat and cold storage with PCM. Springer, Berlin Heidelberg, Berlin, Heidelberg, pp 217–295



38. Scalat S, Bann D, Hawes D, Paris J, Haghghata F, Feldman D (1996) Full scale thermal testing of latent heat storage in wallboard. *Sol Energy Mater Sol Cells* 44:49–61
39. Paspupathy A, Athanasius L, Velraj R, Seeniraj RV (2008) Experimental investigation and numerical simulation analysis on the thermal performance of a building roof incorporating phase change material (PCM) for thermal management. *Appl Therm Eng* 28:556–565. <https://doi.org/10.1016/j.applthermaleng.2007.04.016>
40. Kant K, Shukla A, Sharma A (2017) Heat transfer studies of building brick containing phase change materials. *Sol Energy* 155:1233–1242. <https://doi.org/10.1016/j.solener.2017.07.072>
41. Saxena R, Rakshit D, Kaushik SC (2020) Experimental assessment of Phase Change Material (PCM) embedded bricks for passive conditioning in buildings. *Renew Energy* 149:587–599. <https://doi.org/10.1016/j.renene.2019.12.081>
42. Saxena R, Biplab K, Rakshit D (2018) Quantitative assessment of phase change material utilization for building cooling load abatement in composite climatic condition. *J Sol Energy Eng Trans ASME* 140. <https://doi.org/10.1115/1.4038047>
43. Duffie JA, Beckman WA (2013) *Solar engineering of thermal processes*, fourth. Wiley, Hoboken
44. Saikia P, Azad AS, Rakshit D (2018) Thermodynamic analysis of directionally influenced phase change material embedded building walls. *Int J Therm Sci* 126:105–117. <https://doi.org/10.1016/j.ijthermalsci.2017.12.029>
45. Nghana B, Tariku F (2016) Phase change material's (PCM) impacts on the energy performance and thermal comfort of buildings in a mild climate. *Build Environ* 99:221–238. <https://doi.org/10.1016/j.buildenv.2016.01.023>
46. Baniassadi A, Sajadi B, Amidpour M, Noori N (2016) Economic optimization of PCM and insulation layer thickness in residential buildings. *Sustain Energy Technol Assessments* 14:92–99. <https://doi.org/10.1016/j.seta.2016.01.008>
47. Ascione F, Bianco N, De Masi RF, De'rossi F, Vanoli GP (2014) Energy refurbishment of existing buildings through the use of phase change materials: energy savings and indoor comfort in the cooling season. <https://doi.org/10.1016/j.apenergy.2013.08.045>
48. Han Y, Taylor JE (2016) Simulating the inter-building effect on energy consumption from embedding phase change materials in building envelopes. *Sustain Cities Soc* 27:287–295. <https://doi.org/10.1016/j.scs.2016.03.001>
49. Castell A, Menoufi K, de Gracia A, Rincón L, Boer D, Cabeza LF (2013) Life cycle assessment of alveolar brick construction system incorporating phase change materials (PCMs). *Appl Energy* 101:600–608. <https://doi.org/10.1016/j.apenergy.2012.06.066>
50. Zhang C, Chen Y, Wu L, Shi M (2011) Thermal response of brick wall filled with phase change materials (PCM) under fluctuating outdoor temperatures. *Energy Build* 43:3514–3520. <https://doi.org/10.1016/j.enbuild.2011.09.028>
51. Li L, Yu H, Liu R (2017) Research on composite-phase change materials (PCMs)-bricks in the west wall of room-scale cubicle: mid-season and summer day cases. *Build Environ* 123:494–503. <https://doi.org/10.1016/j.buildenv.2017.07.019>
52. El Omari K, Le Guer Y, Bruel P (2016) Analysis of micro-dispersed PCM-composite boards behavior in a building's wall for different seasons. doi:10.1016/j.jobe.2016.07.013
53. Ryms M, Klugmann-Radziemska E (2019) Possibilities and benefits of a new method of modifying conventional building materials with phase-change materials (PCMs). *Constr Build Mater* 211:1013–1024. <https://doi.org/10.1016/j.conbuildmat.2019.03.277>
54. Bontemps A, Ahmad M, Johannès K, Sallée H (2011) Experimental and modelling study of twin cells with latent heat storage walls. *Energy Build* 43:2456–2461. <https://doi.org/10.1016/J.ENBUILD.2011.05.030>
55. Guarino F, Athienitis A, Cellura M, Bastien D (2017) PCM thermal storage design in buildings: experimental studies and applications to solarium in cold climates. *Appl Energy* 185:95–106. <https://doi.org/10.1016/J.APENERGY.2016.10.046>
56. Dabiri S, Mehrpooya M, Nezhad EG (2018) Latent and sensible heat analysis of PCM incorporated in a brick for cold and hot climatic conditions, utilizing computational fluid dynamics. *Energy* 159:160–171. <https://doi.org/10.1016/j.energy.2018.06.074>

57. Navarro L, de Gracia A, Colclough S, Browne M, McCormack SJ, Griffiths P, Cabeza LF (2016) Thermal energy storage in building integrated thermal systems: a review. Part 1. active storage systems. *Renew Energy* 88:526–547. <https://doi.org/10.1016/j.renene.2015.11.040>
58. Xu B, Li P, Chan C (2015) Application of phase change materials for thermal energy storage in concentrated solar thermal power plants: a review to recent developments. *Appl Energy* 160:286–307. <https://doi.org/10.1016/j.apenergy.2015.09.016>
59. Lo Brano V, Ciulla G, Piacentino A, Cardona F (2013) On the efficacy of PCM to shave peak temperature of crystalline photovoltaic panels: an FDM model and field validation. *Energies* 6:6188–6210. <https://doi.org/10.3390/en6126188>
60. Indartono YS, Suwono A, Pratama FY (2016) Improving photovoltaics performance by using yellow petroleum jelly as phase change material. *Int J Low-Carbon Technol* 11:333–337. <https://doi.org/10.1093/ijlct/ctu033>
61. Abdelrazik AS, Al-Sulaiman FA, Saidur R (2020) Numerical investigation of the effects of the nano-enhanced phase change materials on the thermal and electrical performance of hybrid PV/thermal systems. *Energy Convers Manag* 205:112449. <https://doi.org/10.1016/j.enconman.2019.112449>
62. Fayaz H, Rahim NA, Hasanuzzaman M, Rivai A, Nasrin R (2019) Numerical and outdoor real time experimental investigation of performance of PCM based PVT system. *Sol Energy* 179:135–150. <https://doi.org/10.1016/j.solener.2018.12.057>
63. Al-Waeli AHA, Chaichan MT, Sopian K, Kazem HA, Mahood HB, Khadom AA (2019) Modeling and experimental validation of a PVT system using nanofluid coolant and nano-PCM. *Sol Energy* 177:178–191. <https://doi.org/10.1016/j.solener.2018.11.016>
64. Saxena R, Rakshit D, Kaushik SC (2018) Experimental assessment of characterised PCMs for thermal management of buildings in tropical composite climate. In: MCM2018. Avestia
65. Pereira Da Cunha J, Eames P (2017) Phase change materials to meet domestic hot water demand in the UK—a numerical study. *Avestia Publ J Fluid Flow Heat Mass Transf* 4. <https://doi.org/10.11159/jffhmt.2017.002>
66. Hari Krishnan S, Kalaiselvam S (2013) Experimental investigation of solidification and melting characteristics of nanofluid as PCM for solar water heating systems. 3:628–635
67. Verma A, Shashidhara S, Rakshit D (2019) A comparative study on battery thermal management using phase change material (PCM). *Therm Sci Eng Prog* 11:74–83. <https://doi.org/10.1016/j.tsep.2019.03.003>
68. Rangappa R, Rajoo S, Samin PM, Rajesha S (2020) Compactness analysis of PCM-based cooling systems for lithium battery-operated vehicles. *Int J Energy Environ Eng* 11:247–264. <https://doi.org/10.1007/s40095-020-00339-z>
69. Vignarooban K, Xu X, Arvay A, Hsu K, Kannan AM (2015) Heat transfer fluids for concentrating solar power systems—a review. *Appl Energy* 146:383–396
70. De Falco M Solar power concentration—oil&gas portal. In: Univ. UCBM, Rome. <http://www.oil-gasportal.com/solar-power-concentration/?print=print>. Accessed 24 Aug 2020
71. Saxena R, Rakshit D, Kaushik SC (2019) Phase change material (PCM) incorporated bricks for energy conservation in composite climate: a sustainable building solution. *Sol Energy* 183:276–284. <https://doi.org/10.1016/j.solener.2019.03.035>

# Chapter 14

## Sensitivity Analysis in Solar Systems



Desh Bandhu Singh, Sumit Tiwari, and Sanjay Kumar

### *Nomenclature*

$A_b$	Area of basin, $m^2$
$A_g$	Area of glass cover, $m^2$
$C$	Specific heat capacity, $J/kg\cdot K$
$C_{man}$	Cost of manufacturing the system including cost of piping and labor, Rs.
CRF	Capital recovery factor, fraction
CPC	Compound parabolic concentrator collector
DS	Double-slope solar still
$dx$	Elemental length, m
$F'$	Collector efficiency factor, dimensionless
ETC	Evacuated tubular collector
FPC	Flat plate collector
HTC	Heat transfer coefficient, $W/m^2\cdot K$
$h_{cwGE}$	Convective HTC from water to inner surface of glass cover toward east, $W/m^2\cdot K$

---

D. B. Singh (✉)

Department of Mechanical Engineering, Graphic Era Deemed to be University, Bell Road, Clement Town, Dehradun, Uttarakhand 248002, India  
e-mail: [dbsiit76@gmail.com](mailto:dbsiit76@gmail.com); [deshbandhusingh.me@geu.ac.in](mailto:deshbandhusingh.me@geu.ac.in)

S. Tiwari

Department of Mechanical Engineering, Shiv Nadar University, Greater Noida, G. B. Nagar, Uttar Pradesh 201314, India

S. Kumar

Department of Mechanical Engineering, Galgotias College of Engineering and Technology, Plot no. 1, Knowledge Park II, Greater Noida, Uttar Pradesh 201306, India

$h_{cwgW}$	Convective HTC from water to inner surface of glass cover toward west, $W/m^2-K$
$h_{ewgE}$	Evaporative HTC from water surface to inner surface of glass cover toward east, $W/m^2-K$
$h_{ewgW}$	Evaporative HTC from water surface to inner surface of glass cover toward west, $W/m^2-K$
$h_{ba}$	HTC from blackened surface to water mass, $W/m^2-K$
$h_{bw}$	HTC from blackened surface to water mass, $W/m^2-K$
$h_{rwgE}$	Radiative HTC from water surface to inner surface of glass cover toward east, $W/m^2-K$
$h_{rwgW}$	Radiative HTC from water surface to inner surface of glass cover toward west, $W/m^2-K$
$h_{1wE}$	Total HTC from water surface to inner surface of glass cover toward east, $W/m^2-K$
$h_{1wW}$	Total HTC from water surface to inner surface of glass cover toward west, $W/m^2-K$
$h_{1gE}$	Total HTC from outer surface of glass cover facing east to ambient, $W/m^2-K$
$h_{1gW}$	Total HTC from outer surface of glass cover facing west to ambient, $W/m^2-K$
$I(t)$	Solar intensity on collector, $W/m^2$
$i$	Rate of interest, %
IC	Initial cost of system, Rs.
$I_{SE}(t)$	Solar intensity on glass cover facing east, $W/m^2$
$I_{SW}(t)$	Solar intensity on glass cover facing west, $W/m^2$
$K$	Thermal conductivity, $W/m-K$
$L_g$	Thickness of glass, m
$L$	Latent heat, $J/kg$
$L'$	Length, m
MC	Maintenance cost of NETCDS, Rs.
MCF	Maintenance cost factor
$MFR/\dot{m}_f$	Mass flow rate of fluid/water, $kg/s$
$\dot{m}_{ew}$	Mass of distillate per hour from NETCDS, $kg/h$
$M_w$	Mass of distillate per day from NETCDS, $kg/day$
$N$	Number of collectors
$n$	Life of NETCDS, year
NETCDS	$N$ alike ETCs integrated double-slope solar distiller unit
NPVTFPCSS	$N$ alike partially covered PVT flat plate collectors integrated SS
NPVTCPCSS	$N$ alike partially covered PVT compound parabolic concentrator collectors integrated SS
$PF_c$	Penalty factor due to the glass covers for the glazed portion
$PF_1$	Penalty factor first, dimensionless
$PF_2$	Penalty factor second, dimensionless
PW	Potable water
PCS	Present cost of NETCDS, Rs.

PC	Cost of pump including direct current motor, Rs.
PVT	Photovoltaic thermal
$\dot{Q}_{UN}$	Heat gain from $N$ identical series-connected ETCs
$R_{o1}$	Inner radius of outer glass tube of evacuated coaxial glass tube, m
$R_{o2}/R$	Outer radius of outer glass tube of evacuated coaxial glass tube, m
$R_{i1}$	Inner radius of inner glass tube of evacuated coaxial glass tube, m
$R_{i2}$	Outer radius of inner glass tube of evacuated coaxial glass tube, m
$r$	Radius of copper tube, m
SA	Sensitivity analysis
SF	Sensitivity figure
SV	Salvage value of NETCDS, Rs.
SS	Single-slope solar still
SFF	Sinking fund factor, fraction
$T_{foN}$	Outlet water temperature at the end of $N$ th water collector, °C
$T_a$	Ambient air temperature, °C
$T_{giE}$	Glass temperature at inner surface of glass cover facing east, °C
$T_{giW}$	Glass temperature at inner surface of glass cover facing west, °C
$t$	Time, h
$T_{wo}$	Water temperature at $t = 0$ , °C
$T_w$	Water temperature, °C
$U_L$	Overall heat transfer coefficient, $W/m^2-K$
UEAC	Uniform end-of-year annual cost, Rs.
$V$	Velocity of air, m/s
WD	Water depth, m

### ***Subscript***

eff	Effective
ex	Exergy
f	Fluid
g	Glass
in	Incoming
out	Outgoing
w	Water
E	East
W	West

### ***Greek letters***

$\alpha$	Absorptivity (fraction)
$(\alpha\tau)_{eff}$	Product of effective absorptivity and transmittivity

$\sigma$	Stefan–Boltzmann constant, $\text{W/m}^2\text{-K}^4$
$\tau$	Transmittivity

## 14.1 Introduction

The design analysis and installation of solar energy-driven water purifier are the need of time because the human beings are facing with the shortage of freshwater throughout the globe. The purification of dirty water through conventional source of energy (electric energy) creates polluting elements which adversely affect the environment and is ultimately responsible for the creation of disturbance in ecosystem. So, the purification of water by conventional source of energy needs to be replaced by the renewable source of energy, particularly solar energy. Solar energy is a gift by nature to human beings, and it needs to be harnessed fully. In this direction, solar energy-driven water purifier can be good option as it has the potential to mitigate the shortage of freshwater throughout the globe, particularly locations where sunlight is available in abundance. Solar energy-driven water purifier consists of a box-type structure having inclined top portion for facilitating the movement of condensed water at the inside surface of top portion downward through gravity. The locally available materials can be used for the construction of solar energy-driven water purifier. However, top portion should have high transmittivity and high thermal resistance so that it can easily pass solar flux through it but heat from the inside portion of box should not get lost through top portion. Generally, glass is used for top portion of box-type structure. Some of the popular materials used for the construction of side walls and bottom of solar energy-driven water purifier are fiber-reinforced plastic (FRP), glass-reinforced plastic (GRP), galvanized iron (GI) sheet, concrete, etc. The materials used should have low thermal conductivity so that heat loss through sides and bottom can be minimized.

Active-type solar energy-driven water purifier consists of passive-type solar energy-driven water purifier integrated with some kind of heat supplying system. The heat supplying system to the basin of solar energy-driven water purifier may work on solar energy or some other kind of energy source also. Generally, solar collectors act as heat supplying system to basin. The solar energy-driven water purifier in active mode was introduced by Rai in Tiwari [1] and Zaki et al. [2] in 1983. Since then, a lot of advancements have been reported by various researchers around the globe.

Rai and Tiwari [1] and Zaki et al. [2] examined active solar distiller unit in the laboratory and performed various experimental analyses to identify the application. Later, the continuous variations have been presented and published by various researchers and scientists for its design and analysis. Sahota and Tiwari [3] reviewed the elaborative operational behavior of the similar setup and analyzed active solar distiller combined with photovoltaic module and predicted its self-sustainable behavior. The results thus obtained by Sahota and Tiwari [3] helped a lot in identifying the gaps

in the existing research on solar distiller. Kumar and Tiwari [4] also experimentally investigated such an active solar distiller unit and concluded that the combination enhances the production of PW by more than 3.5 times as compared to conventional solar distiller unit. They made several experimental attempts and calibrated the results obtained as an average value of the number of iterations developed. Later, Tiwari et al. [5] and Singh et al. [6] analyzed the system by partially covering the series-connected flat plate collectors (FPCs) with photovoltaic thermal (PVT). Singh et al. [6] have made a great impact by analyzing the partially covered unit. The analysis reported was helpful in identifying the efficiencies of the combination. The results obtained say that though thermal efficiency is lower than the system reported by Kumar and Tiwari [4] the exergy efficiency and overall thermal efficiency values of the system in partially covered PVTFPCs are better.

Issa and Chang [7] experimentally demonstrated the performance of solar still integrated with evacuated tubes for West Texas climatic condition and reported that the capacity of producing potable water (PW) for the active system was 2.36 times higher than passive system due to increased water temperature in basin by approximately 20 °C. Singh [8] examined single-slope passive solar still and single-slope solar distiller (SS) integrated with  $N$  identical partially covered (25%) photovoltaic thermal (PVT) flat plate collectors (FPCs) and SS integrated with  $N$  identical PVT compound parabolic concentrator collectors (CPCs). The experimentation leads to generation of several runtime and human errors which were thus omitted during the analysis of partially covered distiller units. He clinched that the life cycle conversion efficiency of NPVTFPCSS was higher by 56.25% and 37.5% than NPVTCPCSS and single-slope passive solar still, respectively, under optimized condition. The reason was attributed to higher exergy output of NPVTFPCSS under optimized condition. In a study, it was reported that the life cycle conversion efficiency of evacuated tubular collector integrated solar still as compared to similar passive system was higher due to higher exergy obtained from the active system. The positivity of results leads to the development of the optimized solar still [9]. Fathy et al. [10] concluded that the daily efficiency of double-slope solar still with tracked parabolic trough collector was 29.86% when experimentally studied the performance of double-slope solar still by integrating with parabolic trough collector.

Singh and Tiwari [11] developed analytical characteristic equation for  $N$  identical evacuated tubular collector integrated double-slope solar still. Further, Kumar et al. [12] developed the analytical characteristic equation for SS coupled with  $N$  alike compound parabolic concentrator integrated evacuated tubular collectors and concluded that the performance of the reported system was better than SS integrated with evacuated tubular collectors due to the increased heat collection area. Prasad et al. [13] performed the sensitivity analysis of double-slope active solar still and concluded that the electric power output got enhanced marginally by 0.95% if water depth was changed from 0.07 to 0.14 m for the selected values of MFR and  $N$  due to diminished solar cell temperature at higher water depth. Singh et al. [14] reported the effect of water mass on the performance of SS coupled with PVTFPCs and concluded that the enhancement in daily efficiency and productivity was significant till 1.4 m water depth.

The extant research suggests that the application of sensitivity analysis in solar systems is very limited. Though the method is very old, it has not been explored in the area of renewable energy, particularly solar energy. This chapter focuses on the application of sensitivity analysis to solar systems.

## 14.2 General Methodologies to Carry Out Sensitivity Analysis of Solar System

The sensitivity analysis of solar system provides the designer and installer important information regarding the significance of input parameters with respect to output parameters. The sensitivity analysis provides sensitivity figure which tells us about the relative importance of various input parameters with respect to output parameters. Higher the value of sensitivity figure, more significant the parameter is. Having the information about the relative impact of input parameters on output parameters, designer can take the decision on values of different parameters as per the requirement. The different steps for carrying out sensitivity analysis using one-at-a-time (OAT) technique are as follows:

### Step I

Step I is to carry out thermal modeling which involves writing mathematical equations for different components of solar system based on equating input energy to output energy. These equations are then solved to express unknown parameters in terms of known parameters.

### Step II

Step II is to write the expression of output parameters in terms of input parameters followed by writing the computational programming code in MATLAB. The values of output parameters from MATLAB are then tabulated against values of input parameters and plotted.

### Step III

The value of one input parameter is changed while keeping all other input parameters constant, and values of output parameter so obtained are tabulated and plotted. It is repeated till the variation of all input parameters is completed and corresponding variation of output parameter is noted.

### Step IV

Percentage change in output parameter and percentage change in input parameters are calculated followed by plotting of percentage change in output parameter against the percentage change in input parameter. The slope of this plot gives the sensitivity figure. The average value of sensitivity figure for output parameter with respect to input parameter is calculated.



**Step V**

Step IV is repeated till the calculation of average sensitivity figure for output parameter with respect to all input parameters is completed.

**14.3 Sensitivity Analysis of Solar Energy-Based Active Water Purifier in Forced Mode**

The solar energy-based active water purifier in forced mode consists of a heat supplying system like a number of solar collectors which supply heat to basin, and a DC motor pump is inserted between collectors' combination and pump. The sensitivity analyses of some such types of solar energy-based active water purifier in forced mode are as follows:

**14.3.1 Sensitivity Analysis of N Alike Series-Connected PVT/CPCs Integrated to Single-Slope Solar Energy-Based Water Purifier**

The schematics of  $N$  alike series-connected PVT/CPCs integrated to single-slope solar energy-based water purifier has been depicted in Fig. 14.1. The side view (cross-sectional) and front view (cut section XX') of partly covered PVT/CPC first

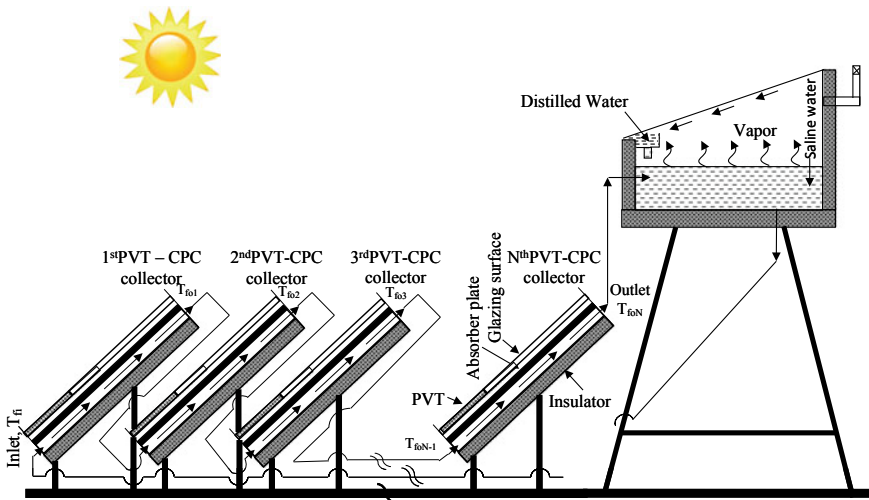


**Fig. 14.1** Schematics of  $N$  equal partly covered PVT/CPCs having series connection and integrated to solar energy-based single-slope water purifier [15]

collector are depicted in Figs. 14.2 and 14.3, respectively. The specification can be seen in Singh et al. [15].

When solar flux from the sun impinging on the surface of solar energy-based active water purifier shown in Fig. 14.1, the solar flux gets reflected and absorbed by the surface and the rest part of incoming solar flux is transmitted to water surface. The water surface reflects and absorbs some part of incoming solar flux, and the remaining part is transmitted to basin liner (painted black) at the bottom where almost all portions of solar flux get absorbed as the basin liner is painted black and acts as the black body. Thus, temperature of basin liner painted in black color rises and transfers heat to water. Water also gets heat from  $N$  equal partly covered PVTCPs having series connection. The PVTCP also generates electrical energy which is used to

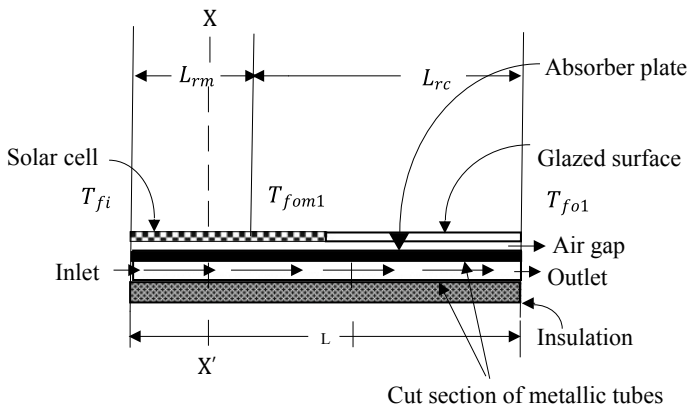


Fig. 14.2 Side view (cross-sectional) of partially covered PVTCP first collector [15]

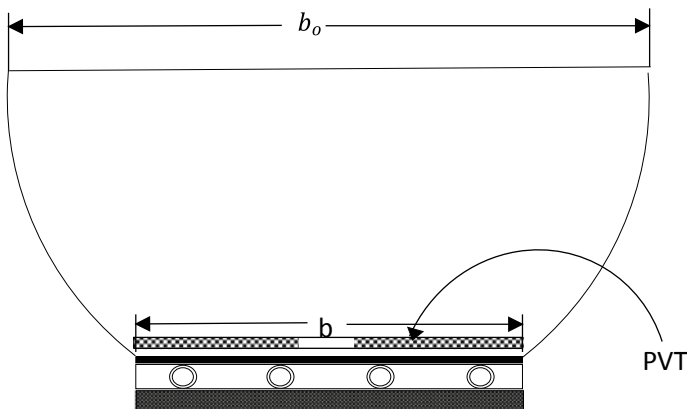


Fig. 14.3 Front view (cut section  $XX'$ ) of partially covered PVTCP first collector [15]

run the pump inserted between  $N$  equal PVTCPs and basin. In this way, water in basin receives water from collectors, basin liner, and directly from incoming solar flux which tend to increase the temperature of water. This results in the creation of temperature difference between water and inside surface of condensing plane. Due to this difference in temperature, evaporation of water occurs and the evaporated water gets condensed at the inside surface of glass and moves down through gravity along the inside surface of glass to tray fixed to the wall. The distilled water is then siphoned off from the tray. This collected distilled water in purest form; however, it cannot be consumed as drinking water directly because the collected distilled water lacks the required minerals. So, distilled water so obtained can be consumed as drinking water after adding minerals in the required proportion.

The expression for temperature at the outlet of first  $N$ th PVTCP can be written as [16, 17]

$$T_{foN} = \left[ \frac{(PF)_2 K(\theta)(\alpha\tau)_{\text{meff}} I_u(t) + T_a}{U_{Lm}} \right] \left[ 1 - \exp \left\{ \frac{-NFU_{LmA_{rm}}}{\dot{m}_f C_f} \right\} \right] + T_{fi} \exp \left\{ \frac{-NFU_{LmA_{rm}}}{\dot{m}_f C_f} \right\} \quad (1)$$

The expression for useful heat collected from  $N$  equal partly covered PVTCPs having series connection can be written as:

$$\dot{Q}_{uN} = \dot{m}_f C_f (T_{foN} - T_{fi}) \quad (2)$$

The value of  $T_{fi}$  will be equal to water temperature at initial time. The expression for electrical energy based on per hour basis electrical exergy on per hour basis can be computed as:

$$\dot{E}_{x_{\text{elec}}} = A_m I_u(t) \sum_1^N (\beta_c \tau_g \eta_{cN}) \quad (4)$$

The value of electrical power on per day basis can be computed by adding electric power on per hour basis for 10 h as solar flux coming from sun subsists for ten hours only.

Following Singh and Tiwari [18], mathematical equation for various components of solar energy-based single-slope water purifier can be written and solved to get the temperature of water in the basin and glass temperatures as follows:

$$T_w = \frac{\bar{f}(t)}{a} (1 - e^{-at}) + T_{w0} e^{-at} \quad (3)$$

$$T_{gi} = \frac{\alpha'_g I_s(t) A_g + h_{1w} T_w A_b + U_{cga} T_a A_g}{U_{cga} A_g + h_{1w} A_b} \quad (4)$$

$$T_{go} = \frac{\frac{K_g}{L_g} T_{gi} + h_{1g} T_a}{\frac{K_g}{L_g} + h_{1g}} \tag{5}$$

Having computed values of water and glass temperatures, one can proceed for the computation of potable water output on per hour basis as

$$\dot{m}_{ew} = \frac{h_{ewg} A_b (T_w - T_{gi})}{L'} \times 3600 \tag{8}$$

The expression for evaporative heat transfer coefficient ( $h_{ewg}$ ) can be evaluated as:

$$h_{ewg} = 16.273 \times 10^{-3} h_{cwg} \left[ \frac{P_w - P_{gi}}{T_w - T_{gi}} \right] \tag{9}$$

Here,

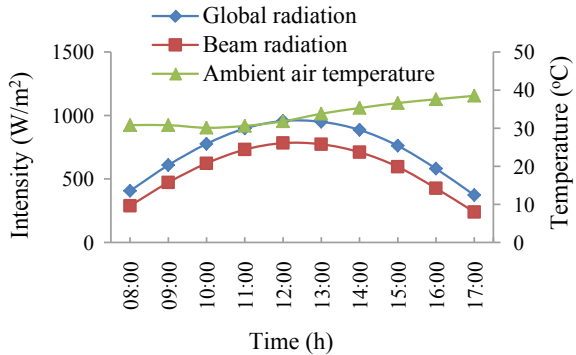
$$h_{cwg} = 0.884 \left[ (T_w - T_{gi}) + \frac{(P_w - P_{gi})(T_w + 273)}{(268.9 \times 10^3 - P_w)} \right] \tag{10}$$

$$P_w = \exp \left[ 25.317 - \frac{5144}{(T_w + 273)} \right] \tag{11}$$

$$P_{gi} = \exp \left[ 25.317 - \frac{5144}{(T_{gi} + 273)} \right] \tag{12}$$

Now, these equations can be fed to the programming code written in MATLAB for the computation of output parameters. The input data required for the evaluation of output parameter has been taken from IMD Pune located in India and has been depicted in Fig. 14.4. The solar flux supplied by IMD Pune is on horizontal plane; so, Liu and Jordan formula has been used to find the value of solar flux on the

**Fig. 14.4** Dissimilarity of intensity on per hour basis and average ambient air temperature on per hour basis for a typical day in the month of May [15]



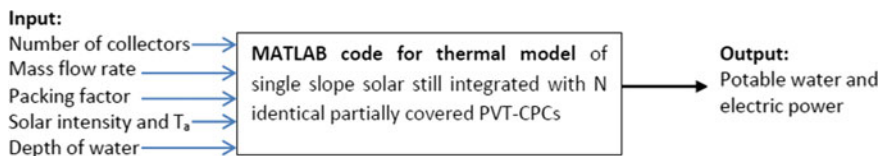


**Fig. 14.5** Conversion of impure water into freshwater using  $N$  equal partly covered PVT-CPCs having series connection and integrated to solar energy-based single-slope water purifier [15]

inclined plane. The input parameters and output parameters for  $N$  equal partly covered PVT-CPCs having series connection and integrated to solar energy-based single-slope water purifier are shown in Fig. 14.5. Out of the input parameters depicted in Fig. 14.5, solar intensity and surrounding temperature are totally dependent on weather and remain same for a particular day. So, they have not been considered.

The outputs received from MATLAB computational programming have been depicted in Figs. 14.6, 14.7, 14.8, and 14.9 and Table 14.2. The dissimilarity of percentage change in potable water (PW) yield with percentage change in mass flow rate/ $N$  for  $N$  equal partly covered PVT-CPCs integrated to solar energy-based single-slope water purifier has been depicted in Fig. 14.6.

The slopes of curves represent the sensitivity figure of PW with respect to  $\dot{m}_f/N$ . It has been observed from Fig. 14.6 that PW yield is more sensitive with respect to  $N$  in comparison with  $\dot{m}_f$ . Also, the values of sensitivity figure are more for lower values of  $\dot{m}_f/N$  and vice versa. Figure 14.7 depicts the dissimilarity of percentage change in PW yield with percentage change in water depth/packing factor for  $N$  equal partly

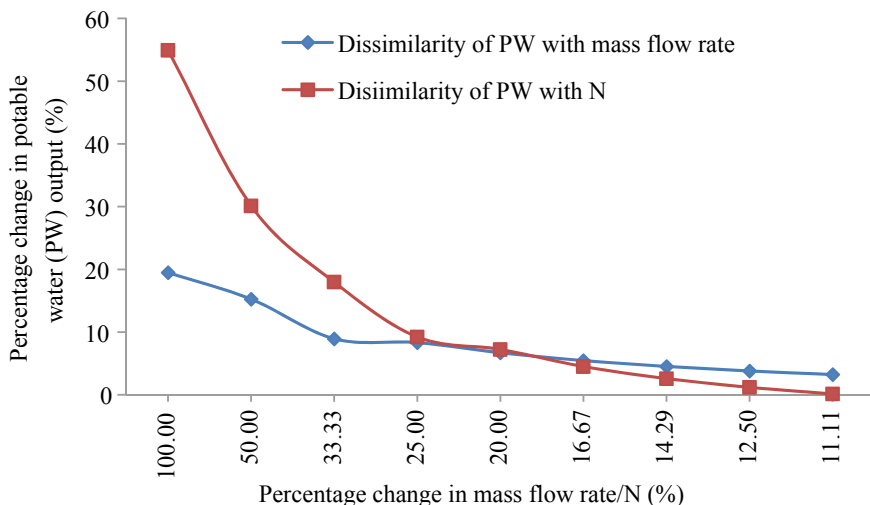


**Fig. 14.6** Dissimilarity of percentage change in PW yield with percentage change in mass flow rate/ $N$  for  $N$  equal partly covered PVT-CPCs integrated to solar energy-based single-slope water purifier (sensitivity analysis) [Source Author]

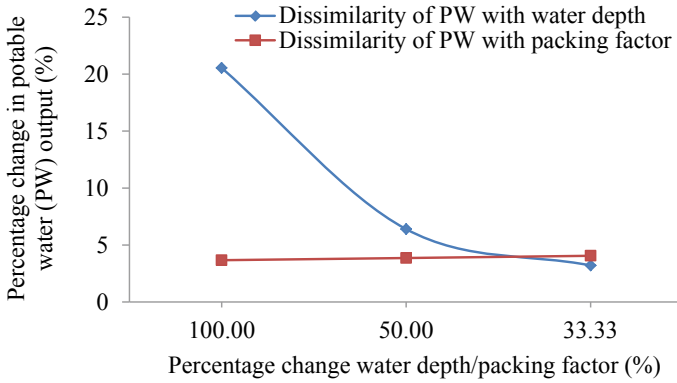


**Fig. 14.7** Dissimilarity of percentage change in PW yield with percentage change in water depth/packing factor for  $N$  equal partly covered PVTCPs integrated to solar energy-based single-slope water purifier (sensitivity analysis) [Source Author]

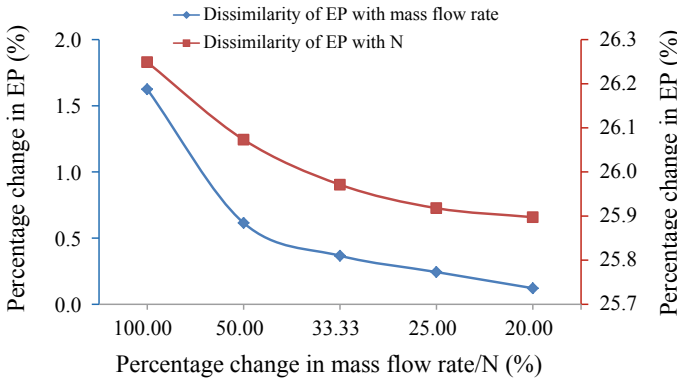


**Fig. 14.8** Dissimilarity of percentage change in electric power (EP) with percentage change in mass flow rate/ $N$  for  $N$  equal partly covered PVTCPs integrated to solar energy-based single-slope water purifier (sensitivity analysis) [Source Author]

covered PVTCPs integrated to solar energy-based single-slope water purifier. The slopes of curves represent the sensitivity figure. It has been observed from Fig. 14.7 that PW yield is more sensitive with respect to water depth as compared to packing factor.

The dissimilarity of percentage change in electric power (EP) with percentage change in mass flow rate/ $N$  for  $N$  equal partly covered PVTCPs integrated to solar energy-based single-slope water purifier has been depicted in Fig. 14.8. The slopes of curves represent the sensitivity figures. It has been observed that the sensitivity figures are more and lower values of mass flow rate/ $N$  and vice versa. The dissimilarity of percentage change in EP with percentage change in packing factor/water depth for  $N$  equal partly covered PVTCPs integrated to solar energy-based single-slope

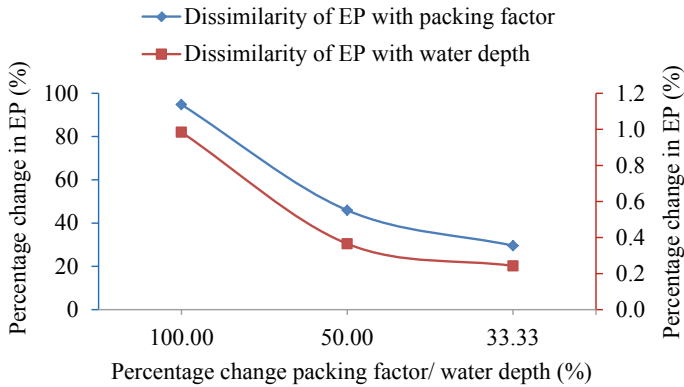


**Fig. 14.9** Dissimilarity of percentage change in EP with percentage change in packing factor/water depth for  $N$  equal partly covered PVTCPs integrated to solar energy-based single-slope water purifier (sensitivity analysis) [Source Author]

water purifier has been depicted in Fig. 14.9. Again, slopes of curves represent the sensitivity figures of EP with respect to packing factor/water depth. The EP has been found to be more sensitive with respect to packing factor as compared to water depth.

The average values of sensitivity figures of PW yield as well as EP with respect to input variables have been depicted in Table 14.1. It has been found from Table 14.1 that the sensitivity figure of PW yield is highest with respect to (w.r.t.)  $N$  followed by  $\dot{m}_f$ , water depth, and packing factor, whereas sensitivity figure of EP is highest with respect to packing factor followed by  $N$ ,  $\dot{m}_f$ , and water depth.

**Table 14.1** Average values of sensitivity figure for  $N$  equal partly covered PVTCPs having series connection and integrated to solar energy-based single-slope water purifier

Average value of sensitivity figure for PW w.r.t. $\dot{m}_f$	Average value of sensitivity figure for PW w.r.t. $N$	Average value of sensitivity figure for PW w.r.t. water depth	Average value of sensitivity figure for PW w.r.t. packing factor
0.298	0.331	0.143	0.078
Average value of sensitivity figure for EPO w.r.t. $\dot{m}_f$	Average value of sensitivity figure for EPO w.r.t. $N$	Average value of sensitivity figure for EPO w.r.t. water depth	Average value of sensitivity figure for EPO w.r.t. packing factor
0.011	0.780	0.008	0.920

### 14.3.2 Sensitivity Analysis of $N$ Alike Series-Connected PVTCPs Integrated to Double-Slope Solar Energy-Based Water Purifier

The schematic of  $N$  equal partly covered PVTCPs integrated to solar energy-based double-slope water purifier has been depicted in Fig. 14.10. The working principle of solar energy-based double-slope active water purifier is same as the working of solar energy-based single-slope water purifier explained earlier. The expression for temperature at the outlet of  $N$ th collector and the expression of heat gain by  $N$  equal partly covered PVTCPs having series connection is also same. The electric energy on per hour basis can be computed using Eq. (4). Following Singh and Tiwari [18], mathematical equation for various components of solar energy-based double-slope water purifier can be written and solved to get the temperature of water in the basin and glass temperatures. The expression for water temperature will be same as Eq. (3); however, values of different terms used in this equation will be different for double-slope-type solar energy-based water purifier. The expression for glass temperatures [18] can be written as:

$$T_{giE} = \frac{A_1 + A_2 T_w}{P} \tag{13}$$

$$T_{giW} = \frac{B_1 + B_2 T_w}{P} \tag{14}$$

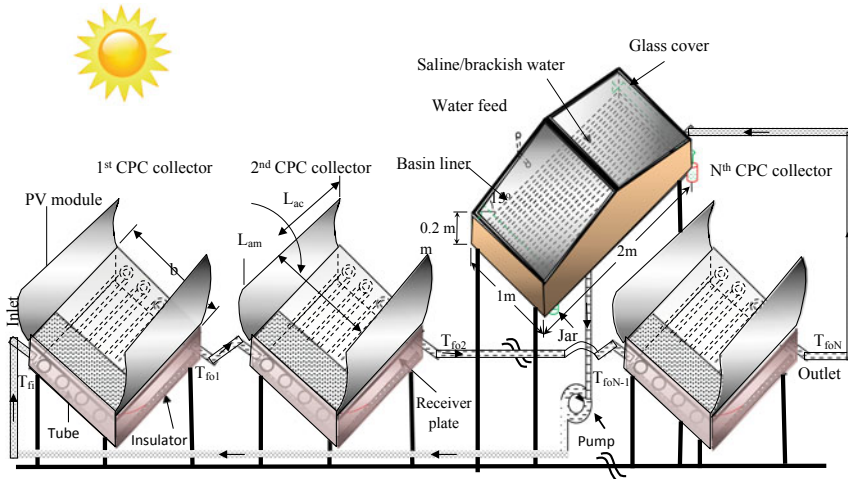


**Fig. 14.10** Schematics of  $N$  equal partly covered PVTCPs having series connection and integrated to solar energy-based double-slope water purifier [18]



$$T_{goE} = \frac{\frac{K_g}{L_g} T_{giE} + h_{1gE} T_a}{\frac{K_g}{L_g} + h_{1gE}} \tag{15}$$

$$T_{goW} = \frac{\frac{K_g}{L_g} T_{giW} + h_{1gW} T_a}{\frac{K_g}{L_g} + h_{1gW}} \tag{16}$$

After evaluating glass temperature from Eqs. (13) and (16) and water temperature using Eq. (3), the computation of PW yield from  $N$  equal partly covered PVTCPs integrated to solar energy-based double-slope water purifier can be done as follows:

$$\dot{m}_{ew} = \frac{[h_{ewgE} \frac{A_b}{2} (T_w - T_{giE}) + h_{ewgW} \frac{A_b}{2} (T_w - T_{giW})]}{L} \times 3600 \tag{17}$$

The values of  $h_{ewgE}$  and  $h_{ewgW}$  can be found out using the expression for  $h_{ewg}$  presented in Eq. (9) by substituting  $T_{giE}$  and  $T_{giW}$ , respectively, in place of  $T_{gi}$ .

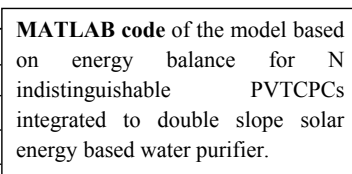
The expression for different unknown terms used in Eqs. (1)–(17) can be seen in Singh and Tiwari [18].

Now, these equations can be fed to the programming code written in MATLAB for the computation of output parameters. The input data required for the evaluation of output parameter has been taken from IMD Pune located in India and has been depicted in Fig. 14.4. The solar flux supplied by IMD Pune is on horizontal plane; so, Liu and Jordan formula has been used to find the value of solar flux on the inclined plane. The input parameters and output parameters for  $N$  equal partly covered PVTCPs having series connection and integrated to solar energy-based double-slope water purifier are shown in Fig. 14.11. Out of the input parameters depicted in Fig. 14.11, solar intensity and surrounding temperature are totally dependent on weather and remain same for a particular day. So, they have not been considered. The output received from MATLAB has been depicted in Figs. 14.12, 14.13, and 14.14 and Table 14.2.

The dissimilarity of percentage change in PW and EP with percentage change in  $\dot{m}_f$  for  $N$  equal partly covered PVTCPs integrated to solar energy-based double-slope water purifier has been depicted in Fig. 14.12. It has been observed from Fig. 14.12 that both PW and EP outputs are more sensitive at lower values of  $\dot{m}_f$

**Input parameters:**

- Number of collectors
- Mass flow rate
- Water depth
- Solar radiation
- Ambient temperature



**Output parameter:**

- Fresh water
- Electric power

**Fig. 14.11** Conversion of impure water into freshwater using  $N$  equal partly covered PVTCPs having series connection and integrated to solar energy-based double-slope water purifier [13]

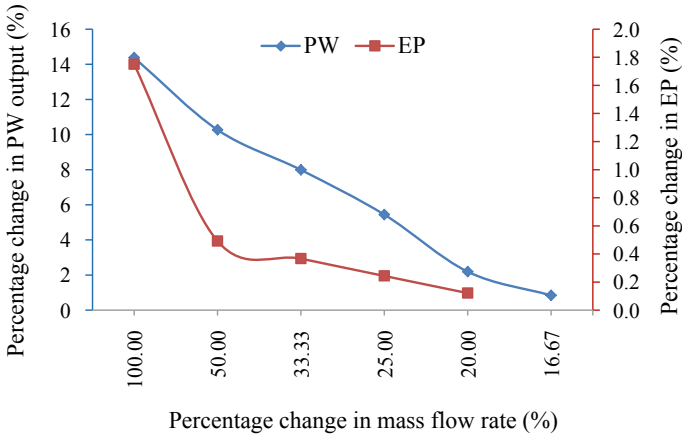


**Fig. 14.12** Dissimilarity of percentage change in PW and EP with percentage change in  $\dot{m}_f$  for  $N$  equal partly covered PVTCPs integrated to solar energy-based double-slope water purifier [Source Author]

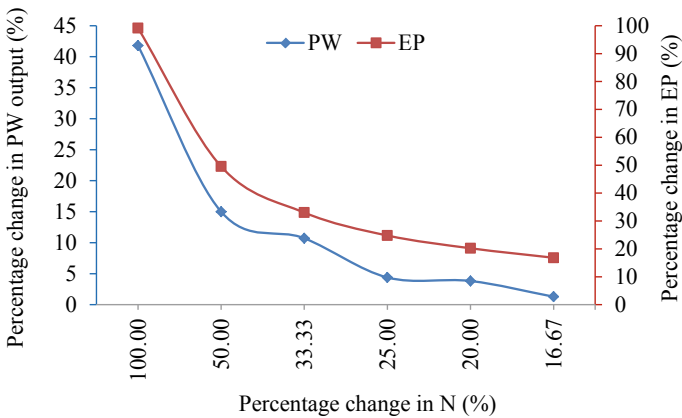


**Fig. 14.13** Dissimilarity of percentage change in PW and EP with percentage change in  $N$  for  $N$  equal partly covered PVTCPs integrated to solar energy-based double-slope water purifier [Source Author]

and the sensitivity decreases as the parameter  $\dot{m}_f$  occupies higher values. The slope of curves represents sensitivity figure.

The dissimilarity of percentage change in PW and EP with percentage change in  $N$  for  $N$  equal partly covered PVTCPs integrated to solar energy-based double-slope water purifier has been depicted in Fig. 14.13. It has been observed from Fig. 14.13 that the sensitivity of both PW and EP outputs is more at lower values of  $N$  and the sensitivity decreases as  $N$  occupies higher values. The slopes of curves represent the sensitivity figure. The dissimilarity of percentage change in PW and EP with

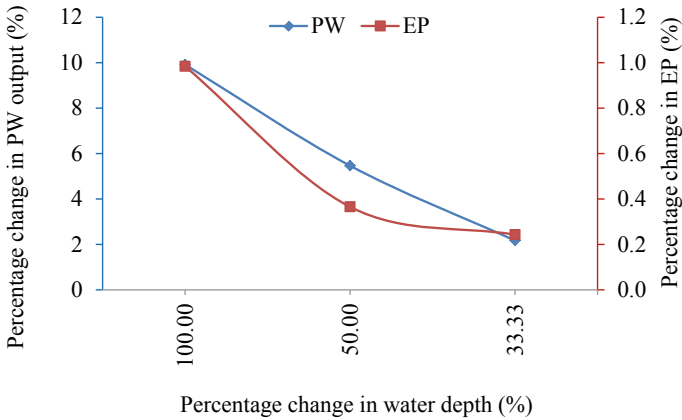


**Fig. 14.14** Dissimilarity of percentage change in PW and EP with percentage change in water depth for  $N$  equal partly covered PVTCPs integrated to solar energy-based double-slope water purifier [Source Author]

**Table 14.2** Average values of sensitivity figure for  $N$  equal partly covered PVTCPs having series connection and integrated to solar energy-based double-slope water purifier

Average value of sensitivity figure for PW w.r.t. $\dot{m}_f$	Average value of sensitivity figure for PW w.r.t. $N$	Average value of sensitivity figure for PW w.r.t. water depth	Average value of sensitivity figure for PW w.r.t. packing factor
0.161	0.247	0.09	0.186
Average value of sensitivity figure for EPO w.r.t. $\dot{m}_f$	Average value of sensitivity figure for EPO w.r.t. $N$	Average value of sensitivity figure for EPO w.r.t. water depth	Average value of sensitivity figure for EPO w.r.t. packing factor
0.019	0.997	0.008	1.07

percentage change in water depth for  $N$  equal partly covered PVTCPs integrated to solar energy-based double-slope water purifier has been depicted in Fig. 14.14. The slopes of these curves in Fig. 14.14 give the values of sensitivity figures. Higher the value of sensitivity figure, more significant the parameter is.

The average values of sensitivity figures for  $N$  equal partly covered PVTCPs having series connection and integrated to solar energy-based double-slope water purifier have been computed using the data given in Prasad et al. [13] and presented in Table 14.2. It is seen that the value of sensitivity figure for PW output is highest with respect to  $N$  followed by packing factor,  $\dot{m}_f$ , and water depth. It means that the designer and installer should focus highest on parameter  $N$  followed by packing factor,  $\dot{m}_f$ , and water depth. Again, the average value of sensitivity figure for EP output is highest with respect to packing factor followed by  $N$ ,  $\dot{m}_f$ , and water depth. The water depth has been found to be least significant for EP output because the

variation in water depth does not affect much the temperature of solar cell. The packing factor has been found to be most significant for EP output because increase in packing factor means increase in the effective area of solar cells which are directly involved in the production of EP.

### 14.3.3 Sensitivity Analysis of N Alike Series-Connected ETCs Integrated to Single-Slope Solar Energy-Based Water Purifier

The schematic of  $N$  equal ETCs integrated to solar energy-based double-slope water purifier has been depicted in Fig. 14.15, and the cross-sectional side view of first ETC has been depicted in Fig. 14.16. The working principle of  $N$  equal ETCs integrated to solar energy-based double-slope water purifier is similar to the working principle of  $N$  equal partly covered PVTCPs having series connection and integrated to

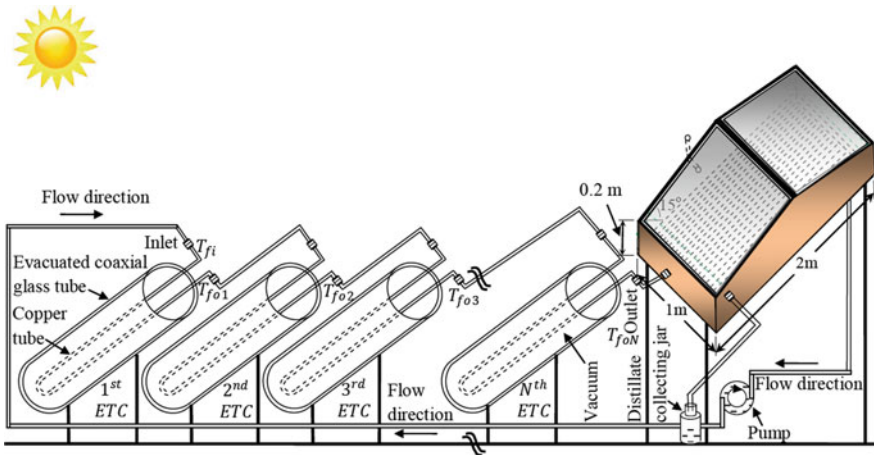
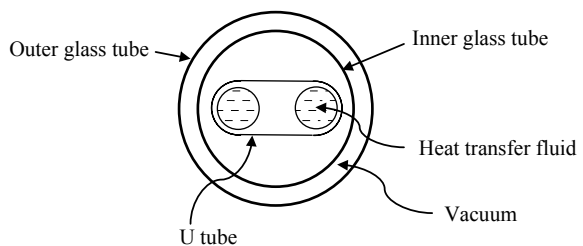


**Fig. 14.15** Schematic of  $N$  equal ETCs integrated to solar energy-based double-slope water purifier [Source Author]

**Fig. 14.16** Schematic of side view (cross section) of the first ETC [Source Author]



solar energy-based single-slope water purifier. However, some technical difference lies between PVTCP and ETC. In the case of PVTCP, loss takes place due to both convection and radiation, whereas, in the case of ETC, loss takes place due to radiation only and there is no loss due to convection as vacuum is present between two concentric glass tubes. The orientation of double slope is in east–west direction for getting higher annual solar energy on the surface of system.

The basic mathematical equation for different components of first ETC can be written, and these equations can be solved to get the temperature of fluid at the outlet of first ETC [19, 20] which can be expressed as:

$$T_{fo1} = \frac{(AF_R(\alpha\tau))_1}{\dot{m}_f C_f} I(t) + \frac{(AF_R U_L)_1}{\dot{m}_f C_f} T_a + K_k^N T_{fi} \quad (18)$$

As ETCs are connected in series, the output of first ETC will be input to second ETC, output of second ETC will be input to the third ETC, and so on. Using this condition and following the approach given in Mishra et al. [19], the temperature at the output of  $N$ th ETC ( $T_{foN}$ ) can be expressed as:

$$T_{foN} = \frac{(AF_R(\alpha\tau))_1}{\dot{m}_f C_f} \frac{(1 - K_k^N)}{(1 - K_k)} I(t) + \frac{(AF_R U_L)_1}{\dot{m}_f C_f} \frac{(1 - K_k^N)}{(1 - K_k)} T_a + K_k^N T_{fi} \quad (19)$$

After obtaining the value of  $T_{foN}$ , one can obtain the useful heat gain ( $\dot{Q}_{uN}$ ) by series-connected  $N$  alike ETCs as:

$$\dot{Q}_{uN} = \dot{m}_f C_f (T_{foN} - T_{fi}) \quad (20)$$

After putting value of  $T_{foN}$  from Eq. (2) into Eq. (3) and simplifying using approach similar to the approach presented in Mishra et al. [19], one can obtain the expression of  $\dot{Q}_{uN}$  as:

$$\dot{Q}_{uN} = \frac{(1 - K_k^N)}{(1 - K_k)} (AF_R(\alpha\tau))_1 I(t) + \frac{(1 - K_k^N)}{(1 - K_k)} (AF_R U_L)_1 (T_{fi} - T_a) \quad (21)$$

where  $T_{foN}$  stands for temperature at the outlet of last collector ( $N$ th collector) and  $T_{fi}$  stands for temperature at the inlet of first collector. The variable  $T_{fi}$  can be taken as identical to  $T_w$  because water from the basin is compelled to go into the inlet of the first collector with the help of pump due to the formation of closed loop with basin. Also, heated water available at the outlet of last collector ( $N$ th collector) is made to flow to the basin of solar still. Hence, the variable  $T_{wo}$  can be taken identical to  $T_{foN}$ . Various unknown terms in Eqs. (18)–(21) can be seen in Mishra et al. [19].

Following Singh and Tiwari [20], the basic mathematical equation for different components of DS can be written and these equations can be solved using Eq. (4) to get the temperature of water ( $T_w$ ) in the basin in terms of some known parameters and can be expressed as:

$$T_w = \frac{\overline{f_2(t)}}{a_2} (1 - e^{-a_2 t}) + T_{w0} e^{-a_2 t} \tag{22}$$

After getting the expression of  $T_w$ , one can proceed for getting the expression for glass temperatures at inner and outer surfaces using the approach similar to the approach presented in Singh and Tiwari [20] and they can be expressed as:

$$T_{giE} = \frac{A_1 + A_2 T_w}{P} \tag{23}$$

$$T_{giW} = \frac{B_1 + B_2 T_w}{P} \tag{24}$$

$$T_{goE} = \frac{\frac{K_g}{L_g} T_{giE} + h_{1gE} T_a}{\frac{K_g}{L_g} + h_{1gE}} \tag{25}$$

$$T_{goW} = \frac{\frac{K_g}{L_g} T_{giW} + h_{1gW} T_a}{\frac{K_g}{L_g} + h_{1gW}} \tag{26}$$

Here,  $T_{giE}$  and  $T_{giW}$  are temperatures of glass at inner surface oriented toward east direction and west direction, respectively.  $T_{goE}$  and  $T_{goW}$  are temperatures of glass at outer surfaces oriented toward east direction and west direction, respectively. Various unknown terms used in Eqs. (22)–(26) can be seen in Singh and Tiwari [20].

After computing the value of water temperature ( $T_w$ ) and glass temperatures ( $T_{giE}$  and  $T_{giW}$ ), the hourly production of potable water ( $\dot{m}_{ew}$ ) can be computed as follows.

$$\dot{m}_{ew} = \frac{h_{ewgE} \frac{A_b}{2} (T_w - T_{giE}) + h_{ewgW} \frac{A_b}{2} (T_w - T_{giW})}{L} \times 3600 \tag{27}$$

where  $L$  stands for the amount of thermal energy required to evaporate unit mass of water (latent heat). The value of daily potable water yield can be evaluated by adding hourly potable water yield for 24 h.

Hourly thermal exergy for the solar distiller ( $\dot{E}x_{thermal}(t)$ ) can be computed as follows [21]:

$$\begin{aligned} \dot{E}x_{thermal}(t) = \frac{A_b}{2} & \left[ h_{ewgE} \times \left\{ (T_w - T_{giE}) - (T_a + 273) \times \ln \left( \frac{T_w + 273}{T_{giE} + 273} \right) \right\} \right. \\ & \left. + h_{ewgW} \times \left\{ (T_w - T_{giW}) - (T_a + 273) \times \ln \left( \frac{T_w + 273}{T_{giW} + 273} \right) \right\} \right] \tag{28} \end{aligned}$$

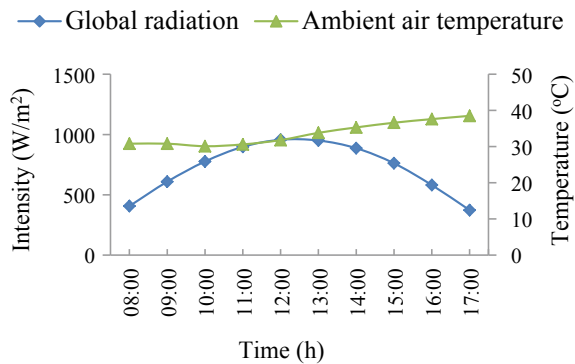
The different terms used in Eqs. (18)–(27) have also been presented in appendix of Singh and Tiwari [19]. The daily exergy can be evaluated by adding hourly exergy for 24 h using Eq. (28).

Now, these equations can be fed to the programming code written in MATLAB for the computation of output parameters. The input data required for the evaluation of output parameter has been taken from IMD Pune located in India and has been depicted in Fig. 14.17. The solar flux supplied by IMD Pune is on horizontal plane; so, Liu and Jordan formula has been used to find the value of solar flux on the inclined plane. The input parameters and output parameters for  $N$  equal partly covered PVTCPs having series connection and integrated to solar energy-based single-slope water purifier are shown in Fig. 14.18. Out of the input parameters depicted in Fig. 14.18, solar intensity and surrounding temperature are totally dependent on weather and remain same for a particular day. So, they have not been considered.

The outputs obtained from MATLAB have been shown in Figs. 14.19 and 14.20 [22] and Table 14.3 [22].

Figure 14.19 presents the comparative study of sensitivity of daily PW yield with the percentage change in one input parameter keeping other input parameters constant. The slope of these curves gives the sensitivity figure for PW yield with respect to one input parameter keeping other input parameters constant. Here, input parameters are MFR,  $N$ , and WD. It has been observed from Fig. 14.19 that the sensitivity in PW yield is higher at lower values of  $N$  and the sensitivity tends to

**Fig. 14.17** Hourly variation of intensity and ambient air temperature for a typical day in the month of May [Source Author]



**Input parameters:**

- Number of collectors
- Mass flow rate
- Water depth
- Solar radiation
- Ambient temperature

MATLAB code of the model based on energy balance for  $N$  indistinguishable evacuated tubular collectors (ETCs) integrated double slope distiller unit

**Output parameter:**

- Fresh water
- Exergy

**Fig. 14.18** Purification of saline/brackish water to potable water using ETCs integrated double-slope solar desalination system [Source Author]

**Fig. 14.19** Comparative sensitivity of PW yield with respect to input variable (MFR/N/WD) for NETCDS [Source Author]

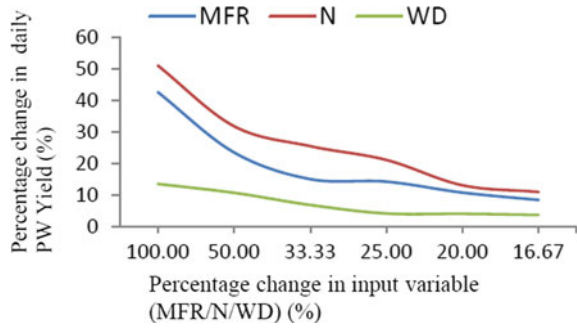


**Fig. 14.20** Comparative sensitivity of daily exergy with respect to input variable [Source Author]

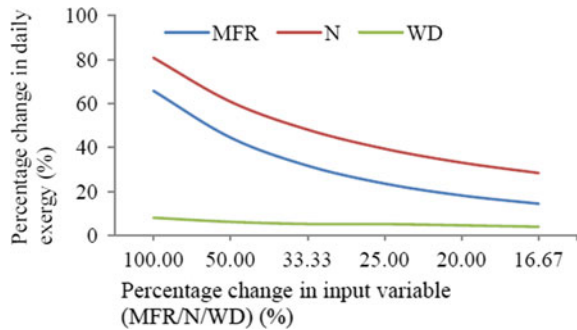


**Table 14.3** Average values of sensitivity figure for  $N$  equal ETCs having series connection and integrated to solar energy-based double-slope water purifier

Average value of sensitivity figure for PW w.r.t. $\dot{m}_f$	Average value of sensitivity figure for PW w.r.t. $N$	Average value of sensitivity figure for PW w.r.t. water depth
0.5	0.68	0.20
Average value of sensitivity figure for EPO w.r.t. $\dot{m}_f$	Average value of sensitivity figure for EPO w.r.t. $N$	Average value of sensitivity figure for EPO w.r.t. water depth
0.019	0.997	0.008

decrease at higher values of  $N$ . It happens because the difference between temperature of absorber plate of ETC and the temperature of fluid below the absorber plate is higher at lower values of  $N$  and vice versa. The heat collection area of each collector is same, and hence the temperature of absorber of the collector is same for each collector; however, fluid coming from the basin will have lower temperature and hence the temperature of fluid flowing below the absorber through copper tubes is lower at lower values of  $N$ . It results in the creation of higher temperature difference between absorber temperature and fluid temperature which is responsible for higher



rate of heat transfer, and ultimately higher amount of heat is added at lower values of  $N$ . Hence, sensitivity in PW yield is higher at lower values of  $N$ .

Further, it has been observed from Fig. 14.19 that the sensitivity in PW yield is higher at lower values of MFR and the sensitivity tends to decrease at higher values of MFR. The reason being that the percentage change in heat gain by  $N$  number of series-connected collectors corresponding to the percentage change in MFR at its lower values is higher which happens due to higher change in temperature. It has also been observed from Fig. 14.6a that the sensitivity in daily PW yield is higher at lower values of WD and the sensitivity tends to decrease at higher values of WD in basin. It occurs due to higher rise in temperature of water in basin at lower water depth as water mass in basin is lesser. Hence, higher evaporation rate is obtained which results in higher change in PW yield. PW yield has been found to be most sensitive with respect to  $N$  followed by MFR and WD. It means that the designer of solar distillation system for industrial use should concentrate most on the selection of  $N$  as this parameter has been found to be most significant for the production of PW. However, the cost of system increases with the increase in the value of  $N$ . So, one should also keep in mind the economy while deciding value of  $N$  for the setup installation. The average values of sensitivity figures with respect to PW yield as depicted in Table 14.3 have been found to be 0.68, 0.50, and 0.20 for  $N$ , MFR, and WD in that order.

Figure 14.20 presents the comparative sensitivity study of exergy output with different input parameters like  $N$ , MFR, and WD. The result says that the most sensitive parameter is  $N$  from the point of view of exergy output followed by MFR and WD. The average value of sensitivity figure with respect to daily exergy output has been presented in Table 14.3. The average values of sensitivity figures for exergy output have been computed as 1.40, 0.87, and 0.17 with respect to  $N$ , MFR, and WD. It means that the designer of NETCDS should focus most on  $N$  followed by MFR and WD from the exergy output point of view.

## 14.4 Conclusions

In this chapter, the sensitivity analysis of solar systems particularly solar energy-based water purifier has been carried out. The methodology for carrying out the sensitivity analysis of solar system has been presented. On the basis of current study, the following conclusions have been drawn:

- (i) The values of sensitivity figure of  $N$  equal partly covered PVTCPs integrated to solar energy-based single-slope water purifier for PW yield are 0.331, 0.298, 0.143, and 0.078 with respect to  $N$ ,  $\dot{m}_f$ , water depth, and packing factor. The values of sensitivity figure of the same system for EP output are 0.920, 0.780, 0.011, and 0.008 with respect to packing factor,  $N$ ,  $\dot{m}_f$ , and water depth.
- (ii) The values of sensitivity figure of  $N$  equal partly covered PVTCPs integrated to solar energy-based double-slope water purifier for PW yield are 0.247,

- 0.186, 0.161, and 0.09 with respect to  $N$ , packing factor,  $\dot{m}_f$ , and water depth. The values of sensitivity figure of the same system for EP output are 1.07, 0.997, 0.019, and 0.008 with respect to packing factor,  $N$ ,  $\dot{m}_f$ , and water depth.
- (iii) The values of sensitivity figure of  $N$  equal ETCs integrated to solar energy-based double-slope water purifier for PW yield are 0.68, 0.5, and 0.20 with respect to  $N$ ,  $\dot{m}_f$ , and water depth. The values of sensitivity figure of the same system for exergy output are 0.997, 0.019, and 0.008 with respect to  $N$ ,  $\dot{m}_f$ , and water depth.
- (iv) The same methodology for carrying out sensitivity analysis can be applied to any solar system. The sensitivity analysis provides the designer and installer a way to find the impact of different input parameters on output parameter so that they can suitably decide on values of input parameters as per the requirement.

## References

1. Rai SN, Tiwari GN (1983) Single basin solar still coupled with flat plate collector. *Energy Convers Manag* 23(3):145–149
2. Zaki GM, Dali El T, Shafie El H (1983) Improved performance of solar still. In: Proceedings of the first Arabic international solar energy conference, Kuwait, pp 331–335
3. Sahota L, Tiwari GN (2017) *Advanced Solar-distillation systems: basic principles, thermal modeling, and its application*. Springer, Singapore
4. Kumar S, Tiwari A (2010) Design, fabrication and performance of a hybrid photo-voltaic/thermal (PVT) active solar still. *Energy Convers Manag* 51:1219–1229
5. Tiwari GN, Yadav JK, Singh DB, Al-Helal IM, Abdel-Ghany AM (2015) Exergoeconomic and enviroeconomic analyses of partially covered photovoltaic flat plate collector active solar distillation system. *Desalination* 367:186–196
6. Singh DB, Yadav JK, Dwivedi VK, Kumar S, Tiwari GN, Al-Helal IM (2016) Experimental studies of active solar still integrated with two hybrid PVT collectors. *Sol Energy* 30:207–223
7. Issa RJ, Chang B (2018) Performance study on evacuated tubular collector coupled solar still in West Texas climate. *Int J Green Energy* 14(10):793–800
8. Singh DB (2018) Improving the performance of single slope solar still by including  $N$  identical PVT collectors. *Appl Therm Eng* 131:167–179
9. Singh DB (2018) Energy metrics analysis of  $N$  identical evacuated tubular collectors integrated single slope solar still. *Energy* 148:546–560
10. Fathy M, Hassan H, Ahmed MS (2018) Experimental study on the effect of coupling parabolic trough collector with double slope solar still on its performance. *Sol Energy* 163:54–61
11. Singh DB, Tiwari GN (2017) Analytical characteristic equation of  $N$  identical evacuated tubular collectors integrated double slope solar still. *J Sol Energy Eng Including Wind Energy Build Energy Conserv ASME* 135(5):051003(1–11)
12. Kumar R, Sharma R, Kumar D, Singh AR, Singh DB, Tiwari GN (2020) Characteristic equation development for single-slope solar distiller unit augmented with  $N$  identical parabolic concentrator integrated evacuated tubular collectors. *J Sol Energy Eng Including Wind Energy Build Energy Conserv ASME* 142:021011 1-11
13. Prasad H, Kumar P, Yadav RK, Mallick A, Kumar N, Singh DB (2019) Sensitivity analysis of  $N$  identical partially covered (50%) PVT compound parabolic concentrator collectors integrated double slope solar distiller unit. *Desalin Water Treat* 153:54–64
14. Singh DB, Kumar N, Harender KS, Sharma SK, Mallick A (2019) Effect of depth of water on various efficiencies and productivity of  $N$  identical partially covered PVT collectors incorporated single slope solar distiller unit. *Desalin Water Treat* 138:99–112

15. Singh DB, Bansal G, Prasad H, Mallick A, Kumar N, Sharma SK (2020) Sensitivity analysis of N undistinguishable PVT compound-parabolic-concentrator-collectors (partly covered, 50%) integrated single slope solar distiller unit. *J Sol Energy Eng ASME* 143:021003-1–021003-11
16. Tripathi R, Tiwari GN, Al-Helal IM (2016) Thermal modeling of N partially covered photovoltaic thermal (PVT)–Compound parabolic concentrator (CPC) collectors connected in series. *Sol Energy* 123:174–184
17. Tiwari GN, Meraj Md, Khan ME (2018) Exergy analysis of N-photovoltaic thermal-compound parabolic concentrator (N-PVT-CPC) collector for constant collection temperature for vapor absorption refrigeration (VAR) system. *Sol Energy* 173:1032–1042
18. Singh DB, Tiwari GN (2016) Effect of energy matrices on life cycle cost analysis of partially covered photovoltaic compound parabolic concentrator collector active solar distillation system. *Desalination* 397:75–91
19. Mishra RK, Garg V, Tiwari GN (2015) Thermal modeling and development of characteristic equations of evacuated tubular collector (ETC). 116:165–176
20. Singh DB, Tiwari GN (2017) Energy, exergy and cost analyses of N identical evacuated tubular collectors integrated basin type solar stills: a comparative study. 55:829–846
21. Nag PK (2004) Basic and applied thermodynamics. Tata McGraw-Hill (ISBN 0-07-047338-2)
22. Singh DB Sensitivity analysis of N identical evacuated tubular collectors integrated double slope solar distiller unit by incorporating the effect of exergy. *Int J Exergy* (Accepted)

# Chapter 15

## Environmental Feasibility of Solar Hybrid Systems



Sumit Tiwari, Prabhakar Tiwari, V. K. Dwivedi, and G. N. Tiwari

### Nomenclature

$A_c$	Area of the crop surface ( $m^2$ )
$A_{cf}$	Opening area of fan ( $m^2$ )
$A_{cl}$	Cross-sectional area of duct of air collector ( $m^2$ )
$A_m$	Area of the PV module ( $m^2$ )
$A_w$	Area of side walls of dryer ( $m^2$ )
$A_t$	Area of the tray ( $m^2$ )
$C_f$	Specific heat of air (J/kg K)
$C_{cr}$	Specific heat of crop (J/kg K)
$d$	Diameter of DC fan (m)
$E_{el}$	Electrical energy (kWh)
$hi$	Heat transfer coefficient inside PVT air collector and solar drying system ( $W/m^2K$ )
$h_{crr}$	Total heat transfer coefficient from crop surface to drying chamber ( $W/m^2K$ )
$h_{crc}$	Convective heat transfer coefficient from crop surface to drying chamber ( $W/m^2K$ )
$h_{crew}$ or $h_{ew}$	Evaporative heat transfer coefficient from crop surface to drying chamber ( $W/m^2K$ )
$h_o$	Heat transfer coefficient from top of module to ambient air ( $W/m^2K$ )

---

S. Tiwari (✉)

Shiv Nadar University, NH-91, Tehsil Dadri, Gautam Buddha Nagar, Uttar Pradesh, India

e-mail: [tiwsumit@hotmail.com](mailto:tiwsumit@hotmail.com)

P. Tiwari · V. K. Dwivedi

MMMUT, Gorakhpur, India

G. N. Tiwari

Indian Institute of Technology, Delhi, India

© The Author(s), under exclusive license to Springer Nature Singapore Pte Ltd. 2021

S. N. Singh et al. (eds.), *Fundamentals and Innovations in Solar Energy*,

Energy Systems in Electrical Engineering,

[https://doi.org/10.1007/978-981-33-6456-1\\_15](https://doi.org/10.1007/978-981-33-6456-1_15)

$h_{pf}$	Heat transfer coefficient from absorbing plate to working fluid (W/m <sup>2</sup> K)
$I_t$	Solar intensity (W/m <sup>2</sup> )
$I_w$	Total solar intensity on the walls of drying chamber (W/m <sup>2</sup> )
$K_g$	Thermal conductivity of glazing (W/mK)
$L_g$	Thickness of the glass (m)
$M_f$	Mass flow rate of working fluid (air) (kg/s)
$M_{cr}$	Mass of crop (kg)
$P_{Tr}$	Partial pressure at greenhouse chamber temperature (N/m <sup>2</sup> )
$P_{Tcr}$	Partial pressure at crop temperature (N/m <sup>2</sup> )
$T_a$	Ambient temperature (°C)
$T_o$	Cell temperature for optimum cell efficiency
$T_c$	Cell temperature (°C)
$T_{cr}$	Crop temperature (°C)
$T_{cro}$	Initial crop temperature (°C)
$T_r$	Drying chamber temperature (°C)
$T_{foN}$	Air temperature at outlet of <i>N</i> th PVT air collector (°C)
$U_{bcf}$	Heat transfer coefficient from bottom of module to working fluid (W/m <sup>2</sup> K)
$U_{tca}$	Heat transfer coefficient from top of module to ambient air (W/m <sup>2</sup> K)
$U_{bpa}$	Heat transfer coefficient from bottom of absorbing plate to ambient air (W/m <sup>2</sup> K)
$Q_{th}$	Thermal energy (kWh)
$Q_{eq,th}$	Equivalent thermal energy (kWh)
$Q_{th,ex}$	Thermal exergy (kWh)
$\alpha_c$	Absorptivity of solar cell
$\alpha_{cr}$	Absorptivity of crop
$\beta_0$	Temperature-dependent efficiency factor
$\beta_c$	Packing factor of module
$\gamma$	Relative humidity
$\eta_0$	Standard efficiency at standard condition
$\eta_c$	Solar cell efficiency
$\eta_m$	Module efficiency
$\eta_{th}$	Thermal efficiency
$\eta_{el}$	Electrical efficiency
$\eta_{eq,th}$	Equivalent thermal efficiency
$\eta_{ex}$	Exergy efficiency
$\eta_{eq,ex}$	Equivalent exergy efficiency
$v$	Wind velocity in ambient (m/s)
$v_1$	Air velocity in duct of air collector (m/s)
$v_2$	Air velocity from fan (m/s)
$v_3$	Air velocity in drying chamber (m/s)
$\tau_g$	Transmittivity of glass

## 15.1 Introduction

In the present era, pollution is increasing continuously, due to quick growth in power demand; there is a great demand of power from renewable sources. Parsa et al. [23] compared active and passive solar purification systems based on environmental/economic/exergy/heat transfer/energy matrices. Singh et al. [32–34] studied the system (ETC with solar still) and evaluated the performance based on CO<sub>2</sub>–SO<sub>2</sub>–NO emissions, EPBT, LCCE, carbon mitigations, etc. Based on 30 years of life, system showed EE (1138.52 kWh) and output of 3.8 l/m<sup>2</sup>/day with 77.2 tons of carbon mitigation. Singh and Tiwari [31] also explored PVT-CPC distillation (active) with thermal modeling and further, based on that EPBT of system analyzed. Sahota et al. [25] explored solar still with nano-fluids (TiO<sub>2</sub>, Al<sub>2</sub>O<sub>3</sub>, and CuO-water based) and exergoeconomic analysis, energy matrices, and enviroeconomic analysis done for system with comparison. Different types of solar still are explored based on environmental economics by Singh et al. [32–34]. Authors also explored different parameters along with energy matrices that have been calculated for PVT drying system and concluded that it is important for the environment [16, 20, 36–43].

Present chapter is an example, which includes complete analysis from scratch to make readers understand how to make thermal model with environmental feasibility of hybrid solar systems. Therefore, PVTAC-connected greenhouse dryer has been considered for analysis.

Drying is the process, which includes both heat and mass transfer. There are different drying technique available as per requirement, namely electrical drying, solar drying, open-air sun drying, and firewood/fuel drying [3, 29, 45]. Sustainable development is only possible with solar drying systems, as it is one of the cleanest forms of energy [30, 37, 38]. Further, solar drying is performed in open or closed system [36, 39]. Due to several shortcomings of open sun drying like decoloration, quality degradation, and insect infestation, solar dryers were developed to enhance the quality of final agricultural residue after drying. Solar dryers operate in forced draught and natural draught mode. Many agricultural scientists and researchers found that forced draught drying gives better results in comparison with natural mode due to better control on drying parameters [5, 22]. Flat plate collectors also can be utilized for solar energy collection and can be used in drying chamber. Dorouzi et al. [10] made a dryer with desiccant material and PV to make it self-sustainable. It was found that if temperature of air increases from 60 to 70 °C, then drying time can be reduced by 10%. The heat from photovoltaic module (PV) can be utilized in several field, namely agricultural, domestic, and buildings [13, 21]; Browne et al. [6, 24]. Thermal modeling with experimental validation of PVT drying systems has been reported by researchers across the globe. Energy matrices have been analyzed and concluded that PV-integrated thermal systems are always better in terms of energy production and environmental protection [26].

Kabeel and Abdelgaied [14] developed a drying system coupled with solar collector (flat plate type) which also contains a rotary desiccant wheel for moisture control. With the help of theoretical model and experimental reading, drying air

temperature is found to be increased from 65–82 °C with reduced humidity ratio for identical situation in contrast to system without desiccant wheel. Adnane et al. [1] found that the drying time can be optimized while testing on henna in drying system integrated with FPC. Several drying systems with or without air heaters have been studied in previous research for efficient use of solar energy [28]. FPCs working with solar energy are popular for its easiness in design with low-cost investment and simplicity in operation [15]. Lamnatou et al. [17] investigated a drying system integrated with air collector having evacuated tube is found good for drying. Akbulut and Durmus [2] investigated the energy utilization ratio, which were 55.2%, 32.19%, 29.2%, 21.5%, and 20.5% for various mass flow rates ranging from 0.014 kg/s to 0.036 kg/s. Azaizia et al. [4] studied solar air collector with dryer and observed good performance in terms of thermal efficiency, which lies between 0.5 and 0.65. Mghazli et al. [18] developed the drying kinetics for rosemary dried solar dryer having distinct drying chamber and air collector. Condorí et al. [8] experimented on an indirect tunnel-type dryer. At no load condition, outlet temperatures reached around 80–90 °C which was 50–60 °C higher than the ambient temperature at 0.06 kg/s mass flow rate. In economic assessment, EPBT of 13 months was found and is still good comparative to other solar heating systems. Some researchers also carried out work in controlled environment using an indirect solar dryer and laboratory. They found that the page model was better for 55 and 65 °C, and Wang and Sing's model showed a better fit at 45 °C [7].

Generally, FPCs integrated drying system requires electricity to run the fan and to operate the system in forced mode. In previous literature, work was found on partially covered FPCs but very less literature is available on partially covered FPCs integrated with drying system. However, in current scenario and environmental condition, grid electricity is not a good choice for running drying system in forced mode. Song et al. [35] found that for environmental and sustainable development point of view, solar drying is important for society. Mishra and Tiwari [19] discussed and compared the energy matrices for five different PV technologies with water heating system and concluded c-Si PV module is better choice for electricity production.

Fterich et al. [12] experimented at Laboratory in Tunisia during September 2015. Through prototype, moisture content of product reduced from 91.94 (%) to 22.32 (%) for tray 1 and to 28.9 (%) for tray 2, in contrast 30.15 (%) for open sun dryer.

This chapter includes

- (i) For the first time, thermal energy (TE), electrical energy (EE), and equivalent (overall) thermal energy (OTE) have been calculated for PVTAC-integrated drying system on yearly basis with the help of data provided by IMD, Pune, India.
- (ii) Analysis has been carried out for various weather conditions which is defined as the ratio of daily diffuse to daily global radiation, namely Type a ( $\leq 0.25$ ), Type b (0.25–0.50), Type c (0.50–0.75), and Type d ( $\geq 0.75$ ).
- (iii) Further, environeconomic analysis (environmental feasibility) has also been carried out for various cell technologies integrated with the system to analyze environmental sustainability.

### 15.2 System Description

Figure 15.1a–b shows diagram of partially covered PVTEC dryer (25% PV coverage) (b) air heater (cross section), respectively. Figure 15.1a contains component, namely drying chamber and PVTAC. The PVTAC comprises PV panel (glass-to-glass type) with FPC. PV has used 25% area of total area of air collector, which is sufficient in making the system viable to perform in forced mode. The PVTAC has been kept at an angle of 30° (latitude angle of New Delhi, India) to explore maximum radiation. One part of the sun rays coming at the top of the PV module is converted into EE and remaining part is absorbed in absorber plate in heat form. Thereafter, heat energy stored in absorber plate has been taken by input air, and further, it flows through the glazing section. Here, solar rays directly absorb at blackened plate and more heat

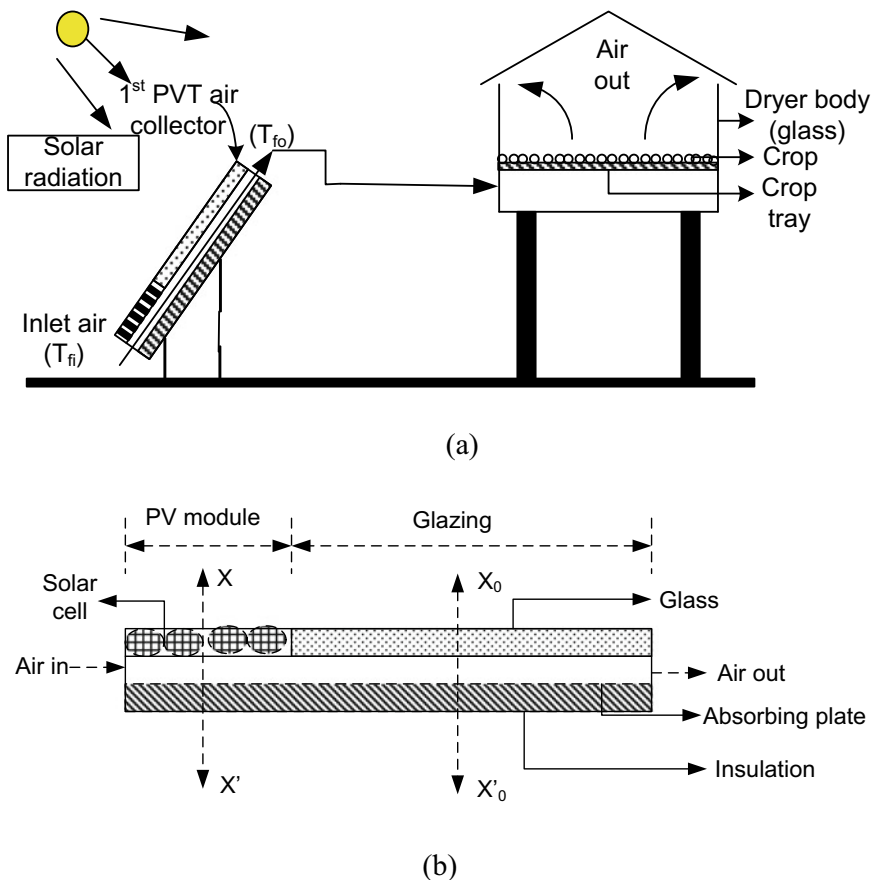


**Fig. 15.1** a Schematic diagram of partially covered PVTEC dryer (25% PV coverage) b air heater (cross section). *Source* Author



gain to heated air compared to PV part. The output-heated air from air collector is fed into the drier by means of a 12 V DC fan to dry crop. Air heater cross section is also included in Fig. 15.1b.

### 15.3 Methodology

To analyze PVTAC-integrated dryer, subsequent methodology is followed.

**Step 1**—The data of ambient air temperature and solar radiation (direct and diffuse) on plane surface provided by IMD, Pune, has been taken and, further, converted for inclined surface at 30° as per experimental setup using Liu and Jordan formula [46].

**Step 2**—With the basic thermal equation, program has been made in MATLAB 2013a. Firstly, cell efficiency formula has been developed in terms of ambient temperature and solar intensity. By using cell efficiency, outlet air temperature ( $T_{fo}$ ) from PVTAC has been evaluated. Further, the temperature of cell and crop at load condition have been evaluated by  $T_{fo}$ .

**Step 3**—To show the behavior of electrical efficiency with respect to temperature for different solar cell technologies (SCTs), calculation for a typical clear day of March month has been done. Then, variation of overall thermal efficiency ( $\eta_{ov,th}$ ) and overall exergy efficiency ( $\eta_{ov,ex}$ ) has also been calculated.

**Step 4**—Energy analysis, which includes electrical, thermal, and overall thermal energy (OTE), has been calculated for all climatic conditions (Type a, Type b, Type c, Type d) possible in a month. Thereafter, same calculation has been carried out for each month of a year and takes the sum of total energy. Abovesaid analysis was followed for all PV technologies considering two different cases, namely 25% (current setup) and 100% (assumed setup) air collector area covered by PV module.

**Step 5**—Further, EPBT, CO<sub>2</sub> mitigation, and CCE for both cases, namely 25% and 100% air collector area covered by PV module have been evaluated and analyzed the comparative benefits of each technology.

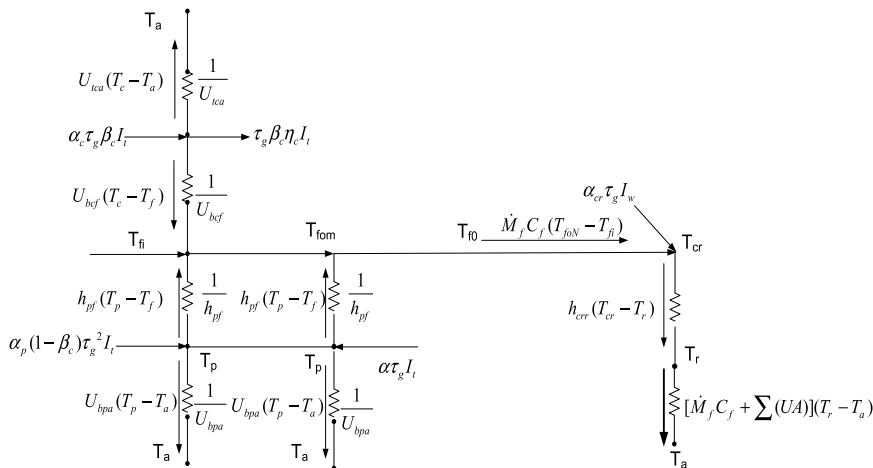
#### 15.3.1 Thermal Modeling

Figure 15.2 shows electrical circuit diagram for the present experimental setup.

#### PV Part PVT air Collector

Equation for PV [27],

$$\alpha_c \tau_g \beta_c I_t b dx = U_{tca}(T_c - T_a) b dx + U_{bcf}(T_c - T_f) b dx + \tau_g \beta_c \eta_c I_t b dx \quad (15.1)$$



**Fig. 15.2** Diagram of thermal resistance along with TE circuit diagram for the present experimental setup. *Source* Author

$$\alpha_c \tau_g \beta_c I_t = U_{tca}(T_c - T_a) + U_{bcf}(T_c - T_f) + \tau_g \beta_c \eta_c I_t \tag{15.2}$$

Temperature-dependent solar cell efficiency [11, 31]

$$\eta_c = \eta_o(1 - \beta_o(T_c - T_o)) \tag{15.3}$$

Equation for absorbing plate [27],

$$\alpha_p(1 - \beta_c) \tau_g^2 I_t b dx = h_{pfa}(T_p - T_f) b dx + U_{bpa}(T_p - T_a) b dx \tag{15.4}$$

$$\alpha_p(1 - \beta_c) \tau_g^2 I_t = h_{pfa}(T_p - T_f) + U_{bpa}(T_p - T_a) \tag{15.5}$$

Equation for working fluid (air) [27],

$$\dot{M}_f C_f \frac{dT_f}{dx} dx = [U_{bcf}(T_c - T_f) + h_{pfa}(T_p - T_f)] b dx \tag{15.6}$$

$$\dot{M}_f C_f \frac{dT_f}{dx} = [U_{bcf}(T_c - T_f) + h_{pfa}(T_p - T_f)] b \tag{15.7}$$

**Conventional (Glazed Part) of PVT Air Collector**

Equation for blackened surface [27]

$$\alpha \tau_g I_t b dx = [U_{bpa}(T_p - T_a) + h_{pfa}(T_p - T_f)] b dx \tag{15.8}$$

$$\alpha \tau_g I_t b dx = U_{bpa}(T_p - T_a) + h_{pf}(T_p - T_f) \quad (15.9)$$

Equation for flowing fluid [27],

$$\dot{M}_f C_f \frac{dT_f}{dx} dx + U_{tfa}(T_f - T_a) b dx = [h_{pf}(T_p - T_f)] b dx \quad (15.10)$$

$$\dot{M}_f C_f \frac{dT_f}{dx} = [h_{pf}(T_p - T_f) - U_{tfa}(T_f - T_a)] b \quad (15.11)$$

### Drying Chamber

Equation for crop [27]

$$\alpha_{cr} \tau_g I_w A_w + h_c(T_{fo} - T_{cr}) A_t = M_{cr} C_{cr} \frac{dT_{cr}}{dt} + h_{crr}(T_{cr} - T_r) A_t \quad (15.12)$$

Equation for drying room [27]

$$\begin{aligned} h_{crr}(T_{cr} - T_r) A_t + \dot{M}_f C_f (T_{fo} - T_{fi}) &= h_c(T_{fo} - T_{cr}) A_t \\ + \dot{M}_f C_f (T_r - T_a) + \left( \sum (UA) \right) (T_r - T_a) & \end{aligned} \quad (15.13)$$

From Eq. (15.2),

$$T_c - T_f = \frac{(\alpha_c \tau_g \beta_c - \eta_m) I_t - U_{tca}(T_f - T_a)}{U_{tca} + U_{bcf}} \quad (15.14)$$

From Eq. (15.4),

$$T_p - T_f = \frac{\alpha_p(1 - \beta_c) \tau_g^2 I_t - U_{bpa}(T_f - T_a)}{h_{pf} + U_{bpa}} \quad (15.15)$$

From Eqs. (15.7), (15.14), (15.15)

$$\frac{dT_f}{dx} + \left( \frac{b U_{Lm}}{\dot{M}_f C_f} \right) T_f = \left( \frac{b}{\dot{M}_f C_f} \right) [(\alpha \tau)_{\text{meff}} I_t + T_a U_{Lm}] \quad (15.16)$$

where,

$$\begin{aligned} U_{Lm} &= U_{tfa} + U_{bfa}, h_{p1} = \frac{U_{bcf}}{U_{tca} + U_{bcf}}, h_{p2} = \frac{h_{pf}}{h_{pf} + U_{bpa}} \\ U_{tfa} &= \frac{U_{tca}}{U_{tca} + U_{bcf}}, U_{bfa} = \frac{U_{bpa}}{h_{pf} + U_{bpa}}, (\alpha \tau)_{\text{meff}} = h_{p1}(\alpha_c \tau_g \beta_c - \eta_m) + h_{p2} \alpha_p (1 - \beta_c) \tau_g^2 \end{aligned}$$

Equation (15.16) can be solved by Eqs. (15.17), (15.18)

$$\frac{dT}{dt} + aT = f(t) \quad (15.17)$$

$$T = \frac{f(t)}{a}(1 - e^{-at}) + T_{cro}e^{-at} \quad (15.18)$$

Solution of the Eq. (15.16) is

$$T_{fom} = \left[ \frac{(\alpha\tau)_{meff}I_t}{U_{Lm}} + T_a \right] \left[ 1 - \exp\left(-\frac{bU_{Lm}L_m}{\dot{M}_f C_f}\right) \right] + T_{fi} \exp\left(-\frac{bU_{Lm}L_m}{\dot{M}_f C_f}\right) \quad (15.19)$$

(at initial condition  $x = 0$ ,  $T_f = T_{fi}$  and  $x = L_m$ ,  $T_f = T_{fom}$ )

From Eq. (15.8)

$$T_p - T_f = \frac{\alpha\tau_g I_t - U_{bpa}(T_f - T_a)}{U_{bpa} + h_{pf}} \quad (15.20)$$

From Eqs. (15.11) and (15.20)

$$\frac{dT_f}{dx} + \left( \frac{bU_{Lc}}{\dot{M}_f C_f} \right) T_f = \left( \frac{bU_{Lc}}{\dot{M}_f C_f} \right) \left[ \frac{(\alpha\tau)_{ceff}I_t}{U_{Lc}} + T_a \right] \quad (15.21)$$

where

$$h_{p2} = \frac{h_{pf}}{U_{bpa} + h_{pf}}, U_{pfa} = \frac{U_{bpa}h_{pf}}{U_{bpa} + h_{pf}}, U_{Lc} = U_{pfa} + U_{ifa}$$

$$(\alpha\tau)_{c,eff} = h_{p2}(\alpha_p\tau_g)$$

Equation (15.21) can be compared with Eqs. (15.17) and (15.18)

$$T_{fo} = \left[ \frac{(\alpha\tau)_{ceff}I_t}{U_{Lc}} + T_a \right] \left[ 1 - \exp\left(-\frac{U_{Lc}A_c}{\dot{M}_f C_f}\right) \right] + T_{foi} \exp\left(-\frac{U_{Lc}A_c}{\dot{M}_f C_f}\right) \quad (15.22)$$

And

$$T_{foi} = T_{fom} = \left[ \frac{(\alpha\tau)_{meff}I_t}{U_{Lm}} + T_a \right] \left[ 1 - \exp\left(-\frac{bU_{Lm}L_m}{\dot{M}_f C_f}\right) \right] + T_{fi} \exp\left(-\frac{bU_{Lm}L_m}{\dot{M}_f C_f}\right) \quad (15.23)$$

From Eqs. (15.22) and (15.23)

$$T_{fo} = \frac{I_t}{\dot{M}_f C_f} [AF_R(\alpha\tau)] + \frac{T_a}{\dot{M}_f C_f} [AF_R U_L] + T_{fi} \left[ 1 - \frac{[AF_R U_L]}{\dot{M}_f C_f} \right] \quad (15.24)$$

where

$$\begin{aligned} \frac{\dot{M}_f C_f}{U_{Lm}} \left( 1 - \exp\left(-\frac{A_m U_{Lm}}{\dot{M}_f C_f}\right) \right) &= A_m F_{Rm}, \quad \frac{\dot{M}_f C_f}{U_{Lc}} \left( 1 - \exp\left(-\frac{A_c U_{Lc}}{\dot{M}_f C_f}\right) \right) = A_c F_{Rc} \\ \exp\left(-\frac{A_m U_{Lm}}{\dot{M}_f C_f}\right) &= 1 - \frac{A_m U_{Lm} F_{Rm}}{\dot{M}_f C_f}, \quad \exp\left(-\frac{A_c U_{Lc}}{\dot{M}_f C_f}\right) = 1 - \frac{A_c U_{Lc} F_{Rc}}{\dot{M}_f C_f} \\ [AF_R(\alpha\tau)] &= (\alpha\tau)_{\text{ceff}} A_c F_{Rc} + (\alpha\tau)_{\text{meff}} A_m F_{Rm} \left( 1 - \frac{A_c F_{Rc} U_{Lc}}{\dot{M}_f C_f} \right) \\ [AF_R U_L] &= U_{Lc} A_c F_{Rc} + U_{Lm} A_m F_{Rm} \left( 1 - \frac{A_c F_{Rc} U_{Lc}}{\dot{M}_f C_f} \right) \end{aligned}$$

To calculate cell efficiency, average solar cell temperature is required, and average temperature of cell can be calculated by average fluid temperature. Average air temperature (from PV portion)

$$\bar{T}_f = \frac{T_{\text{fom}} + T_{fi}}{2} \quad (15.25)$$

$$\bar{T}_f = \frac{1}{2} \left[ \frac{I_t}{\dot{M}_f C_f} [A_m F_{Rm}(\alpha\tau)_{\text{meff}}] + (1 + K_m) [AF_R(\alpha\tau)] \left[ \frac{1 - K_K}{1 - K_K} \right] + T_{fi} \right] \quad (15.26)$$

Further

$$\begin{aligned} \bar{T}_{cN} &= \frac{I_t}{U_{tca} + U_{bcf}} \left[ (\alpha_c \tau_g \beta_c - \eta_c \tau_g \beta_c) + \frac{U_{bcf}}{2\dot{M}_f C_f} [[A_m F_{Rm}(\alpha\tau)_{\text{meff}}] \right. \\ &\quad \left. + (1 + K_m) [AF_R(\alpha\tau)] \left( \frac{1 - K_K}{1 - K_K} \right) \right] \\ &\quad + \frac{T_a}{U_{tca} + U_{bcf}} \left[ U_{tca} + \frac{U_{bcf}}{2\dot{M}_f C_f} [A_m F_{Rm} U_{Lm}] \right. \\ &\quad \left. + (1 + K_m) [AF_R U_L] \left( \frac{1 - K_K}{1 - K_K} \right) + \frac{(1 + K_m)}{2(U_{tca} + U_{bcf})} T_{fi} \right] \quad (15.27) \end{aligned}$$

$$\eta_{cN} = \eta_0 [1 - \beta_0 (\bar{T}_{cN} - T_0)] \quad (15.28)$$

$$\begin{aligned}
 & \eta_0 \left[ 1 - \frac{\beta_0}{U_{tca} + U_{bcf}} \left[ I_t \left[ \alpha_c \tau_g \beta_c + \frac{U_{bcf}}{2M_f C_f} \left( h_{p1} \alpha_c \tau_g \beta_c + h_{p2} \alpha_p (1 - \beta_c) \tau_g^2 \right) A_m F_{Rm} \right. \right. \right. \right. \\
 & \left. \left. \left. \left. \left( 1 + K_m \right) \left[ (\alpha \tau)_{eff} A_c F_{Rc} + \left( h_{p1} \alpha_c \tau_g \beta_c + h_{p2} \alpha_p (1 - \beta_c) \tau_g^2 \right) A_m F_{Rm} \left( 1 - \frac{A_c F_{Rc} U_{Lc}}{M_f C_f} \right) \right] \right] \right] \right] + \\
 & + \eta_{cN} \\
 & \frac{T_a \left[ U_{tca} + \frac{U_{bcf}}{2M_f C_f} \left[ A_m F_{Rm} U_{Lm} \right] + (1 + K_m) \left[ A F_R U_L \right] \left( \frac{1+K_m}{2} \right) T_{ji} - T_0 \right] \left[ U_{tca} + \frac{U_{bcf}}{2M_f C_f} \left[ A_m F_{Rm} U_{Lm} \right] + (1 + K_m) \left[ A F_R U_L \right] \left( \frac{1+K_m}{2} \right) T_{ji} - T_0 \right]}{1 - \frac{\eta_0 \beta_0 I_t}{U_{tca} + U_{bcf}} \left[ \tau_g \beta_c + \frac{U_{bcf}}{2M_f C_f} \left( h_{p1} \tau_g \beta_c \right) + \frac{U_{bcf}}{2M_f C_f} \left( 1 + K_m \right) h_{p1} \tau_g \beta_c A_m F_{Rm} \left( 1 - \frac{A_c F_{Rc} U_{Lc}}{M_f C_f} \right) \left( \frac{1-K_K}{1-K_K} \right) \right]} \\
 & \hspace{15em} (15.29)
 \end{aligned}$$

From Eq. (15.13),

$$T_r = \frac{(h_{crr} + h_c)T_{cr}A_t + \dot{M}_f C_f (T_{foN} - T_{fi}) - h_c T_{foN} A_t + \dot{M}_f C_f T_a + (\sum (UA))T_a}{h_{crr}A_t + \dot{M}_f C_f + \sum (UA)} \tag{15.30}$$

From Eqs. (15.12) and (15.33),

$$\alpha_{cr} \tau_g I_w A_w + h_c (T_{fo} - T_{cr})A_t = M_{cr} C_{cr} \frac{dT_{cr}}{dt} + h_{crr} \left( T_{cr} - \frac{(h_{crr} + h_c)T_{cr}A_t + \dot{M}_f C_f (T_{fo} - T_{fi}) - h_c T_{fo} A_t + \dot{M}_f C_f T_a + (\sum (UA))T_a}{h_{crr}A_t + \dot{M}_f C_f + \sum (UA)} \right) A_t \tag{15.31}$$

$$\frac{dT_{cr}}{dt} + \frac{U_{cra}(\dot{M}_f C_f + \sum (UA) - h_c A_t) + h_c A_t}{M_{cr} C_{cr}} T_{cr} = \left( \frac{1}{M_{cr} C_{cr}} \right) (\alpha_{cr} \tau_g I_w A_w + h_c T_{fo} A_t + U_{cra} \dot{M}_f C_f (T_{fo} - T_{fi}) + \dot{M}_f C_f T_a + (\sum (UA))T_a - h_c T_{fo} A_t) \tag{15.32}$$

where

$$U_{cra} = \frac{h_{crr} A_t}{h_{crr} A_t + \dot{M}_f C_f + \sum (UA)}$$

From Eqs. (15.17) and (15.18), solution of Eq. (15.32),

$$T_{cr} = \frac{f(t)}{a} (1 - e^{-at}) + T_{cro} e^{-at} \tag{15.33}$$

(at  $t = 0, T_{cro} = T_a$ )Where,

$$f(t) = \left( \frac{1}{M_{cr} C_{cr}} \right) (\alpha_{cr} \tau_g I_w A_w + h_c T_{fo} A_t + U_{cra} (\dot{M}_f C_f (T_{fo} - T_{fi}) + \dot{M}_f C_f T_a + (\sum (UA))T_a - h_c T_{fo} A_t))$$

$$a = \frac{U_{cra} (\dot{M}_f C_f + \sum (UA) - h_c A_t) + h_c A_t}{M_{cr} C_{cr}}$$

$$T_{cr} = \left( \frac{\alpha_{cr} \tau_g I_w A_w + h_c T_{fo} A_t + U_{cra} (\dot{M}_f C_f (T_{fo} - T_{fi}) + \dot{M}_f C_f T_a + (\sum (UA))T_a - h_c T_{fo} A_t)}{U_{cra} (\dot{M}_f C_f + \sum (UA) - h_c A_t) + h_c A_t} \right) (1 - e^{-at}) + T_{cro} e^{-at} \tag{15.34}$$

The PV module's efficiency

$$\eta_m = \tau_g \beta_c \eta_c \tag{15.35}$$

Electrical energy

$$\dot{E} = \eta_m A_m I(t) \quad (15.36)$$

Thermal energy

$$\dot{Q}_{th} = \dot{M}_f C_f (T_r - T_a) \quad (15.37)$$

Thermal exergy N-PVT air collector

$$\dot{Q}_{th,ex} = \dot{M}_f C_f (T_r - T_a) - \dot{M}_f C_f (T_a + 273) \ln((T_{f0N} + 273)/(T_a + 273)) \quad (15.38)$$

Overall (equivalent) exergy

$$\dot{Q}_{eq,ex} = \dot{Q}_{th,ex} + \dot{E} \quad (15.39)$$

Overall (equivalent) thermal energy gain

$$\dot{Q}_{eq,th} = \dot{Q}_{th} + (\dot{E}/0.38) \quad (15.40)$$

Thermal efficiency

$$\eta_{th} = (\dot{M}_f C_f (T_r - T_a)) / (A_m I_t + A_c I_t) \quad (15.41)$$

Overall (equivalent) thermal efficiency

$$\eta_{eq,th} = \eta_{th} + \frac{\eta_c}{0.38} \quad (15.42)$$

Thermal exergy efficiency

$$\eta_{th,ex} = (\dot{Q}_{th,ex}) / \left( (A_m I_t + A_c I_t) \left( 1 - \left( \frac{4}{3} \right) \frac{(T_a + 273)}{6000} + \left( \frac{1}{3} \right) \left( \frac{T_a + 273}{6000} \right)^4 \right) \right) \quad (15.43)$$

Overall exergy efficiency of the system

$$\eta_{eq,ex} = \eta_c + \eta_{th,ex} \quad (15.44)$$

Values of constants in Appendix I and Appendix II are used in the above thermal modeling.

### 15.3.2 Embodied Energy (EmE)

EmE energy is defined as the total energy required for making a system [9].



### 15.3.3 Energy Payback Time (EPBT)

EPBT is the time taken to recover the investment [9, 19].

$$\text{EPBT} = \frac{\text{Embodied Energy } (E_{\text{in}}, \text{ kWh})}{\text{Annual Energy Output } (E_{\text{out}}, \text{ kWh/y})} \quad (15.45)$$

### 15.3.4 CO<sub>2</sub> Emission

The average carbon dioxide (CO<sub>2</sub>) emission in environment from thermal power plant for generation of electricity from coal is nearly 0.98 kg/kWh at the source [9, 44].

$$\text{CO}_2\text{emission per year} = \frac{E_{\text{in}}}{L} \times \frac{1}{1 - L_a} \times \frac{1}{1 - L_t} \times 0.98 \text{ kg} \quad (15.46)$$

where  $E_{\text{in}}$ ,  $L$ ,  $L_a$ , and  $L_t$  show EmE, life of system, transmission losses, and  $L_a$  = domestic appliances losses.

After considering  $L_t = 0.40$  and  $L_a = 0.20$ , then Eq. (15.46) may be written as follows:

$$\text{CO}_2\text{emission per year} = \frac{E_{\text{in}}}{L} \times \frac{1}{1 - 0.20} \times \frac{1}{1 - 0.40} \times 0.98 \text{ kg} = \frac{E_{\text{in}}}{L} \times 2.042 \quad (15.47)$$

### 15.3.5 CO<sub>2</sub> Mitigation (Net)

The difference of total CO<sub>2</sub> saved and total CO<sub>2</sub> emitted for whole life of system is known as net CO<sub>2</sub> mitigation.

CO<sub>2</sub> mitigation (Net) = total CO<sub>2</sub> mitigation – total CO<sub>2</sub> emission

$$= (E_{\text{aout}} \times L - E_{\text{in}}) \times \frac{1}{1 - L_a} \times \frac{1}{1 - L_t} \times 0.98 \text{ kg} = (E_{\text{aout}} \times L - E_{\text{in}}) \times 2.04 \text{ kg} \quad (15.48)$$

where  $L$  and  $E_{\text{aout}}$  represent life of system (30 years) and yearly energy output (kWh/y) [19].

### 15.3.6 Carbon Credit Earned (CCE)

The CCE of present system may be calculated as follows [9, 19].

$$CCE = \text{Net CO}_2\text{mitigation(in t)} \times 10 \text{ US\$/t} \tag{15.49}$$

## 15.4 Result and Discussion

The hourly change of solar radiation (beam ( $I_t$ ) and diffuse ( $I_d$ )) along ambient air temperature ( $T_a$ ) with respect to time for a typical clear day of March month has been shown in Fig. 15.3. Figure 15.4 represents hourly variation of solar cell temperature ( $T_c$ ) and solar cell efficiency ( $\eta_c$ ) for different PV technologies with respect to time. The shape of graph for all PV technologies is almost the same with different values, i.e., as the temperature of solar cell efficiency increases, its electrical efficiency reduces. The figure also reveals that maximum temperature goes in a-Si and minimum in c-Si, so electrical efficiency points of view for c-Si and a-Si are best and worst, respectively. Figure 15.5 shows the hourly variation of overall thermal efficiency ( $\eta_{ov,th}$ ) and overall exergy efficiency ( $\eta_{ov,ex}$ ) for different PV technology with respect to time. The sequence of average energy and exergy efficiency for the system is found to be c-Si (48.70%, 24.08%) > p-Si (46.46%, 23.24%) > CIGS (36.60%, 19.39%) > CdTe (34.62%, 18.64%), and a-Si (29.41%, 16.67%).

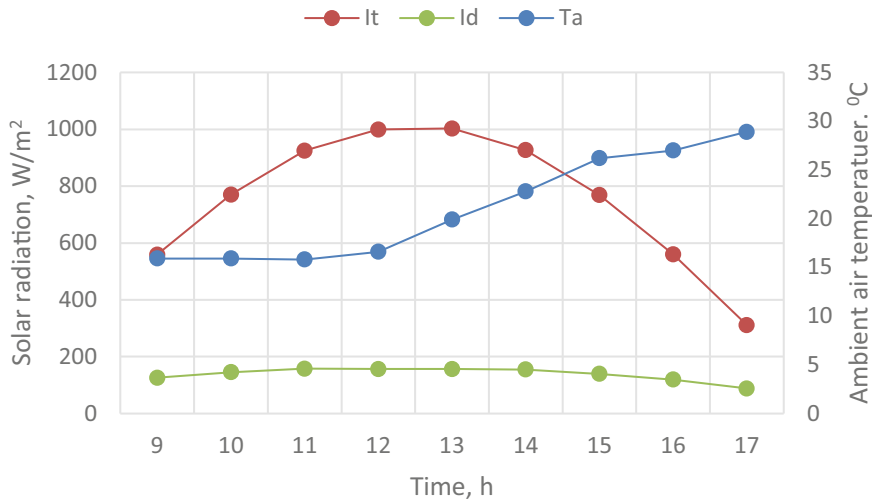


**Fig. 15.3** Hourly variation of beam radiation ( $I_t$ ), diffuse radiation ( $I_d$ ), and ambient air temperature ( $T_a$ ) with respect to time for a typical clear day of March month. *Source* Author

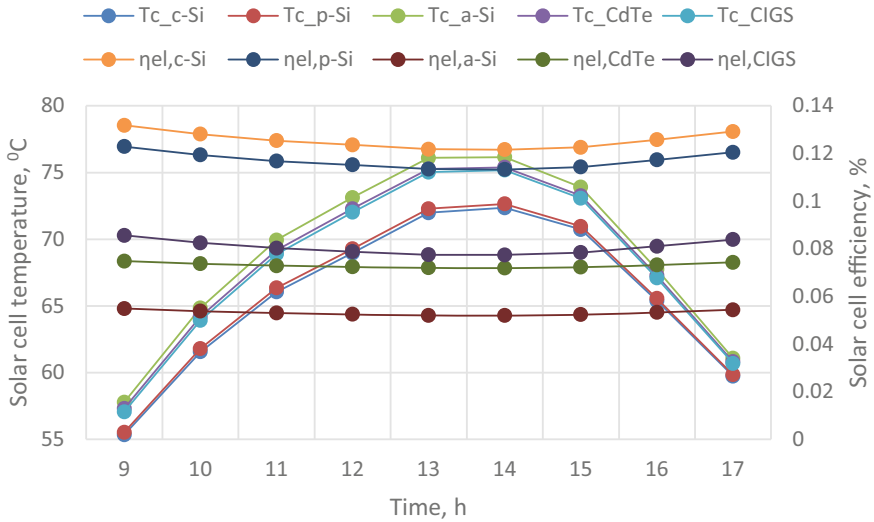


**Fig. 15.4** Hourly variation of solar cell temperature ( $T_c$ ) and solar cell efficiency ( $\eta_c$ ) for different PV technology with respect to time for a typical clear day of March month. *Source* Author

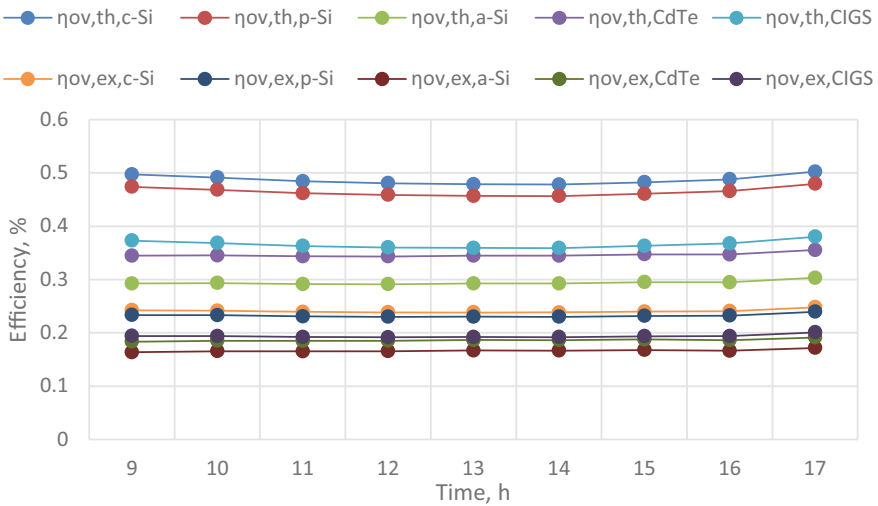


**Fig. 15.5** Hourly variation of overall thermal efficiency ( $\eta_{ov,th}$ ) and overall exergy efficiency ( $\eta_{ov,ex}$ ) for different PV technology with respect to time for a typical clear day of March month. *Source* Author

When the energy graph is fitted with polynomial equation of order two, then it can be clear that the effect of temperature on overall thermal efficiency ( $\eta_{ov,th}$ ) is maximum in the case of c-Si and minimum in the case of a-Si and CdTe. This shows that a-Si and CdTe are more stable thermally comparative to other technologies.

Figures 15.6 and 15.7 show hourly variation of ambient temperature and average solar intensity with respect to time for different month. Figures 15.8, 15.9, 15.10, 15.11, and 15.12 showing monthly variation of (a) TE and (b) EE from c-Si, p-Si, a-Si, CdTe, CIGS, PVT air collector-integrated greenhouse dryer for all weather conditions, respectively. The TE and EE for c-Si PVTAC drying system in Fig. 15.8

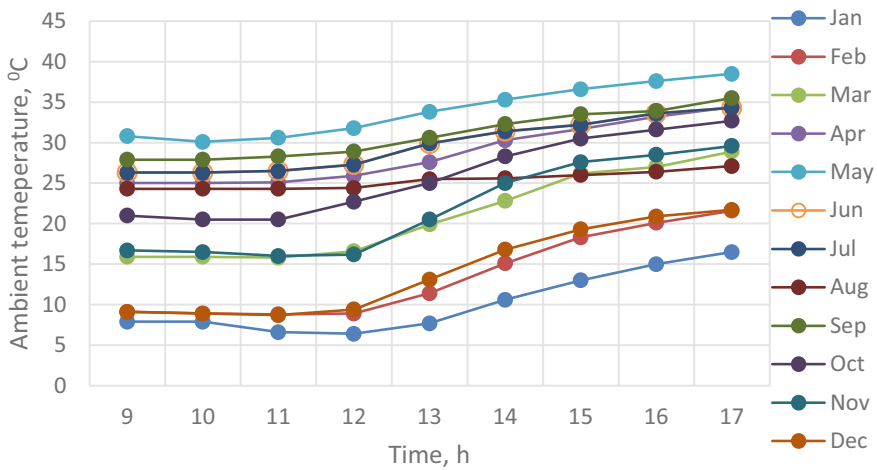


Fig. 15.6 Hourly variation of ambient temperature [19]

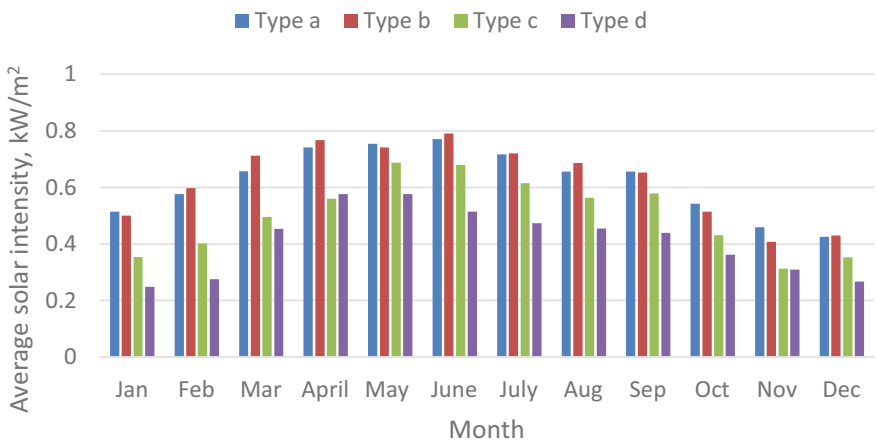
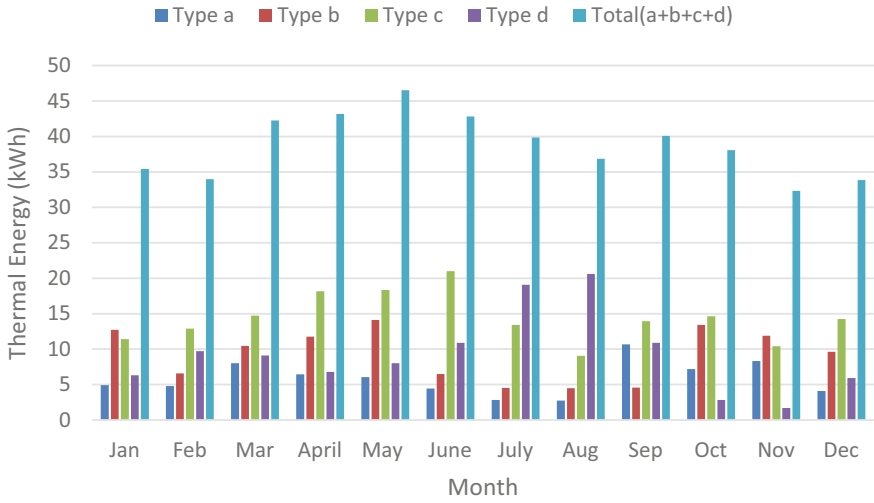
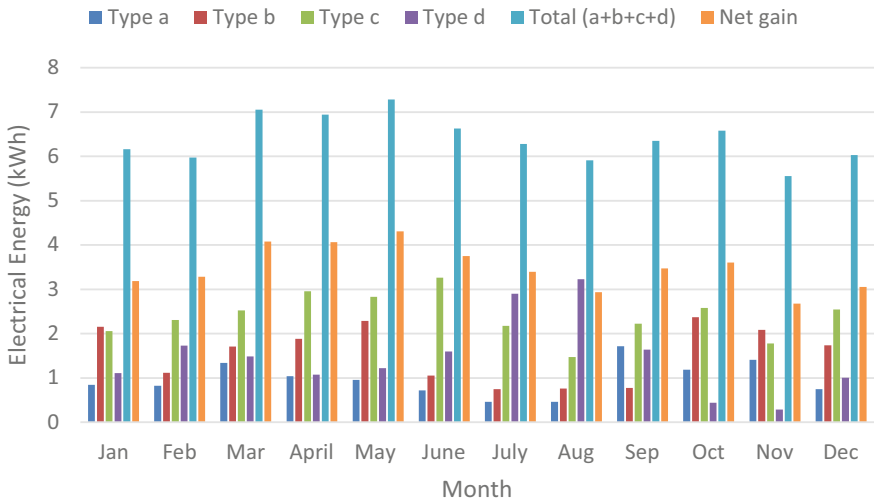


Fig. 15.7 Monthly variation of average solar intensity [19]

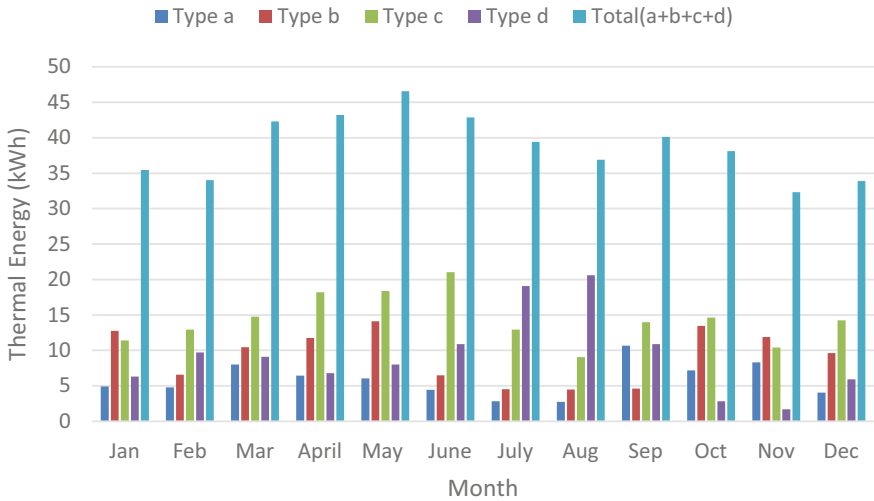


(a)

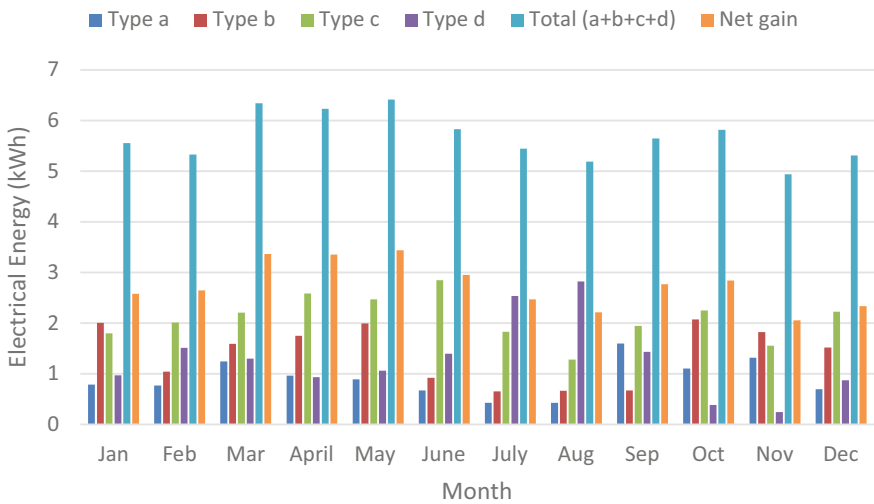


(b)

**Fig. 15.8** Monthly variation of **a** TE and **b** EE from c-Si-PVT air collector-integrated dryer. *Source* Author)



(a)

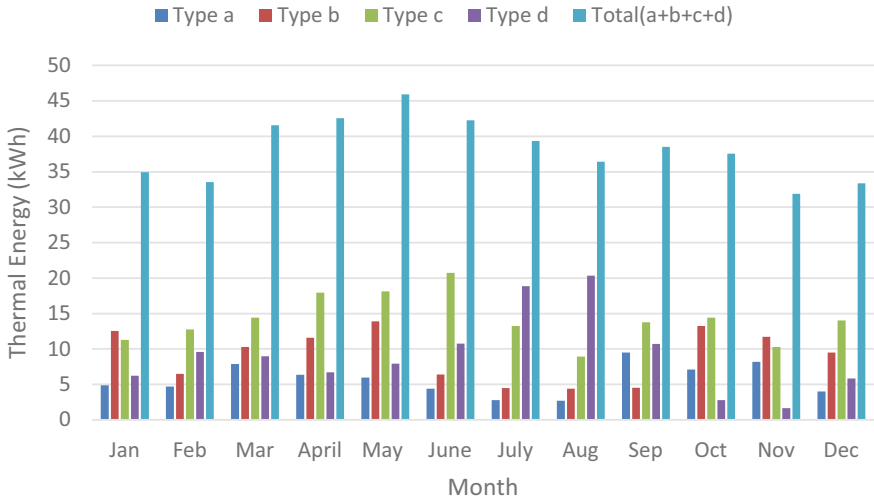


(b)

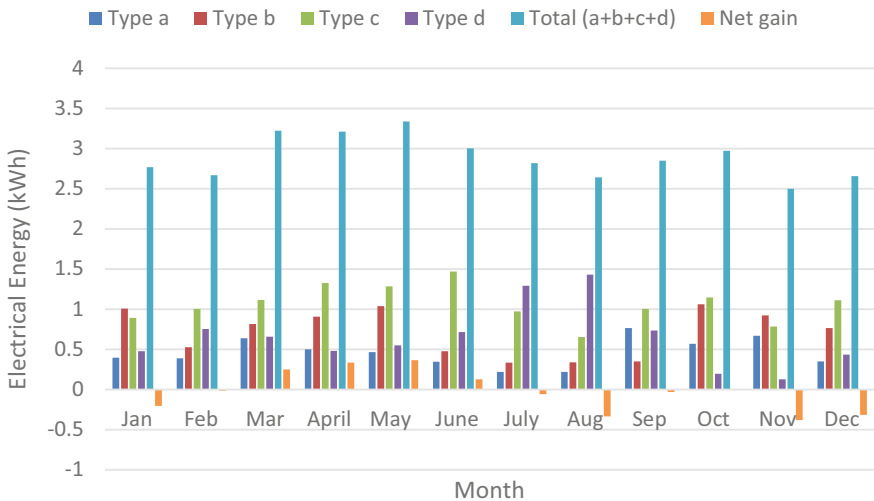
**Fig. 15.9** Monthly variation of **a** TE and **b** EE from p-Si-PVT air collector-integrated dryer. *Source* Author

are found to be for Type a (70.55, 11.68), Type b (110.62, 18.66), Type c (172.27, 28.71) and Type d (111.81, 17.70), respectively, in kWh/year.

The TE and EE for p-Si PVTAC drying system shown in Fig. 15.9 are found to be for Type a (70.59, 10.89), Type b (110.74, 16.70), Type c (172.02, 25.01), and Type d (111.94, 15.47) weather conditions, respectively, in kWh/year.



(a)



(b)

**Fig. 15.10** Monthly variation of **a** TE and **b** EE from a-Si-PVT air collector-integrated dryer.  
 Source Author

The TE and EE for a-Si PVTAC drying system in Fig. 15.10 are found to be for Type a (68.48, 5.52), Type b (109.04, 8.54), Type c (169.91, 12.76), and Type d (110.44, 7.84), respectively, in kWh/year.

In Fig. 15.11, the TE and EE for CdTe PVTAC drying system are found to be for Type a (69.34, 7.69), Type b (108.85, 11.75), Type c (169.74, 17.50), and Type d

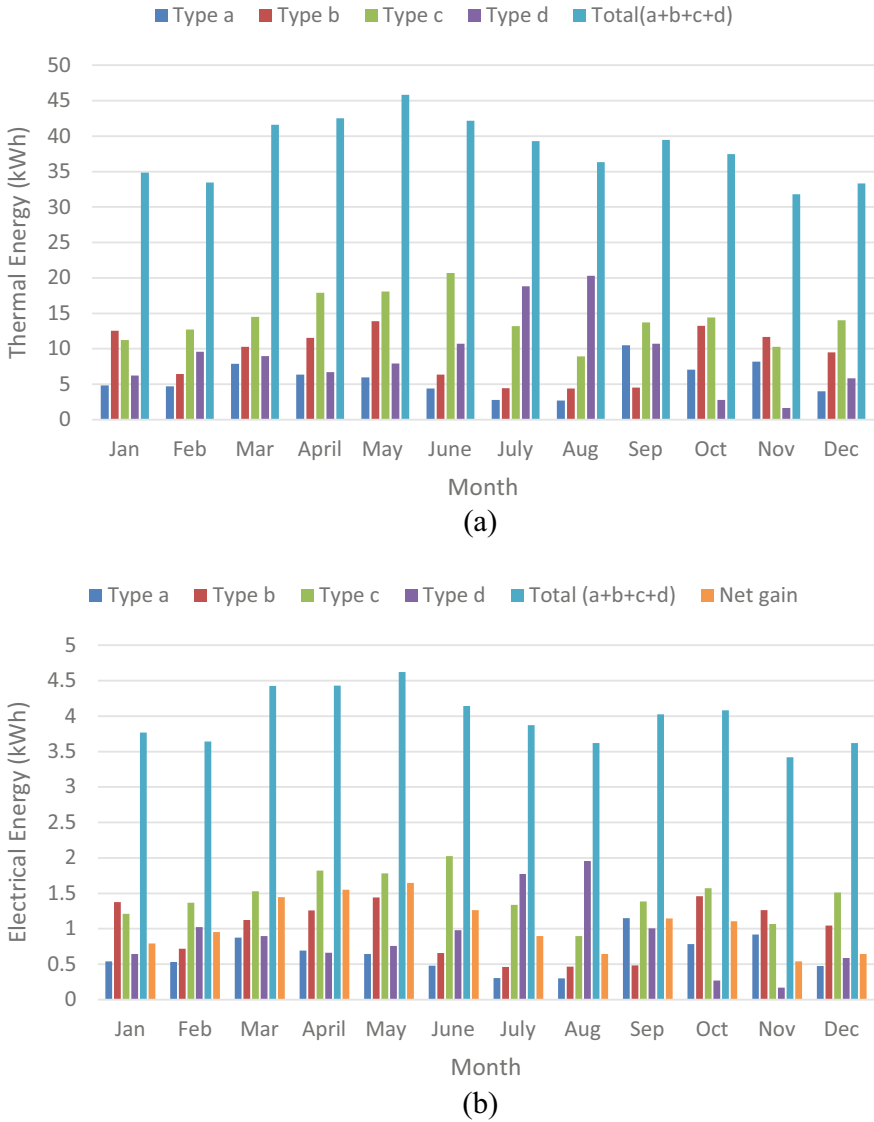
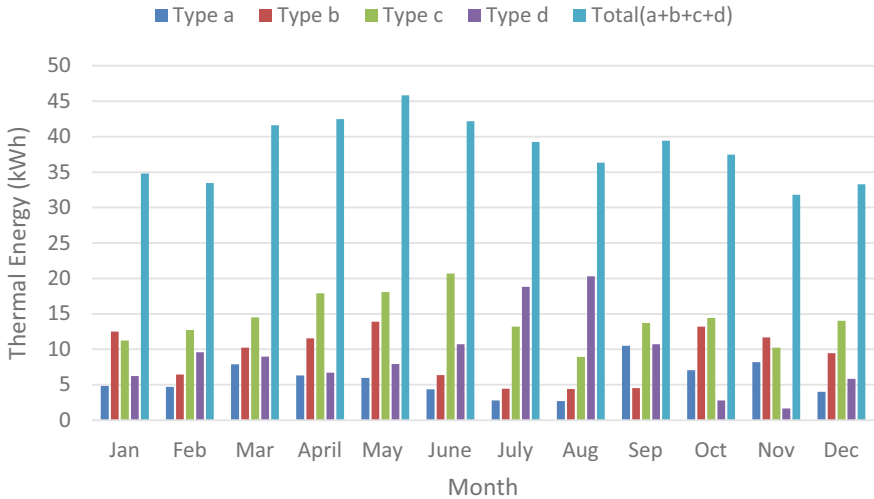


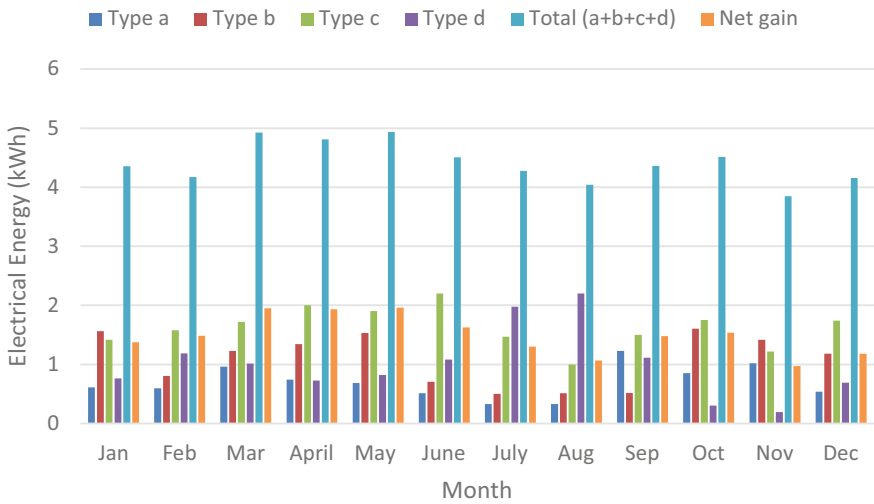
**Fig. 15.11** Monthly variation of **a** TE and **b** EE from CdTe-PVT air collector-integrated dryer. Source Author

(110.27, 10.73), respectively, in kWh/year. In Fig. 15.12, the TE and EE for CIGS PVTAC drying system are found to be for Type a (69.30, 8.41), Type b (108.78, 12.91), Type c (169.62, 19.50), and Type d (110.19, 12.07), respectively, in kWh/year.





(a)



(b)

**Fig. 15.12** Monthly variation of **a** TE and **b** EE from CIGS-PVT air collector-integrated dryer. Source Author

Figure 15.13 shows variation in TE and EE given by system in the complete year. The values show that a-Si PVTAC drying system has negative electricity value which means a-Si technology is not enough for operating the 12 W DC fan with 25% covered area. Even though research shows fan works at lesser wattage with lower

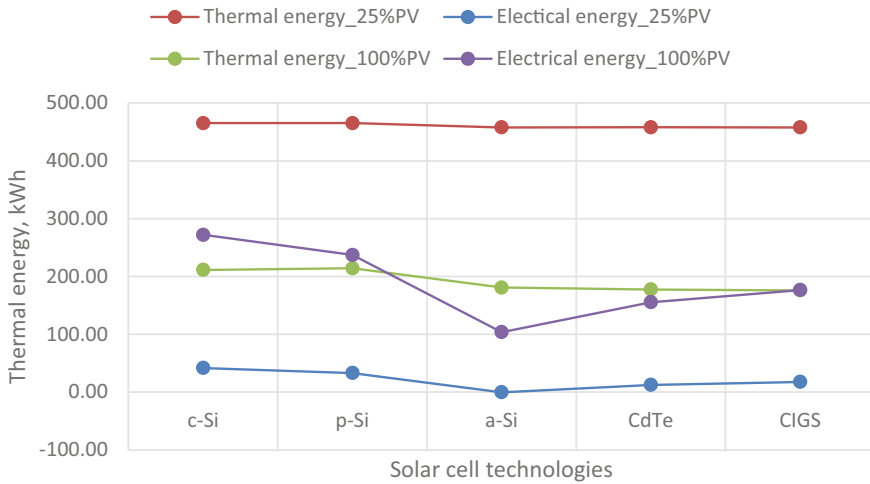


**Fig. 15.13** TE and EE given by the system in a year *Source* Author

speed, it is seen that 100% PV module on dryer is capable of providing sufficient EE to run 30 W DC fan and 10 W CFL for 10 h/day/year (Fig. 15.14).

The environmental feasibility can be checked by calculating CO<sub>2</sub> emission and mitigation and CCE. The EmE required for solar dryer (except PV) is included in Table 15.1. The properties of different PV technologies are listed in Table 15.2. Through OTE gain, EPBT and EmE for 100% and 25% PV area are listed in Tables 15.3, 15.4, 15.5, and 15.6.

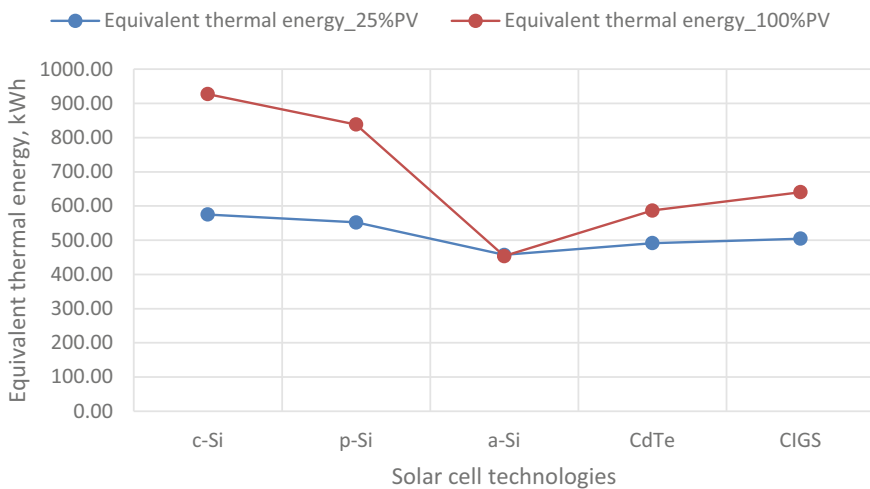


**Fig. 15.14** OTE given by the system in a year. *Source* Author

**Table 15.1** EmE for PVTEC with solar dryer [27]

S. No.	Material	Quantity (kg)	EmE (kWh/kg)	Total EmE (kWh)
1	Glass	14	7.28	101.92
2	Steel	10	8.89	88.90
3	Paint	1	25.11	25.11
4	Rubber gasket and polyethylene sheet	1	25.64	25.64
5	Fittings (Nut bolt with washer, steel screws and rivets etc.)	1	8.89	8.89
6	Aluminum sheet	10	55.28	552.80
7	Wool material	20	2.89	57.80
8	Wire mesh tray	1.3	9.67	25.14
9	Exhaust fan (DC)			
	(a) Aluminum	0.39	55.28	21.56
	(b) Iron	0.22	8.89	1.95
	(c) Plastic	0.12	19.44	2.33
	(d) Copper wire	0.050	19.61	0.98
Total EE				913.02

From Tables 15.3 and 15.4, it is clear that EmE and EPBT are found to be least and maximum for CIGS and c-Si. If PV area increases from 25% to 100%, the EPBT increased for p-Si, a-Si c-Si, and CdTe by 17.76%, 39.69%, 21.17%, and 22%, respectively, with 14.58% reduction for CIGS. For large system, CIGS is advisable not only due to least embodied energy, EPBT but also both reduce as PV area or setup area increases. Tables 15.5 and 15.6 show calculation for CO<sub>2</sub> emission, net CO<sub>2</sub> mitigation, and CCE for 25% and 100% PV area of system. Calculation shows that after increasing the PV area from 25% to 100%, the carbon credit increased for c-Si, p-Si, CdTe, and CIGS by 58.34%, 49.67%, 16.87%, and 28.13%, respectively, and decreased for a-Si by 3.98%. This shows a-Si is the worst technology of hybrid system till date and c-Si is best in terms of CCE. Though CCE is maximum for c-Si PV technology, i.e., \$325.06 and \$514.70 for 25% and 100% PV area of total PVTAC, but carbon emission in production of CIGS is least.

## 15.5 Conclusions

- The results showed that a-Si and CdTe are more stable thermally comparative to other technologies.
- EPBT is found best in the case of CIGS.

**Table 15.2** Specifications of various SCTs [19, 27]

PV technologies	Module efficiency, $\eta_0$ (%)	Expected life (y)	Specific energy content ( $\text{kWhm}^{-2}$ )	$E_{in}$ for 0.358 $\text{m}^2$ ( $\text{kWh}$ for 30 y)	$E_{in}$ for 1.431 $\text{m}^2$ ( $\text{kWh}$ for 30 y)	Temperature coefficient $\beta_{ref}$ ( $^{\circ}\text{C}^{-1}$ )	Packing factor	Absorptivity
c-Si	16	30	1189.5	425.84	1702.17	0.0040	0.89	0.9
p-Si	14	30	910	325.78	1302.21	0.0040	0.89	0.9
a-Si	6	20	378	135.32	540.92	0.0026	1	0.85
CdTe	8	15	266	190.45	761.29	0.0020	1.	0.8
CIGS	10	10	24.5	26.313	105.18	0.0045	1	0.8

**Table 15.3** Total EmE and EPBT for solar dryer integrated with SCTs (25% PV area of total PCPVTAC) (Source Author)

Different PV	$E_{in}$ for 0.358 m <sup>2</sup> module (kWh for 30 y)	EmE for different parts of greenhouse	Total EmE for system ( $E_{in}$ , kWh)	Energy out from the system ( $E_{out}$ , kWh)	EPBT (y)
c-Si	425.84	913.02	1338.86	575.26	2.33
p-Si	325.78	913.02	1238.80	552.18	2.24
a-Si	135.32	913.02	1048.34	457.14	2.29
CdTe	190.45	913.02	1103.48	491.46	2.25
CIGS	26.31	913.02	939.33	504.86	1.86

**Table 15.4** Total embodied energy and EPBT for solar dryer integrated with various SCTs (100% PV area of total PCPVTAC) (source Author)

PV Technologies	$E_{in}$ for 1.431 m <sup>2</sup> module (kWh for 30 y)	EmE for different parts of greenhouse	Total EmE for system ( $E_{in}$ , kWh)	Energy out from the system ( $E_{out}$ , kWh)	EPBT (y)
c-Si	1702.17	913.02	2615.19	927.36	2.82
p-Si	1302.21	913.02	2215.23	838.50	2.64
a-Si	540.92	913.02	1453.94	453.86	3.20
CdTe	761.29	913.02	1674.31	587.18	2.85
CIGS	105.18	913.02	1018.20	640.68	1.59

**Table 15.5** CO<sub>2</sub> emission, net CO<sub>2</sub> mitigation, and CCE for system with diverse SCTs (25% PV area of total PCPVTAC) (source Author)

PV Technologies	c-Si	p-Si	a-Si	CdTe	CIGS
CO <sub>2</sub> emission (In kg)	91.13	84.32	71.36	75.11	63.94
Net CO <sub>2</sub> mitigation (In t)	32.51	31.30	25.86	27.85	29.01
CCE (In \$)	325.06	312.97	258.64	278.54	290.09

**Table 15.6** CO<sub>2</sub> emission, net CO<sub>2</sub> mitigation, and CCE for system with diverse SCTs (100% PV area of total PCPVTAC) (source Author)

PV Technologies	c-Si	p-Si	a-Si	CdTe	CIGS
CO <sub>2</sub> emission (In kg)	178.01	150.78	98.96	113.96	69.31
Net CO <sub>2</sub> mitigation (In t)	51.47	46.84	24.83	32.55	37.17
CCE (In \$)	514.70	468.43	248.35	325.52	371.69

- Results showed that a-Si is the worst technology of hybrid system till date and c-Si is the best technology in terms of CCE.

Present paper reveals very important outcomes especially related to hybrid thermal systems. Thermal analysis of system showed CIGS PV-integrated system has less embodied energy and payback time comparative to other technologies which may encourage scientist and engineers to give more attention to CIGS PV technology. Results also showed CIGS is the only technology for hybrid system in which after increasing the area, payback period decreased which encourages its uses in large hybrid systems. It is very interesting, though, CCE is maximum for c-Si PV technology, i.e., \$325.06 and \$514.70 for 25% and 100% PV area of total PVTAC but carbon emission in production of CIGS is least which is important in making the environment healthier.

## Appendix I

Formulae used to compute various heat transfer coefficient are as follows:

$A_{cf} = (\pi/4) \times d^2$	$v_2 = \dot{M}_f / (\rho \times A_{cf})$
$v_1 = ((\pi/4) \times d^2 \times v_2) / A_{c1}$	$v_3 = ((\pi/4) \times d^2 \times v_2) / A_t$
$h_i = 2.8 + 3v_1$	$h_o = 5.7 + 3.8v$
$h_{crr} = h_{crc} + h_{crew}$	$h_{erc} = 2.8 + 3v_3$
$h_{crew} = \frac{0.01667h_{erc}(P_{Tcr} - \gamma P_{Tr})}{T_{cr} - T_r}$	$P_{Tcr} = \exp(25.317 - (5144/(273 + T_{cr})))U_{bpa} = 1/((L_p/K_p) + (1/h_i))$
$P_{Tr} = \exp(25.317 - (5144/(273 + T_r)))$	$U_{bcf} = 1/((L_g/K_g) + (1/h_i))$
$U_{tca} = 1/((L_g/K_g) + (1/h_o))$	$U_{wra} = 1/((L_g/K_g) + (1/h_o))$
$UA = A_w U_{wra}$	

## Appendix II

Various design parameters taken for the calculation of different temperatures

$\alpha_c = 0.85$	$\tau_g = 0.9$	$\beta_c = 0.83$
$\eta_o = 0.15$	$\alpha_{cr} = 0.4$	$M_{cr} = 2 \text{ kg}$
$C_{cr} = 3900 \text{ J/kg K}$	$\gamma = 0.4$	$v = 2 \text{ m/s}$
$A_m = 0.358 \text{ m}^2$	$A_w = 0.390 \text{ m}^2$	$A_c = 1.073 \text{ m}^2$
$C_f = 1005 \text{ J/kg K}$	$K_g = 1.1 \text{ W/mK}$	$d = 0.01 \text{ m}$

(continued)

(continued)

$L_g = 0.003 \text{ m}$	$L_p = 0.002 \text{ m}$	$K_p = 0.8 \text{ W/mK}$
$\rho = 1.17 \text{ kg/m}^3$	$T_0 = 25 \text{ }^\circ\text{C}$	$A_t = 0.169 \text{ m}^2$

## References

1. Adnane L, Noureddine M, Kamel A, Adel B (2016) Solar drying of henna (*Lawsonia inermis*) using different models of solar flat plate collectors: an experimental investigation in the region of Biskra (Algeria). *J Clean Prod* 112:2545–2552
2. Akbulut A, Durmus A (2010) Energy and exergy analyses of thin layer drying of mulberry in a forced solar dryer. *Energy* 35:1754–1763
3. Anyanwu CN, Okonkwo WI (2006) Experimental determination of the drying rate constant of chilly yellow pepper. In: *Proceedings of National Solar Energy Forum*, Nnamdi Azikiwe University Awka
4. Azaizia Z, Kooli S, Elkhadraoui A, Hamdi I, Guizani A (2017) Investigation of a new solar greenhouse drying system for peppers. *Int J Hydrogen Energy*. <https://doi.org/10.1016/j.ijhydene.2016.11.180>
5. Barnwal P, Tiwari GN (2008) Grape drying by using hybrid photovoltaic-thermal (PV/T) greenhouse dryer: an experimental study. *Sol Energy* 82:1131–1144
6. Browne MC, Norton Brian, McCormack Sarah J (2016) Heat retention of a photovoltaic/thermal collector with PCM. *Solar Energy* 133:533–548
7. Castillo-Téllez M, Pilatowsky-Figueroa I, López-Vidaña EC, Sarracino-Martínez O, Hernández-Galvez G (2017) Dehydration of the red chilli (*Capsicum annum* L., costeño) using an indirect-type forced convection solar dryer. *Appl Thermal Eng* 114:1137–1144
8. Condorí M, Condorí G, Echazú R, Altobelli F (2017) Semi-industrial drying of vegetables using an array of large solar air collectors. *Energy Sustain Dev* 37:1–9
9. Crawford RH, Treloar GJ, Fuller RJ, Bazilian M (2006) Life-cycle energy analysis of building integrated photovoltaic systems (BIPVs) with heat recovery unit. *Renew Sust Energy Rev* 10(6):559–575
10. Dorouzi M, Morteza pour H, Akhavan H-R, Moghaddam AG (2018) Tomato slices drying in a liquid desiccant-assisted solar dryer coupled with a photovoltaic-thermal regeneration system. *Sol Energy* 162:364–371
11. Evans DL (1981) Simplified method for predicting PV array output. *Sol Energy* 27:555–560
12. Fterich M, Chouikhi H, Bentaher H, Maalej A (2018) Experimental parametric study of a mixed-mode forced convection solar dryer equipped with a PV/T air collector. *Sol Energy* 171:751–760
13. Hussain CMI, Norton B, Duffy A (2017) Technological assessment of different solar-biomass systems for hybrid power generation in Europe. *Renew Sustain Energy Rev* 68:1115–1129
14. Kabeel AE, Abdelgaied M (2016) Performance of novel solar dryer. *Process Saf Environ Prot* 102:183–189
15. Kalogirou SA (2004) Solar thermal collectors and applications. *Prog Energy Combust Sci* 30:231–295
16. Kumar M, Sahdev RK, Tiwari S, Panchal H, Manchanda H (2019) Experimental free convection thin layer groundnut greenhouse drying. *Agric Eng Int CIGR J* 21(3):203–211
17. Lamnatou C, Papanicolaou E, Belessiotis V, Kyriakis N (2012) Experimental investigation and thermodynamic performance analysis of a solar dryer using an evacuated-tube air collector. *Appl Energy* 94:232–243

18. Mghazli S, v M, Hidar N, Lahnine L, Idlimam A, Mahrouz M (2017) Drying characteristics and kinetics solar drying of moroccan rosemary leaves. *Renew Energy*. <https://doi.org/10.1016/j.renene.2017.02.022>
19. Mishra RK, Tiwari GN (2013) Energy matrices analyses of hybrid photovoltaic thermal (HPVT) water collector with different PV technology. *Sol Energy* 91:161–173
20. Muthukarupan KS, Eashwar SS, Subramanian V, Tiwari S, Singh DB (2020) Performance improvement of PVT module with applications of nano-fluids and phase change materials: a review. In: *International conference on electrical and electronics engineering (ICEEE) 2020*
21. Odeh N, Grassie T, Henderson D, Muneer T (2006) Modelling of flow rate in a photovoltaic-driven roof slate-based solar ventilation air preheating system. *Energy Convers Manage* 47:909–925
22. Pawar RS, Takwale MG, Bhide VG (1995) Solar drying of custard powder. *Energy Convers Manage* 36:1085–1096
23. Parsa SM, Rahbar A, Davoud Javadi Y, Koleini MH, Afrand M, Amidpour M (2020) Energy-matrices, exergy, economic, environmental, exergoeconomic, enviroeconomic, and heat transfer (6E/HT) analysis of two passive/active solar still water desalination nearly 4000 m: Altitude concept. *J Cleaner Prod* 261:121243
24. Saeedi F, Sarhaddi F, Behzadmehr A (2015) Optimization of a PV/T (photovoltaic/thermal) active solar still. *Energy* 87:142–152
25. Sahota L, Shyam, Tiwari GN (2017) Energy matrices, enviroeconomic and exergoeconomic analysis of passive double slope solar still with water based nanofluids. *Desalination* 409:66–79
26. Saini V, Tiwari S, Tiwari GN (2017) Environ economic analysis of various types of photovoltaic technologies integrated with greenhouse solar drying system. *J Cleaner Prod* 156:30–40
27. Saini V, Tiwari S, Jain VK, Tiwari GN (2020) Performance evaluation of different types PV materials for PVTAC with solar drying system. *Mater Today Proc* 25(4):544–550
28. Sami S, Rahimi A, Etesami N (2011) Dynamic modeling and a parametric study of an indirect solar cabinet dryer. *Dry Technol* 29:825–835
29. Scanlin D, Renner M, Domermuth D, Moody H (1997) The design, construction and use of an indirect, through – pass solar food dryer. *Home Power* 57:62–72
30. Singh AK, Samsher (2020) Material conscious energy matrix and enviro-economic analysis of passive ETC solar still. *Mater Today Proc*
31. Singh DB, Tiwari GN (2016) Effect of energy matrices on life cycle cost analysis of partially covered photovoltaic compound parabolic concentrator collector active solar distillation system. *Desalination* 397:75–91
32. Singh DB, Raturi A, Kumar N, Nirala A, Singh AK, Tiwari S (2020a) Effect of flow of fluid mass per unit time on life cycle conversion efficiency of single slope solar desalination unit coupled with N identical evacuated tubular collectors. *Mater Today Proc* 28(4):2096–2100
33. Singh DB, Bansal G, Yadav JK, Kumar N, Tiwari S, Raturi A (2020) Exergoeconomic and enviroeconomic analyses of single slope solar desalination unit loaded with/without nanofluid: a comprehensive review. *MS&E* 748(1):012031
34. Singh DB, Bansal G, Yadav JK, Kumar N, Tiwari S, Raturi A (2020) Exergoeconomic and enviroeconomic analyses of single slope solar desalination unit loaded with/without nanofluid: A comprehensive review. *Mater Sci Eng* 748:012031
35. Song H, Starfelt F, Daianova L, Yan J (2012) Influence of drying process on the biomass-based polygeneration system of bioethanol, power and heat. *Appl Energy* 90:32–37
36. Tiwari S, Tiwari GN, Al-Helal IM (2016) Performance analysis of photovoltaic–thermal (PVT) mixed mode greenhouse solar dryer. *Sol Energy* 133:421–428
37. Tiwari S, Tiwari GN (2016) Thermal analysis of photovoltaic-thermal (PVT) single slope roof integrated greenhouse solar dryer. *Sol Energy* 138:128–136
38. Tiwari S, Tiwari GN (2016b) Exergoeconomic analysis of photovoltaic-thermal (PVT) mixed mode greenhouse solar dryer. *Energy* 114:155–164
39. Tiwari S, Tiwari GN, Al-Helal IM (2016) Development and recent trends in greenhouse dryer: a review. *Renew Sustain Energy Rev* 65:1048–1064



40. Tiwari S (2020a) ANN and mathematical modelling for moisture evaporation with thermal modelling of bitter gourd flakes drying in SPVT solar dryer. *Heat Mass Transfer*
41. Tiwari S, Srivastava AK, Sahu R (2020b) 2nd international conference on computational and experimental methods in mechanical engineering. *Mater Today Proc* 25(4): 537–960
42. Tiwari S, Tiwari P, Sahdev RK, Dwivedi VK (2020c) Environmental feasibility of PVT drying system. In: 2020 International conference on electrical and electronics engineering (ICE3), Gorakhpur, India, pp 773–777. <https://doi.org/10.1109/ICE348803.2020.9122886>
43. Tiwari S, Tiwari P, Singh SN (2020d) Study to improve the efficiency of c-Si material in photovoltaic power plant. *Mater Today Proc* 25:691–694
44. Watt M, Jhonson A, Ellis M, Quthred N (1998) Life cycle air emission from PV power systems. *Prog Photovoltaic Res Appl* 6(2):127–136
45. Whitefield D (2000) Solar dryer systems and the Internet: important resources to improve food preparation. In: conference paper: international conference on solar cooking, Kimberly, South Africa
46. Wong LT, Chow WK (2001) Solar radiation model. *Appl Energy* 69:191–224

# Chapter 17

## Impact of the Photovoltaic Integration on the Hydrothermal Dispatch on Power Systems



Walter A. Carranza, Wilfredo C. Flores, Harold R. Chamorro, Margarita M. Diaz-Casas, Roozbeh Torkzadeh, Francisco Gonzalez-Longatt, Wilfredo Sifuentes, Vijay K. Sood, and Wilmar Martinez

### 17.1 Introduction

The significant inclusion of non-synchronous generation is creating several challenges on the power systems operation [1, 2]. Current electricity markets require innovative solutions to include the non-synchronous generation into the economic

---

W. A. Carranza · W. C. Flores  
Universidad Tecnológica Centroamericana, Tegucigalpa, Honduras  
e-mail: [walter.carranza@unitec.edu.hn](mailto:walter.carranza@unitec.edu.hn)

W. C. Flores  
e-mail: [wilfredo.flores@unitec.edu.hn](mailto:wilfredo.flores@unitec.edu.hn)

H. R. Chamorro (✉)  
KU Leuven, Katholieke Universiteit Leuven, Leuven, Belgium  
e-mail: [hr.chamo@ieee.org](mailto:hr.chamo@ieee.org)

M. M. Diaz-Casas  
Universidad de Buenos Aires, Buenos Aires, Argentina  
e-mail: [margarita.diaz@ieee.org](mailto:margarita.diaz@ieee.org)

R. Torkzadeh  
Eindhoven University of Technology, Eindhoven, The Netherlands

F. Gonzalez-Longatt  
University of South-Eastern Norway, Porsgrunn, Norway  
e-mail: [f.gonzalez-longatt@usn.no](mailto:f.gonzalez-longatt@usn.no)

W. Sifuentes  
Comite de Operacion Economica del Sistema Interconectado Nacional del Peru, COES,  
Lima, Peru  
e-mail: [wsifuentes@gmx.net](mailto:wsifuentes@gmx.net)

V. K. Sood  
Institute of Technology, University of Ontario, Ontario, Canada  
e-mail: [vijay.sood@uoit.ca](mailto:vijay.sood@uoit.ca)

W. Martinez  
Department of Electrical Engineering (ESAT) at KU Leuven, Diepenbeek, Belgium  
e-mail: [wilmar.martinez@kuleuven.be](mailto:wilmar.martinez@kuleuven.be)

© The Author(s), under exclusive license to Springer Nature Singapore Pte Ltd. 2021  
S. N. Singh et al. (eds.), *Fundamentals and Innovations in Solar Energy*,  
Energy Systems in Electrical Engineering,  
[https://doi.org/10.1007/978-981-33-6456-1\\_17](https://doi.org/10.1007/978-981-33-6456-1_17)

dispatch to cope with the integration and minimize the risk in the operation [3]. Since hydroelectrical and thermal power are the most common sources in traditional power generation, research into the impact on the renewable energy sources on them is required [4].

Several authors have formulated the hydrothermal economic dispatch including different factors. For instance, in [5], hydrothermal economic dispatch with significant wind power penetration is formulated. In [6], a method to analyze the amount of operation reserves applied to the Spanish hydrothermal system to determine the impact of the time period in the use of the reserves is presented.

Short-term hydrothermal coordination, unit commitment, and economic load dispatch are studied in [7]. It considers a scheduling horizon period of a week. Hourly generation schedules are obtained for each of both hydro and thermal units. Future cost curves of hydro generation, obtained from long and mid-term models, have been used to optimize the amount of hydro energy to be used during the week. In [8], the impacts on the resulting market dispatch outcomes and assess the economic costs over more extended periods of operation including renewables are investigated.

The economical impact of the load forecasting errors on the daily power system operation including the probability of generating units outages in order to estimate the energy not served due outages is considered in [9]. A reserve dispatch model that outputs hourly scheduled energies and both commodities' prices is studied in [10]. In such kind of model, units of each generation company are simplified into technologies and sub-technologies for faster performance, but still considering intertemporal constraints such as ramps and responding time for reserves, and unit commitment decisions such as start-up and shut-down costs.

An optimization model with adjustable uncertainty budget dispatch model is built for hybrid power system to achieve coordination between reliability and economy including renewables in [11]. A combination of wind power, photovoltaic power, hydropower and pumped storage power to form a complementary generation system is presented in [12]. The study proposes two-optimal scheduling models of multi-energy power generation. The first model aims to minimize the cost of thermal units; the second model aims to minimize the fluctuation of the complementary generation system.

A hydro and thermal power generation to support secure and economical wind power integration coordination is presented in [13]. Several reserves, including an online generation reserve, a ramping reserve and a transmission capacity reserve, are identified and considered in such model to counteract the variability and uncertainty inherent in wind power [13].

Then, study in [14] presents an optimisation strategy for solving coordinated economic dispatch problem with wind hydrothermal complex power source structure. The wind hydrothermal coordinated dispatch aims to minimize the total fuel costs of coal-fired thermal power units while satisfying operating constraints. Authors in [15] study the incorporation of the wind and solar power and pumped hydro energy storage into the dispatch and do the reserve cost and penalty cost of over and under estimation of renewable energy sources and power ramp rate constraints of co-generation units and thermal generators. In [16], it is addressed how well the

solar power and hydropower could be coordinated in power system operation based on a multi-scenario dispatch model considering the uncertainty of water inflow and solar irradiation coordination.

In [17], the economic dispatch model considering risk indices of spinning reserve and interruptible load regarded as a spinning reserve to improve the system economy is formulated. The solar units are incorporated in economic dispatch problems in order to minimize the overall generating cost of electric power in [18]. Another example of combined emission economic dispatch model for a solar photovoltaic (PV) integrated power system with multiple solar and thermal generating plants is presented in [19]. A real-time economic dispatch which incorporates the variability cost in the optimization using sequential and dynamic models is proposed in [20]. The impact of non-dispatchable power plants is analyzed in Belitung System in [21], where it concluded that the economic feasibility of existing power plants could be compensated by the delta of system electricity production cost before and after solar PV plants injected into system.

A practical example of the impact of a PV installation on the hydrothermal generation is studied in this document using the Honduras power system case.

The Honduran generation matrix went from being a matrix with the operation of hydroelectric, thermal and biomass power plants until 2010 to a current operation with a significant installed capacity of intermittent renewable sources power plants like wind and photovoltaic solar, both installed and operated in the south of the country [22].

The increase of photovoltaic solar power plants installed is the result of an incentive policy for this type of technology published in the Decree 70-2007 “Law to promote the generation of electricity from renewable sources” and its reform, the Decree 138-2013. The operation of Honduran the electrical system and its operational security is the primary concern as well as the cost decrease in the minimal operation.

The rapid growth of the installed capacity of variable energies requires to adapt the electrical system to avoid a negative impact on its stability and reliability [23]. The aim of this study case is to analyze the energy dispatch prior to incorporate variable sources generation, the current impact of electricity penetration coming from them and develop an optimal hydrothermal dispatch model which allows a lower cost in the horizon proposed for the medium term.

Honduran economy is one of the smallest in Central America. In 2016, the nominal GDP was US 21.5 billion and its population is 9.1 million inhabitants, placing the GDP per capita at US 2.360.

The electricity generation matrix in the Honduran market has a stake of power plants operated by the state company ENEE and other power plants operated by private investors. Actually, the installed capacity is 2602 MW, 38.4% uses fossil fuel sources and the 61.6% remaining renewable resources sources.

Most of the PV solar power plants that currently are operating in Honduras are located in Choluteca and Valle department at the south of the country. The policies in favor of electricity generation using renewable sources were an accelerator for installing this technology. The profit for installing this type of power plants was the

value added of 0.03 USD per kW-h, within the first two years of the Decree's validity or when the installed power reached 300 MW.

The lack of planning a strategy for expanding the electrical network and the type of technologies that could supply the electricity demand and the development of energy efficiency projects in the country is a major challenge for the operative management of the system. It is mentioned in [24] that in Honduras does not exist a long-term energy policy, until now there only has government policies every four years.

At the National Electric System, the hydrothermal dispatch had changed due to the incorporation of electric generation using intermittent sources like photovoltaic solar mainly. The added uncertainty because of the use of this kind of technologies is another challenge for the operation system. Likewise, it is important to have backup power plants which could supply the variable demand; however, the cost could increase. In order to have a suitable resources disposal, it is important to estimate them considering reliable data, new methodologies, systems and information technologies.

At present, the system operator faces a new stage of managing both the demand and the supply of electricity.

The purpose of this document is to determine the optimal hydrothermal dispatch due to the solar power inclusion in the south of Honduras. The situation due to energy purchases during 2017 is analyzed, and the current and future potential of the solar power impact, considering several restrictions, is studied.

As a result of the changes in the Honduran electric system operation, it is necessary to define a suitable strategy for estimating the available energy resources and planning an optimal dispatch which allows for a decrease in the operation cost according to the horizon of this study case.

The rest of this chapter is organized as follows: Sect. 17.2 describes the energy background and the power systems in Central America and their interaction in the economic dispatch. Section 17.3 explains the optimization model used and the subsets established for the economic dispatch. Section 17.4 presents the results obtained, focusing on the marginal dispersion costs and future generation value. Finally, the conclusion is given in Section in 17.5.

## 17.2 Preliminary Background

This section presents the following background of the generation market in the region:

- First, it describes the hydrothermal dispatch problem.
- Second, it presents a review of how the intermittent renewable resources as part of the overall power generation sources take part in the USA market; and, in particular, a study case of California is examined.
- Third, it presents an overview of the region, and
- Finally, it presents a summary about the past and present states of the Honduran electrical power system.

### 17.2.1 Hydrothermal Dispatch

The main objective of hydrothermal dispatch is to optimize the use of water in the hydroelectric power plants as well as to minimize the total operative cost affected by the fuel used in the thermo-electric power plants, plus any penalties for rationing.

The total cost is defined by the sum of the present operation cost and future operation cost. To generate energy to zero cost in the present, using the hydroelectric dams is a decision which implies high generation costs in the future due to depletion or reduction of water as a resource regardless of using thermal plants. On the other hand, if the decision is to store water for future use while dispatching today's thermal energy, and if the future flows are humid, it will be necessary to pour water, which means a waste of energy.

The meteorological factors not only affect the energy supply when to use hydro power or not, for instance, air conditioning systems or the number of light hours during the day.

The dispatch is composed of subsets of in one step, where the objective is to minimize the aforementioned immediate and future operative costs.

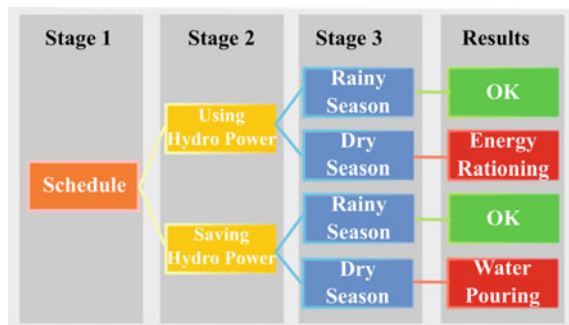
There are many possible uncertainty sources; because of that, it is essential to have planning tools. From the point of view of the thermal generators, the uncertainty is that the price of fuels like coal or gas is unknown; during the planning exploitation stages, it is necessary to consider that the final cost incurred may vary depending on the evolution of these raw materials in international markets [25].

Failures on generation equipment and transport represent a relevant uncertainty. For a robust system planning, the demand on the system must be known and it includes the future electrification projects.

As Fig. 17.1 shows, the operator has the options to use hydropower today, and with this to reduce the costs of the complementary thermal energy, or to store it to use it in the next stage. If the decision today is to use hydroelectric power and in the future the flow rates are high—allowing the reservoirs to be filled—the operation was efficient.

However, if a drought occurs in the future, the reservoirs will not recover, and it will be necessary to use more expensive thermal generation, or even interrupt the

**Fig. 17.1** Simplified example of hydrothermal dispatch steps. *Source* Author



supply of demand. On the other hand, if today's decision is to store water for future use through the use of more thermal generation, and future flows are high it will be necessary to pour the water, which it means a waste of energy. However, if a drought occurs in the future, storage will be used to avoid more expensive generation or power rationing.

### ***17.2.2 Stochastic Dual Dynamic Programming Hydrothermal Model***

The model is solved using on stochastic dual programming, a highly well-known model for dispatch centers in several countries including Guatemala, El Salvador and Panama. SDDP is a model that represents the transmission network and uses the operative short, medium and long terms.

The SDDP model uses the Stochastic Dual Dynamic Programming (SDDP) methodology, developed by PSR team in the 80s. This methodology allows representing the future cost function of traditional "PDE" (stochastic dynamic programming) as a linear function by parts.

### ***17.2.3 Californian Power System***

The growing economic competition of the renewable energy sources such as wind and solar power has attracted great attention worldwide. Several countries have considered in their energy policy the inclusion of this power generation systems to reduce the impact on the environment while the countries that import fossil fuels are trying to reduce their dependence on them [26].

However, incorporating intermittent technologies it is a challenge for electrical system planners and operators since most of this generation sources can not be dispatched; it is not possible for the system operator to control the generation due to its highly volatile nature, and it can change significantly from one hour to the next (Fig. 17.2).

During 2015, the renewable energy represented 13.44% of the electricity produced in the USA. California is leading state in renewable energy integration with approximately 29% of its energy produced by renewables, including micro-hydropower plants. Moreover, California leads the climate change policies which are committed to reduce the CO<sub>2</sub> emissions in the electrical sector in 40% to 2030. In order to achieve such target, the reliability of the power network, including the renewables energy sources, should be maintained.

Figure 17.3 shows the system demand in the past and the prospect subtracting the renewable generation.

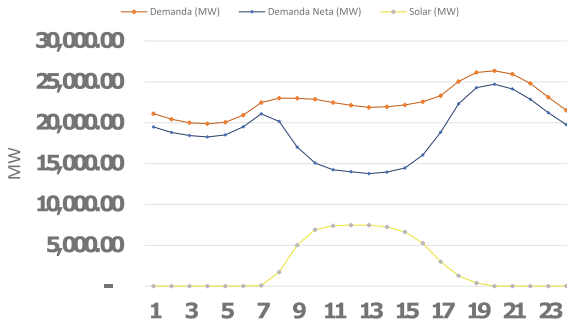


**Fig. 17.2** Electricity demand in California during January 1, 2018. *Source* Author

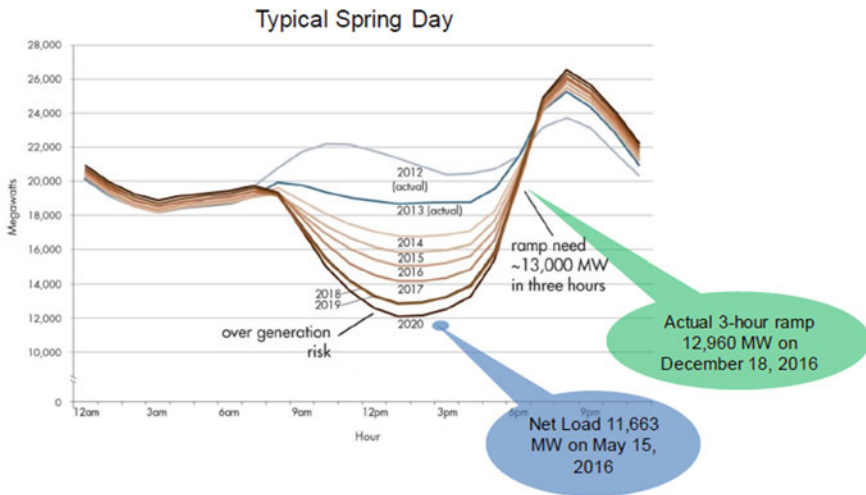


**Fig. 17.3** Net demand of the CAISO system [26]

The rapid penetration of renewable generation into the Californian grid is changing the network operator standards [27]. Figure 17.4 shows the ramp increment of 12,000 MW in 3 hours approximately, which requires to have a generation reserve enough to supply this abrupt change.

Additionally, California Independent System Operator (CAISO) reports an increasing integration of solar power in its generation portfolio coming from PV self-installed roof-mounted producers. As a consequence, the power systems operator is challenged during the sunrise and sunset.

The solar thermal generation resources used during the night need to be practically disconnected during the sunrise. Special attention and control should be given due to the over-production and volatility (Table 17.1).



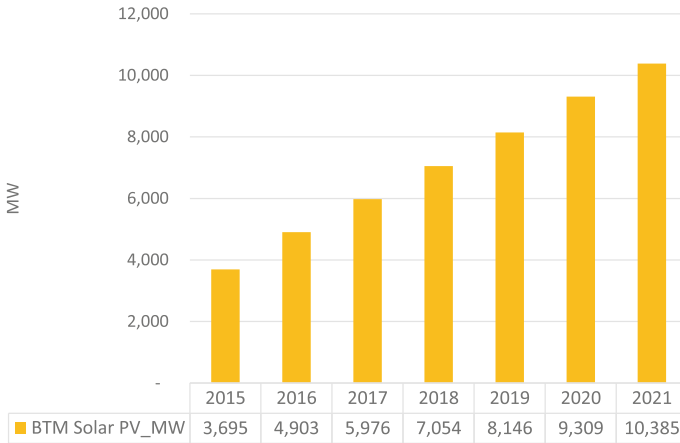


**Fig. 17.4** Rooftop installation projection in California. *Source* Author

**Table 17.1** Renewable generation in the CAISO operation

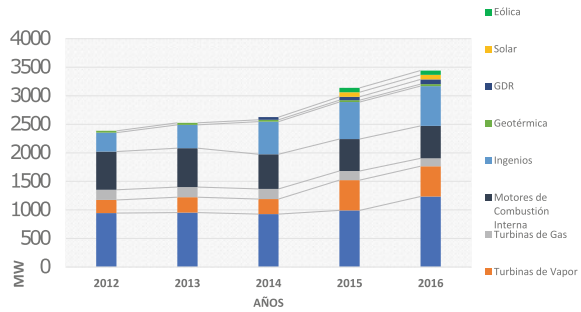
Source	Hour	Generation peak (MW)	Daily energy production (MWh)
Thermal-solar	14:06	650	6653
PV solar	14:22	10,054	104,181
Wind	19:28	4948	90,108
Micro hydro	19:20	560	9338
Biogas	04:40	258	5794
Biomass	03:30	399	9012
Geo-thermal	23:58	995	23,404

*Source* Author

### 17.2.4 Central American Power System

On December 2016, the installed capacity in the Central American region was 20.237 MW, larger 6.9% than the capacity observed back in 2015. This represents an increase of a total 1.312 MW (not taken into account the finishing contracts, maintenance or aging). The generation in the region is divided as 20.8% in Guatemala, 17.9% in Dominican Republic, 17.1% in Costa Rica, 16.5% in Panama, 12% en Honduras, 8.3% in El Salvador, 6.8% in Nicaragua, and 0.9% in Belice. 54.4% of the total capacity in the eight regions (10.327 MW) corresponds to the renewable energy plants.

**Fig. 17.5** Installed capacity during 2016 in Guatemala.  
Source Author



#### 17.2.4.1 Guatemalan Power System

The Guatemalan electrical system mainly is formed by thermal generation and hydroelectric generation systems. The installed capacity 3207.642 and 90MW from a photovoltaic solar system. The main hydroelectric power plants in the Guatemalan Power System are Chixoy (300 MW), Hydro Xacbal (94 MW), Palo Viejo (85 MW), Aguacapa (90 MW) and Renace II (100 MW).

The participation of Guatemala in the regional market is significant, in accordance with the “Administrador del Mercado Mayorista (AMM)” and the CNEE statistics, on 2016 Guatemala exported to the “Mercado Eléctrico Regional (MER)” 1284.49 GWh, reaching a participation of 57.01% in the energy injections to MER, it means the 11.05% of the total generation of the country (Fig. 17.5).

The structure and its related process of the electric industry in Guatemala are being somewhat similar to the developed on the electric market of Honduras. It is expected in the future to have a competitive market that provide as a result lower operating costs (Table 17.2).

#### 17.2.4.2 El Salvador Power System

El Salvador is the country which imports the most energy in the central American region. During 2016, the total electricity energy imported was around of 12,012 GWh that corresponds to 61.82% of the total energy importation. The total installed capacity of El Salvador is based on thermal, hydroelectric and geothermal power plants. During 2016, the participation of renewable energy sources (such as solar power) was 10.9% only.

The Salvadorian power system has been changing in history as follows: In the 40s decade, the energy development was in charge of the government, the geothermal plants were operated by the state and, the first hydropower centrals were built. During the 90s, the Salvadorian energy sector redefined the state’s role. During 2007, the National Energy Council was created as an authority empowered to coordinate the different energy sectors and to promulgate the policies and grid codes [28] (Fig. 17.6).

**Table 17.2** Main stakeholders in guatemalan electricity market regulation

Ministry of energy and mines	National electric energy commission (CNEE)	Wholesale market administration (AMM)
It is responsible of ensuring strict compliance with the laws and regulations pertaining to its functions and powers as well as formulating and coordinating State policies and indicative programs for various energy sources	It is responsible of enforcing the law and its regulations, imposing sanctions, protecting the rights of users and preventing conduct against free competition and abusive and discriminatory practices, defining transmission and distribution fares and promulgating the policies	It is responsible of coordinating the of plants, lines and interconnections at minimum cost, establishing short-term market prices for power and energy transfers, when they do not correspond to freely agreed long-term contracts, operation programming and electrical dispatch

Source Author

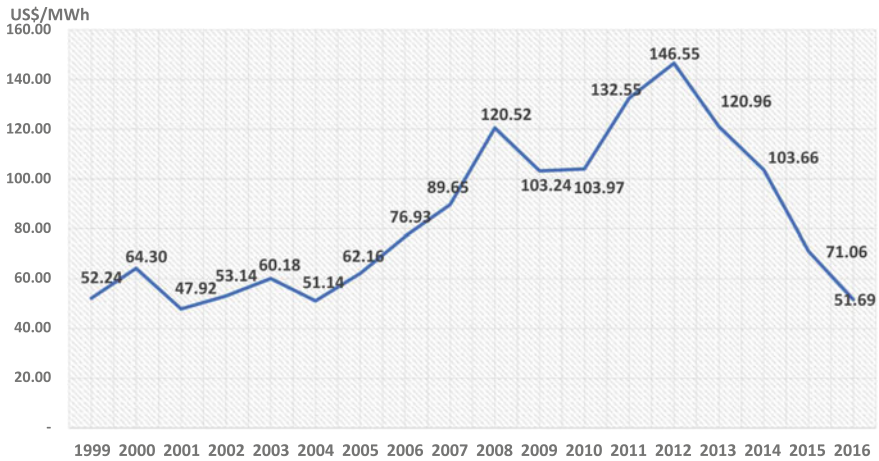


**Fig. 17.6** Spot prices in the Salvadoran electricity. Source Author

During 2009, the Energy National Council of El Salvador started to develop the national energy policy, that aims to envision a comprehensive energy market information, the decisions about the renewable integration and the laws to reinforce it (Figs. 17.7 and 17.8; Table 17.3).

**17.2.4.3 Costa Rican Power System**

The Costa Rican power system is dominated by renewable generation based on hydropower. During April of 2018, the installed capacity was 1683.818 MW that corresponds to 67.88% of the total installed capacity. The second biggest generation is the thermal power with a capacity of 571.69% MW and participation of 23.05% of the generation matrix. A clear example of the Costa Rican commitment to renewable

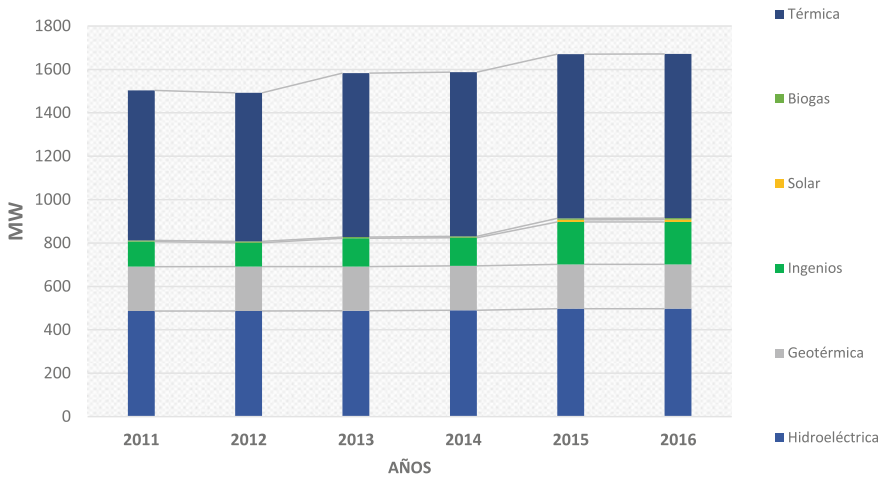


Fig. 17.7 Installed capacity in the Salvadorian system. Source Author

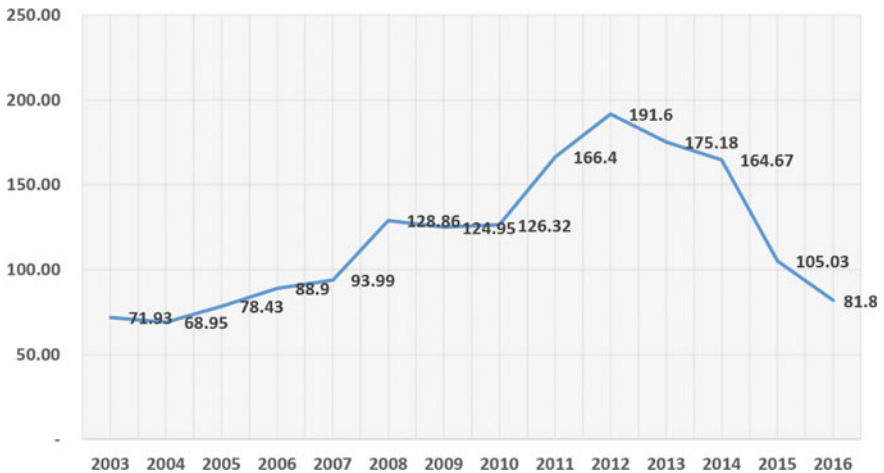


Fig. 17.8 Energy prices during 2017 in El Salvador. Source Author

power generation happened during June 7, 2018, when there was zero participation of thermal power, and the geothermal generation was produced 11% of the energy demand, and the wind power registered a maximum power of 327.5 MW. In Costa Rica, the electricity generation from solar power is almost null with an installed capacity of 1 MW [29].

The Costa Rican electricity sector is characterized by the main state participation. The power production, transmission, and distribution of the electricity are considered a public good. The state formulates the tariffs policies applicable to the electricity service (Fig. 17.9).

**Table 17.3** Electricity market regulatory institutions in El Salvador

National energy council (CNE)	General superintendence of electricity and telecommunications (SIGET)	Transaction unit (UT)
The CNE is the highest authority which govern and regulate the energy policies. Its aim is establishing the policy and strategy for promoting an efficient development of the energy sector	The SIGET is an autonomous public service institution with powers to apply laws and regulations which govern electric sector, the regulations from international treaties on electric and communications	The UT is an anonymous society created according to the LGE, and its aim is to operate the transmission system and the wholesales electric energy market

Source Author

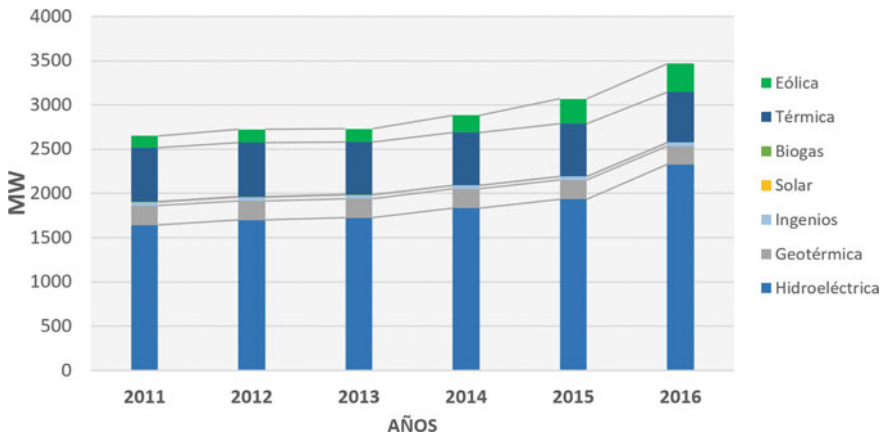


**Fig. 17.9** Installed capacity in the Costa Rican power system. Source Author

The Costa Rican electricity market is vertically structured, and it is governed by the state company, the Costa Rican Institute of Electricity (ICE). The private companies that participate in the power production are under several conditions to enter the market, such the power plants sizes and the power produced that can sell to the ICE, the monopolist buyer. The ICE is the only company authorized by the Costa Rican Law to generate thermal power (Table 17.4).

### 17.2.5 Honduran Power System

Since 2011, the Honduran Electric system went through a significant change in its generation matrix, which until 2010 had been mainly composed by hydroelectric, thermal and biomass power plants. The Francisco Morazán (300 MW) power dam, Cañaveral (80 MW), Río Lindo (29 MW) and El Nispero (22.5) are state hydroelectric power plants, while ENERSA (276.1 MW), Lufusa III (267.4), Lufusa Valle (80 MW)

**Table 17.4** Electricity market regulatory institutions in Costa Rica

Ministry of environment and energy (MINAE)	Regulatory authority for public services (ARESEP)	National center for energy control Costa Rica—CENCE	
The MINAE is the authority of the executive branch which execute the govern and political direction of the energetic sector	It is responsible of enacting the environmental policies, management and use of natural resources and promotion of renewable resources in order to compliance with the objectives and goals proposed in the ministerial programs and in the National Development Plan	The ARESEP is in charge of approving and applying the methodologies for setting rates, knowing the rate requests made by operators under the approved methodologies, and receiving and investigating complaints from users of public services	The CENCE is the operator of the electrical National System from Costa Rica, and it is responsible of the security of electricity supply

Source Author

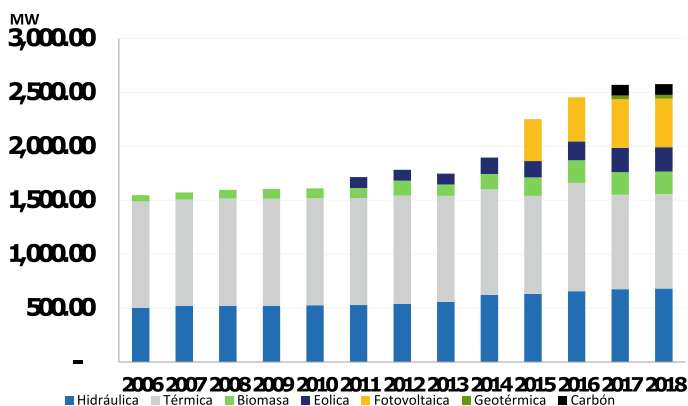


**Fig. 17.10** Installed capacity in the Honduras power system. Source Author

and ELCOSA (80 MW) are part of the thermal park of power generation owned by private companies (Fig. 17.10).

Since 2011, the power generation started using non-synchronous generation, and it was increasing in 2015 when PV power plants were incorporated into the system. The reduction of the dependence of using fossil fuels was one of the main objectives.

The generation sources based on renewable sources do not show a significant seasonality; it just evidences the sugar cane harvesting and milling period in the sugar mills for biomass power plants.

Due to the structure of the electrical market in Honduras, almost all private generation companies based its commercial operation on Power Purchase Agreements (PPA) with ENEE as the counterpart.

The type of contracts differs one from others; however, the dispatch from each plant is carried out according to the cost or variable prices of production and fulfilling the technical conditions and safety of supply. “An annual growth rate of demand of 4% is considered for the period 2015–2030”.

The Honduran electric market offers a significant share of variables renewable power generation (wind and solar) and, also a significant number of hydroelectric power plants on the edge of water whit minimum flow regulation (hourly). As a result, there is an energy production which is not steady; it means that the availability for using those energies in a electric system critical situation is uncertain.

### **17.2.5.1 Honduran Electricity Market Opening**

The Decree 404-2913 “General Law of the Electric Industry” was published on May, 2014, and the aim is the regulation of generation, transmission, distribution and commercialization of electricity, as well as the operation of the Honduran Electric System and the import and export of electrical energy within the Regional Electricity Market (REM).

The “General Law of the Electric Industry” also mentions the creation of an entity in charge of regulating the energetic activities and the country’s energy policy. Due to the Decree 404-2913 and as a result of many attempts to form it, the Executive Branch enacts the Executive Decree “PCM 48-2017”, which creates the “Secretary of State in the Office of Energy” (SEN), and it is attached to the Sector Cabinet of Economic Development.

Figure 17.11 shows the scenario of electric energy participation using intermittent renewable sources (photovoltaic solar) across the region.

## ***17.2.6 Regulatory Framework for the Honduran Electricity Market***

Honduras is the country which has experiment a significant growth of installed capacity using intermittent renewable sources of power generation at the Central America context. For that reason, Honduras should be pioneer in optimization analyses in order to guarantee the lowest generation cost in the electricity market. The fact that Honduras has a high photovoltaic solar energy penetration forces the study of natural events that could put on risk the SIN operation, i.e., during the eclipse of August 21, 2017, was possible to identify a close connection between this kind of natural phenomenon and the electrical Honduran network operation.

This study incorporates the entry into operation of plants of different types, and strategic plan by ENEE is taken as reference.

As a result of the above, the simulation was done using SDDP as a way of determining the operative statistics, marginal operation cost and the effects of photovoltaic

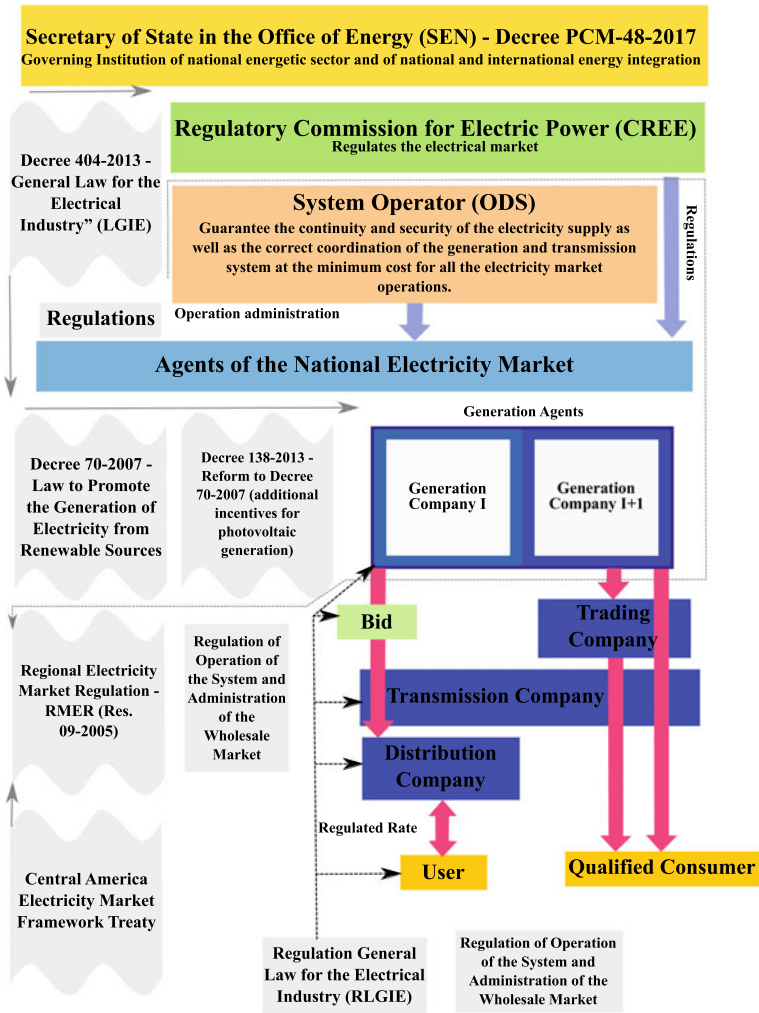


Fig. 17.11 Installed capacity in Central America. Source Author

solar generation for the Honduran electric system according to the horizon in the medium term for this study case. It was mentioned in Sect. 17.2.2.

For approximately 60 years, the Honduran electric sub-sector was organized based on the traditional monopoly model: a vertically integrated state company, named National Electric Power Company (ENEE). The liberalization of the electric market by the Honduran government started on May, 2014, with the enactment of the “General Law for the Electrical Industry” (LGIE).



An electricity wholesale market was established by the law. According to this model, the producing agents can sell electricity to distributors, qualified consumers, other generators and to the regional market of Central America. Implementing this new system has been a slow process, after the enactment of LGIE on May, 2014, there has been hardly published a few regulations:

- Firm Capacity Purchase Regulations on November 15, 2015.
- General Regulation of the Electricity Industry on November 18, 2015.
- Regulation of Operation of the System and Administration of the Wholesale Market on November 18, 2015.
- Internal Regulations of the Regulatory Commission for Electric Power on November 17, 2015.
- Electric Service Regulation on November 14, 2017.
- Distribution Quality Technical Standard (NT-CD) on November 14, 2017.
- Transmission Quality Technical Standard (NT-CT) on November 14, 2017.
- Technical Standard of the Electricity Opportunity Market (NT-MEO) on June 7, 2018.

Figure 17.12 shows the summary of the regulatory framework of the sector in Honduras as well as the current structure of the sector including the incorporation of the new Secretary State of Energy Dispatch. This state entity who governs the National Electric Sector is responsible mainly of formulation, planning, coordination, execution, monitoring and evaluation of strategies and policies in the energy sector. The structure was defined in the LGIE, Decree 404-2013, its regulations and standards (Table 17.5).

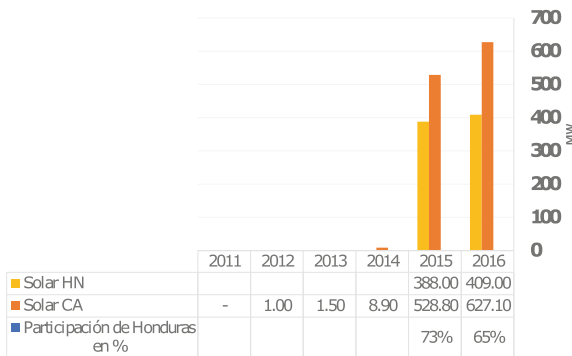


**Fig. 17.12** Installed capacity in the Honduras power system. *Source* Author

**Table 17.5** Electricity market regulatory institutions in Honduras

Secretary of state in the energy office (SEN)	Regulatory commission for electric power (CREE)	System operator (ODS)
<p>The SEN is the governing institution for the national energy sector and also for the regional and international energy integration. It is in charge of proposing Energetic National Strategy and the policies related with the integral and sustainable development of the energetic sector to the National Energy Council. Likewise, the SEN is in charge of formulation, planning, coordination, execution, monitoring and evaluation of energy sector strategies and policies</p>	<p>The CREE is a decentralized, with sufficient administrative powers, functional and budgetary independence entity of the Sectorial Ministry from Economic Driving and Regulation. It regulates the electrical market, define transmission and distribution fares and promulgate regulations and policies</p>	<p>The ODS must guarantee the continuity and security of the electricity supply as well as the correct coordination of the generation and transmission system at the minimum cost for all the electricity market operations. Also, supervising and controlling all the SIN operations, including the electrical dispatch and operation programming coordination with companies and operators of the electricity system, under the principles of transparency, objectivity, independence and economic efficiency</p>

Source Author

## 17.3 Proposed Methodology

### 17.3.1 Solar Power Penetration Impact

The analysis of the operation cost impact of the National Interconnected System “SIN” due to the release of PV solar power plants is based on the optimization and simulation of the whole system including the solar power plants.

Using the SDDP software, the SIN could be simulated in order to get the operative statistics and the marginal operation costs.

The impact on the reduction of greenhouse emissions from the use of renewable sources is not considered in this analysis due to the hydrothermal release emissions; hence, this is beyond the objectives for this study case.

Figure 17.13 shows the structure for entering data to the SDDP model

Each one of the modules showed in the last figure are described below.

The “SIN” is energized by different generation sources like hydroelectric systems, thermal plants based on combustion engines powered with fossil fuel. In recent years, generation sources supplied with biomass and coal plants have been incorporated and operated within the system.

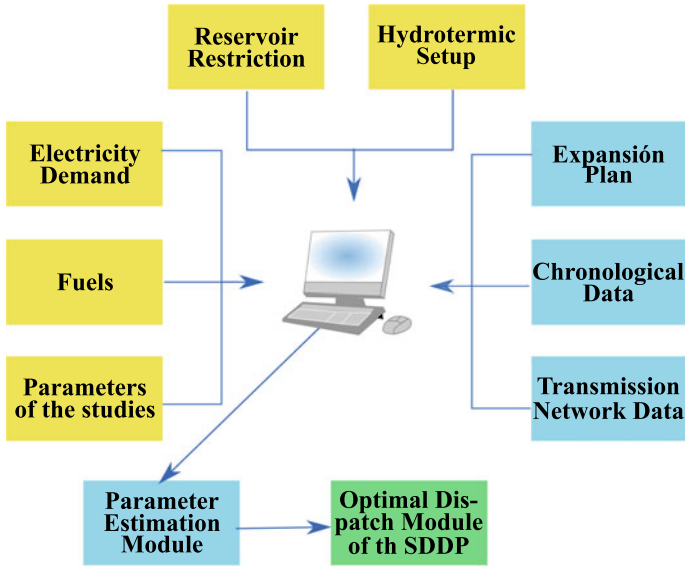


Fig. 17.13 Methodology representation. *Source* Author

### 17.3.1.1 Study Parameters

The operation of the SIN is simulated for six (06) years according to the hydrologic schedule, which starts on January 1, 2019, until December 31, 2024. The resolution stages are monthly. The data used, related to Honduras, was updated on October and November, 2017, from the database. The variables considered in this analysis are: demand for electrical energy, fuel prices, hydrologic conditions, addition of new generation systems with operative restriction.

### 17.3.1.2 Transmission Network

The database of SIN are transmission network models simulated according to the technical parameters and its restrictions. The networks which have a voltage lower than 138 KV had been simplified and replaced with equivalents. Those changes do not affect the electrical flow and the voltage is always under 138 KV.

In this case study, the new transmission networks from Honduran electrical system are not incorporated.

Figure 17.14 shows a simplified model of the Honduras transmission system which includes most of the transmission used for SIN operation. The SDDP model simulated included the whole network until December, 2017.

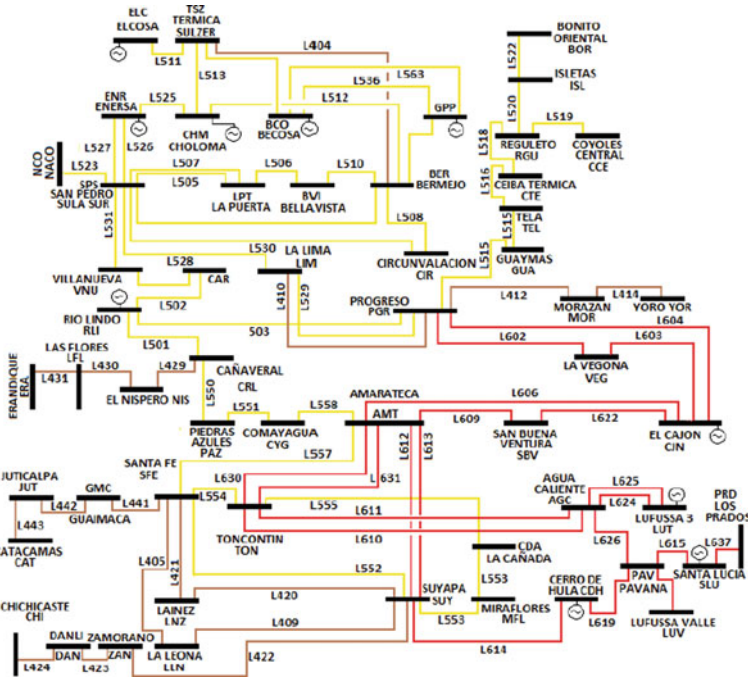


Fig. 17.14 Honduras power system. Source Author

### 17.3.1.3 Hydrothermal Setup

The generation matrix used as reference is part of the strategic plan of ENEE Group 2016–2020, and is in compliance with the “Centro Nacional de Despacho”, the Planning Management Office and the newsletter of March 2018.

#### 17.3.1.4 Parameters Estimation

The energy demand has been divided on five (5) energy blocks. The block 1 represents the highest energy demand, while block 5 represents the lowest demand. According to the objective of this analysis, the Patuca 3 Hydroelectric Plant (capacity 104 MW) and Tornillito Power Plant should be included on October, 2018 and December, 2021, respectively. Including these power plants has an impact on the estimation of future costs, which will tend to decrease.

### **17.3.1.5 Electricity Demand**

The electricity demand is included on the Strategic Plan 2016–2020 by ENEE Group. This plan specifies which power plants will be closed and which ones will be connected to the network during the period of this analysis.

### **17.3.1.6 Fuels**

In Honduras, like in Latin America, the prices of electric energy are linked to the variation of the fuels prices because most of the generation sources use fossil fuels as first source of energy. Those prices are indexed according to the international oil prices.

The prices used on this analysis are based on the Annual Energy Outlook (AEO) published on January, 2017, for the next years.

## ***17.3.2 Economic Dispatch Including PV Power Plants***

In order to get a detailed analysis of the energetic dispatch, it is necessary to simulate the system including all the power plants for optimizing the renewable resources.

### **17.3.2.1 Hydrothermal Dispatch**

For the analysis of the hydrothermal power system is necessary the simulation programming stochastic models, which minimize the operation cost during time. The total cost of the system is calculated by summing the present operation cost and the future operation cost.

The main limiting for enlarging the electrical power system in Honduras is that most of the hydroelectric power plants have a regulatory reservoir, and it is necessary to define how much water must be stocked on the reservoirs for energy generation and minimizing the cost.

The main restrictions for an hydrothermal power dispatch at low cost in short term, according to [30], are the following:

- Thermal units
- Hydroelectrical units
- Reservoirs
- Primary resources
- Contractual
- Maintenance of system components
- Safety system
- Nodal Balance

- Operation
- International interconnection.

According to the objective of this study case were considered, the restriction listed before except for the primary resources restriction.

### 17.3.2.2 PV Power Plants Incorporation

Including intermittent renewable generation sources causes major impacts on the net demand profile (electricity demand less renewable generation sources). It should be noted that in this type of operation using PV solar plants the ramp increases in the morning and decreases in the afternoon; Fig. 17.15 shows those changes. In order to cover the national energetic demand, respond to the changes in the electrical network maintaining the reliability and stability of the system, it is necessary include thermal generations sources. However, this would imply an increase in the starts and stops of thermal plants.

### 17.3.3 Power Plants Modeling

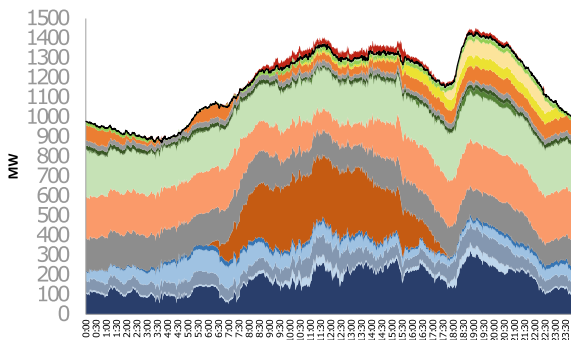
In order to simulate the system operation and consider the restrictions, aforementioned is necessary to model the basic components of the system as follows:

#### 17.3.3.1 Thermal Power Plants

In purely thermal power systems, the power plant cost depends on the fuel cost. Therefore, the thermal power plant is represented by its unitary cost  $\{c_j, j = 1, \dots, J\}$  and the generation capacity:

$$g_r(j) \leq \bar{g}(j), \tag{17.1}$$

**Fig. 17.15** Ramps due to the solar power generated.  
Source Author



where  $j$  is the number of thermal power plants,  $J$  is the total number of thermal power plants,  $g_t(j)$  is the energy produced by the plant  $j$  in the stage  $t$ , and  $\bar{g}(j)$  is the generation capacity of the power plant.

### 17.3.3.2 Hydroelectrical Power Plants

The storage at the end of the stage  $t$  (begin of the stage  $t + 1$ ) is equal to the initial storage minus the total discharge (turbine, pouring and irrigation) plus the tributary volume (lateral flows plus the discharge of the upstream plants).

$$v_{t+1}(i) = v_t(i) - u_t(i) - s_t(i) + a_t(i) + \delta r_t(t) + \sum_{m \in v_i} [u_t(m) + s_t(m)] \quad (17.2)$$

where  $I$  is the number of hydro power plants,  $v_{t+1}(i)$  is the stored volume in the power plant  $i$  at the end of the step  $t$ ,  $v_t(i)$  is the stored volume in the power plant  $i$  at the beginning of the step  $t$ ,  $a_t(i)$  is lateral flow of the power plant  $i$  in the step  $t$ ,  $r_t(t)$  is the watering in the power plant  $i$  in the step  $t$ ,  $\delta r_t(t)$  watering flow violation for the power plant  $i$  in the step  $t$ ,  $u_t(m)$  turbine volume in the step  $t$ ,  $s_t(i)$  is the volume after in the step  $t$ ,  $m \in v_i$  is the set of power plants over the plant  $i$ .

The stored and draining limits are defined as follows:

$$v_t(i) \leq \bar{v}(i) \quad (17.3)$$

$$u_t(i) \leq \bar{u}(i) \quad (17.4)$$

where  $\bar{v}(i)$  is the storage capacity of the power plant  $i$ , and  $\bar{u}(i)$  is the turbine capacity of the power plant  $i$ .

Hydroelectric power plants convert the potential energy from the stored water into kinetic energy, which is used to move the turbines coupled to generators.

The produced power is defined as follows:

$$g_t(i) = \rho(v_t(i)) u_t(i) \quad (17.5)$$

where  $\rho(v_t(i))$  is the production coefficient of the central  $i$ , and  $u_t(i)$  is the hydro central turbination  $i$  at the stage  $t$ .

The production coefficient is calculated as:

$$\rho(v_t(i)) = \eta(i) \phi \gamma h(v_t(i)) \quad (17.6)$$

where  $\eta(i)$  is the hydro generators/turbines efficiency set  $i$ ,  $\phi$  is the specific mass of water,  $\gamma$  is the gravity factor,  $h(v_t(i))$  is the water falling distance between dam superior limit and the downstream outlet.

The hydrological uncertainty is based on the historical data of the main hydrologic power plants provided by the ENEE in the period 1965–2014.

The operation cost is affected by the variation of thermal power plants generation connected to SIN, considering that other kind of power plants has not variable cost operation. Due to that variability, it is important to evaluate the impact of photovoltaic power plants during the stage of modelling thermal power plants and its restrictions.

The hydrological uncertainty is based on the historical data of main hydroelectric power plants according to the “Empresa Nacional de Energia (ENEE) for the period 1965–2014”.

### 17.3.3.3 PV Power Plants

Using the statistics of real generation power plants available in the SIN for the period 2015–2018, the maximum generation power was determined.

The procedure used for determining the solar power generation is:

- For high-capacity photovoltaic generation power plants, the SIN defines a profile according to the generation schedule with a monthly data representation (Fig. 17.16).
- Block-hour mapping generates as a result the average of demand per block and the lasting of each block. Next Figure shows the block-hour mapping of one of the high-capacity photovoltaic solar plant in the Honduran electrical network. Values in values per unit (p.u.) (Table 17.6).

Table 17.7 shows the lasting of each block as a percentage. This percentage is used as the input of the model.

Table 17.8 shows a block-hour map of energy demand in GWh for the SIN.

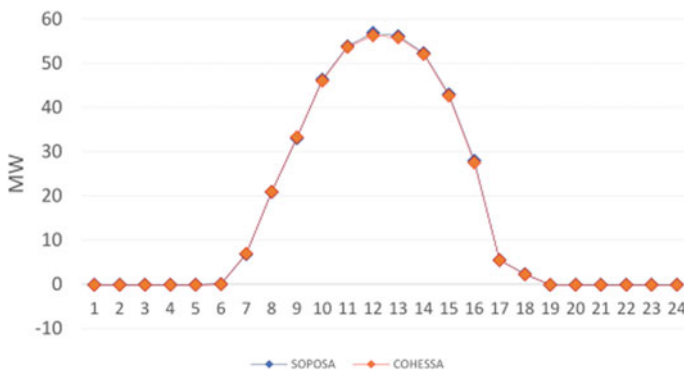


Fig. 17.16 Daily solar power plants generation on the September 26, 2017. Source Author



**Table 17.6** Generator replacement for each case

Block	Jan	Feb	Mar	Apr	May	May	May
1	–	–	–	–	–	–	
2	0.82	0.82	0.82	0.82	0.82	0.82	0.82
3	0.50	0.50	0.50	0.50	0.50	0.82	0.82

Source Author

**Table 17.7** Blocks demand in %

Blocks	Duration
1	8.55
2	28.43
3	21.00
4	20.60
5	21.42
Total	100

Source Author

**Table 17.8** Energy demand

Year	Block	Jan	Feb	Mar	Apr
2019	1	55.24	61.31	122.05	225.64
2019	2	287.65	251.01	297.93	336.59
2019	3	204.67	224.69	220.98	187.81
2019	4	189.00	158.59	192.65	149.99
2019	5	198.85	154.63	153.62	109.13

Source Author

### 17.3.4 Hydrothermal Dispatch

The economic dispatch is composed of various subsets of one step which objective is to minimize the sum of the immediate and future operative costs.

As it is shown in Fig. 17.17, the immediate cost function reduces when the turbinated volume in the hydropower units is reduced. However, the future cost function increases when the turbinated volume increases due to the necessity of using the thermal unit to supply the demand.

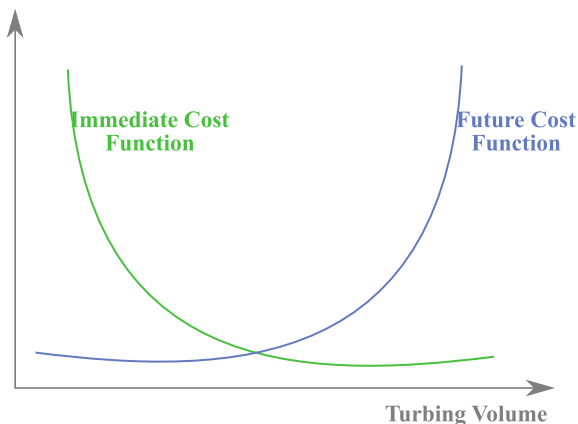
The hydrothermal dispatch for the step is presented as follows:

$$\min (FCI + FCF) \tag{17.7}$$

According to the basic operative restrictions of each step.

The immediate cost FCI is given by the thermal cost in the step plus the penalties for breaking the restrictions of each step.

**Fig. 17.17** Immediate and future costs per turbinated volume. *Source* Author



$$FCI = \sum_{k=1}^K \sum_{j=1}^J c(j) g_{tk}(i) + c_{\delta} + \delta_{gt} \tag{17.8}$$

where  $k$  are the demand blocks at the stage  $i$ ,  $K$  number of blocks,  $j$  is the thermal central index,  $J$  is the thermal central set,  $c(j)$  is the variable cost of the central operation  $j$ ,  $g_{tk}(i)$  is the energy produced by the plant  $j$  at the time  $t$  and block  $k$ ,  $c_{\delta}$  is the cost of violating a restriction,  $\delta_{gt}$  is the violating amount at the stage  $t$ .

The function of future costs FCF is represented as:

$$FCF = \alpha_{t+1}(v_{t+1}, a_t) \tag{17.9}$$

where  $v_{t+1}$  is the storage at the end of the stage  $t$ ,  $a_t$  is the dam flow stream during the stage  $t$ .

In this study, the hydroelectrical model shows the tributary flows of the main hydroelectric power plants in Honduras; as well as the final dimension in meters for the most important hydroelectric power plant (Hydroelectric Francisco Morazán Dam) in the system.

### 17.4 Analysis and Results

This section shows how the PV power plants affect the electrical dispatch, using different scenarios. Additionally, the operation system projected costs and the optimal operation scenario which lets perform the power generation park with the lower costs is presented. The simulation of the SIN was done using the SDDP software used to carry out the scenarios.

### 17.4.1 Definition of the Model Parameters

The parameters used in the simulation in order to solve the optimization problem are shown in Table 17.9.

#### 17.4.1.1 Hydroelectric Power Plants Used in the Simulation

Table 17.10 shows the information of all the power plants included in the simulation like downstream, amount of units per power plant, its capacity and the production coefficient, as well as power plants with regulatory reservoir and power plants installed in the future (Fig. 17.18).

#### 17.4.1.2 Thermal Plants Considered in the Simulation

Table 17.11 presents the thermal plants based on fossils, used for the simulation.

#### 17.4.1.3 Solar Plants Considered in the Simulation

Most photovoltaic solar power plants are located in Valle and Choluteca departments in the southern area of the country. The installed capacity in each power plant and the incorporation year are shown in Table 17.12.

Due to the incentives of the Decree 138-2013 for the electric generation using solar resources, it was possible that in 2015 most of the power plants, that currently are operating, could start their operation.

**Table 17.9** SDDP model parameters

Parameter	Value
Analysis horizon	2019–2024
Initial stage	January 2019
Final stage	December 2024
Hydrology stage year	2012
Discount rate%	12%
Type	Stochastic
Flow number n	Synthetic ARP
Number of forward scenarios	100
Number of backward scenarios	50
Minimum number of iterations	1
Maximum number of iterations	15

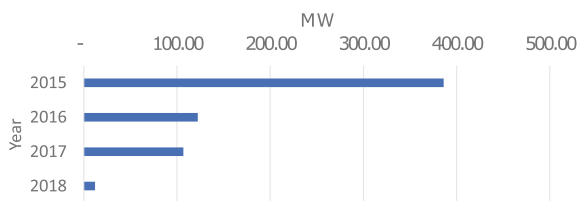
Source Author

**Table 17.10** SDDP model parameters

Parameter	Downstream	Downstream	Units	Capacity	Prod.
El Cajón	La Vegona	La Vegona	4	300	0.84
Cañaveral	Río Lindo-H		2	29	1.04
Río Lindo-H			4	80	3.03
Nispero-H			1	22.5	0.95
Nacaome			3	28.1	0.2
Cuyamapa			2	12.5	3.4
Cuyamel-H			2	7.8	0.89
Esperanz			2	12.8	5.7
RioBlanc-H			1	5	1.08
Cortesis-H			2	5.5	2.15
Gloria			2	5.8	1.38
Juan-H			1	6.6	2.4
Chamelec			2	11	0.6
LaVegona			2	38.5	0.2
Laureles			2	3.5	3
Patuca3	3Patuca2AH		2	104	0.38518
OjoAgua			2	19.5	2.6
Llanitos	3-JicatuyoH		2	98.186	0.6533
Patuca2			3	270	0.6527
Tablon			2	20	0.417
Jicatuyo			4	172.9	0.5753
Tornillt			3	160.2	0.42381
Patuca2A	3-Patuca2H		3	150	0.46875
Cangrejl			2	40.2	1.4337

Source Author

**Fig. 17.18** Generation capacity due to the additional solar power. Source Author



### 17.4.2 Model Results

The study case was designed and executed on the simulation SDDP model version 14.0.17 using information from the Honduran electric system database, updated on October and November, 2017.

**Table 17.11** SDDP model parameters

Name	Units	Capacity MW
Lufusa III-AGC-TV	14	247.9
Enersa-MT	1	235.2
BECOSA1-TV	8	120
Elcosa1-MT	8	80
LUFUSA-Valle-MT	5	80
Emce Choloma-MT	1	55
Geoplatanares-GT	1	35
GPP-KG	1	35
TFIC06070193	1	35
EXC-LUFUSA-MT	1	30.5
KG-HGP-C	1	30
CAHSA-TV	1	24
Envasa Nac-TV	1	20
NAINSA-MT	1	20
TFIC05730150	1	20
VETASA	1	20
UDEHSA	15	20
Elcatex-MT	1	19.9
Tres Valles-TV	1	19.5
TFIC05600169	1	19.5
CELSUR-TV	1	18.75
CELSR-C-TV	1	18.75
LPT-HI-TG	1	18
KG-MPP-G	1	16
LPT-GE-TG	1	15
CHUMB	1	15
La Grecia-TV	2	12
CARACOL-G	1	12
KG-HGP-G	1	11
Emce Ceiba-MT	4	10
Park-naco	6	10
CAHSA-C-TV	1	10
AZUNOSA-G-TV	1	10
GREC-C-TV	1	7
SantaFe-MT	2	5
CHUMB-C-TV	15	5
JUT5-MT	15	5
AZU-C-TV	1	4
PARKDAL-C	1	4
MPP-C	1	2
ELCTX-C-TV	1	2
PALMASA	1	1.8
ECOPALS-TV	1	1.2
ACEYDES-TV	1	1.1
YODECO-TV	1	0.3
CEIBDIE-MT	1	0
TFIC06060191	1	0

Source Author

**Table 17.12** PV solar plants considered in the simulation

Number	Name	Date	Installed power
1	SOPOSA	01/05/2015	50.00
2	COHESSA	01/05/2015	50.00
3	FOTERSA	01/05/2015	20.00
4	ENERSOL	01/10/2016	6.73
5	FOTOSOL	01/10/2016	5.39
6	PRADOS	01/10/2016	10.00
7	SURENA	01/10/2016	11.20
8	MECER	01/05/2015	25.00
9	GENERSA	01/06/2015	11.20
10	MARCVIA	01/06/2015	35.00
11	CHOL1	01/06/2015	20.00
12	CHOL2	01/06/2015	30.00
13	CAGUAN	01/06/2015	50.00
14	MANZANI	01/01/2017	21.90
15	GEN-ENR	01/03/2016	25.00
16	LLA-SUR	01/10/2016	14.00
17	FRAY	01/01/2017	48.00
18	PACIFIC	01/10/2016	50.00
19	NACA2	01/07/2015	50.00
20	POLLITO	01/07/2015	20.00
21	ENERBSA	01/07/2015	25.00
22	LAJAS	01/01/2017	11.90
23	HELIOS	01/07/2017	25.00
23	SNMARCO	15/05/2018	12.00

Source Author

#### 17.4.2.1 Demand and Dispatch

The demand of power for supply the Honduran System during the period of the study case (January, 2019 to December, 2024) is mainly provided by hydroelectric and thermal power generators. For this study case, there has been modeled two scenarios for simulating. The first one includes in the system the power generation park using photovoltaic solar generation and the second one without those injection. Below shown are the results.

### 17.4.2.2 Dispatch with PV Generation

The objective of this analysis is defining which operation represents the lowest cost for the system. During the development of the model simulation, there are no deficit problems for the Honduran electricity system.

Considering only the marginal cost, the operational system cost is affected directly by the use of photovoltaic solar power plants. This cost decreases when the dispatch to the system is obligatory, according to the LGIE.

Figure 17.19 shows the behavior of marginal cost generation during the first 12 steps of the study. The average for each step is showed as a possible variation considering lower percentiles to 10 and 20% as well as upper percentiles. This behavior allows to have a better price estimation in order to evaluate the risks of participating on the electrical market.

The required generation capacity for supplying the demand on this scenario is showed in the Table 17.19, where are the hydroelectric and thermal power plants of generation as the main supply sources (Tables 17.13 and 17.14).

The Hydroelectric power plant Francisco Morazán, known as Dam El Cajón, is the most important in Honduras. The volume behavior for this power plant, during the 12 stages of the study case, was simulated using the SDDP model for 2019, and

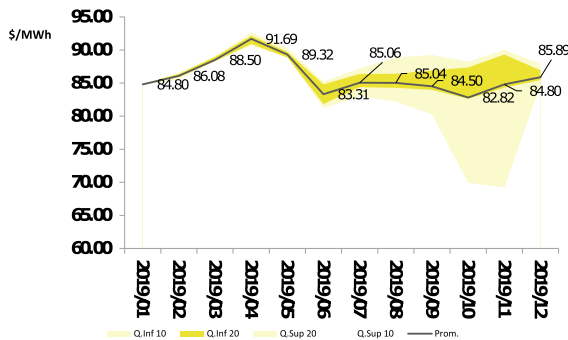


Fig. 17.19 Marginal cost dispersion including solar power. Source Author

Table 17.13 Generation including PV

Source	Jan–Dec 2019	Jan–Dec 2020	Jan–Dec 2021
Hydro	3384.00	3298.00	3587.00
Thermal	4703.00	5197.00	5350.00
Renewable	2611.00	2611.00	2611.00
Generation	10,698.00	11,106.00	11,548.00
Losses	206.00	199.00	196.00
Demand	10,491.00	10,907.00	11,356.00

Source Author

**Table 17.14** Generation including PV

Source	Jan–Dec 2022	Jan–Dec 203	Jan–Dec 2024
Hydro	4348.00	4241.00	4267.00
Thermal	4703.00	5197.00	5350.00
Renewable	2611.00	2611.00	2611.00
Generation	10,698.00	11,106.00	11,548.00
Losses	206.00	199.00	196.00
Demand	10,491.00	10,907.00	11,356.00

Source Author

**Fig. 17.20** El Cajón Dam volume and demand projected. Source Author

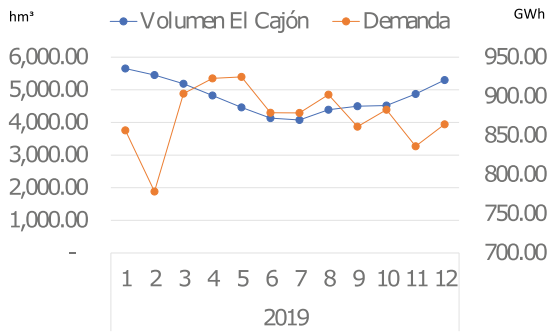
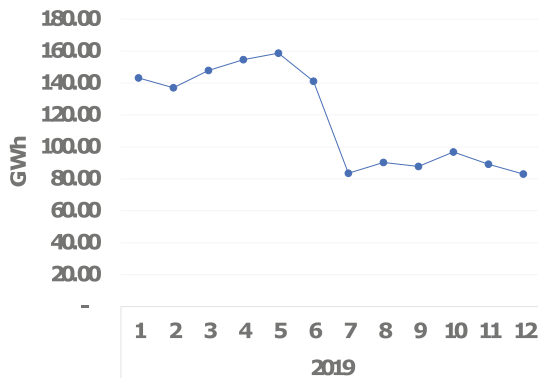


**Fig. 17.21** Generation of the solar PV plants during 2019 in GWh. Source Author



it is possible to compare the variation of marginal cost of generation and the future demand, showed in Fig. 17.20.

Figure 17.21 shows the contribution of photovoltaic solar power plants for the first 12 stages of this study case.

Considering the prices paid for photovoltaic solar generation power, the total cost increases. This behavior reinforces the results obtained by Pablo Meraz in his analysis (2017): “Comparative analysis of the economic dispatch in the Honduran electric power system considering the power purchase contracts as of 2017” The



**Table 17.15** Simulation results with SDDP

Year	Generation	Total demand	Marginal cost	Marginal cost
2019	1413.10	10,491.00	83.32	89.68
2020	1413.10	10,907.00	90.47	99.31
2021	1413.10	11,356.00	111.67	122.03
2022	1413.10	11,820.00	95.88	105.01
2023	1413.10	11,820.00	84.49	93.17
2024	1,413.10	11,820.00	77.3	87.17

Source Author

**Table 17.16** Simulation Results with SDDP

Year	Economic D	PPA Solar	PPA	ED
2019	874,110.12	24.25	107.57	1128,468.34
2020	986,756.29	23.32	113.79	1241,114.51
2021	1268,124.52	22.40	134.07	1522,482.74
2022	1133,301.60	21.52	117.40	1387,659.82
2023	998,671.80	21.52	106.01	1253,030.02
2024	913,686.00	21.52	98.82	1168,044.22

Source Author

model results for the study horizon considering the photovoltaic solar generation park operation are shown in Table 17.11. If the photovoltaic solar generation is excluded, the increase of operation cost can be appreciated (Tables 17.15 and 17.16).

Table 17.11 shows the results of incorporating the photovoltaic solar power generation park to the considered future generation. The results showed the total value of photovoltaic solar power dispatched to the system has an average marked difference of \$254 358,220 additional annual in the study case horizon in relation to the economic dispatch analysis with a greater participation of a thermal power generation park.

### 17.4.2.3 Dispatch Without the PV Inclusion

The second scenario simulated excludes the photovoltaic solar power generation; for this reason, the variation of power is supplied by the thermal power generation park as is shown in Tables 17.17 and 17.18.

The thermal sources of generation are mainly affected by the availability or not of the photovoltaic power generation park because thermal power generation plants replace the photovoltaic solar power injection to the system. Figure 17.22 shows the results of the SDDP model simulation for both scenarios.

Table 17.13 shows a comparative analysis of marginal generation cost by stages for both simulation scenarios. There is an increase estimated in the value of the marginal cost when the photovoltaic solar power generation park is excluded, due

**Table 17.17** Generation including PV

Source	Jan–Dec 2019	Jan–Dec 2020	Jan–Dec 2021
Hydro	3387.00	3293.00	3524.00
Thermal	6098.00	6605.00	6823.00
Renewable	1170.00	1170.00	1170.00
Generation	10,655.00	11,069.00	11,517.00
Losses	164.00	162.00	165.00
Demand	10,491.00	10,907.00	11,356.00

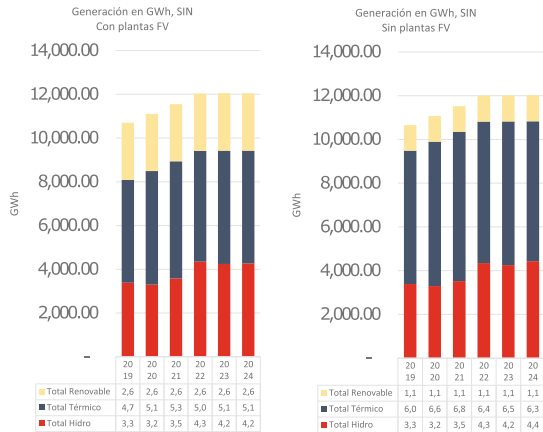
Source Author

**Table 17.18** Generation including PV

Source	Jan–Dec 2022	Jan–Dec 203	Jan–Dec 2024
Hydro	4344.00	4250.00	4431.00
Thermal	6469.00	6575.00	6397.00
Renewable	1188.00	1188.00	1188.00
Generation	12,001.00	12,013.00	12,016.00
Losses	181.00	193.00	196.00
Demand	11,820.00	11,820.00	11,820.00

Source Author

**Fig. 17.22** Generation capacity due to the additional solar power. Source Author



to the increase of power generation by thermal power plants. This increase causes an impact on the fossil fuel importation necessary for operating the thermal power plants which replace the photovoltaic solar power plants generation (Fig. 17.23; Table17.19).

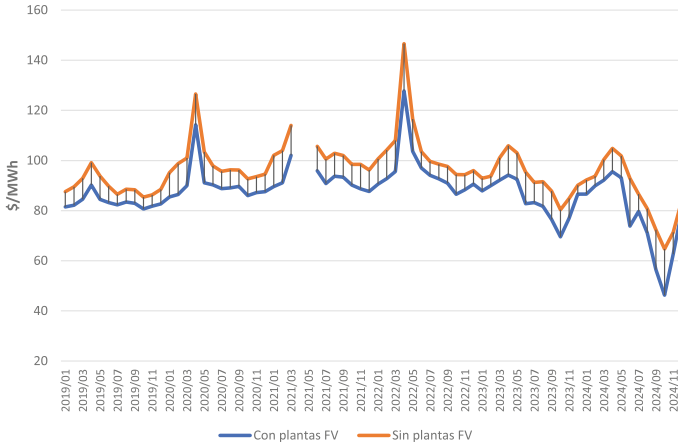


**Fig. 17.23** Marginal cost by stage for both simulation scenarios. *Source* Author

**Table 17.19** Marginal cost by stage for both simulation scenarios

Stage	Using solar PV	
2019/01	81	88
2019/02	82	90
2019/03	85	93
2019/04	90	99
2019/05	84	94
2019/06	83	90
2019/07	82	87
2019/08	83	89
2019/09	83	88
2019/10	81	85
2019/11	82	86
2019/12	83	88
2020/01	85	95
2020/02	86	99
2020/03	90	101
2020/04	114	127
2020/05	91	103
2020/06	90	98
2020/07	89	96
2020/08	89	96
2020/09	90	96
2020/10	86	93

(continued)

**Table 17.19** (continued)

Stage	Using solar PV	
2020/11	87	94
2020/12	88	95
2021/01	90	102
2021/02	91	104
2021/03	102	114
2021/04	268	277
2021/05	149	163
2021/06	96	106
2021/07	91	101
2021/08	94	103
2021/09	93	102
2021/10	90	98
2021/11	89	98
2022/01	91	101
2022/02	93	104.1616
2022/03	96	108
2022/04	128	147
2022/05	104	117
2022/06	97	104
2022/07	94	100
2022/08	93	99
2022/09	91	98
2022/10	87	94
2022/11	88	94
2022/12	91	96
2023/01	88	93
2023/02	90	94
2023/03	92	101
2023/04	94	106
2023/05	92	103
2023/06	83	95
2023/07	83	91
2023/08	82	92
2023/09	76	88
2023/10	70	80
2023/11	77	85
2023/12	87	90
2024/01	87	92
2024/02	90	94

(continued)

**Table 17.19** (continued)

Stage	Using solar PV	
2024/03	92	100
2024/04	96	105
2024/05	93	102
2024/06	74	93
2024/07	80	87
2024/08	71	81
2024/09	57	72
2024/10	46	65
2024/11	63	71
2024/12	80	84.30508

Source Author

## 17.5 Conclusions

During this study case, each one of the proposed steps had been fulfilled according to the methodology exposed on section III and considering the objectives presented on Chapter I, we can conclude as follows:

The injection of electricity using photo-voltaic solar power plants has developed a new way of dispatch on the Honduran electric system. However, a high uncertainty has been produced during the thermal park operation because it is obligatory to dispatch and the available resources vary. Figure 17.20 shows an overview of this behaviour. Considering an economic dispatch without the price impact of the electric energy generated by the photo-voltaic solar power plants, the SDDP model result during the horizon of the study case is that an estimated of US254 358,220/annual would be saved due to the increase in the marginal cost of generation, this cost increased from 91.96 US/MWh to 112.94 US/MWh.

In order to adequate the optimal electric dispatch operation of Honduran system, the specific case of the photo-voltaic solar power plants needs a deep analysis because, it is a variable source with a high generation potential but it does not provide steady power.

Optimal dispatch considers minimize the sum of immediate cost and generation future cost, estimating the injection of photo-voltaic solar generation to reduce using the thermal sources of generation as shows the Fig. 17.21. It is necessary to review the prices established in the supply contracts between producers and buyers due to the excessive cost compared to the growth based on conventional generation.

## References

1. Chamorro HR, Sevilla FRS, Gonzalez-Longatt F, Rouzbehi K, Chavez H, Sood VK, Innovative primary frequency control in low-inertia power systems based on wide-area RoCoF sharing. <https://doi.org/10.1049/iet-esi.2020.0001>. <https://digital-library.theiet.org/content/journals/10.1049/iet-esi.2020.0001>
2. Chamorro HR, Ordonez CA, Peng JC, Ghandhari M (2016) Non-synchronous generation impact on power systems coherency. *IET Gener Transm Distrib* 10(10):2443–2453. <https://doi.org/10.1049/iet-gtd.2015.1233>
3. Bouffard F, Galiana FD (2008) Stochastic security for operations planning with significant wind power generation. In: 2008 IEEE power and energy society general meeting—conversion and delivery of electrical energy in the 21st Century, pp 1–11
4. Hogan WW (2019) Market design practices: which ones are best? [in my view]. *IEEE Power Energy Mag* 17(1):100–104
5. Ma H, Du W, Wang Q, Gong N (2019) Research on wind-hydro-thermal power system multi-time scale coordinated optimal dispatch. In: IEEE innovative smart grid technologies—Asia (ISGT Asia), pp 2815–2819
6. Ramos A, Rivier M, Garcia-Gonzalez J, Latorre JM, Morales-Espaa G (2016) Assessment of operation reserves in hydrothermal electric systems with high wind generation. In: 2016 13th international conference on the European energy market (EEM), pp 1–5
7. Gil E, Bustos J, Rudnick H (2003) Short-term hydrothermal generation scheduling model using a genetic algorithm. *IEEE Trans Power Syst* 18(4):1256–1264
8. Degeilh Y, Cadoux F, Navid N, Gross G (2012) Economic assessment of the explicit representation of ramping requirements on conventional generators in systems with integrated intermittent resources. In: IEEE power and energy society general meeting, pp 1–5
9. Ortega-Vazquez MA, Kirschen DS (2006) Economic impact assessment of load forecast errors considering the cost of interruptions. In: 2006 IEEE power engineering society general meeting, p 8
10. Gonzalez P, Villar J, Daz CA, Campos FA (2013) Hourly energy and reserve joint dispatch with a hydro-thermal technological based representation. In: 2013 10th International conference on the European energy market (EEM), pp 1–8
11. Peng C, Xie P, Pan L, Yu R (2016) Flexible robust optimization dispatch for hybrid wind/photovoltaic/hydro/thermal power system. *IEEE Trans Smart Grid* 7(2):751–762
12. Zhang Q, Wang X, Yang T (2017) Liang J (2017) Research on scheduling optimisation for an integrated system of wind-photovoltaic-hydro-pumped storage. *J Eng* 13:1210–1214
13. Zhou B, Geng G, Jiang Q (2016) Hydro-thermal-wind coordination in day-ahead unit commitment. *IEEE Trans Power Syst* 31(6):4626–4637
14. Shi L, Wang R, Yao L (2017) Modelling and solutions of coordinated economic dispatch with windhydrothermal complex power source structure. *IET Renew Power Gener* 11(3):262–270
15. Basu M (2019) Combined heat and power dynamic economic dispatch with demand side management incorporating renewable energy sources and pumped hydro energy storage. *IET Gener Transm Distrib* 13(17):3771–3781
16. Yang J, Zhang H, Kang C, Xia Q, Miao M, Tian X (2016) Assessing the dispatch flexibility of coordinated solar and hydro generation. In: 2016 IEEE power and energy society general meeting (PESGM), pp 1–5
17. Meng J, Li G, Du Y (2013) Economic dispatch for power systems with wind and solar energy integration considering reserve risk. In: IEEE PES Asia-Pacific power and energy engineering conference (APPEEC), pp 1–5
18. Das D, Bhattacharya A, Ray RN (2018) Solution of probabilistic economic dispatch in presence of solar power. In: International electrical engineering congress (iEECON), pp 1–4
19. Khan NA, Sidhu GAS, Gao F (2016) Optimizing combined emission economic dispatch for solar integrated power systems. *IEEE Access* 4:3340–3348

20. Surender Reddy S, Bijwe PR, Abhyankar AR (2015) Real-time economic dispatch considering renewable power generation variability and uncertainty over scheduling period. *IEEE Syst J* 9(4):1440–1451
21. Ramadhani P, Sasmono S, Hariyanto N (2018) Impact of intermittency costs due to injection of solar photovoltaics to grid on economic feasibility of existing power plant case study of belitung system. In: Conference on power engineering and renewable energy (ICPERE), pp 1–7
22. Flores WC (2016) Some issues related to the regulatory framework and organizational structure of the Central American electricity market. In: 2016 IEEE PES transmission distribution conference and exposition-Latin America (PES T D-LA), pp 1–5
23. Tobon AG, Chamorro HR, Gonzalez-Longatt F, Sood VK (2019) Reliability assessment in transmission considering intermittent energy resources. In: 2019 IEEE 10th Latin American symposium on circuits systems (LASCAS), pp 193–196
24. Flores WC, Meraz P, Berrios J, Melara D, Barahona C, Sifuentes W (2018) The solar eclipse of august 21, 2017 in Honduras: Evidence of the impact on the power system operation. In: 2018 IEEE PES transmission distribution conference and exhibition—Latin America (T D-LA), pp 1–5
25. Gloria Ramos AA-A, Optimizacin bajo incertidumbre. Universidad Pontificia Comillas
26. Green I (2015) Caiso experience with impact of high penetration of renewable resources on short-term voltage stability. In: IEEE power energy society general meeting, pp 1–18
27. Makarov YV, Loutan C, Ma J, de Mello P (2009) Operational impacts of wind generation on california power systems. *IEEE Trans Power Syst* 24(2):1039–1050. <https://doi.org/10.1109/TPWRS.2009.2016364>
28. Elizondo M, Vallem M, Samaan N, Makarov Y, Vyakaranam B, Nguyen T, Muoz C, Herrera R, Midence D, Shpitsberg A (2016) Transmission reinforcements in the Central American regional power system. In: IEEE power and energy society general meeting (PESGM), pp 1–5
29. Quiros-Tortos J, Valverde G, Arguello A, Ochoa LN (2017) Geo-information is power: using geographical information systems to assess rooftop photovoltaics in costa rica. *IEEE Power Energy Mag* 15(2):48–56
30. Sifuentes WS, Vargas A (2007) Hydrothermal scheduling using benders decomposition: accelerating techniques. *IEEE Trans Power Syst* 22(3):1351–1359

# Chapter 18

## Potential and Financial Analysis of the Floating PV in Hydropower Dams of Thailand



Wanwisa Peanpitak and Jai Govind Singh

### 18.1 Introduction

Global warming and climate changes become increasingly crucial for global issues in recent years. Thus, all countries around the globe should mitigate greenhouse gas emissions, mainly by changing the sources of energy from fossil fuel to renewables. Solar power is one of the alternative sources of energy that is the most widely used because it is clean and abundant. However, installing solar modules on the ground may lead to some issues in the nation that there is insufficient space for installation. During 2014–2018, the cumulative global FPV installed capacity has been growing exponentially (Fig. 18.1). The advantages of reducing evaporation, increasing efficiency, and the utilization of the existing infrastructure and the installation of large-scale FPV in hydropower dams have attracted attention.

The study to find the potential of FPV installation on Lake Pleasant Reservoir in Arizona, USA, found that the possible capacity of FPV can be determined by the total usable area of the reservoir and the mean of the energy density of the existing FPV projects (100 MW/km<sup>2</sup>). The annual energy is approximated by multiplication of capacity with state capacity factor, measured by solar insolation and the number of hours in a year [14]. Kim et al. [18] analyzed the FPV system potential for reservoirs in Korea by considering the water level. The limitations of average water depth in the reservoir higher than 5 m and a minimum of the water depth higher than 1 m were considered. Assuming that 10% of all reservoir areas fulfill the conditions, the annual

---

W. Peanpitak · J. G. Singh (✉)

Department of Energy Environment and Climate Change, School of Environment, Resources and Development, Asian Institute of Technology, 58 Moo 9—Paholyothin Highway, Khlong Nueng, Pathum Thani 12120, Thailand  
e-mail: [jgsingh@ait.ac.th](mailto:jgsingh@ait.ac.th)

W. Peanpitak

e-mail: [wanwisa.p@egat.co.th](mailto:wanwisa.p@egat.co.th)



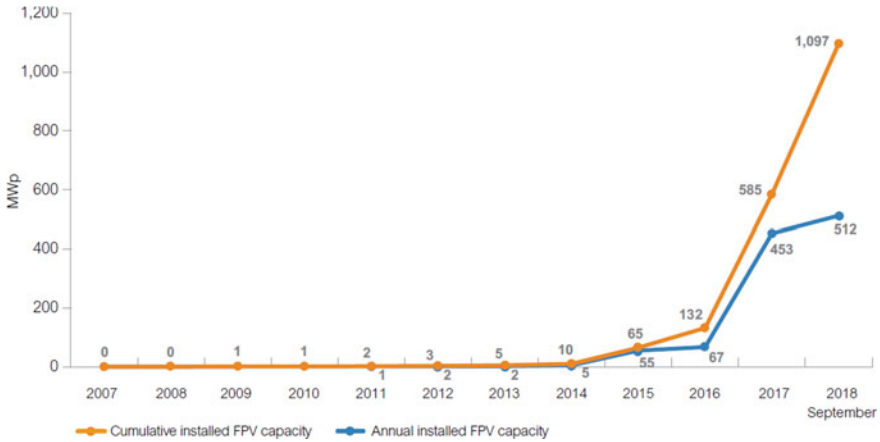


**Fig. 18.1** Global installed floating PV capacity [38]

energy production was approximated to 2932 GWh, and the yearly GHG emission was reduced around 1,294,450 tons. According to a recent study of integrated floating PV (FPV) with the hydroelectric power plant in Pakistan, the potential of the FPV capacity of Ghazi Barotha Reservoir is estimated by using Google Earth to access the ground elevation. This location has a potential of 200 MW at 20% of the surface area [30]. In the case of using FPV in India [35], the total generating capacity of 909.05 Gigawatt and the water saving of 16,233 billion liters would exist. The feasibility analysis of 1 MW FPV at two different locations is determined by using the PVWatts calculation from the National Renewable Energy Laboratory (NREL).

The potential FPV energy productions have been studied in a variety of locations and methods. However, there were some limitations to solar radiation prediction accuracy, which can be improved by using the measured data at the installed site or the nearest station. Also, the detailed economic assessment of FPV projects that include the water-saving benefits and GHG reduction income has not been done. For the comparative financial analysis, the results between the FPV and ground-mounted PV systems, different operating temperatures and the difference in degradation and soiling loss of both systems should be considered. There have been many studies on individual large or small FPV systems in reservoirs, lakes, and shrimp farms. However, very little has been studied on installing FPV systems in the reservoirs having existing hydropower in the whole country. Countries like Thailand need to increase the proportion of electricity production from renewable energy in the long run. Therefore, this study's overall objective is to assess the potential of floating solar PV in hydropower dams of Thailand and analyze their financial viability.

This chapter is divided into four sections. The first section presents the modeling of the components. The second part illustrates the data sources and methods to predict the solar radiance and energy production of FPV systems. The third section demonstrates the results and discussions of potential energy production of FPV and

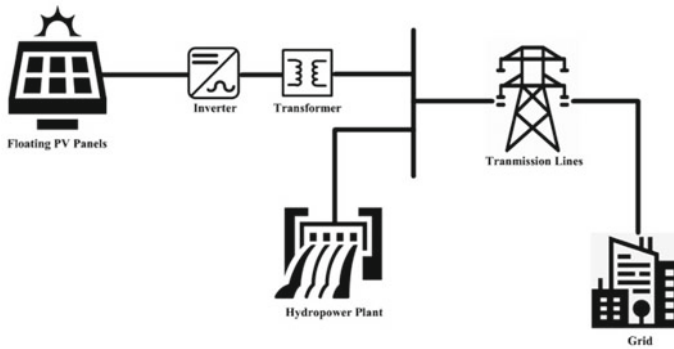


**Fig. 18.2** Schematic diagram of the FPV system connected to the existing hydropower plant and grid. *Source* Author

financial analysis results of FPV compared to the ground-mounted PV system, which is the hypothesis case. The final section presents the conclusion of the study.

## 18.2 Methodology

### 18.2.1 Components Modeling

#### 18.2.1.1 System Description

The reservoir dams chosen in this study are hydropower dams (impoundment type). Figure 18.2 shows the system which consists of PV panels, DC to AC inverter, transformer, hydropower plant, and transmission lines connected to the grid. The transmission lines and the substation of the FPV system are existing equipments of hydropower plants.

#### 18.2.1.2 PV System Parameters, Losses, and Other Assumptions

The PV panel type is assumed to be polycrystalline silicon, widely used because of the balance between performance and price. The characteristics of the PV system considered in this study are described in Table 18.1. In this study, the technical parameters of solar panels and inverters are the values of products that are commercially available and manufactured at an industrial level. The overall energy production and the environmental benefits will also increase if the equipment with better efficiency than Table 18.1 is installed in the reservoir. However, in this case, the total cost will also increase, resulting in an increment in the economic burden. Therefore, the suitable selection should be made according to the technological level and economic

**Table 18.1** Parameters of the PV system considered in this study [18, 36]

Type	Parameters	Value
Solar cell module	Model	SMX-250P
	Length (m)	1.65
	Width (m)	0.94
	Maximum (kW/unit)	0.25
	Efficiency (%)	15.2
	Nominal operating cell temperature (°C)	45 ± 2
	Temperature coefficient (%/°C)	-0.4
Inverter	Model	SPR-12000f
	Efficiency (%)	95.5
	Capacity (kW/unit)	12.5

conditions of installation. According to the National Renewable Energy Laboratory [12], the efficiency of crystalline silicon cells has continuously increased. In 2019, the best research-cell efficiencies for silicon cell technology had achieved more than 26%. Therefore, it is expected that more efficient devices will be installed at a lower price in the future.

The power losses of the grid-connected PV system occur in various components under actual operating conditions. In this study, the losses are estimated as detail given in Table 18.2 [21].

Losses due to temperature effects are included in the energy generation calculation formula in Eq. 18.2. The FPV operating temperature is approximately 3.5 °C lower

**Table 18.2** System loss estimation [21]

Losses	Ground-mounted PV system (%)	FPV system (%)
Miscellaneous capture losses	10.00	9.00
• PV losses due to irradiance level	3.10	3.10
• Array soiling losses	2.10	1.10
• Module array mismatching losses	2.10	2.10
• Module quality losses	1.60	1.60
• DC wiring losses	1.10	1.10
• Other power conditioning losses	1.20	1.20
• Transformer and AC cabling losses	1.20	1.20

than terrestrial PV [23]. The degradation mechanism may be influenced by different climatic zones and for each type of technology. The crystalline silicon remains at around 0.5% per year for systems installed before and after 2000 [16]. The study of [4] states that the degradation rate of the FPV systems is lower than 0.5% p.a. Therefore, the degradation rate of ground-mounted PV systems can be estimated around 0.5% p.a., and the FPV system degradation is assumed to be 0.4% p.a.

Designing at the DC/AC ratio of 1.2 (the module's power rating is 20% larger than the maximum power rating of the inverter) frequently leads to the lowest losses. At the same time, a value of 1.25 or 1.3 can increase the economics of a project, mainly when the restriction of a project size is AC power output [13].

### 18.2.1.3 Energy Delivered by FPV

Akbarzadeh et al. [1] stated that excessive solar radiation and high environmental temperatures could limit the operation of PV modules. Kalogirou et al. [17] have pointed out that module efficiency could be dropped by 0.45% for monocrystalline (c-Si) and polycrystalline (pc-Si) for the rise of each degree of temperature. Another factor that reduces the efficiency of the PV module is dirtiness or dust [25]. FPV systems' efficiency is higher than ground-mounted PV systems due to the cooling effect of water and less dust accumulation. The PV module's temperature can be obtained by the following equation [8].

$$T_m = T_a + \left( \frac{G_T}{G_{T,NOCT}} \right) \left( \frac{9.5}{5.7 + 3.8V} \right) (T_{NOCT} - T_{a,NOCT}) \left[ 1 - \frac{m}{\tau\alpha} \right] \quad (18.1)$$

where  $T_m$  represents the temperature of the PV module (°C),  $T_a$  means to the environmental or ambient temperature (°C),  $G_T$  is sun irradiation (W/m<sup>2</sup>),  $G_{T,NOCT}$  is sun irradiation at nominal operating cell temperature (NOCT) condition (W/m<sup>2</sup>),  $V$  wind speed (m/s),  $T_{NOCT}$  and  $T_{a,NOCT}$  mean the PV module and ambient temperature in the NOCT condition (°C), respectively,  $m$  is the efficiency of the module (%), and  $\tau\alpha$  is the effective transmittance-absorptance product [8].

The yearly electricity production of the PV system can be calculated by applying the RETScreen software formula, which is the development of Natural Resources Canada [29]. RETScreen calculates the amount of power produced by the PV system through Eq. 18.2.

$$E_A = H_t \times S \times \eta_m \times \eta_{inv} \times [1 - \beta_p \times (T_m - 25)] \times (1 - \lambda_p) \times (1 - \lambda_c) \quad (18.2)$$

where  $E_A$  is the power (kWh/h) generated by a PV system,  $H_t$  is solar irradiance per unit area per unit time (kWh/m<sup>2</sup>/h),  $S$  means the total surface area of PV modules (m<sup>2</sup>),  $\eta_m$  is PV module efficiency (0–1),  $\eta_{inv}$  is inverter efficiency,  $\beta_p$  is temperature coefficient associated with the efficiency of the PV module,  $T_m$  (°C) is mean temperature of the PV module,  $\lambda_p$  is loss coefficient of the PV module, and  $\lambda_c$  is loss coefficient of the inverter [29].

## 18.2.2 Proposed Methodology

### 18.2.2.1 Data Sources

The data for predicted PV module temperature and estimated electricity generation consists of solar irradiation, ambient temperature, and wind speed, which are historical data during 2014–2017, and PV module parameters. All data was checked using Microsoft Excel to filter out some missing or error to ensure that blank or abnormal values were neglected. Figure 18.3 demonstrates yearly average hourly solar radiation data, which was global radiation collected from 5 am to 7 pm from January 2014 to December 2017 (48 months) at each location. The ambient temperature and wind speed data came from meteorological stations for four years (the same period as solar radiation).

The ambient temperature data was collected every three hours at 7 am, 10 am, 1 pm, and 4 pm. The hourly ambient temperature was averaged from these four records. Also, the hourly wind speed data collection was the same frequency and time as ambient temperature. The average wind speed was calculated from four values at 7 am, 10 am, 1 pm, and 4 pm, respectively. Then, the PV module temperature was estimated by the input data of ambient temperature, solar radiation, wind speed, and PV module specification.

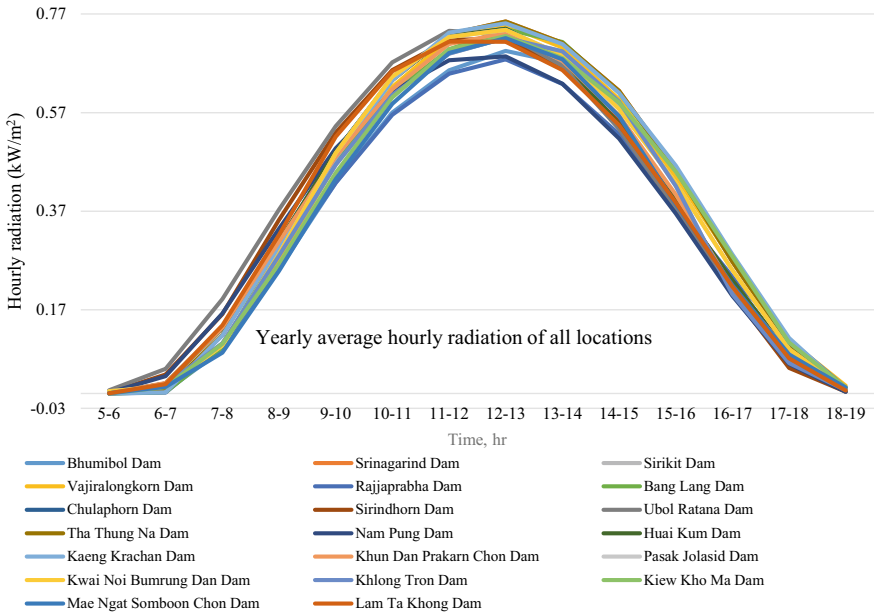


**Fig. 18.3** Yearly average hourly irradiation data of all locations (department of alternative energy and development and efficiency 2019)

**18.2.2.2 Method for Energy Production Estimation**

The energy production and plant capacity factor of the floating PV system at each site is estimated based on the historical data of solar radiation, meteorological info, and FPV system design parameters. Figure 18.4 demonstrates the flowchart used to determine FPV energy production.

The capacity factor value refers to the use of that power plant in production capacity and operating time. A higher capacity value indicates that the power plant is being used more [9].

$$\text{Capacity Factor} = \frac{\text{Gross Actual Generation}}{\text{Gross Maximum Capacity} \times \text{Period Hours}} \times 100 \quad (18.3)$$

The installed FPV capacity at each location is calculated from the formula given in Table 18.3. Here, five different cases are considered as follows:

- Case-I:** the FPV having the same capacity as the hydropower plant with the DC/AC ratio of 1.25;
- Case-II:** the FPV having the same capacity as the hydropower plant with the DC/AC ratio of 1.70;

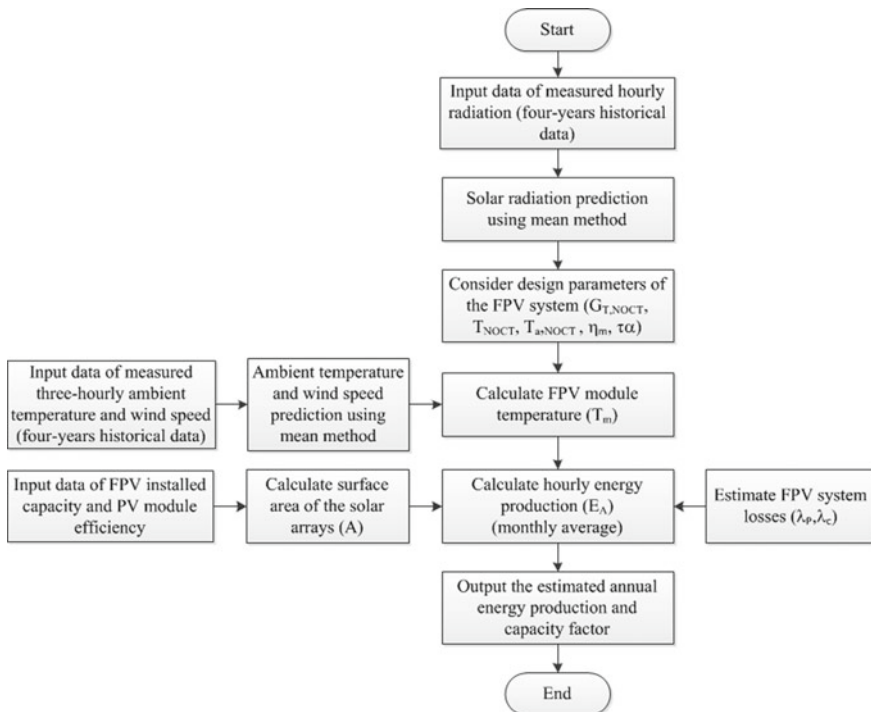


**Fig. 18.4** Flowchart for the estimation of FPV energy production. *Source* Author

**Table 18.3** Input data, method, and formula used to calculate the FPV installed capacity [9, 14, 33]

Cases	Input data to calculate FPV installed capacity	Method	Formula
Case-I	<ul style="list-style-type: none"> <li>Installed capacity of hydropower plants (AC)</li> <li>DC/AC ratio</li> </ul>	Using DC/AC ratio of 1.25 (Oversizing)	FPV installed capacity = 1.25 × HPP installed capacity (AC)
Case-II	<ul style="list-style-type: none"> <li>Installed capacity of hydropower plants (AC)</li> <li>DC/AC ratio</li> </ul>	Using DC/AC ratio of 1.70 (Oversizing)	FPV installed capacity = 1.70 × HPP installed capacity (AC)
Case-III	<ul style="list-style-type: none"> <li>Annual HPP production</li> <li>FPV capacity factor (from Case-I)</li> </ul>	Using gross capacity factor formula	FPV installed capacity = (Annual HPP production)/(FPV capacity factor × 8760) × 100
Case-IV, Case-V	<ul style="list-style-type: none"> <li>% area covered by FPV</li> <li>Reservoir water surface</li> <li>The FPV energy density (power per unit area)</li> </ul>	Using the FPV energy density of 100 MWp/km <sup>2</sup>	FPV installed capacity = (% area covered by FPV) × Reservoir water surface × FPV energy density

**Case-III:** the condition in which the installation of FPV plants can replace the electricity produced from hydropower plants;

**Case-IV:** the FPV power plants covering the water surface of 5%, and

**Case-V:** the FPV power plants covering the water surface of 10%.

For Cases-I, II, and III, the surface area of the solar array can be computed by applying Eq. 18.4.

$$\eta_{el} = \frac{P_{max}}{S \times A} \times 100\% \tag{18.4}$$

where  $\eta_{el}$  refers to the electrical efficiency of the PV module (%),  $P_{max}$  represents the power produced from the PV module (W),  $S$  is the solar radiation intensity incident on the PV module (W/m<sup>2</sup>) and  $A$  refers to the front PV module surface exposed to the solar radiance (m<sup>2</sup>). Then, the PV system’s annual electricity production is computed, applying the expression of Eq. 18.2 [29].

### 18.2.3 Test System and Data

The accuracy of the method used to calculate PV module temperature and energy production was verified by comparing the measured module temperature and energy

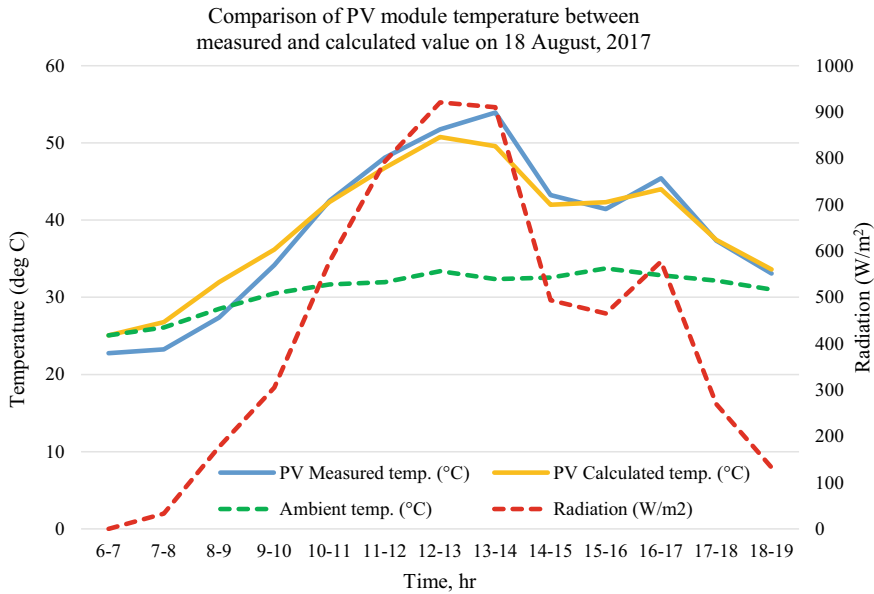


**Fig. 18.5** Comparison of PV module temperature between measured and calculated value. *Source* Author

read from the meter with the calculated values. The hourly data of the PV system at the ET buildings in Asian Institute of Technology (AIT), Thailand, on August 18, 2017, was collected. The result in Fig. 18.5 shows that the calculated module temperature is approximately 0.9% higher than the measured value. Also, the energy from the AC meter is higher than the calculation of around 4.7%, as shown in Fig. 18.6. Therefore, the methodology used for PV module temperature and energy production prediction has an error of approximately 1–5%, which is acceptable.

### 18.3 Results and Discussions

The economic analysis is evaluated for all five cases of potential energy production. Then, the financial analysis of FPV projects is compared with terrestrial PV projects to analyze the differences.

#### 18.3.1 The Energy Production Estimation Results

The condition of 125% oversizing presents that the total electricity produced from all FPV locations is estimated at around 5771 GWh/year, which accounts for 1.96 km<sup>2</sup>



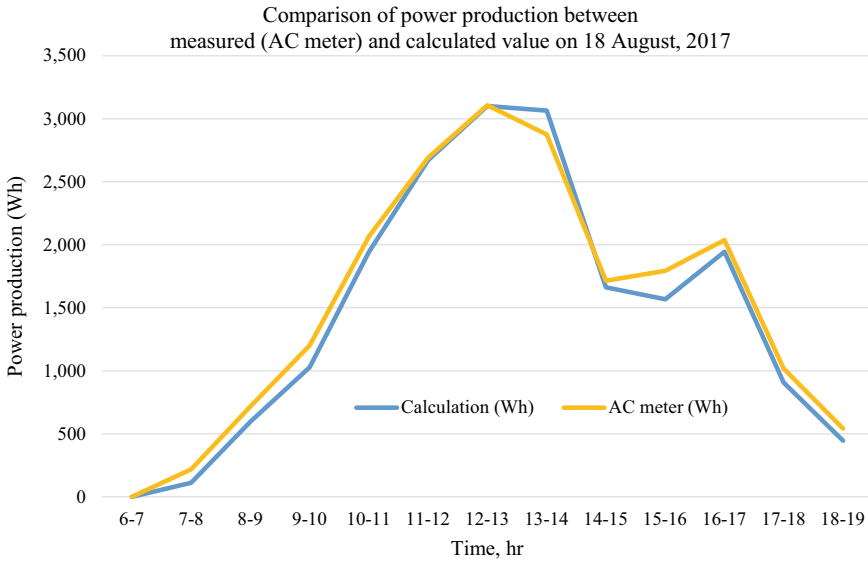


**Fig. 18.6** Comparison of power production between measured and calculated value. *Source* Author

or only 2% of surface area coverage (on average). The condition of the DC/AC ratio of 170% illustrates that it can produce total annual electricity of about 7648 GWh, with the average surface area of 2.6 km<sup>2</sup> or 2.5%. The energy output and surface area coverage of FPV systems in the condition that DC/AC ratio is 170% can generate more electricity than the DC/AC ratio of 125% about 1877 GWh or 32.5% per year.

Case-III is when the installation of FPV plants can replace the electricity produced from hydroelectric plants (around 5511 GWh/year). While the total installed capacity of the hydropower plant is 3845 MW, the total installed capacity of the floating solar system, in this case, is 3758 MWp, which is close to the Case-I (the installed capacity is 3928 MWp).

Cases-IV and V are assumed that the FPV power plants are installed, covering the water surface of 5% and 10%, respectively. The installation of FPV plants covering the 5% of surface area can produce electric energy around 20,049 GWh/year, with the average water surface area of 6.7 km<sup>2</sup>. The installation of FPV systems covering 10% of the surface area is expected to produce 40,096 GWh/year, which accounts for 13.4 km<sup>2</sup> of surface area coverage (on average).

### 18.3.2 Financial Assessment

#### 18.3.2.1 Evaporation Reduction

Table 18.4 demonstrates the energy density (power per unit area) of utility-scale FPV systems in the existing literatures. The average energy density of all considered projects is about 105 MWp/km<sup>2</sup>. In this study, a standard energy density of 100 MWp/km<sup>2</sup> is used to assess the installation area of the FPV system.

The energy density is one of the input data to estimate the area covered by FPV. The water surface area covered by floating PV structure results in the saving of water evaporation. Water evaporation evaluation is complex, and there are many models and factors to consider [31]. Therefore, the detail finding of evaporated water is outside the scope and capability of this study. Based on the FPV installation experience by various installers, the amount of water saving from FPV system installation can be considered at 1.25 million m<sup>3</sup> per year per km<sup>2</sup> of the FPV area [34].

For the financial evaluation of water saving, the amount of saved water can be converted into two forms, i.e., energy and agricultural value. Converting water saving to the electricity can be done by dividing the amount of water that can be saved by the average water rate (water consumption for a kWh of electricity) of each hydropower plant from Eq. 18.5.

$$\text{Electricity} \left[ \frac{\text{MWh}}{\text{year}} \right] = \frac{\text{Water - saving} \times 1000 [\text{million m}^3]}{\text{HPP water rate} \left[ \frac{\text{m}^3}{\text{kWh}} \right]} \quad (18.5)$$

Due to the water use throughout the life of each plant in each region, the water value for agriculture is different. In estimating the value of water for agriculture, it is important to know the parameters, e.g., including the type of plants, the amount of water used throughout the plant's life, the yield per rai, the selling price per ton, and the farming costs. In this study, the reference plant is jasmine rice, the main agricultural product of Thailand. Water consumption throughout the life of rice is

**Table 18.4** Energy density of large FPV projects [3, 14, 20, 27]

Project location	Installed capacity	Area coverage	Energy density	Reference
India	82 MW	20%	1 kWp/10 m <sup>2</sup> or 100 MWp/km <sup>2</sup>	[27]
Global	Same as the first 20 largest HPP in the world	3.5% (average)	120 Wp/m <sup>2</sup> or 120 MWp/km <sup>2</sup>	[3]
India	4 MW	–	10 kWp/100 m <sup>2</sup> or 100 MWp/km <sup>2</sup>	[20]
USA	12 MW	0.70%	100 MWp/km <sup>2</sup>	[14]
Average	–	–	105 MWp/km <sup>2</sup>	–

**Table 18.5** Input parameters for evaluation of water value for agriculture [6, 28, 32, 37]

Parameters	Value	Unit	Reference/comments
Average annual rice production	0.453	ton/rai	[28]
Average water consumption of rice throughout the life	1122	m <sup>3</sup> /rai	[32]
Average paddy price in year 2018	542.72	USD/ton	[37]
Average farming cost	152.64	USD/rai	[6]
Average farming income	93.21	USD/rai	Calculation (Eq 18.6)
Water value for agriculture	0.083	USD/m <sup>3</sup>	Calculation (Eq 18.7)

calculated from the national average. Table 18.5 shows the input parameters used to evaluate the value of water for agriculture, which can be calculated from the Eqs. 18.6 and 18.7.

$$\begin{aligned}
 \text{Average farming income} &= \left( \text{Average annual rice production} \left[ \frac{\text{ton}}{\text{rai}} \right] \right. \\
 &\quad \times \text{Average paddy price} \left[ \frac{\text{USD}}{\text{ton}} \right] \Bigg) \\
 &\quad - \text{Average farming cost} [\text{USD}/\text{rai}] \quad (18.6)
 \end{aligned}$$

$$\begin{aligned}
 \text{Water value for agriculture} [\text{USD}] &= \frac{\text{water saving} [\text{m}^3]}{\text{Average water consumption of plant} \left[ \frac{\text{m}^3}{\text{rai}} \right]} \\
 &\quad \times \text{Average farming income} [\text{USD}/\text{rai}] \quad (18.7)
 \end{aligned}$$

### 18.3.2.2 Greenhouse Gas Emissions Reduction

In this study, greenhouse gas emission reduction is calculated to determine the amount of CO<sub>2</sub> that can be reduced from electricity production by floating solar power plants. The standard values of Thailand greenhouse gas emissions promulgated by the Greenhouse Gas Management Organization on September 28, 2017, (0.5692 tCO<sub>2</sub>/MWh) and the average loss of power/energy transmission and distribution (0.06112) from the EIA statistics data source are used for the analysis of greenhouse gas emissions gained from the installation of a floating PV system (Eq. 18.8).

$$G_t = E_s \times 10^{-3} \times G \times (1 + b) \quad (18.8)$$

Here,  $G_t$  refers to the amount of greenhouse gas emissions that can be reduced (tCO<sub>2</sub>/year).  $E_s$  is the electrical energy generated from the FPV power plant per year (MWh/year).  $G$  is the standard value of each country’s greenhouse gas emissions

( $\text{tCO}_2/\text{year}$ ) and  $\beta$  represents the average rate of transmission and distribution loss (6.1112% in the year 2014).

Currently, it seems there is no actual market for carbon trading in Thailand. There is only a purchase called over the counter (OTC) or voluntary market trading, which the CDM project developers and countries in Annex-I are trading credits through financial funds agents and brokers. However, the Greenhouse Gas Management Organization has studied the appropriate carbon credit price in Thailand. The purpose of their study is to evaluate the feasibility of carbon prices in Thailand. The result shows that the cost of implementing a typical greenhouse gas reduction project is between 190 and 1390 Baht/ $\text{tCO}_2\text{e}$  (6.08–44.48 USD/ $\text{tCO}_2\text{e}$ ) [24]. Therefore, the carbon price of Thailand should not lower than 6.08 USD/ $\text{tCO}_2\text{e}$ . This study considers the average value of the carbon price of 25.28 USD/ $\text{tCO}_2\text{e}$  for economic evaluation. Compared with EU ETS (32.46 USD/ $\text{tCO}_2\text{e}$ ), this reference price is lower, but it is close to Korea ETS (24.20 USD/ $\text{tCO}_2\text{e}$ ). Nevertheless, this price is somewhat higher than Switzerland's ETS (7.19 USD/ $\text{tCO}_2\text{e}$ ) and Shanghai's ETS (5.81 USD/ $\text{tCO}_2\text{e}$ ).

### 18.3.2.3 Financial Evaluation

The detailed financial evaluation of FPV projects that include the water-saving value from evaporation reduction and GHG emissions reduction benefit is discussed in Sections-A.1 and A.2, respectively. This section describes the overall results of the annual economic benefits of each case study (Case-I to Case-V). Table 18.6 shows a summary of the annual financial assessment of all case studies. The outcomes illustrate that the minimal benefits occurred in Case-III (to replace HPP production), which correspond with the estimated energy yield and water surface area coverage. In Case-III, it presents that the amount of saving 46.98 million  $\text{m}^3$  of evaporated water from nineteen reservoirs can be used to produce annual electricity of about 9487 MWh, and saving water for agriculture is worth approximately 3.90 million USD per year. The total FPV energy production of 5511 GWh results in a reduction of around 3.33 million  $\text{tCO}_2/\text{year}$ , which equals to the revenue of 84.15 million USD/year if the carbon price is implemented. The financial evaluation results of Case-I (FPV capacity equals to HPP, with DC to AC ratio of 1.25) and Case-III (to replace HPP production) are slightly different. The economic benefits of Case-II (FPV capacity equals to HPP, with 170% DC to AC ratio) have improved from Cases-I and II around 30–40%. The maximum economic outcomes were found in Case-V (FPV covers 10% of the surface area), according to the estimated maximum energy and surface area; as a result, it was expected to produce the energy of 40,096 GWh/year. This equals the amount of GHG reduction of approximately 24.22 million  $\text{tCO}_2/\text{year}$ . The total GHG revenue is worth nearly 612 million USD/year. The annual water evaporation reduction of 335.55 million  $\text{m}^3/\text{year}$  is valuable for agriculture, about 27.85 million USD/year, and approximately 50,461 MWh/year for electricity production. Also, the economic advantages of Case-V are twice as much as the Case-IV (FPV covers 5% of the surface area).

**Table 18.6** Summary of annual economic benefits of FPV systems

Cases	Description	Estimated energy production (GWh/year)	Water evaporation reduction			GHG emissions reduction	
			Amount (million m <sup>3</sup> )	Equivalent to electricity (MWh/year)	Water value for agriculture (million USD)	Amount (million tCO <sub>2</sub> /year)	Revenue (million USD/year)
Case-I	FPV equals to the existing HPP with DC/AC ratio of 1.25	5770.99	49.10	9625.90	4.076	3.486	88.12
Case-II	FPV equals to existing HPP with DC/AC ratio of 1.70	7648.05	65.11	13,091.30	5.404	4.619	116.78
Case-III	FPV energy can replace hydropower production	5511.04	46.98	9486.50	3.899	3.329	84.15
Case-IV	FPV covers 5% of the surface area	20,047.76	167.77	25,230.60	13.925	12.109	306.1
Case-V	FPV covers 10% of the surface area	40,095.53	335.55	50,461.10	27.850	24.217	612.21

Source Author

### ***18.3.3 Financial Evaluation of FPV Compared to the Ground-Mounted PV Systems***

In this study, the financial assessment was made in terms of the FPV systems' cost, the profits from electricity generation, GHG emission reduction, and evaporated water saving. The 16 projects in nine hydropower dams [26] and the other 10 projects are considered in this study. To simplify the financial study, five projects in different sizes chosen as the representative for financial viability study whose capacities are close to 5, 50, 100, 200, and 300 MW, respectively. These projects are at four locations included Sirikit Dam, Bang Lang Dam, Chulaphorn Dam, and Kiew Kho Ma Dam. To compare the financial benefits, the same capacity of ground-mounted PV systems is assumed as the hypothesis case to install at the same site (same solar radiance and weather conditions). Then, the financial analysis of both systems is

**Table 18.7** Wholesale electricity rates for MEA and PEA [10]

Trans. line voltage	Electricity cost		Transmission cost		Total wholesale cost		Average electricity cost	
	Peak	Off-Peak	Peak	Off-Peak	Peak	Off-Peak	(Baht/kWh)	(USD/MWh)
230 kV	3.1192	2.3316	0.2730	–	3.3922	2.3316	3.035	94.8
69–115 kV	3.1286	2.3341	0.4913	–	3.6199	2.3341	3.187	99.6
At the end of the trans. line 69–115 kV	3.1948	2.3555	0.8528	–	4.0476	2.3555	3.477	108.7
11–33 kV	3.2017	2.3567	1.0226	–	4.2243	2.3567	3.595	112.3

performed throughout the lifetime to compare their profitability. The financial parameters include net present value (NPV), payback period, internal rate of return (IRR), benefit–cost ratio (BC ratio), and levelized cost of electricity (LCOE).

For electricity tariff, the average electricity price that EGAT wholesale to PEA and MEA is used here. The average wholesale price is derived from the time of use rate (TOU) by excluding wholesale Ft (variable fuel cost). The average electricity price is calculated by considering that the floating PV plant operating time is from 6 am to 6 pm every day. Total peak day and the off-peak day in one year are 242 and 123 days, respectively. Table 18.7 shows the average electricity price of each transmission voltage level (the exchange rate on January 28, 2020, is 31.25 THB/USD).

Peak period           09:00–22:00 Monday-Friday  
Off-Peak period       22:00–09:00 Monday-Friday  
                              00:00–24:00 Saturday-Sunday, National Labor Day and public holidays (excluding substitution holidays and The Royal Plowing Ceremony Day)

The cost of the FPV system can be divided into the initial installation and operating and maintenance expenditures. The capital investment of projects sized equal to or larger than 2 MW is considered utility-scale according to NREL’s assumption [12]. Figure 18.7 presents the capital cost versus the installed capacity of the FPV systems according to the compilation from the floating solar market report and previous studies of the FPV systems. Due to the investment cost of FPV, projects larger than 150 MWp are not available. The linear extrapolation in excel is created to forecast the FPV installation cost. However, using the extrapolate trend of the existing capital cost of FPV projects (blue dot) could not predict the cost of FPV, which is more than 350 MWp capacity (the cost has a negative value). This results from the fluctuation of the FPV system cost, especially on small systems (less than 10 MW). To solve this problem, this study considers the cost of an FPV system with a capacity higher than 10 MWp and adjusts the slope of FPV cost by implementing the deviation of the PV system cost. Figure 18.7 also shows the comparison of FPV investment cost before and after the slope adjustment. After that, the expenditures versus the installed capacity of the FPV compared to ground-mounted PV systems are presented in

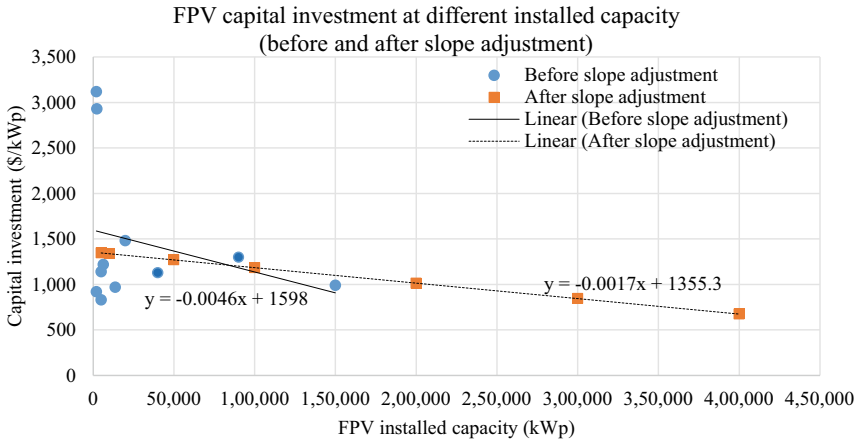


**Fig. 18.7** Capital investment of FPV projects versus the system size. *Source* Author

Fig. 18.8. The linear lines are estimated according to the capital cost of the previous projects and the assumed cost of 200, 300, and 400 MWp systems by using the deviation in cost of PV systems sized 50 and 100 MWp. From this estimation, the installation cost of the FPV system is higher than the PV system, about 7% on average. In this study, if the project size is more than 400 MWp, the initial cost is estimated to be the same as the 400 MW cost. It is crucial to note that these are estimated costs that need to be revised when more data from large-scale FPV systems around the world is available. In addition, the design and location also affect the expenditure of a specific FPV project.

Table 18.8 illustrates the approximated operating and maintenance costs of land-based PV and floating PV systems. The literature survey results on annual operation

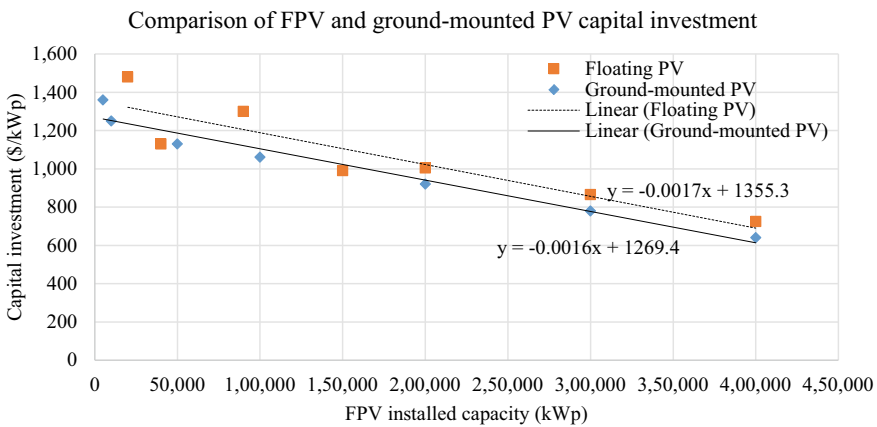


**Fig. 18.8** Comparison of FPV and ground-mounted PV installation cost. *Source* Author

**Table 18.8** Estimated operating and maintenance costs for terrestrial PV and FPV systems [2, 5, 7, 11, 18, 19, 22, 38]

Utility-scale fixed tilt	O&M (\$/Wp/year)	Geographic focus	PV system type
[11]	0.0154	United States	Ground-mounted
[22]	0.0090	United States	Ground-mounted
[19]	2.5% of CAPEX	Germany	Ground-mounted
[38]	0.0110	General assumption	Ground-mounted/FPV
Domnoen et al. (2017)	0.0128	Thailand	Ground-mounted
[7]	0.0180	Montenegro (Europe)	FPV
[2]	2% of CAPEX	Thailand	Ground-mounted/FPV
[18]	0.0104	Korea	FPV
Average ground-mounted PV	0.0121	–	–
Average FPV	0.0131	–	–

and maintenance expenditures during 2017–2019 show that the average operating and maintenance cost of ground-mounted PV and FPV systems is approximately 0.0121 and 0.0131 USD/kWp, respectively.

The sources of parameters in financial analysis are shown in Table 18.9.

The two scenarios of financial analysis in this study are shown in Fig. 18.9. For FPV power plants, the first scenario (Scenario-I) considers direct benefits, including revenue from FPV electricity and energy production from the amount of water that can be saved by reducing evaporation. In the second scenario (Scenario-II), all economic benefits are included to be revenue (energy production, GHG emissions reduction, and water saving from evaporation reduction). However, for land-based PV systems, Scenario-I includes only energy generation, while Scenario-II consists of revenue from GHG emission reduction and electricity generation. The two scenarios are analyzed in both FPV and land-based PV systems to compare the financial analysis results. The ground-mounted PV system is the hypothesis for the comparison purpose.

**Table 18.9** Reference of parameters for financial analysis [15, 38] (Bank of Thailand 2019)

Parameters	References
Project lifetime	Based on the longest lifetime of the system’s component
Discount rate	The standard discount rate for non-OECD countries [15]
Inflation rate	Thailand inflation rate 10 years average
Lending interest rate	World Bank lending interest rate [38]



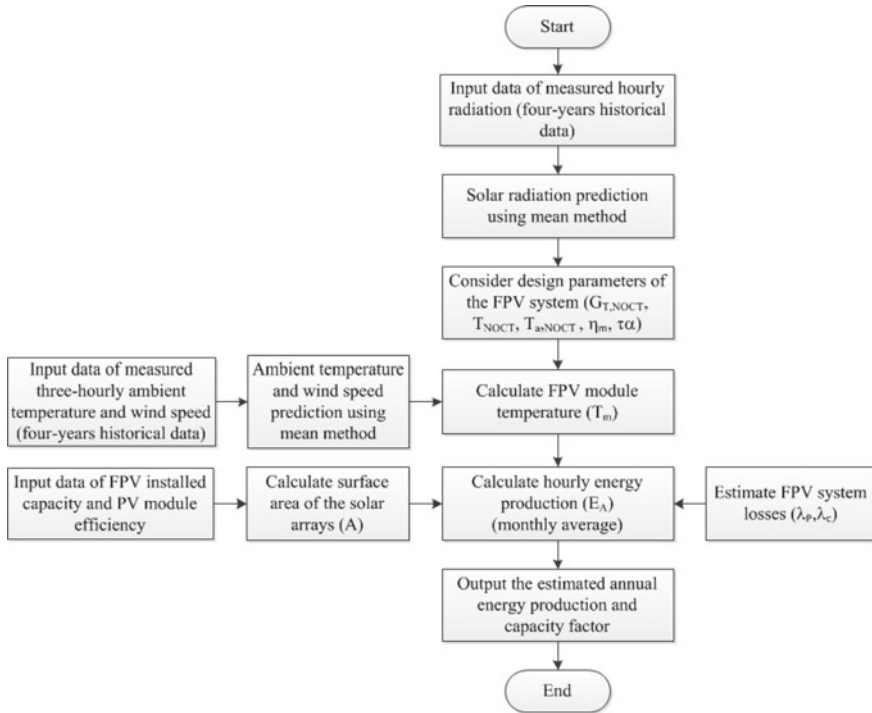


Fig. 18.9 Two scenarios of financial analysis. Source Author

The amount of energy yield and economic outcomes of FPV and ground-mounted PV systems are estimated in which all parameters of FPV and ground-mounted PV are the same except the module temperature, soiling losses, and degradation rate because of the effect of different operating conditions. The financial feasibility of the project is performed using RETScreen software. It is assumed that the FPV and ground-mounted PV systems are in the same location. The economic analysis for the equal installed capacity of FPV and ground-mounted PV systems were performed throughout the 25 years lifetime to compare their profitability.

**18.3.3.1 Financial Evaluation Results of Case-I and Case-II**

This section performs the financial evaluation of FPV and ground-mounted PV systems for Case-I and Case-II with two scenarios for each PV system type. Case-I and Case-II are the conditions that the installed capacity of FPV must equal to existing HPP capacity (AC power output is limited to equal to hydropower plant). The differences between these two cases are DC/AC ratio which is 1.25 and 1.70 for Case-I and Case-II, respectively. The results show that although a greater DC/AC ratio in Case-II results in an increase in capital expenditures, it could produce more

energy. The financial evaluation can perform to compare the difference in profits between these two cases.

Table 18.10 presents the financial analysis results of FPV compared to ground-mounted PV projects for Case-I (FPV equals to HPP capacity with DC/AC ratio of 1.25). All projects have positive NPV values. The payback periods of all studied sites are shorter than the project's lifetime, and the IRR value is higher than the discount rate.

Figure 18.10 illustrates the comparison of NPV on FPV and land-based PV projects. In Scenario-I, the NPV of all FPV systems is positive and close to the ground-mounted PV projects. In Scenario-II, when all benefits are included, the NPV of the FPV systems is mostly equal or higher than the on-ground PV system.

Figure 18.11 demonstrates the IRR for FPV and terrestrial PV systems. The IRR of FPV projects in Case-I ranges between 16 and 33%. However, its value of FPV plants is about 1–2% lower than terrestrial PV plants. When all economic benefits are considered, the IRR value increases by about 2–8% from only energy production.

The comparison of payback periods between FPV and land-based PV systems is shown in Fig. 18.12. The FPV's values are longer than ground-mounted PV around 0.4 years on average.

Figure 18.13 illustrates the comparison of the BC ratio on FPV and ground-mounted PV projects. All FPV projects achieve the BC ratio of more than one. The FPV projects sized more than or higher than 300 MW have the highest BC ratio. The BC ratios of all terrestrial PV plants are higher than FPV plants, but it is not significant (about 0.1% on average).

The cost of electricity or the LCOE of Scenario-II is not calculated because some benefits are not directly affected by the cost of FPV power plants (GHG emissions reduction revenue). Figure 18.14 shows the cost of electricity of floating PV systems compared with global average utility-scale PV projects. The FPV project, whose size is more than or equal to 76 MW, has an electricity cost that is competitive with global terrestrial PV systems. The average electricity cost of the FPV project is approximately 0.081 USD/kWh, which is lower than the global weighted-average LCOE of utility-scale solar PV projects commissioned in 2018 (0.085 USD/kWh).

Table 18.11 presents the financial analysis results of FPV compared to land-based PV projects for Case-II (FPV equals to HPP capacity with DC/AC ratio of 1.70). From the results of financial analysis, it could be observed that the FPV projects are still attractive even after increasing its size or capacity (increase in installation cost). The comparison of financial indicators between FPV and terrestrial PV systems in Case-II found that there is a tendency for differences like Case-I, as shown in Figs. 18.15, 18.16, 18.17 and 18.18.

Figure 18.19 shows the average FPV electricity price of 0.078 USD/kWh, which is lower than Case-I.

Figures 18.20 and 18.21 illustrate the comparing of NPV and IRR of Case-I (FPV capacity equals to HPP capacity with the DC/AC ratio of 1.25) and Case-II (FPV capacity equals to HPP capacity with the DC/AC ratio of 1.70). The NPV of Case-II tends to increase from Case-I considerably following the project size, while the IRR slightly improves.

**Table 18.10** Financial analysis results of FPV compared to ground-mounted PV projects in Case-I (FPV equals to HPP capacity with DC/AC ratio of 1.25)

Project type	Scenario	Project size (MW)	Reservoir name	NPV (million USD)	Payback period (years)	IRR (%)	BC ratio
FPV	Scenario-I: include only energy production benefit	5.5	Kiew Kho Ma Dam	2.8	8.9	16.3	1.8
		40.0	Chulaphorn Dam	16.9	9.2	15.5	1.7
		76.0	Bang Lang Dam	39.6	8.6	17.2	1.9
		175.0	Sirikit Dam Phase I	93.0	8.0	18.9	2.1
		325.0	Sirikit Dam Phase II	284.3	5.4	32.6	3.6
	Scenario-II: include all economic benefits	5.5	Kiew Kho Ma Dam	4.6	7.7	20.2	2.2
		40.0	Chulaphorn Dam	29.9	7.8	19.7	2.2
		76.0	Bang Lang Dam	64.9	7.3	21.9	2.4
		175.0	Sirikit Dam Phase I	147.1	6.8	24.3	2.7
		325.0	Sirikit Dam Phase II	384.8	4.6	41.1	4.6
Ground-mounted PV (hypothesis)	Scenario-I: include only energy production benefit	5.5	Kiew Kho Ma Dam	3.0	8.5	17.2	1.9
		40.0	Chulaphorn Dam	17.6	8.9	16.2	1.7
		76.0	Bang Lang Dam	41.8	8.2	18.2	2.0
		175.0	Sirikit Dam Phase I	96.3	7.7	20.0	2.2
		325.0	Sirikit Dam Phase II	284.2	5.2	34.7	3.8
	Scenario-II: include all economic benefits	5.5	Kiew Kho Ma Dam	4.6	7.4	21.2	2.3
		40.0	Chulaphorn Dam	29.8	7.6	20.4	2.3
		76.0	Bang Lang Dam	65.2	7.0	22.9	2.5
		175.0	Sirikit Dam Phase I	146.7	6.5	25.4	2.8
		325.0	Sirikit Dam Phase II	377.6	4.4	43.2	4.8

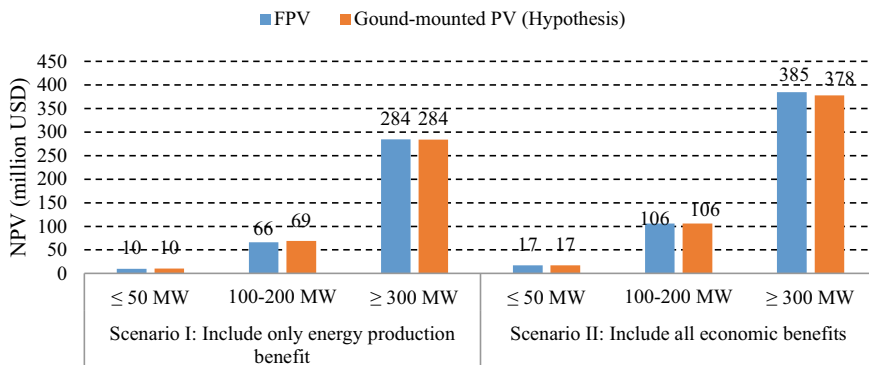


Fig. 18.10 NPV for FPV compared to ground-mounted PV projects (Case-I). Source Author

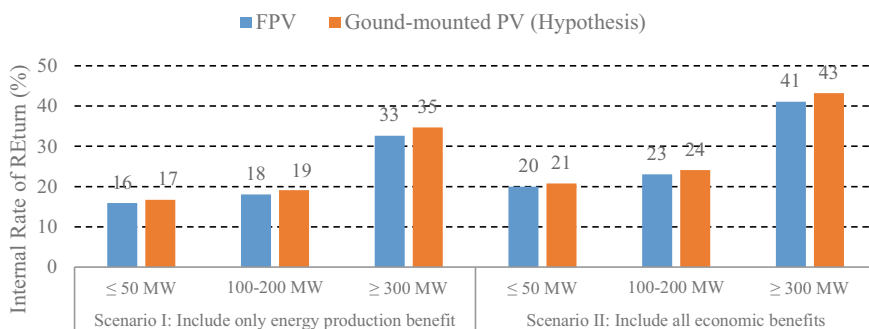


Fig. 18.11 IRR for FPV and terrestrial PV systems (Case-I). Source Author

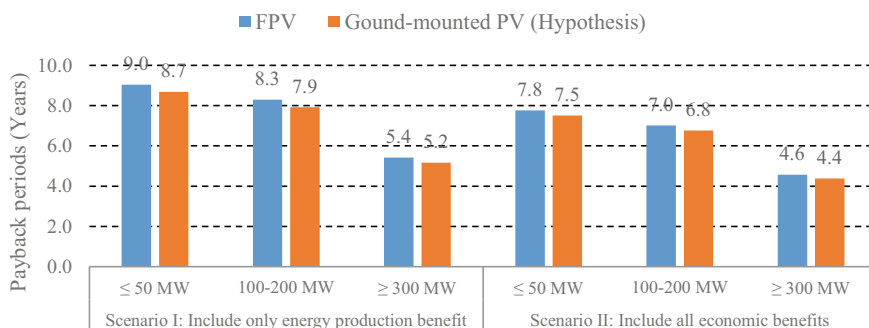
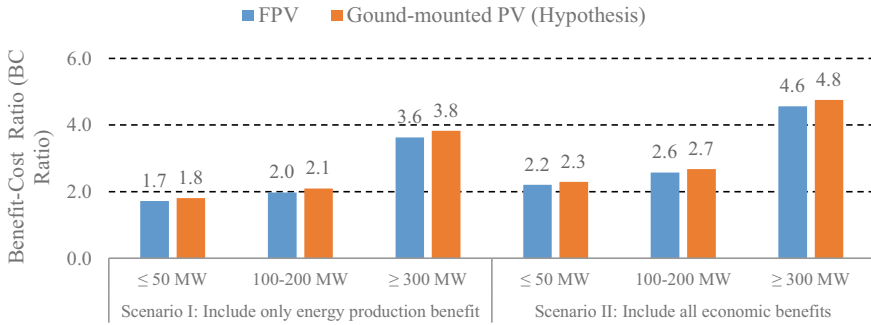
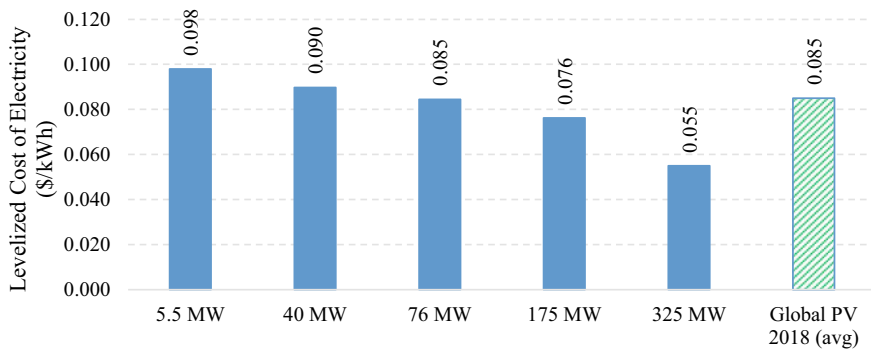


Fig. 18.12 Payback period of FPV compared to land-based PV plants (Case-I). Source Author



**Fig. 18.13** BC ratio of FPV compared to land-based PV plants (Case-I). *Source* Author



**Fig. 18.14** Electricity cost of different FPV system sizes (Case-I). *Source* Author

**18.3.3.2 Financial Evaluation Results of Case-IV and Case-V**

The financial evaluation results of Case-IV (FPV covers 5% of the surface area) are demonstrated in Table 18.12. The simulation results show that all projects can get profits. Comparing with the land-based PV systems, it is the same trend as the previous three case studies. The terrestrial projects are likely to be better than FPV, but not much different.

Table 18.13 shows the financial results of Case-V (FPV covers 10% of the surface area). The FPV power plant size of more than 300 MW can generate the highest profit compared to the Case-I to Case-IV.

Overall, larger FPV projects tend to have lower electricity costs and higher profitability. When all the FPV benefits in this study are included in the economic analysis in Scenario-II, all financial indicators of the FPV system except NPV are still less than the ground-mounted PV system, but it is not notable. Even the FPV systems’ costs are higher than the overland PV system; there are benefits gained from energy production due to the reduction in operating temperature and water-saving.

**Table 18.11** Financial analysis results of FPV compared to ground-mounted PV projects in Case-II (FPV equals to HPP capacity with DC/AC ratio of 1.70)

Project type	Scenario	Project size (MW)	Reservoir name	NPV (million USD)	Payback period (years)	IRR (%)	BC ratio
FPV	Scenario-I: include only energy production benefit	5.5	Kiew Kho Ma Dam	3.9	8.8	16.4	1.8
		40.0	Chulaphorn Dam	24.7	9.0	16.0	1.7
		76.0	Bang Lang Dam	60.7	8.1	18.5	2.0
		175.0	Sirikit Dam Phase I	160.7	6.9	23.3	2.6
		325.0	Sirikit Dam Phase II	386.7	5.4	32.6	3.6
	Scenario-II: include all economic benefits	5.5	Kiew Kho Ma Dam	6.3	7.7	20.3	2.3
		40.0	Chulaphorn Dam	42.4	7.7	20.4	2.3
		76.0	Bang Lang Dam	94.8	6.9	23.4	2.6
		175.0	Sirikit Dam Phase I	234.2	5.8	29.6	3.3
		325.0	Sirikit Dam Phase II	523.3	4.6	41.1	4.6
Ground-mounted PV (hypothesis)	Scenario-I: include only energy production benefit	5.5	Kiew Kho Ma Dam	4.1	8.5	17.3	1.9
		40.0	Chulaphorn Dam	25.6	8.7	16.7	1.8
		76.0	Bang Lang Dam	62.9	7.8	19.6	2.1
		175.0	Sirikit Dam Phase I	163.4	6.6	24.7	2.7
		325.0	Sirikit Dam Phase II	386.5	5.2	34.7	3.8
	Scenario-II: include all economic benefits	5.5	Kiew Kho Ma Dam	6.3	7.4	21.3	2.4
		40.0	Chulaphorn Dam	42.1	7.4	21.1	2.3
		76.0	Bang Lang Dam	94.7	6.7	24.5	2.7
		175.0	Sirikit Dam Phase I	231.8	5.6	31.1	3.5

(continued)

**Table 18.11** (continued)

Project type	Scenario	Project size (MW)	Reservoir name	NPV (million USD)	Payback period (years)	IRR (%)	BC ratio
		325.0	Sirikit Dam Phase II	513.6	4.4	43.2	4.8

Source Author

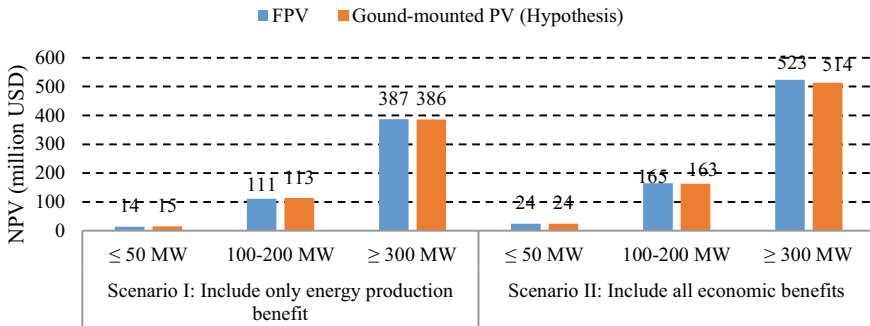


**Fig. 18.15** NPV for FPV compared to ground-mounted PV projects (Case-II). Source Author

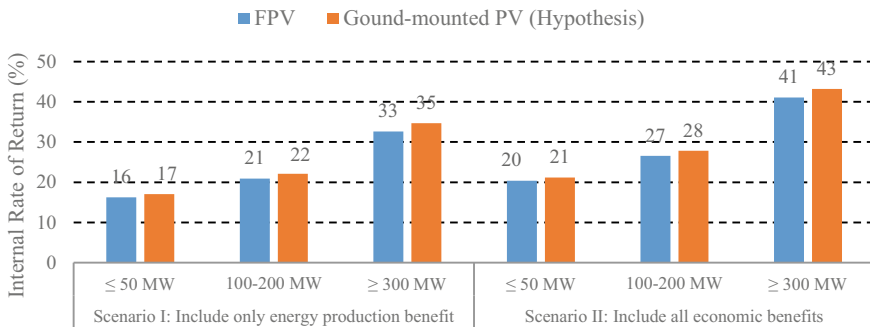


**Fig. 18.16** IRR for FPV and terrestrial PV systems (Case-II). Source Author

Although the financial analysis results of all five cases cannot be directly compared because of different conditions, the pros and cons of the FPV installation in all five case studies can be discussed. Case-I and Case-II are the most possible because the existing transmission system can be utilized without the transmission system constraint. Also, the installation of the FPV system with a DC to AC ratio of 170% (Case-II) can obtain more profits in terms of NPV than an installation with a DC to AC ratio of 125% because the energy production grows up around 36%, while the installation costs increase about 30%. In Case-III, though, the overall results are close to the first case. However, to produce the same amount of electricity as

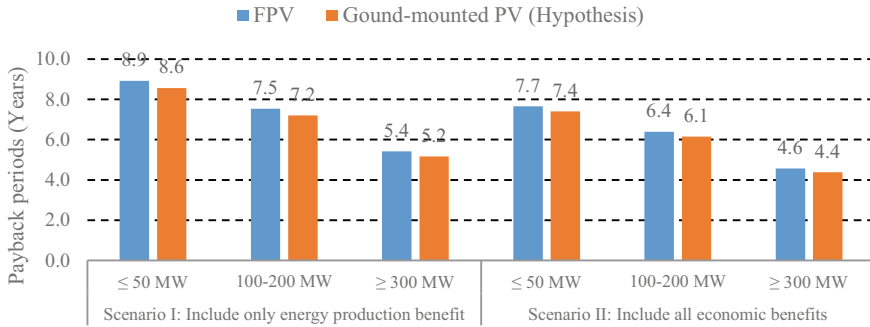


**Fig. 18.17** Payback period of FPV compared to land-based PV power plants (Case-II). *Source Author*

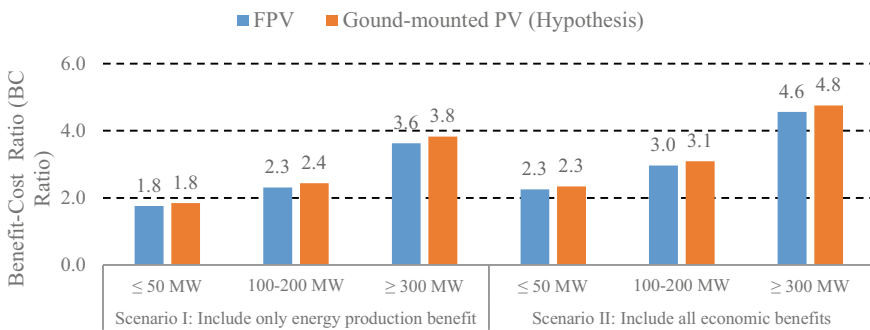


**Fig. 18.18** BC ratio of FPV compared to land-based PV power plants (Case-II). *Source Author*

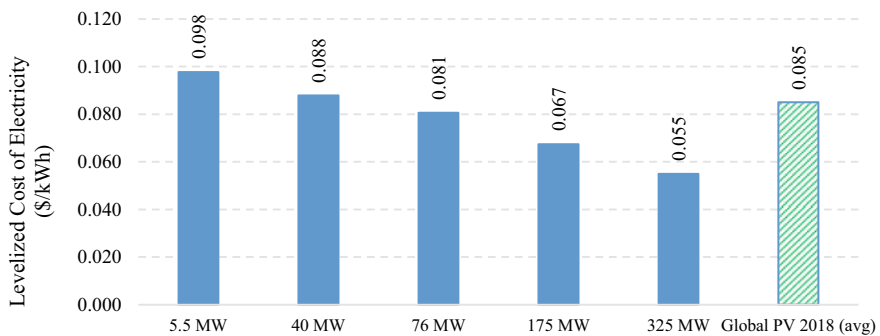


**Fig. 18.19** Electricity cost of different FPV system sizes (Case-II). *Source Author*

hydropower plants, some locations need to have a larger floating solar system than the hydropower plant. This can cause the transmission system in some locations to be expanded, which might affect an increase in the project costs. The maximum



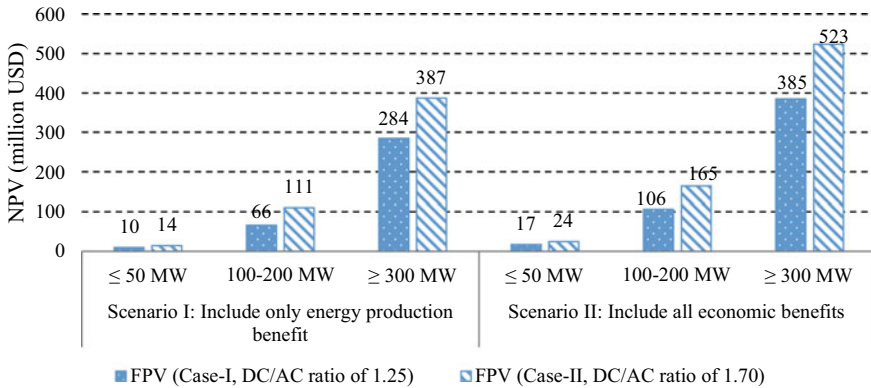


**Fig. 18.20** Comparison of NPV of FPV systems in two different oversizings. *Source* Author

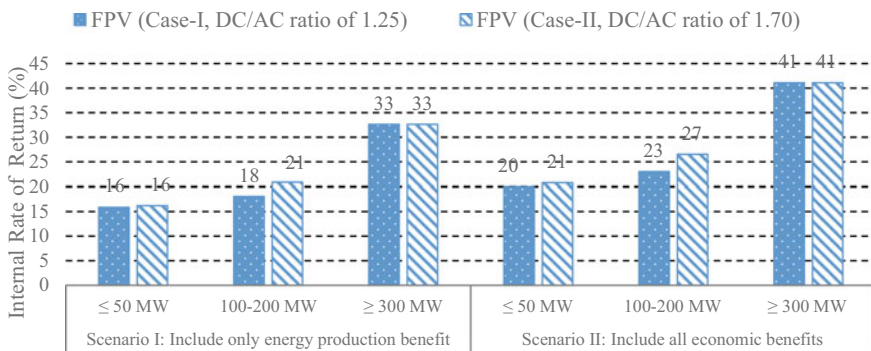


**Fig. 18.21** Comparison of IRR of FPV plants having 125% and 170% DC/AC ratio. *Source* Author

financial benefits occur in Case-V, followed by Case-IV, because it has the highest power capacity and water surface area coverage.

### 18.4 Conclusions

The key findings in this study can be summarized as follows.

- (a) The measured hourly solar irradiance and weather data (ambient temperature and wind speed) during 2014–2017 were applied to estimate the potential energy production of FPV power plants. It is assumed that the FPV system’s capacity is equal to the power plant at each location. From all locations in case the DC to AC ratio of 125% would apply, energy production was estimated to be 5771 GWh/year, covering the surface of about 2% on average. Considering the higher oversizing with the DC to AC ratio of 170%, the estimated annual energy

**Table 18.12** Financial analysis results of FPV compared to ground-mounted PV projects in Case-IV (FPV covers 5% of the surface area)

Project type	Scenario	Project size (MW)	Reservoir name	NPV (million USD)	Payback period (years)	IRR (%)	BC ratio	
FPV	Scenario-I: include only energy production benefit	61.4	Kiew Kho Ma Dam	39.7	8.1	18.7	2.1	
		48.0	Chulaphorn Dam	21.1	9.1	15.8	1.7	
		164.0	Bang Lang Dam	119.1	7.2	22.0	2.4	
		364.0	Sirikit Dam Phase I	318.4	5.4	32.6	3.6	
		676.0	Sirikit Dam Phase II	591.4	5.4	32.6	3.6	
	Scenario-II: include all economic benefits	61.4	Kiew Kho Ma Dam	59.1	7.0	23.1	2.6	
		48.0	Chulaphorn Dam	36.7	7.7	20.1	2.2	
		164.0	Bang Lang Dam	173.2	6.1	27.7	3.1	
		364.0	Sirikit Dam Phase I	431.0	4.6	41.1	4.6	
		676.0	Sirikit Dam Phase II	800.4	4.6	41.1	4.6	
	Ground-mounted PV (hypothesis)	Scenario-I: include only energy production benefit	61.4	Kiew Kho Ma Dam	41.1	7.7	19.7	2.2
			48.0	Chulaphorn Dam	22.0	8.8	16.5	1.8
			164.0	Bang Lang Dam	121.4	6.9	23.3	2.6
			364.0	Sirikit Dam Phase I	318.3	5.2	34.7	3.8
676.0			Sirikit Dam Phase II	591.1	5.2	34.7	3.8	
Scenario-II: include all economic benefits		61.4	Kiew Kho Ma Dam	59.2	6.8	24.1	2.7	
		48.0	Chulaphorn Dam	36.5	7.5	20.8	2.3	
		164.0	Bang Lang Dam	171.9	5.9	29.0	3.2	
		364.0	Sirikit Dam Phase I	423.0	4.4	43.2	4.8	

(continued)

**Table 18.12** (continued)

Project type	Scenario	Project size (MW)	Reservoir name	NPV (million USD)	Payback period (years)	IRR (%)	BC ratio
		676.0	Sirikit Dam Phase II	785.5	4.4	43.2	4.8

Source Author

production and the area coverage were 7648 GWh and 2.5%, respectively. It is approximately 32.5% increase from that of the oversizing at 125%. Also, to replace the annual hydropower production (about 5511 GWh), the total capacity of the FPV would be installed at around 3758 MWp, which is close to the capacity of the first supposition. The installation of the FPV systems covered 5% and 10% of the surface area. It produced the highest electric power, which was more than the power generated from the existing hydropower plants, about 3.5 and 7 times, respectively.

- (b) All five cases of potential energy production were considered for economic analysis. The highest financial benefit was found in the condition that FPV covers 10% of the surface area. As a result, it was expected to produce 40,096 GWh of electricity per year. This equals the amount of GHG reduction of approximately 24.22 million tCO<sub>2</sub>/year. The annual water evaporation reduction of 335.55 million m<sup>3</sup>/year is worth for agriculture, about 27.85 million USD/year and for the electricity production of about 50,461 MWh/year.
- (c) Based on the evaluation of various financial indicators, namely NPV, IRR, payback period, benefit–cost ratio (BCR), and electricity production cost (LCOE), the economic analysis results can ensure that all the FPV projects studied are profitable. Large-scale FPV projects tend to have lower electricity costs and higher profitability. The financial analysis result of the FPV system was logically less than the ground-mounted PV system because of the higher investment and O&M costs. However, FPV projects still maintained profit even if only energy production benefit was considered.
- (d) The case that the FPV system’s capacity equals the hydroelectric plant was the most possible because the existing transmission system could be utilized without the need of its capacity expansions. The best option among the cases studied was that FPV covered 10% of the water surface because it gained the highest financial benefit. However, installing FPV in a large area should consider other factors such as transmission system costs, fishing, tourism, and navigator.

**Table 18.13** Financial analysis results of FPV compared to ground-mounted PV projects in case-V (FPV covers 10% of the surface area)

Project type	Scenario	Project size (MW)	Reservoir name	NPV (million USD)	Payback period (years)	IRR (%)	BC ratio
FPV	Scenario-I: include only energy production benefit	122.9	Kiew Kho Ma Dam	96.7	7.2	22.0	2.4
		96.0	Chulaphorn Dam	52.9	8.3	17.9	2.0
		328.0	Bang Lang Dam	359.3	4.8	38.8	4.3
		728.0	Sirikit Dam Phase I	636.9	5.4	32.6	3.6
		1352.0	Sirikit Dam Phase II	1182.8	5.4	32.6	3.6
	Scenario-II: include all economic benefits	122.9	Kiew Kho Ma Dam	135.6	6.3	27.0	3.0
		96.0	Chulaphorn Dam	84.0	7.1	22.6	2.5
		328.0	Bang Lang Dam	467.6	4.1	48.0	5.3
		728.0	Sirikit Dam Phase I	861.9	4.6	41.1	4.6
		1352.0	Sirikit Dam Phase II	1600.7	4.6	41.1	4.6
Ground-mounted PV (hypothesis)	Scenario-I: include only energy production benefit	122.9	Kiew Kho Ma Dam	98.5	6.9	23.2	2.6
		96.0	Chulaphorn Dam	54.0	8.0	18.7	2.0
		328.0	Bang Lang Dam	356.9	4.5	41.2	4.5
		728.0	Sirikit Dam Phase I	636.6	5.2	34.7	3.8
		1352.0	Sirikit Dam Phase II	1182.2	5.2	34.7	3.8
	Scenario-II: include all economic benefits	122.9	Kiew Kho Ma Dam	134.7	6.0	28.2	3.1
		96.0	Chulaphorn Dam	83.0	6.9	23.5	2.6
		328.0	Bang Lang Dam	457.9	3.9	50.4	5.5
		728.0	Sirikit Dam Phase I	846.0	4.4	43.2	4.8

(continued)

**Table 18.13** (continued)

Project type	Scenario	Project size (MW)	Reservoir name	NPV (million USD)	Payback period (years)	IRR (%)	BC ratio
		1352.0	Sirikit Dam Phase II	1570.9	4.4	43.2	4.8

Source Author

## References

- Akbarzadeh A, Wadowski T (1996) Heat pipe-based cooling systems for photovoltaic cells under concentrated solar radiation. *Appl Therm Eng* 16(1):81–87
- Campana PE, Wästhage L, Nookuea W, Tan Y, Yan J (2019) Optimization and assessment of floating and floating-tracking PV systems integrated in on-and off-grid hybrid energy systems. *Sol Energy* 177:782–795
- Cazzaniga R, Rosa-Clot M, Rosa-Clot P, Tina GM (2019) Integration of PV floating with hydroelectric power plants. *Heliyon* 5(6):e01918
- Charles Lawrence Kamuyu W, Lim J, Won C, Ahn H (2018) Prediction model of photovoltaic module temperature for power performance of floating PVs. *Energies* 11(2):447
- Damnoen P, Ketjoy N (2019) Analysis of investment models for megawatt scale photovoltaic power plant in Thailand. *J Renew Energy Smart Grid Technol* 14(1)
- Department of Foreign Trade (DFT) (2019) Rice production and trade information. Retrieved 8 Feb 2020, from <http://www.thairiceinfo.go.th/?page=DataL3.ShowData&codeData=A1008>
- Durković V, Đurišić Ž (2017) Analysis of the potential for use of floating PV power plant on the Skadar Lake for electricity supply of aluminium plant in Montenegro. *Energies* 10(10):1505
- Edalati S, Ameri M, Iranmanesh M, Tarmahi H, Gholampour M (2016) Technical and economic assessments of grid-connected photovoltaic power plants: Iran case study. *Energy* 114:923–934. <https://doi.org/10.1016/j.energy.2016.08.041>
- Electricity Generating Authority of Thailand (EGAT) (2016) Retrieved 10 Jan 2020, from [https://www.egat.co.th/index.php?option=com\\_content&view=article&id=1454:article-20160420-01&catid=49&Itemid=251](https://www.egat.co.th/index.php?option=com_content&view=article&id=1454:article-20160420-01&catid=49&Itemid=251)
- Electricity Generating Authority of Thailand (EGAT) (2019) Wholesale electricity rates for MEA and PEA. Retrieved 10 Jan 2020, from [http://www.egat.co.th/index.php?option=com\\_content&view=article&id=174&Itemid=222](http://www.egat.co.th/index.php?option=com_content&view=article&id=174&Itemid=222)
- Fu R, Feldman D, Margolis R, Woodhouse M, Ardani K (2017) US solar photovoltaic system cost benchmark: Q1 2017 (No. NREL/TP-6A20-68925). EERE Publication and Product Library
- Fu R, Feldman DJ, Margolis RM (2018) US solar photovoltaic system cost benchmark: Q1 2018 (No. NREL/TP-6A20-72399). National Renewable Energy Lab. (NREL), Golden, CO (United States)
- Grana P (2016) Solar inverters and clipping: what DC/AC inverter load ratio is ideal? Retrieve 10 Nov 2019, from <https://www.solarpowerworldonline.com/2016/07/solar-inverters-clipping-dcac-inverter-load-ratio-ideal/>
- Hartzell TS (2016) Evaluating potential for floating solar installations on Arizona water management infrastructure
- IRENA (2017) Renewable energy outlook: Thailand. International Renewable Energy Agency, Abu Dhabi
- Jordan DC, Wohlgemuth JH, Kurtz SR (2012) Technology and climate trends in PV module degradation (No. NREL/CP-5200-56485). National Renewable Energy Lab. (NREL), Golden, CO (United States)

17. Kalogirou SA, Tripanagnostopoulos Y (2006) Hybrid PV/T solar systems for domestic hot water and electricity production. *Energy Convers Manag* 47(18–19):3368–3382
18. Kim SM, Oh M, Park HD (2019) Analysis and prioritization of the floating photovoltaic system potential for reservoirs in Korea. *Appl Sci* 9(3):395
19. Kost C (2018) Levelized cost of electricity renewable energy technologies, fraunhofer institute for solar energy system ISE
20. Krishnaveni N, Anbarasu P, Vigneshkumar D (2016) A survey on floating solar power system. *Int J Current Res Modern Edu* 152–158
21. Kumar BS, Sudhakar K (2015) Performance evaluation of 10 MW grid connected solar photovoltaic power plant in India. *Energy Rep* 1:184–192
22. Lazard N (2018) Lazard's levelized cost of energy analysis—version 12
23. Liu L, Wang Q, Lin H, Li H, Sun Q (2017) Power generation efficiency and prospects of floating photovoltaic systems. *Energy Procedia* 105:1136–1142
24. Lohsomboon P (2017) Combating climate change with carbon pricing. Retrieved 3 Feb 2020, from. [http://www.dsdw2016.dsdw.go.th/doc\\_pr/ndc\\_2560-2561/PDF/8459sc/8459PongwipaLorsomboon.pdf](http://www.dsdw2016.dsdw.go.th/doc_pr/ndc_2560-2561/PDF/8459sc/8459PongwipaLorsomboon.pdf)
25. Mekhilef S, Saidur R, Kamalisarvestani M (2012) Effect of dust, humidity and air velocity on efficiency of photovoltaic cells. *Renew Sustain Energy Rev* 16(5):2920–2925
26. Ministry of energy (2018) Power development plan 2018 (PDP 2018). Retrieved 7 Aug 2019, from. [http://www.eppo.go.th/images/Information\\_service/public\\_relations/PDP2018/PDP2018.pdf](http://www.eppo.go.th/images/Information_service/public_relations/PDP2018/PDP2018.pdf)
27. Mittal D, Saxena BK, Rao KVS (2017) Floating solar photovoltaic systems: An overview and their feasibility at Kota in Rajasthan. In: International conference on circuit, power and computing technologies (ICCPCT), pp 1–7. IEEE
28. Office of Agricultural Economics (OAE) (2019) White rice: arable land, harvesting area, yield and yield per rai, year 2018, by province. Retrieved 8 Feb 2020, from. <http://www.oae.go.th/view/1/table showing details of rice paddies/TH-TH>
29. RETScreen international clean energy decision support centre (2005) Clean energy project analysis, RETScreen engineering and cases textbook. CANMET energy technology centre: Montreal, QC, Canada
30. Rauf H, Gull MS, Arshad N (2019) Integrating floating solar pv with hydroelectric power plant: analysis of ghazi Barotha reservoir in Pakistan. *Energy Procedia* 158:816–821
31. Rosa-Clot M, Tina GM, Nizetic S (2017) Floating photovoltaic plants and wastewater basins: an Australian project. *Energy Procedia* 134:664–674
32. Royal Irrigation Department (RID) (2019) Water consumption of plants (Evapotranspiration; ET). Retrieved Feb 8 2020, from. <http://water.rid.go.th/hwm/cropwater/CWRdata/ET/index.htm>
33. SMA Solar Technology AG. Oversizing White Paper. Retrieved 28 Apr 2020, from. [https://www.sma.de/fileadmin/content/global/specials/documents/oversizing/Whitepaper\\_Oversizing\\_EN\\_180530\\_01.pdf](https://www.sma.de/fileadmin/content/global/specials/documents/oversizing/Whitepaper_Oversizing_EN_180530_01.pdf)
34. Sharma AK, Kothari DP (2016) Floating solar PV potential in large reservoirs in India. *Int J Innov Res Sci Technol* 2:97–101
35. Song J, Choi Y, Yoon SH (2015) Analysis of photovoltaic potential at abandoned mine promotion districts in Korea. *Geosyst Eng*
36. SunSpark Technology Inc (2019) Poly Module 250 W, 255 W, 260 W, 265 W. Retrieved 7 Nov 2019, from. <https://www.enfsolar.com/pv/paneldatasheet/crystalline/38332>
37. Thai Rice Mills Association (2018) Average rice price for the year 2018. Retrieved 8 Feb 2020, from. <http://www.thairicemillers.org/index.php?lay=show&ac=article&Ntype=16>
38. World Bank Group, ESMAP and SERIS (2019) Where sun meets water: floating solar market report. World Bank, Washington, DC

# Chapter 19

## Voltage Fault Ride-Through Operation of Solar PV Generation



Bonu Ramesh Naidu and Prabodh Bajpai

### 19.1 Introduction

The ambitious targets for the installation of grid-connected SPV generation in many nations are direct result of action plan for climate change [1]. However, SPV generation is characterized with uncontrolled variability and certain unpredictability. On the other hand, faults are an unavoidable phenomenon on the utility network, and they perturb the voltage and frequency across the network. However, in most of the cases, the faults are either temporary in nature or they are quickly isolated by suitable protection devices in the network. Tripping of the distributed generation units during such temporary voltage events under high penetration scenarios may lead to voltage collapse and/or risk of frequency variations due to cascade tripping. SPV units are interfaced through inverter technology. Few major faults across the globe in last 5 years and their impact on the network in terms of disconnection of the generating units are given in Table 19.1. The SPV generating units during all these events isolated themselves from the network due to their stringent protection settings in terms of voltage and frequency variations [2]. In the event of high penetration of such generating units, the rest of the network is prone to severe disturbances in frequency and voltage which may trigger a chain reaction of disconnection of loads and generating units. This triggers a need to curtail the relative capacity of SPV installations with respect to the grid capacity or bring in reforms to the way SPV generation interacts with the utility grid so as to ensure seamless inclusion of solar energy and safe operation of the utility grid. One possible reform is to shift from traditional *instantaneous trip* control setting to the *wait, watch, and act* control setting for the generators.

---

B. R. Naidu (✉) · P. Bajpai  
Department of Electrical Engineering, Indian Institute of Technology Kharagpur,  
Kharagpur, West Bengal 721302, India  
e-mail: [b.r.naidu.1006@gmail.com](mailto:b.r.naidu.1006@gmail.com)

P. Bajpai  
e-mail: [pbajpai@ee.iitkgp.ac.in](mailto:pbajpai@ee.iitkgp.ac.in)

© The Author(s), under exclusive license to Springer Nature Singapore Pte Ltd. 2021  
S. N. Singh et al. (eds.), *Fundamentals and Innovations in Solar Energy*,  
Energy Systems in Electrical Engineering,  
[https://doi.org/10.1007/978-981-33-6456-1\\_19](https://doi.org/10.1007/978-981-33-6456-1_19)

**Table 19.1** Network faults and SPV generating units' trip events

S. No.	Date	Details of the event	Loss of generation (MW)
1	August 2016	Blue cut fire incident led to a normally cleared fault on 500 kV line, Southern California, USA	1200
2	October 2017	Canyon 2 fire incident caused two transmission faults (220 and 500 kV), Los Angeles, USA	900

Source Authors

Fault ride-through (FRT) operation of the generating units is an essential and emerging dynamic operating feature that mandates the generating unit to stay connected to the utility network and continue serving the loads even during short-term abnormal variations in the network parameters [3, 4]. Such an operation is desirable to avoid any common mode tripping of generating units due to the abnormal frequency and/or voltage. This requires the generating unit to widen its protection settings and deploy means and methods to withstand the impact of the excursions. FRT operation includes both voltage and frequency FRT operation. This chapter primarily elucidates various aspects of the voltage FRT operation. Voltage FRT operation of SPV units requires the generating unit to stay connected and support the network during short-term high- or low-voltage excursions in the network.

## 19.2 Grid Code for Voltage FRT Operation

The power system network is formed by a coherent interaction of multiple generating units, loads, and storage devices with distinct characteristics through a complex set of transmission and distribution lines. The transition from passive to active network through rapid deployment of renewable energy units led to the need for rules and regulations that dictate the way these generating units interact with the network. Grid code is an operative collection of regulations to coordinate the inclusion of and interaction among different generating units in an interconnected power system network. The grid code for voltage FRT operation falls into the category of dynamic operation of the network. In the recent years, most of the countries published or have updated their grid code related to the voltage FRT operation of the SPV units. The voltage FRT requirements are often embedded in the grid code through a voltage versus time curve and a reactive current variation versus voltage curve that dictates the operation of the generating unit during short-term voltage disturbances in the network [3].

The voltage versus time curve is indicative of the extent of voltage sag and the duration of impact that the generating unit should withstand to avoid disconnection during the short-term voltage deviations. Typical voltage versus time curve is shown



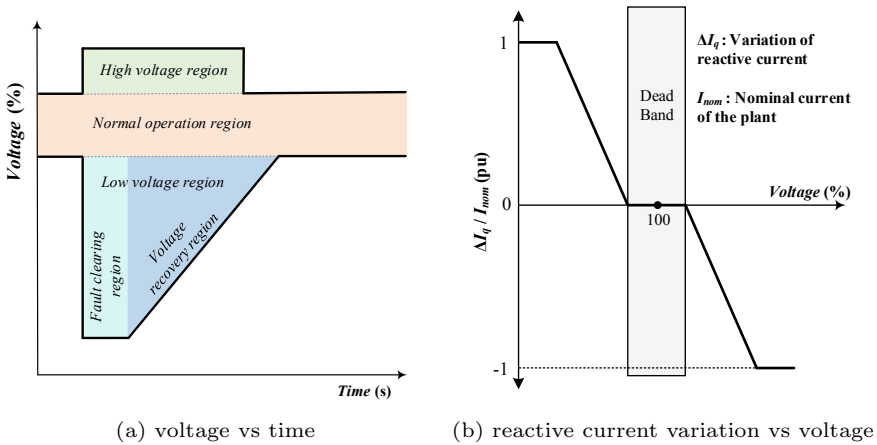


**Fig. 19.1** Voltage FRT characteristics for a generating unit. *Source* Authors

in Fig. 19.1a. Broadly, the voltage versus time curve can be divided into the following regions (i) normal operating region; (ii) low-voltage region; and (iii) high-voltage region as shown in Fig. 19.1a. The normal operating region specifies the voltage limits within which the generating unit can continue its intended operation. Typically, the voltage limits for this region are 90–110%. The low-voltage region corresponds to the voltage limits below normal operating region and within the characteristic curve within which the generating unit needs to stay connected to the network irrespective of the drop in voltage. This region can be further classified as (a) fault clearing region<sup>1</sup> and (b) voltage recovery region [5]. The fault clearing region represents the phase during which the network voltage undergoes a significant dip in the voltage resulting from a fault and settles at a voltage level depending on the severity and type of the fault. The time duration of this region and the allowed voltage sag mainly depend on the maximum time taken by the protection system to isolate the faults and the severity of the fault. Post successful isolation of the fault, the network voltage starts recovering back to the normal operating region. The region within the low-voltage region other than the fault clearing region is generally referred as the voltage recovery region. The rate of recovery of voltage in this region depends on the strength of the network, reactive power capability, generation–load mix, etc. High voltages in the network typically occur due to switching transients and/or sudden disconnection of loads. The region above the normal operating region and below the voltage FRT characteristics is the high-voltage region that bears the same operational norms as their low-voltage counterpart.

In the event of high or low voltages in the network, the network requires suitable reactive power to counteract the cause. This requirement is represented by a reac-

<sup>1</sup>The voltage versus time curve specified by the grid code is unique and equally applicable for voltage deviations due to all possible causes, yet, the focus of this chapter is on the voltage deviations due to the network faults as they are much severe in nature.

tive current variation versus voltage curve as shown in Fig. 19.1b [6]. The reactive current variation versus voltage curve depicts the requirements for reactive current exchange during network voltage deviations in a view to stabilize and quickly regain normal operating condition of the network voltage. Going the distributed way, during network faults, few grid codes mandate the reactive current compensation from the distributed generating units. Typically, a fall in network voltage should be counteracted by an appropriate injection of reactive current by the generating unit and vice versa. The dead band in Fig. 19.1b corresponds to the network voltage limits for which no reactive current compensation is required. This region generally aligns with the normal operating region of the voltage versus time curve. Beyond the dead band, droop settings are in place to determine the required reactive current variation as a ratio of nominal current of the generating unit against the voltage level. The generating unit may either curtail the real current or be oversized to meet this reactive current requirement.

### 19.2.1 Voltage FRT Characteristics of Different Countries

Low-voltage FRT operation is more dominant requirement in many nations as the possibility of its occurrence is very high compared to the high-voltage counterpart. Hence, the low-voltage FRT characteristics of different countries are given in Table 19.2 [7]. Referring to Table 19.2,  $T_{\text{lVRT}}$  indicates the maximum time for fault clearing,  $V_{\text{lVRT}}$  corresponds to the minimum voltage the generating unit needs to withstand during voltage FRT operation. Similarly,  $T_{\text{lres}}$  indicates the maximum time for reaching the steady-state operation following a voltage fault, and  $V_{\text{lres}}$  corresponds to the voltage limit for continuous operating region. The diversity in the voltage FRT characteristics among different nations is primarily due to the difference in their network topology, network parameters, load-generation mix, and renewable energy penetration levels.

**Table 19.2** LVRT specifications for different countries

Country	$T_{\text{lVRT}}$ (ms)	$V_{\text{lVRT}}$ (%)	$T_{\text{lres}}$ (ms)	$V_{\text{lres}}$ (%)
India	300	15	3000	85
UK	140	15	500	94
Canada <sup>a</sup>	150	0	1000	75
Germany	150	0	1500	90
Egypt	250	0	3000	90
China	625	20	2000	90

<sup>a</sup>HQ Hydro-Québec region

Source Authors

## 19.2.2 Voltage FRT Characteristics in IEEE 1547:2018 Standard

The Institute of Electrical and Electronics Engineers (IEEE) 1547 standard is established to provide technical guidelines for interconnecting distributed generating units to the utility grid. The evolution of this standard with respect to the voltage FRT operation is shown in Fig. 19.2. In its very first version, i.e., IEEE 1547:2003 standard, there is no mention of the FRT operation as the penetration level for various distributed generation units is very low at that point of time. Further in its first amendment (IEEE 1547:2014), the concept of voltage FRT operation is introduced, and the settings for voltage versus time curve and the reactive current variation versus voltage curve are mentioned. Finally, in the wake of increasing penetration levels, the recent version, i.e., IEEE 1547:2018, introduced more add-on features to the existing guidelines like abnormal performance categorization, multiple operating regions within the voltage versus time curve, multiple FRT operation requirements, guidelines for dynamic voltage support, etc. [2, 4]. Hereon, the guidelines in the IEEE 1547:2018 standard will be elucidated due to their relevance to the present scenario.

Most of the available distributed generation technologies like SPV, wind, fuel cell, hydro generation, and energy storage technologies are classified into abnormal performance category (APC) I, II, and III with respect to the voltage FRT operation. The basis for this classification is not straightforward, yet it depends on both technical and non-technical factors like generation type, capacity, type of application, future penetration of generation technology, grid configuration, generation technology use case, impacts on environment, emissions, and sustainability. The methodology and an example classification of the existing distributed generation units are presented in Appendix-B of the IEEE 1547:2018 standard. Based on this classification, unique voltage versus time curve is published for each APC. The fundamental difference lies in the voltage and time settings of the voltage versus time characteristic curve. Inverters sourced by SPV units either fall into APC-II or III depending on the level of penetration with APC-III having the most wider voltage versus time settings.

The voltage versus time curve is sub-divided into multiple performance regions in IEEE 1547:2018 for each APC. The low-voltage region (below 0.88 pu) and high-voltage region (above 1.1 pu) are further divided into mandatory operation region,

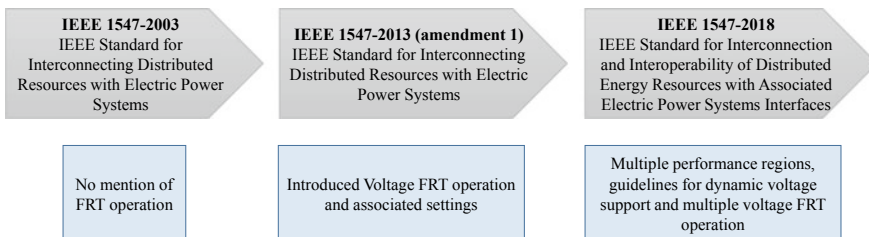


**Fig. 19.2** Evolution of IEEE 1547 standard with respect to voltage FRT operation. *Source* Authors

permissive operation region, and momentary cessation region. It is important to note that the presence of a particular performance region within the voltage versus time curve depends on the type of APC. The performance regions and the requirements for the distributed generation unit while operating in that performance regions are elucidated below.

- **Mandatory Operation Region:** The generating unit shall<sup>2</sup> stay in synchronization and shall continue to exchange energy with the network. For APC-II and III, the generating unit shall not reduce its total apparent current during the disturbance period below 80% of the pre-disturbance value or of the corresponding real current level subject to the available real power, whichever is less. Active and reactive current oscillations in the post-disturbance period that are positively damped are acceptable.
- **Permissive Operation Region:** The generating unit shall stay in synchronization and may<sup>3</sup> continue to exchange energy with the network or may cease to energize. If the generating unit rides through a voltage disturbance with cease to energize function, the generating unit shall restore output of real current to at least 80% of pre-disturbance real current level within 0.4 s once the permissive operation region is surpassed. Active and reactive current oscillations in the post-disturbance period that are positively damped are acceptable.
- **Momentary Cessation Region:** The generating unit shall stay in synchronization and shall cease to energize. The restore output conditions are same as described for permissive operation region.

The structure of the voltage versus time curve for APC-II is presented in Fig. 19.3. The high-voltage region comprises only permissive operation region, whereas the low-voltage region is sub-divided into mandatory operation region and permissive operation region. The momentary cessation region is absent in APC-II characteristics. The summary of different performance regions is depicted in Fig. 19.4. The reader may refer to Appendix-H of IEEE 1547:2018 standard [4] for detailed figures of voltage versus time characteristics for APC-I to III.

Multiple consecutive voltage events may arise due to (i) a reasonable tripping and reclosing sequence (ii) separate faults that might occur due to multiple reasons (iii) dynamic voltage swings that cyclically transition in and out of the continuous operation region, etc., and can result in repeating periods of abnormal voltages separated by periods of relatively normal voltages. To deal with such scenarios, the concept of multiple ride-through operation is introduced in IEEE 1547: 2018 standard. The requirements corresponding to the same are given in Table 19.3 for all three types of APC and are illustrated in Fig. 19.5 for APC-II. The generating unit falling under

---

<sup>2</sup>The word *shall* represents a *mandatory* requirement.

<sup>3</sup>The word *may* represents an *optional* requirement.

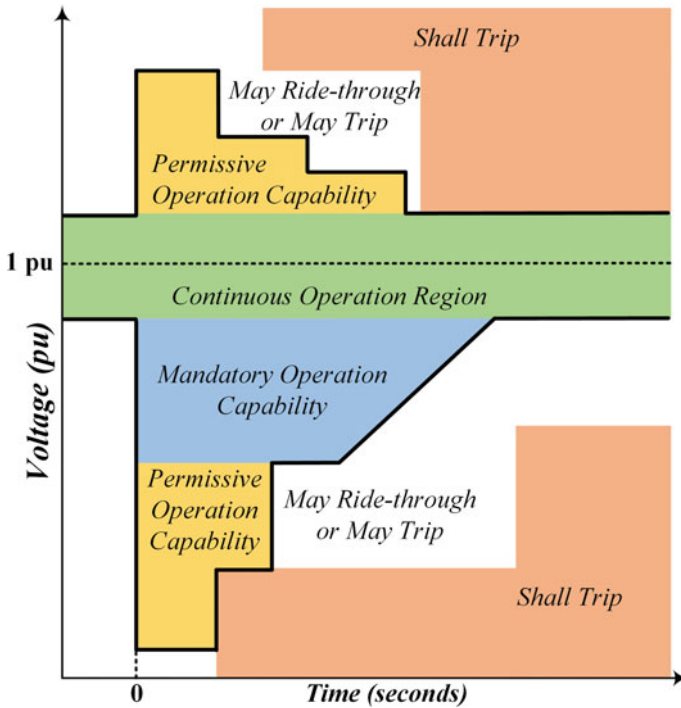


Fig. 19.3 Structure of voltage versus time curve for APC-II. Source Authors

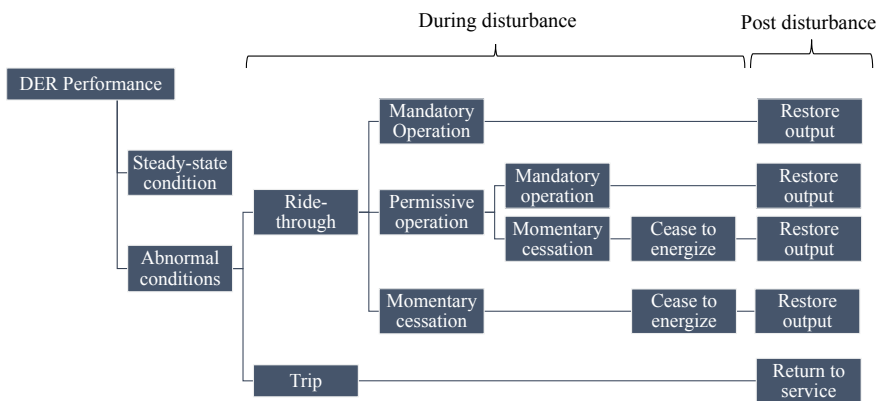


Fig. 19.4 Overview of performance regions for voltage FRT operation. Source Authors

APC-II requirements shall ride-through a maximum of two consecutive voltage dis-

**Table 19.3** Consecutive voltage FRT requirements

APC	Maximum number of voltage FRT events	Minimum time between consecutive events (s)	Minimum time to reiterate new set of FRT events (min)
I	2	20	60
II	2	10	60
III	3	5	20

Source Authors

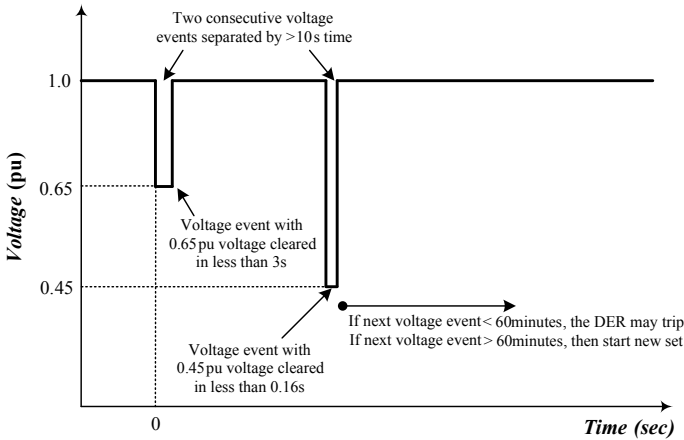


**Fig. 19.5** Illustration of multiple voltage FRT operation for APC-II settings. Source Authors

turbance events, separated by at least 10 s, and may prohibit doing so for further voltage events until next 60min.<sup>4</sup>

Of late, the dynamic voltage support is being mandated from the generating units performing voltage FRT operation in a view to quickly regain the voltage normalcy in the network. Dynamic voltage support requires the generating unit to inject appropriate current during voltage events to regulate the voltage of the network. In the literature, multiple such methods exist to determine the current during voltage support. As per the IEEE 1547:2018 standard

- Under a mutual agreement with the network operator and the generating unit, the dynamic voltage support may be utilized during voltage FRT operation
- The dynamic voltage support in addition to the voltage FRT operation shall not lead the generating unit into trip operation during the case where the generator would not have tripped in the absence of dynamic voltage support.

<sup>4</sup>Note that this standard allows an unlimited number of multiple consecutive voltage disturbances that DER are required to ride through within a single disturbance “set,” as long as the cumulative duration of all the disturbances in this set does not exceed the maximum required ride-through duration for the respective voltage disturbance severity (and performance category).

- The generating unit *shall* maintain reactive current output (if any during dynamic voltage support) until 5 s after the voltage enters the continuous operating limits.

With these new set of requirements introduced for voltage FRT operation, the need for a detailed study on the capability of the generating unit to cater to these requirements has increased manifold.

### 19.3 Grid-Connected SPV Generating Unit

Grid codes are mandating fail-proof voltage FRT operation from the generating units. It is therefore the need of the hour to understand the operation and different aspects related to the grid interaction of the generating unit. The layout of a grid-connected SPV generating unit along with its control strategy is depicted in Fig. 19.6 [8]. Typically, grid-connected SPV unit involves a two-stage power conversion, i.e., first DC-DC and then DC-AC, often performed by DC-DC converter and two-level inverter, respectively. The DC-DC converter is often controlled to tap maximum power from SPV panels by taking the voltage and current at the panel terminals as feedback. Maximum power point tracking (MPPT) controller hosts the tracking algorithms like incremental conductance, perturb & observe, fractional open-circuit voltage, etc. [9]. The resulting effect of the MPPT algorithm is an uncontrolled variation of the DC bus voltage. Therefore, the two-level inverter is often controlled to stabilize the DC bus voltage at a preset reference value by transferring the incoming maximum power from PV panels to the utility grid. Often, voltage and current variables from the point of common coupling (PCC) are measured and processed for further control. While PCC voltage is used for synchronizing the output of inverter with that of the PCC, the PCC current is used to control the power flow through the inverter. The DC bus voltage controller takes DC bus voltage as input and generates a real power reference ( $P_{inv}^*$ ) in a process to control the voltage to a predefined reference value.<sup>5</sup> Similarly, the SPV system can either host an AC voltage controller that generates the reactive power reference ( $Q_{inv}^*$ ) or a predefined reactive power/current versus voltage curve that defines the level of reactive power/current required with respect to variations in PCC voltage. Post reference power generation, the information of the real and reactive powers will be converted to an apparent current reference ( $i_{inv}^*$ ) and is passed on to the AC current controller that compares the reference current with the actual current ( $i_{inv}$ ) measured from the PCC and generates modulation signals for generating the switching pulses for the SPV inverter. The entire system therefore behaves as a grid-following entity with maximum power transfer from SPV panels to the utility grid at any point of time [10]. This two-stage grid-connected SPV unit is required to provide voltage FRT operation as mandated by the grid code.

---

<sup>5</sup>The superscript \* and subscript pu for any variable represent the reference value and per unit value of that variable respectively.

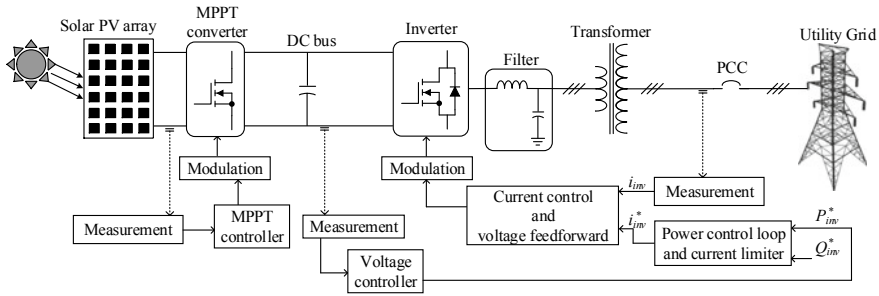


**Fig. 19.6** Grid-connected SPV generation unit along with its control. *Source* Authors

### 19.3.1 Voltage Fault Response of SPV Generation Unit

The requirements of the voltage FRT operation apply at the PCC and are achieved by tweaking the control logic of the inverter and appending suitable hardware components. Inverters are current limited devices due to the limited current rating of the switches deployed in it [8]. Hence, at any point of time, the user needs to appropriately modify the real and reactive currents subject to the available maximum current limit. The response of different variables in a SPV inverter for both low- and high-voltage symmetrical faults is shown in Fig. 19.7. The black, blue, and red color lines indicate the response of the system to nominal voltage, low voltage and high voltage at the PCC, respectively. The subscript *nom* of the variables used in Fig. 19.7 represents its nominal/rated value. A sudden drop in the PCC voltage at time  $t_1$  in Fig. 19.7a results in an increase in the inverter current by virtue of its constant power operation as shown in Fig. 19.7b. If the rise in current is well below the current limit of the inverter switches, the inverter power and DC bus voltage return back to the nominal value irrespective of the low voltage at the PCC as shown in blue dotted lines in Fig. 19.7c and d. On the other hand, if the increase in current is beyond the inverter current limit, the inverter control hard limits the inverter current, and thus, there will be a power imbalance at the DC bus that results in a rise in DC bus voltage as depicted with solid blue lines in Fig. 19.7c and d. Similarly, the response of the SPV inverter for a high voltage at the PCC is also shown in Fig. 19.7. The rise in PCC voltage actually demands a decrease in the inverter current to maintain constant power flow through the inverter as shown in Fig. 19.7b. Hence, the inverter momentarily transfers higher power than the available SPV power (until the inverter reaches the new operating point, i.e., until  $t_3$ ) as shown in Fig. 19.7c by draining the energy from DC bus resulting in a decrease in the DC bus voltage as shown in Fig. 19.7b.<sup>6</sup> Please note that the DC bus voltage should be high enough to push power into the utility grid even during high voltage at the PCC; otherwise, there will indeed be a boost in the DC bus voltage due to the imbalance arising at the DC bus.

<sup>6</sup>This phenomenon depends on the speed of response of the inverter controller in adjusting its current reference to a variation in the voltage.



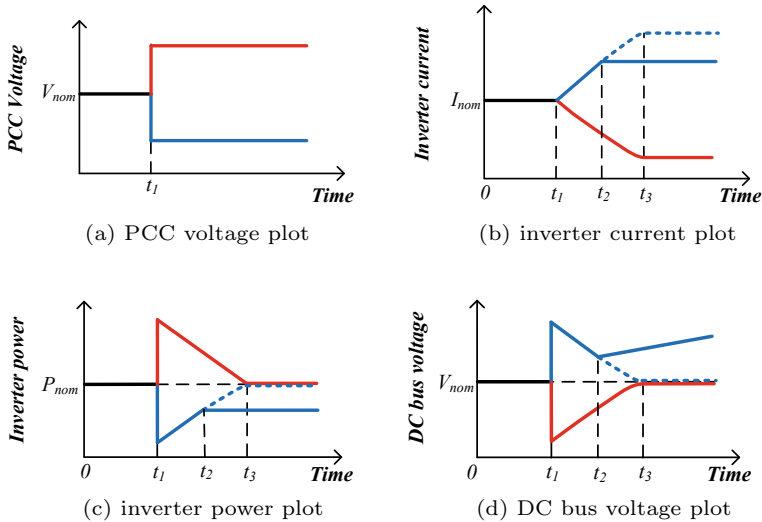


**Fig. 19.7** Response of a SPV unit to low/high voltage at the PCC. *Source* Authors

It is therefore evident that there will be serious perturbations in the DC bus voltage resulting from limitation in the switch current rating of the inverter which may lead to the tripping of SPV unit due to the stringent protection settings. The effect worsens for APC-III characteristics as the voltage versus time requirements are very wide in this case. SPV units without voltage FRT operation capability end up in tripping for short-term voltage disturbances leading to a loss of revenue for plant owners and stability issues to the utility grid (every time the unit trips and reconnects to the grid). Therefore, the upcoming solar installations should be designed adhering to the required grid code, whereas the existing solar SPV installations need to be retrofitted in terms of both system components and/or control strategy to comply with the ride-through operation. The above analysis suggests that suitable hardware or control mechanism is imperative to facilitate stable and reliable voltage FRT operation from SPV units. A simple current limiting control can limit the inverter current and possible solutions based on control methods only or using both hardware and control-based methods exist for stabilizing the DC bus during voltage FRT operation. They are summarized below and are presented in Fig. 19.8.

1. OFF-MPP control of DC-DC converter; [11, 12]
2. Crowbar circuit at the DC bus; [13, 14]
3. Energy storage at the DC bus. [15, 16]

The voltage FRT operation of the SPV unit with the above-mentioned methods will be elucidated in the following subsection.

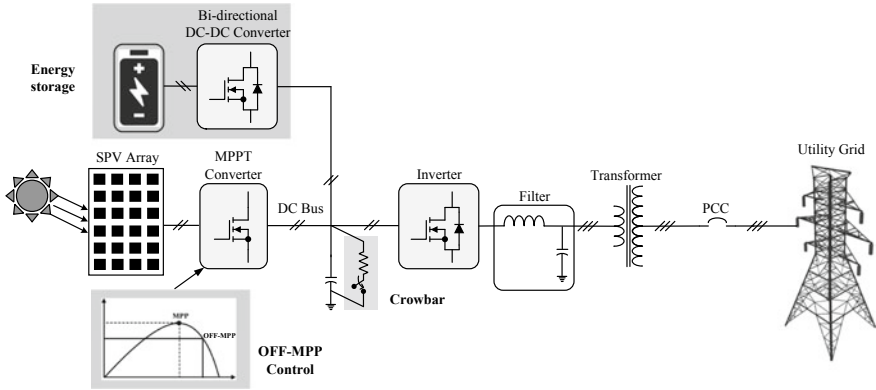
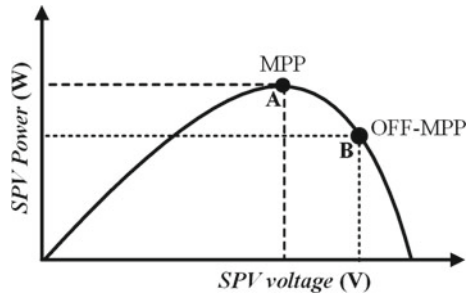


**Fig. 19.8** Methods to achieve reliable voltage FRT operation of SPV unit. *Source* Authors

**Fig. 19.9**  $P-V$  curve of SPV array with different operating points. *Source* Authors



### 19.3.2 Control of SPV Generation for Voltage FRT Operation

In the event of voltage FRT operation, if the inverter enters into the current limit mode and is unable to transfer the available real power, the DC bus voltage rises and settles at a new value depending on the imbalance power at the DC bus. Besides the inverter control strategy for voltage FRT operation, additional control or hardware methods are required to stabilize the DC bus voltage. Three possible methods to support the voltage FRT operation of the SPV unit by restricting the rise in DC bus voltage are discussed in detail and classified as only control-based method and both hardware and control-based method.

1. *OFF-MPPT control of DC-DC converter:* This is only control-based method since it involves a change in the control principle of the DC-DC converter interfacing the SPV array with the DC bus. As long as the DC bus voltage is within the prescribed voltage limits, the converter is controlled by the MPPT algorithm which measures and controls the SPV terminal voltage to achieve maximum power transfer. In the event of voltage FRT operation, the control logic switches from input voltage control to output voltage control and thereby limits the power fed to the DC bus

and arrests the rise in DC bus voltage. Accordingly, the operating point of the SPV array changes on the  $P-V$  curve from A to B as shown in Fig. 19.9.

2. *Crowbar circuit at the DC bus:* A crowbar is an electrical circuit used to prevent an over-voltage condition of a power supply unit, which may lead to damaging the circuits attached to the power supply unit. It consists of a suitably sized resistor in series with a high-frequency switch as shown in Fig. 19.8. In the event of voltage FRT operation, the crowbar connected at the DC bus switches ON the resistor circuit that absorbs the excess energy at the DC bus and thereby limits the DC bus voltage close to its reference value [13, 14]. However, the crowbar circuit cannot arrest a fall in the DC bus voltage which might arise during high-voltage FRT operation.
3. *Energy storage at the DC bus:* An energy storage device at the DC bus coupled with a bidirectional DC-DC converter can arrest both positive and negative variations in the DC bus voltage (refer Fig. 19.8). The bidirectional converter is controlled to track the DC bus voltage to a preset reference value through appropriate voltage and current controllers. Suitable energy storage device should be chosen to meet the requirements of power variation and energy requirement during the voltage FRT operation. In addition, energy management strategy is required to maintain the state of charge (SoC) levels of energy storage device. The energy storage option at DC bus can assist in both high- and low-voltage FRT operation.

Out of these methods, the first method is purely control logic-based while the other two methods require additional hardware along with control. However, the first two methods result in a loss of solar power, while the energy storage-based method stores the same. Also, by using suitably sized energy storage at the DC bus and by slightly tweaking the control strategy of the inverter, additional grid-supporting functions like frequency FRT and black start operation can be achieved. Proper control and energy management strategy of energy storage plays a vital role in achieving the required functionalities from the energy storage. The inverter control for achieving voltage FRT operation is described below.

The grid-connected solar PV system along with the auxiliary hardware, i.e., crowbar circuit or energy storage for facilitating voltage FRT operation is depicted in Fig. 19.10. The specifications of the system are listed in Table 19.4. The SPV array is the primary source, and hence, it is always preferred to operate at maximum power point. The grid-connected inverter is prioritized to control the DC bus voltage. Accordingly, the inverter control hosts a DC voltage controller that regulates the voltage to the given set-point by injecting or absorbing required active power from the DC bus. In this regard, the voltage controller generates a current/power reference based on DC voltage deviations which is further tracked by the current/power controllers. The  $P_{inv}$  controller in Fig. 19.10 contains the above-mentioned voltage controller that takes in the reference voltage ( $v_{dc,pu}^*$ ) and actual voltage ( $v_{dc,pu}$ ) of the DC bus and generates the current reference for real power control of the inverter, i.e.,  $i_{pcc,pu}^{(d)*}$ .

The control strategy employed to achieve voltage FRT operation from the solar PV inverter is depicted in Fig. 19.10. The local variables, i.e., three-phase PCC voltage

**Table 19.4** Technical specification of the test setup considered for voltage FRT study

Device/system	Specifications
PV array	430 V, 11.75 A, 5 kW, $N_s = 14$ , $N_p = 3$
DC-DC converter (solar PV)	500 V/380 V, 5 kW
Crowbar circuit	30 $\Omega$ , 20k Hz
DC-AC inverter	3-ph, 380 V(DC)/220 V(AC), 5 kVA
Inverter current limit	1.2 pu
Transformer	3-ph, 415/220 V, 50Hz, $D_{yn}1$ , 5 kVA, 2.1%
AC load	3-ph, 415 V, 5 A, 3.6 kW
Utility grid	3-ph, 415 V, 50Hz, SCR = 16, $\frac{X_g}{R_g} = 0.5$

Source Authors

and current ( $v_{pcc}$  and  $i_{pcc}$ ), are sensed using appropriate sensing circuit and fed to the inverter controller. A synchronous reference frame (SRF) phase-locked loop (PLL) extracts the phase angle information ( $\psi$ ) of  $v_{pcc}$  which is used in calculating the dq-axis components of  $v_{pcc,pu}$  and  $i_{pcc,pu}$  (i.e.,  $v_{pcc,pu}^{(dq)}$  and  $i_{pcc,pu}^{(dq)}$ ). The  $v_{pcc,pu}$  is compared with the voltage FRT characteristics for detecting the occurrence of voltage FRT condition. Accordingly, the FRT signal is either 1 or 0. During the steady-state operation, the real current reference of the inverter ( $i_{pcc,pu}^{(d)*}$ ) is generated using the  $P_{inv}$  controller, while the reactive current reference ( $i_{pcc,pu}^{(q)*}$ ) can be either generated from the PCC voltage controller for static voltage compensation or can be kept zero. During voltage FRT operation, the inverter prioritizes the reactive current as per the reactive current requirement specified in the grid code, and the real current is

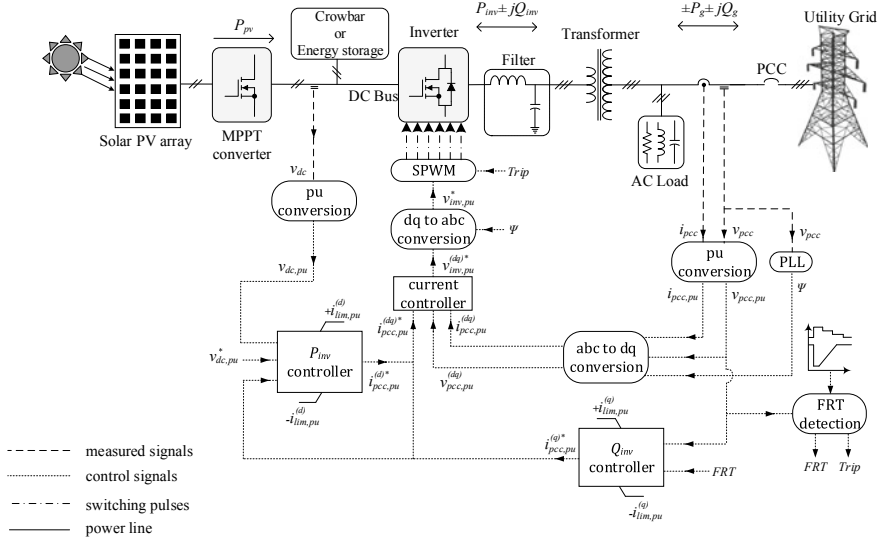


**Fig. 19.10** Schematic diagram of SPV units with voltage FRT control. Source Authors

generated adhering to the following equation.

$$\sqrt{(i_{pcc,pu}^{(d)*})^2 + (i_{pcc,pu}^{(q)*})^2} = I_{inv,pu}^{\max} \quad (19.1)$$

where  $I_{inv,pu}^{\max}$  is the maximum current limit of the inverter switches. Further, using current control and sinusoidal pulse width modulation technique, the switching pulses of inverter are generated. Under any circumstances, if the PCC voltage deviates beyond the voltage FRT characteristics, the *Trip* command is activated and the pulses to the inverter will be stopped.

## 19.4 Numerical Design Examples

The following design examples illustrate the process of retrofitting an existing SPV plant with the crowbar option and energy storage option to meet the requirements of voltage FRT operation.

**Design Example 1:** A 500 kW SPV plant as shown in Fig. 19.11a is connected to the distribution network at 11 kV and is exporting power at unity power factor (UPF) under steady-state operating conditions. The grid code mandates the PV plant to ride through symmetrical or asymmetrical voltage faults as per the voltage versus time curve depicted in Fig. 19.11b. Correspondingly, the PV plant is required to support the network voltages by exchanging suitable reactive current as dictated by Fig. 19.11c. The inverter in the SPV plant is capable of withstanding an over-current of 1.2 pu of its rated current for a duration of not more than 1 s. Neglect losses in the converters, transformer, and lines from PV to the PCC. The retrofitting of the solar SPV plant is to be performed to meet the grid code requirements.

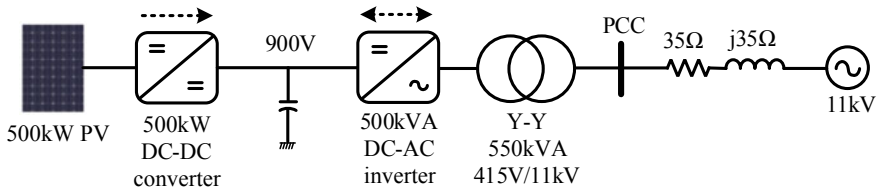
Calculate the following for two different options as given below assuming that the SPV plant is not operating in islanding condition under any circumstance.

### 1. DC crowbar circuit option

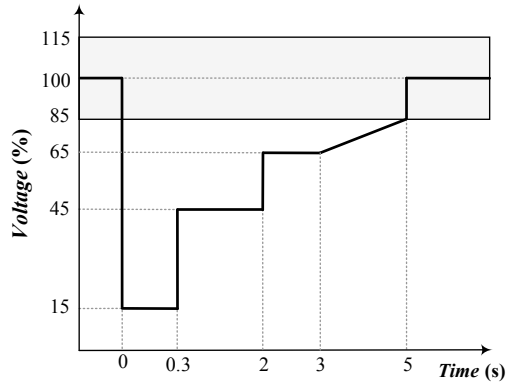
- (a) Calculate the worst-case power imbalance at the DC bus;
- (b) Calculate the suitable value of crowbar resistance for voltage FRT operation.

### 2. Supercapacitor energy storage option at the DC bus

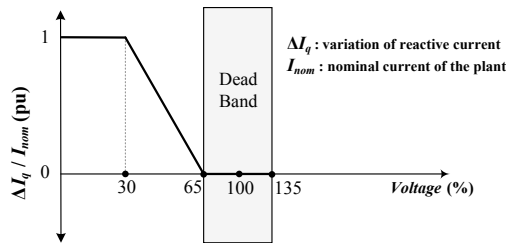
- (a) Calculate the peak power rating of the DC-DC bidirectional converter for interfacing the energy storage with the DC bus.
- (b) Calculate the total energy absorbed by the storage unit and the size of the supercapacitor bank required for the voltage FRT operation of the SPV plant considering 55 V, 130 F supercapacitor units. The limit on the charge/discharge current of the supercapacitor unit is 1900 A. Consider a DC-DC bidirectional converter with a voltage rating of 600 V/900 V ( $\pm 10\%$ ) with supercapacitor bank connected on the low-voltage side and DC bus connected to the high-voltage side.



(a) Grid-connected SPV plant



(b) voltage vs time curve



(c) reactive current variation vs voltage curve

**Fig. 19.11** Voltage FRT operation design example. *Source* Authors

- (c) Draw the schematic diagram showing the arrangement of the supercapacitor bank along with series/parallel combination if any.

**Solution:** The response of the PV plant needs to be analyzed under both steady-state operation and fault conditions. Since the transformer is lossless and is of Y-Y configuration, the FRT characteristics are equivalently applicable at the inverter output terminals (i.e., 415 V) without any modifications. In addition, assume that the inverter controller response is almost instantaneous.

### Steady-state Operation

The rated power of the inverter is  $S_{\text{inv}} = 500$  kVA, the nominal DC bus voltage is  $V_{\text{dc}} = 900$  V, and the rated line-line terminal voltage at the inverter is  $V_{\text{inv}} = 415$  V. The RMS value and peak value of the phase voltage at the inverter terminals are  $V_{\text{inv(ph)}} = 240$  V and  $V_{\text{inv(ph-pk)}} = 339.40$  V, respectively. Hence, the rated RMS and peak values of the line current of the inverter are given by

$$I_{\text{inv}} = \frac{S_{\text{inv}}}{\sqrt{3}V_{\text{inv}}} = 695.54 \text{ A} \quad (19.2)$$

$$I_{\text{inv(pk)}} = \sqrt{2}I_{\text{inv}} = 983.64 \text{ A} \quad (19.3)$$

The inverter state variables, i.e., phase voltage and line current, are converted to  $dq0$  components for control purpose, i.e.,  $V_{\text{inv}}^{(d)}$ ,  $V_{\text{inv}}^{(q)}$ ,  $I_{\text{inv}}^{(d)}$ , and  $I_{\text{inv}}^{(q)}$ . For proper decoupling of the real and reactive powers flowing through the inverter, synchronous reference frame-based phase-locked loop is generally used to reduce the  $V_{\text{inv}}^{(q)}$  component to zero such that the real and reactive powers through the inverter are controlled independently by controlling the  $I_{\text{inv}}^{(d)}$  and  $I_{\text{inv}}^{(q)}$ , respectively. Also, it is mentioned that the system is operating under UPF conditions during steady-state operation. Hence,

$$V_{\text{inv}}^{(d)} = 339.40 \text{ V}, V_{\text{inv}}^{(q)} = 0 \text{ V}, I_{\text{inv}}^{(d)} = 983.64 \text{ A} \quad \text{and} \quad I_{\text{inv}}^{(q)} = 0 \text{ A}.$$

The expressions for real and reactive powers through the inverter are therefore given by

$$P_{\text{inv}} = 1.5 \times V_{\text{inv}}^{(d)} \times I_{\text{inv}}^{(d)} = 500 \text{ kW} \quad (19.4)$$

$$Q_{\text{inv}} = 1.5 \times V_{\text{inv}}^{(d)} \times I_{\text{inv}}^{(q)} = 0 \text{ kVAR} \quad (19.5)$$

### Voltage FRT Operation

During FRT operation, as mandated by the grid code, the inverter moves away from UPF operation and injects certain reactive current as dictated by the grid code. As per Fig. 19.11c, the expression for reactive current during grid voltage sags is given below

$$I_{\text{inv}}^{(q)} = \begin{cases} 0 \text{ pu}, & \text{for } 65\% < \% V_{\text{inv}}^{(d)} < 135\% \\ 1.857 - \frac{\% V_{\text{inv}}^{(d)}}{35} \text{ pu}, & \text{for } 30\% < \% V_{\text{inv}}^{(d)} \leq 65\% \\ 1 \text{ pu}, & \text{for } \% V_{\text{inv}}^{(d)} \leq 30\% \end{cases} \quad (19.6)$$

**1(a)** It is imperative that the worst-case power imbalance at the DC bus occurs when the SPV unit is generating its rated power ( $P_{\text{mpp}} = 500$  kW) and the inverter is performing voltage FRT operation with the lowest possible voltage on the grid, i.e., 15% in this case. Also, from the reactive current requirement plot, the reactive current that is to be injected by the inverter during voltage drop to 15% is 1 pu, i.e., 983.64 A. However, the inverter over-current capability of 1.2 pu will be utilized to

inject certain amount of real current as per the following equation

$$I_{inv}^{(d)} = \sqrt{1.2^2 - (I_{inv}^{(q)})^2} = 0.6633 \text{ pu} \quad (19.7)$$

Hence, the real power transferred to the grid during a grid voltage dip down to 15% is

$$P_{inv} = 1.5 \times V_{inv}^{(d)} \times I_{inv}^{(d)} = 1.5 \times 0.15 \times 339.40 \times 0.6633 \times 983.64 = 49.82 \text{ kW} \quad (19.8)$$

Hence, the worst-case power imbalance ( $P_{imb}$ ) at the DC bus is

$$P_{imb} = P_{mpp} - P_{inv} = 500 - 49.83 = 450.18 \text{ kW} \quad (19.9)$$

**1(b)** The value of the crowbar resistance required at the DC bus is therefore determined from the worst-case power imbalance at the DC bus by the following equation

$$R_{cb} = \frac{V_{dc}^2}{P_{imb}} = \frac{900^2}{450.18 \times 1000} = 1.80 \Omega \quad (19.10)$$

**2(a)** Consider a supercapacitor bank connected at the DC bus through a DC-DC bidirectional converter for facilitating successful voltage FRT operation of the SPV plant. The minimum peak power rating of the supercapacitor bank converter required for a successful voltage FRT operation of the SPV plant is equal to the worst-case power imbalance at the DC bus, i.e., 450.18 kW. Assume that the DC-DC bidirectional converter is lossless.

**2(b)** To compute the rating of the supercapacitor bank, the worst-case energy diverted to the bank during the voltage FRT operation needs to be computed.

For % $V_{inv}^{(d)} = 15\%$ , the power imbalance is already calculated in 1(a). This imbalance is to be absorbed by the energy storage for a duration of 0.3 s as dictated by the grid code.

For % $V_{inv}^{(d)} = 45\%$ , the reactive current requirement can be computed from (19.6) and is equal to 0.57 pu. The inverter can operate at 1.2 pu current rating for a duration not exceeding 1 s. Hence, from 0.3 to 1 s,

$$I_{inv}^{(d)} = \sqrt{1.2^2 - (I_{inv}^{(q)})^2} = 1.055 \text{ pu} \quad (19.11)$$

Hence, the real power transferred to the grid during this duration is

$$P_{inv} = 1.5 \times V_{inv}^{(d)} \times I_{inv}^{(d)} = 1.5 \times 0.45 \times 339.40 \times 1.055 \times 983.64 = 237.74 \text{ kW} \quad (19.12)$$

Hence, the worst-case power imbalance at the DC bus is

$$P_{imb} = P_{mpp} - P_{inv} = 500 - 237.74 = 262.26 \text{ kW} \quad (19.13)$$



This power imbalance needs to be absorbed by the energy storage for a duration of  $1 - 0.3 = 0.7$  s.

The grid code mandates a voltage ride-through operation at 0.45 pu voltage until 2 s. However, beyond 1 s, the inverter current is limited to only 1 pu. Hence,

$$I_{\text{inv}}^{(d)} = \sqrt{1^2 - (I_{\text{inv}}^{(q)})^2} = 0.821 \text{ pu} \quad (19.14)$$

Hence, the real power transferred to the grid during this duration is

$$P_{\text{inv}} = 1.5 \times V_{\text{inv}}^{(d)} \times I_{\text{inv}}^{(d)} = 1.5 \times 0.45 \times 339.40 \times 0.821 \times 983.64 = 185 \text{ kW} \quad (19.15)$$

Hence, the worst-case power imbalance at the DC bus is

$$P_{\text{imb}} = P_{\text{mpp}} - P_{\text{inv}} = 500 - 185 = 315 \text{ kW} \quad (19.16)$$

This power imbalance should be absorbed by the energy storage for a duration of  $2 - 1 = 1$  s.

From 2 to 3 s, the  $\%V_{\text{inv}}^{(d)} = 65\%$ , for which the reactive current requirement is 0 pu. Hence,

$$I_{\text{inv}}^{(d)} = \sqrt{1^2 - (I_{\text{inv}}^{(q)})^2} = 1 \text{ pu} \quad (19.17)$$

Hence, the real power transferred to the grid during this duration is

$$P_{\text{inv}} = 1.5 \times V_{\text{inv}}^{(d)} \times I_{\text{inv}}^{(d)} = 1.5 \times 0.65 \times 339.40 \times 1 \times 983.64 = 325.50 \text{ kW} \quad (19.18)$$

Hence, the worst-case power imbalance at the DC bus is

$$P_{\text{imb}} = P_{\text{mpp}} - P_{\text{inv}} = 500 - 325.50 = 174.50 \text{ kW} \quad (19.19)$$

This power imbalance should be absorbed by the energy storage for a duration of  $3 - 2 = 1$  s.

From 3 to 5 s, the voltage FRT characteristics in Fig. 19.11b follow a ramp fashion with the following equation.

$$V_{\text{inv}}^{(d)} = \begin{cases} 0.1t + 0.35 \text{ pu,} & \text{for } 3 \text{ s} < t < 5 \text{ s} \end{cases} \quad (19.20)$$

However, the reactive current requirement for  $V_{\text{inv}}^{(d)} > 65\%$  is 0 pu. Hence,

$$I_{\text{inv}}^{(d)} = \sqrt{1^2 - (I_{\text{inv}}^{(q)})^2} = 1 \text{ pu} \quad (19.21)$$

Hence, the real power transferred to the grid during this duration is

$$\begin{aligned}
 P_{\text{inv}} &= 1.5 \times V_{\text{inv}}^{(d)} \times I_{\text{inv}}^{(d)} = 1.5 \times (0.1t + 0.35) \times 339.40 \times 1 \times 983.64 \\
 &= (50t + 175)\text{kW}
 \end{aligned} \tag{19.22}$$

Hence, the worst-case power imbalance at the DC bus is

$$P_{\text{imb}} = P_{\text{mpp}} - P_{\text{inv}} = 500 - (50t + 175) = (325 - 50t)\text{kW} \tag{19.23}$$

This power imbalance should be absorbed by the energy storage for a duration of  $5 - 3 = 2$  s.

Considering all possible cases calculated above, the worst-case energy that will be diverted to the energy storage device during voltage FRT operation as dictated by the given voltage versus time and reactive current variation versus voltage curves considering the inverter over-current rating is given by

$$\begin{aligned}
 E_{\text{ess}} &= (450.18 \times 0.3) + (262.26 \times 0.7) + (315 \times 1) + (174.50 \times 1) \\
 &+ \int_3^5 (325 - 50t)dt = 1058.14 \text{ kW s}
 \end{aligned} \tag{19.24}$$

This energy should be absorbed by the supercapacitor bank with a maximum power of 450.18 kW. Each supercapacitor unit can vary its voltage anywhere 0 V 55 V, but the DC-DC bidirectional converter interfacing the energy storage should be applied with the given  $\pm 10\%$  limit so a minimum voltage of  $V_{\text{sc}(\text{min})} = 600 \text{ V} - 60 \text{ V} = 540 \text{ V}$  and a maximum voltage of  $V_{\text{sc}(\text{max})} = 600 \text{ V} + 60 \text{ V} = 660 \text{ V}$ . Hence, multiple supercapacitor units need to be connected in series such that the fully charged voltage on the string does not exceed 660 V. Hence,

$$N_{\text{series}} = \frac{660}{55} = 12 \tag{19.25}$$

Hence, the maximum number of series units are 12, which gives a string voltage of 660 V. Now, since the lowest voltage allowed at the terminals of the string is 540 V, the minimum voltage until which each supercapacitor unit can be allowed is

$$V_{\text{sc,unit}(\text{min})} = \frac{540}{12} = 45 \text{ V} \tag{19.26}$$

The peak current through the DC-DC converter during voltage FRT operation occurs when the supercapacitor bank is absorbing 450.18 kW with the lowest string voltage 540 V and is equal to

$$I_{\text{sc,unit}(\text{max})} = \frac{450.18 \times 1000}{540} = 834.47 \text{ A} \tag{19.27}$$

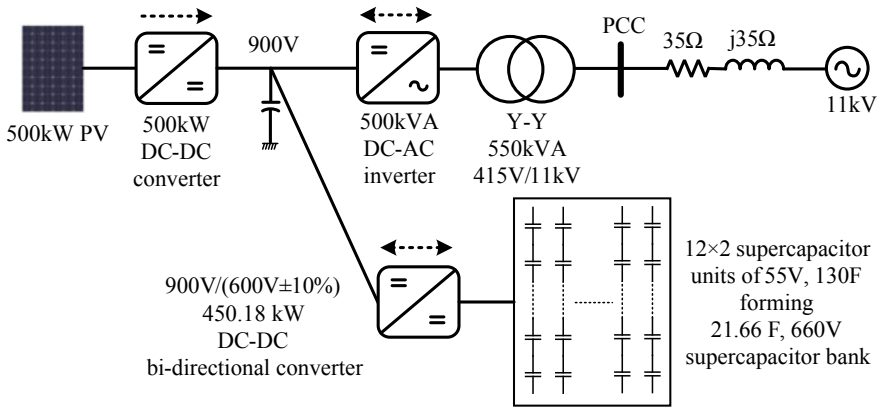


**Fig. 19.12** SPV plant with supercapacitor bank for voltage FRT operation. *Source* Authors

Since each supercapacitor unit can handle a current of 1900 A, their series combination can equally 1900 A which is greater than 837.47 A. Hence, as per the current requirement, no further parallel combinations are required. Therefore, the minimum capacitance of the supercapacitor bank required to perform one voltage FRT operation is thus given by

$$C_{sc} = \frac{E_{ess} \times 2}{V_{sc(max)}^2 - V_{sc(min)}^2} = \frac{1058.14 \times 1000 \times 2}{660^2 - 540^2} = 14.70 \text{ F} \quad (19.28)$$

However, series combination of 12 units of 55 V, 130 F gives an equivalent capacitance 10.83 F which is less than 14.70 F. Hence, one more string should be connected in parallel to achieve an equivalent capacitance of  $2 \times 10.83 = 21.66$  F. Hence, 24 units of 55 V, 130 F supercapacitor units should be connected to successfully support voltage FRT operation of the SPV plant.

**2(c)** The schematic diagram of the SPV plant retrofitted with the supercapacitor bank for support during voltage FRT operation is shown in Fig. 19.12.

**Design Example 2:** A 500 kW SPV plant as shown in Fig. 19.13a is connected to the distribution network at 11 kV and is exporting power at UPF under steady-state operating conditions. The grid code mandates the PV plant to ride through two consecutive symmetrical or asymmetrical voltage faults as per the voltage versus time curve depicted in Fig. 19.13b. Correspondingly, the PV plant is required to support the network voltages by exchanging suitable reactive current as given below.

$$I_{inv}^{(q)} = \begin{cases} 0 \text{ pu,} & \text{for } 85\% < \%V_{inv}^{(d)} < 115\% \\ 2.125 - \frac{\%V_{inv}^{(d)}}{40} \text{ pu,} & \text{for } 45\% < \%V_{inv}^{(d)} \leq 85\% \\ 1 \text{ pu,} & \text{for } \%V_{inv}^{(d)} \leq 45\% \end{cases} \quad (19.29)$$

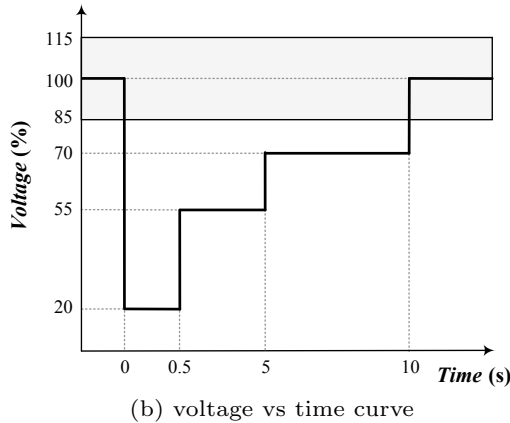
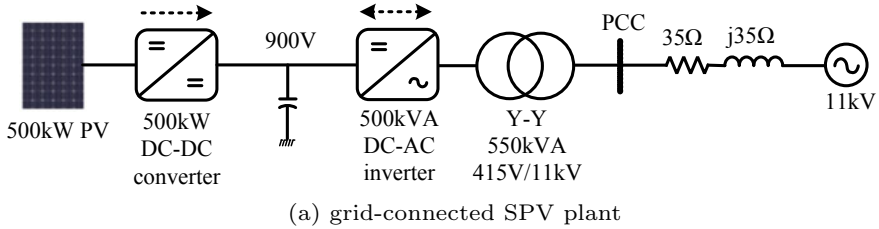


Fig. 19.13 Voltage FRT operation design example. Source Authors

The inverter in the SPV plant is capable of withstanding an over-current of 1.3 pu of its rated current for a duration of not more than 1 s. Neglect losses in the converters, transformer, and lines from PV to the PCC. The retrofitting of the solar SPV plant is to be performed to meet the grid code requirements.

Calculate the following assuming that the SPV plant is not operating in islanding condition under any circumstance.

1. Battery energy storage option at the DC bus

- (a) The peak power rating of the DC-DC bidirectional converter of 900 V/500 V ( $\pm 10\%$ ) for interfacing the energy storage device with the DC bus.
- (b) The total energy absorbed by the energy storage coupled to the DC bus for two consecutive voltage FRT operations.
- (c) The size of the battery bank for the voltage FRT operation. In addition, determine and depict the configuration of the battery bank required with battery units of 2 V, 800 Ah. Consider C/10 rate for safe charge/discharge operation of the battery bank.

**Solution:** The response of the PV plant needs to be analyzed under both steady-state operation and fault conditions. Since the transformer is lossless and is of Y-Y configuration, the FRT characteristics are equivalently applicable at the inverter

output terminals (i.e., 415 V) without any modifications. In addition, assume that the inverter controller response is almost instantaneous.

### Steady-state Operation

The rated power of the inverter is  $S_{\text{inv}} = 500$  kVA, the nominal DC bus voltage is  $V_{\text{dc}} = 900$  V, and the rated line-line terminal voltage at the inverter is  $V_{\text{inv}} = 415$  V. The RMS value and peak value of the phase voltage at the inverter terminals are  $V_{\text{inv(ph)}} = 240$  V and  $V_{\text{inv(ph-pk)}} = 339.40$  V, respectively. Hence, the rated RMS and peak values of the line current of the inverter are given by

$$I_{\text{inv}} = \frac{S_{\text{inv}}}{\sqrt{3}V_{\text{inv}}} = 695.54 \text{ A} \quad (19.30)$$

$$I_{\text{inv(pk)}} = \sqrt{2}I_{\text{inv}} = 983.64 \text{ A} \quad (19.31)$$

The inverter state variables, i.e., phase voltage and line current, are converted to  $dq0$  components for control purpose, i.e.,  $V_{\text{inv}}^{(d)}$ ,  $V_{\text{inv}}^{(q)}$ ,  $I_{\text{inv}}^{(d)}$ , and  $I_{\text{inv}}^{(q)}$ . Also, it is mentioned that the system is operating under UPF conditions during steady-state operation. Hence,

$$V_{\text{inv}}^{(d)} = 339.40 \text{ V}, V_{\text{inv}}^{(q)} = 0 \text{ V}, I_{\text{inv}}^{(d)} = 983.64 \text{ A} \quad \text{and} \quad I_{\text{inv}}^{(q)} = 0 \text{ A}.$$

The expressions for real and reactive powers through the inverter are therefore given by

$$P_{\text{inv}} = 1.5 \times V_{\text{inv}}^{(d)} \times I_{\text{inv}}^{(d)} = 500 \text{ kW} \quad (19.32)$$

$$Q_{\text{inv}} = 1.5 \times V_{\text{inv}}^{(d)} \times I_{\text{inv}}^{(q)} = 0 \text{ kVAR} \quad (19.33)$$

### Voltage FRT Operation

During FRT operation, as mandated by the grid code, the inverter moves away from UPF operation and injects certain reactive current as dictated by the grid code. As per Fig. 19.11c, the expression for reactive current during grid voltage sags is given in Eq. 19.29.

**1(a).** It is imperative that the worst-case power imbalance at the DC bus occurs when the SPV unit is generating its rated power and the inverter is performing voltage FRT operation with the lowest possible voltage on the grid, i.e., 20% in this case. Also, from the reactive current requirement plot, the reactive current that is to be injected by the inverter during 20% drop is 1 pu, i.e., 983.64 A. However, the inverter over-current capability of 1.3 pu will be utilized to inject certain amount of real current as per the following equation

$$I_{\text{inv}}^{(d)} = \sqrt{1.3^2 - (I_{\text{inv}}^{(q)})^2} = 0.831 \text{ pu} \quad (19.34)$$

Hence, the real power transferred to the grid during a grid voltage dip down to 20% is

$$P_{\text{inv}} = 1.5 \times V_{\text{inv}}^{(d)} \times I_{\text{inv}}^{(d)} = 1.5 \times 0.20 \times 339.40 \times 0.831 \times 983.64 = 83.23 \text{ kW} \quad (19.35)$$

Hence, the worst-case power imbalance at the DC bus is

$$P_{\text{imb}} = P_{\text{mpp}} - P_{\text{inv}} = 500 - 83.23 = 416.77 \text{ kW} \quad (19.36)$$

Therefore, the minimum peak power rating of the DC energy storage converter for a successful voltage FRT operation of the SPV plant is equal to the worst-case power imbalance at the DC bus, i.e.,  $P_{\text{imb}} = 416.77 \text{ kW}$ .

**1(b).** For  $\%V_{\text{inv}}^{(d)} = 20\%$ , the power imbalance is already calculated previously. This imbalance is to be absorbed by the energy storage for a maximum duration of 0.5 s as dictated by the grid code.

For  $\%V_{\text{inv}}^{(d)} = 55\%$ , the reactive current requirement can be computed from (19.29) and is equal to 0.75 pu. The inverter can operate at 1.3 pu current rating for a duration not exceeding 1 s. Hence, from 0.5 to 1 s,

$$I_{\text{inv}}^{(d)} = \sqrt{1.3^2 - (I_{\text{inv}}^{(q)})^2} = 1.0615 \text{ pu} \quad (19.37)$$

Hence, the real power transferred to the grid during this duration is

$$P_{\text{inv}} = 1.5 \times V_{\text{inv}}^{(d)} \times I_{\text{inv}}^{(d)} = 1.5 \times 0.55 \times 339.40 \times 1.0615 \times 983.64 = 292.36 \text{ kW} \quad (19.38)$$

Hence, the worst-case power imbalance at the DC bus is

$$P_{\text{imb}} = P_{\text{mpp}} - P_{\text{inv}} = 500 - 292.36 = 207.64 \text{ kW} \quad (19.39)$$

This power imbalance needs to be absorbed by the energy storage for a duration of  $1 - 0.5 = 0.5 \text{ s}$ .

The grid code mandates a voltage ride-through operation at 0.55 pu voltage until 5 s. However, beyond 1 s, the inverter current is limited to only 1 pu. Hence,

$$I_{\text{inv}}^{(d)} = \sqrt{1^2 - (I_{\text{inv}}^{(q)})^2} = 0.6614 \text{ pu} \quad (19.40)$$

Hence, the real power transferred to the grid during this duration is

$$P_{\text{inv}} = 1.5 \times V_{\text{inv}}^{(d)} \times I_{\text{inv}}^{(d)} = 1.5 \times 0.55 \times 339.40 \times 0.6614 \times 983.64 = 182.16 \text{ kW} \quad (19.41)$$

Hence, the worst-case power imbalance at the DC bus is

$$P_{\text{imb}} = P_{\text{mpp}} - P_{\text{inv}} = 500 - 182.16 = 317.84 \text{ kW} \quad (19.42)$$

This power imbalance should be absorbed by the energy storage for a duration of  $5 - 1 = 4 \text{ s}$ .

From 5 to 10 s, the  $\%V_{inv}^{(d)} = 70\%$ , for which the reactive current requirement is 0.375 pu. Hence,

$$I_{inv}^{(d)} = \sqrt{1^2 - (I_{inv}^{(q)})^2} = 0.927 \text{ pu} \quad (19.43)$$

Hence, the real power transferred to the grid during this duration is

$$P_{inv} = 1.5 \times V_{inv}^{(d)} \times I_{inv}^{(d)} = 1.5 \times 0.7 \times 339.40 \times 0.927 \times 983.64 = 324.95 \text{ kW} \quad (19.44)$$

Hence, the worst-case power imbalance at the DC bus is

$$P_{imb} = P_{mpp} - P_{inv} = 500 - 324.95 = 175.05 \text{ kW} \quad (19.45)$$

This power imbalance should be absorbed by the energy storage for a duration of  $10 - 5 = 5$  s.

Considering all possible cases calculated above, the worst-case energy that will be diverted to the energy storage device during two consecutive voltage FRT operation as dictated by the given voltage versus time and reactive current variation versus voltage curves considering the inverter over-current rating is given by

$$E_{ess} = 2 \times [(416.770.5) + (207.64 \times 0.5) + (317.84 \times 4) + (175.05 \times 5)] = 4917.64 \text{ kW s} \quad (19.46)$$

This energy should be absorbed by the energy storage unit with a maximum power of 416.77 kW.

**1(c).** The peak power rating of the DC-DC bidirectional converter is 416.77 kW, and the energy required during ride through is 4917.64 kW s. The battery terminal voltage does not vary much with respect to the state of charge, but the DC-DC bidirectional converter interfacing the energy storage should be applied with the given voltage limits of  $\pm 10\%$  so a voltage between the minimum voltage of  $500 \text{ V} - 50 \text{ V} = 450 \text{ V}$  and a maximum voltage of  $500 \text{ V} + 50 \text{ V} = 550 \text{ V}$ . Hence, the rated voltage, i.e., 500 V can be considered for the battery sizing. Hence, 250 battery units of 2 V, 800 Ah can be connected in series to achieve a rated voltage of 500 V. Therefore, the charging current required for the battery bank is given by

$$I_{bat(max)} = \frac{416.77 \times 1000}{500} = 833.54 \text{ A} \quad (19.47)$$

Considering a 2 V, 800 Ah lead–acid battery unit, the safe discharge or charging current limit is at C/10 rate, i.e.,  $800/10 = 80 \text{ A}$ . However, the peak current fed to the battery bank during the voltage FRT operation is 833.54 A. Hence, more parallel combinations of battery units are required to achieve a higher current rating, i.e., a parallel combination of 11 battery units that give a rated current of the bank 880 A is required. Hence, 250 units of 2 V, 800 Ah battery units are required in each string to obtain a terminal voltage of 500 V and 11 such strings should be connected in parallel

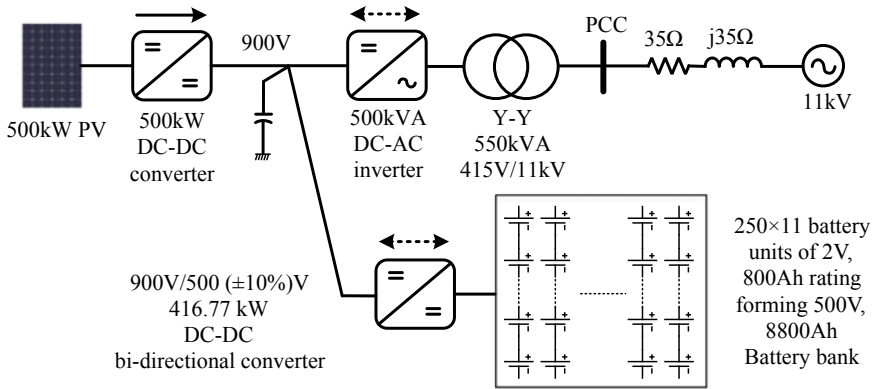


**Fig. 19.14** SPV plant with battery bank for voltage FRT operation. *Source* Authors

to achieve the required current rating for the DC-DC converter. Hence, a total of  $250 \times 11 = 2750$  battery units are required. With this configuration of battery bank, the energy available is  $E_{bat} = 2 \times 250 \times 800 \times 11 \text{ Wh} = 15,840 \text{ MW s}$  which is sufficiently higher than the requirement of  $4917.64 \text{ kW s}$ . The schematic diagram of the SPV plant retrofitted with the battery bank for support during voltage FRT operation is shown in Fig. 19.14.

These examples present a generic methodology for designing the additional hardware required in support of the voltage FRT operation of SPV units for a given set of voltage versus time characteristics, reactive current variation versus voltage characteristics, and inverter over-current rating.

### 19.5 Simulation Study

The system depicted in Fig. 19.10 is simulated for two scenarios, i.e., low-voltage FRT operation and high-voltage FRT operation adhering to the Indian Grid Code [17]. As per the Indian Grid Code for voltage FRT operation,

- *The generating station connected to the grid shall remain connected to the grid when voltage at the interconnection point on any or all phases lies within the given voltage FRT curve.*
- *Provided that during the voltage dip, the supply of reactive power has first priority, while the supply of real power has the second priority and the real power preferably be maintained during voltage drops, provided, a reduction in real power within the plant’s design specifications is acceptable and real power be restored to at least 90% of the pre-fault level within 1 s of restoration of voltage.*

There is no mention of the reactive current variation versus voltage curve in the Indian Grid Code. A study determining the appropriate reactive current exchange



**Table 19.5** Base values for per unit conversion

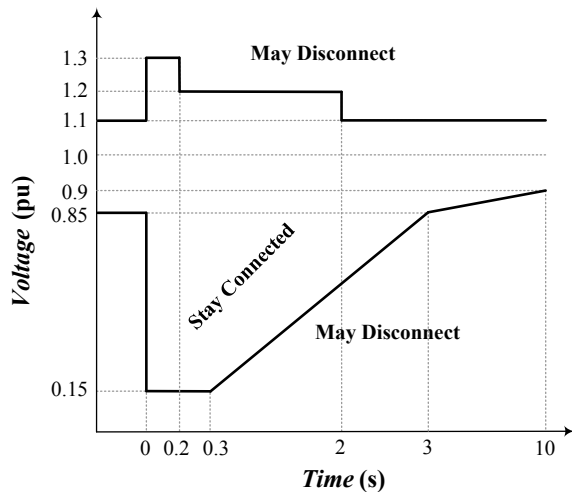
Parameter	Base value
AC/DC power	5 kW
AC voltage HV side (L-L)	415 V
AC voltage LV side (L-L)	150 V
DC voltage	380 V
Frequency	50Hz

Source Authors

during voltage FRT operation is not in the scope of this chapter. Accordingly, for simulation study, the reactive current contribution from the SPV unit is kept zero. The crowbar method is used to regulate the DC bus voltage during voltage FRT operation. The specifications of the system under study are given in Table 19.4. The base values for converting the system variables into pu values are given in Table 19.5. The simulation results therefore depicted in pu values for easy understanding. The simulation study is carried out in MATLAB/Simulink for a duration of 10 s. The test conditions within this 10 s duration are listed below

- The SPV generation is programmed to its rated value, i.e., 5 kW or 1 pu throughout the simulation.
- At 2.5 s, a low-voltage fault down to 0.15 pu for a duration of 0.3 s is simulated.
- At 5 s, a high-voltage fault of 1.2 pu for a duration of 0.2 s is simulated.
- At 7.5 s, another high-voltage fault with a higher fault magnitude, i.e., 1.3 pu, is simulated for a duration of 0.2 s (Fig. 19.15).

**Fig. 19.15** Voltage versus time curve for Indian grid.  
Source Authors



### 19.5.1 Low-Voltage FRT Operation

The response of the system is shown in Fig. 19.16a. The DC bus voltage and PCC voltage represented in pu values are presented in Fig. 19.16b. Between 0 and 2 s, the SPV generation reaches 1 pu from 0 pu, and accordingly, the DC bus and PCC voltage witnessed a rise in voltage. However, the DC bus voltage variation is within the permissible limit of  $\pm 5\%$  due to the prompt action from its voltage controller. At 2.5 s, due to the low voltage down to 0.15 pu at the PCC, the inverter controller detects the occurrence of voltage FRT event as shown in Fig. 19.16b. By virtue of the low-voltage operation, the inverter controller pushes the inverter real current reference ( $i_{pcc,pu}^{(d)*}$ ) to a higher value but gets limited to 1.2 pu as shown in Fig. 19.16c. Since the reactive current component is zero, the entire inverter capacity is used to push the real

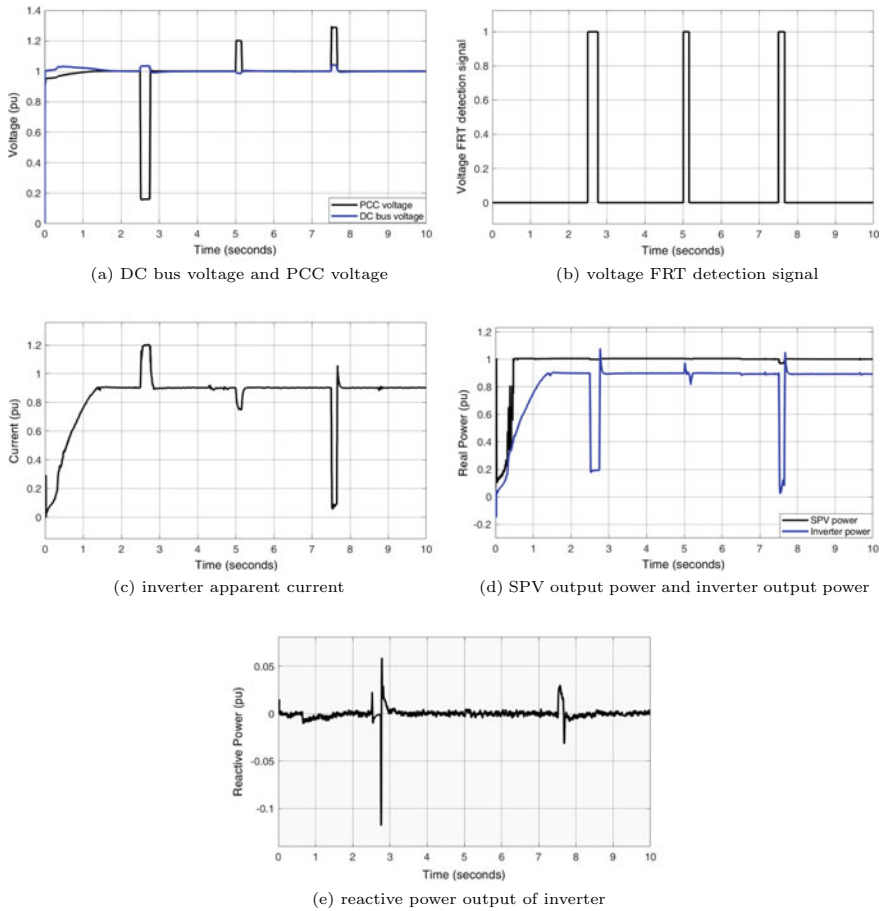


Fig. 19.16 Response of SPV unit for voltage FRT events. Source Authors

power even during the low-voltage conditions. Accordingly, the real power that gets transferred to the grid is 0.2 pu, i.e., approximately 1 kW as shown in Fig. 19.16d. The same can be obtained through (19.8) as discussed in the numerical. However, the SPV power output is maintained at 1 pu by virtue of the MPPT control which thus leads to a rise in the DC bus voltage as shown in Fig. 19.16a. The rise in the DC bus voltage can be arrested by the prompt action by any method discussed previously for voltage FRT support; otherwise, the SPV unit can trip due to the voltage violation at the DC bus. In this simulation study, crowbar method is used to arrest the rise in DC bus voltage. The value of crowbar calculated from (19.10) is used in this simulation study and is given in Table. 19.5. The reactive power contribution from the SPV unit is depicted in Fig. 19.16c. Except for transients during the transition in PCC voltage, the steady-state contribution of reactive power from the SPV inverter is zero. It is thus evident that the voltage FRT control of the inverter along with the crowbar circuit method is effective in facilitating a reliable voltage FRT operation of the SPV unit.

### ***19.5.2 High-Voltage FRT Operation***

A high voltage of 1.2 pu is applied at 5 s due to which the inverter current reference tends to reduce to 0.75 pu in order to keep the overall power transferred from the SPV unit equal to the available maximum power. This effect therefore induces negligible variations in the DC bus voltage and the inverter output power as depicted in Fig. 19.16a and d, respectively. However, at 7.5 s, when the magnitude of PCC voltage is increased to 1.3 pu, the inverter is unable to push power to grid due to the limitation in the modulation index which led to the power imbalance at the DC bus resulting in a rise in DC bus voltage as shown in Fig. 19.16a. As discussed previously, the DC bus voltage is limited to 1.04 pu (well within  $\pm 5\%$  variation) in this scenario too. However, after the high-voltage event, the system quickly returned to the steady-state operation. Thus, a SPV unit can be retrofitted with appropriate hardware device and control to facilitate a reliable voltage FRT operation.

## **19.6 Conclusions**

This chapter presented an overview of different aspects of the voltage FRT operation of SPV units. Apart from a review of the existing grid codes, important aspects pertaining to the voltage FRT operation in the IEEE 1547:2018 standard are discussed. The new features introduced in the IEEE 1547:2018 standard tend to increase the benefits from voltage FRT operation and thus should be quickly adapted by the generating units. With a brief review of good practices for achieving reliable voltage FRT operation of SPV units, it can be concluded that option of energy storage device has high initial cost but can help in many other ancillary services to the system. Numerical design examples are presented to discuss the methodology for retrofitting

of an existing SPV unit with the crowbar circuit or energy storage devices at the DC bus. These design examples considering different scenarios can act as reference for designing the hardware solution for achieving/enhancing the voltage FRT operation of the SPV units considering different scenarios. A simulation case study is also presented to illustrate the impact of fault on system performance and mitigation through FRT operation in a grid-connected SPV unit.

The voltage FRT techniques discussed here can be further extended in future regarding type of storage device and appropriate mix of multiple storage devices for more reliable operation and multifold benefits. Further, the control and sizing of energy storage for various other ancillary services like frequency FRT operation and black start can be investigated for effective use of the energy storage.

## References

1. Palchak D et al (2017) Greening the grid: pathways to integrate 175 gigawatts of renewable energy into India's electric grid, vol 1, national study. Tech. rep., National Renewable Energy Laboratory
2. Michael P, Joe P (2018) Impact of IEEE 1547 standard on smart inverters. Tech. rep., IEEE PES Industry Technical Support Task Force
3. Boemer JC (2016) On stability of sustainable power system: network fault response of transmission system with very high penetration of distributed generation. PhD thesis, Delft University of Technology, Delft, The Netherlands [online; Accessed 29 May 2019]
4. IEEE standard for interconnection and interoperability of distributed energy resources with associated electric power systems interfaces (IEEE 1547: 2018 standards) (2018) IEEE Standards Association
5. Jerin RA, Kaliannan P, Subramaniam U (2018) Testing of low-voltage ride through capability compliance of wind turbines—a review. *Int J Ambient Energy* 39(8):891–897
6. Popavath L, Kaliannan P (2018) Photovoltaic-STATCOM with low voltage ride through strategy and power quality enhancement in a grid integrated wind-PV system. *Electronics* 7:51
7. Naidu BR, Bajpai P, Chakraborty C (2019) Voltage fault ride-through operation of solar PV units: a review and way forward. In: 2019 8th international conference on power systems (ICPS), pp 1–6
8. Shuai Z, Shen C, Yin X, Liu X, Shen ZJ (2018) Fault analysis of inverter-interfaced distributed generators with different control schemes. *IEEE Trans Power Deliv* 33:1223–1235
9. Atri PK, Modi PS, Gujar NS (2020) Comparison of different MPPT control strategies for solar charge controller. In: 2020 international conference on power electronics IoT applications in renewable energy and its control (PARC), pp 65–69
10. Cornelis AP (2011) Fault response of inverter-based distributed generation. PhD thesis, Imperial College London, London, UK [online; Accessed 25 June 2019]
11. Sandali A, Cheriti A (2017) New adapted forms of P-V optimal slope MPPT for a better grid connected PV system integration. In: IEEE international conference on industrial technology, Toronto, ON, pp 446–451. <https://doi.org/10.1109/ICIT.2017.7913272>
12. Sandali A et al (2015) LVRT control strategy for PV grid connected system based on P-V optimal slope MPPT technique. In: IEEE 3rd international renewable and sustainable energy conference, Marrakech, pp 1–6. <https://doi.org/10.1109/IRSEC.2015.7455087>
13. Geng Y, Yang K, Lai Z, Zheng P, Liu H, Deng R (2019) A novel low voltage ride through control method for current source grid-connected photovoltaic inverters. *IEEE Access* 7:51735–51748
14. Wang M, Xu W, Hongjie J, Yu X (2012) A new control system to strengthen the LVRT capacity of DFIG based on both crowbar and DC chopper circuits. In: IEEE PES Innovative Smart Grid Technologies, pp 1–6

15. Yank Y et al (2015) Wide-scale adoption of photovoltaic energy: grid code modifications are explored in the distribution grid. *IEEE Ind Appl Mag* 21(5):21–31
16. Worku MY, Abido MA (2015) Grid-connected PV array with supercapacitor energy storage system for fault ride through. In: *IEEE international conference on industrial technology (ICIT)*, pp 2901–2906
17. Technical standards for connectivity to the grid (amendment) regulations (2019) Central Electricity Authority